



HAL
open science

Stabilized finite element method for heat transfer and turbulent flows inside industrial furnaces

Elie Hachem

► **To cite this version:**

Elie Hachem. Stabilized finite element method for heat transfer and turbulent flows inside industrial furnaces. Mechanics [physics.med-ph]. École Nationale Supérieure des Mines de Paris, 2009. English. NNT : 2009ENMP1645 . tel-00443532

HAL Id: tel-00443532

<https://pastel.hal.science/tel-00443532>

Submitted on 30 Dec 2009

HAL is a multi-disciplinary open access archive for the deposit and dissemination of scientific research documents, whether they are published or not. The documents may come from teaching and research institutions in France or abroad, or from public or private research centers.

L'archive ouverte pluridisciplinaire **HAL**, est destinée au dépôt et à la diffusion de documents scientifiques de niveau recherche, publiés ou non, émanant des établissements d'enseignement et de recherche français ou étrangers, des laboratoires publics ou privés.

...to Alexa, Ejeý and my parents

Acknowledgments

First and foremost I want to thank my advisor Thierry Coupez. It has been an honor to be his Ph.D. student. I appreciate all his contributions of time, challenging ideas, critical remarks, constant guidance and support to make my Ph.D. experience productive and stimulating. My special thanks to you for providing me all the theoretical insight for many problems and especially for allowing me knocking your door without appointments. I would like also to convey my deepest gratitude to my second advisor Elisabeth Massoni for her support, constructive suggestions and kind help that paved a joyful and enthusiastic way in accomplishing this thesis.

I am highly indebted and grateful to my friend and co-worker Thibaud, for his generous help, encouragements and his particular peeping in my manuscripts that helped me enormously in reaching my goals.

The members of CIM research team, the *Cimliber*, have contributed immensely to my personal and professional time at CEMEF. The group has been a source of friendships as well as good advice and collaboration: Hugues, Rudy, Marc, Luisa, Patrice and Julien. My special thanks go also for many friends and contributors especially Benjamin, Guillaume and Greg.

I am grateful to the secretaries and librarians for helping and assisting me during the last three years in particularly Marie-Francoise, Sylvie, Genevieve, Florence and Nadine. Brigitte and Sylvie deserve special mention.

My time at CEMEF was made enjoyable in large part due to the many friends and groups that became a part of my life. I am grateful for time spent with my colleagues in DE16: Marc, David and Olivier. I would like to thank also all the staff at CEMEF, Group EII and special mention to the directors: Jean-Loup Chenot and Yvan Chastel.

I gratefully acknowledge the funding sources from ADEME and SCC, and all the industrial partners involved in the THOST project. My earnest gratitude goes for the architect of this project, the Davids, for introducing me to the field of industrial computations.

I am very grateful to Patrick Coels for his advices, motivation, inspiration and immense knowledge in life and managements that, taken together, make him my best mentor.

Last but not least, I would like to thank my family: my parents, brothers and nieces for their support. To Alexa, the little one and my other nieces I dedicate my thesis.

Abstract

The development of efficient methods to understand and simulate conjugate heat transfer for multi-components systems appears in numerous engineering applications and still a need for industrials, especially in the case of the heat treatment of high-alloy steel by a continuously heating process inside industrial furnaces. The thermal history of the load and the temperature distribution in the furnace are critical for the final microstructure and the mechanical properties of the treated workpieces and can directly determined their final quality in terms of hardness, toughness and resistance. The main objectives of this thesis is then to understand and better model the heat treatment process at the same time in the furnace chamber and within the workpieces under specified furnace geometry, thermal schedule, parts loading design, initial operation conditions, and performance requirements. The Computational Fluid Dynamics (CFD) simulation provides a useful tool to predict the temperature evolution and such processes. In the first part of this work, various stabilized finite element methods required for computing the conjugate heat transfer and the incompressible flows are proposed and analyzed. Two turbulence models, the k-epsilon and the Large Eddy Simulations (LES) models were introduced and used to simulate and take into account the complex turbulent flows inside the furnace chamber. The effect of thermal radiation was appropriately accounted for by means of a volumetric model known as the P1-model. In the latter part of this work, a multidomain approach referred as the immersed volume method (IVM) is introduced and applied to treat the fluid-solid interactions. It is based on the use of an adaptive anisotropic local grid refinement by means of the level-set function to well capture the sharp discontinuities of the fluid-solid interface. The proposed method showed that it is well suited to treat simultaneously the three modes, convective, conductive and radiative heat transfer that may interfere in both the fluid part and the solid part using anisotropic finite element meshes.

Résumé

La connaissance du comportement thermique des fours et des pièces est un problème difficile et cependant essentiel dans les thématiques de recherche industrielles actuelles. L'industrie cherche à se doter de moyens numériques de plus en plus efficaces tout en réduisant sans cesse le temps de calcul afin de modéliser des pièces et des assemblages de plus en plus réalistes. Les cinétiques de chauffe ainsi que la distribution de la température dans l'enceinte et dans les pièces traitées doivent également être maîtrisées, afin d'améliorer la qualité des produits chauffés en terme de résistance et dureté.

Le travail présenté dans cette thèse porte donc sur le développement de méthodes de résolution numérique pour la simulation du transfert thermique. Ces méthodes permettent le calcul couplé de la température des pièces avec l'environnement du four afin d'optimiser la géométrie de ces pièces, leur position dans le four mais également les conditions initiales de chauffe. Le calcul de dynamique des fluides (CFD) peut être considéré comme un puissant outil technique de prédiction de l'écoulement des fluides et du transfert thermique dans des cas industriels réalistes.

La première partie de la thèse porte sur l'étude de schémas numériques avancés relatifs aux méthodes éléments finis stabilisés. Ces méthodes de calculs efficaces ont été utilisées pour simuler des écoulements instationnaires et des transferts thermiques conjugués. Par la suite, deux modèles de turbulence (modèle k-epsilon et modèle Large Eddy Simulation) sont introduits et utilisés pour prendre en compte les écoulements complexes et turbulents dans l'enceinte du four. Le transfert radiatif est assuré par la résolution du modèle P1 tout en calculant un terme source volumique qui sera intégré dans l'équation de la chaleur.

La deuxième partie de cette thèse se consacre à la mise en place d'une méthodologie de discrétisation robuste qui permet aux utilisateurs de générer de façon entièrement automatique un seul maillage. Ce maillage contient à la fois des domaines axés sur la résolution d'un problème fluide (air, eau, ...) mais également solides spécifiques aux structures, et ce quel que soit le niveau de détail et donc de complexité du cas étudié. Cette approche, connue sous le nom d' « immersion de volume », garantit un maillage anisotrope précis aux interfaces fluide-solide afin de capturer plus précisément les gradients thermiques et la forte discontinuité des propriétés physiques. Cette méthode offre donc une grande flexibilité dans la mise en données du problème mixte fluide-structure et aussi dans la prise en compte de plusieurs géométries (four, pièces, supports) et elle est également bien adaptée aux solveurs thermomécaniques développés.

Contents

Chapter 1

General introduction	11
1.1 Introduction to heat treatment furnaces	12
1.2 Role of computational modeling in heat furnace design	13
1.3 Brief literature on heat transfer modeling	15
1.4 Objectives of the thesis	16
1.5 Work environment	20
1.6 Layout of the thesis	20
References	21

Chapter 2

Stabilized finite element method of convection-diffusion-reaction equations	23
2.1 The need of stabilization methods	24
2.2 Standard Galerkin solution	25
2.2.1 Problem setting	25
2.2.2 Space discretization	26
2.2.3 Temporal discretization	27
2.2.4 Introduction to stabilized method	27
2.3 Stabilized finite element methods	31
2.3.1 Streamline Upwind Petrov-Galerkin FEM	31
2.3.2 Shock Capturing Petrov-Galerkin	36
2.3.3 Residual Free Bubbles	40
2.4 Application to heat transfer equation	44
2.5 Thermal shock treatment for unsteady diffusion problems	47
2.6 Numerical tests and validation	48
2.6.1 Transient CDR problems	48
2.6.2 Transient pure convection	50
2.6.3 Transient heat transfer	55
2.7 Conclusion	58
References	59

Chapter 3

Stabilised finite element methods for incompressible flows with high Reynolds number	85
3.1 Basic formulation of the equation	86
3.1.1 Initial and boundary conditions	87
3.1.2 Classical mixed formulation	88
3.2 Stable mixed variational formulation	90
3.3 Stabilized finite element method	91
3.3.1 Multiscale approach	92
3.3.2 Matrix formulation of the problem	99
3.3.3 Stabilization parameter	100
3.4 Numerical examples and validation	102
3.4.1 A convergence test	103
3.4.2 Driven flow cavity problem (2-D)	106
3.4.3 Flow over a circular cylinder	115
3.4.4 The flow over a backward-facing step	118
3.5 Conclusion	124
References	125

Chapter 4

Implementation of turbulence models in incompressible flow solvers based on a finite element discretization	131
4.1 Introduction to turbulence	132
4.2 Turbulence simulation	133
4.3 The k-epsilon turbulence model	135
4.3.1 The standard formulation	136
4.3.2 The boundary conditions	138
4.3.3 Enhanced wall treatment	144
4.3.4 Low Reynolds formulation	145
4.3.5 Finite element solution	148
4.3.6 Positivity of the solution	150
4.4 Large Eddy Simulation	151
4.4.1 Filtering equations	152
4.4.2 Subgrid-scale modeling	153
4.5 Benchmarks for the k-epsilon model	156
4.5.1 Validation: grid turbulence	156
4.5.2 Comte-Bellot	157
4.5.3 Flow over a backward-facing step	162
4.6 Flow behind an obstacle using LES model	169
4.7 Conclusion	172
References	173

Chapter 5

Immersed volume method for solving conjugate heat transfer	179
5.1 Introduction.....	180
5.2 The immersed volume method.....	183
5.2.1 The signed distance function	183
5.2.2 The anisotropic mesh adaptation	185
5.2.3 Mixing laws	190
5.3 Radiative heat transfer	194
5.3.1 Introduction.....	195
5.3.2 The radiative transport equation (RTE).....	196
5.3.3 Diffusive grey medium assumption.....	197
5.3.4 P1-model.....	199
5.3.5 Rosseland model.....	200
5.3.6 Conclusion and discussion.....	200
5.3.7 Combined natural convection and radiation in a square cavity	201
5.4 Applications	206
5.4.1 Forced and natural convection of conducting solids.....	206
5.4.2 Results and discussion	211
5.5 Conclusion	212
References.....	213

Chapitre 6

Immersed volume method for solving conjugate heat transfer and turbulent flows	219
6.1 Immersed volume method for solving natural convection, conduction and radiation of a hat-shaped disk inside an enclosure.....	221
6.2 Stable mixed-finite element method for incompressible flows with high Reynolds number	245
6.3 Finite element solution to handle complex heat and fluid flows in industrial furnaces using the immersed volume method	275
6.4 Numerical simulation in a full-scale industrial furnace.....	303

Chapter 7

Conclusions and Perspectives	319
---	-----

Chapter 1

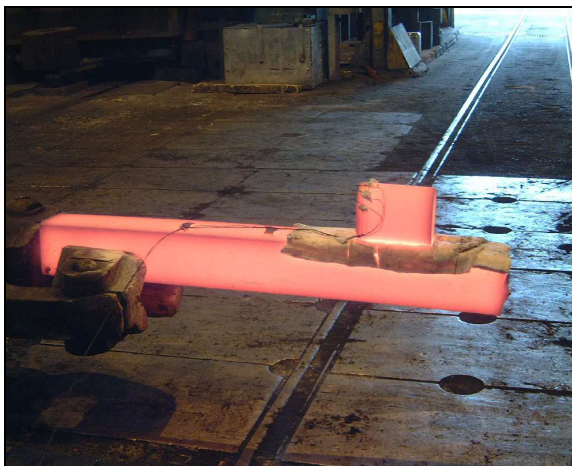
General introduction

Chapter 1	11
General introduction.....	11
1.1 Introduction to heat treatment furnaces.....	12
1.2 Role of computational modeling in heat furnace design.....	13
1.3 Brief literature on heat transfer modeling	15
1.4 Objectives of the thesis	16
1.5 Work environment.....	20
1.6 Layout of the thesis	20
References	21

1.1 Introduction to heat treatment furnaces

Heat transfer is involved in several physical processes, and in actual fact it can be the limiting factor for many processes. The modeling of heat transfer effects inside industrial furnaces has started drawing attention of many more investigators as a result of the demand for energy conservation through efficiency improvement and for reduction of pollutant emissions. It also has become ever more important in the design of the products itself in many areas such as the electronics, automotive, machinery and equipment manufacturing industries. Research in both experimental and numerical areas and through mathematical models has proven to be effective in accelerating the understanding of complex problems as well as helping decrease the development costs for new processes. In the past, the optimizations and savings in large productions was made by only large companies that could support and afford the cost of sophisticated heat transfer modeling tools, specialized engineers and computer software. Nowadays, modeling has become an essential element of research and development for many industrial; and realistic models of complex three dimensional structure of the furnace can be feasible on a personal computer.

A heat treatment furnace is a manufacturing process to control the mechanical and physical properties of metallic components. It involves furnace control, turbulent flows, conduction within the load, convection and thermal radiation simultaneously. The thermal history of each part and the temperature distribution in the whole load are critical for the final microstructure and the mechanical properties of workpieces and can directly determined the final quality of parts in terms of hardness, toughness and resistance. To achieve higher treatment efficiency, the major influencing factors such as the design of the furnace, the location of the workpieces, thermal schedule and position of the burners should be understood thoroughly.



Thermocouples on a heated pieces



Large hollow metal ingot outside the furnace

Figure 1. Heat treatment study on industrial parts

The damage to the global environment and the prospective depletion of essential resources caused by growing human activity constitute a dual challenge that calls for coordinated measures by multilateral organizations such as ADEME, French Environment and Energy Management Agency. This is an industrial and commercial public agency, under the joint supervision of French Ministries for Ecology, Sustainable Development and Spatial Planning (MEDAD) and for Higher Education and Research with a mission to encourage, to supervise, to coordinate, to facilitate and to undertake operations aiming in protecting the environment and managing energy.

Since simulation of the heating up process of workpieces in heat treatment furnaces is of great importance for the prediction and control of the ultimate microstructure of the workpieces but specially the reduction of both energy consumption and pollutant emissions, this agency supports our research program and encourages all players and partners in this project to save energy, particularly sectors that consume high quantities of energy on daily basis.



Figure 2. Continuous heating inside a furnace.

1.2 Role of computational modeling in heat furnace design

As mentioned previously, the major factor to be considered in the working of a furnace is the heat transfer by all the modes, which occur simultaneously. To either study a new furnace or to optimize the heating process in existing ones, the heat transfer in the furnace has to be modeled in the same way of a real situation as closely as possible. Given the geometry of the furnace, different boundary conditions along the furnace length, gas composition and properties and other complexities, an analytical solution is not feasible and computational modeling has to be resorted to. Over the last 20 years, the CFD (Computational Fluid Dynamics) has gained its reputation of being an efficient tool in identifying and solving such problems.

Modeling the heating process involves solving coupled heat transfer equations. By solving them computationally, the method should be capable of doing so in an accurate way and within a reasonable time. In the heat transfer of heat treatment furnace, there are conduction, convection, radiation, turbulent flow and furnace control. Conduction mainly occurs in all solids materials. Turbulent convection exists between the atmosphere and solid

materials exposed to it, and furnace walls to the ambient air. Radiation exists between solid materials exposed to each other and to all walls. The tools used in this thesis are the Finite Element Method (FEM) and Computational Fluid Dynamics (CFD). This method is shown as an attractive way to solve the turbulent flow and heat transfer in the furnace chamber and it can be applied for a variety of furnace geometry and boundary conditions. The entire heat transfer process is a transient one, and iterations are necessary. The main process is detailed in the following flowchart:

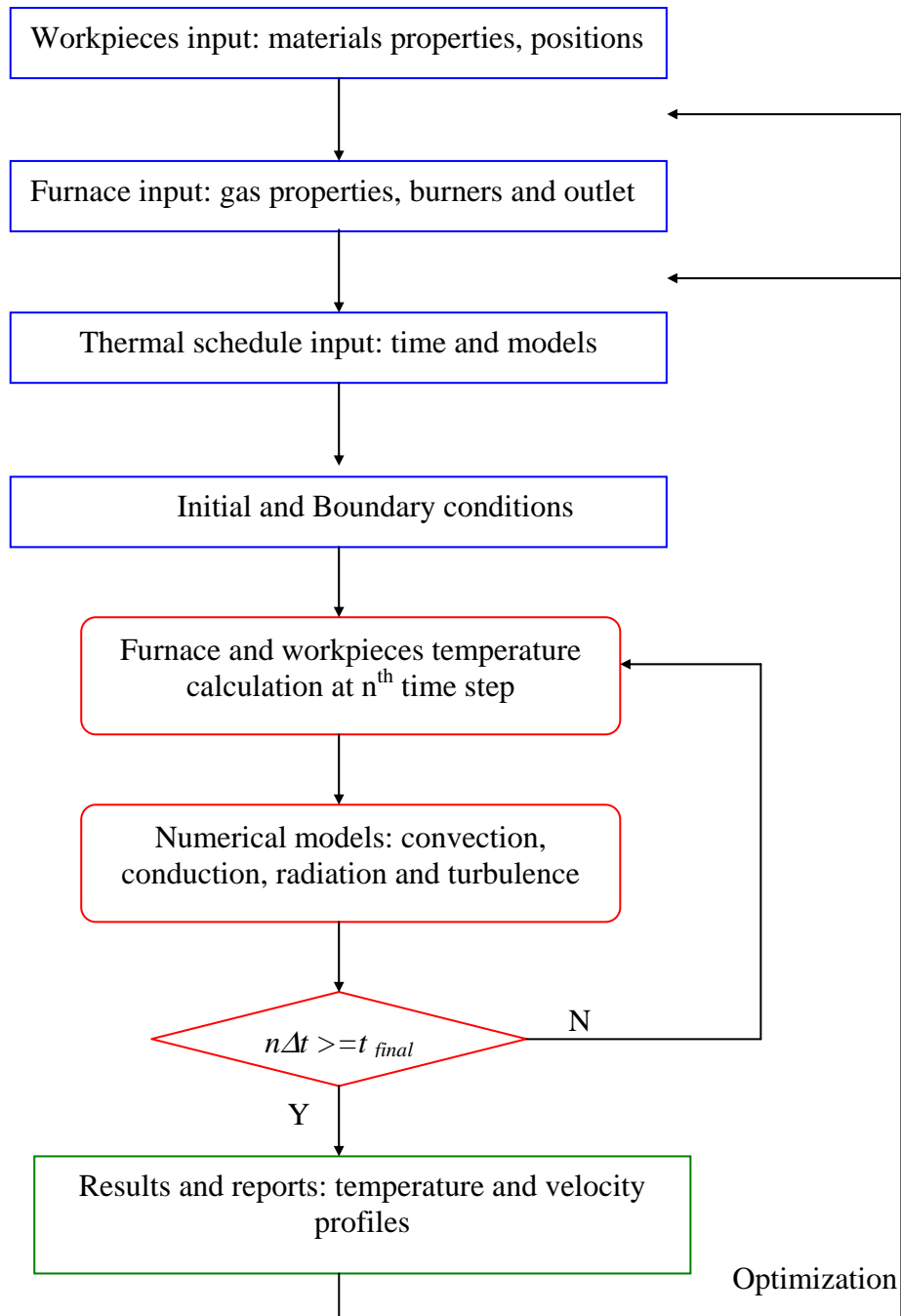


Figure 3. General flowchart for a heat treatment process

1.3 Brief literature on heat transfer modeling

In order to give an idea of the evolution of the modelling process for transient heating in heat furnaces, a brief review will be presented here. Different methods and models have been used and each model can be characterized upon the assumptions made. Numerous practical methods and models for the prediction of thermal heating process have been developed and applied to various different furnace geometries. For a complete description about computational modelling of heat transfer in reheat furnaces, the readers may refer to Harish J. in [1]. Patankar and Spalding (1973) [2] modelled combustions chambers and furnaces using the composite-flux radiation model. The steady state heat transfer was modelled by Krivandin and Markov (1980) [3] using some empirical relations in both the pusher-type and walking beam furnaces. Only radiation was considered and convection was neglected.

Minaev et. al. (1983) in [4] showed by studying walking beam furnaces that the convective heat transfer coefficient changes very little along the furnace. In [5], Tucker and Lorton (1984) investigated the effects of non-gray combustion products using the zone method proposed by Hottel and Cohen (1958) [6]. This method was used for absorbing, emitting and non-scattering homogeneous gas to predict radiative heat transfer in a reheating furnace. The zonal energy balance method was used to compute the gas temperature. However, it was stated that the coupling of the temperature distribution in the load and refractories with heat transfer from the combustion gases was not completely accurate.

In the work of Gerasimov et. al. (1984) [7], passive experiments were conducted as an addition to a statistical mathematical model, monitoring the dimensions of the load, speed of movement and thermocouple readings. They found out that by considering only a uniform continuous entry of workpieces in to the furnace and by assuming that the temperature of the furnace atmosphere was constant in a zone, good results can be obtained.

Kohlgrüber (1985) in [8] developed a simplified model capable of determining detailed temperatures profiles in the load for a continuous reheating furnace. This model consists in computing the gas temperature as a function of the distance though the furnace. The mean-beam length technique was used to compute the radiation effects using the gray model assumption for gases.



Figure 4. Automotive, machinery and equipment manufacturing industries

Li et al (1988) [9] developed a mathematical model for predicting steady state heat transfer. The radiation effects were computed using the zone method while transient 2D conduction equation was solved to compute the temperature profiles in the slab. They pointed out that the computing cost of the zone-method is too expensive and should be replaced.

In [10], Ramamurthy et al. (1991) developed a model of an indirectly fired continuous furnace capable of predicting the fuel consumption. The radiation heat transfer was calculated using the radiosity method assuming that the gases are a nonparticipating medium. A 1D model was used for the conduction in the solid.

A mathematical system model for modelling direct fired continuous reheat furnaces was developed in [11] by Chapman et al (1991). The convective heat-transfer rate to the load and refractory surfaces was calculated using existing correlations from the literature. The zone method was applied for computing the radiation heat exchange between the load, the combustion gases, and the refractory. A parametric investigation was also conducted to study the effects of the load and refractory emissivities and the height of the combustion space on the thermal performance of the continuous reheating furnace.

Barr (1995) [12], developed an interesting simplified approach for on-line temperature control of a pusher type furnace. The temperature was computed in the longitudinal section of each bloom inside a long-furnace type. An implicit finite-difference method was used to solve the convection heat transfer and a zonal method was applied to calculate the radiation effects.

Marino (2000) developed in [13] a simplified on-line model for controlling a rotating reheat furnace. The radiation effects between individual load segments and between the burners and the load as well as the convection were neglected.

Altschuler et. al. (2000) [14] developed both offline and online models of the pusher-type and walking beam furnaces. The problem was divided into the load problem and the radiation problem for the purpose of analysis. The zonal method was used to calculate the radiation heat transfer and a finite volume approach was used to calculate the conduction heat transfer in the load.

Harish and Dutta (2005) [15] developed a computational model to predict the heat transfer in a direct-fired pusher type reheat furnace. The finite volume method was used to compute the gas radiative heat transfer.

Recently, Man Y. Kim (2007) [16] developed a mathematical model to predict the radiative heat flux impinging on the slab surface and temperature distribution inside the slab. The furnace is modelled as radiating medium with spatially varying temperature and constant absorption coefficient.

1.4 Objectives of the thesis

As explained previously, heat treatment represents a critical step within the steelmaking process. It can be defined as a combination of heating and cooling operations applied to a metal alloy in solid state which controls its mechanical properties, therefore contributes to the product quality in terms of hardness, resistance and toughness. Therefore, the objective of the proposed project is to develop a computational methodology able to predict the furnace atmosphere as well as the transient heat transfer to the load in a continuous heat treatment process.

Due to the complexities of the physics that may occur for such applications, many mathematical models have been proposed over the past years. Of course this complexity has decreased with the available computing power but most of the time, the general idea of these models was to solve only for heat conduction within the load and employ different assumption and simplification about the surrounding gas temperature within the furnace using different heat transfer coefficients derived from known furnaces or previous experimental

works [17-18-19]. Additionally, in recent years, different environmental constraints pushed the industrials to change their previous regulations. Consequently, many experimental tests must be made to deduce such transfer coefficients that ensure both the convective and radiation effects on and from the treated solid. However, when dealing with a large diversity of shapes, dimensions and physical properties of these metals to heat or to quench, such operations can become rapidly very costly and time consuming.

The development of efficient methods to understand and simulate conjugate heat transfer for multi-components systems (fluid-solid) is then highly demanded. In recent years, there has been increasing interest in studying numerically a variety of engineering applications that involve such coupling (fluids-solids) [20-21-22]. Typically, the general idea of these techniques consists in dividing the global domain and solving on each subdomain the corresponding equation independently. The global solution can then be constructed by suitably constructing local solutions from individually modeled subdomains. However, during the assembly, the coordination between the meshes can become complicated or even sometimes not feasible.

Other alternative approaches have been applied for multi-phase flows problems and are available in the literature, such as the ghost fluid method introduced by Fedkiw et al. (1999) in [23], the immersed boundary method [24], the domain decomposition [25], the X-FEM [26]. They introduced and improved enrichment functions for material interfaces and voids by means of the level set representations of surfaces.

Nevertheless, in general when using all these techniques, one still needs to know the value of the heat transfer coefficients between the two domains which ensures, as a Neumann/Dirichlet boundary conditions, the heat exchange at the air/solid interface.

The main objective of this work aims to overcome this drawback and to present a multidomain approach to solve the conjugate heat transfer for which the three modes, convective, conductive and radiative heat transfer interfere simultaneously and in both the fluid part and the solid part. The proposed numerical method for modeling such multimaterial flows (fluid/solid) will be referred as the immersed volume method (IVM). It allows an improved, simple and accurate resolution; in particular at the interface between the fluid and solid. A full description and details about this method will be given. To complete, the three-dimensional finite-element (FEM) methods needed for solving the transient heat transfer and turbulent flows inside the furnaces must be capable of taking into account also the proposed thermal coupling.

Therefore, the first part of the thesis consists in developing different numerical methods for modeling the heat transfer and turbulent flow. At the burner's level and inside the domain, it is well known that for convection-dominated problems, spurious oscillations may appear in the standard finite element resolution of the advection-diffusion equations. In order to overcome this numerical difficulty, different stabilized finite element methods will be presented, such as SUPG (Streamline Upwind Petrov-Galerkin) and SCPG (Shock Capturing Petrov-Galerkin). At ingot's level, where diffusion is the sole mechanism for heat mass transfer, there are still some conditions for which the Galerkin method fails to solve the transient conduction problem. A new approach will be presented to obtain stabilized finite element formulation that ensures an oscillation-free solution and treats the thermal shocks. The velocity and the pressure fields are computed by solving the Navier-Stokes equations coupled to heat equations. This finite element solver is already implemented in our library

CIMLIB*. It uses the so called P1+/P1 or “MINI-element” formulation as a stabilization method. An extension of this solver will be studied, analyzed and added to take into account the convection dominated terms for simulating high Reynolds numbers. The work mainly involves the implementation of turbulence models. Two models will be added to this project, the k-epsilon model and the Large Eddy Simulation (LES) method (Smagorinsky model). In addition, it has been reported in the literature that radiation is the dominant mode of heat transfer inside the furnace or in quenching process. Therefore to capture accurately the temperature evolution, different thermal radiation models are discussed, only two are implemented and adapted to the proposed immersed volume method. All the numerical results obtained for benchmark problems are compared with other numerical models and analytical solutions for validation purposes. This will be the subject of the last part where also several industrial applications will be presented.

To summarize, the originality of this work is the combination of stabilization methods, unstructured grids, anisotropic mesh adaptation, transient flows, heat transfer, turbulence models and radiation models in a multidomain approach. All those elements represent the features dedicated to industrial abilities of the method.

This work was done within the THOST, “Thermal Optimization SysTem” project context, which includes the following industrial members:

- ADEME (www.ademe.fr): industrial and commercial public agency
- Snecma (www.snecma.fr) : aeronautic equipment
- ArcelorMittal – Industeel (www.arcelormittal.com) : steelmaker company
- EDF (www.edf.fr) : Electricity of France
- Aubert & Duval (www.aubertduval.com) : world leader in alloys, manganese and nickel activities
- Terreal (www.terreal.com) : producer of terra-cotta
- Manoir Industries (www.manoir-industries.com): cast and forged metal components
- Creusot Forge, group Areva (www.sfarsteel.com): heavy steel fabrication and mechanised welding of complex assemblies
- SCC, Sciences Computers Consultants (www.sccconsultants.com) industrialization and commercialization of material forming software (Ximex, THOST, Ludovic, Fakuma)

The main tasks within this project were:

- The establishment of physics-mathematical models for temperature and heat transfer analysis during a continuous heating inside the furnace. This will mainly include a turbulent flow model, a heat radiation model, a heat convection-conduction model in a multi-domain approach.
- The development of a numerical calculation method for estimating the temperature distributions in the furnace and workpieces by using stabilized finite element methods, under a specified furnace geometry, thermal schedule, part loading design, initial operation conditions, and performance requirements.

- Finally, the development of knowledge-based CAD tool, which will provide a CAD user interface for the information input of the furnace, workpieces, thermal and physical properties, and initial operation conditions that are used in the simulation.

The first two points can resume the present work. The last point was conducted and managed by SCC. Another encouraging point for the industrial partners is the establishment of such user friendly interface. The project is built not only on the idea of offering accurate results for the heat furnace treatment but also in answering all our partner's needs in a custom-made software. Here is a list of some industrial demands.

1. Accurate prediction of temperature profiles in the furnace chamber.
 - a. Temperature capturing at different positions (walls, corners...).
 - b. Temperature capturing at the surface or core of every loaded parts.
 - c. Capable of handling multiple parts in three-dimensional simulations.
2. Ability to simulate various configurations
 - a. Ability to arrange or randomly distribute loaded parts.
 - b. Simulating different thermal schedule.
 - c. Ability to insert or remove ingots at anytime during the simulation
3. Facility to calculate important terms such as:
 - a. The heat losses from the furnace.
 - b. The heat and energy required for the load under different conditions.
 - c. The heat stored in the furnace or in the load as a function of time.
4. Ability to change the environment
 - a. Opening or closing the doors
 - b. Turning on or cutting off some burners during the simulation



Figure 5. Large heated industrial workpieces

1.5 Work environment

In this thesis, all the numerical implementations of the developed methods are carried out using the finite element library CIMLIB. CIMLIB, which stands for CIM as Advanced Computing in Material forming research group and LIB for library, is developed by the team of T. Coupez and H. Digonnet [27]. It is the base for different numerical applications developed at CEMEF (www.cemef.mines-paristech.fr), in collaboration with other research team and industrial partners. This scientific library represents an Object Oriented Program and a fully parallel code, written in C++, gathers the numerical development of the group (Ph.D. students, researcher, associate professor...). CIMLIB aims at providing a set of components that can be organized to build numerical simulation of a certain process, such as REM3D, XIMEX, Forge3 and the present project THOST.

1.6 Layout of the thesis

The thesis is divided into seven chapters. Chapter 1 is an introduction to the topic considered in this thesis. Chapter 2 summarizes the basic governing equation for the heat transfer equation which leads to the common convection-diffusion-reaction equation. The mathematical modelling with emphasis on stabilized finite element in industrial applications is presented. Chapter 3 gives a detailed description of the computational procedure needed to solve the flow problem. Special attention is given to the use of different stabilization methods for solving the Navier-Stokes equation at high Reynolds number. The computation of different benchmarks tests has been also carried out. Chapter 4 is devoted to the numerical approach of two turbulence models, k-epsilon and LES (Large Eddy Simulation). The Immersed Volume Method (IVM) coupled to the mesh adaptation for solving thermal coupling of fluids and solids and for the representation of the loads inside the furnace is presented and discussed in chapter 5. The radiative heat transfer models are detailed in the second part of this chapter. Chapter 6 summarizes the results obtained computationally along with the validation of the code on some industrial applications. Several comparisons with experimental works will be also presented in four preprints for publications. In chapter 7, conclusion and the possible extension of the present work to include more features is explored.

References

- [1] J. Harish, ,Computational Modelling Of Heat Transfer In Reheat Furnaces, *M.S. Thesis, Dept. of Mechanical Engineering, Indian Institute of Science*, 2000, Available from: <http://hdl.handle.net/2005/234>
- [2] S.V. Patankar and D.B. Spalding, Simultaneous prediction of flow patterns and radiation for three-dimensional flames, *Seminar of the International Center for Heat and Mass Transfer*, Yugoslavia, 1973
- [3] V.A. Krivandic, and B.L. Markov, *Metallurgical Furnaces*, Mir Publishers, 1980
- [4] A. N. Minaev, S.I. Reshetnyak, , and I.G. Butenko, Heat Transfer in Walking Beam Furnaces, *Steel in the USSR*, vol. 13, pp. 417-418, 1983
- [5]. R.J. Tucker and R. Lorton, Mathematical modelling of load-recuperative gas-fired furnaces, *First UK National Heat Transfer Conference, Inst Chem Engrs, Symposium Series No 86*, 1984
- [6] H. C. Hottel and E. S. Cohen., Radiant Heat Exchange in Gas-Filled Enclosure, *Journal of American Institute of Chemical Engineers*, vol. 4, pp. 3, 1958
- [7] S. I. Gerasimov, S. Yu. Efrogimovich, M.D. Klimovitskii, and V.N. Khloponin, Stastical Modelling of Heating of Metal in Conveyor Furnaces Taking into Account Heating-Atmosphere Temperature profile, *Steel in the USSR*, vol. 14, pp. 461-462, 1984
- [8] S. I. Gerasimov, S. Yu. Efrogimovich, M.D. Klimovitskii, and V.N. Khloponin, Stastical Modelling of Heating of Metal in Conveyor Furnaces Taking into Account Heating-Atmosphere Temperature profile, *Steel in the USSR*, vol. 14, pp. 461-462, 1984
- [9] Z. Li, P.V. Barr and J.K. Brimacombe, Computer simulation of the slab reheating furnace, *Can. Metall. Quarterly* 27, pp. 187–196, 1988
- [10] H. Rarnarnurthy , S. Ratnadhyan, and R. Viskanta, Modeling of heat transfer in indirectly-fired batch reheating furnace, *Procceding of the 3rd ASME/JSME Thermal Engineering Joint Conference*, pp. 205-2 15, 1991
- [11] K.S. Chapman, S. Ramadhyan and R. Viskanta, Modeling and parametric studies of heat transfer in a direct-fired continuous reheating furnace, *Metallurgical transactions, Part B*, vol. 22, pp. 513-521, 1991
- [12] Barr, P.V., The Development, Verification and Application of a Steady-State Thermal Model for the Pusher-Type Reheat Furnace, *Metallurgical and Materials Transactions B*, Volume 26B, pp 851-869, 1995
- [13] Marino, P., Numerical Modeling of Steel Tube Reheating in Walking Beam Furnaces, *Proceedings of The Fifth European Conference on Industrial Furnaces and Boilers*, Porto, Portugal, 2000

- [14] Altschuler, E., Marino, P. and A. Pignotti, Numerical Models of Reheating Gas Furnaces in the Steel Industry, *Proceedings of the Fourth ISHMT/ASME Heat and Mass Transfer Conference*, Pune, India, 2000
- [15] J. Harish and P. Dutta, Heat transfer analysis of pusher type reheat furnace, *Ironmaking Steelmaking*, 32 pp. 151–158, 2005
- [16] M. Y. Kim. A heat transfer model for the analysis of transient heating of the slab in a direct-fired walking beam type reheating furnace, *International Journal of Heat and Mass Transfer* 50, 3740–3748, 2007
- [17] F.Fitzgerald, A.T. Sheridan, Heating of a Slab in a Furnace, *Journal of Iron and Steel Institute*, Vol.208, 1970
- [18] R. Collin, A Flexible Mathematical Model for the Simulation of Reheating Furnace Performance, *Proc. of Conference for Hot Working*, 1968
- [19] M. Venturino, P.A. Rubini. Coupled fluid flow and heat transfer analysis of steel reheat furnaces. *3rd European Conference on Industrial Furnaces and Boilers*, Lisbon, Portugal, 18-21 April 1995
- [20] Houzeaux G, Codina R. An overlapping Dirichlet/Robin domain decomposition method. *Journal of Computational and Applied Mathematics*; 158(2):243–276, 2003
- [21] Felippa CA. Partitioned analysis for coupled mechanical systems, *Engineering Computations*, 5:123–133, 1988
- [22] Principe J, Codina R. A numerical approximation of the thermal coupling of fluids and solids, *Int. J. Numer. Meth. Fluids*, 59:1181–1201, 2009
- [23] FEDKIW, R., ASLAM, T., MERRIMAN, B., AND OSHER, S, A Non-oscillatory Eulerian Approach to Interfaces in Multimaterial Flows (The Ghost Fluid Method). *J. Comput. Phys.* 152, 457, 1999
- [24] C. S. Peskin, The immersed boundary method, *Acta Numerica*, 11, pp. 1–39, 2002
- [25] Rixen D. & Gosselet P., Domain decomposition methods applied to challenging engineering problems, *16th International Conference on Domain Decomposition Method*, New-York, 12-15 January, 2005.
- [26] N. Sukumar, N. Moës, B. Moran and T. Belytschko, `Extended Finite Element Method for Three-Dimensional Crack Modeling, *International Journal for Numerical Methods in Engineering*, Vol. 48, Number 11, pp.1549-1570, 2000
- [27] H. Digonnet, T. Coupez, Object-oriented programming for fast and easy development of parallel applications in forming processes, in: K. Bathe (Ed.), *Second MIT conference on computation Fluid and Solid Mechanics*, MIT, 2003.

Chapter 2

Stabilized finite element method of convection-diffusion-reaction equations

The present chapter is dedicated to the modelling of the heat transfer equation in fluid mechanics which leads to the common convection-diffusion-reaction equation. The need for stabilisation of the discrete equation is explained and a review on the stabilisation methods is discussed. After briefly reviewing the reason for the observed non-physical oscillations in the numerical solutions due to the presence of sharp gradients of temperature or in highly convected schemes, some methods to circumvent these oscillations are considered. The main part of the chapter is devoted to the family of residual based stabilisations methods which are discussed, implemented and validated on several numerical examples. Our motivation and our future goal are to resolve the transient heat transfer equation by a continuous finite element approximation using the above mentioned stabilized methods.

Chapter 2	23
Stabilized finite element method of convection-diffusion-reaction equations.....	23
2.1 The need of stabilization methods.....	24
2.2 Standard Galerkin solution.....	25
2.2.1 Problem setting.....	25
2.2.2 Space discretization.....	26
2.2.3 Temporal discretization.....	27
2.2.4 Introduction to stabilized method.....	27
2.3 Stabilized finite element methods	31
2.3.1 Streamline Upwind Petrov-Galerkin FEM.....	31
2.3.2 Shock Capturing Petrov-Galerkin	36
2.3.3 Residual Free Bubbles.....	40
2.4 Application to heat transfer equation	44
2.5 Thermal shock treatment for unsteady diffusion problems.....	47
2.6 Numerical tests and validation	48
2.6.1 Transient CDR problems.....	48
2.6.2 Transient pure convection	50
2.6.3 Transient heat transfer	55
2.7 Conclusion.....	58
References	59

2.1 The need of stabilization methods

The finite element method has been used widely in simulating many physical situations due to its flexibility to represent complex geometric domains especially for mechanical applications: airplanes, industrial furnaces and many others. Since in most cases analytical solutions are difficult or impossible to obtain, the finite element method can provide an interesting alternative way to solve and simulate physical situations governed by well established mathematical equations. Although it has been used extensively in structural mechanics, it was noticed that during recent years more advanced development are still being continued to extend its application in complex fluid mechanics.

The solution of the transient convection-diffusion-reaction problem represents a very important subject in numerical modelling for a wide class of problems in fluid mechanics in particularly the heat transfer equation. Usually the Galerkin Finite Element (FE) method is the first mentioned among the various numerical techniques available to solve these problems. This can be explained due to its simplicity and ease of implementation in different codes.

This method is usually based on the Eulerian formulation in which a fixed position control volume is used to derive the governing equations. Consequently, the resulting governing equation contains a convective term that has first order spatial derivatives. However, when using the standard Galerkin finite element procedure on this governing equation, the convective term creates a skew matrix which is the source of non-physical oscillations. These non-physical oscillations therefore are a result of the discretization of the first order spatial derivative in the convective term when dominating the other terms, like diffusion or reaction terms, in the same governing equation.

We can find in the literature many papers with different methods proposed to avoid these numerical oscillations. These methods are known as the upwinding techniques. The idea in upwinding is that the node in the upstream direction gives more weight to the solution than the node in the downstream direction.

Since 1950, many upwinding techniques have been the object of extensive investigations in the literature. This idea was first proposed by Courant *et al.* [1] in 1952 then outlined by [2] and [3]. The very first procedures have been proposed by Hughes *et al.* [4, 5, 6], Donea *et al.* [7], Patankar [8], etc. For a review of literature relating to this subject, the readers are referred to a complete summary reported in [9] and [15]. These methods are quite efficient and stable in certain applications, with the use of specific discretization, but improvements and generalizations for finite element analysis with optimal accuracy characteristics are still under active development. In this chapter, we will discuss the need of such upwinding methods specifically for the convection dominated heat transfer equation inside the furnace.

Other instabilities may occur where transient conduction is the sole mechanism for heat mass transfer in particularly at ingot's level. There are still some conditions for which the Galerkin method fails to solve unsteady diffusion problem. A new approach based on the variational multiscale method will be presented here to obtain stabilized finite element formulation that ensures an oscillation-free solution and treats the thermal shocks. Many related ideas was proposed like, mesh refinement [10], M-matrix theory [11], finite volume method [12], discontinuous Galerkin models [13] and the diffusion-split method [14]. Compared to all these methods, the new approach works for general meshes, can use any time step and has not only a good accuracy order, but also a smaller computational cost.

2.2 Standard Galerkin solution

In this section the general equation of convection-diffusion-reaction is described and solved. The main interest is then to highlight the reason of the occurring unphysical oscillations. This can be easily done by analyzing a one dimension discrete equation as proposed by Donea and Heurta [16].

2.2.1 Problem setting

The convection-diffusion-reaction equation over a bounded and polyhedral domain $\Omega \subset \mathfrak{R}^d$ (d being the space dimension) consists in finding a scalar $u(x,t)$ such that:

$$\begin{aligned} \partial_t u + \mathcal{L} u &= f & \text{in } \Omega \times (0, T) \\ u &= 0 & \text{on } \partial\Omega \times (0, T) \\ u(\cdot, 0) &= u_0 & \text{in } \Omega \end{aligned} \quad (2.1)$$

Where \mathcal{L} is the convection-diffusion-reaction operator:

$$\mathcal{L} u := a \cdot \nabla u - \nabla \cdot (k \nabla u) + \sigma u \quad (2.2)$$

Here, a is a given divergence-free velocity field, $k > 0$ is the diffusion coefficient and $\sigma \geq 0$ is the reaction coefficient, f is a source function and u_0 the initial data. First let us introduce some notation [15]. For a given $\Omega \subset \mathfrak{R}^d$, the space of functions whose distributional derivatives of order up to $m \geq 0$ belong to $L^2(\Omega)$ is denoted by $H^m(\Omega)$. The subspace of $H^1(\Omega)$ consisting of functions vanishing on the boundary is denoted by $H_0^1(\Omega)$. The norm of $H^m(\Omega)$ is denoted by $\|\cdot\|_{m,\Omega}$. The L^2 norm is denoted by $\|\cdot\|_{0,\Omega}$ and its inner product by (\cdot, \cdot) . The topological dual of $H_0^1(\Omega)$ is denoted by $H^{-1}(\Omega)$ and $\langle \cdot, \cdot \rangle_\Omega$ is used to denote the duality pairing between them.

The Galerkin variational formulation corresponding to (2.1) is obtained by multiplying this equation by test functions and integrating over the computational domain. The problem can be written in a weak form as follows: given $f \in H^{-1}(\Omega)$ and $a \in L^\infty(\Omega)$, find $u \in V := H_0^1(\Omega)$ such that :

$$\begin{aligned} (\partial_t u, v) + b(u, v) &= l(v) \quad \forall v \in V \\ b(u, v) &:= (a \cdot \nabla u, v) + (k \nabla u, \nabla v) + (\sigma u, v) \\ l(v) &:= \langle f, v \rangle \end{aligned} \quad (2.3)$$

2.2.2 Space discretization

For the spatial discretization, we consider the finite element partition \mathcal{T}_h of Ω into set of N_{el} elements K such that they cover the domain and there are either disjoint or share a complete edge (face). Using this partition, the above-defined functional space V is approached by a finite dimensional space V_h spanned by continuous piecewise polynomials.

$$V_h = \left\{ v_h \in H_0^1(\Omega), v_{h/K} \text{ is linear for } K \in \mathcal{T}_h \right\} \quad (2.4)$$

The Galerkin discrete problem consists now in finding $u_h \in V_h$ such that:

$$(\partial_t u_h, v_h) + b(u_h, v_h) = l(v_h) \quad \forall v_h \in V_h \quad (2.5)$$

Finally, the matrix systems follow from introduction of linear shape functions into the variational formulations (2.5). The linear matrix system for the convection-diffusion-reaction equation reads after assembly of the element matrices a system of first order differential equations:

$$\mathbf{M}\dot{U} + \mathbf{K}_c U + \mathbf{K}_d U + \mathbf{K}_r U = \mathbf{F} \quad (2.6)$$

where U is the vector of nodal unknown temperatures, \mathbf{M} is the mass matrix, \mathbf{K}_c the stiffness matrix from the conductive term, \mathbf{K}_d the stiffness matrix from the diffusion term, \mathbf{K}_r the stiffness matrix from the reaction term and \mathbf{F} is the internal source. The finite element matrix equation must be solved to obtain the numerical solution for the convection-diffusion-reaction problem with specified boundary conditions. The coefficient matrices and load vectors are defined as follows:

$$\begin{aligned} \mathbf{M} &= \mathcal{A}_{i=1}^{N_{el}} \int_{K_i} N_i N_j dK \\ \mathbf{K}_c &= \mathcal{A}_{i=1}^{N_{el}} \int_{K_i} a \cdot \nabla N_i N_j dK \\ \mathbf{K}_d &= \mathcal{A}_{i=1}^{N_{el}} \int_{K_i} k \nabla N_i \cdot \nabla N_j dK \\ \mathbf{K}_r &= \mathcal{A}_{i=1}^{N_{el}} \int_{K_i} \sigma N_i N_j dK \\ \mathbf{F} &= \mathcal{A}_{i=1}^{N_{el}} \int_{K_i} f N_j dK \end{aligned} \quad (2.7)$$

being N_i the linear interpolation function at node i and \mathcal{A} is the matrix assembly operator.

2.2.3 Temporal discretization

The system of ordinary differential equations (2.6) has to be integrated in time. Using the finite difference family of approximations, the derivative of the temperature with respect to time can be approximated at time $t=n\Delta t$ by:

$$M \frac{U^n - U^{n-1}}{\Delta t} + \mathbf{K} (\theta U^n + (1-\theta)U^{n-1}) = \theta \mathbf{F}^{n+1} + (1-\theta)\mathbf{F}^n \quad (2.8)$$

Here, Δt denotes the chosen time step, $n-1$ the previous time level subject to $n=0, \dots, (T/\Delta t)-1$, T the simulation time and θ the parameter of the method, taken to be in the interval $[0,1]$. We remind that this family includes the backward Euler scheme ($\theta=1$), the Crank-Nicolson scheme ($\theta=1/2$) and the forward Euler scheme ($\theta=0$). The forward and backward Euler schemes have first-order accuracy. However, the Crank-Nicolson scheme it is the only scheme bearing second-order accuracy. The critical disadvantage of last mentioned method lies in the potential occurrence of oscillations during the development of the solution. The reason is usually due to a chosen time step being too large for the underlying problem. Using, for example, the backward Euler scheme such an ‘incorrect’ time step may be overcome by the strong damping feature which comes into play by choosing $\theta > 1/2$. For a general analysis of these methods with regard to the damping feature, one may consult e.g. Hughes (2000) [17].

The explicit forward Euler method is subject to the so-called CFL ($\Delta t |a|/h$) (Courant-Friedrich-Levy)-condition governing the size of the time step depending on the velocity and the chosen spatial discretization h . When using extremely small time steps, the CFL-condition may become very restrictive. Despite the simplicity of this scheme, implicit scheme whose parameter lies between $1/2$ and 1 are favoured here. Another alternative was suggested by [18] to increase slightly θ above $1/2$ in order to cure the oscillations, but at the same time it sacrifices the second-order accuracy.

2.2.4 Introduction to stabilized method

In this section, the one dimensional convection-diffusion equation is considered to highlight the numerical problem when using the standard Galerkin finite element method. Although the following example is simple, it reflects the real situations even when simulating an industrial application. Assuming a steady state condition, a zero source term and without a reaction term, the problem will reduce as follow:

$$a \frac{du}{dx} - k \frac{d^2u}{dx^2} = 0 \quad \text{in } \Omega \quad (2.9)$$

A uniform mesh domain $[0,L]$ to be considered with the element length h and its linear interpolation functions is shown in Figure 1:

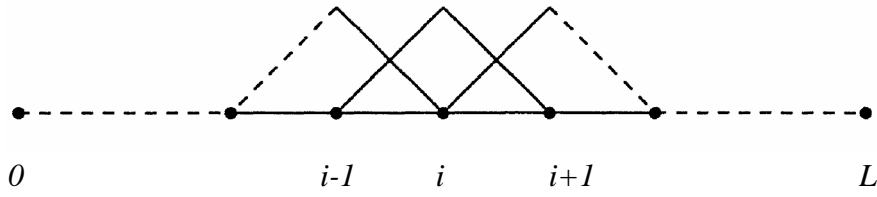


Figure 1. Interpolation function for the node i

By applying the Galerkin method to equation (2.9) we obtain the following equation,

$$\int_{\Omega} \left(a \frac{du}{dx} - k \frac{d^2u}{dx^2} \right) v \, d\Omega = 0 \quad (2.10)$$

Solving equation (2.10) leads the following discrete form for the i^{th} node of a uniform mesh with element size h ,

$$a \frac{-u_{i-1} + u_{i+1}}{2h} - k \frac{u_{i-1} - 2u_i + u_{i+1}}{h^2} = 0 \quad (2.11)$$

where u_{i-1} , u_i and u_{i+1} are the nodal values of u at nodes $i-1$, i and $i+1$ respectively. It can be seen that the Galerkin method gives rise to central-difference type approximations of differential operators, same as of the central finite difference method, which are well suited for elliptic problems, see for example Huerta *et al.* (2003) [19]. This equation can be simplified to obtain the following

$$(-1 - Pe^e)u_{i-1} + 2u_i + (-1 + Pe^e)u_{i+1} = 0 \quad (2.12)$$

where Pe^e is the element Péclet number, $Pe^e = ah/2k$. It is a dimensionless number relating the rate of advection term of a flow to its rate of diffusion. So the flow is assumed to be convection-dominated for $Pe \gg 1$ and diffusion-dominated when $Pe \ll 1$. When the convective terms dominate, these anti-symmetric terms create instability in the finite element solution which is indicated by oscillations. A simple illustration is given in the following example.

Consider the 1D boundary value problem on the interval $[0,1]$ with $u(0)=1$ and $u(1)=0$. The velocity field is prescribed by $a=1$ uniformly and constant diffusivity is assumed, $k=10^{-2}$. If the element size $h = 0.1$ then the global Péclet number will be 100. This outflow boundary layer problem have the following analytical solution:

$$u(x) = \frac{e^{\frac{ax}{k}} - e^{\frac{a}{k}}}{1 - e^{\frac{a}{k}}} \quad (2.13)$$

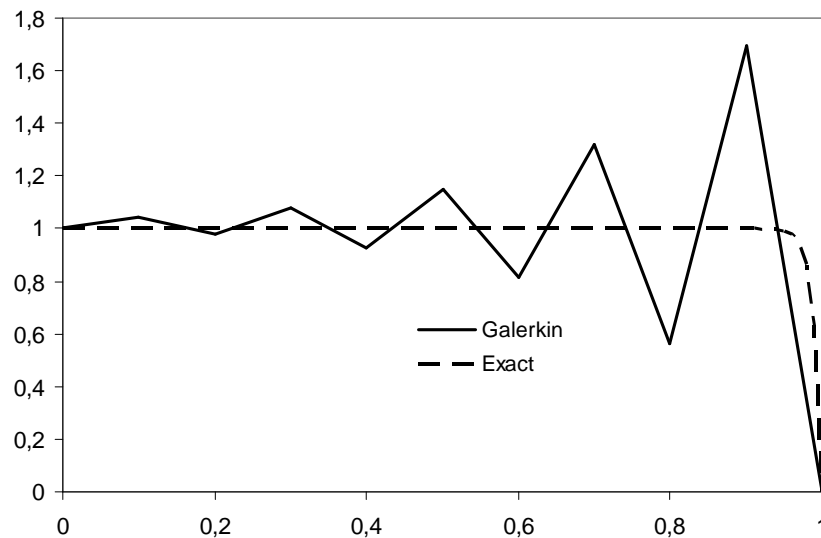


Figure 2. Solution of the 1D convection-diffusion problem using the Galerkin method

Notice that the boundary layer is located at the right end of the interval (at $x=1$). In this region the gradient is important. As stated previously, for high Péclet numbers, i.e. when the flow is dominated by advection, it can be seen from figure 2 that the Galerkin discretization gives rise to node-to-node oscillations of the solution or “wiggles”. Such numerical instabilities pollute the global solution and create critical problems when solving couple heat transfer problems. One way to eliminate these oscillations is the use of upwind techniques such as stabilized finite element.

In general, as stated in [9], the basic upwinding technique consists in replacing the central difference method obtained from the Galerkin finite element procedure for the convective terms by the forward difference method, of first order accuracy. This will give a stable calculation. However, using the complete forward difference method yields numerical results that are not satisfactory since they are overly diffused. To improve accuracy, several modified versions were proposed and developed by introducing an adjusted variable, which is a function of the Péclet number. The most popular formulation is known as the Streamline Upwind Petrov-Galerkin method (SUPG). It was proposed by Hughes and Brooks in [3] and [20] for advection dominated problems. In brief, the basic idea of the streamline upwind method (SU) is to add artificial diffusion which acts only in the direction of the flow.

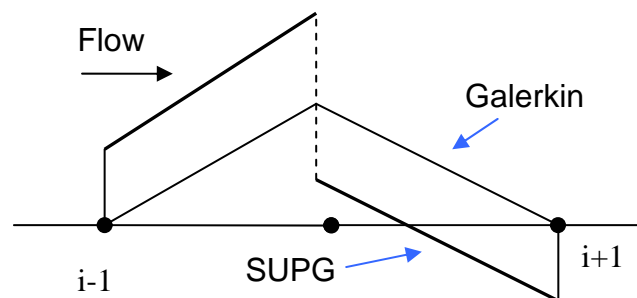


Figure 3. Weighting function of the Galerkin method and the SUPG method for linear elements

Then it was extended to a Petrov-Galerkin formulation by modifying the standard Galerkin weighting functions v_h for all terms in the equation. This modification is interpreted by allowing more weight to the node in the upstream direction and reducing the weight to the node in the downstream direction (see figure 3). The modified equation will take the following form

$$\int_{\Omega} \left(a \frac{du}{dx} - k \frac{d^2u}{dx^2} \right) \tilde{v} d\Omega = 0 \quad (2.14)$$

where $\tilde{v} = v + \tau a \frac{dv}{dx}$ is the new modified weighting function. Note also that since a linear interpolation is used, second derivative cancels out. The parameter τ , known as stabilizing parameter, will govern the amplitude of the added artificial diffusion. Finally equation (2.14) will be modified into

$$\left(-1 - Pe^e - \frac{\tau a^2}{k}\right)u_{i-1} + \left(2 + 2\frac{\tau a^2}{k}\right)u_i + \left(-1 + Pe^e - \frac{\tau a^2}{k}\right)u_{i+1} = 0 \quad (2.15)$$

As a result, an exact nodal solution is obtained for one dimensional analysis. (Figure 4)

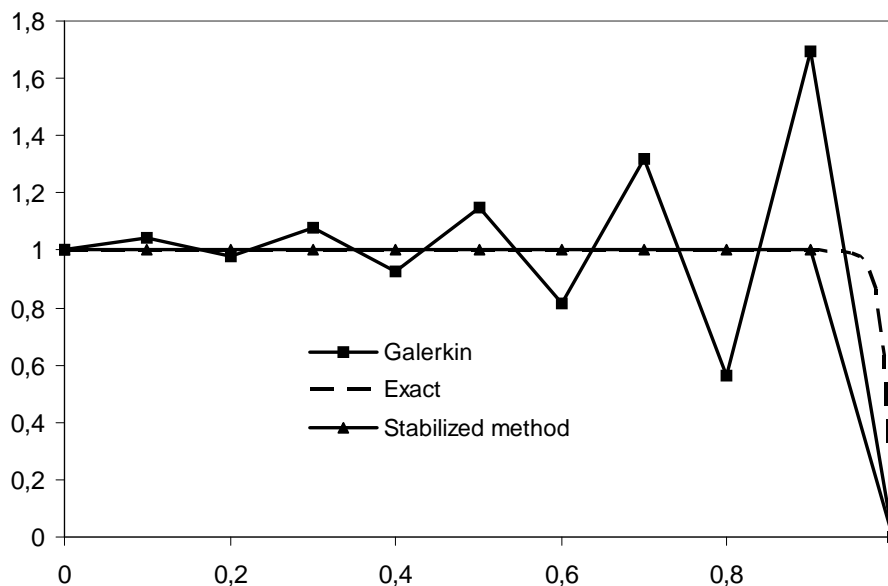


Figure 4. Solution of the 1D convection-diffusion problem using the stabilized method

The previous simple example illustrates some of the difficulties that motivated much of the development of upwind and stabilized finite element methods. For multidimensional cases, the idea of upwinding can not be easily applied. However, various methods have been proposed to implement the basic idea of upwinding to multidimensional analyses. In the following subsection, we shall discuss these methods for time-dependent convection-diffusion-reaction specifically with respect to their use in heat transfer applications.

2.3 Stabilized finite element methods

The numerical solution of convection-diffusion-reaction equation using Galerkin formulation normally exhibits global spurious oscillations in convection-dominated problems, especially in the vicinity of sharp gradients. In heat transfer applications, it is important to design a numerical methods guaranteeing that the discrete it temperature solution satisfies the physical conditions, in particular for convection dominated and sharp gradient problems. Another typical example is the simulation of process which involves solving the two-equation turbulence models. Such equations might be either convection or reaction dominated. Therefore, the main objective in this section is to revisit these numerical methods to obtain stable form for any regime without loss of accuracy. Over, the last two decades, a variety of finite elements approaches have been proposed to deal with such situations. These methods add a perturbation term to the weighting functions with aim to get an oscillation-free solution. These terms are mesh-dependent and allow getting a consistent and stabilizing numerical scheme. Recently, such methods have grown in popularity, especially in application to fluid dynamics. Starting with Hughes and Brooks in [3, 4, 5] with the SUPG method, a generalization was proposed for multidimensional advective–diffusive systems in [22] and [23]. Later, as pointed out in Harari and Hughes [24–25], the Galerkin/Least-Squares (GLS) and gradient Galerkin/least-squares (GGLS) methods were used to optimize the performance of finite element formulations for advection-diffusion equation with production.

At the same time, a number of interesting stabilized formulations have been proposed based on the multiscale methods [26] and related work on the residual free bubbles (RFB) by Russo [27] and Brezzi [28]. Further attempts to develop a stabilized finite element method with good stability in the presence of reactive terms are presented with the unusual stabilized method (USFEM) by Franca *et al.* [29, 30]. For a detailed comparison of some finite element methods for solving these equations, the readers are referred to the work of Codina [31]. Some advancement in this direction has been done in [31] and in [32] with the presentation of a subgrid scale method with a simple intrinsic time-scale parameter.

In this section, we discuss the use of the SUPG and the RFB methods to solve the transient advection-diffusion-reaction equation. Different structure of the stabilizing parameters will be presented and conclusions will be drawn.

2.3.1 Streamline Upwind Petrov-Galerkin FEM

We reconsider the time-dependent convection-diffusion-reaction equation using the same homogeneous Dirichlet boundary condition and initial condition as (2.1), find $u_h \in V_h$ such that :

$$(\partial_t u_h, v_h) + (a \cdot \nabla u_h, v_h) + (k \nabla u_h, \nabla v_h) + (\sigma u_h, v_h) = (f, v_h) \quad \forall v_h \in V_h \quad (2.16)$$

The original SUPG method was first designed for the steady version of Eq. 2.1 as a method to avoid the numerical oscillations found using the Galerkin approach when the diffusion term is

small. The extension to the transient problem that we consider here is based on a previous discretization in time of the equation and then on the use of stabilized finite element method for the resulting spatially-continuous problem. This approach is mostly used in the literature (see [31] and [32]).

For illustration purposes, we apply the backward implicit Euler method to equation (2.16) and we obtain the followed: given u^n , find u^{n+1} satisfying the boundary conditions and: $\forall v_h \in V_h$

$$\left(\frac{u_h^{n+1}}{\Delta t}, v_h\right) + (a \cdot \nabla u_h^{n+1}, v_h) + (k \nabla u_h^{n+1}, \nabla v_h) + (\sigma u_h^{n+1}, v_h) = \left(\frac{u_h^n}{\Delta t}, v_h\right) + (f, v_h) \quad (2.17)$$

By adding a streamline upwind perturbation which acts mainly in the flow direction:

$$\tilde{v}_h = v_h + \tau a \cdot \nabla v_h \quad (2.18)$$

and inserting it into (2.17), the SUPG method is formulated as follow: $\forall v_h \in V_h$

$$\begin{aligned} \left(\frac{u_h^{n+1}}{\Delta t}, v_h\right) + (a \cdot \nabla u_h^{n+1}, v_h) + (k \nabla u_h^{n+1}, \nabla v_h) + (\sigma u_h^{n+1}, v_h) + \sum_K (\mathcal{R} u_h, \tau_K a \cdot \nabla v_h) \\ = \left(\frac{u_h^n}{\Delta t}, v_h\right) + (f, v_h) \end{aligned} \quad (2.19)$$

Where $\mathcal{R}(u_h)$ is the appropriate residual of the finite element components u_h . We can see that this method is consistent in the sense that the additional stabilizing term is zero if u_h is the solution of the continuous equation.

$$\begin{aligned} \mathcal{S}^{SUPG}(u_h, v_h) &= \sum_K (\mathcal{R} u_h, \tau_K a \cdot \nabla v_h)_K \\ &= \sum_K \tau_K \underbrace{\left(\frac{u_h^{n+1}}{\Delta t} + a \cdot \nabla u_h^{n+1} - \nabla \cdot (k \nabla u_h^{n+1}) + \sigma u_h^{n+1} - \frac{u_h^n}{\Delta t} - f\right)}_{\text{time-dependent convection-diffusion-reaction residual}}, a \cdot \nabla v_h)_K \end{aligned} \quad (2.20)$$

This method up to now has been extensively used in convection dominated problems by introducing the streamline diffusion in the context of weighted residual methods. The added stabilizing terms are indicated by a subscript K which denotes integration over the element, (only added on the element interiors). Note that the third term vanishes in (2.20) while using linear interpolations. It remains to define how to compute the parameter τ_K called often ‘intrinsic time’ which can determines and calibrate the amount of upwinding weighting locally in each element. The definition of this parameter was originally computed for 1D problem. Then it was extended for multidimensional cases using some ‘ad hoc’ modifications.

More recently, other ways of computing τ_K have been proposed on the basis of the convergence and error analysis of the method. The purpose of the next subsection is to present some definitions of the stabilization parameters that can be directly implemented in our finite element code.

2.3.1.1 Proposal for the parameters

The critical question in the SUPG method remains in the choice of the parameter τ_K . *How much of the perturbation term we must add to obtain the desirable effects of additional stability with high accuracy?* There is a large amount of literature concerning this choice and design of the stability parameters in both presence and absence of the reaction term. However, very few of them have been so far used in the simulation of time-dependent equations. In our case, as we can see in the discretized equation (2.19), the transient term can act like an additional reaction term which might dominate the diffusion and the convection term, in particular for small time steps. Thus, appropriate parameters should take both the reaction and the transient term into account yielding modified stabilizing parameters.

The standard design for τ_K comes from advection-diffusion theory and computed as follow:

$$\tau_{ad} = \frac{h}{2|a|} \xi(Pe) \quad (2.21)$$

where $\xi(Pe)$, function of the Péclet number is derived from nodal exactness as:

$$\xi(Pe) = \coth Pe - \frac{1}{Pe} \approx \min\left(\frac{1}{3} Pe, 1\right) \quad (2.22)$$

For negative reaction terms, Codina in [31] and [33] derived the following formula for τ_K which emanates from the discrete maximum principle:

$$\tau_{cod} = \left(\frac{4k}{h^2} + \frac{2|u|}{h} + |\sigma| \right)^{-1} \quad (2.23)$$

A similar symmetric expression with respect to the sign of the reaction term is proposed by Shakib *et al.* [34] where each contribution is squared

$$\tau = \left(9 \left(\frac{4k}{h^2} \right)^2 + \left(\frac{2|u|}{h} \right)^2 + \sigma^2 \right)^{-1/2} \quad (2.24)$$

From convergence and stability theory, Franca and Valentin [30] derived the following expression

$$\begin{aligned} \tau_{FV} &= \left(\frac{2k}{m_k h^2} \zeta(Pe_2) + \sigma \zeta(Pe_1) \right)^{-1} \\ \zeta(Pe_i) &= \max(Pe_i, 1) \\ Pe_1 &= \frac{2k}{m_k h^2 |\sigma|} \quad \text{and} \quad Pe_2 = \frac{m_k |a| h}{k} \end{aligned} \quad (2.25)$$

where m_k equal to $1/3$ is the optimal value for piecewise linear elements and $|a|$ is the norm of the velocity. Here h , as mentioned in previous section, is an appropriate measure for the size of the mesh cell K .

A Fourier analysis strategy was used by Codina [35] in the variational multiscale context. The subgrid scale equation from which we can derive the form of the stability parameter is expressed in the Fourier space within each element and approximated taking into account the subscales that contain only high wave numbers λ . This assumption enables us to get rid of the boundary term and to express the Fourier transform of a given variable $g(x)$ in the physical space as follow:

$$\hat{g}(\lambda) := \int_{\Omega_K} \exp\left(-i \frac{\lambda \cdot x}{h}\right) g(x) d\Omega_x \quad (2.26)$$

where h is an elemental length parameter. The obtained approximate spatial derivative gives:

$$\frac{\partial \hat{g}}{\partial x_j}(k) \approx i \frac{k_j}{h} \hat{g}(k), \quad \frac{\partial^2 \hat{g}}{\partial x_i \partial x_j}(k) \approx -\frac{k_i k_j}{h^2} \hat{g}(k) \quad (2.27)$$

where $\lambda = (\lambda_1, \dots, \lambda_d)$ is the dimensionless wave number. It was shown that by substituting the obtained expressions into the subgrid scale equation, we obtain:

$$\hat{\tau}(k) \approx \left(\varepsilon \frac{|k|^2}{h^2} + i \frac{u \cdot k}{h} + \sigma \right)^{-1} \quad (2.28)$$

Note also that in the above expression, the assumption of velocity being constant within an element is required. Using the Pancheral's formula and the mean value theorem, it leads us back to the definition of the stabilizing parameter [36]:

$$\tau \approx \left[\left(c_1 \frac{k}{h^2} \right)^2 + \left(c_2 \frac{u}{h} \right)^2 + \sigma^2 \right]^{-1/2} \quad (2.29)$$

Furthermore, the asymptotic behaviour of τ in the advection limit is dominated by the term h/u , the asymptotic behaviour in the diffusive limit is dominated by the term h^2/k and the one in the reaction limit is dominated by σ . The link between equation (2.29) and the SUPG-like stabilization methods reside in the choice of the random constants as $c_1=4$ and $c_2=2$.

2.3.1.2 The modified parameters

For a complete review with examples about the proposed parameters presented in the previous section, we recommend the following reference [37]. So far, most efforts have been invested to deal with steady-problem, while less attention has been devoted to unsteady problem. The goal here is to study how stabilization methods designed for steady problem could be adapted for non-stationary cases. A direct simple way is to use the above proposed parameters and apply them on the time-dependent equation (2.19). Recently, the same idea was proposed by [38] and consists in taking into account the transient term as an extra reaction term and inserting the time step Δt into (2.23) and (2.25). This will provide the following stabilizing parameter:

$$\begin{aligned}\tau_K^{cod} &\approx \frac{\Delta t h^2}{4k\Delta t + 2|u|h\Delta t + h^2(1 + \Delta t\sigma)} \\ \tau_K^{FV} &\approx \frac{\Delta t h^2}{6k\Delta t\zeta(Pe_2) + h^2\zeta(Pe_1)(1 + \Delta t\sigma)}\end{aligned}\quad (2.30)$$

where

$$Pe_1 = \frac{6\Delta tk}{h^2(1 + \Delta t\sigma)} \quad \text{and} \quad Pe_2 = \frac{|a|h}{3k}$$

It turns out that these proposed time-dependent parameters give identical results in some interesting limit cases. In order to analyze the asymptotic behavior, we consider first the convection-dominated regime, where the local Péclet number is large, $Pe_K = |a|h/2k \gg 1$. If the velocity is of the unity order from which follows $k \ll h$ two cases could occurs: ($h=1/64$, $\kappa=10^{-6}$)

$\Delta t \ll h \ll 1$	$\tau_K^{cod} \sim \tau_K^{FV} \sim \frac{\Delta t}{(1 + \Delta t\sigma)}$
$\Delta t \sim h \ll 1$	$\tau_K^{cod} \sim \tau_K^{FV} \sim \frac{\Delta t h}{2 u \Delta t + h(1 + \Delta t\sigma)}$

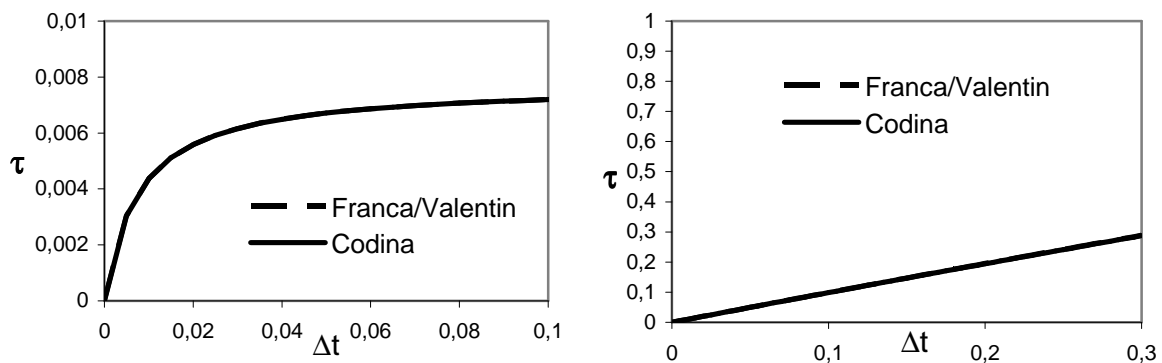


Figure 5. The profile of τ_K for $u=1$ and $c=1$ (left); $u=10^{-3}$ and $c=0$ (right)

For diffusion dominated regime, when the velocity norm is too small and zero reaction term is used, we can obtain $\tau_K^{cod} \sim \tau_K^{FV} \sim \Delta t$ in particular when $h^2 \gg k\Delta t$. Figure 5 illustrates the behavior of the stabilizing terms in function of the time step for both convection and diffusion dominated regimes.

2.3.1.3 Element length definitions

The characteristic element length h has a significant impact on the amount of the stabilizing parameter. It is shown that it can be proportional to h^2 at the diffusion limit and linear in the element length at the convective limit. Therefore, the choice of the mesh cell is not obvious specifically in the presence of distorted mesh or highly elongated elements. It could be simply the diameter of the mesh cell or could be chosen as the mesh cell in the direction of the convection for convection-diffusion equations. This choice is the most recommended in the literature, see for example [30,39].

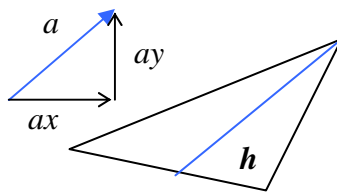


Figure 6. The support length in the streamline direction

$$h = 2 \left(\sum_{\alpha}^{n_e} \left| \frac{a_i}{\|a\|} \frac{\partial N_{\alpha}}{\partial x_i} \right| \right)^{-1} \quad \text{where} \quad \|a\| = \sqrt{\sum_i a_i^2} \quad (2.31)$$

Where n_e is the number of nodes in the element, N_{α} is the basis function associated with the local node α , and a is again the local velocity. For more details about the determination of the element length taking into account anisotropy of the mesh, the work of J. Principe and R. Codina in [40] is highly recommended.

2.3.2 Shock Capturing Petrov-Galerkin

The SUPG method is a popular upwinding scheme. Many researchers have successfully applied this scheme to solve numerical problems in many fields, such as coupled heat transfer and fluid flow, turbulence models and transient incompressible flow. The numerical solution to a convection-dominated problem using this method is quite satisfactory when approximating smooth functions. Some numerical examples will be presented at the end of this chapter. However, when the function contains a shock front in the interior of the domain or a boundary layer, the numerical results exhibits some spurious oscillations know as overshoots and undershoots. To improve the result, beyond SUPG upwinding scheme were

introduced in [4], [5] and [41] with an objective to reduce or even to remove out these oscillations near a sharp gradients.

The basic idea of these methods is to add a non-linear term to the SUPG formulation, allowing for more regulation of the function's derivative in the direction of the gradient. One can distinguish several classes of these methods usually referred as discontinuity capturing or shock capturing methods. See [41] and [42]. The most familiar one are known as the Consistent Approximate Upwind (CAU) methods [43, 44, 45] and the Spurious Oscillations at Layers Diminishing (SOLD) methods, see [46, 47] for review. However, very few of them have been so far used in the simulation of time-dependent equations, in particular for heat transfer.

As an extension for the SUPG method, this scheme adds an extra term called discontinuity-capturing operator. The extra term affects only the numerical solution in the direction of the gradient of the solution u . The weighting function is then modified to include this term and is defined as follows:

$$\tilde{v}_h = v_h + \tau a \cdot \nabla v_h + \tau^c a_{//} \cdot \nabla v_h \quad (2.32)$$

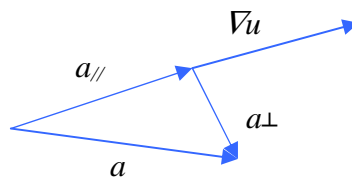


Figure 7. Projection of the advection direction onto the solution gradient ∇u

Where the $\tau^c a_{//} \cdot \nabla v_h$ is the discontinuity-capturing term. It creates an artificial diffusivity in the gradient of the solution direction. The auxiliary vector $a_{//}$ is a projection of the advection in the direction of the gradient ∇u_h as shown in figure 7. It is defined as follows

$$a_{//} = \begin{cases} \frac{a \cdot \nabla u_h}{\|\nabla u_h\|_2} \nabla u_h & \text{if } \nabla u_h \neq 0 \\ 0 & \text{if } \nabla u_h = 0 \end{cases} \quad (2.33)$$

As we can see, since the new vector depends on the unknown discrete solution u_h , the resulting method is nonlinear. Applying the Galerkin procedure to equation with the new weighting function, we obtain

$$\mathcal{R}(u_h, \tilde{v}_h) = \mathcal{R}(u_h, v_h) + \mathcal{S}^{SUPG}(u_h, v_h) + \underbrace{\sum_K (\mathcal{R} u_h, \tau_K^c a_{//} \cdot \nabla v_h)_K}_{\text{discontinuity-capturing}} = 0 \quad (2.34)$$

Therefore, the interaction of the new weighting function with the convective term of the equation will yield the following additional terms:

$$\begin{aligned}
\dots + (a \cdot \nabla u_h^{n+1}, \tilde{v}_h) + \dots &= \dots + (a \cdot \nabla u_h^{n+1}, \tilde{v}_h) \\
&+ \sum_K \tau_K (a \cdot \nabla u_h^{n+1}, a \cdot \nabla v_h)_K \\
&+ \sum_K \tau_K^c (a_{//} \cdot \nabla u_h^{n+1}, a_{//} \cdot \nabla v_h)_K + \dots
\end{aligned} \tag{2.35}$$

In the expression above, we can see that the first term is the convective term obtained using the classical Galerkin method; the second term represents the artificial diffusivity term along the streamline direction obtained using the SUPG method while the last, the new extra term is the artificial diffusivity in the gradient direction. This last additional term controls the derivatives in the direction of the solution gradient, thus smoothing out the numerical result around a shock front or a boundary layer. Note also that all these additional terms are added in a way to preserve consistency.

Due to the large number of various discontinuity-capturing methods and the comparatively small amount of theoretical research on them, the correct choice of the respective stabilization parameters is even less clear than for the SUPG method. For more details, see [4]. Often, the determination of τ_K^c is similar to the one in the SUPG method when replacing the velocity vector a by the new vector $a_{//}$ into the calculation of all needed terms. Therefore, to simplify the notation, these terms will be indicated by a subscript c . Note also that using the same procedure to determine τ_K^c will introduce the effect of the transient terms into its definition.

Another important issue is when $a \cong a_{//}$, a double artificial diffusivity effect occurs. Therefore, to avoid the double effect, the following ‘*ad hoc*’ correction was firstly introduced [4].

$$\tau_K^c = \max(0, \tau_K^c - \tau_K) \tag{2.36}$$

Another definition that assures a single effect was also introduced by Tezduyar *et. al* in [49] and [50]:

$$\tau_K^c = \frac{h^c}{2|a_{//}|} \eta \left(\frac{|a_{//}|}{2|a|} \right) \tag{2.37}$$

with

$$\eta(x) = 2x(1-x) \quad , \quad x \in [0,1] \tag{2.38}$$

In certain cases, for smooth problems, these techniques can introduce some undesirable crosswind diffusion that leads to less accurate solution than the SUPG methods. In order to minimize the effect of the discontinuity-capturing terms in regions where the solution is smooth, the idea in [43] and [45] was to introduce a feedback function about the regularity of the approximate solution. This locally defined function is added to the stabilizing parameter. It is given by:

$$\alpha_h = \frac{a \cdot \nabla u_h}{\mathcal{R}(u_h)} \quad (2.39)$$

Therefore, the modified methods will take the following form:

$$\begin{aligned} S^{SCPG}(u_h, v_h) &= \sum_K (\mathcal{R} u_h, \tau_K^c a_{//} \cdot \nabla v_h)_K \\ a_{//} &= \begin{cases} \frac{\mathcal{R} u_h}{\|\nabla u_h\|_2^2} \nabla u_h & \text{if } \nabla u_h \neq 0 \\ 0 & \text{if } \nabla u_h = 0 \end{cases} \\ \tau_K^c &= \tau_K^c \max \left\{ 0, \frac{|a|}{|a_{//}|} - \zeta \right\} \quad \text{with } \zeta = \max \{1, \alpha_h\} \end{aligned} \quad (2.40)$$

Remarks

1. The parameter τ_K^c is influenced by the time step Δt only indirectly through the residual and over the SUPG parameters.
2. All these techniques are nonlinear since they need the computation of the approximated residual. This can be solved iteratively using a fixed-point technique. Recall that usually for nonlinear problems, the computational cost will increase since the storage of the previous solution in time is required for the whole iteration. But small variation of the solution occurs when small time step are chosen, therefore the residual can be approximated directly using the previous time solution.

$$\mathcal{R} u_h \approx \frac{u_h^n}{\Delta t} + a \cdot \nabla u_h^n - \nabla \cdot (k \nabla u_h^n) + \sigma u_h^n - \frac{u_h^{n-1}}{\Delta t} - f \quad (2.41)$$

As a result and without significant efforts and development of new software, these algorithms allow reuse of existing spatial finite element frameworks and deploy a time dependent solution method. Thus, in practice, for several reasons, implicit, fully discrete formulations in which spatial and temporal discretizations are affected separately are in much more common use than the coupled time-space formulations. Note also that for a large number of computational applications like in the present work, the heating of an ingot inside industrial furnaces, the increased cost in the number of unknowns for coupled time-space formulations is a significant drawback.

2.3.3 Residual Free Bubbles

As pointed out before, the previous stabilized methods add some consistent terms providing additional diffusion in the streamline direction (SUPG) or in the gradient direction (SCPG). However, the amount of such additional artificial diffusion is tuned by a stabilizing parameter that must be chosen in a suitable way. Despite the progress of these methods in theory and application, their essential drawback lies in the choice of τ . One way to remedy to this problem is the use of variational multiscale methods which offers a suitable convincing argument for the definition of such parameter and can provide the required theoretical foundation to classical stabilization techniques.

The residual-free bubble method, as an example, started by Brezzi and Russo [50] and further developed by Franca and Russo [51], will be briefly described here. The variational multiscale method was proposed by Hughes [26] as an alternative viewpoint. An interesting error analysis on this subject can be found in [52] and [53]. In [54] the authors showed that the two approaches were completely equivalent. The basic idea behind those techniques is the search for an optimal τ through the solution of a suitable boundary problem solved in each element K .

For further explanation on this subject, the reader could refer to many publications about the residual-free bubbles authored by [29], [50] and [51]. The purpose of this section is to have a brief review to justify the definition and the choice of the stabilizing parameters and to offer an introduction for the following subsections.

Let $\tilde{B}_h \subset V$ be a finite dimensional bubble space on \mathcal{T}_h such that

$$\tilde{B}_h = \bigoplus_{K \in \mathcal{S}_h} B_K \quad (2.42)$$

where $B_K = H_0^1(K)$.

For each element K , we enrich and enlarge the following space V_a defined by

$$V_a = V_h \oplus \tilde{B}_h \quad (2.43)$$

so that any element of this space admits a unique decomposition into the sum of an element of V_h and \tilde{B}_h .

By (2.43) we have that any $u_a \in V_a$ can be split into a linear part $u_h \in V_h$ and into a bubble part $u_b \in \tilde{B}_h$ in a unique way:

$$u_a = u_h + u_b \in V_h \oplus \tilde{B}_h \quad (2.44)$$

Moreover, for any element K , we can write

$$u_{b|K} = u_{b,K} \text{ with } u_{b,K} \in B_K \quad (2.45)$$

Thus, the variational problem in V_a can be re-stated as follows:

$$\left\{ \begin{array}{l} \text{find } u_a = u_h + u_b = u_h + \sum_{K \in \mathcal{S}_h} u_{b,K} \in V_a \text{ such that} \\ \mathcal{L}(u_h, v_h) + \sum_{K \in \mathcal{S}_h} \mathcal{L}_K(u_{b,K}, v_h) = (f, v_h) \quad \forall v_h \in V_h \\ \mathcal{L}_K(u_{b,K}, v_{b,K}) + \mathcal{L}_K(u_h, v_{b,K}) = (f, v_{b,K})_K \quad \forall v_{b,K} \in B_K \quad \forall K \in \mathcal{T}_h \end{array} \right. \quad (2.46)$$

Where the subscript $\mathcal{L}_K(\cdot, \cdot)$ and $(\cdot, \cdot)_K$ indicates that the integrals involved are restricted to the element K .

The static condensation consists in solving element-wise the second equation in (2.46) for $u_{b,K}$, known as the small scale equation, and then substituting the resulting expression into the first equation, called also the large scale equation. (see [55] for details).

$$\left\{ \begin{array}{l} \text{find } u_{b,K} \in B_K \text{ such that} \\ \mathcal{L}_K(u_{b,K}, v_{b,K}) = (f, v_{b,K})_K - \mathcal{L}_K(u_h, v_{b,K}) = (f - Lu_h, v_{b,K}) \quad \forall v_{b,K} \in B_K \end{array} \right. \quad (2.47)$$

At this stage, simplifications must be done to solve for the subgrid scale equation. In the literature, the usual approximation consists in taking the subgrid scale as element wise and solving (2.47) in each element:

$$\begin{aligned} L_K(u_{b,K}) &= f - Lu_h|_K \\ &= \mathcal{R}(u_h) \end{aligned} \quad (2.48)$$

Thus, for each u_h , the unique solution of problem (2.47) can be written as

$$u_{b,K} = L_K^{-1} (f - Lu_h)|_K \quad \forall K \in \mathcal{T}_h \quad (2.49)$$

where $L_K^{-1}: H^{-1}(K) \rightarrow H_0^1(K)$ is the bounded linear operator. Inserting the resulting expression of the bubble part into the large scale equation (2.46) we obtain:

$$\left\{ \begin{array}{l} \text{find } u_h \in V_h \text{ such that} \\ \mathcal{L}(u_h, v_h) + \underbrace{\sum_{K \in \mathcal{T}_h} \mathcal{L}_K(L_K^{-1} (f - Lu_h)|_K, v_h)}_{\text{stabilisation term}} = (f, v_h) \quad \forall v_h \in V_h \end{array} \right. \quad (2.50)$$

It's clear that the fact of introducing and eliminating the bubble has modified the Galerkin formulation by adding a residual-free stabilizing term. By applying the Green's formula to the stabilization term, we can rewrite the problem as

$$\left\{ \begin{array}{l} \text{find } u_h \in V_h \text{ such that} \\ \mathcal{L}(u_h, v_h) + \sum_{K \in \mathcal{T}_h} (L_K^{-1} (f - Lu_h)|_K, L^* v_h)_K = (f, v_h) \quad \forall v_h \in V_h \end{array} \right. \quad (2.51)$$

where L^* is the formal adjoint operator of L on K coming from the second integration by parts with Dirichlet boundary conditions and given by:

$$L^* v := -\nabla \cdot (k \nabla v) - a \cdot \nabla v + \sigma v \quad (2.52)$$

Recall that the purpose of this section is to show that the use of these methods can reproduce the streamline-diffusion scheme and, at the same time, will provide a suitable definition of the stabilizing parameter. However the implementation of the RFB method requires the solution of the subgrid scales problem which is of the same complexity of the original problem. Hence, by following the same approximations of the bubbles made and described in Brezzi *et al.* [28] we retain only the effect of these unresolved scales. Therefore, the result of the local inversion L_K^{-1} can be reduced to a multiplication by a constant on each element K that depends on the equation coefficient and the finite element mesh as:

$$\tau_K^{RFB} = \frac{1}{|K|} \int_K L_K^{-1}(1) \quad (2.53)$$

Then, the resulting stabilized scheme on V_h takes the following form:

$$\left\{ \begin{array}{l} \text{find } u_h \in V_h \text{ such that} \\ \mathcal{L}(u_h, v_h) + \sum_{K \in \mathcal{T}_h} \tau_K^{RFB} (\mathcal{R} u_h, L^* v_h)_K = (f, v_h) \quad \forall v_h \in V_h \end{array} \right. \quad (2.54)$$

By comparing (2.54) and (2.19) we immediately see that stabilization term introduced by the SUPG method and the RFB method are identical specifically when v_h is linear on every element and under the assumption of piecewise constant coefficients. However, the advantage of the RFB method is that the stabilization parameter is produced by the approach rather than by ‘*ad hoc*’ tuning. Several publications regarding the link between the stabilized methods and the element wise residual-free bubbles were proposed in Franca and Farhat [29] and Franca and Russo [54].

At this point, the calculation of the stabilization parameter has to be specified. Recall that several strategies were proposed to model the subscales. For example, Codina derived in [31] his version using the maximum principle. Franca and Valentin in [56] proposed a definition of the stabilizing parameters based on the convergence theory. More general derivation was proposed later by Codina and Blasco using a Fourier analysis [57]. In [58] the authors used the element Green’s function to provide a suitable definition of this parameter. Let’s consider here an instructive example for the computation of τ_K^{RFB} . Let L be the convection-diffusion operator using piecewise constant coefficients, that V_h is the space of continuous, piecewise linear functions, on each element $K \in \mathcal{T}_h$ we have

$$f - Lu_h = f - (-\nabla \cdot (k \nabla u_h) + a \cdot \nabla u_h) = f - a \cdot \nabla u_h \quad (2.55)$$

Giving that (2.55) is a constant and by the definition of (2.48) and (2.49) we obtain:

$$L_K^{-1}(f - Lu_h)|_K = (f - a \cdot \nabla u_h)|_K b_k \quad (2.56)$$

In particular the stabilizing term in (2.51) will reduce to

$$(L_K^{-1}(f - Lu_h)_K, L^* v_h)_K = \frac{\int_K b_K}{|K|} \int_K (a \cdot \nabla u_h - f)(a \cdot \nabla v_h) \quad (2.57)$$

Finally, the resulting scheme becomes

$$\begin{cases} \text{find } u_h \in V_h \text{ such that} \\ \mathcal{L}(u_h, v_h) + \sum_{K \in \mathcal{T}_h} \tau_K^{RFB} \int_K (a \cdot \nabla u_h - f)(a \cdot \nabla v_h) = (f, v_h) \quad \forall v_h \in V_h \end{cases} \quad (2.58)$$

Both SUPG and RFB have an identical structure with a particular choice of the stabilizing parameter. In most interesting case, the convection-dominated case, we can approximate the stabilizing term as discussed in [51]. For convection dominated problem, it was shown that the solution of the fine-scale can be approximated by solving the following reduced purely convective problem:

$$\begin{cases} a \cdot \nabla \tilde{b}_K = 1 & \text{in } K \\ \tilde{b}_K = 0 & \text{on } \partial K^- \end{cases} \quad (2.59)$$

If h_a is the length of the longest segment parallel to a and contained in K , then the solution \tilde{b}_K of this reduced problem can be seen as the volume of the pyramid of base K and height $h_a/|a|$ (see Figure 8)

$$\tau_K^{RFB} = \frac{1}{|K|} \int_K b_K \approx \frac{1}{|K|} \int_K \tilde{b}_K = \frac{1}{|K|} \left(\frac{1}{3} |K| \frac{h_a}{|a|} \right) = \frac{h_a}{3|a|} \quad (2.60)$$

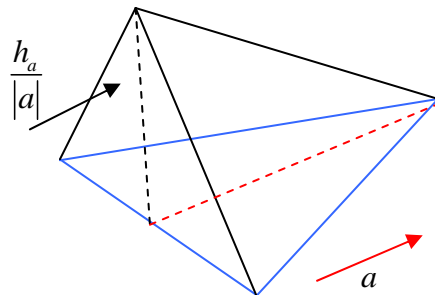


Figure 8. The adjoint residual-free bubble in 2D

This value is straight-forward to compute and gives similar and good approximation of τ_K in the convection-dominated regime. In the diffusion limit case [59], when the diffusion term is large with respect to the convection term, we have

$$\tau_K^{RFB} = \frac{\int_K b_K}{|K|} \approx c \frac{h_K^2}{k} \quad (2.61)$$

where c is a constant that depends on K and h . We can see that in both regimes, these stabilizing parameters are very similar to those presented in the previous section.

2.4 Application to heat transfer equation

In this section, the equations governing the heat transfer in the heat treatment furnaces are presented. The treatment processes inside industrial furnaces involves three modes: the radiation, conduction and convection. The unknown temperature T (Kelvins) must be found from an equation that simultaneously incorporates all three heat transfer processes. Recall that the conduction heat transfer occurs in fixed solids that experience internal temperature gradients (Figure 9). The conduction heat flow is defined by Fourier's law as

$$\mathbf{q}_{cond}'' = -k\nabla T \quad (2.62)$$

where k (W/mK) is the thermal conductivity of the solid multiplied by the temperature gradient. When the heat is transferred between the ingot and its surroundings, the furnace, via a flowing fluid, at a certain velocity, transport mechanisms occur, and the process is known as the thermal convection.

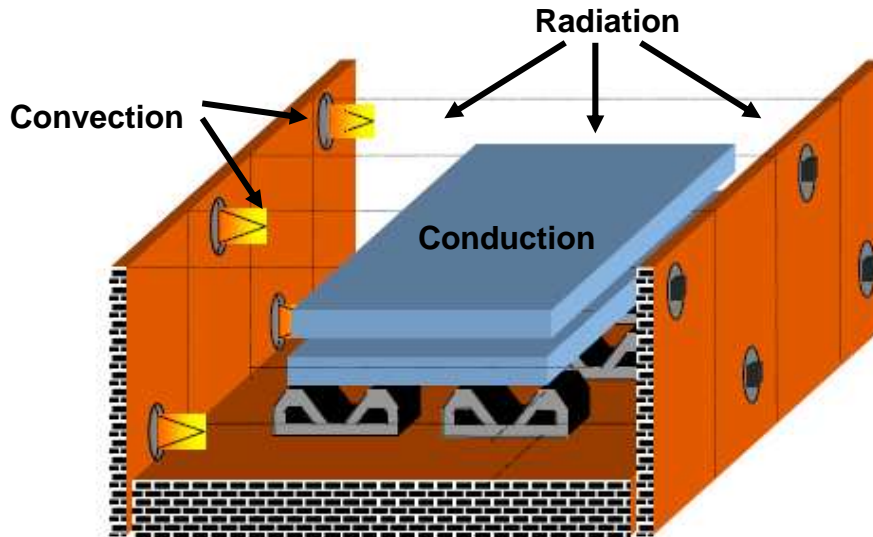


Figure 9. Heating process of an immersed solid inside an industrial furnace

Radiation heat transfer is concerned with the exchange of thermal radiation energy between two or more bodies (wall, solid,...). The heat transferred into or out of an object by thermal radiation is a function of several components. These include its surface reflectivity, emissivity, surface area, temperature, and geometric orientation with respect to other thermally participating objects. More details about the radiative heat transfer will be treated later in chapter 5.

By combining those modes, the energy conservation equation will be governed by a time-dependent conduction-convection equation as follow:

$$\rho c_p \left(\frac{\partial T}{\partial t} + \mathbf{v} \cdot \nabla T \right) - \nabla \cdot (\kappa \nabla T) = f \quad (2.63)$$

where, again T is the temperature of the treated domain (fluid or solid) having the respective material properties: κ is the thermal conductivity, ρ (kg/m^3) is the mass density, c_p is the specific heat (J/kg.K), v is a computed velocity (m/s) and f is the energy source term. The following initial condition is applied $T(x, t_0) = T_0(x)$ where T_0 is the initial temperature distribution over the domain.

Different boundary conditions can be considered for the problem:

$$\begin{aligned} T &= g \quad \text{on } \Gamma_s \\ -k\nabla T \cdot \mathbf{n} &= q_w \quad \text{on } \Gamma_q \\ -k\nabla T \cdot \mathbf{n} &= h_c(T - T_{out}) + q_r \quad \text{on } \Gamma_c \end{aligned} \quad (2.64)$$

Here, g represents the wall temperature imposed on a portion of the boundary Γ_s , q_w is a prescribed inflow heat flux imposed on the wall Γ_q , while the convection boundary conditions are imposed on the wall Γ_c with h_c as a convection heat transfer coefficient, T_{out} as the external temperature and q_r is the radiative heat flux. The dimensionless numbers relevant in this problem, the Péclet number take the following form:

$$P_e^K = \frac{\rho c_p |v| h_K}{2\kappa} \quad (2.65)$$

Discretization of the time derivative can be made as shown previously by means of the θ scheme. For simplicity in the notation, when $\theta = 1$, backward Euler method, Eq. (2.63) yields the following linear ordinary differential equation at each time step:

$$\rho c_p \frac{T^{n+1} - T^n}{\Delta t} + \rho c_p v \cdot \nabla T^{n+1} - \nabla \cdot (\kappa \nabla T^{n+1}) = f \quad \text{in } \Omega \times (0, t_f) \quad (2.66)$$

The stabilized variational formulation for the now discrete-in-time problem reads

$$\begin{aligned} \mathcal{L}(T_h, v_h) + S^{SUPG}(T_h, v_h) + S^{SCPG}(T_h, v_h) + (h_c T_h^{n+1}, v_h)_{\Gamma_c} \\ = \left(\frac{\rho c_p}{\Delta t} T_h^n + f, v_h \right) + (q_w, v_h)_{\Gamma_q} + (h_c T_{out} + q_r, v_h)_{\Gamma_c} \end{aligned} \quad (2.67)$$

Where

$$\begin{aligned} \mathcal{L}(T_h, v_h) &= \left(\frac{\rho c_p}{\Delta t} T_h^{n+1}, v_h \right) + (\rho c_p v \cdot \nabla T_h^{n+1}, v_h) + (k \nabla T_h^{n+1}, \nabla v_h) \\ S^{SUPG}(T_h, v_h) &= \sum_K (\mathcal{R} T_h, \tau_K v \cdot \nabla v_h)_K \\ S^{SCPG}(T_h, v_h) &= \sum_K (\mathcal{R} T_h, \tau_K^c v_{||} \cdot \nabla v_h)_K \\ \mathcal{R} T_h &= \frac{\rho c_p}{\Delta t} T_h^{n+1} + v \cdot \nabla T_h^{n+1} - \nabla \cdot (\kappa \nabla T_h^{n+1}) - \frac{\rho c_p}{\Delta t} T_h^n - f \end{aligned} \quad (2.68)$$

The resulting equation shows at each time step an identical structure with respect to the stationary convection-diffusion-reaction equation. The space-discrete formulation for the heat transfer equation is now complete.

Additional stabilizing terms are added in a consistent way to reduce and possibly to eliminate numerical oscillations in the streamline direction and the temperature gradient direction specifically at the burner's level, where the convection is dominated. In the last section, some numerical examples will illustrate the behavior of the proposed method. These terms are tuned by the local stabilizing parameters given here for the thermal problem by: (see equation (2.22), (2.25) and (2.30))

$$\tau_K \approx \frac{\Delta t h^2}{6k\Delta t \zeta(Pe_2) + \rho c_p h^2 \zeta(Pe_1)}$$

where

$$Pe_1 = \frac{6k\Delta t}{\rho c_p h^2} \quad \text{and} \quad Pe_2 = \frac{\rho c_p |v| h}{3k} \tag{2.69}$$

At ingot's level, the only mechanism for heat mass transfer is the conduction. It is well known that the numerical solution of unsteady conduction problems using the Galerkin finite element method, based on piecewise polynomial interpolations, is often affected by severe numerical instabilities unless appropriately refined meshes are used in the solution's layers. In this case, the solution exhibits steep gradients known usually as thermal shocks, that usually appear in the boundary of a domain initially hot (or cold) that is suddenly cooled (resp. heated). In particular, the Galerkin method might fail to solve unsteady diffusion problems when either the diffusion parameter is low and/or small time steps are used in time discretization ($\varepsilon \leq h^2 \Delta t^{-1}$). For the thermal mechanical analysis, the problem can be serious in some cases specifically when the material behavior is temperature dependent.

This difficulty has been object of research for the last decades, the purpose being to get finite element formulations that are stable for problems with boundary layers and coarse mesh accurate enough for smooth problems. In the next section, a new approach based on the variational multiscale method will be presented here to obtain a space-time stabilized finite element formulation that ensures an oscillation-free solution and treats the thermal shocks.

2.5 Thermal shock treatment for unsteady diffusion problems

Abstract

This paper presents an original technique via finite elements to treat numerically the thermal shocks in heat transfer finite element analysis using a continuous P1 element. The method consists in a slight modification on the standard enriched finite element approaches. It will be applied here to the transient conduction heat equation where the classical Galerkin method is shown to be unstable. The proposed method consists in adding and eliminating bubbles to the finite element space and then to interpolate the solution to the real time step. This modification is equivalent to the addition of a stabilizing term tuned by a local time-dependent stability parameter, which ensures an oscillating-free solution. To validate this approach, the numerical results obtained in classical 2D and 3D benchmark problems are compared with the Galerkin and the analytical solutions.

Keywords: Finite elements, stabilization, heat conduction, static condensation

*** see attached paper at the end of the chapter (p. 65)**

2.6 Numerical tests and validation

In this section a series of numerical calculations is performed to assess the effectiveness of the methods described previously. Numerical examples for stationary and time-dependent problems are given in the following. The main interest of these examples is to test how well the space-time stability theory developed herein matches with computation. More applications on thermally coupled flows and heat transfer inside industrial furnaces will be treated later in chapter 5 and 6.

2.6.1 Transient CDR problems

In the section, several cases are considered in a unit square domain given by $\Omega = [0,1] \times [0,1]$. These problems have been widely studied in literature, e.g., (see [4] and [5]) as good examples for the accuracy of various numerical schemes. Two tests series will be considered here. In the first one, no reaction term will be considered and zero Dirichlet boundary conditions are imposed on all sides. The source term is assumed to be equal to one and the domain is spatially discretized by 16×16 elements such that $h \approx 0.0625$. The simulations were performed with final time $T=2s$ and the time step $\Delta t=0.1s$. The flow is unidirectional and constant with velocity components: $a_x = \cos \alpha$, $a_y = \sin \alpha$ as shown in Figure 10.

Recall that the element Péclet number and the element Damköhler number are given by:

$$P_e(K) = \frac{h|a|}{2k} \quad \text{and} \quad Da_e = \frac{\sigma h}{|a|} \quad (2.70)$$

The diffusion and reaction coefficients may have different values, leading to different Péclet and Damköhler numbers respectively.

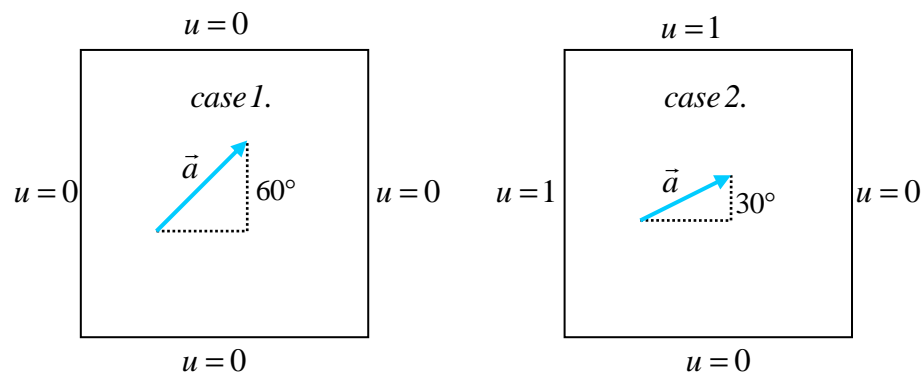


Figure 10. Dirichlet boundary conditions and flow direction: case 1 (left) and case 2 (right)

The results obtained from the first test series for different Péclet numbers are shown in Figure 11. As expected, all methods give good results for low Péclet number without extra diffusivity. All solutions are wiggle free and indistinguishable. When the diffusion coefficient is decreased, the Péclet number increases over the unity, the discontinuity in the boundary data propagates into the computational region, and some wiggles originate at the boundary.

As k decreased further, the Galerkin solution blows up and the SUPG method produces smaller oscillations towards the outflow boundary. These remaining wiggles are due to cross-wind instabilities. On the other hand, the SCPG method show no oscillations and a smoothed solution is obtained.

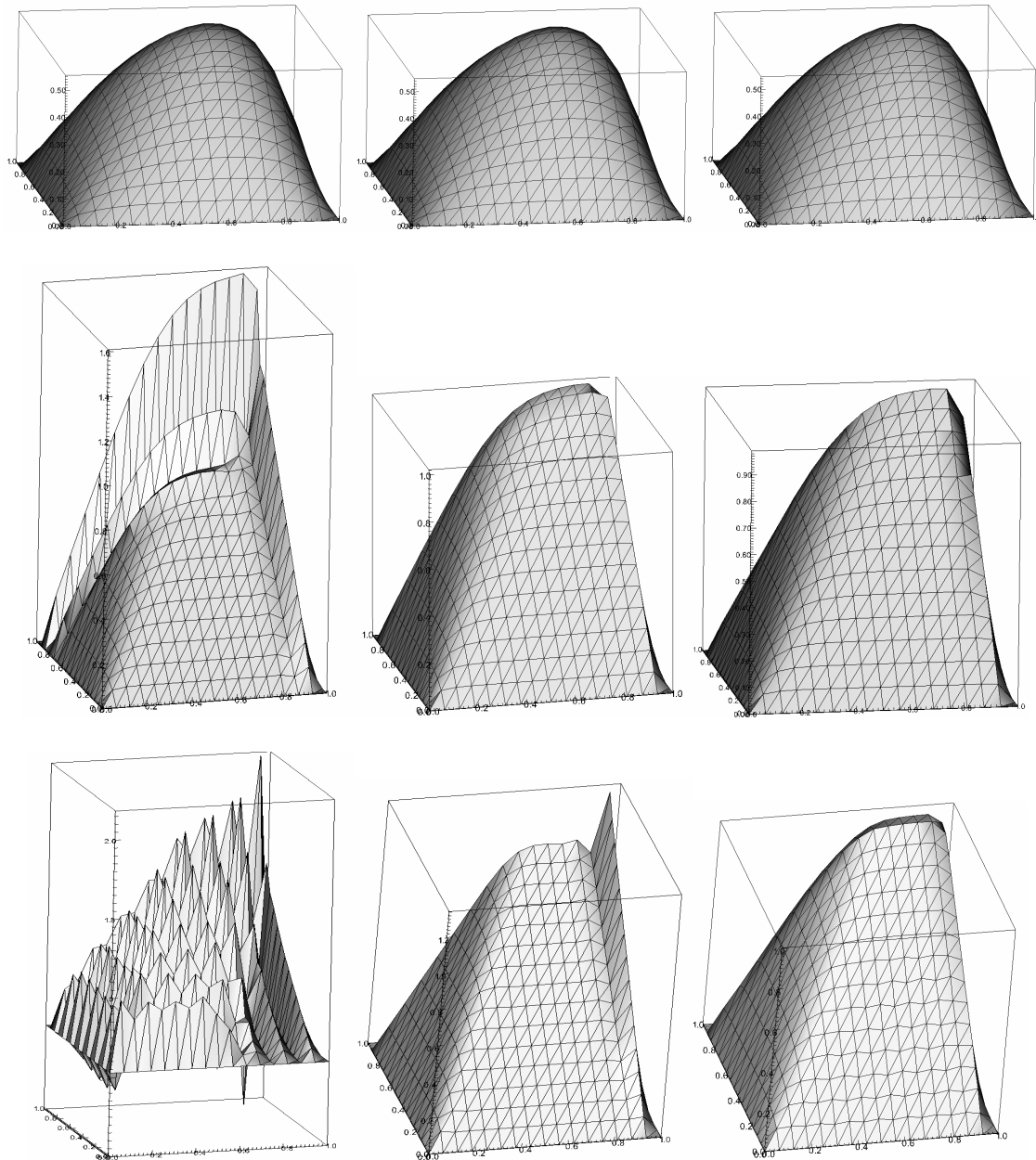


Figure 11. Comparison of the Galerkin (left), the SUPG (center) and the SCPG(right). From top to bottom, $Pe_K=0.5$, $Pe_K=5$, $Pe_K=50$

In the second example, different Dirichlet boundary conditions and flow direction are considered, (see case 2 in Figure 10). Here the parameters are chosen to have both convection and reaction-dominated problem; $Pe_K = 10$ and $Da_K = 8$. Figure 12 shows the results obtained with the Galerkin, the SUPG and the SCPG methods.

As expected in the flow direction, the Galerkin solution yields oscillations towards the boundary $y=1$ whereas the SUPG produces oscillations with smaller amplitude towards the boundary $x=0$. Even on this coarse grid, the SCPG succeeded to remove most of the oscillations and to provide a good approximation of the solution in both directions.

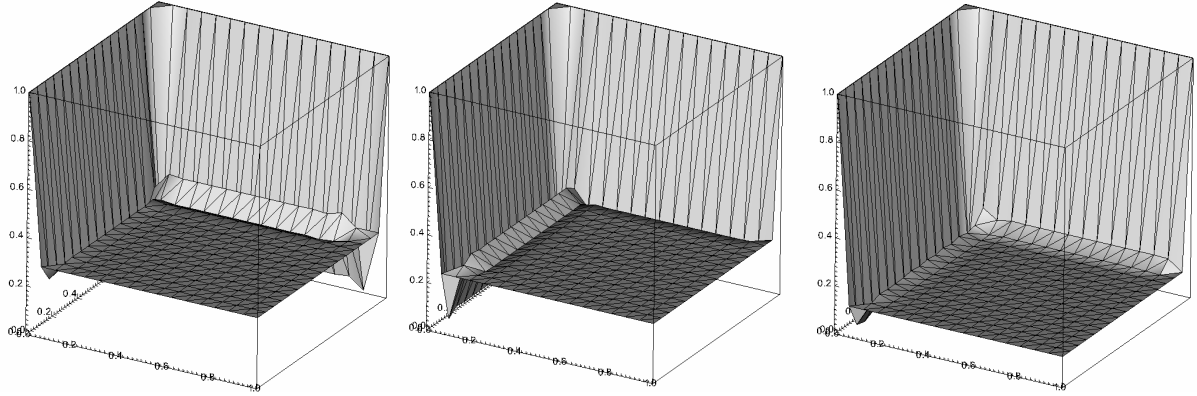


Figure 12. Comparison of the Galerkin (left), the SUPG (center) and the SCPG(right).

2.6.2 Transient pure convection

We begin to compare the Galerkin, SUPG and the SCPG methods in the pure advection limit, i.e. for $\kappa = 0$. In order to provide a representative range of CFL values for each example, different time steps are used. Two dimensional unit square $\Omega = [0,1] \times [0,1]$ with zero source term is considered. The problem is solved using an unstructured mesh of 41×41 elements. This gives a partition of 2024 degrees of freedom, 3897 triangles and a mesh parameter $h \approx 0.025$. This problem was first considered by P.B. Bochev *et. al* in [61] for studying transient advection of a cylinder with radius of 0.2, initially positioned at \mathbf{x}_c using a given velocity \mathbf{v} . For further details about transient advection-diffusion problems, we highly recommend this reference. In this paper, a full comparison was only made between the Galerkin and the SUPG solutions. Here we have added the SCPG method, as pointed out in the conclusion and recommended by the authors, to preclude the overshoots and undershoots in the neighborhood of the vicinity.

The boundary and initial condition values are as follow (Figure 13):

$$u_0(x) = \begin{cases} 1 & \text{if } |x - x_c| \leq 0.2 \\ 0 & \text{elsewhere} \end{cases}, \quad x_c = \begin{pmatrix} 0.25 \\ 0.25 \end{pmatrix}, \quad CFL = v \frac{\Delta t}{h} \quad (2.71)$$

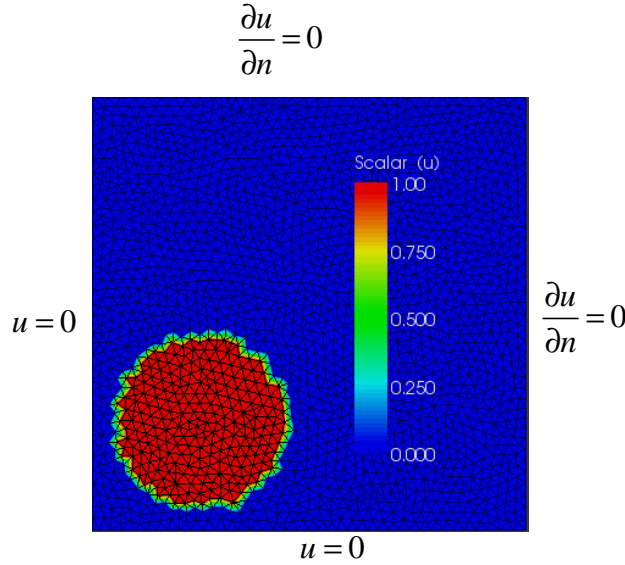


Figure 13. Problem domain with initial and boundary conditions.

Two advection fields were considered:

$$\begin{aligned} \text{case 1. } \mathbf{v} &= \begin{bmatrix} 1.0 \\ 0.7 \end{bmatrix} && \text{i.e. constant velocity} \\ \text{case 2. } \mathbf{v} &= \begin{bmatrix} y + 1.0 \\ x + 0.7 \end{bmatrix} && \text{i.e. variable solenoidal velocity} \end{aligned} \tag{2.72}$$

Both examples are discretized in time using the Crank-Nicolson method. In order to study the behaviour of the method in respect with the time step, we used the following data:

Δt	0.1s	0.01s	0.001s	0.0005s
CFL	4.884	0.4884	0.04884	0.02441

Each refinement of the time step leads to a change in the CFL number, above and below one. In both examples, we can see that the SUPG and SCPG methods perform better than the Galerkin solution by suppressing the global spurious oscillations even for small time steps. These conclusions are confirmed by plots of solution profiles along the lines $x=0.75$ and $y=0.6$ in the case 1 and along the lines $x=1$ and $y=0.85$ in the case 2.

However, in the vicinity of sharp gradient and internal layer, the SUPG solution still contains some remained oscillations. Figures 14 and 15 show graphically these remarks. By adding an artificial diffusion in the gradient solution direction, the SCPG method displays no non-physical oscillations and removes these over and undershoots in the neighbourhood of the discontinuities. Furthermore, the graphical comparisons between snapshots of the solutions at the finest time step in Figures 16 and 17 validate our remarks. Recall that the numerical results presented here are in excellent agreement with the chosen article.

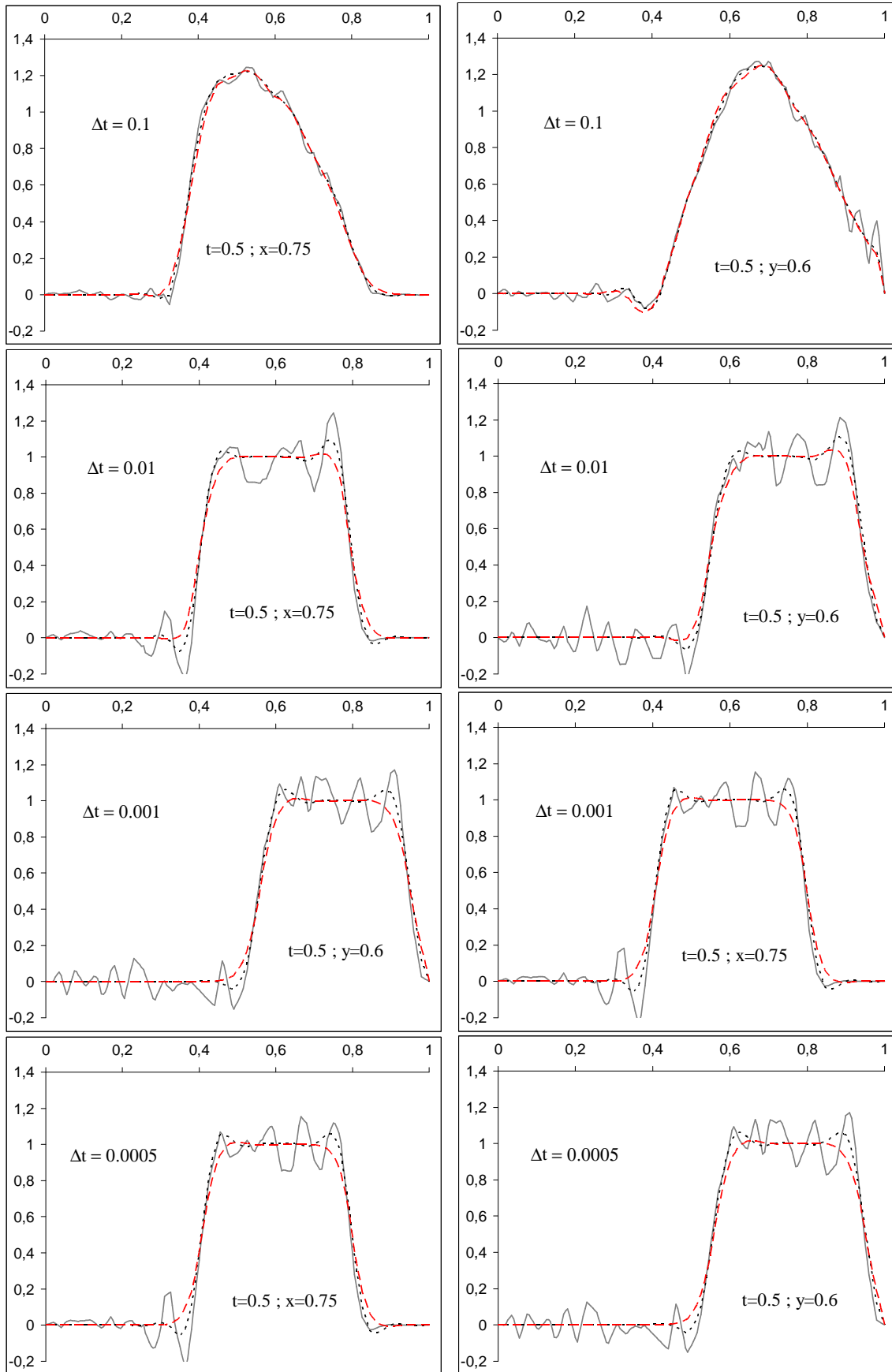


Figure 14. Profile of the solutions: Galerkin (solid), SUPG (dotted) and SCPG (dashed)

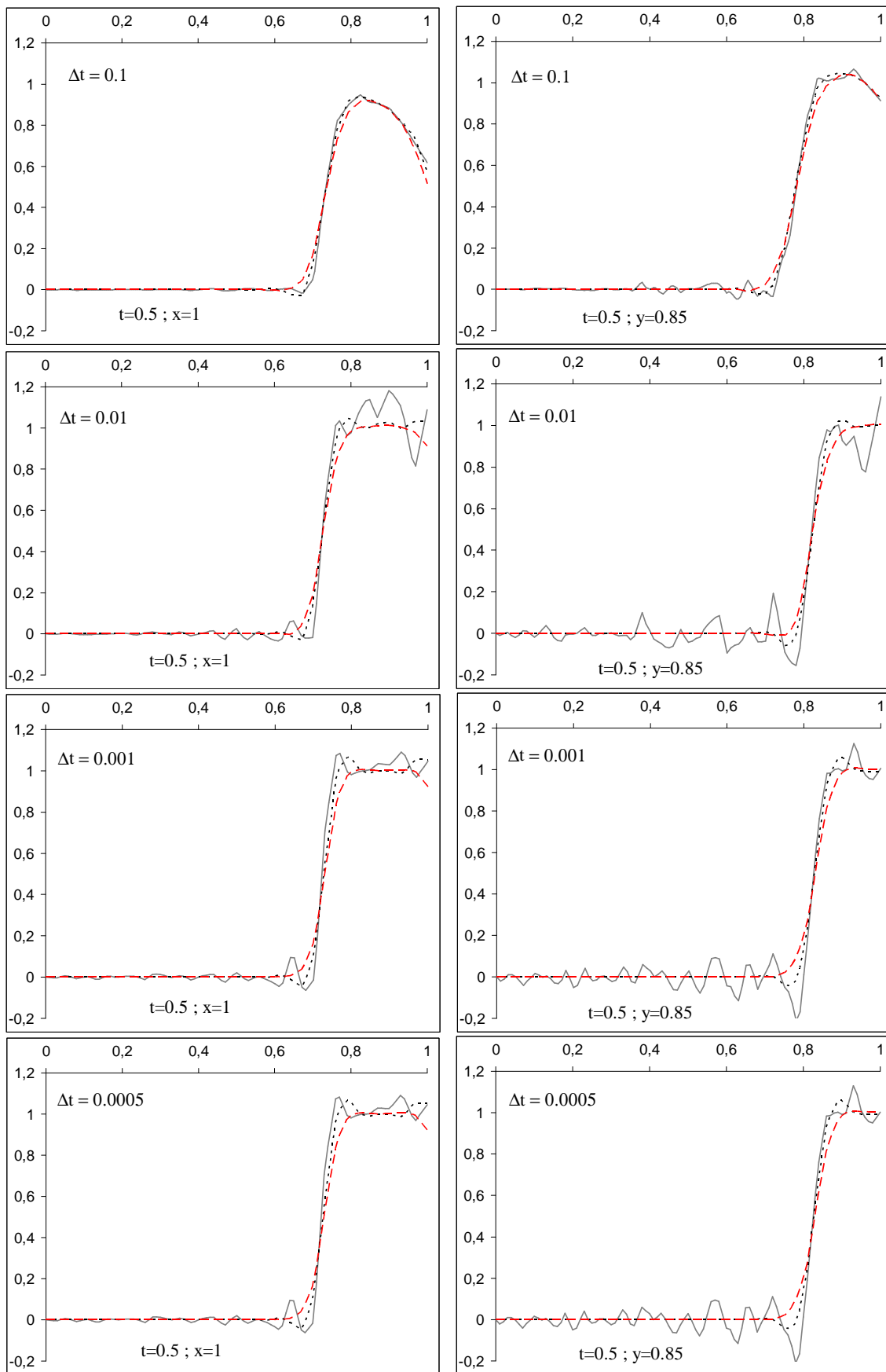


Figure 15. Profile of the solutions: Galerkin (solid), SUPG (dotted) and SCPG (dashed)

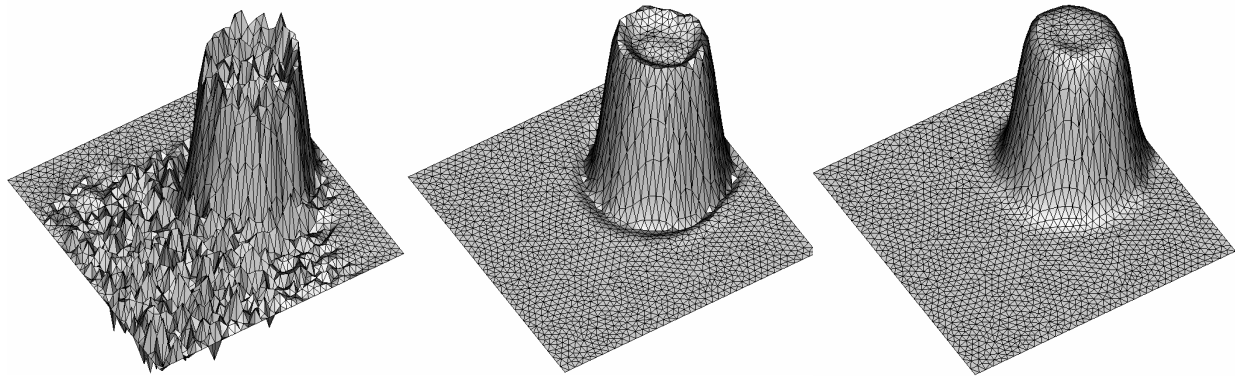


Figure 16. Profile of the solutions at $t=0.5$, $\Delta t=10^{-3}$: Galerkin (left), SUPG (centre) and SCPG (right)

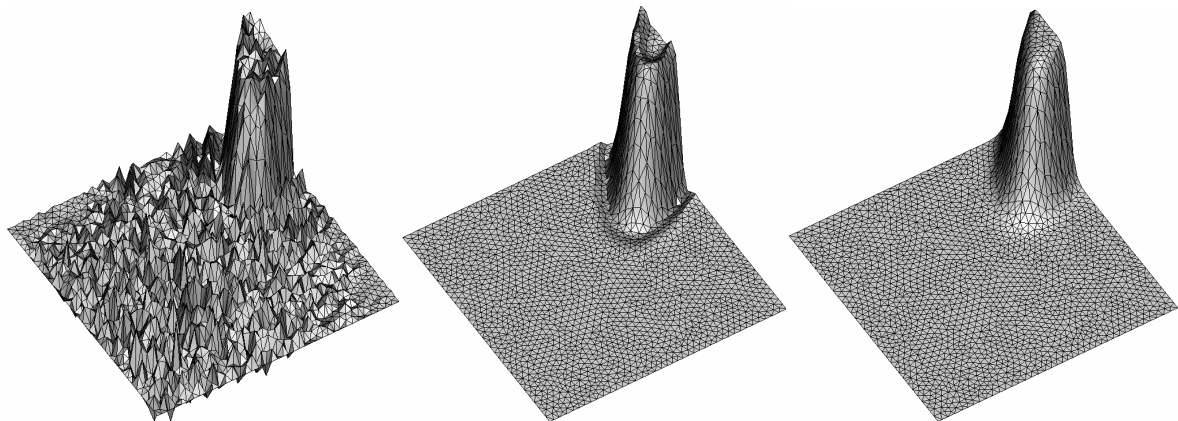


Figure 17. Profile of the solutions at $t=0.5$, $\Delta t=10^{-3}$: Galerkin (left), SUPG (centre) and SCPG (right)

2.6.3 Transient heat transfer

An interesting internal flow used for validation of unsteady flow code is the forced convection heat transfer between two parallel plates. A diagram of the calculation domain and boundary conditions is shown in Figure 18. This situation may be viewed as the modelling of a high temperature burner inside the furnace facing a 2D cold wall or cold solid. Near that region, a formation of a thermal boundary layer will be observed. Here, the diffusion coefficient is fixed to one and the source term assumed to be zero. Therefore, the chosen velocity will determine the Péclet number. Three numerical experiments have been performed using the following constant convecting velocities: *60, 200 and 2000* respectively. Recall that these experiments are inspired from the work of Lim *et al.* in [63] and then followed by S.J. DeSilva *et al.* in [64]. These interesting papers deal with the boundary element method applied on transient convection-conduction problems. It's shown that for the above example we can obtain a closed form analytical solution specifically for high Péclet numbers. For further details about the derivation of the asymptotic solution, the reader could refer to Lim *et al.* More recent article about the same subject applied on different numerical examples can be also found in [62].

The exact solution is given by:

$$T(x,t) = \begin{cases} 0.5 \left[2 - \operatorname{erfc}\left(-\frac{x - Pe.t}{2\sqrt{t}}\right) \right] & \text{if } x \leq Pe.t \\ 0.5 \left[\operatorname{erfc}\left(-\frac{x - Pe.t}{2\sqrt{t}}\right) \right] & \text{if } x > Pe.t \end{cases} \quad (2.73)$$

A mesh sensitivity study was conducted to validate the capability of the method. Therefore, three different unstructured grids are used for this comparisons with a mesh size $h \approx 0.05, 0.025$ and 0.01 respectively. (Figure 19)

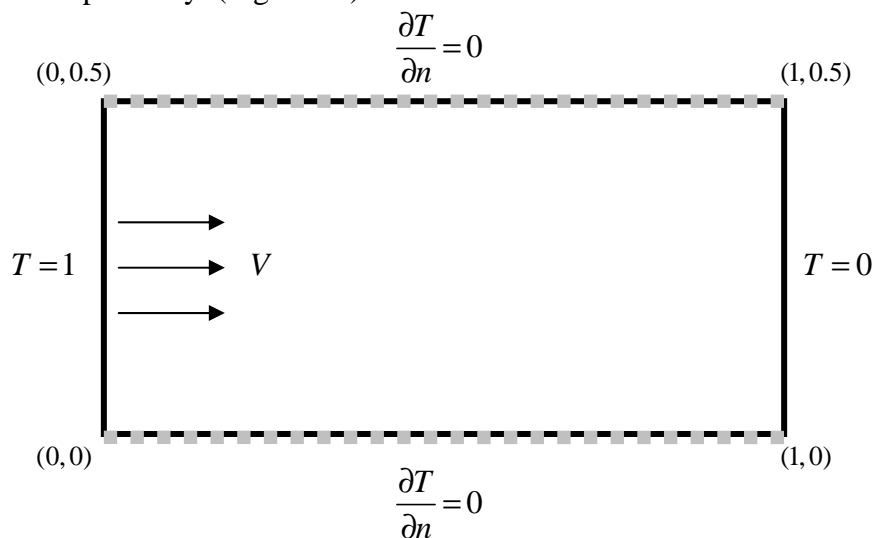


Figure 18. Thermal boundary layer: problem statement

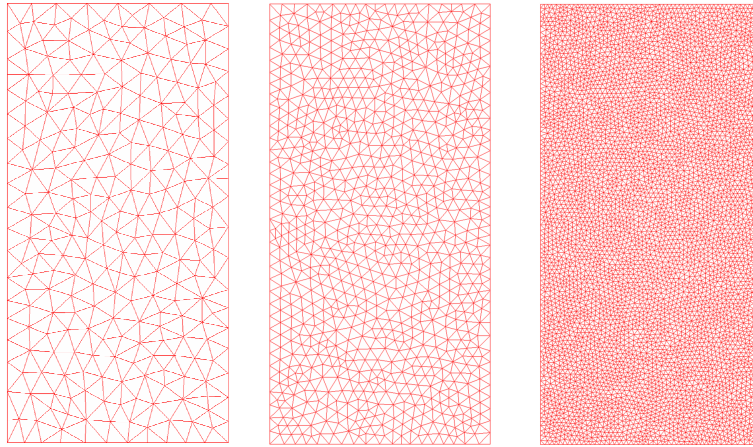


Figure 19. Different meshes with h equal to 0.05, 0.025 and 0.01

The temperature profiles for different times and different Pe numbers are illustrated in Figures 20-22. As expected, for low Pe , the solutions are accurate and coincide with the exact solution. As the Péclet number increases, the convection dominates and the flow gives rise to travelling waves with sharp gradient. One can clearly observe that the standard Galerkin formulation produces some oscillations specifically near the boundary layer on coarse mesh. The stabilized scheme yields satisfactory results on all meshes. With finer discretization, good improvements in the results are observed. These remarks can be seen graphically on mesh 3.

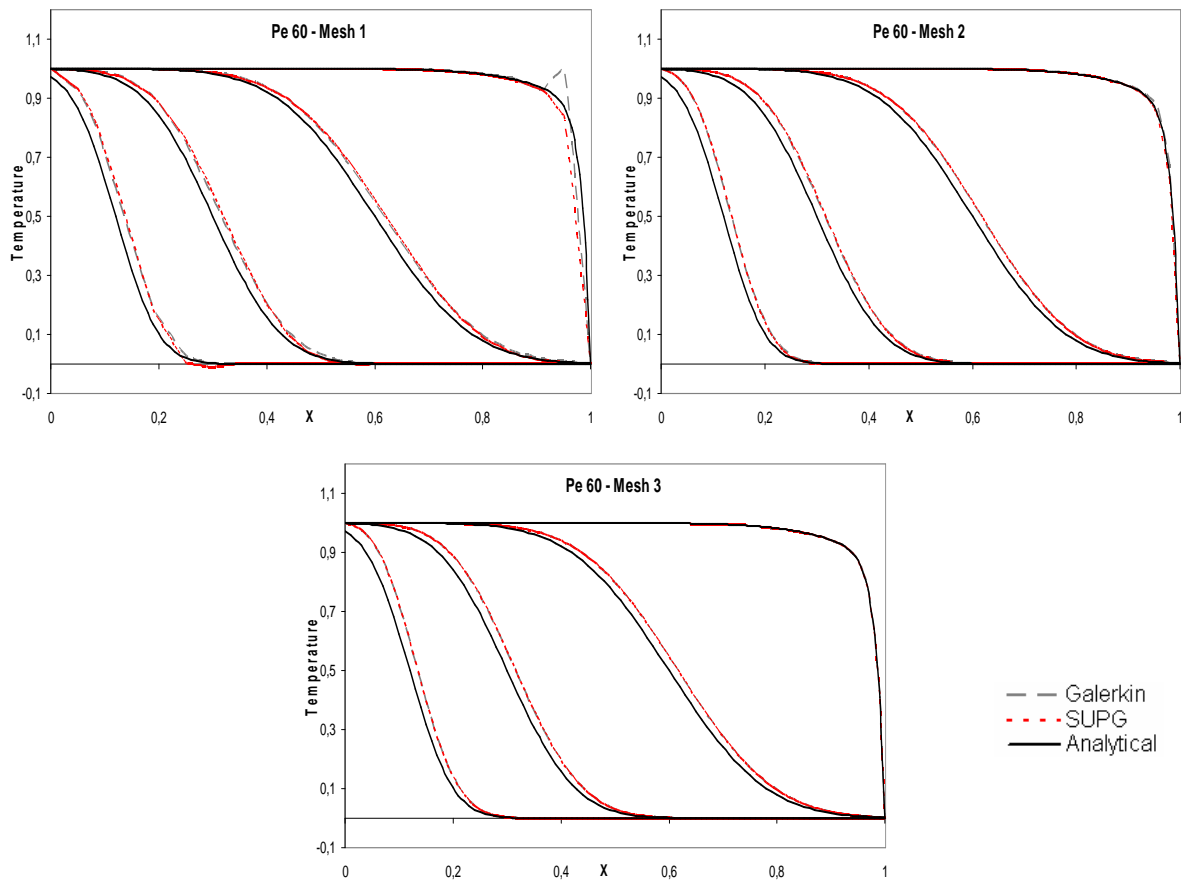


Figure 20. Predicted temperature profiles at different time $t=2 \cdot 10^{-3}$, $5 \cdot 10^{-3}$, 0.01 and 0.02s

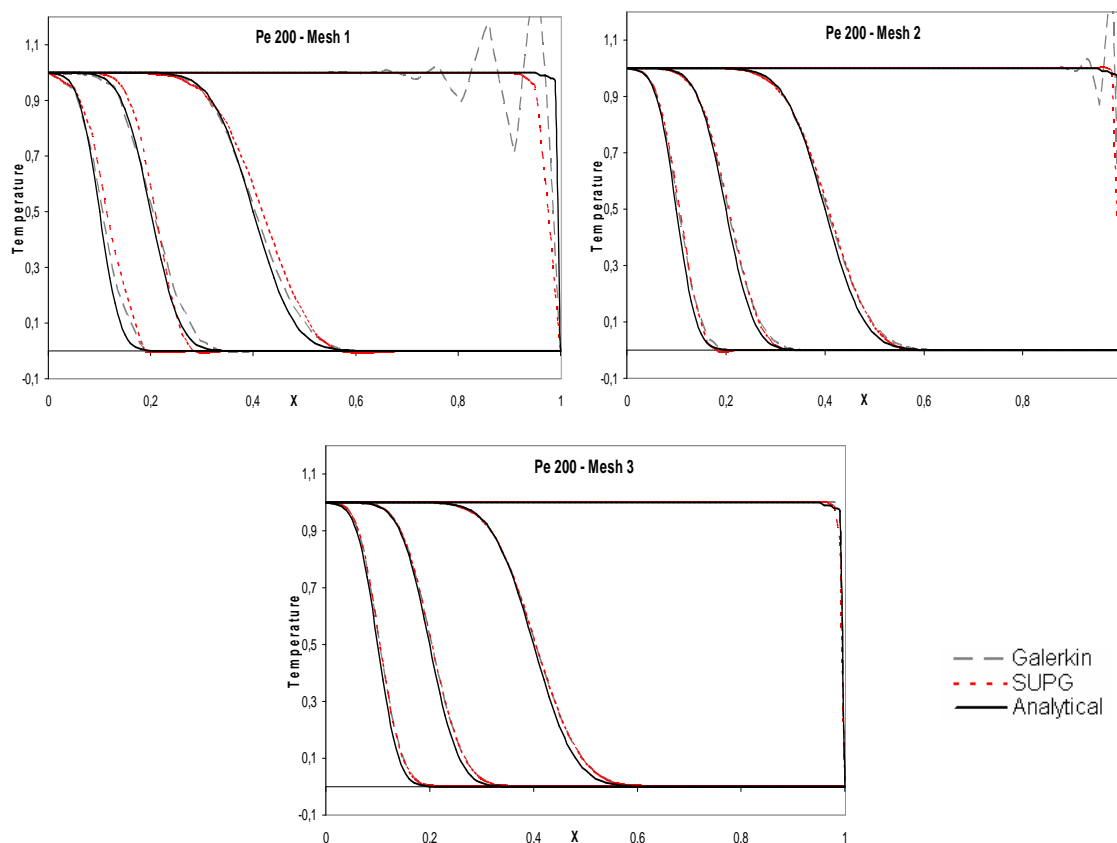


Figure 21. Predicted temperature profiles at different time $t=5 \cdot 10^{-4}$, $1 \cdot 10^{-3}$, $2 \cdot 10^{-3}$ and $5 \cdot 10^{-3}$ s

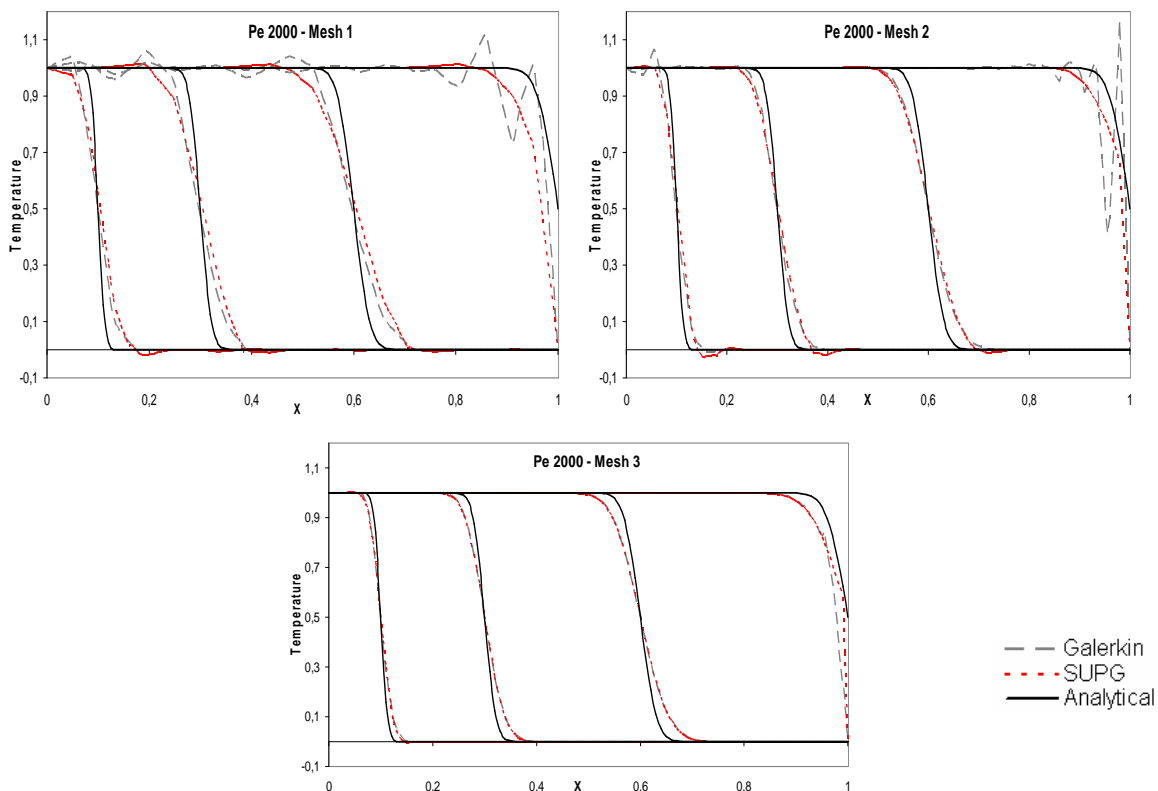


Figure 22. Predicted temperature profiles at different time $t=5 \cdot 10^{-5}$, $1.5 \cdot 10^{-4}$, $3 \cdot 10^{-4}$ and $5 \cdot 10^{-4}$ s

2.7 Conclusion

The need for stabilization methods in the case of time-dependent convection diffusion reaction problems has been revisited. Different stabilized methods were introduced and discussed. Extension of these methods to transient problems was proposed and analysed. For convection-dominated problems, it is shown that the SUPG and the SCPG methods are free of oscillations, yield satisfactory results and easy to implement. In the case of transient diffusion problems, a space-time stabilized finite element method has been presented and analysed to treat thermal shock in numerical heat transfer. The most important part of this chapter is the application of these stabilized formulations to the heat transfer equation needed later for simulation of heat treatment inside industrial furnaces. Finally, some numerical examples are given to study the efficiency of the proposed methods.

References

- [1] R. Courant, E. Isaacson, and M. Rees. On the solution of nonlinear hyperbolic differential equations by finite differences. *Comm. on Pure and Applied Math.*, 5:243-255, 1952.
- [2] I. Christie, D.F. Griffiths, A.R. Mitchell, and O.C. Zienkiewicz. Finite element methods for second order differential equations with significant first derivatives. *Internat. J. Numer. Methods Engrg.*, 10:1389-1396, 1976.
- [3] A.N. Brooks and T.J.R. Hughes. Streamline upwind/Petrov-Galerkin formulations for convection dominated flows with particular emphasis on the incompressible Navier-Stokes equations. *Comput. Methods Appl. Mech. Engrg.*, 32:199-259, 1982.
- [4] T.J.R. Hughes, M. Mallet, and A. Mizukami. A new finite element formulation for computational fluid dynamics: II. beyond SUPG. *Comput. Methods Appl. Mech. Engrg.*, 54:341-355, 1986.
- [5] T.J.R. Hughes and M. Mallet. A new finite element formulation for computational fluid dynamics : IV. a discontinuity-capturing operator for multidimensional advective-diffusive systems. *Comput. Methods Appl. Mech. Engrg.*, 58:329- 336, 1986.
- [6] T.J.R. Hughes, L.P. Franca, and G.M. Hulbert. A new finite element formulation for computational fluid dynamics: VIII. the Galerkin/least-squares method for advective-diffusive equations. *Comput. Methods Appl. Mech. Engrg.*, 73:173-189, 1989.
- [7] J. Donea, V. Selmin, and L. Quartapelle. Recent developments of the Taylor- Galerkin method for the numerical solution of hyperbolic problems. In *Numerical Methods for Fluid Dynamics III*, pages 171-185, New York, 1988. Oxford Univ. Press.
- [8] S.V. Patankar. *Numerical Heat Transfer and Fluid Flows*. McGraw-Hill, New York, 1980.
- [9] Dena Hendriana , Computational Modelling Of Heat Transfer In Reheat Furnaces, *M.S. Thesis, Dept. of Mechanical Engineering*, Massachusetts Institute of Technology (MIT), 1994, Available from: <http://hdl.handle.net/1721.1/37735>
- [10] Sheu, T. W. H. and Chen, H. Y. H., A multi-dimensional monotonic finite element model for solving the convection-diffusion-reaction equation, *International Journal for Numerical Methods in Fluids*, Vol. 39, pp. 639-656, 2002
- [11] Putti, M. and Cordes, C., Finite element approximation of the diffusion operator in tetrahedral, *SIAM Journal on Scientific Computing*, Vol. 19 No. 4, pp. 1154-1168, 1998
- [12] Kosik, R., Fleischmann, P., Haindl, B., Pietra, P. and Selberherr, S. , On the interplay between meshing and discretization in three-dimensional diffusion simulation, *IEEE Transactions on Computer-Aided Design of Integrated Circuits and Systems*, Vol. 19 No. 11, pp. 1233-1240, 2000

- [13] Pichelin, E. and Coupez T., A Taylor discontinuous Galerkin method for the thermal solution in 3D mold filling, *Comput. Methods Appl. Mech. Engrg.* 178, 153-169, 1999
- [14] Fachinotti V. and Bellet M., Linear tetrahedral finite elements for thermal shock problems, *International Journal of Numerical Methods for Heat & Fluid Flow*, Vol. 16, pp. 590-601, 2004
- [15] Zienkiewicz, O. C. and Taylor, R. L., *The finite element method - The basis*, Butterworth-Heinemann, Oxford, 2000
- [16] Donea, J. and Huerta, A. *Finite Element Methods for Flow Problems*, J. Wiley & Sons, Chichester, 2002, 352 pp. ISBN 0-471-496669
- [17] T.J.R. Hughes, *The Finite Element Method: Linear Static and Dynamic Finite Element Analysis*, Dover Publications, Mineola, 2000.
- [18] Heywood J, Rannacher R, Finite-element approximation of the nonstationary Navier-Stokes problem. IV. Error analysis for second-order time discretization. *SIAM J Numer Anal* 27(2):353–384, 1990
- [19] Huerta, A.; Fernández-Méndez, S., Time accurate consistently stabilized mesh-free methods for convection dominated problems. *International Journal For Numerical Methods in Engineering* , 56 (9) : 1225-1242. ISSN: 0029-5981, 2003
- [20] Hughes, T.J.R. and A.N. Brooks, A Multi-Dimensional Upwind Scheme with No Crosswind Diffusion, in: *Finite Element Methods for Convection Dominated Flows*, T.J.R. Hughes (ed.), *ASME Monograph AMD-34*, (1979), pp. 19–35.
- [21] G. Hauke and T.J.R. Hughes, A comparative study of different sets of variables for solving compressible and incompressible flows, *Comp. Meth. Appl. Mech. Eng.*, pp1–44, 1998
- [22] A. Mizukami and T.J.R. Hughes. A Petrov-Galerkin finite element method for convection dominated flows: an accurate upwinding technique for satisfying the maximum principle. *Comput. Methods Appl. Mech. Engrg*, 50:181-193, 1985.
- [23] A. Mizukami. An implementation of the streamline-upwind/Petrov-Galerkin method for linear triangular elements. *Comput. Methods Appl. Mech. Engrg*, 49:357-364, 1985.
- [24] I. Harari and T.J.R. Hughes, Galerkin/least-squares finite element methods for the reduced wave equation with non-reflecting boundary conditions in unbounded domains, *Computer Methods in Applied Mechanics and Engineering*, 98(3), 411-454 (1992).
- [25] I. Harari and T.J.R. Hughes, Stabilized finite element methods for steady advection diffusion with production, *Computer Methods in Applied Mechanics and Engineering*, 115(1-2), 165-191, 1994.
- [26] T.J.R. Hughes. Multiscale phenomena: Green's functions, the Dirichlet-to-Neumann formulation, subgrid scale models, bubbles and the origins of stabilized methods. *Comput. Methods in Applied Mechanics and Engineering*, 127:387-401, 1995.

- [27] A. Russo F. Brezzi, L.D.Marini. On the choice of a Stabilizing Subgrid for Convection Diffusion Problems. *Comput. Methods Appl. Mech. Engrg.*, 194(2-5):127{148, 2005.
- [28] F.Brezzi, L.P. Franca, T.J.R. Hugues, A.Russo. “ $b = \int g$ ”, *Computer methods in applied mechanics and engineering*, 145, 329-339 (1997).
- [29] L.P.Franca, C.Farhat. Bubble functions prompt unusual stabilized finite element methods. *Comput. Methods. in Applied Mech. and Eng.*, 123:299, 1995.
- [30] L.P.Franca, F. Valentin. On an improved unusual stabilized finite element method for the advection-reactive- diffusive equation. *Comput. Methods. in Applied Mech. and Eng.*, 190:1785, 2001.
- [31] R.Codina. Comparison of some finite element methods for solving the diffusion convection-reaction equation. *Comput. Methods. in Applied Mech. and Eng.*, 156:185-210, 1998.
- [32] G.Hauke. A simple subgrid scale stabilized method for the advection-diffusion-reaction equation. *Comput. Methods. in Applied Mech. and Eng.*, 191:2925-2947, 2002.
- [32] E. Dick. Accurate Petrov-Galerkin methods for transient convective diffusion problems. *Inter. J. Num. Methods in Engrg*, 19:1425-1433, 1983.
- [33] R. Codina , On stabilized finite element methods for linear systems of convection–diffusion-reaction equations. *Comput. Methods Appl. Mech. Engrg.* 188 , pp. 61–88, 2000
- [34] F. Shakib, T.J.R. Hughes and Z. Johan , A new finite element formulation for computational fluid dynamics: X. The compressible Euler and Navier–Stokes equations. *Comput. Methods Appl. Mech. Engrg.* 89, pp. 141–219, 1991
- [35] R. Codina, Stabilized finite element approximation of transient incompressible flows using orthogonal subscales, *Comput. Methods Appl. Mech. Engrg.* 191, pp. 4295–4321, 2002.
- [36] R. Codina, Analysis of a stabilized finite element approximation of the transient convection–diffusion equation using orthogonal subscales, *Comput. Visual. Sci.* 4 (3), pp. 167–174, 2002
- [37] Velamur Asokan Badri Narayanan , Nicholas Zabaras, Variational multiscale stabilized FEM formulations for transport equations: stochastic advection-diffusion and incompressible stochastic Navier-Stokes equations, *Journal of Computational Physics*, v.202 n.1, p.94-133, 2005
- [38] Volker John, Ellen Schmeier Finite element methods for time-dependent convection-diffusion-reaction equations with small diffusion , *Comput. Meth. Appl. Mech. Engrg.*, 198, 475 - 494, 2008

- [39] V. John and P. Knobloch, A comparison of spurious oscillations at layers diminishing (sold) methods for convection–diffusion equations: part I – a review, *Comput. Methods Appl. Mech. Engrg.* 196, pp. 2197–2215, 2007
- [40] Javier Principe, Ramon Codina, On the stabilization parameter in the subgrid scale approximation of scalar convection-diffusion-reaction equations on distorted meshes, *Comput. Methods Appl. Mech. Engrg.*, available online 15 August 2009, ISSN 0045-7825, DOI: 10.1016/j.cma.2009.08.011
- [41] E.G.D. Carmo and A.C. Galeao. Feedback Petrov-Galerkin methods for convection-dominated problems. *Comput. Methods Appl. Mech. Engrg.* 88:1-16, 1991.
- [42] R. Codina, E. Oñate and M. Cervera, The intrinsic time for the streamline upwind Petrov–Galerkin formulation using quadratic elements. *Comput. Methods Appl. Mech. Engrg.* 94, pp. 239–262, 1992.
- [43] A.C. Galeão and E.G. Do Carmo, A consistent approximate upwind Petrov–Galerkin method for convection-dominated problems. *Comput. Methods Appl. Mech. Engrg.* 68, pp. 83–95, 1988.
- [44] E.G.D. do Carmo and G.B. Alvarez, A new stabilized finite element formulation for scalar convection–diffusion problems: the streamline and approximate upwind/Petrov–Galerkin method. *Comput. Methods Appl. Mech. Engrg.* 192, pp. 3379–3396, 2003.
- [45] A. C. Galeão , R. C. Almeida , S. M. C. Malta , A. F. D. Loula, Finite element analysis of convection dominated reaction-diffusion problems, *Applied Numerical Mathematics*, v.48 n.2, p.205-222, 2004
- [46] V. John and P. Knobloch, On discontinuity-capturing methods for convection–diffusion equations. In: A. Bermúdez de Castro, D. Gómez, P. Quintela and P. Salgado, Editors, *Numerical Mathematics and Advanced Applications, Proceedings of ENUMATH 2005*, Springer-Verlag, Berlin, pp. 336–344, 2006.
- [47] V. John and P. Knobloch, On spurious oscillations at layers diminishing (SOLD) methods for convection–diffusion equations: Part I – A review, *Comput. Methods Appl. Mech. Engrg.* 196, pp. 2197–2215, 2007
- [48] T.E. Tezduyar and Y.J. Park, Discontinuity-capturing finite element formulations for nonlinear convection–diffusion–reaction equations, *Comput. Methods Appl. Mech. Engrg.* 59, pp. 307–325, 1986.
- [49] T.E. Tezduyar, Finite element methods for fluid dynamics with moving boundaries and interfaces. In: E. Stein, R. De Borst and T.J.R. Hughes, Editors, *Encyclopedia of Computational Mechanics, Fluids* vol. 3, Wiley, New York (2004) (Chapter 17).
- [50] F. Brezzi and A. Russo, Choosing bubbles for advection–diffusion problems, *Math. Models Methods Appl. Sci.* 4, pp. 571–587, 1994.

- [51] L.P. Franca and A. Russo, Deriving upwinding, mass lumping and selective reduced integration by residual-free bubbles, *Appl. Math. Lett.* 9, pp. 83–88, 1996
- [52] G. Sangalli, Global and local error analysis for the residual-free bubbles method applied to advection-dominated problems, *SIAM J. Numer. Anal.* 38, pp. 1496–1522, 2000
- [53] G. Sangalli, A robust a posteriori estimate for the residual-free bubbles method applied to advection–diffusion problems, *Numer. Math.* 89, pp. 379–399, 2001.
- [54] A. Russo, Streamline-upwind Petrov/Galerkin method (SUPG) vs residual-free bubble (RFB), *Comput. Methods Appl. Mech. Engrg.* 195, 1608-1620, 2006.
- [55] F. Brezzi, D. Marini and E. Süli, Residual-free bubbles for advection–diffusion problems: the general error analysis, *Numer. Math.* 85 (2000), pp. 31–47
- [56] L.P.Franca, F. Valentin. On an improved unusual stabilized finite element method for the advection-reactive-diffusive equation. *Comput. Methods. in Applied Mech. and Eng.*, 190:1785-1800, 2001.
- [57] R. Codina and J. Blasco. Analysis of a stabilized finite element approximation of the transient convection-diffusion-reaction equation using orthogonal subscales. *Comput. Visual. Sci.*, 4(3):167-174, 2002..
- [58] G. Hauke and A. Garcia-Olivares. Variational subgrid scale formulations for the advection-diffusion-reaction equation. *Comput. Methods Appl. Mech. Eng.* 6847-6865, 2001.
- [59] A. Russo, Bubble stabilization of finite element methods for the linearized incompressible Navier–Stokes equations, *Comput. Methods Appl. Mech. Engrg.* 132, pp. 335–343, 1996.
- [60] Gravemeier, W.A. Wall, A "divide-and-conquer" spatial and temporal multiscale method for transient convection-diffusion-reaction equations, *International Journal for Numerical Methods in Fluids* 54, 779-804, 2007.
- [61] P.B. Bochev, M.D. Gunzburger and J.N. Shadid, Stability of the SUPG finite element method for transient advection–diffusion problems, *Comput. Methods Appl. Mech. Engrg.* 193, pp. 2301–2323, 2004.
- [62] M.M. Grigoriev and G.F. Dargush, Boundary element methods for transient convective diffusion. Part III: numerical examples, *Comput. Methods Appl. Mech. Engrg.* 192, pp. 4313–4335, 2003.
- [63] J. Lim, C.L. Chan and A. Chandra, A BEM analysis for transient conduction–convection problems. *Int. J. Numer. Methods Heat Fluid Flow* 4, pp. 31–45, 1994.
- [64] S.J. DeSilva, C.L. Chan, A. Chandra and J. Lim, Boundary element method analysis for the transient conduction–convection in 2-D with spatially variable convective velocity, *Appl Math Modelling* 22, pp. 81–112, 1998.

Enriched finite element spaces for transient conduction heat transfer

E. Hachem^{*}, H. Dignonnet, E. Massoni, T. Coupez
*Centre For Material Forming (CEMEF), École des Mines de Paris
06904 Sophia-Antipolis, France*

Abstract

This paper presents an original technique via finite elements to treat numerically the thermal shocks in heat transfer finite element analysis. The method consists in a slight modification on the standard enriched finite element approaches. It will be applied here to the transient conduction heat equation where the classical Galerkin method is shown to be unstable. The proposed method consists in adding and eliminating bubbles to the finite element space and then to interpolate the solution to the real time step. This modification is equivalent to the addition of a stabilizing term tuned by a local time-dependent stability parameter, which ensures an oscillating-free solution. To validate this approach, the numerical results obtained in classical 2D and 3D benchmark problems are compared with the Galerkin and the analytical solutions.

Keywords: Finite elements, stabilization, heat conduction, static condensation

^{*} Corresponding author. Tel. : +33 4 93 95 74 58 ; fax : +33 4 92 38 97 52

E-mail address: elie.hachem@mines-paristech.fr

1. Introduction

The scalar diffusion equation is generally used as a linear model for simulating time-dependent phenomena in domains like fluid dynamics and heat transfer. It is well known that the numerical solution of unsteady diffusion problems using the Galerkin finite element method, based on piecewise polynomial interpolations, is often affected by severe numerical instabilities unless appropriately refined meshes are used in the solution's layers. In this case, the solution exhibits steep gradients known usually as thermal shocks, that usually appear in the boundary of a domain initially hot (or cold) that is suddenly cooled (resp. heated). In particular, the Galerkin method might fail to

solve unsteady diffusion problems when either the diffusion parameter ε , is low and/or small time steps Δt are used in time discretization ($\varepsilon \leq h^2 \Delta t^{-1}$). This difficulty has been object of research for the last decades; the purpose is to obtain solutions that are stable and coarse mesh accurate. Such formulations, known as stabilized or enriched methods, consist generally in adding to the Galerkin formulation additional terms balanced by stabilization parameters [1-2-3-4-5]. This allows the control of spurious oscillations giving accurate results for real industrial applications like solidification, hot forming and casting, polymer injection molding.

The present work aims to retain the advantages of using linear approximations (P1 finite elements) regarding the accuracy and the computational cost, especially for 3D applications. This is the common choice when solving heat transfer problems making possible at the same time to overcome thermal shocks when small enough time increments are used. In this context, we will use the enriched method that employs bubble functions satisfying strongly the differential equations in each element subjected to homogeneous boundary conditions on the element boundary. Nevertheless, one limitation of this method is that, when applied to a steady diffusion problem, it has no distinction to the original one if approximated with linear shape functions [4-5]. If instead, we apply this technique to an unsteady diffusion problem, we can show in this paper that static condensation procedure of the bubble yields a stabilized finite element method of the Galerkin Least Squares (GLS) type [8-9]. The authors show that the use of the GLS method in this conditions can be interpreted as the solution of the standard the Galerkin method, but with a much larger time step. To overcome this drawback, we propose the extension of the enriched method by interpolating the solution to the real time step, referred as an enriched method with interpolation (EM-I). This will result a local definition of stabilization parameters that resembles the one used in well-known stabilized formulations but whose origins are based on the use of local time-steps combined with a kind of synchronization scheme. This method shows good properties of stability and accuracy, both for smooth problems and for problems with boundary and internal layers. We can also mention that the proposed method can be helpful for computational engineers in the field of heat transfer analysis and it can be easily implemented in finite element codes.

So far, most efforts have been invested to deal with steady-problem, while less attention has been devoted to unsteady problem, especially to transient conduction heat transfer. The most favored and efficient approach to such problems was proposed by [6]. In this paper, like in here, both temporal and spatial ingredients were used in order to get a stabilized solution in particularly for small time steps. Similarly, the authors in [7] discussed the use of such coupling between stabilized finite elements and finite difference time integration on more general problems such as the advection-diffusion-reaction problems. Other related ideas was proposed like, mesh refinement [10], M-matrix theory [11], finite volume method [12], discontinuous Galerkin models [13] and the diffusion-split method [14]. Compared to all these methods, the new approach works for general meshes, can use any time step or diffusion parameter and, with low computational cost offers a good accuracy order. The outline of the paper is as follows: first, we present the unsteady diffusion model and the associated Galerkin finite element formulation. Section 3 presents the enriched method with and without time-interpolation. We perform several numerical validations in Section 4, which confirm the

good performance of the method. Finally, conclusions and perspectives are conclusions are draw in Section 5.

2. The heat equation

The model equation for transient heat transfer by conduction is:

$$\rho c_p \frac{\partial T}{\partial t} - \nabla \cdot (k \nabla T) = f \quad \text{in } \Omega \times (0, t_f) \quad (1)$$

where T is the temperature (the problem's unknown), Ω is the spatial computational domain, t the time, t_f the final time, ρ is the material's density, c_p its specific heat, k the thermal conductivity and f represents a heat source. The following initial condition is applied: $T(x, t_0) = T_0(x)$ where T_0 is the initial temperature distribution over the domain. For the heat equation, various types of boundary conditions can be considered:

$$T = T_s \quad \text{on } \Gamma_s \quad (2)$$

$$k \nabla T \cdot n = q_w \quad \text{on } \Gamma_q \quad (3)$$

$$k \nabla T \cdot n = -h_c (T - T_{out}) \quad \text{on } \Gamma_c \quad (4)$$

where T_s represents the wall temperature imposed on a portion of the boundary Γ_s , q_w is a prescribed inflow heat flux imposed on Γ_q , while the convection boundary conditions are imposed on Γ_c using h_c as the convection heat transfer coefficient and T_{out} as the temperature outside this boundary of the domain.

2.1. Galerkin finite element formulation

The Galerkin finite element formulation is obtained by multiplying Eq. (1) by an appropriate test function w and by integrating over the computational domain [15]. For that, let us consider first the functional spaces $H_s^1(\Omega)$ in which we are searching the solution in accordance with its regularity:

$$H_s^1 = \left\{ w \in H^1(\Omega) \mid w = s \quad \forall x \in \Gamma \right\}$$

where $H^1(\Omega)$ is a Sobolev space, classically defined as

$$H^1(\Omega) = \left\{ w \in L^2(\Omega), \|\nabla w\| \in L^2(\Omega) \right\}$$

and $L^2(\Omega)$ is the Hilbert vector space of the functions quadratically summable on Ω :

$$L^2(\Omega) = \left\{ w(x) \mid \int_{\Omega} |w(x)|^2 dx < \infty \right\}$$

By applying the Galerkin weighted residual method and the Green's theorem, the variational formulation corresponding to Eq. (1) became:

Find $T \in H_s^1(\Omega)$ such that

$$a\left(\frac{\partial T}{\partial t}, w\right) + b(T, w) = l(w) \quad \forall w \in H_0^1(\Omega) \quad (5)$$

where

$$\begin{aligned} a\left(\frac{\partial T}{\partial t}, w\right) &= \int_{\Omega} \rho c_p \frac{\partial T}{\partial t} w d\Omega \\ b(T, w) &= \int_{\Omega} k \nabla T \cdot \nabla w d\Omega + \int_{\Gamma_c} h_c T w d\Gamma \\ l(w) &= \int_{\Omega} f w d\Omega + \int_{\Gamma_q} q w d\Gamma + \int_{\Gamma_c} h_c T_{out} w d\Gamma \end{aligned}$$

For the spatial discretization, we consider the finite element partition \mathfrak{S}_h of Ω into tetrahedral elements K . Using these representations, the above-defined functional spaces $H_s^1(\Omega)$ and $H_0^1(\Omega)$ are approached by discretized spaces $H_s^{1h}(\Omega)$ and $H_0^{1h}(\Omega)$. The Galerkin approximation of (5) is formulated on these finite-dimensional subspaces as follows:

Find $T_h \in H_s^{1h}(\Omega)$ such that

$$a\left(\frac{\partial T_h}{\partial t}, w_h\right) + b(T_h, w_h) = l(w_h) \quad \text{for all } w_h \in H_0^{1h} \quad (6)$$

Finally, the problem defined by equations (1)-(6) yields the system of first order differential equations:

$$\mathbf{C} \frac{\partial \mathbf{T}}{\partial t} + \mathbf{K} \mathbf{T} = \mathbf{F} \quad (7)$$

where T is the vector of nodal unknown temperatures, C is the capacitance matrix, K the conductivity matrix, and F is the internal source and external flux vector, defined as

$$C_{ij} = \int_{\Omega} \rho c_p N_i N_j dV \quad (8)$$

$$K_{ij} = \int_{\Omega} k \nabla N_i \cdot \nabla N_j dV + \int_{\Gamma_c} h N_i N_j dS \quad (9)$$

$$F_i = \int_{\Omega} f N_i dV + \int_{\Gamma_c} q_w N_i dS + \int_{\Gamma_c} h T_{out} N_i dS \quad (10)$$

being N_i the linear interpolation function at node i .

2.2. Time integration scheme

The system of ordinary differential equations (7) has to be integrated in time. Using the θ finite difference family of approximations, the derivative of the temperature with respect to time can be approximated at time $t = n\Delta t$ by

$$\mathbf{C} \frac{T^n - T^{n-1}}{\Delta t} + \mathbf{K} (\theta T^n + (1-\theta)T^{n-1}) = \mathbf{F} \quad (11)$$

where $\Delta t = t_f / N$ is the time step, $n = 1, \dots, N$, and $0 \leq \theta \leq 1$. We remind that this family includes the backward Euler scheme ($\theta = 1$), the Crank-Nicolson scheme ($\theta = 0.5$) and the forward Euler scheme ($\theta = 0$). For simplicity, we consider the first case, usually known as the implicit Euler scheme, and equation (11) can be written at time $t + \Delta t$ as:

$$\mathbf{C} \frac{T^n - T^{n-1}}{\Delta t} + \mathbf{K} T^n = \mathbf{F} \quad (12)$$

where T^{n-1} is the temperature at the previous time step.

3. Stabilized finite element method

When diffusion is the only mechanism for heat transfer, there are conditions for which the Galerkin method fails to produce smooth solutions. It is well known that this method, based on piecewise polynomial approximations, yields poor solutions for low thermal diffusivity materials ε and/or when the time step is small ($\varepsilon \leq h^2 \Delta t$). Thus, one way to overcome such limitations consists in using stabilized finite element methods. In the following, we discuss the use of enriched method on our unsteady diffusion problem.

3.1. The enriched space approach (without time-interpolation)

The concept of enriched methods has been developed and explored in [1-2-3]. This method is based on a local enrichment of the finite element space instead of a modification of the variational formulation. The idea is to add to the usual space of piecewise polynomials, referred to as macro-scales, the so-called bubbles, representing the micro-scales. In here, bubbles are functions whose support remains inside the elements of the triangulation. In other word, one solves additionally a micro-scale equation on individual elements with zero Dirichlet boundary conditions. The numerical method turns out to be stable (see, for example, [3] and [4]), even though there is a computational cost associated to the fact that the solution of local problems is necessary in order to approximate, and possibly eliminate, the bubble degrees of freedom. For sake of simplicity, we consider all of Γ to be the zero Dirichlet boundary condition. Generalization to other types of boundary conditions will be subject of a future work.

We start with the model problem given by: find a scalar valued function $T(x)$ define in $\Omega \subset \mathfrak{R}^n$ with initial condition $T(x, t_0) = T_0(x)$ such that

$$\begin{aligned} \rho c_p \frac{\partial T}{\partial t} - \nabla \cdot (k \nabla T) &= f \quad \text{in } \Omega \times (0, t_f) \\ T &= 0 \quad \text{on } \Gamma \times (0, t_f) \end{aligned} \quad (13)$$

where $f(x)$ is a given source function assumed to be square integrable in Ω . Using Euler implicit scheme, the classical Galerkin approximation of (13) is the following:

Find $T_h \in V_h^{(1)} \subset H_0^1(\Omega)$ such that

$$\left(\frac{\rho c_p}{\Delta t} T_h^n, w_h \right) + (k \nabla T_h^n, \nabla w_h) = (f, w_h) + \left(\frac{\rho c_p}{\Delta t} T_h^{n-1}, w_h \right) \quad \forall w_h \in V_h^{(1)} \quad (14)$$

where

$$V_h^{(1)} = \left\{ w_h \in C^0(\overline{\Omega}) \mid w_{h/K} \in P_1(K), \forall K \in \mathfrak{S}_h \right\}$$

is the finite element space of continuous, piecewise linear functions on \mathfrak{S}_h used to approximate the exact solution.

For sake of simplicity in the notation, we replace all the second hand term, the source term and the previous time step solution by g , from (14) we get:

$$\begin{aligned} \left(\frac{\rho c_p}{\Delta t} T_h^n, w_h \right) + (k \nabla T_h^n, \nabla w_h) &= (f, w_h) + \left(\frac{\rho c_p}{\Delta t} T_h^{n-1}, w_h \right) \quad \forall w_h \in V_h^{(1)} \\ \left(\frac{\rho c_p}{\Delta t} T_h^n, w_h \right) + (k \nabla T_h^n, \nabla w_h) &= (g, w_h) \quad \forall w_h \in V_h^{(1)} \end{aligned} \quad (15)$$

Remark 1. As noted in [7], equation (16) can be seen as a family of steady diffusion-reaction problems that could be either diffusion or reaction dominated. Note also, that the proposed scheme deals with both regimes.

The notation $(f, g) = \int_{\Omega} fg \, d\Omega$ and $(u, v) = \int_{\Omega} u \cdot v \, d\Omega$ represents the inner product between scalar and vector fields respectively.

We enrich and enlarge the following subspace $V_h^{(1)}$ into:

$$V_h^b = \left\{ w \in H_0^1(\Omega) \mid w_K \in P_1(K) \oplus B(K), K \in \mathfrak{S}_h \right\} \quad (16)$$

$B(K)$ denotes the space of bubble functions.

The bubble basis function satisfies:

$$\begin{cases} \varphi(x) > 0 \quad \forall x \in K \\ \varphi(x) = 0 \quad \forall x \in \partial K \\ \varphi(x) = 1 \quad \text{at the barycenter of } K \end{cases} \quad (17)$$

Consequently, the unknown solution $T_h \in V_h^b$ can be decomposed into its linear part

$T_1 \in V_h^{(1)}$ and its part spanned by the bubble:

$$T_h = T_1 + \sum_{K \in \mathfrak{S}_h} T_{b_K} \varphi \quad (18)$$

where T_{b_K} is the unknown bubble coefficient .

First, we begin by solving equation (15) on the local-scale, called ‘‘bubble equation’’:

$$\left(\frac{\rho c_p}{\Delta t} T_h^n, \varphi \right)_K + (k \nabla T_h^n, \nabla \varphi)_K = (g, \varphi)_K \quad (19)$$

By using the decomposition of the solution T_h (18) and substituting it into (19), we get:

$$\left(\frac{\rho c_p}{\Delta t} T_1^n, \varphi \right)_K + T_{b_K} \left(\frac{\rho c_p}{\Delta t} \varphi, \varphi \right)_K + (k \nabla T_1^n, \nabla \varphi)_K + T_{b_K} (k \nabla \varphi, \nabla \varphi)_K = (g, \varphi)_K \quad (20)$$

Using linear shape functions, the third term vanishes. Solving (20) for the bubble coefficient in each element $K \in \mathfrak{S}_h$ leads to:

$$T_{b_K} = \frac{1}{\frac{\rho c_p}{\Delta t} \|\varphi\|_{0,K}^2 + k \|\nabla \varphi\|_{0,K}^2} \left(g - \frac{\rho c_p}{\Delta t} T_1^n, \varphi \right)_K \quad (21)$$

where $\|\varphi\|_{0,K}^2 = \int_K \varphi^2 d\Omega$.

Remark 2. The bubbles considered here are quasi-static, i.e., that the effect of their time variation may be neglected. Note that following the evolution of small-scales in time is an interesting method [18], but for this type of equation, it could increase the computational cost without considerable gain in accuracy.

Hereafter, we need to solve equation (15) on the macro-scale. The static condensation procedure will eliminate the bubbles function at the element level

$$\left(\frac{\rho c_p}{\Delta t} T_1^n, w_1 \right) + \sum_{K \in \mathfrak{S}_h} T_{b_K} \left(\frac{\rho c_p}{\Delta t} \varphi, w_1 \right)_K + (k \nabla T_1^n, \nabla w_1) = (g, w_1) \quad (22)$$

The solution of the small-scale can be expressed using (21) and (22) on each element K :

$$T_{b_k} \left(\frac{\rho c_p}{\Delta t} \varphi, w_1 \right)_K = \frac{1}{\frac{\rho c_p}{\Delta t} \|\varphi\|_{0,K}^2 + k \|\nabla \varphi\|_{0,K}^2} \left(g - \frac{\rho c_p}{\Delta t} T_1^n, \varphi \right)_K \left(\frac{\rho c_p}{\Delta t} \varphi, w_1 \right)_K \quad (23)$$

Following the lines in [16], one can simplify the expression of (23) into:

$$T_{b_k} \left(\frac{\rho c_p}{\Delta t} \varphi, w_1 \right)_K = \frac{C_1 h_k^2}{\underbrace{\frac{\rho c_p}{\Delta t} h_k^2 + k C_2}_{\tau_k}} \left(g - \frac{\rho c_p}{\Delta t} T_1^n, \frac{\rho c_p}{\Delta t} w_1 \right)_K \quad (24)$$

where C_1 and C_2 are positive constants. The stabilizing parameter τ_k is computed for each element separately. (we take $C_1 = 1$ and $C_2 = 6$, see [1] for more details)

Therefore, the resulting variational equation (14) is equivalent to use the standard Galerkin method with piecewise linear functions plus a stabilization term weighted by τ_k :

$$\begin{aligned} \left(\frac{\rho c_p}{\Delta t} T_1^n, w_1 \right) + (k \nabla T_1^n, \nabla w_1) - \sum_{K \in \mathcal{S}_h} \tau_k \left(\frac{\rho c_p}{\Delta t} T_1^n, \frac{\rho c_p}{\Delta t} w_1 \right)_K \\ = (g, w_1) - \sum_{K \in \mathcal{S}_h} \tau_k \left(g, \frac{\rho c_p}{\Delta t} w_1 \right)_K \end{aligned} \quad (25)$$

The bubble contribution took effect in one hand on transient term and in other hand on the modified source term g which represents the previous time step solution and the source term. The stabilization term contains a zero order term in the test function w_1 and is equivalent to a change in the test function as follows:

$$\tilde{w}_1 = w_1 \left(1 - \tau_k \frac{\rho c_p}{\Delta t} \right) \quad (26)$$

In the absence of the source term f , this can be seen as a modified problem by the Galerkin method with a much larger time step. The authors in [9] pointed out that the solution is free of oscillations but will no longer be the solution to the original problem.

3.2. The modified formulation (with time-interpolation)

The previous method improves stability by adding a stabilizing term obtained after condensation of the bubble function in the original problem. But as mentioned before, this can work only in particular case when the source term is zero. To fix ideas, we rewrite the new stabilized formulation of (25) after replacing g by its value:

$$\left(\rho c_p \frac{T^n}{\Delta t}, w \left(1 - \tau_k \frac{\rho c_p}{\Delta t} \right) \right) + (k \nabla T^n, \nabla w) = \left(f + \rho c_p \frac{T^{n-1}}{\Delta t}, w \left(1 - \tau_k \frac{\rho c_p}{\Delta t} \right) \right) \quad (27)$$

It is clear when this method is applied to an unsteady diffusion problem without a source term, it can be interpreted as a Galerkin method with a modified larger time step:

$$(\rho c_p \frac{T^*}{\Delta t^*}, w) + (k \nabla T^*, \nabla w) = (\rho c_p \frac{T^{n-1}}{\Delta t^*}, w) \quad (28)$$

where T^* is the modified solution and Δt^* is the new time step given on each K by:

$$\frac{\Delta t}{\Delta t^*} = (1 - \tau_K \frac{\rho c_p}{\Delta t}) = \frac{1}{\xi}, \quad \xi > 0 \quad (29)$$

An easy way to correct the time step distortion introduced by the previous stabilization is to use an interpolation of the solution to the real time step:

$$T^* = \xi T^n + (1 - \xi) T^{n-1} \quad (30)$$

By substituting (30) into (28) we obtain:

$$\begin{aligned} & (\frac{\rho c_p}{\Delta t^*} (\xi T^n + (1 - \xi) T^{n-1}), w) + (k \nabla (\xi T^n + (1 - \xi) T^{n-1}), \nabla w) = (\frac{\rho c_p}{\Delta t^*} T^{n-1}, w) \\ \Rightarrow & (\rho c_p \frac{T^n}{\Delta t}, w) + (\frac{\rho c_p}{\Delta t^*} (1 - \xi) T^{n-1}, w) + (\xi k \nabla T^n, \nabla w) \\ & + ((1 - \xi) k \nabla T^{n-1}, \nabla w) = (\frac{\rho c_p}{\Delta t^*} T^{n-1}, w) \\ \Rightarrow & (\rho c_p \frac{T^n}{\Delta t}, w) + (\xi k \nabla T^n, \nabla w) = (\rho c_p \frac{T^{n-1}}{\Delta t}, w) + ((\xi - 1) k \nabla T^{n-1}, \nabla w) \end{aligned} \quad (31)$$

Finally, we get:

$$(\rho c_p \frac{T^n - T^{n-1}}{\Delta t}, w) + (\xi k \nabla T^n, \nabla w) = ((\xi - 1) k \nabla T^{n-1}, \nabla w) \quad (32)$$

Comparing (32) with the original version (15), we see that the process of enlarging our space with bubbles and then modifying the time step yields a stabilized finite element formulation for the unsteady heat diffusion problem. This contribution acts as a new artificial, time-dependent thermal conductivity (ξk) integrated over the element's interior and tuned by a local stabilization term τ_K that ensures an oscillating-free solution.

Remark 3. If we reconsider the heat source f , equation (28) can be always interpreted as a Galerkin method using a modified larger time step but in addition of a modified source term. The extension to the use of this term can be straightforward by simply considering the equivalent term ξf . The numerical example in section 4.3 will assess this matter.

In conclusion, the new approach formulation of the transient heat conduction with a source term will take the following form:

$$\int_{\Omega} \rho c_p \frac{T^n - T^{n-1}}{\Delta t} w d\Omega + \sum_K \int_{\Omega_K} \xi_K k \nabla T^n \cdot \nabla w d\Omega = \int_{\Omega} f w d\Omega + \sum_K \int_{\Omega_K} (\xi_K - 1) k \nabla T^{n-1} \cdot \nabla w d\Omega + \sum_K \int_{\Omega_K} \tau_K \nabla f \cdot \nabla w d\Omega \quad (33)$$

3.3. Diffusion reduction factor

Furthermore, in order to avoid an extra diffusion effect and thus a non-realistic result toward the steady state, a cut-off strategy is introduced. This strategy consists in modifying the stabilization parameter making it varying with time and depending on the regularity of the approximate solution. In practice, this diffusion correction factor can be seen as the coth-formula, function of the element Peclet number often used in convection-dominated problems. In conclusion, this strategy will at the same time ensure stability in the initial iterations and convergence toward the steady state without extra diffusivity.

Correspondingly, we define the following dimensionless number in order to evaluate the regularity, computed at each time step by:

$$\alpha = \frac{h |R_e(h)|}{\varepsilon |\nabla T_h|} \quad (34)$$

where ε is the heat diffusivity (m^2/s)

and $|R_e(h)|$ is the residual of the approximate solution. Thus, the choice of the new parameter will ensure the following properties:

$$\xi_k = \begin{cases} \xi_k & \text{if } \alpha \geq 1 \\ 1 & \text{if } \alpha < 1 \end{cases} \quad (36)$$

- stability in the proximity of boundary layers, when α is very large
- accuracy when we converge to a steady state, where α tends towards less than unity

4. Numerical results

4.1. Unsteady diffusion in a semi-infinite solid with Dirichlet boundary conditions

In order to evaluate the efficiency of the new formulation, we consider test problems that present analytical solutions. First, we consider equation (1) subject to homogenous boundary conditions in a semi-infinite solid cooled from the side. We take our domain initially at a uniform temperature of 800°C . The Dirichlet boundary condition for temperature is set to 25°C (cooled side). The conductivity is set to $5 \cdot 10^{-5} \text{ W/mK}$ while the material's density and specific heat are equal to 1 kg/m^3 and 1 J/KgK . We use a 3D unstructured triangulation with an uniform element size $h \approx 10^{-3}$ and equal time steps of $\Delta t = 10^{-2} \text{ s}$, (see Figure 1).



Figure 1: 3D bar - geometry and boundary conditions

Subject only to the boundary condition T_s , the problem can be considered as one-dimensional case for which the exact solution takes the following form [19]:

$$T(x,t) = T_s + (T_0 - T_s) \operatorname{erf} \left(\frac{x}{2\sqrt{at}} \right) \quad (37)$$

In Figure 2, we plot the evolution in time of the temperature for a node placed $2h$ far from the cooled side. We compare the results given by the Galerkin and the new method with the exact solution. We do not consider the solution given by the new method without time-interpolation since it is the solution at different time step. The Galerkin method is affected by thermal shocks and spurious oscillations near the cooled boundary. These instabilities appear at the initial time steps and decrease as the solution converges to the steady state. The new solution has no oscillations. Both predictions converges to the analytical solution at the end of the simulation.

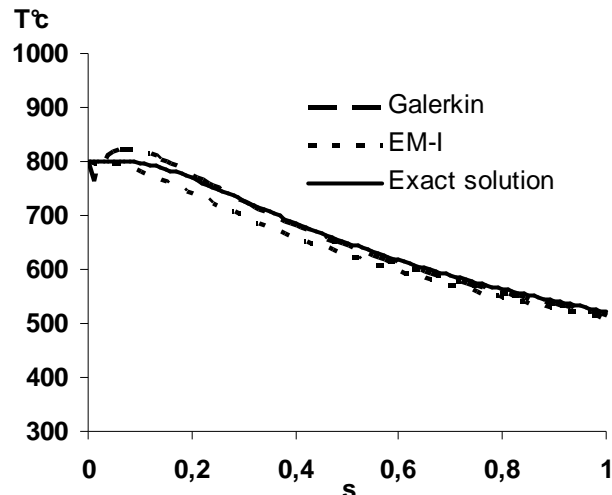


Figure 2: Evolution of the temperature at a node situated 2h far from the cooled side.

4.2. Study of the thermal conductivity influence

The previous example illustrates the performance of the new method on a 3D mesh for a given conductivity with an equal time step. One interesting aspect is to investigate the behavior in time of the solution when changing the conductivity value. For this, we consider another simple test adopted from [9] where we propose the solution of problem (1) subject to homogenous boundary conditions in a 1D semi-infinite from $x = 0$ to 1. The Dirichlet boundary condition for the temperature is set to 0°C (cooled side at $x = 0$).

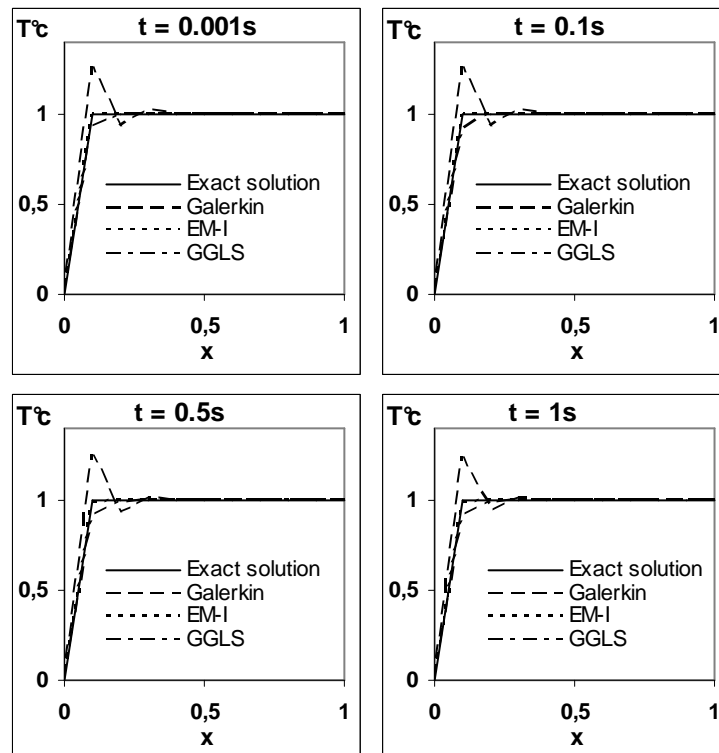


Figure 3: Comparison between solutions obtained by the different methods ($\varepsilon = 10^{-4}$)

The different values of conductivity are selected to 10^{-4} , 10^{-2} and 1, while the material's density and specific heat are equal to the unity. The domain discretization is uniform with $h = 0.1$ and $\Delta t = 10^{-3} s$.

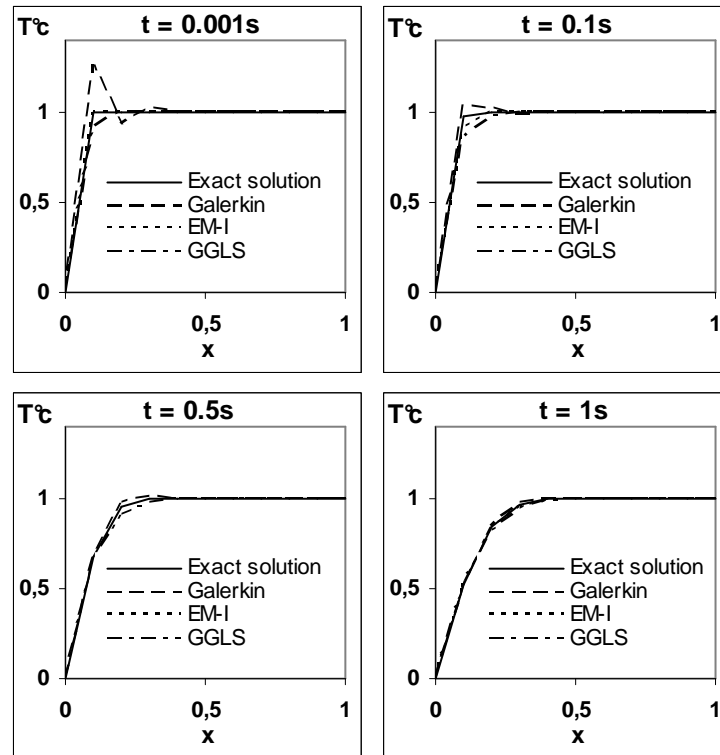
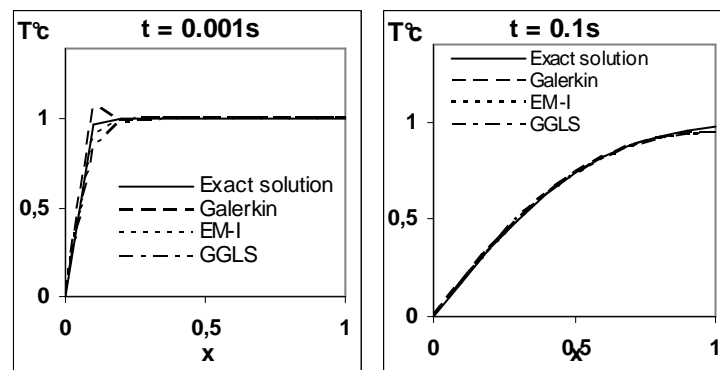


Figure 4: Comparison between solutions obtained by the different methods ($\varepsilon = 10^{-2}$)

In Figure 3, similar behaviour is observed in the predicted solutions: both stabilized methods, the GGLS and the EM-I provide exact nodal and oscillating-free solutions at all simulation times whereas, oscillations appear in the Galerkin resolution. Figures 4 and 5 show that if we increase the conductivity, the Galerkin solution still presents some oscillations near the boundary layer but with small amplitude. However, when the temperature gradient is diffused over more than two elements, the oscillations disappear. At the end of the simulation, it is important to see that the proposed method does not present an excess of numerical diffusion, however, the GGLS solution seems to be a little bit diffusive. This matter was pointed out by authors in [9]: "This is the price to be paid to avoid oscillations".



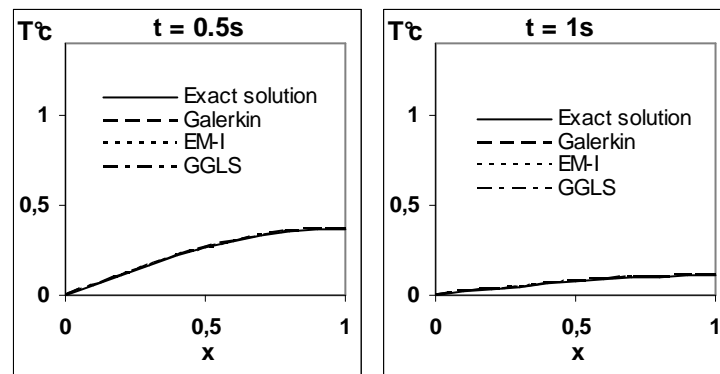


Figure 5: Comparison between solutions obtained by the different methods ($\varepsilon = 1$)

4.3. Source problem

4.3.1. Case 1: constant source term ($f=1$)

Here we consider the classical unit square subject to a homogeneous boundary condition ($T=0$). For a fixed conductivity $k=1$, initial temperature $T=1$ and very small time step $\Delta t = 10^{-5}$ boundary layers appear close to the wall. Figure 6 shows as expected the oscillations at the initial iteration near the walls where the high temperature gradients are localized. the Galerkin solution still suffer from numerical instabilities even in the presence of a constant source term. Again, the behaviour of the proposed method is satisfactory. Note also, towards the steady state, both methods have comparable performance without additional diffusivity, (see Figure 6 - right).

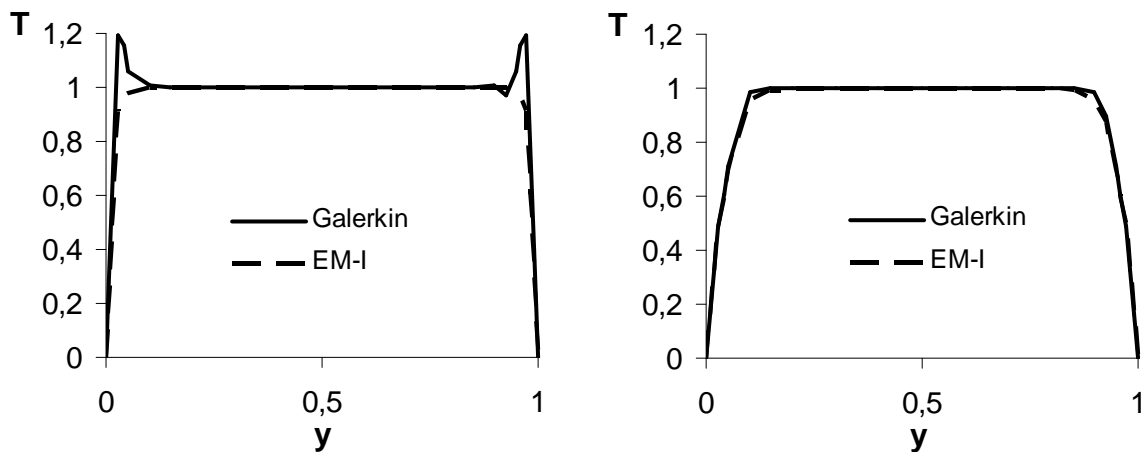


Figure 6: Solution at $x=0.5$ for $t = 10^{-5}$ (left) $t = 10^{-3}$ (right)

4.3.2. Case 2: *piecewise linear source term*

For fixed time step equal to 1 and small $\varepsilon = 10^{-6}$, we consider the following piecewise linear source term :

$$f(x, y) = \begin{cases} x & \text{if } 0 \leq x \leq 0.5 \\ 1-x & \text{if } 0.5 \leq x \leq 1 \end{cases} \quad (38)$$

The unstructured mesh consists of 20x20 elements and all the parameters were adopted from [16]. Again, the proposed method performs better than the Galerkin solution as shown in figure 7. Results are in complete accordance with the reference

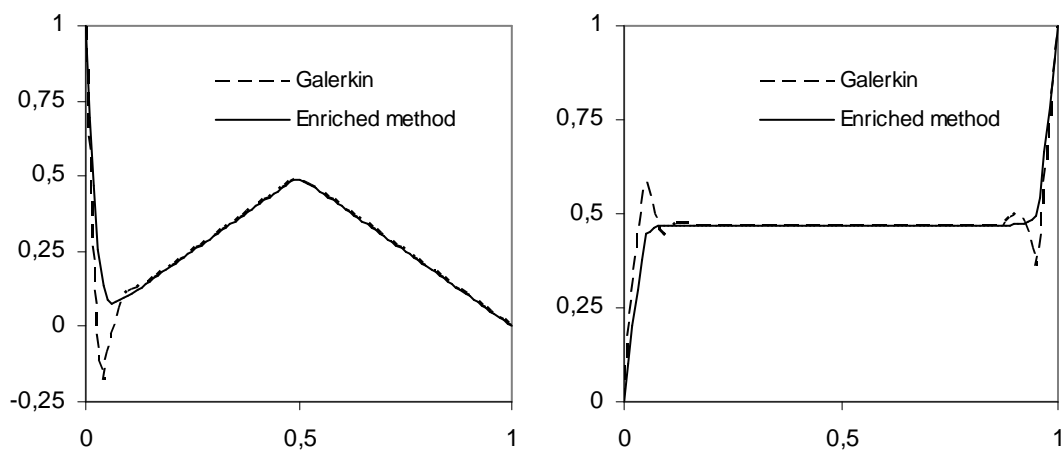


Figure 7: Solution at $y=0.5$ for (left) and $x=0.5$ (right)

4.4. 3D Multi-domain application using refined mesh

In order to demonstrate the efficiency of this approach, we consider in this example a 3D computational domain that presents heterogeneous thermal properties. This domain is discretized using a single mesh on which we use an immersion technique [19-20] to place an object inside. This is a typical case illustrating the problems posed by thermal shocks in current 3D industrial applications. In our case, this object is a hot ingot that will be heated or cooled thanks to the surrounding air (Figure 8).

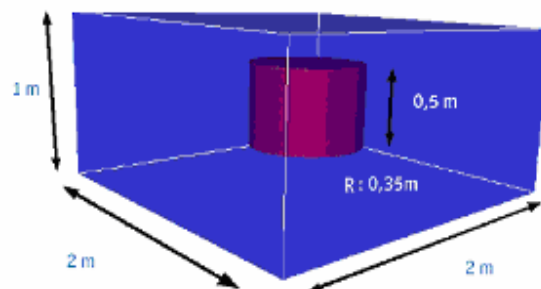


Figure 8: 3D computational domain with an immersed solid

The purpose of this example is to check the performance of new method in the presence sharp gradients inside the domain without any Dirichlet boundary conditions. To define the position of ingot/air interface of the ingot, we use a signed distance function χ :

$$\begin{cases} \chi > 0 & \text{inside} \\ \chi < 0 & \text{outside} \\ \chi = 0 & \text{at the interface} \end{cases} \quad (39)$$

In Figure 7 (a), we can see that the isosurface of χ at $t=t_0$ is accurately interpolated.

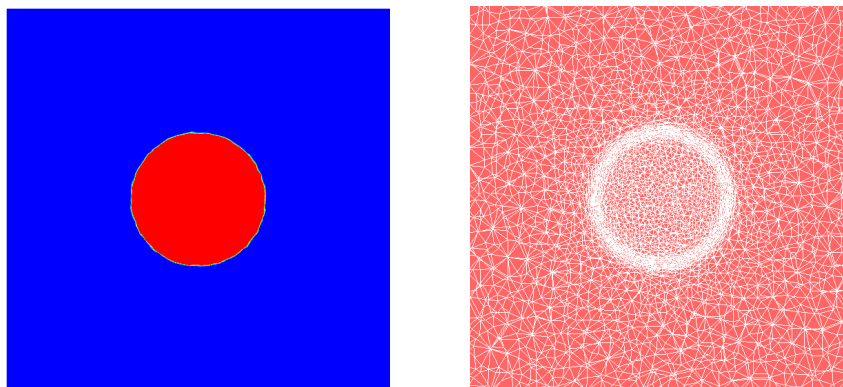


Figure 9: Mesh refinement at the interface level

Moreover, since χ is signed, so we can compute homogeneous material parameter's distribution, from the different material properties of each component (Table I, air/solid). Based on a mixture law, we define all thermal properties (T, ρ, c_p, k) as follows:

$$T(x, t) = T_{solid} f(\chi) + T_{air} (1 - f(\chi)) \quad (40)$$

If $T_{solid} = 400^\circ C$ in the ingot and $T_{air} = 20^\circ C$ outside, the temperature distribution is represented in Figure 9 (left).

$f(\chi)$ is a function between 0 and 1 (straight, abrupt or gradual...) that will decide the amount of each property inside elements crossed by the interface. To gain high precision at the interface, we used an anisotropic mesh adaptation technique based on variations of χ which allows a better capture of the discontinuities of the thermal parameters that characterize the strongly heterogeneous domain (air/solid) (Figure 9 - right). See [19] for further details.

We assume adiabatic conditions imposed in the outer boundary. For $\Delta t = 0.01s$, the obtained solution using the Galerkin method still, in the presence of mesh refinement, presents spurious oscillations specially in early iterations. As shown in figure 10, the present method captures the thermal shocks without oscillatory behavior.

All these instabilities decrease as the solutions converge to the steady state (figure 11). At this stage, the new approach yields equivalent results to the Galerkin method without extra diffusivity.

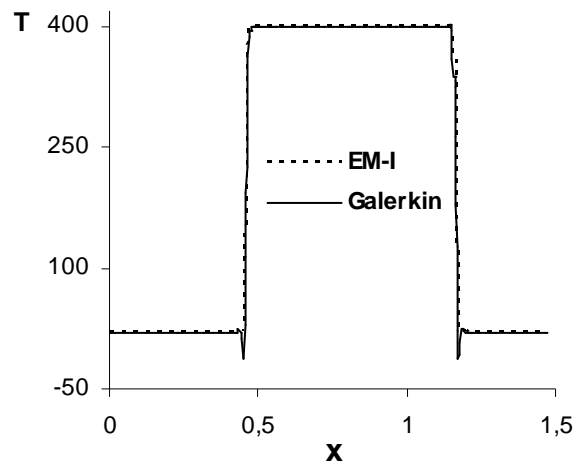


Figure 10: Profile of the solution at $z=0.5$ ($t=0.1s$)

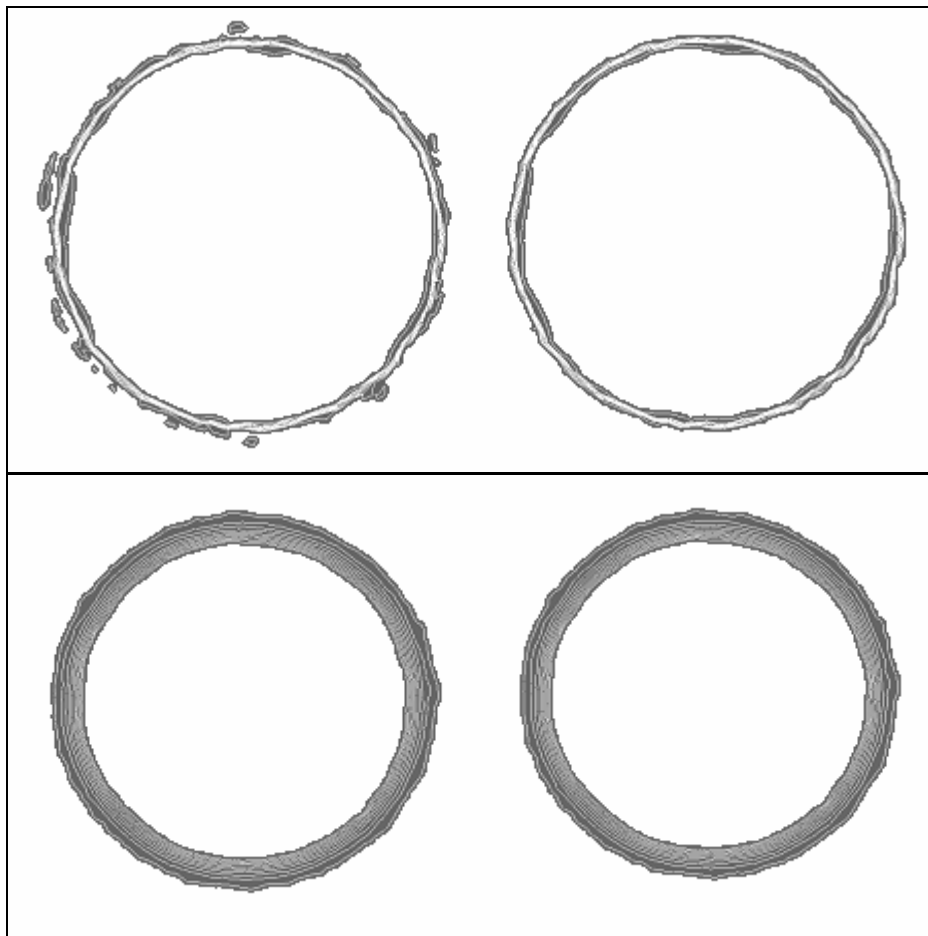


Figure 11: Isovalues of the solutions by Galerkin (left) and by EM-I method (right).
Top ($t = 0.1s$) and bottom ($t=10s$)

Solid	
Density ρ	2500 kg/m ³
Heat capacity c_p	1000 J/(kg°C)
Thermal conductivity k	175 W/(m°C)
Initial temperature T	400 °C
Fluid	
Density ρ	1,2 kg/m ³
Heat capacity c_p	1000 J/(kg°C)
Thermal conductivity k	0.02 W/(m°C)
Initial temperature T	20°C

Table I: Material properties for the multi-domain problem

5. Conclusions and perspectives

The new idea was first to apply the enriched method on an unsteady diffusion problem and then, to use a time interpolation for the modified problem (EM-I). The proposed method results in improved resolution compared with the standard Galerkin formulation on problems having sharp gradients. It avoids undesirable oscillations resulting in possible unphysical values of the solution. The concept of this stabilization method is to add an artificial conductivity controlled by space-time stabilization parameters that leads to a better representation of the solution in particularly for small time steps. More investigations are necessary to extend this approach to the boundary condition and this will be subject of future works.

Acknowledgements

The authors gratefully acknowledge support from the ADEME, CIM Team and the companies involved in the THOST project managed by Science Computer and Consultants (SCC).

References

1. C. Baiocchi, F. Brezzi and L.P. Franca, Virtual bubbles and the Galerkin-least-squares method, *Comput. Methods Appl. Mech. Engrg.* 105, (1993) 125-141
2. F. Brezzi, M.O. Bristeau, L.P. Franca, M. Mallet and G. Roge, A relationship between stabilized finite element methods and the Galerkin method with bubble functions, *Comput. Methods Appl. Mech. Engrg.* 96, (1992) 117-129
3. L.P. Franca and C. Farhat, Bubble functions prompt unusual stabilized finite element methods, *Comput. Methods Appl. Mech. Engrg.* 123, (1995) 299-308
4. L.P. Franca and C. Farhat, On the limitations of bubble functions, *Comput. Methods Appl. Mech. Engrg.* 117, (1994) 225-230
5. L.P. Franca, C. Farhat, A.P. Macedo and M. Lesoinne, Residual-free bubbles for the Helmholtz equation, *Int. J. Num. Meth. Eng.* 40, (1997) 4003-4009
6. Isaac Harari, Stability of semidiscrete formulations for parabolic problems at small time steps, *Comput. Methods Appl. Mech. Engrg.* 193, (2004) 1491-1516
7. M.I. Asensio, B. Ayuso, G. Sangalli, Coupling stabilized finite element methods with finite difference time integration for advection–diffusion–reaction problems, *Comput. Methods Appl. Mech. Engrg.* 196, (2007) 3475-3491
8. L.P. Franca and E.G. Dutra Do Carmo , The Galerkin gradient least-squares method. *Computer Methods in Applied Mechanics and Engineering* **74** (1989), pp. 41–54.
9. Ilinca F. Héту J-F, Galerkin gradient least-squares formulation for transient conduction heat transfer, *Comput. Methods Appl. Mech. Engrg.* 191, (2002) 3073-3097
10. Sheu, T. W. H. and Chen, H. Y. H. (2002), “A multi-dimensional monotonic finite element model for solving the convection-diffusion-reaction equation”, *element International Journal for Numerical Methods in Fluids*, Vol. 39, pp. 639-656.
11. Putti, M. and Cordes, C. (1998), “Finite element approximation of the diffusion operator in tetrahedral”, *SIAM Journal on Scientific Computing*, Vol. 19 No. 4, pp. 1154-1168.
12. Kosik, R., Fleischmann, P., Haindl, B., Pietra, P. and Selberherr, S. (2000), “On the interplay between meshing and discretization in three-dimensional diffusion simulation”, *IEEE Transactions on Computer-Aided Design of Integrated Circuits and Systems*, Vol. 19 No. 11, pp. 1233-1240.
13. Pichelin, E. and Coupez T., “A Taylor discontinuous Galerkin method for the thermal solution in 3D mold filling”, *Comput. Methods Appl. Mech. Engrg.* 178, (1999) 153-169.

14. Fachinotti V. and Bellet M. (2006), "Linear tetrahedral finite elements for thermal shock problems", *International Journal of Numerical Methods for Heat & Fluid Flow*, Vol. 16, pp. 590-601.
15. Zienkiewicz, O. C. and Taylor, R. L. (2000), "The finite element method - The basis", Butterworth-Heinemann, Oxford
16. Isaac Harari and Thomas J. R. Hughes, What are C and h?: Inequalities for the analysis and design of finite element methods, *Comput. Methods Appl. Mech. Engrg.* 97 (1992) 157-192
17. L.P. Franca, J.V.A. Ramalho and F. Valentin, Multiscale and residual-free bubble functions for reaction-advection-diffusion problems, *International Journal for Multiscale Computational Engineering*,. Vol. 3, pp. 297-312 (2005).
18. R. Codina, J. Príncipe, O. Guasch and S. Badia, Time dependent subscales in the stabilized finite element approximation of incompressible flow problems, *Comput. Methods Appl. Mech. Engrg.* **196** (2007), pp. 2413–2430.
19. J.F. Agassant, P. Avenas, J.P. Sergent, B. Vergnes, M. Vincent, "La mise en forme des matières plastiques", Lavoisier, TEC & DOC . 199
20. C. Gruau et T. Coupez , "3D tetrahedral, unstructured and anisotropic mesh generation with adaptation to natural and multidomain metric", *Comput. Methods Appl. Mech. Engrg* 194, (2005) 4951-4976.
21. T. Coupez, H. Digonnet and R. Ducloux, "Parallel meshing and remeshing", *Appl. Math. Modelling*,. 25, 153-175, Elsevier, (2000).

Chapter 3

Stabilised finite element methods for incompressible flows with high Reynolds number

The present chapter is dedicated to the modelling of the flow inside the furnace. The stabilized finite element approximation from the previous chapter will be extended and applied for the resolution of the 3D transient Navier-Stokes equation. Recall that inside the furnace at the burner's level, a forced convection is applied; therefore this chapter will focus on the stabilization of the convection-dominated flows for high Reynolds number. The Newton-Raphson linearization strategy will be adopted to deal with the nonlinear convective terms. The implementation algorithm of the equal velocity-pressure linear interpolation with additional bubble functions needed to satisfy the inf-sup condition will be considered here. The developed stabilized formulation is tested on four standard benchmarks and conclusions are drawn.

Chapter 3	85
Stabilised finite element methods for incompressible flows with high Reynolds number	85
3.1 Basic formulation of the equation	86
3.1.1 Initial and boundary conditions.....	87
3.1.2 Classical mixed formulation.....	88
3.2 Stable mixed variational formulation.....	90
3.3 Stabilized finite element method.....	91
3.3.1 Multiscale approach	92
3.3.2 Matrix formulation of the problem.....	99
3.3.3 Stabilization parameter.....	100
3.4 Numerical examples and validation	102
3.4.1 A convergence test	103
3.4.2 Driven flow cavity problem (2-D)	106
3.4.3 Flow over a circular cylinder	115
3.4.4 The flow over a backward-facing step	118
3.5 Conclusion.....	124
References	125

3.1 Basic formulation of the equation

It is known that the property of incompressibility is a feature of the flow performed by the fluid. The flow is said to be incompressible if we neglect the density changes. Usually, we consider liquids, in particular the water, as incompressible flows. Whereas, the gases are mostly considered as compressible flows. For low *Mach* number around 0.3, they can be also be treated as incompressible [1]. This non-dimensional number quantifies the relation between a characteristic velocity u of the flow and the velocity of the sound c by:

$$Ma = \frac{u}{c} \quad (3.1)$$

The Mach number is named after physicist and philosopher Ernst Mach (1836-1916). Since the velocity of the sound is $340m/s$ in the air, then the conditions of incompressibility is well respected up to fluid velocity of $100m/s$. In this work, these values for the velocity can be almost reached inside some of our partner's industrial furnaces. Therefore, some assumptions and simplifications are made.

Another important non-dimensional number that quantifies the properties of a particular flow is the REYNOLDS number given by

$$Re = \frac{LU}{\nu} \quad (3.2)$$

where L is a characteristic length scale, U is a measure velocity and ν is the kinematic viscosity of the respective flow. It gives a measure of the ratio of inertial forces to viscous forces and, consequently it quantifies the relative importance of these two types of forces for given flow conditions. Reynolds numbers is frequently used to characterize different flow regimes, such as laminar or turbulent flow: laminar flow occurs at low Reynolds numbers, where viscous forces are dominant, and is characterized by smooth, constant fluid motion, while turbulent flow occurs at high Reynolds numbers and is dominated by inertial forces, which tend to produce random eddies, vortices and other flow fluctuations. Reynolds number is named after Osborne Reynolds (1842–1912), who proposed it in 1883.

The transient equation of the fluid to be solved in a domain $\Omega \subset \mathfrak{R}^d$ (d being the space dimension) for a time period T consists in finding the velocity $u(x,t)$ and the pressure $p(x,t)$ such that:

$$\begin{aligned} \rho(\partial_t u + u \cdot \nabla u) - \nabla \cdot \sigma &= f \quad \text{in } \Omega \times (0, T) \\ \nabla \cdot u &= 0 \quad \text{in } \Omega \times (0, T) \end{aligned} \quad (3.3)$$

where σ is the stress tensor, ρ the density of the fluid and f is a given force vector. The stress tensor for a Newtonian fluid *i.e.*, the viscosity is assumed to be constant, is given by the constitutive equation:

$$\sigma = 2\mu \varepsilon(u) - pI \quad (3.4)$$

where μ is the dynamic viscosity, I the identity tensor, and p is the pressure. The strain rate tensor $\varepsilon(u)$, is defined by

$$\varepsilon(u) = \frac{1}{2} [\nabla u + \nabla u^t] \quad (3.5)$$

Combining (3.3)-(3.5) yields the following momentum equation

$$\begin{aligned} \rho(\partial_t u + u \cdot \nabla u) - 2\mu \nabla \cdot \varepsilon(u) + \nabla p &= f \quad \text{in } \Omega \times (0, T) \\ \nabla \cdot u &= 0 \quad \text{in } \Omega \times (0, T) \end{aligned} \quad (3.6)$$

The transient incompressible Navier-Stokes equations (3.6) constitute a nonlinear system of mixed hyperbolic-parabolic partial differential equations for the vector u and the scalar p . In order to solve this system, initial-boundary values must be set and specified.

3.1.1 Initial and boundary conditions

The initial condition at $t=0$ must satisfy $\nabla \cdot u_0 = 0$ in order to obtain a well-posed problem and has the following form:

$$u = u_0 \quad \text{in } \Omega \times (0) \quad (3.7)$$

Recall that for an incompressible flow there is no initial condition for the pressure. Usually, two types of boundary conditions can be applied, the Dirichlet boundary conditions on a Γ_D , and the Neumann boundary conditions on Γ_N , where $\partial\Omega = \Gamma = \Gamma_D \cup \Gamma_N$ and $\Gamma_D \cap \Gamma_N = \emptyset$. These conditions are defined as follow:

$$\begin{aligned} u &= u_D \quad \text{on } \Gamma_D \times (0, T) \\ n \cdot \sigma &= h_N \quad \text{on } \Gamma_N \times (0, T) \end{aligned} \quad (3.8)$$

where n is the unit outward normal vector to Γ_N .

In our context, inside an industrial furnace, two particular conditions can be characterized:

- The inflow boundary conditions imposed at the burner's level, which will be modelled by a fixed Dirichlet boundary conditions using a prescribed velocity u_D .
- The outflow boundary conditions which are not an easy task. It stills a challenge and an open problem. More details about this subject are discussed by Gresho [2] and Heywood *et al.* [3]. Within our case, the most popular "do nothing" boundary condition will be used, which means a zero Neumann boundary conditions.
- The pressure boundary condition is critical when there is no Neumann boundary. When only Dirichlet boundary conditions are imposed everywhere on our domain, the resulting pressure is obtained only up to an arbitrary constant. Therefore, two ways to define pressure field uniquely, either in prescribing an average value with respect to the complete domain having: $\int_{\Omega} p \, d\Omega = p_0$ where p_0 is a constant that can be zero, or by prescribing discrete value of the pressure at a point which is computationally the most convenient.

3.1.2 Classical mixed formulation

First let us define the function spaces that will be used in the remainder of this chapter. The function spaces for the velocity, the weighting function space and the scalar function space for the pressure are respectively defined by:

$$\begin{cases} \mathcal{V} = \left\{ u, u \in (H^1(\Omega))^d \mid u = g \text{ on } \Gamma_D \right\} \\ \mathcal{W} = \left\{ u, u \in (H^1(\Omega))^d \mid u = 0 \text{ on } \Gamma_D \right\} \\ \mathcal{Q} = \left\{ p, p \in L^2(\Omega) \right\} \end{cases}$$

Then the weak form of (3.6) consists in finding $(u, p) \in (\mathcal{V}, \mathcal{Q})$ such that:

$$\begin{cases} \rho \left(\frac{\partial u}{\partial t}, v \right) + \rho (u \cdot \nabla u, v) + (2\eta \mathcal{E}(u) : \mathcal{E}(v)) - (p, \nabla \cdot v) = (f, v) + (h_N, v)_{\Gamma_N} \\ (\nabla \cdot u, q) = 0 \end{cases} \quad (3.9)$$

Note that when integrating-by-parts the viscous and the pressure term, the Neumann boundary term appears naturally in the formulation.

As mentioned in previous chapter, the Galerkin approximation consists in decomposing our domain Ω into N_{el} elements K such that they cover the domain and there are either disjoint or share a complete edge (face). Using this partition, the above-defined functional spaces are approached by a finite dimensional spaces spanned by continuous piecewise polynomials such that:

$$\begin{cases} \mathcal{V}_h = \left\{ v_h \in (C^0(\Omega))^d \mid v_h|_K \in P^1(K)^d, \forall K \in \mathcal{T}_h \right\} \\ \mathcal{V}_{h,0} = \left\{ v_h \in \mathcal{V}_h, v_h|_{\Gamma} = 0 \right\} \\ \mathcal{Q}_h = \left\{ q_h \in C^0(\Omega) \mid q_h|_K \in P^1(K), \forall K \in \mathcal{T} \right\} \end{cases}$$

The Galerkin discrete problem consists now in solving the mixed problem by:

find the pair $(u_h, p_h) \in (\mathcal{V}_h, \mathcal{Q}_h)$, $\forall (v_h, q_h) \in (\mathcal{V}_{h,0}, \mathcal{Q}_h)$ such that:

$$\begin{cases} \rho \left(\frac{\partial u_h}{\partial t}, v_h \right) + \rho (u_h \cdot \nabla u_h, v_h) + (2\eta \mathcal{E}(u_h) : \mathcal{E}(v_h)) - (p_h, \nabla \cdot v_h) = (f, v_h) + (h_N, v_h)_{\Gamma_N} \\ (\nabla \cdot u_h, q_h) = 0 \end{cases} \quad (3.10)$$

It is known that the finite element approximation (3.10) may fail because of two reasons: the inf-sup condition (Brezzi-Babuska) which required an appropriate pair of the function spaces for the velocity and the pressure [4, 5].

The second one is the dominance of the nonlinear convective term which can generate spurious oscillations that will pollute the whole numerical solution. In the present work we aim to retain the advantages of using linear approximations (P1 finite elements) regarding the accuracy and the computational cost, especially for 3D real applications. But it is well known that the combination of P1-P1 approximation for the velocity and the pressure does not lead to a stable discretization of (3.10) since it fails to satisfy the inf-sup condition:

$$\inf_{q_h \in Q_h} \sup_{u_h \in \mathcal{V}_{h,0}} \frac{(\nabla \cdot u_h, q_h)_\Omega}{|q_h|_0 |u_h|_1} \geq \beta > 0 \quad (3.11)$$

where β is a constant independent of h .

Many measures may be distinguished to solve and get around these two difficulties, the instabilities in advection-dominated regime and the velocity-pressure compatibility condition. A very popular method was firstly proposed by Arnold, Brezzi and Fortin [6] for the Stokes problem. It was suggested to enrich \mathcal{V}_h with space of bubble functions known as MINI element. Since the bubble functions vanish on each element boundary, they can be eliminated and statically condensed giving rise to a stabilized formulation for equal-order linear element. Later it was pointed out in [7] that using these local bubbles is equivalent to residual-based stabilized schemes with a natural way of choosing the stabilization parameters. Therefore, the selection of the “optimal” bubble function will reproduce the appropriate choice of the stability parameter. Thus, it’s clear that the bubble will have different shape on the diffusive dominated regime then the advection-dominated flow regime. For example, it was shown in [8, 9] that upwind bubbles must be used to reproduce the SUPG stabilization.

A standard reference for mixed finite element methods is the book of Brezzi and Fortin [10]. A brief history on residual based stabilisation methods can be found in Brezzi *et al.* [11], the book of Donea and Huerta [12], all the articles by Hughes *et al.* [13, 14, 15] on multiscale methods and SUPG/PSPG methods by Tezduyar [16]. The Unusual Stabilised finite element method was introduced by Franca and Farhat in [17]. Codina and co-workers introduced lately recent developments of residual based stabilisation methods using orthogonal subscales and time dependent subscales [18, 19, 20, 21]. These methods are very promising and considered to be an open door to turbulence. At the same level, we can find a complete description on the use of variational multiscale method for turbulent flows in Gravemeier [22, 23, 24] where a three scale separation method was developed and applied.

The main interest of this chapter will focus on stabilizing the convection-dominated flows and to retain the use of equal velocity-pressure linear interpolation. A detailed description on the parallelisation of the 2D finite element solver using the Mini-element P1+/P1 can be found in T. Coupez [25, 26] and [27]. The implementation of the code in our finite element library CIMLIB and the stabilization for the 3D Stokes problem has to be credited to [28]. Recently, an extension to transient Navier-Stokes was considered and added by [29]. In this sense, the present work can be considered as a continuation of those references to deal with highly convection-dominated flows. Several numerical examples for solving the transient problems will show the benefits of the proposed scheme and conclusion will be drawn.

3.2 Stable mixed variational formulation

The primary aim of the next two sections is twofold: we begin to present briefly the classical stable mixed-formulation for the Stokes problem which can be derived by introducing the MINI element and the corresponding static condensation [6]. This formulation is stable for equal-order interpolation for the velocity and the pressure fields (satisfies the inf-sup condition) and already implemented in the CIMLIB library and validated by [27, 29]. Once we illustrate the basic enrichment of the functional spaces and the corresponding condensation procedure, we extend the presentation in the second part of this chapter for solving the transient Navier-Stokes equations using the general framework of the multiscale methods.

The finite element formulation of the classical mixed formulation for Stokes equations reads: find the pair $(\mathbf{u}_h, p_h) \in (\mathcal{V}_h, \mathcal{Q}_h)$ such that:

$$\begin{cases} (2\eta\mathcal{E}(\mathbf{u}_h) : \mathcal{E}(\mathbf{v}_h)) - (p_h, \nabla \cdot \mathbf{v}_h) = (f, \mathbf{v}_h) \\ (\nabla \cdot \mathbf{u}_h, q_h) = 0 \end{cases} \quad (3.12)$$

We enrich the velocity functional space by the discrete space associated to the bubble function [6]:

$$\tilde{\mathcal{V}}_h = \left\{ \tilde{\mathbf{u}}_h, \tilde{u}_{h|K_i} \in P^1(K_i) \cap H_0^1(K_i), \forall K \in \mathcal{T}_h, i=1, \dots, D \right\}$$

where D is the topological dimension and K_i is a decomposition of K in D subsimplex (subtriangle in two-dimension and subtetrahedra in three-dimension), that have as common vertex the barycentre of K . In other words, the choice of this bubble function is continuous inside the element, considered as linear on each sub-triangle and vanishes at the boundary of K .

The velocity field is now an element of the function space generated by the following direct sum $\mathcal{V}_h \oplus \tilde{\mathcal{V}}_h$. Hence, we use continuous piecewise linear functions enriched by bubbles for the velocity and piecewise linear functions for the pressure. The mixed-finite element approximation of problem (3.12) can now be written: find $\mathbf{u}_h \in \mathcal{V} = \mathcal{V}_h \oplus \tilde{\mathcal{V}}_h$ and $p_h \in \mathcal{Q}_h$ such that:

$$\begin{cases} (2\eta\mathcal{E}(\mathbf{u}_h) : \mathcal{E}(\mathbf{v}_h)) - (p_h, \nabla \cdot \mathbf{v}_h) = (f, \mathbf{v}_h) \\ (\nabla \cdot \mathbf{u}_h, q_h) = 0 \end{cases} \quad (3.13)$$

Since the fine-scale problem is independent and uncoupled at the element level and vanishes on the element boundaries, the system in (3.13) can be decomposed into:

$$\begin{cases} (2\eta\mathcal{E}(u_h) : \mathcal{E}(v_h)) - (p_h, \nabla \cdot v_h) = (f, v_h) \\ (2\eta\mathcal{E}(\tilde{u}_h) : \mathcal{E}(\tilde{v}_h)) - (p_h, \nabla \cdot \tilde{v}_h) = (f, \tilde{v}_h) \\ (\nabla \cdot (u_h + \tilde{u}_h), q_h) = 0 \end{cases} \quad (3.14)$$

Remark 1. Note that the fine-scale space is assumed to be orthogonal to the finite element space, the crossed viscous terms in both equations of (3.14) vanished [24].

Equations in (3.14) give rise to the following global system to solve:

$$\begin{pmatrix} A_{vv} & 0 & A_{vp}^T \\ 0 & A_{bb} & A_{bp}^T \\ A_{vp} & A_{bp} & 0 \end{pmatrix} \begin{pmatrix} u_h \\ \tilde{u}_h \\ p_h \end{pmatrix} = \begin{pmatrix} B_v \\ B_b \\ B_p \end{pmatrix} \quad (3.15)$$

where :

$$A_{vv} = (2\eta\mathcal{E}(u_h) : \mathcal{E}(v_h)), \quad A_{bb} = (2\eta\mathcal{E}(\tilde{u}_h) : \mathcal{E}(\tilde{v}_h)), \quad A_{vp} = (\nabla \cdot u_h, q_h), \quad A_{bp} = (q_h, \nabla \cdot \tilde{u}_h)$$

$$B_v = (f, v_h), \quad B_b = (f, \tilde{v}_h), \quad B_p = 0$$

The static condensation process consists into solving the second line for the bubble function \tilde{u} which by inserting into the third line of (3.15) results the condensed matrix scheme for large-scale unknowns u_h and p_h reading:

$$\begin{pmatrix} A_{vv} & A_{vp}^T \\ A_{vp} & \tilde{A}_{pp} \end{pmatrix} \begin{pmatrix} u_h \\ p_h \end{pmatrix} = \begin{pmatrix} B_v \\ \tilde{B}_p \end{pmatrix} \quad (3.16)$$

where:

$$\tilde{A}_{pp} = -A_{bp} A_{bb}^{-1} A_{bp}^T \quad \text{and} \quad \tilde{B}_p = -A_{bp}^T A_{bb}^{-1} B_b$$

It is clear that taking into account locally the influence of fine scales (bubble functions) upon the resolved large scales has introduced new stabilizing terms and has modified the components of the global matrix giving rise to a stable mixed formulation for the velocity and pressure system of equations (see [29] for more details).

3.3 Stabilized finite element method

In this section the time-dependent Navier-Stokes equation is solved. The stabilizing schemes from a variational multiscale view point will be described and presented. The velocity and the pressure spaces will be enriched by a space of bubbles that will cure the spurious oscillations in the convection-dominated regime as well as the pressure instability.

3.3.1 Multiscale approach

Following the lines in Hughes *et al.* [30], we assume an overlapping sum decomposition of the velocity and the pressure fields into resolvable coarse-scale and unresolved fine-scale $u = u_h + \tilde{u}$ and $p = p_h + \tilde{p}$. The fine-scale part is usually modelled via residual based terms that are derived consistently. The static condensation consists in substituting the fine-scale solution into the large-scale problem. Consequently, additional stabilized terms, tuned by a local time-dependent stabilizing parameter, will enhance the stability and accuracy of the standard Galerkin formulation for the transient nonlinear Navier-Stokes equations. Likewise, we consider the same decomposition for the weighting functions $v = v_h + \tilde{v}$ and $q = q_h + \tilde{q}$. Note also, that the fine-scale may be represented via different bubbles functions (similar to the MINI element) and the selection of the ‘‘optimal’’ bubble function will reproduce the appropriate choice of the stability parameter [7, 8].

The enrichment of the functional spaces is then as follow: $\mathcal{V} = \mathcal{V}_h \oplus \tilde{\mathcal{V}}$, $\mathcal{V}_0 = \mathcal{V}_{h,0} \oplus \tilde{\mathcal{V}}_0$, $\mathcal{Q} = \mathcal{Q}_h \oplus \tilde{\mathcal{Q}}$ and $\mathcal{Q}_0 = \mathcal{Q}_{h,0} \oplus \tilde{\mathcal{Q}}_0$. The mixed-finite element approximation of problem (3.10) can now be written:

find $(u, p) \in (\mathcal{V}, \mathcal{Q})$ such that:

$$\begin{aligned} & \rho \left(\frac{\partial(u_h + \tilde{u}_h)}{\partial t}, v_h + \tilde{v}_h \right) + \rho \left((u_h + \tilde{u}) \cdot \nabla(u_h + \tilde{u}_h), v_h + \tilde{v}_h \right) - (p_h + \tilde{p}, \nabla \cdot (v_h + \tilde{v}_h)) \\ & + (2\eta \varepsilon(u_h + \tilde{u}_h) : \varepsilon(v_h + \tilde{v}_h)) = (f, v_h + \tilde{v}_h) + (h_N, v_h + \tilde{v}_h)_{\Gamma_N} \quad \forall v_h + \tilde{v}_h \in \mathcal{V}_{h,0} \oplus \tilde{\mathcal{V}}_0 \end{aligned} \quad (3.17)$$

$$(\nabla \cdot (u_h + \tilde{u}), q_h + \tilde{q}_h) = 0 \quad \forall q_h + \tilde{q}_h \in \mathcal{Q}_{h,0} \oplus \tilde{\mathcal{Q}}_0 \quad (3.18)$$

As shown previously, these equations can be split also into two sub-problems by separating the two scales:

Integrating by parts within each element we obtain:

- *the coarse-scale problem:*

$$\begin{aligned} & \rho \left(\frac{\partial(u_h + \tilde{u}_h)}{\partial t}, v_h \right) + \rho \left((u_h + \tilde{u}_h) \cdot \nabla(u_h + \tilde{u}_h), v_h \right) - (p_h + \tilde{p}_h, \nabla \cdot v_h) + (2\eta \varepsilon(u_h) : \varepsilon(v_h)) \\ & = (f, v_h) + (h_N, v_h)_{\Gamma_N} \quad \forall v_h \in \mathcal{V}_{h,0} \end{aligned} \quad (3.19)$$

$$(\nabla \cdot (u_h + \tilde{u}_h), q_h) = 0 \quad \forall q_h \in \mathcal{Q}_{h,0} \quad (3.20)$$

- the fine-scale problem:

$$\rho \left(\frac{\partial(u_h + \tilde{u}_h)}{\partial t}, \tilde{v}_h \right) + \rho((u_h + \tilde{u}_h) \cdot \nabla(u_h + \tilde{u}_h), \tilde{v}_h) - (p_h + \tilde{p}, \nabla \cdot \tilde{v}_h) + (2\eta \mathcal{E}(\tilde{u}_h) : \mathcal{E}(\tilde{v}_h)) \quad (3.21)$$

$$= (f, \tilde{v}_h) + (h_N, \tilde{v}_h)_{\Gamma_N} \quad \forall \tilde{v}_h \in \tilde{\mathcal{V}}_0$$

$$(\nabla \cdot (u_h + \tilde{u}_h), \tilde{q}_h) = 0 \quad \forall \tilde{q}_h \in \tilde{\mathcal{Q}}_0 \quad (3.22)$$

To derive the stabilized formulation, we first solve the fine scale problem, defined on the sum of element interiors and written in terms of the time-dependant large-scale variables. Then we substitute the fine-scale solution back into the coarse problem (3.19 - 3.20), thereby ‘eliminating the explicit appearance of the fine-scale while still modelling their effects’.

Remark 1. Recall that for linear interpolation functions, the second derivatives vanish as well as all terms involving integrals over the element interior boundaries.

Remark 2. Since the fine-scale space is assumed to be orthogonal to the finite element space, the crossed viscous terms vanished in (3.19) and (3.21). [25-26]

Remark 3. For the sake of simplicity in the notation, we consider all of $\partial\Omega$ to be zero Dirichlet boundary condition. Generalization to other types of boundary conditions is straightforward.

Rearranging the terms, equation (3.21) is equivalent to:

$$\underbrace{\rho \left(\frac{\partial \tilde{u}}{\partial t}, \tilde{v} \right)}_{\text{time-dependent subscale}} + \underbrace{\rho((u_h + \tilde{u}) \cdot \nabla \tilde{u}, \tilde{v}) + (2\eta \mathcal{E}(\tilde{u}) : \mathcal{E}(\tilde{v})) + (\nabla \tilde{p}, \tilde{v})}_{\text{nonlinear convection term}} \quad (3.23)$$

$$= \left(f - \rho \frac{\partial u_h}{\partial t} - \rho(u_h + \tilde{u}) \cdot \nabla u_h - \nabla p_h, \tilde{v} \right) \quad \forall \tilde{v} \in \tilde{\mathcal{V}}_0$$

$$= (\mathcal{R}_m, \tilde{v}) \quad \forall \tilde{v} \in \tilde{\mathcal{V}}_0$$

$$(\nabla \cdot \tilde{u}, \tilde{q}) = (-\nabla \cdot u_h, \tilde{q}) = (\mathcal{R}_c, \tilde{q}) \quad \forall \tilde{q} \in \tilde{\mathcal{Q}}_0 \quad (3.24)$$

As we can observe, the subscale equation (3.23) is time dependent and highly nonlinear. To our knowledge, the first attempt to apply and use a time-dependent subscale for the Navier-Stokes equations has to be credited to Codina [19]. It was shown later in [31, 32] that by tracking the subscales in time and keeping their nonlinear contributions in the advection velocity will guarantee the global conservation of the momentum equation and can also open the door to turbulence modelling. These methods can be considered very promising and interesting and they will be for sure the subject of further research on the stabilization methods.

Here in our context, following the evolution and the storage of the small-scales in time together with the need of fine computational meshes can easily increase the computation cost in particular when long time simulation of heat treatment furnaces are considered. Therefore, for the time being, their effects will be replaced by the standard turbulence models such as the Smagorinsky-type eddy viscosity or k-epsilon-type eddy viscosity. These two models will be used later to deal with turbulent flows inside the furnace (see next chapter).

Before the description of the temporal discretization, we follow the work already made and implemented by [29] on the use of Newton-Raphson linearization method for treating the nonlinear convective terms. Here in our context, inspired by the work of Codina in [31], we will extend the use of this method to the multiscale finite element formulation. Recall that Newton-Raphson method is attractive because it converges rapidly from any sufficiently good initial guess; however, one drawback of this method is the need to solve the Newton equation at each iteration. This can be expensive specifically when the number of unknowns is large.

The nonlinear convective term in the large-scale problem can be approximated by keeping terms only to first order at the i^{th} iteration as:

$$\begin{aligned} (u_h \cdot \nabla u_h, v)^i &= (u_h^{i-1} + (u_h^i - u_h^{i-1}) \cdot \nabla (u_h^{i-1} + (u_h^i - u_h^{i-1})), v) \\ &= (u_h^{i-1} \cdot \nabla u_h^i, v) + (u_h^i \cdot \nabla u_h^{i-1}, v) - (u_h^{i-1} \cdot \nabla u_h^{i-1}, v) + ((u_h^i - u_h^{i-1}) \cdot \nabla (u_h^i - u_h^{i-1}), v) \quad (3.25) \\ &\approx (u_h^i \cdot \nabla u_h^{i-1}, v) + (u_h^{i-1} \cdot \nabla u_h^i, v) - (u_h^{i-1} \cdot \nabla u_h^{i-1}, v) \end{aligned}$$

where u^{i-1} is the previous know Newton-Raphson's iteration.

At this stage, before solving the fine-scale equation, the above mentioned assumptions will be detailed and then applied:

- 1- First, the subscales will not be tracked in time, therefore, 'quasi-static' subscales are considered here. This choice is justified in [33]. Since additional turbulence model will be used, this approximation is reasonable for the time being. Moreover, we can say that the subscale equation is 'quasi' time-dependent since it is driven by the large-scale time-dependent residual [31].
- 2- Second, the convective velocity of the nonlinear term may be approximated using only the large-scale part: $(u_h + \tilde{u}) \cdot \nabla (u_h + \tilde{u}) \approx u_h \cdot \nabla u_h + u_h \cdot \nabla \tilde{u}$. This choice will provides us with some reduction of computational cost.

Consequently, the fine-scale problem will reduce to the following:

$$\begin{aligned} \rho(u_h^{i-1} \cdot \nabla \tilde{u}, \tilde{v}) + (2\eta \varepsilon(\tilde{u}) : \varepsilon(\tilde{v})) + (\nabla \tilde{p}, \tilde{v}) &= (\mathcal{R}_m, \tilde{v}) \quad \forall \tilde{v} \in \tilde{\mathcal{V}}_0 \\ (\nabla \cdot \tilde{u}, \tilde{q}) &= (\mathcal{R}_c, \tilde{q}) \quad \forall \tilde{q} \in \tilde{\mathcal{Q}}_0 \end{aligned} \quad (3.26)$$

With regard to the work of [29], we can identify at this point two important extensions. The first consists in considering the advection terms in equation (3.26) and the second is that the small-scale pressure is included. These two extensions are essential for simulating high convection-dominated flows.

It is also known, from [44, 45] that by considering the small-scale pressure as an additional variable we complete the continuity condition on the small-scale level. This will provide additional stability in particular with increasing Reynolds number. However, solving the small-scale equation for both the velocity and the pressure is somewhat complicated. Franca and co-workers [4] proposed a separation technique of the small-scale unknowns. They replaced the small-scale continuity equation by the small-scale pressure Poisson equation (PPE). Since only the effect of the small-scale pressure Poisson equation on the large-scale equation must be retained, Franca and Oliveira (2003) [34] showed that rather than solving this equation it could be approximated by way of an additional term in the fashion of a stabilizing term. This leads to an approximation of the form

$$\tilde{p} \approx -\tau_c \nabla \cdot u_h \quad (3.27)$$

The result (3.27) can now be integrated directly into the large-scale equation (3.19). For additional details about solving the PPE equation, see the thesis [46] and the work of Gravemeier [22, 23, 24, and 41]. In these references, a complete review on considering two-scales and even three-scales for the convection-diffusion-reaction and the Navier-Stokes equations is fully described. Additionally, the author as in [36, 11] confirms that the effect of considering the small-scale pressure is important for high Reynolds applications.

For the definition of τ_c , we adopt the definition made by Codina and co-workers [21, 31]:

$$\tau_c = \left[v^2 + \left(\frac{c_2 |u|_K}{c_1 h} \right)^2 \right]^{1/2} \quad (3.28)$$

where c_1 and c_2 are two constants, independent of h , h is the characteristic element length defined in (2.31) and $\nu = \eta/\rho$ is the kinematic viscosity. More details about the choice of the stabilizing parameter will be addressed in the following section.

According to the previous assumptions, this method is then considered as a combined of stable formulation (MINI-element) / (stabilizing strategy). The stable formulation, as described previously for the Stokes problem, is applied to the velocity field whereas the fine-scale pressure is modelled using a stabilizing methods. After all, the main assumption that $\tilde{p} = 0$ in the small scale momentum equation and eliminating its effect in (3.26) comes down to the fact that ‘the small scale velocity is exclusively driven by the residual of the large scale momentum equation and not by the residual of the continuity equation’ [31].

In the last part of this section, we go back to the small-scale momentum equation. Please note that our objective is to compute the small-scale velocity and then integrate the solution into the large-scale problem. Many methods have been proposed to solve and approximate this fine-scale system (3.26). Since solving directly this problem is difficult, therefore, only their effects must be retained.

We can find in the literature the Green's function approach method proposed by Hughes [14] and Masud [35] and the two-level finite element approach proposed by Franca *et al.* [4]. The use of orthogonal subscales and the Fourier analysis approach was introduced and developed by Codina [31, 32]. The close relationship, the comparison between different stabilization techniques and the significantly contribution on the analysis of these method are credited to Codina in [18].

Without loss of generality, using the arguments of chapter 2 together with the previous section 3.2, the fine-scale problem is solved and the structure of the stability parameter is extracted by employing bubble functions on individual elements. Following all the earlier efforts made by Masud [47, 48, 49, 50], the fine-scale fields are expanded as follow:

$$\tilde{u}_h = \sum_{K \in \mathcal{T}_h} u'_K b_K \quad \text{and} \quad \tilde{v}_h = \sum_{K \in \mathcal{T}_h} v'_K b_K \quad (3.29)$$

where b_K represents the bubble shape functions, u'_K represents the coefficients for the fine-scale velocity field and v'_K represents the coefficient for the fine-scale weighting function.

Introducing (3.29) into the fine-scale momentum equation we get on each element K :

$$\rho \left(u_h^{i-1} \cdot \nabla b_K u'_K, b_K v'_K \right)_K + \left(2\eta \mathcal{E}(b_K u'_K) : \mathcal{E}(b_K v'_K) \right)_K = (\mathcal{R}_m, b_K v'_K)_K \quad (3.30)$$

As stated previously in chapter 2, we can reconstruct the fine scale velocity by taking, out of the integral, the vectors of constant coefficients.

Therefore, since v'_K is arbitrary, the fine-scale velocity will take the following form:

$$u'_K = \frac{1}{\underbrace{\left[\rho \left(u_h^{i-1} \cdot \nabla b_K, b_K \right)_K + \left(2\eta \mathcal{E}(b_K) : \mathcal{E}(b_K) \right)_K \right]}_{\tau_K}} (\mathcal{R}_m, b_K) \quad \forall K \in \mathcal{T}_h \quad (3.31)$$

As expected, the structure of the elemental stabilisation parameter τ_K has appeared naturally via the solution of the fine-scale problem. Consequently, the effect of the bubble is now condensed in this elemental parameter.

As mentioned before, it is clear that the choice of the bubble functions affects the value of the stability parameter. In (3.31) both convection and viscous regime are represented. But it is important to note that when using the same bubble function for the trial solution and the weighting function leads to the cancellation of the convection term in the definition of the needed stabilisation parameter τ_K . Under the assumption that u_h is piecewise constant, it is easy to see that the choice of the MINI-element bubbles yields:

$$\left(u_h^{i-1} \cdot \nabla b_K, b_K \right)_K = 0 \quad \forall K \in \mathcal{T}_h \quad (3.32)$$

One way to recover the convection terms it was pointed out by [8, 9], is the use of additional upwind bubbles. Such choice can reproduce naturally the coefficients of SUPG stabilization methods. This matter was highlighted by also Masud *et al.* [49, 50] by proposing the use of different order interpolation functions for the trial solution and the weighting function in the skew part of (3.31) (see figure 1 for an example). In order to keep the presentation simple, and to extract the structure of the stability parameter τ_K , we employ a combination of standard bubble shape functions b_K and upwind shape functions b_K^* in the fine-scale field \tilde{v}_h . More details about this section are given in chapter 6 section 2.

Therefore, by introducing the modified \tilde{v}_h in (3.30), the fine-scale velocity will take the modified following form:

$$u'_K = \left[\underbrace{\rho(u_h^{i-1} \cdot \nabla b_K, b_K^*)}_K}_{\text{advection term}} + \underbrace{(2\eta \varepsilon(b_K) : \varepsilon(b_K))}_K}_{\text{viscous term}} \right] (\mathcal{R}_m, b_K) \quad \forall K \in \mathcal{T}_h \quad (3.33)$$

Remark 4. Using linear interpolations, the upwind part drops out directly in the viscous term.

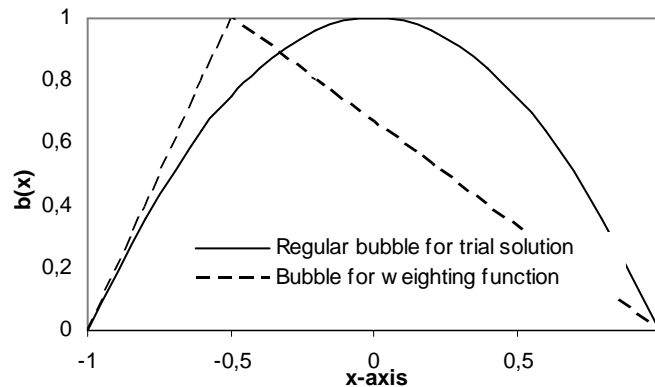


Figure 1. Example of 1-D bubble function for the trial solution and the weighting function adopted from [50]

Now, let us reconsider the coarse-scale problem given by (3.19-3.20)

$$\left(\rho \frac{\partial u_h}{\partial t}, v_h \right) + (\rho u_h \cdot \nabla u_h, v_h) + (\rho u_h^{i-1} \cdot \nabla \tilde{u}_h, v_h) + (2\eta \varepsilon(u_h) : \varepsilon(v_h)) \quad (3.34)$$

$$-(p_h, \nabla \cdot v_h) - (\tilde{p}, \nabla \cdot v_h) = (f, v_h) \quad \forall v_h \in \mathcal{V}_{h,0}$$

$$(\nabla \cdot u_h, q_h) + (\nabla \cdot \tilde{u}_h, q_h) = 0 \quad \forall q_h \in \mathcal{Q}_{h,0} \quad (3.35)$$

Applying integration by parts to the third terms in equation (3.34) and to the second term in equation (3.35), and then substituting the expressions of both the fine-scale pressure (3.27) and the fine-scale velocity (3.33), we get:

$$\begin{aligned} & \left(\rho \frac{\partial u_h}{\partial t}, v_h \right) + (\rho u_h \cdot \nabla u_h, v_h) - \sum_{K \in \mathcal{T}_h} \left(\tau_K \mathcal{R}_m, \rho u_h^{i-1} \cdot \nabla v_h \right) + (2\eta \mathcal{E}(u_h) : \mathcal{E}(v_h)) \\ & - (p_h, \nabla \cdot v_h) + \sum_{K \in \mathcal{T}_h} (\tau_C \nabla \cdot u_h, \nabla \cdot v_h) = (f, v_h) \quad \forall v_h \in \mathcal{V}_{h,0} \end{aligned} \quad (3.36)$$

$$(\nabla \cdot u_h, q_h) - \sum_{K \in \mathcal{T}_h} (\tau_K \mathcal{R}_m, \nabla q_h) = 0 \quad \forall q_h \in \mathcal{Q}_{h,0} \quad (3.37)$$

Finally, substituting the residual of the momentum equation and expanding all the additional terms, we obtain from (3.36) a modified coarse scale equations expressed solely in coarse scale functions. For illustration purposes, the new modified problem can now be decomposed into four main terms: the first one is the Galerkin contribution; the second and the third terms take into account the influence of the fine-scale velocity on the finite element components and the last term models the influence of the fine-scale pressure onto the large-scale problem.

$$\begin{aligned} & \underbrace{\left(\rho \frac{\partial u_h}{\partial t}, v_h \right) + (\rho u_h \cdot \nabla u_h, v_h) + (2\eta \mathcal{E}(u_h) : \mathcal{E}(v_h)) - (p_h, \nabla \cdot v_h) + (\nabla \cdot u_h, q_h) - (f, v_h)}_{\text{Galerkin terms}} \\ & + \underbrace{\sum_{K \in \mathcal{T}_h} \left(\tau_K \rho \frac{\partial u_h}{\partial t} + \rho u_h \cdot \nabla u_h + \nabla p - f, \rho u_h^{i-1} \cdot \nabla v_h \right)}_{\text{Upwind stabilization terms}} \\ & + \underbrace{\sum_{K \in \mathcal{T}_h} \left(\tau_K \rho \frac{\partial u_h}{\partial t} + \rho u_h \cdot \nabla u_h + \nabla p - f, \nabla q_h \right)}_{\text{Pressure stabilization terms}} \\ & + \underbrace{\sum_{K \in \mathcal{T}_h} (\tau_C \nabla \cdot u_h, \nabla \cdot v_h)}_{\text{grad-div stabilization term}} = 0 \quad \forall v_h \in \mathcal{V}_{h,0}, \quad \forall q_h \in \mathcal{Q}_{h,0} \end{aligned} \quad (3.38)$$

When compared with the Galerkin method (3.9), the proposed stable formulation involves additional integrals that are evaluated element wise. These additional terms, obtained by replacing the approximated \tilde{u} and \tilde{p} into the large-scale equation, represent the effects of the sub-grid scales. As a result, different stabilization terms were introduced in a consistent way to the Galerkin formulation. As for the additional grad-div stabilization term, it was introduced to the large-scale momentum equation controlled by a suitable parameter τ_C . All of these terms will overcome the instability of the classical formulation found in convection dominated flows and the need to satisfy the inf-sup condition for the velocity and pressure interpolations. While the last term in equation (3.38) provides additional stability at high Reynolds number.

Remark 1. The addition of the stabilizing terms does not compromise the consistency of the formulation, since these terms are weighted with the residuals of the equations, which vanish for exact solutions.

Remark 2. Recall that when using linear elements (triangular and tetrahedral) all second order derivatives vanishes. These terms were directly omitted from the formulations.

Remark 3. For sake of simplicity in the notation and for a better representation of all the additional terms in equation (3.38), the condensation procedure of the small-scale into the large scale is masked under these stabilizing parameters. However, from the implementation point of view, the structure of the stabilizing parameters will be computed naturally via the element-level matrices.

3.3.2 Matrix formulation of the problem

Let us summarize and rewrite the resulting variational stabilized formulation in the usual matrix scheme. Following the work of [29] on the development of the Navier-Stokes solver in CIMLIB library, it is adequate that we keep here the same matrix notations. All new additional stabilizing terms needed for the convection-dominated problems will be then highlighted. Note also that the structure of the stabilizing parameters will be computed naturally via the element-level matrices.

For sake of simplicity in the notation, the Euler implicit temporal discretization is applied, the linearization (3.25) is introduced into the variational formulation for the space-time discretized Navier-Stokes equations and the modified fine-scale weighting function \tilde{v}_h is used. Correspondingly, the matrix equivalent of the stabilized problem simplifies to

$$\begin{pmatrix} A_{vv} & A_{vb}^T & A_{vp}^T \\ A_{bv} & A_{bb} & A_{bp}^T \\ A_{vp} & A_{bp} & 0 \end{pmatrix} \begin{pmatrix} u_h \\ \tilde{u}_h \\ p_h \end{pmatrix} = \begin{pmatrix} B_v \\ B_b \\ B_p \end{pmatrix} \quad (3.39)$$

where

$$A_{vv} = \left(\rho \frac{u_h}{\Delta t}, v_h \right) + \left(\rho u_h^{i-1} \cdot \nabla u_h^i, v_h \right) + \left(\rho u_h^i \cdot \nabla u_h^{i-1}, v_h \right) + \left(2\eta \varepsilon(u_h) : \varepsilon(v_h) \right) + \underbrace{\left(\tau_C \nabla \cdot u_h, \nabla \cdot v_h \right)}_{\text{Effect of } \tilde{p}}$$

$$A_{bv} = \left(\rho \frac{u_h}{\Delta t}, \tilde{v}_h \right) + \left(\rho u_h^{i-1} \cdot \nabla u_h^i, \tilde{v}_h \right) + \left(\rho u_h^i \cdot \nabla u_h^{i-1}, \tilde{v}_h \right)$$

$$A_{bb} = \rho \left(u_h^{i-1} \cdot \nabla \tilde{u}_h, \tilde{v}_h \right) + \left(2\eta \varepsilon(\tilde{u}_h) : \varepsilon(\tilde{v}_h) \right)$$

$$A_{vp} = \left(\nabla \cdot u_h, q_h \right)$$

$$A_{bp} = \left(q_h, \nabla \cdot \tilde{u}_h \right)$$

$$B_v = (f, v_h) + \rho \left(\frac{u_h^-}{\Delta t}, v_h \right) + \rho (\nabla u_h^{i-1}, u_h^{i-1}, v_h)$$

$$B_p = 0$$

$$B_b = (f, \tilde{v}_h) + \rho \left(\frac{u_h^-}{\Delta t}, \tilde{v}_h \right) + \rho (\nabla u_h^{i-1}, u_h^{i-1}, \tilde{v}_h)$$

The static condensation process consists into solving the second line for \tilde{u} and by inserting it into the first and third line of (3.39) it gives rise to the condensed matrix scheme for large-scale unknowns u_h and p_h reading

$$\begin{pmatrix} \tilde{A}_{vv} & \tilde{A}_{vp}^T \\ \tilde{A}_{vp} & \tilde{A}_{pp} \end{pmatrix} \begin{pmatrix} u_h \\ p_h \end{pmatrix} = \begin{pmatrix} \tilde{B}_v \\ \tilde{B}_p \end{pmatrix} \quad (3.40)$$

where:

$$\tilde{A}_{vv} = A_{vv} - A_{vb}^T A_{bb}^{-1} A_{bv} \quad \tilde{A}_{vp} = A_{vp} - A_{bv} A_{bb}^{-1} A_{bp}$$

$$\tilde{A}_{vp}^T = A_{vp}^T - A_{vb}^T A_{bb}^{-1} A_{bp}^T \quad \tilde{A}_{pp} = -A_{bp} A_{bb}^{-1} A_{bp}^T$$

$$\tilde{B}_v = B_v - A_{vb}^T A_{bb}^{-1} B_b \quad \tilde{B}_p = -A_{bp}^T A_{bb}^{-1} B_b$$

It is clear that taking into account locally the influence of unresolved fine scales upon the resolved large scales has introduced new stabilizing terms and modified the components of all the matrices. The effect of the fine-scale pressure was added directly to the first matrix by a stabilizing term. These terms seems to play an important role in particularly for high Reynolds number flows. Later on, several numerical examples will show the benefits of the proposed scheme.

Remark 4. In order to keep the presentation simple, we advise the reader to consult [29] as well as section 2 from chapter 6 for more details about the time discretization combined with the Newton-Raphson linearization.

3.3.3 Stabilization parameter

The selection of the stabilization parameter has attracted a significant amount of attention and research. This subject was also discussed in the previous chapter. Here, for the Navier-Stokes equation, these stabilizing parameters will involve in their structure the spatial and temporal discretization, the equation coefficients as well as the local Reynolds number. Various definitions were proposed and tested for the SUPG, GLS and the PSPG methods.

These definitions can be easily implemented in any finite element codes. Please consult [45, 36, 51, 52] for more details.

In the previous subsection, we showed that the stabilizing parameter was constructed naturally in a consistent manner by incorporating the coarse-scale residual evaluated over the element. This forms the advantage of using variational multiscale approach, i.e. unlike other SUPG/PSPG implementations, the multiscale approach allows a local tuning of the size of the stabilization term, thus enhancing flexibility and accuracy. But at the same time, it seems interesting to discuss the structure of these parameters and there limits in different regimes.

Recall that the importance of stabilization is related to the local nature of the flow that is commonly characterized by a local Reynolds number to be defined. This leads us to set up different strategies for the choice of the stabilizing parameter depending on the local Reynolds number. However, using bubble approach to SUPG will lead to efficient strategies for an automatic choice of these parameters.

Most of the strategies involve first of all the computation of a local Reynolds number

$$\text{Re}_K = \frac{m_K |u|_K h}{4\nu} \quad (3.41)$$

Next, if we set

$$\zeta(\text{Re}_K) = \begin{cases} \text{Re}_K & \text{if } 0 \leq \text{Re}_K \leq 1 \\ 1 & \text{if } \text{Re}_K > 1 \end{cases} \quad (3.42)$$

Then this common used stabilizing parameter will take the following form:

$$\tau_K = \frac{h}{2|u|_K} \zeta(\text{Re}_K) = \begin{cases} m_K \frac{h^2}{8\nu} & \text{if } 0 \leq \text{Re}_K \leq 1 \\ \frac{h}{2|u|_K} & \text{if } \text{Re}_K > 1 \end{cases} \quad (3.43)$$

where m_K is 1/3 is the optimal value for piecewise linear elements and $|u|_K$ is the norm of the velocity.

Here h , as mentioned previously, is an appropriate measure for the size of the mesh cell K [45, 51]. Observe that in the expression (3.43) τ_K switches between different dominated regimes; i.e. in diffusion dominated case, τ_K is $O(h_K^2/\nu)$ and in the advection dominated case is $O(h_K/|u|_K)$ [47, 50].

A similar expression of the stabilizing parameters was suggested by Codina [31, 32] from a Fourier analysis of the subscale problem

$$\tau_K = \left[\left(\frac{c_1 \nu}{h^2} \right)^2 + \left(c_2 \frac{|u|_K}{h} \right)^2 \right]^{-1/2} \quad (3.44)$$

where c_1 and c_2 are algorithmic constants chosen equal to 4 and 2 respectively for linear elements. Similarly, the two terms in the right-hand expression can be interpreted as the diffusion-dominated regime and the advection-dominated regime.

For time-dependent problems, the time step is introduced into the definition of τ_K . Tezduyar and Osawa [45] supposed that

$$\tau_K = 1 / \sqrt{\left(\frac{2}{\Delta t} \right)^2 + \left(\frac{4\nu}{h^2} \right)^2 + \left(\frac{2|u|_K}{h} \right)^2} \quad (3.45)$$

This is the most common used definition for the transient Navier-Stokes problems. However, for small time step, the expression of τ_K can degenerate in that $\tau_K \rightarrow 0$. One way to remedy this problem is the use of dynamic subgrid scales introduced by Codina *et al.* [21], i.e. the fine-scale velocity becomes a history variable that needs to be stored. This seems like a promising step in the direction of more accurately representing the fine scales and can also open the door to turbulence modeling.

To conclude, it is clear that in all the definitions given in this section, the structure of the stabilization parameter contains mainly two terms: convection term and viscous terms, which is identical to the structure given in the previous section (eq. 3.33).

3.4 Numerical examples and validation

In this section, four numerical calculations are performed to assess the effectiveness of the method described previously. Numerical examples for time-dependent flow problems are given in the following. The main interest of these examples is to test how well the stabilized formulation developed herein matches with computation in particular for high Reynolds number. More applications on thermally coupled flows for heat treatment furnaces will be given later in chapter 5 and 6. The previous implementation of the Navier-Stokes solver [29] will also be used and referred as 'previous version' or 'old scheme'. Recall that the difference between the new implemented method and the previous version resides only in the extension to deal with high convection dominated flows. In order to highlight the role of these additional terms, some comparisons are made and results are discussed.

3.4.1 A convergence test

In this example, already presented in [53] and [46], we consider the Navier-stokes equations in the unit square $\Omega=[0,1]\times[0,1]$. The objective of this test is to check the convergence of the approximation to the exact solution and to compare the effect of the new additional stabilizing terms in respect to the previous version implemented in CIMLIB [29]. This problem consists of a jet impinging upon a wall with a controlled body force f given by

$$\begin{aligned} f_1 &= 5xy^8 + 10xy^3 + 60vxy^2 \\ f_2 &= 0 \end{aligned} \quad (3.46)$$

The exact velocity components and the pressure are then defined on the domain by:

$$\begin{aligned} u_1 &= -5xy^4, \quad u_2 = -\frac{1}{2} + y^5 \\ p &= \frac{1}{2}(y^5 - y^{10}) + 5vy^4 \end{aligned} \quad (3.47)$$

The boundary conditions as well as the expected velocity distribution are depicted in Fig. 2.

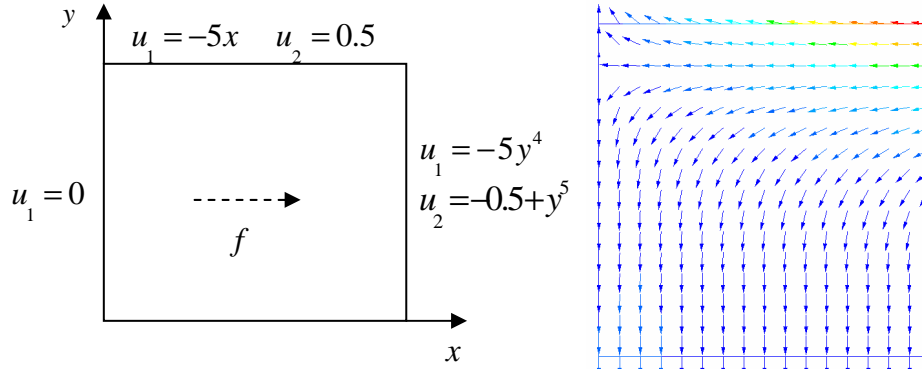


Figure 2. Boundary conditions (left) and expected velocity distribution (right)

The convergence study is divided into two parts. In the first part we study the convergence for low Reynolds number $Re=0.5025$ with $v=10$ (diffusion-dominated flow), and in the second part we present the convergence rates for high Reynolds number $Re=5025$ with $v=0.001$ (convection-dominated flow). Uniform meshes of 4×4 , 8×8 and 16×16 linear triangular elements have been used to discretize the computational domain. We compute the error of the velocity and the pressure solution using the L^2 -norm as follow:

$$e_h^u = \frac{\|u - u_h\|_0}{\|u\|_0} = \left(\frac{\int_{\Omega} (u - u_h)^2 d\Omega}{\int_{\Omega} u^2 d\Omega} \right)^{\frac{1}{2}}, \quad e_h^p = \frac{\|p - p_h\|_0}{\|p\|_0} = \left(\frac{\int_{\Omega} (p - p_h)^2 d\Omega}{\int_{\Omega} p^2 d\Omega} \right)^{\frac{1}{2}} \quad (3.48)$$

In the given reference [46], the objective being different, a full study of convergence was conducted for testing higher-order elements using different methods. Here, we retain the use of linear triangular elements and we investigate the effects of ignoring both the pressure subscale and the added stabilizing convective terms in different regimes.

In Figure 3, the values of the pressure are shown and measured along the y -axis at $x=0.5$. For diffusion-dominated flow, both methods are in very good agreements with the exact solution. As expected, when the flow becomes convection-dominated, some numerical oscillations appear in the solution (see Figure 3 and Figure 4). On the other hand, the new modified scheme yields good results when comparing to the analytical solution.

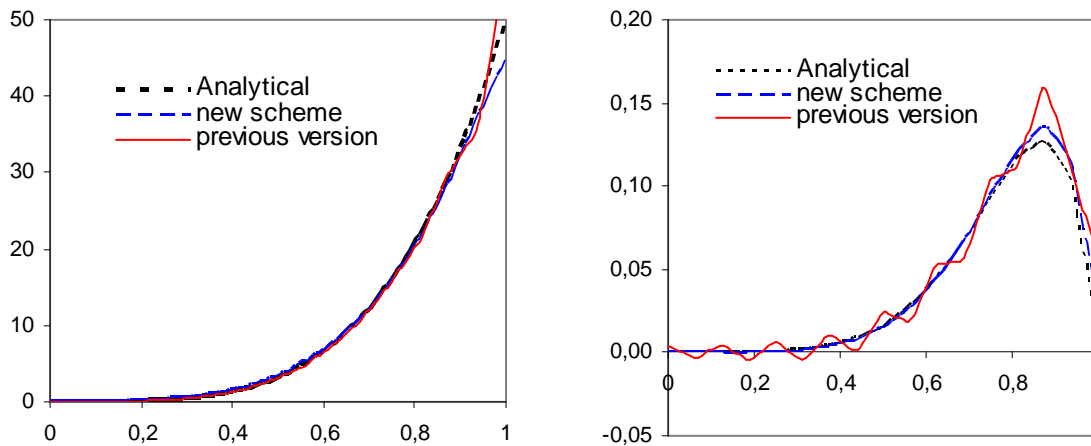


Figure 3. Pressure solution obtained by using 16×16 linear triangular elements: diffusion-dominated flow (left) and convection-dominated flow (right)

Moreover, it was pointed out also in [46] that the use of linear elements in this numerical test leads to relatively ‘satisfactory’ results for the pressure. This can be observed in Figure 4 showing the pressure distribution for both methods. For more details about the use of higher-order elements and curing these instabilities, the readers could refer to [46].

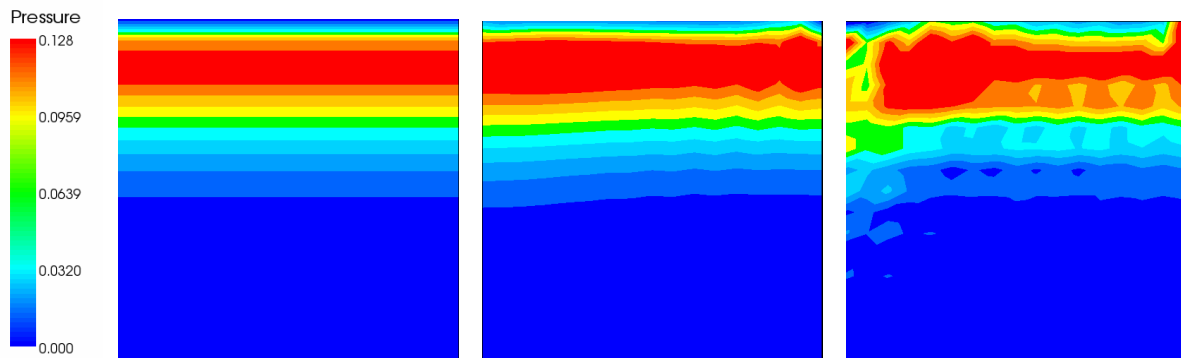


Figure 4. Pressure distribution obtained by using 16×16 linear triangular elements for convection-dominated flow: analytical (left), new scheme (center) and previous version (right)

Figure 5 and 6 present the convergence rates in the L_2 -norm for the velocity and the pressure fields. In the diffusion-dominated flow (Figure 5), the convergence rates are in complete accordance with the theoretical predictions and both methods accurately matched.

However, it is interesting to note that the error increases when the convection terms become dominant as showing in figure 6, whereas the new scheme exhibits smaller error and keeps the same order of convergences. These rates are in agreement with the references.

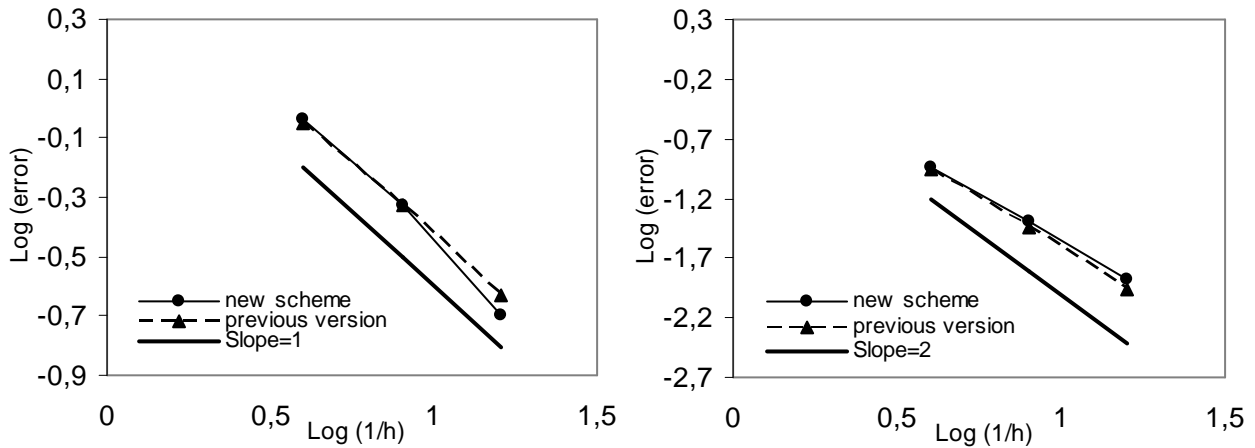


Figure 5. L^2 -norm for diffusion-dominated flow: pressure (left) and velocity (right)

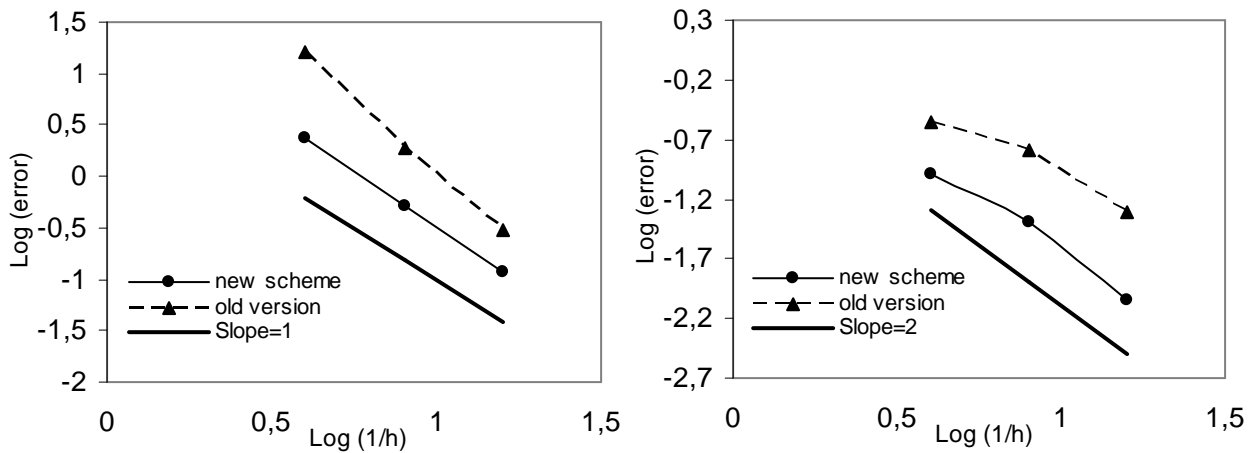


Figure 6. L^2 -norm for convection-dominated flow: pressure (left) and velocity (right)

3.4.2 Driven flow cavity problem (2-D)

Now we numerically solve the lid-driven flow problem. This test has been widely used as a benchmark for numerical methods and has been analyzed by a number of authors (for example, see [37, 38, 39, 40]). The problem description, boundary conditions and the corresponding meshes are depicted in figure 7. Dirichlet boundary conditions prescribe $\bar{u}(1,0)$ on the upper boundary at $y=1$, and $\bar{u}(0,0)$ elsewhere on Ω . The source term is identical to zero. The viscosity is adjusted in order to obtain Reynolds number of 1000, 5000, 10000, 20000, 33000 and 50000. Zero pressure is prescribed at the lower left corner.

Two meshes of linear finite elements have been used in the calculations. The “coarse” one is made of 64×64 elements, refined near the walls of the cavity. The “fine” mesh consists of 180×180 elements. All numerical experiments will be compared to the very known references of Ghia *et al.* (1982) [37] and Erturk *et al.* [42]. The authors in [37] applied a second-order accurate finite difference method using a fine grid of 257×257 while in [42] the 2-D steady incompressible Navier-Stokes equations was solved using a very efficient finite difference numerical method (fourth order compact formulation) on a very fine grid of 601×601 . We consider that the steady state is reached when the normalized velocity deviations within one step are lower than a chosen tolerance of 10^{-6} . Recall that the main interest is to compare the performance of the new scheme described in the previous section and the behavior of the solution for high Reynolds number flows.

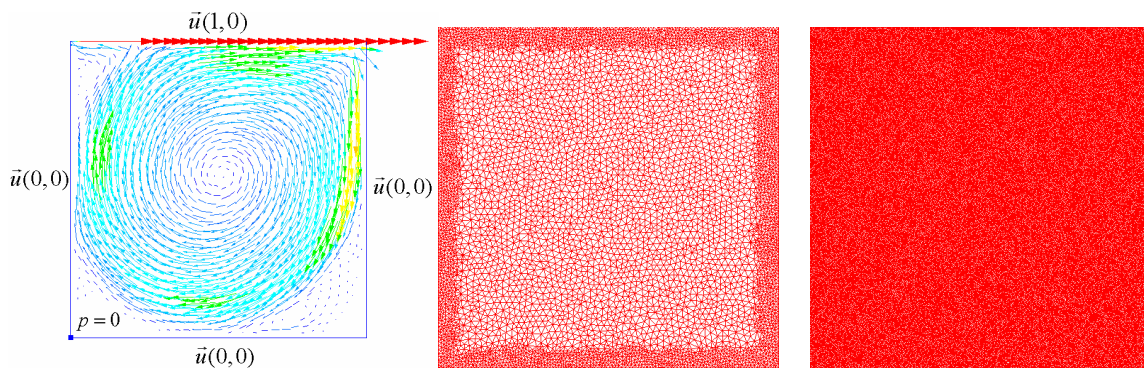


Fig 7. Problem settings: boundary conditions (left), coarse mesh (center), fine mesh (right)

A first set of numerical experiments has been performed using both methods i.e., the previous version and the new modified scheme. The velocity profiles for u_x and u_y along $x=0.5$ and $y=0.5$ respectively are shown in figure 8 and 9. Comparing these results with the given reference, one can clearly see the improvement of the new scheme in the solution in particular when the Reynolds number increases. Hence, we conclude that the absence of the pressure subscale and the convection terms in the small-scale problem renders an extremely diffusive solution even on a very fine mesh. For high Reynolds number, the results are underestimated with respect to the new formulation. However, the solution of the modified scheme is in a very agreement with the reference in all situations.

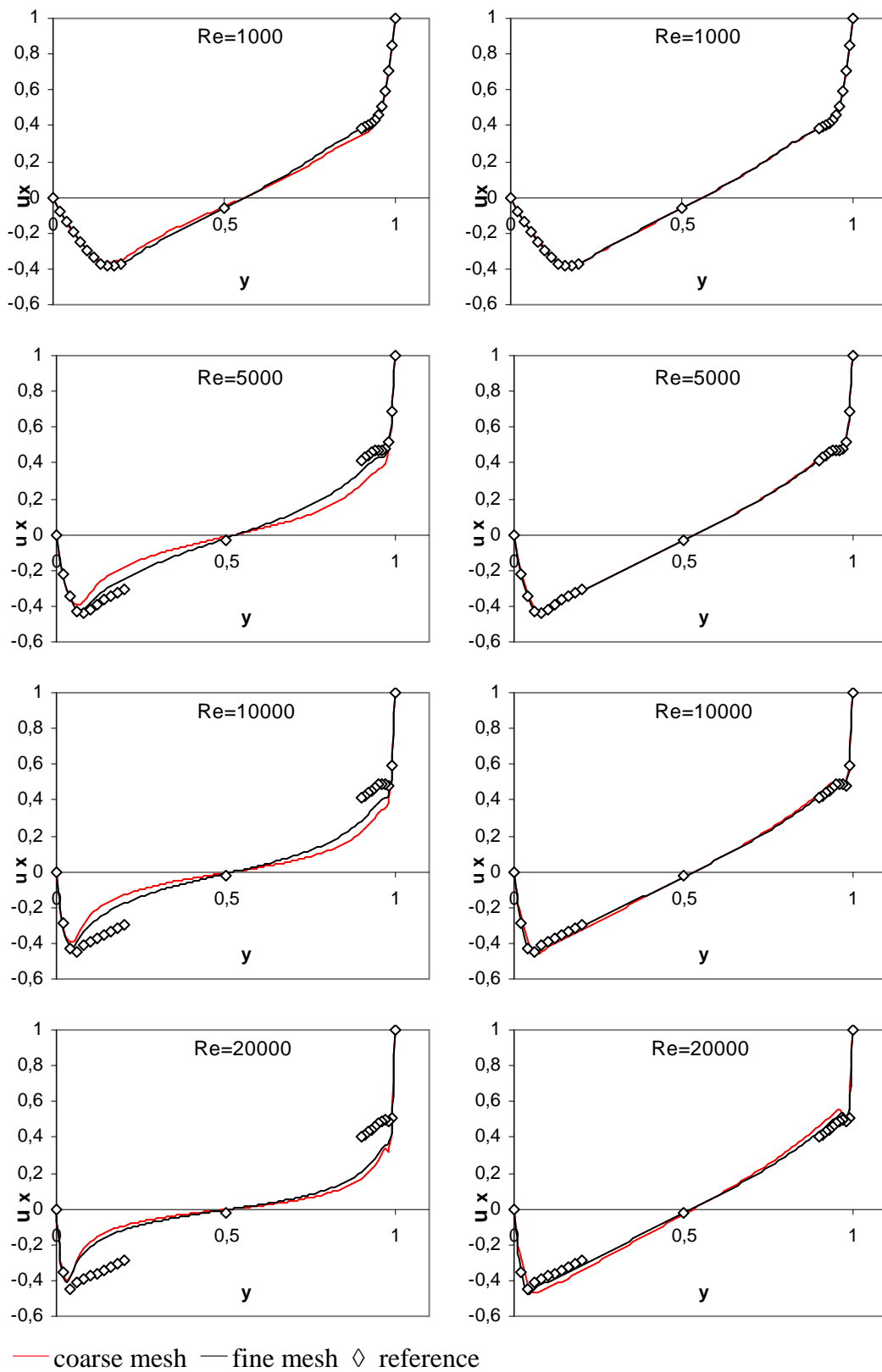


Fig 8. Velocity profile for u_x along $x=0.5$: previous version (left) and modified scheme (right)

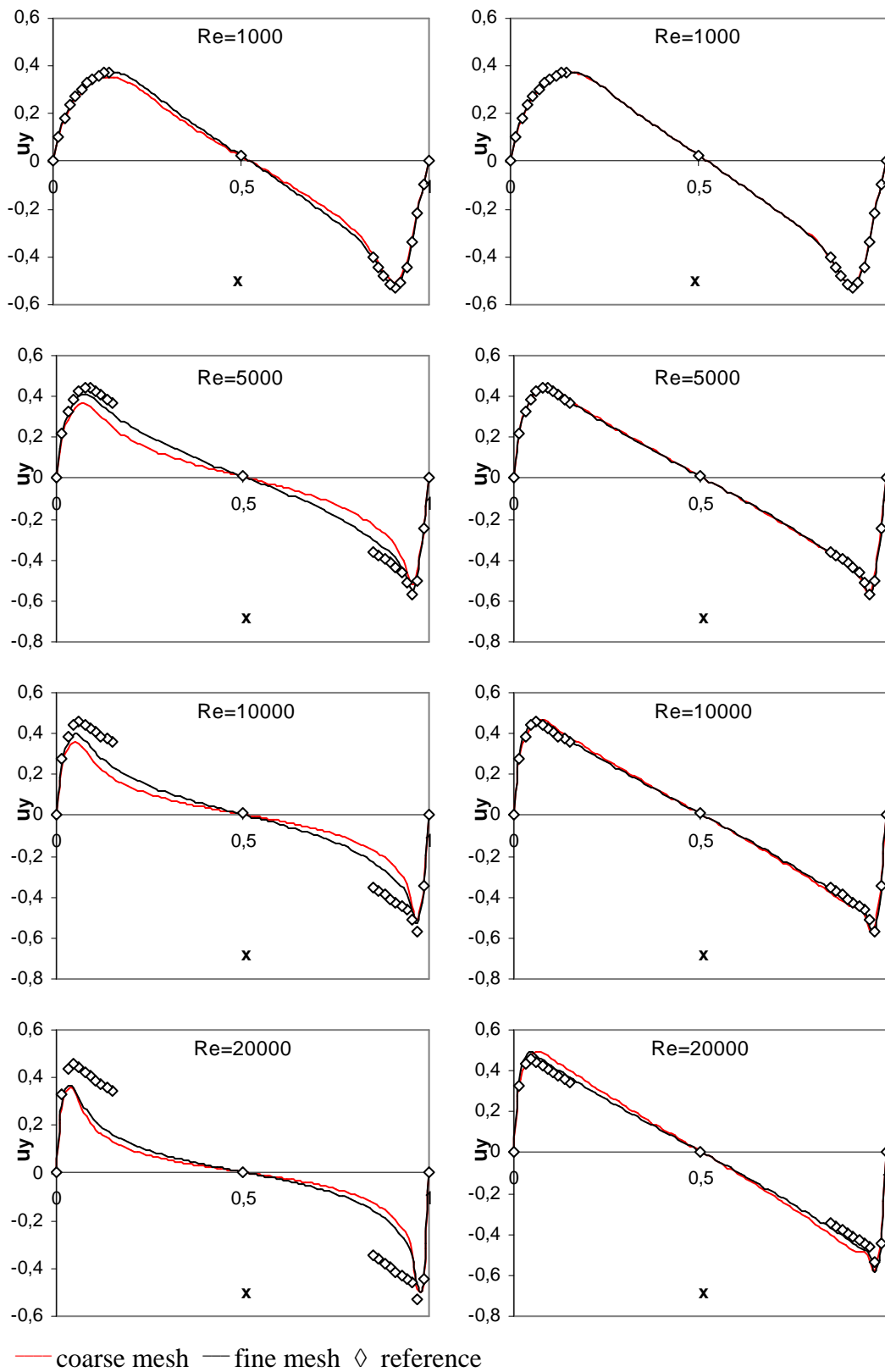


Fig 9. Velocity profile for u_y along $y=0.5$: previous version (left) and modified scheme (right)

Some other interesting quantities than plotting the velocity profiles are available in the literature. For instance, in [46] the author have studied and analyzed the pressure and the vortex formation and comparisons were made using several numerical methods for different Reynolds number. In the following, we will get a closer look on the pressure isolines for Reynolds number 10000 and compared our results to the given reference. Table I and figure 10 show a very good agreement of the new modified scheme with the given reference.

	<i>previous version</i>	<i>new scheme</i>	USFEM	two-level method	Three-level method
Re=10000, mesh 64x64	-0.0372 / 0.8056	-0.1319 /0.9142	-0.0975 /0.8774	-0.0730 /1.0465	-0.0904 /1.1278

Table I. Minimum and maximum values of the pressure for various numerical methods

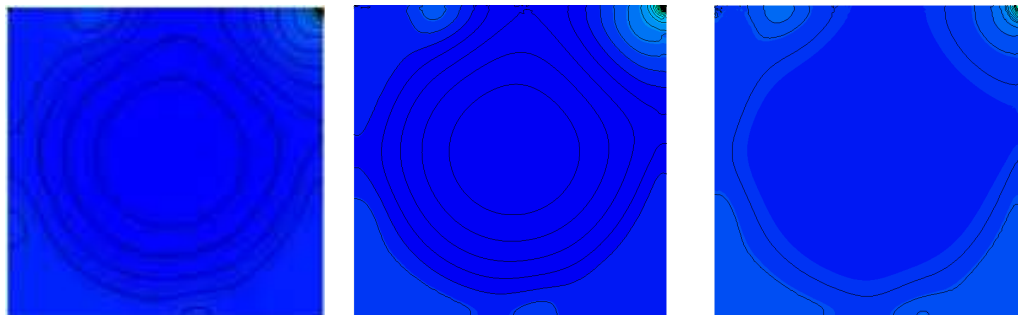


Figure 10. Pressure isolines on colored pressure distribution: two-level method adapted from [46] (left), the new modified scheme (middle) and the previous version (right)

As in [29] we will continue our comparisons by investigating the location of the respective vortex centers. Figure 11 shows the computed flow fields in terms of the velocity magnitude and the corresponding streamlines.

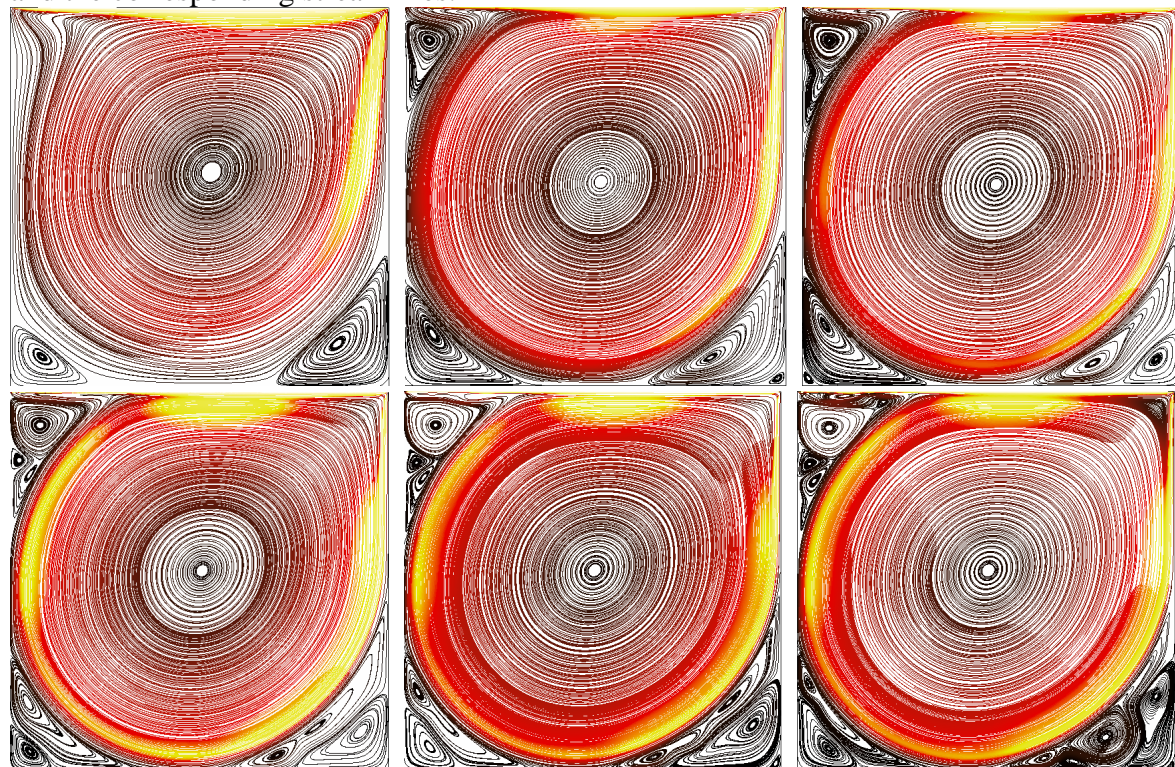


Figure 11. Streamline on colored velocity distribution from top-left to bottom-right: Re=1000, 5000, 10000, 20000, 33000 and 50000 with 180x180 mesh

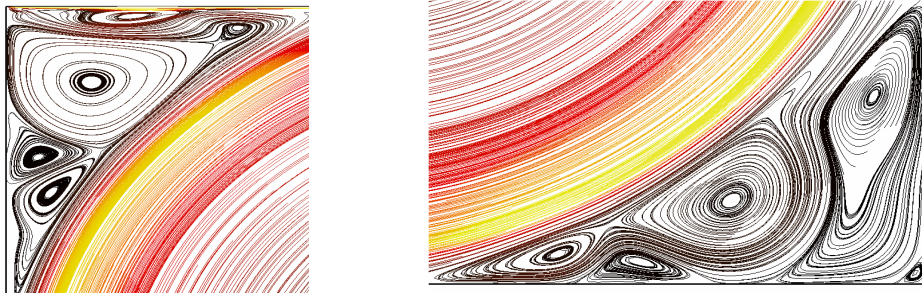


Figure 12. A magnified view of various secondary vortices near the cavity corners, $Re=50000$

As expected, using the fine mesh 180×180 the solutions exhibit additional counter-rotating vortices in or near the cavity corners as Re increases. It is known that this problem involves a primary vortex, while for higher Reynolds numbers secondary vortices appear in the corners of the domain. As the Reynolds number increases, the location of the centers of these vortices change, secondary vortex has the tendency to break on two new vortex and consequently their number increases (see figure 11 and 12). The effect of Re on the genesis of new vortices inside the cavity is presented in the following graph.

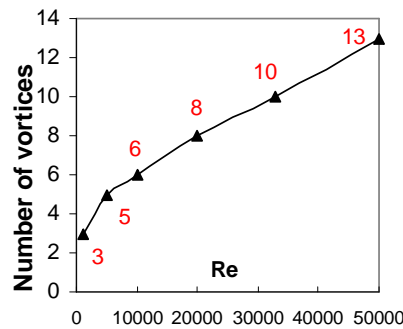


Figure 13. Number of resolved vortices in function of the Reynolds number

Figure 14 highlights by order of appearance the location of these expected vortices. The location of the centers of these vortices together with corresponding values from references solutions are summarized in Table II. Qualitatively and quantitatively, the results are similar to reference solutions and a good agreement is observed, although the mesh used here is coarser than the one used in the reference.

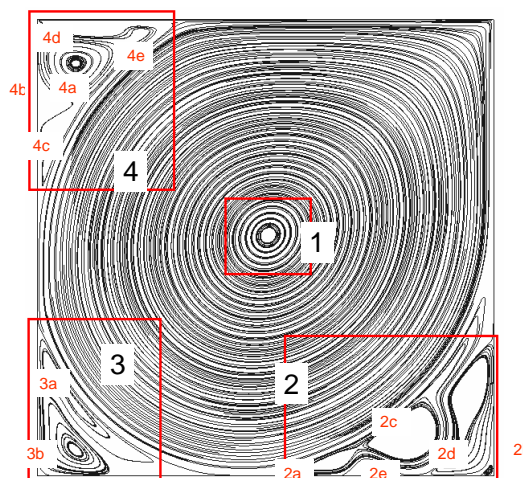


Figure 14. Location of the resolved vortices in order of appearance

Reynolds		1000	5000	10000	20000	33000	50000
Vortex 1a	Present	0,532 / 0,566	0,514 / 0,536	0,511 / 0,531	0,508 / 0,528	0,506 / 0,527	0,506 / 0,526
	Reference	0,5313 / 0,5625	0,5117 / 0,5352	0,5117 / 0,533	0,5100 / 0,5267	-	-
Vortex 2a	Present	0,864 / 0,112	0,802 / 0,0733	0,767 / 0,0594	0,706 / 0,0416	0,667 / 0,035	0,654 / 0,0309
	Reference	0,8594 / 0,1094	0,8086 / 0,0742	0,7656 / 0,0586	0,7267 / 0,0450	-	-
Vortex 3a	Present	0,0828 / 0,0785	0,0733 / 0,136	0,0589 / 0,16	0,0489 / 0,182	0,0375 / 0,206	0,0307 / 0,226
	Reference	0,0859 / 0,0781	0,0703 / 0,1367	0,0586 / 0,1641	0,0483 / 0,1817	-	-
Vortex 4a	Present		0,0641 / 0,909	0,071 / 0,911	0,0802 / 0,912	0,0852 / 0,911	0,0839 / 0,908
	Reference		0,0625 / 0,9102	0,0703 / 0,9141	0,0817 / 0,9133	-	-
Vortex 2b	Present		0,978 / 0,0189	0,933 / 0,0689	0,929 / 0,106	0,926 / 0,119	0,99 / 0,0112
	Reference		0,9805 / 0,0195	0,9336 / 0,0625	0,9300 / 0,1033	-	-
Vortex 3b	Present			0,016 / 0,0191	0,0536 / 0,0511	0,0692 / 0,0602	0,0831 / 0,0556
	Reference			0,0156 / 0,0195	0,0567 / 0,0533	-	-
Vortex 2c	Present				0,808 / 0,115	0,863 / 0,178	0,816 / 0,0857
	Reference				-	-	-
Vortex 4b	Present				0,0255 / 0,82	0,0339 / 0,811	0,0317 / 0,809
	Reference				0,0233 / 0,82	-	-
Vortex 4c	Present				0,0539 / 0,783	0,0537 / 0,774	0,0446 / 0,763
	Reference				-	-	-
Vortex 2d	Present					0,986 / 0,017	0,95 / 0,194
	Reference					-	-
Vortex 2e	Present						0,732 / 0,0218
	Reference						-
Vortex 4d	Present						0,126 / 0,988
	Reference						-
Vortex 4e	Present						0,228 / 0,972
	Reference						-

Table II. Location of vortex centers (coordinate x / coordinate y)

Remark 1. We have used as reference [37] for number of Reynolds less than 10000, and [42] for $Re = 20000$. To our knowledge, results for Reynolds number 33000 and 50000 using linear stabilised finite elements methods are considered very rare. We notice a very interesting behaviour of these computations which will be subject of further investigations and of future publication (see section 2 in chapter 6). The velocity profiles for u_x and u_y along $x=0.5$ and $y=0.5$ respectively for Reynolds number 33000 and 50000 are shown in figure 15.

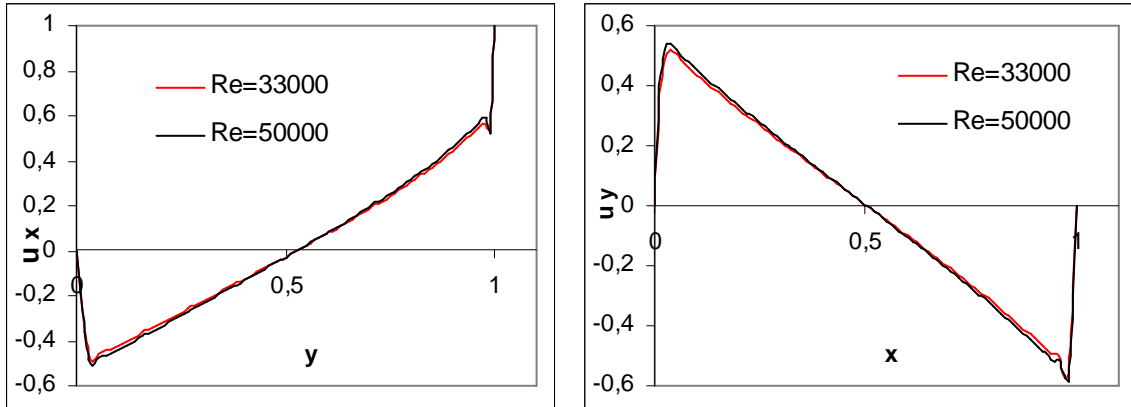


Figure 15. Velocity profile for u_x along $x=0.5$ (left) and u_y along $y=0.5$ (right)

Another set of numerical experiments was conducted in order to study the convergence of the new scheme. We performed a mesh sensitivity study to validate the capability of the method. Therefore, five different unstructured grids were used for these comparisons with a mesh of 16×16 , 32×32 , 64×64 , 80×80 and 125×125 elements respectively. The Reynolds number is chosen to be equal 5000. We compute the error of the velocity solution using the L^2 -norm:

$$err(h) = \left(\sum_{x,y} (u_{ref}^i - u_h^i)^2 \right)^{\frac{1}{2}} \quad \forall h \quad (3.4.1)$$

Results are compared to [42] obtained by employing a high-order accurate finite difference method on a 601×601 mesh. The approximation error is plotted in figure 16 and shows the expected improvement in the results. The velocity profiles employing different grid resolutions together with the reference solution are shown in figure 17 and 18. Note that the new implemented scheme converges rather rapidly to the given benchmark solution.

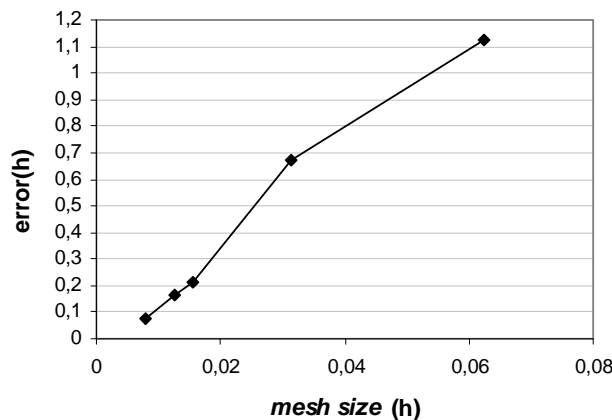


Figure 16. Evolution of the error in function of the mesh size h

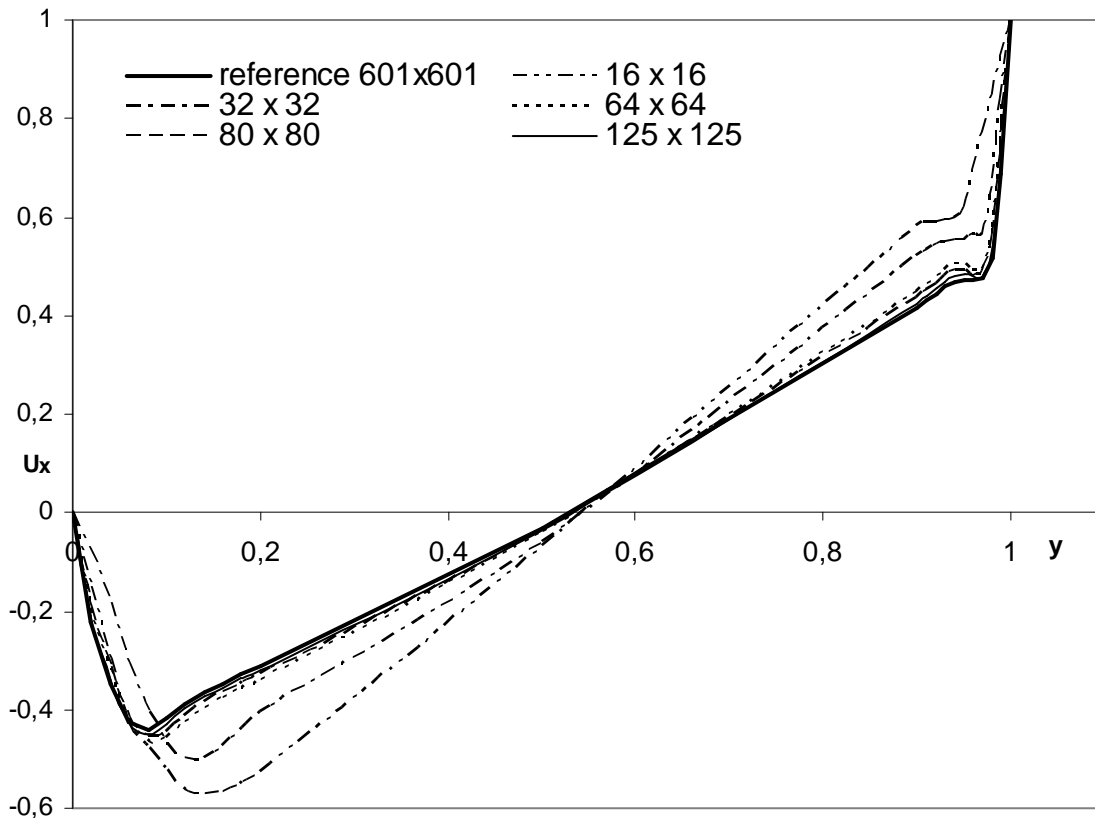


Figure 17. Velocity profile for u_x along $x=0.5$ using different meshes

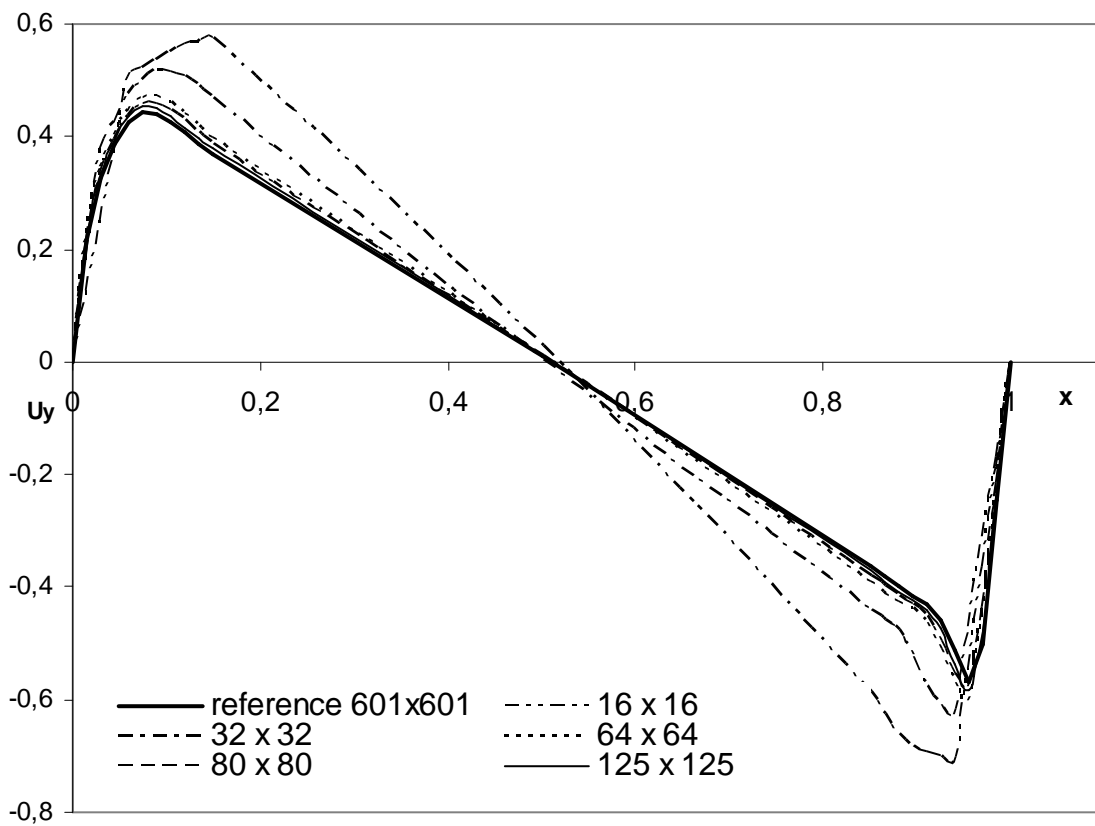


Figure 18. Velocity profile for u_y along $y=0.5$ (left) using different meshes

We conclude this numerical example by a short discussion on the computer demands. The computational costs for both methods are compared next. The number of time steps needed to reach the steady state with $\Delta t=0.1s$, as well as the required CPU time, are reported in figure 19 and 20 respectively. Within each time step only a single iteration is performed. It can be observed that the old method requires less time steps to reach the steady state in particularly for high Reynolds number. The reason for this behavior is maybe due to the higher numerical diffusion of the scheme. Figure 19 illustrates the expected behavior in increasing the CPU time with respect to the increase of Reynolds number.

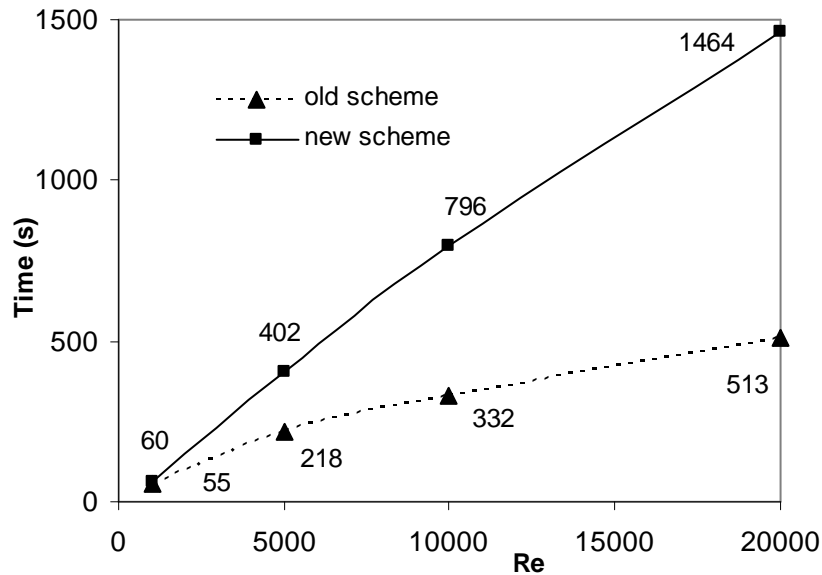


Figure 19. Physical time (s) required to reach the steady state for different Reynolds number

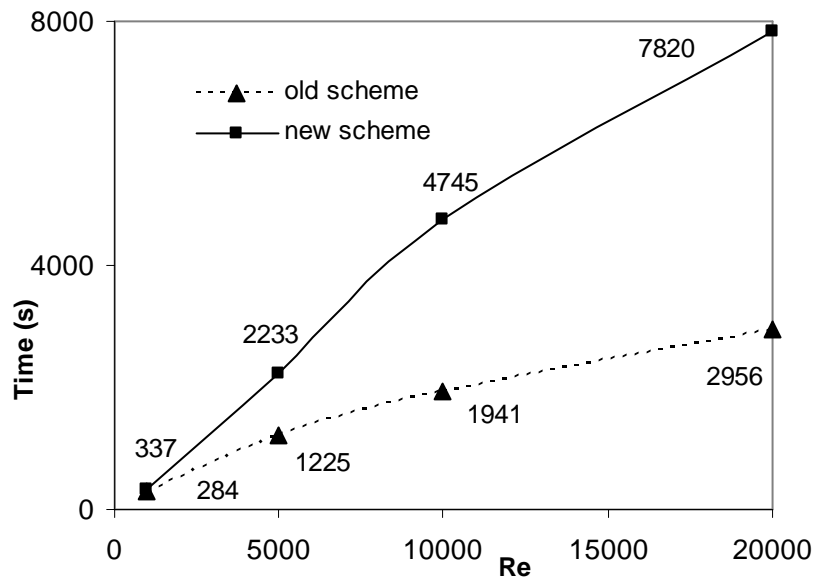


Figure 20. CPU-Time (s) to reach the steady state for different Reynolds number

3.4.3 Flow over a circular cylinder

This example describes a widely solved benchmark problem; the flow over a certain object (a circular cylinder here). Inside the furnace, this solid body can be considered as the heated part. At a moderate Reynolds number, two symmetrical vortices will be stationary attached behind the cylinder. By increasing the Reynolds number, these vortices become starched and the flow will be disorted and broken apart, leading to an alternative vortex shedding known as Karman vortex street. The Reynolds number is defined by $Re = UD/\nu$, where D is the diameter of the cylinder, U is the free-stream velocity and ν the kinematic viscosity. Having the diameter and the free-stream velocity equal to the unity, the kinematic viscosity was set to 0.01 to achieve a Reynolds number of 100.

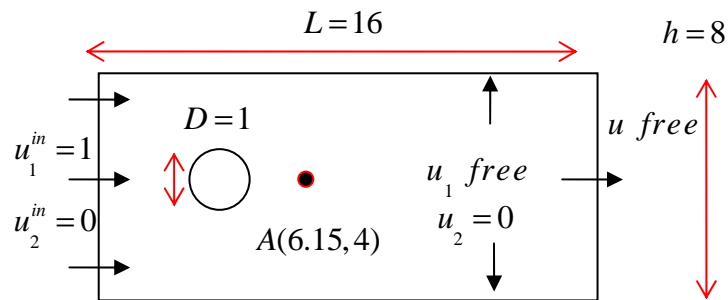


Figure 21. Geometry and boundary condition of the problem

The mesh used for this simulation contains 4000 nodes and it was adapted and refined near the cylinder. We used $\vec{u}(1,0)$ as initial condition except at the cylinder surface with a fixed time step $\Delta t = 0.1$. A backward Euler time scheme is used for the simulations. Within each time step, only one iteration is performed. The flow situation and boundary condition are depicted in figure 21. A complete description of this problem can be found in [54]. A detailed study on the use of different stabilization methods and time discretization for this benchmark can be found in [46] and [32].

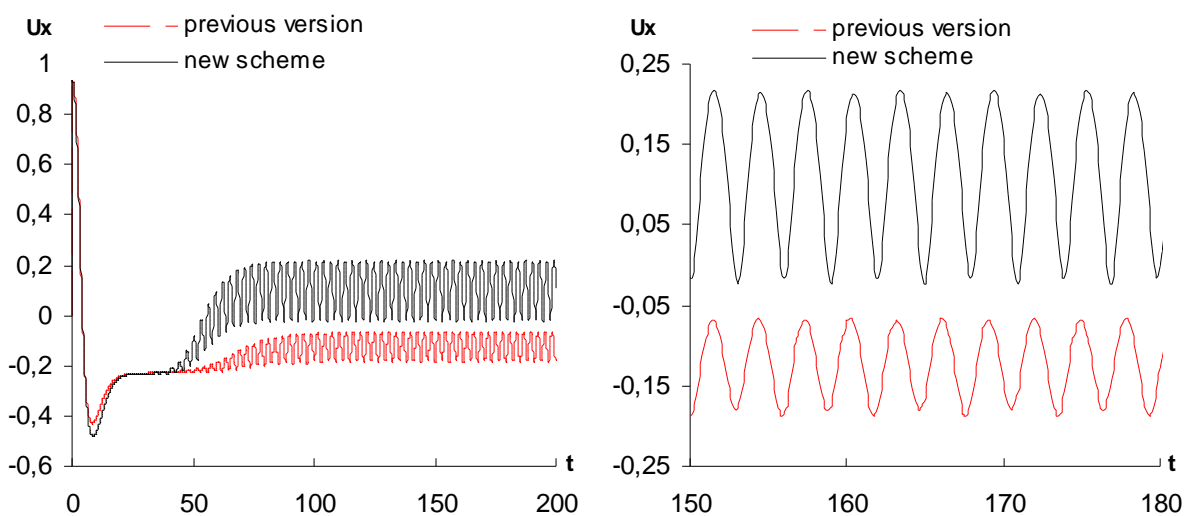


Fig 22. Temporal evolution of U_x at $A(6.15,4)$ using both methods (left) and its detail (right)

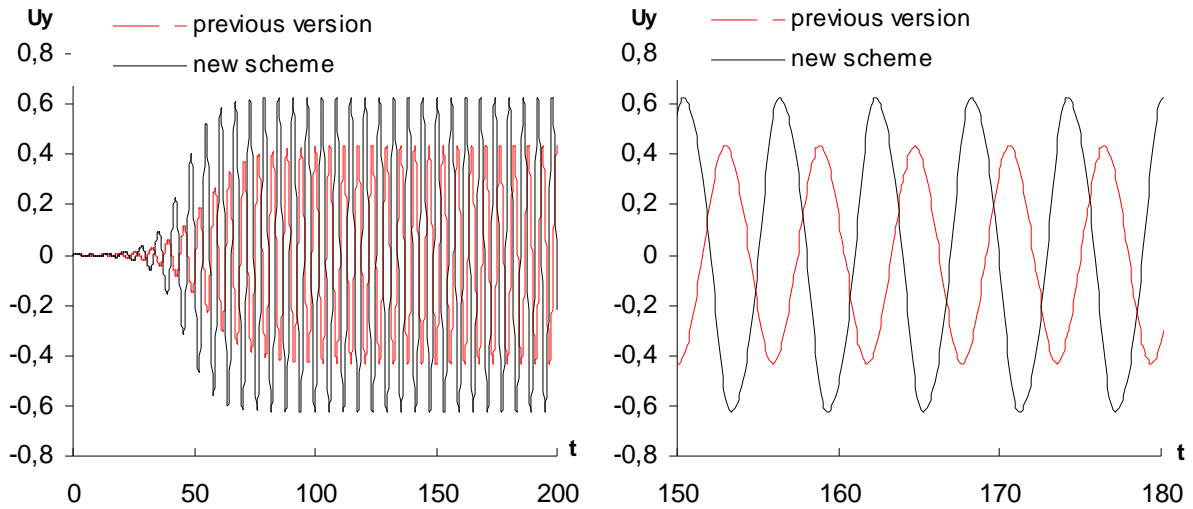


Fig 23. Temporal evolution of U_y at $A(6.15,4)$ using both methods (left) and its detail (right)

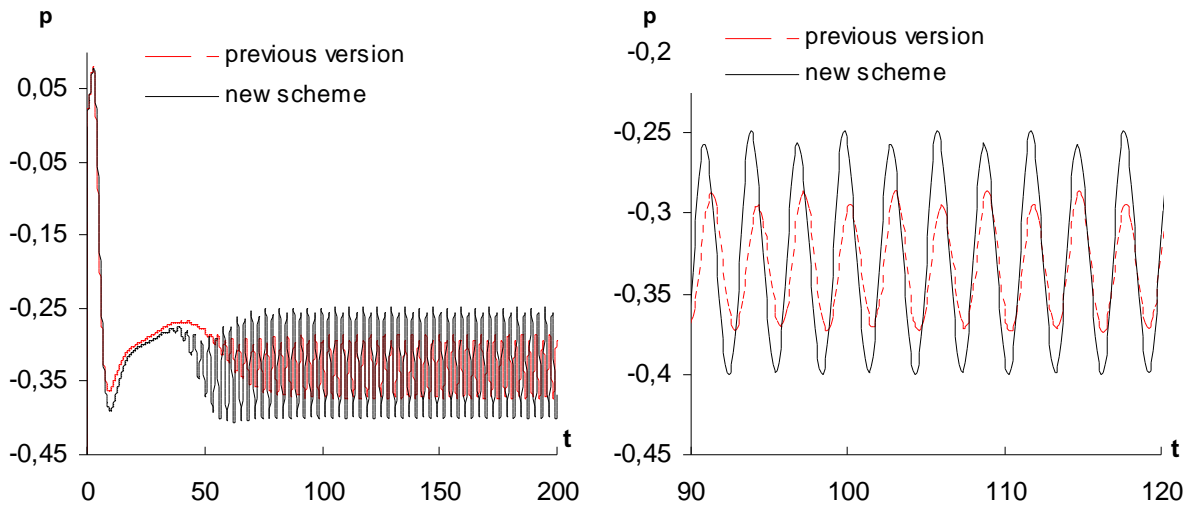


Fig 24. Pressure evolution at $A(6.15,4)$ using both methods (left) and its detail (right)

For the comparisons, we choose [32] as the reference solution. In this study, we plot the time history at point $A(6.15, 4)$ of the velocity components and the pressure. The obtained frequency of the oscillations is in accordance with the benchmark solution. (Figure 22-24)

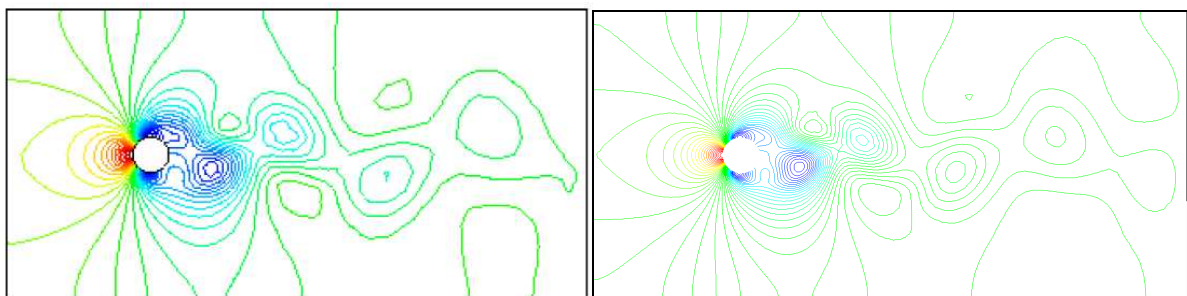


Fig 25. The pressure distribution at $t=160s$: reference [32] (left) and modified scheme (right)

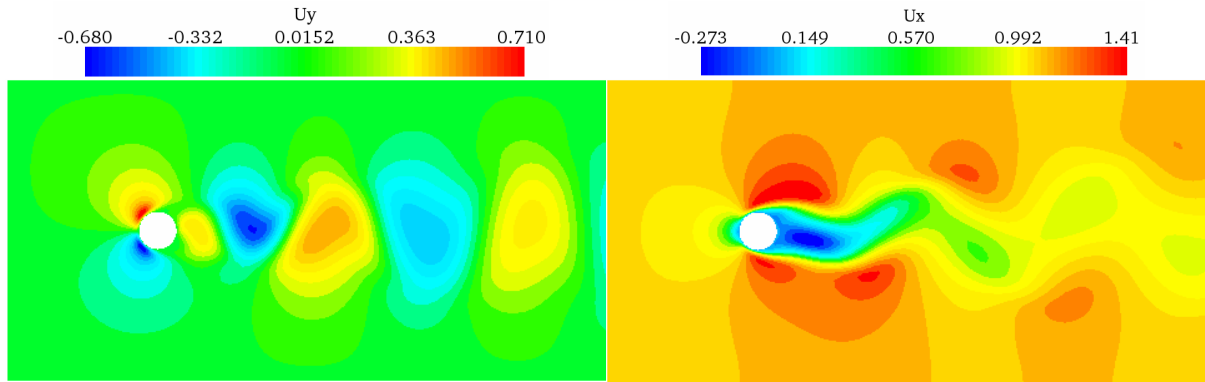


Fig 26. The predicted U_x and U_y contours near the wake of the circular cylinder at $t=160s$

However, it can be seen from these plots that the previous version of the solver gives a lower amplitude and lower frequency of the oscillation. The reason for this behavior is due once again to the higher numerical dissipation of the scheme. Figure 25 and 26 shows the pressure and the velocity contours respectively in the near wake of the circular cylinder at $t=160s$. All these results are in good agreement with the benchmark solution [32] as well as other published solution [46] and show the vortex-shedding as expected. Finally the Strouhal number will be calculated for the sake of comparisons with other numerical methods. This non-dimensional number can be considered important to quantify the properties of the periodic solution of the vortex street. It is given by

$$St = \frac{D}{u_1^{in} T_p} \quad (3.4.2)$$

T_p denotes the dimensionless time period. For $Re=100$, the Strouhal number corresponding to this benchmark is known to be equal 0.164 . Using the old scheme and the new modified scheme yields a Strouhal number of approximately 0.169 and 0.166 respectively. These values are matched more or less exactly by both methods. In Codina [31], employing a Crank-Nicholson scheme in time and coarser mesh the St number was reported equal to 0.174 . A value of 0.167 was stated by Hughes and Brooks (1982) [13] using a stabilized method of SUPG-type and a predictor-multicorrector algorithm in time. It was pointed out by [46] that the use of backward Euler scheme introduces more numerical viscosity which yields quite satisfactory results.

flow undergoes rapid distortion in the region surrounding the reattachment point and subsequently relaxes downstream at this point.

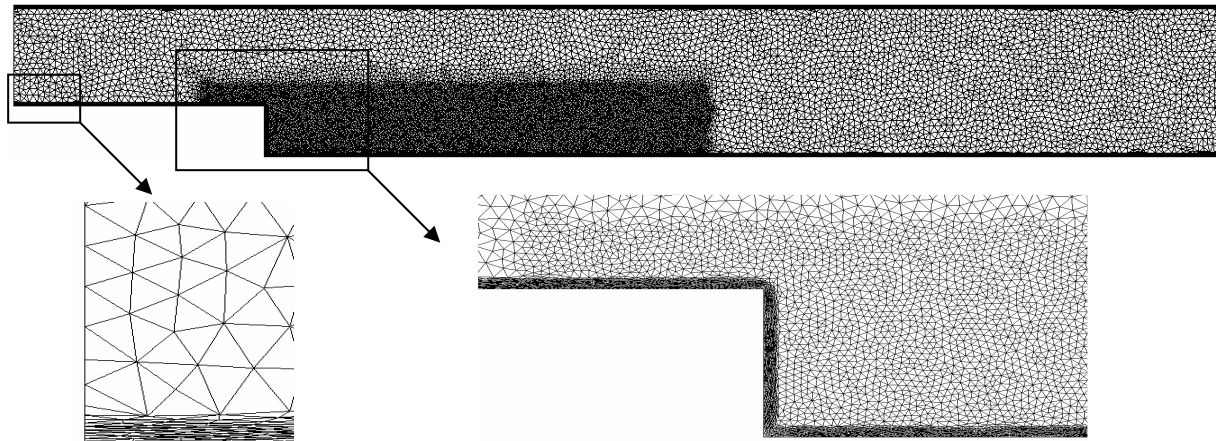


Figure 28. Geometry and boundary condition of the problem

The variation in the development of the streamlines, the pressure and the velocity is shown in Figure 29, 30 and 31 respectively starting from an arbitrary reference time.

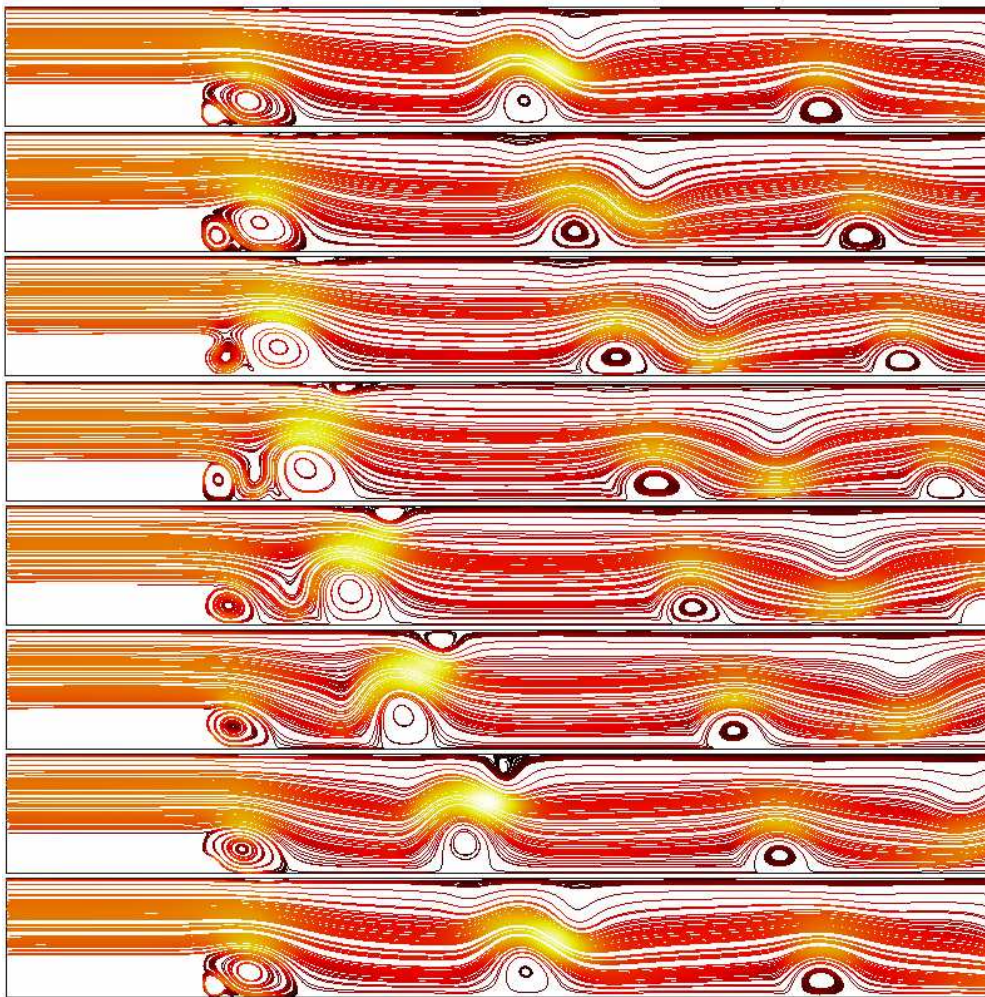


Figure 29. Periodic evolution of streamlines from $t=3.04s$ to $t=3.11s$

In two-dimensional simulations at high Reynolds numbers, the authors in [59] have indicated the presence of oscillatory flow behaviour in the solution. This is clearly shown in the basic characteristics of the flow given by these plots. Moreover, the velocity components and the pressure fields appear to be qualitatively appropriate without any non-physical oscillations.

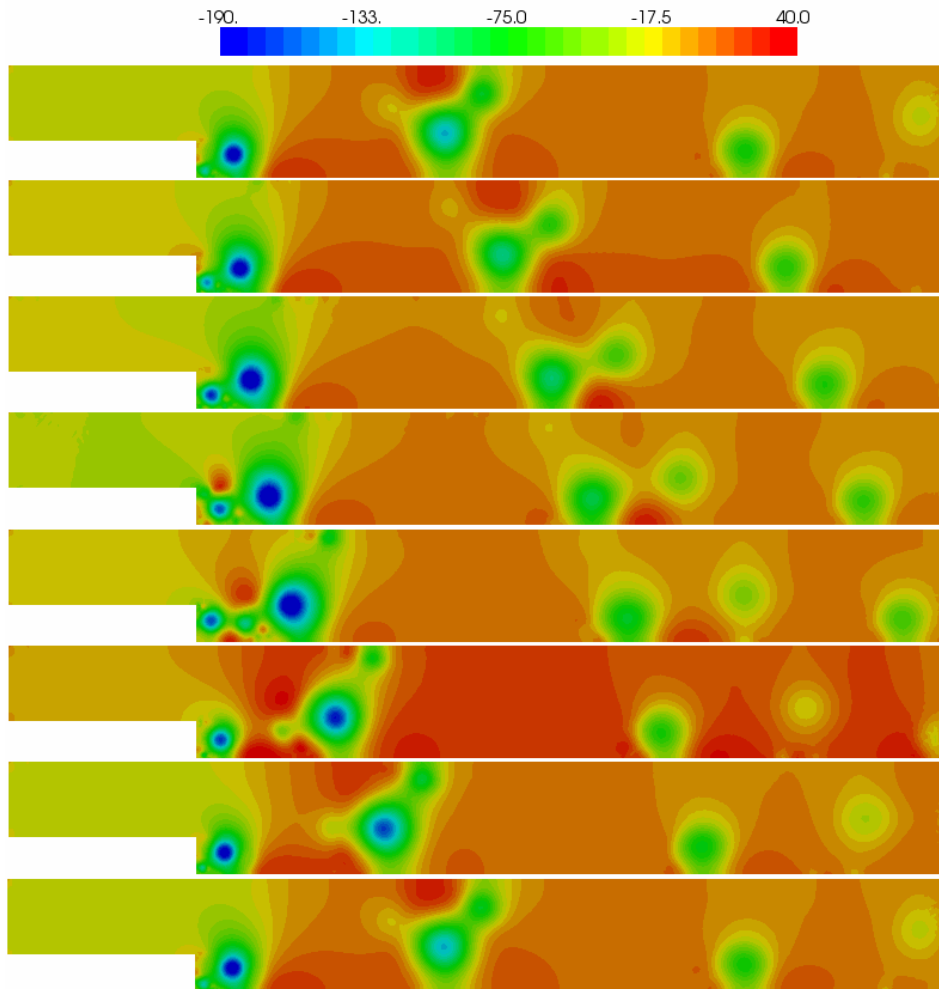


Figure 30. Periodic evolution of the pressure from $t=3.04s$ to $t=3.11s$

The shear layer rolls up forming a large-scale structure behind the step. As the large-scale structure grows, the reattachment location travels downstream then suddenly decreases indicating a detachment of the turbulent large-scale from the step. This movement of turbulent vortices is also described by the pressure field. From figure 30, one can clearly see that the low-pressure regions have been shown to correspond to the centres of coherent vortices.

The velocity and pressure fluctuations as a function of time at two locations A and B; the first near the reattachment zone ($x \approx 6h$) and the second in the middle of the channel (see figure 27) are plotted in figure 32 and 33. Similar oscillatory responses are detected at those points in the flow fields. The Strouhal number corresponding to the dominant frequency is roughly $St = fh / U_0 \approx 0.06$, corresponding to period $T \approx 17h/U_0$. These values are in total accordance with previous experimental and numerical deductions given by [59]. This reference contains full details about the direct numerical simulation of the backward-facing step together with the entire statistical results.

In figures 33 and 34 we represent the periodic evolution of both velocity components and the pressure.

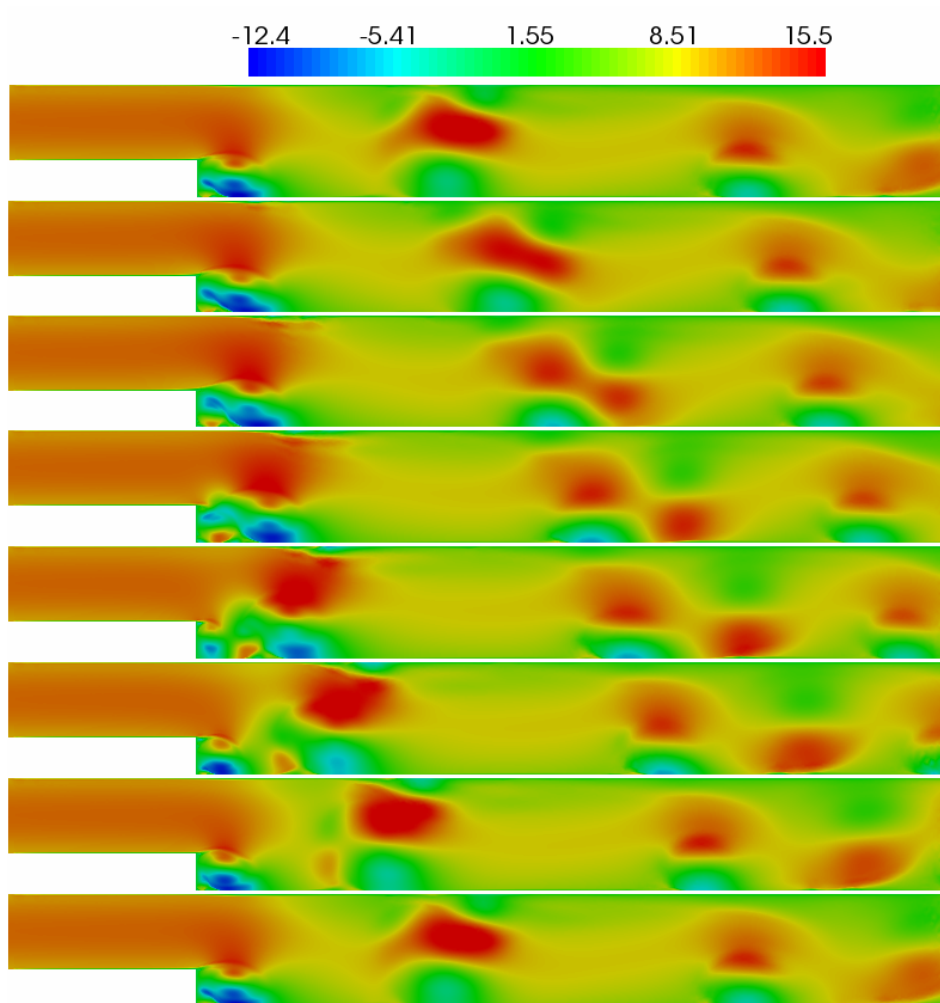


Figure 31. Periodic evolution of the streamwise velocity from $t=3.04s$ to $t=3.11s$

Finally, we can conclude that from all these illustrations, we demonstrate that there is no presence of any spurious oscillations in the solutions, in particular for the pressure. The implemented method has proved to work well on such heterogeneous meshes with highly stretched elements near the walls.

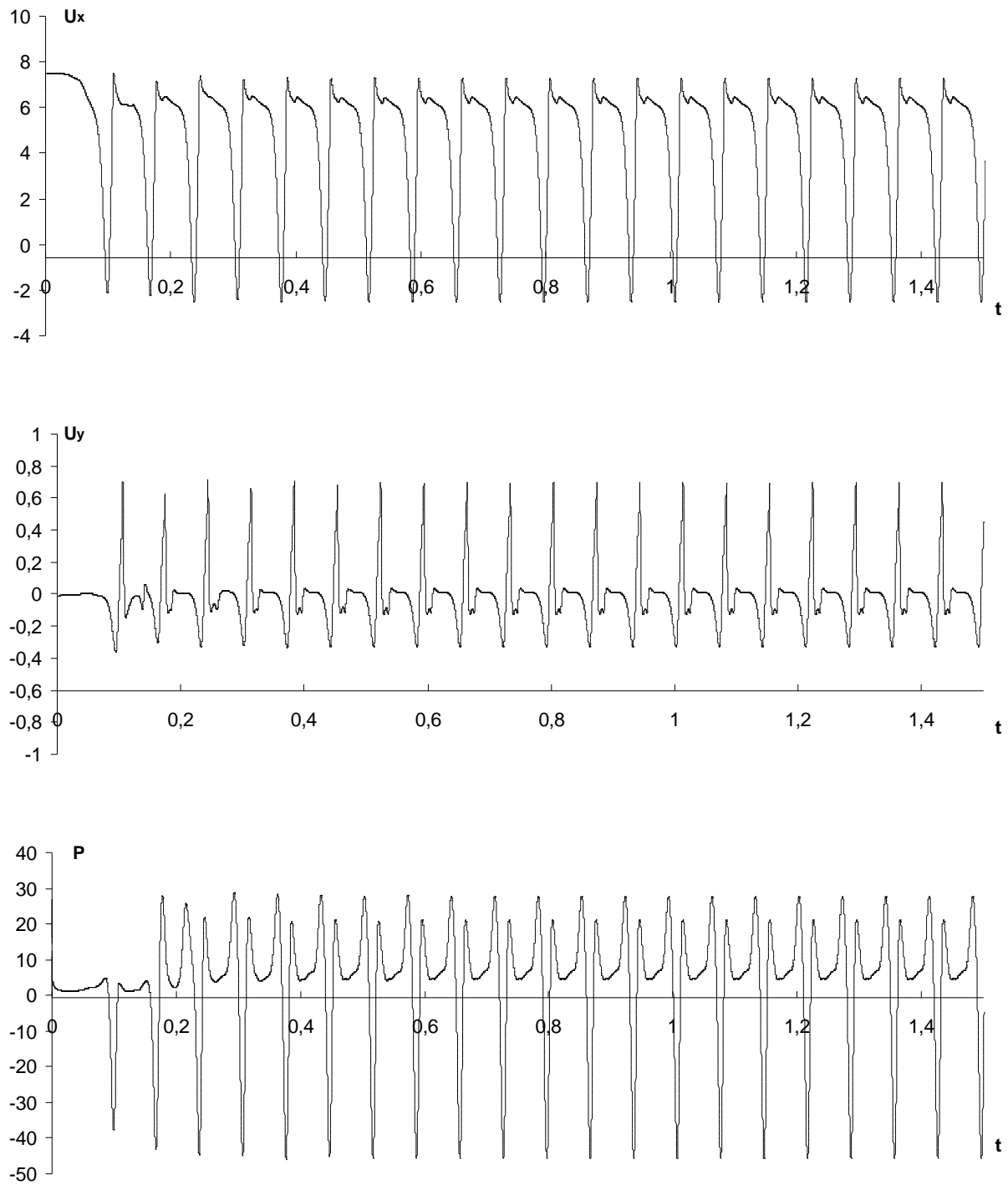


Figure 32. Periodic evolution of the velocity and the pressure at point A

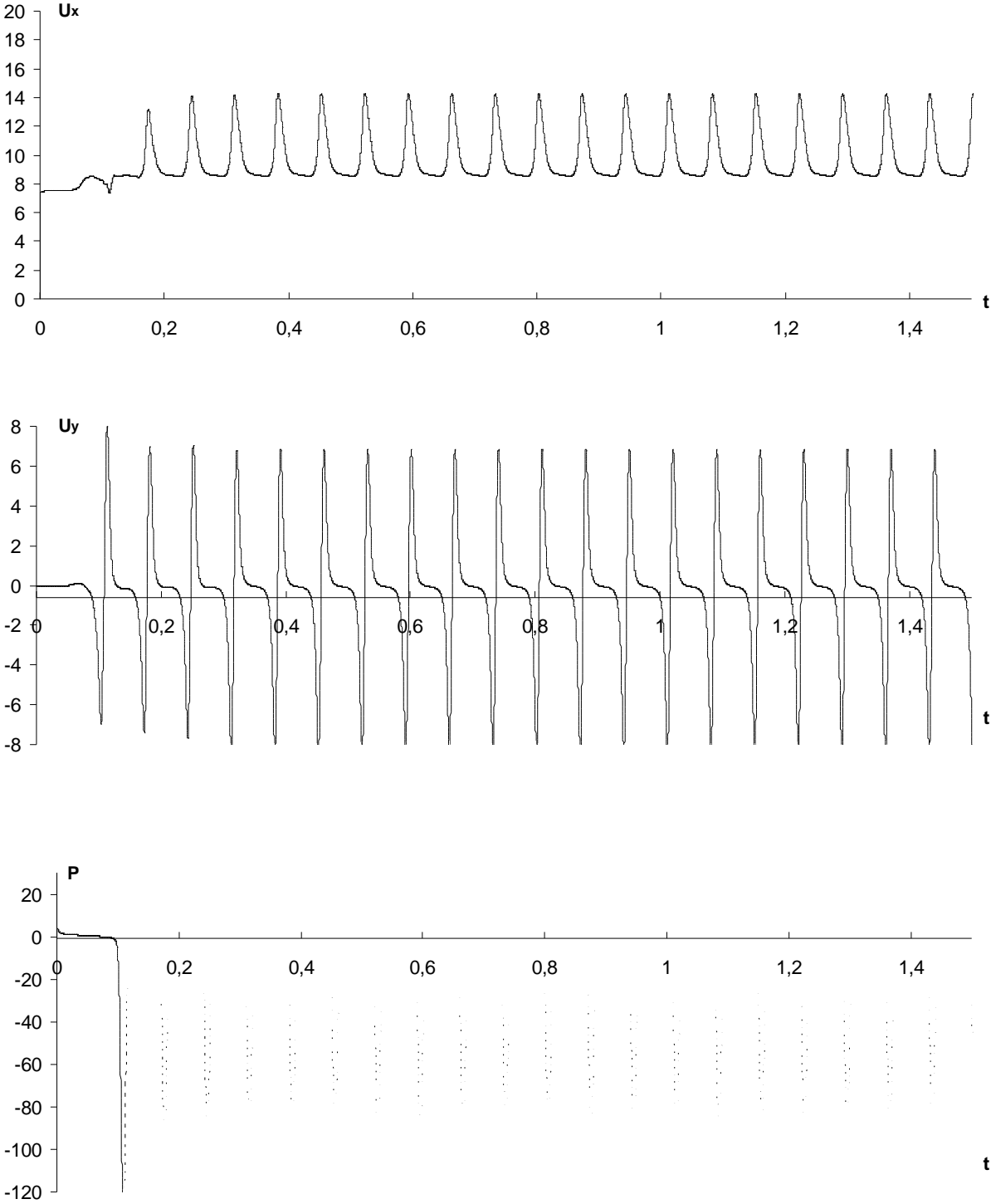


Figure 33. Periodic evolution of the velocity and the pressure at point B

3.5 Conclusion

“A lot must be achieved in order to obtain a complete Navier-Stokes solver, but the least in this chapter has been done: an extension of the previous scheme that takes into account the convection dominated flows”. In other words, a solver able to handle flows at high Reynolds number. In this chapter we have described a stabilized finite element method for the transient incompressible Navier-Stokes equations based on the decomposition of the unknowns into large scale and fine scale. The motivation of using these techniques comes from the desire of solving problems for higher Reynolds numbers. Note that the implementation of such efficient solver will be later used for solving heat transfer and convection-dominated flows inside industrial furnaces. The bottom line of the new approach was to take into account the small-scale pressure and to add the convection terms into the fine scale equations. Results for the unsteady Navier-Stokes equations obtained via the new modified scheme have been compared and analyzed. The numerical experiments show that the method is stable and the gain with respect to the previously implemented method is notorious in particularly for high Reynolds numbers. The performance and the efficiency of the overall new scheme have been demonstrated using four benchmarks. Detailed accurate and new results have been presented for the model problem of flow in a driven cavity. Reynolds number up to 50000 has been considered. Upcoming, more tests will be presented for three-dimensional computations (section 2, chapter 6) and coupled heat problem (section 1 and 3, chapter 6).

References

- [1] Ferziger, J.H. and Peric, M.. *Computational methods for fluid dynamics* (2nd edition). Springer-Verlag, Berlin, 1999
- [2] P.M. Gresho, Some current CFD issues relevant to the incompressible Navier-Stokes equations, *Comput. Methods Appl. Mech. Eng.* **87** (1991), pp. 201–252.
- [3] J. Heywood, R. Rannacher and S. Turek, Artificial boundaries and flux and pressure conditions for the incompressible Navier–Stokes equations, *Int. J. Numer. Methods Fluids* **22** (1996), pp. 325–352
- [4] Franca L, Nesliturk A, Stynes M. On the stability of residual-free bubbles for convection diffusion problems and their approximation by a two-level finite element method. *Computer Methods in Applied Mechanics and Engineering* 1998; 166:35-49.
- [5] Nesliturk A. Approximating the incompressible Navier-Stokes equations using a two level finite element method. *PhD Thesis, University of Colorado* 1999.
- [6] Arnold D, Brezzi F, Fortin M. A stable finite element for the Stokes equations. *Calcolo* 1984; 23(4):337- 344.
- [7] Canuto C, Van Kemenade V. Bubble-stabilized spectral methods for the incompressible navier-stokes equations. *Computer Methods in Applied Mechanics and Engineering* 1996; 135:35-61.
- [8] Brezzi F, Russo A. Choosing bubbles for advection-diffusion problems. *Mathematical Models and Methods in Applied Sciences* 1994; 4:571-587.
- [9] Russo A. Bubble stabilization of finite element methods for linearized incompressible Navier-Stokes equations. *Computer Methods in Applied Mechanics and Engineering* 1996; 132:335-343.
- [10] Brezzi F, M F. Mixed and Hybrid Finite Element Methods. *No. 15 in Springer Series in Computational Mathematics*, Springer-Verlag: New-York, 1991.
- [11] Brezzi F, Franca L, Hughes T, Russo A. Stabilization techniques and subgrid scales capturing. *Conference of the State of the Art in Numerical Analysis*, York, England, 1996.
- [12] Donea J, Huerta A. Finite Element Methods for Flow Problems. *New-York*, 2003.
- [13] Brooks A, Hughes T. Streamline upwind/Petrov-Galerkin formulations for convection dominated flows with particular emphasis on the incompressible Navier-Stokes equations. *Computer Methods in Applied Mechanics and Engineering* 1982; 32:199-259.
- [14] Hughes T. Multiscale phenomena: Green's functions, the Dirichlet-to-Neumann formulation, subgrid scale models, bubbles and the origin of stabilized methods. *Computer Methods in Applied Mechanics and Engineering* 1995; 127:387-401.

- [15] F. Brezzi, L.P. Franca, T.J.R. Hugues, A. Russo. “ $b = \int g$ ”, *Computer methods in applied mechanics and engineering*, 145, 329-339 (1997).
- [16] Tezduyar T, Shih R, Mittal S, Ray S. Incompressible flow computations with stabilized bilinear and linear equal-order-interpolation velocity-pressure elements. *Computer Methods in Applied Mechanics and Engineering* 1992; 95:221-242.
- [17] Franca L, C F. Bubble functions prompt unusual stabilized finite element methods. *Computer Methods in Applied Mechanics and Engineering* 1995; 123:229-308.
- [18] Codina R. Stabilization of incompressibility and convection through orthogonal subscales in finite element methods. *Computer Methods in Applied Mechanics and Engineering* 2000; 190(13-14):1579-1599.
- [19] Codina R. Stabilized finite element method for the transient Navier-Stokes equations based on a pressure gradient projection. *Computer Methods in Applied Mechanics and Engineering* 2000; 182(3-4):277-300.
- [20] Codina R. Pressure stability in fractional step finite element methods for incompressible flows. *Journal of Computational Physics* 2001; 170(1):112-140.
- [21] Codina R, Principe J. Dynamic subscales in the finite element approximation of thermally coupled incompressible flows. *International Journal for Numerical Methods in Fluids* 2007; 54:707-730.
- [22] Gravemeier V. Scale-separating operators for variational multiscale large eddy simulation of turbulent flows. *Journal of Computational Physics* 2006; 212(2):400-435.
- [23] Gravemeier V. A consistent dynamic localization model for large eddy simulation of turbulent flows based on a variational formulation. *Journal of Computational Physics* 2006; 218(2):677-701.
- [24] Gravemeier V, Gee MW, Kronbichler M, Wall WA. An algebraic variational multiscale-multigrid method for large eddy simulation of turbulent flow. *Computer Methods in Applied Mechanics and Engineering* 2009; (In Press).
- [25] Coupez T. Stable-stabilized finite element for 3D forming calculation. *Technical Report, CEMEF* 1996. 23.
- [26] Coupez T, Marie S. From a direct to a parallel iterative solver in 3D forging simulation, *International Journal of Supercomputer Applications And High Performance Computing* 1997; 11(4):277-285.
- [27] Perchat E. Mini-élément et factorisation incomplètes pour la parallélisation d'un solveur de Stokes 2D : application au forgeage. *PhD Thesis, Ecole Nationale Supérieure des Mines de Paris*, 2000.
- [28] Digonnet H, Coupez T. Object-oriented programming for fast and easy development of parallel applications in forming processes simulation. *Computational Fluid and Solid Mechanics* 2003, 2003; 1922-1924.

- [29] Basset O. Simulation numérique d'écoulements multi-fluides sur grille de calcul. *PhD Thesis, Ecole Nationale Supérieure des Mines de Paris* 2006.
- [30] Hughes TJR, Feijoo GR, Mazzei L, Quincy JN. The variational multiscale method a paradigm for computational mechanics. *Computer Methods in Applied Mechanics and Engineering* 1998; 166:3-24.
- [31] R. Codina. Stabilized finite element approximation of transient incompressible flows using orthogonal subscales. *Comput. Methods Appl. Mech. Engrg.*, 191(39-40):4295-4321, 2002.
- [32] R. Codina, J. Principe, O. Guasch and S. Badia, Time dependent subscales in the stabilized finite element approximation of incompressible flow problems, *Comput. Methods Appl. Mech. Engrg.*, 196 (21-24) : 2413-2430, 2007.
- [33] Dubois T, Jauberteau F, Temam R. Dynamic Multilevel Methods and the Numerical Simulation of Turbulence. *Cambridge University Press: Cambridge*, 1999.
- [34] Franca LP, Oilveira SP. Pressure bubbles stabilization features in the Stokes problem. *Computer Methods in Applied Mechanics and Engineering* 2003; 192:1929-1937.
- [35] Masud A, Khurram RA. A multiscale/stabilized finite element method for advection diffusion equation. *Computer Methods in Applied Mechanics and Engineering* 2004; 193:1997-2018.
- [36] Behr MA, Franca LP, E TT. Stabilized finite element methods for the velocity-pressure-stress formulation of incompressible flows. *Computer Methods in Applied Mechanics and Engineering* 1993; 104(1):31-48.
- [37] Ghia U, Ghia KN, Shin CT. High-Re solutions for incompressible flow using the Navier Stokes equations and a multigrid method. *Journal of Computational Physics* 1982; 48(3):387-411.
- [38] Schreiber R, Keller HB. Driven cavity flows by efficient numerical techniques. *Journal of Computational Physics* 1983; 49:310-333.
- [39] Botella O, Peyret R. Benchmark spectral results on the lid-driven cavity flow. *Computers and Fluids* 1998; 27(4):421-433.
- [40] Sahin M, Owens RG. A novel fully-implicit finite volume method applied to the lid-driven cavity problem. part i: high Reynolds number flow calculations. *International Journal for Numerical Methods in Fluids* 2003; 42:57-77.
- [41] Gravemeier V, Wall WA, Ramm E. Numerical solution of the incompressible Navier Stokes equations by a three-level finite element method. *Computational Fluid and Solid Mechanics* 2003; :915-918.
- [42] Erturk E, Corke TC, Gokcol. Numerical solutions of 2-D steady incompressible driven cavity flow at high Reynolds numbers. *International Journal for Numerical Methods in Fluids* 2005; 48(7):747-774.

- [43] Koseff JR, Street RL, Gresho PM, Upson CD, Humphrey JAC, To JW. A three dimensional lid-driven cavity flow: experiment and simulation. *Third International Conference on Numerical Methods in Laminar and Turbulent Flow*, Seattle, WA, 1983; 564-581.
- [44] Wall WA, Bischoff M, Ramm E. A deformation dependent stabilization technique, exemplified by EAS elements at large strains. *Computer Methods in Applied Mechanics and Engineering* 2000; 188(4):859-871.
- [45] Tezduyar TE, Osawa Y. Finite element stabilization parameters computed from element matrices and vectors. *Computer Methods in Applied Mechanics and Engineering* 2000; 190(3-4):411-430.
- [46] V. Gravemeier, The variational multiscale method for laminar and turbulent incompressible flow, *PhD Thesis, Report No. 40*, Institute of Structural Mechanics, University of Stuttgart, 2003
- [47] A. Masud and T. J. R. Hughes. A stabilized mixed finite element method for Darcy flow. *Comput. Methods Appl. Mech. Engrg.*, 191(39{40):4341{4370, 2002.
- [48] A. Masud L.P.Franca, G.Hauke. Stabilized Finite Elements Methods, *chapter Finite Element Methods: 1970's And beyond*. CIMNE, Barcelona, Spain, 2003.
- [49] Masud A, Khurram RA. A multiscale finite element method for the incompressible Navier-Stokes equations. *Computer Methods in Applied Mechanics and Engineering* 2006; 195: 1750-1777
- [50] Masud A, Khurram RA. A multiscale/stabilized finite element method for the advection-diffusion equation. *Computer Methods in Applied Mechanics and Engineering* 2004; 193: 1997-2018
- [51] T.E. Tezduyar, R. Glowinski and F. Glaisner, Streamline-upwind/Petrov-Galerkin Procedures for the Vorticity-Stream Function Form of the Navier-Stokes Equations, *Numerical Methods in Laminar and Turbulent Flow* (eds. C. Taylor, W.G. Habashi and M.M. Hafez), Vol. 5, Pineridge Press, Swansea, U.K. (1987).
- [52] T.E. Tezduyar, S. Mittal, R. Shih and S.E. Ray, "Stabilized Incompressible Flow Computations Using Bilinear and Linear Equal-order-interpolation Velocity-Pressure Elements", *Computational Mechanics '91--Theory and Applications* (eds. S.N. Atluri, D.E. Beskos, R. Jones and G. Yagawa), ICES Publications, Atlanta, Georgia (1991).
- [53] Hendriana, D. and Bathe, K.--J. (2000): On upwind methods for parabolic finite elements in incompressible flows, *International Journal for Numerical Methods in Engineering*, 47, 317--340.
- [54] Engelman MS, Jaminia M-A. Transient flow past a circular cylinder: a benchmark solution. *International Journal for Numerical Methods in Fluids* 1990; 11: 985-1000

- [55] J.J. KIM, 'Investigation of separation and reattachment of turbulence shear layer: flow over a backward facing step', *Ph.D. Thesis, Stanford University*, 1978
- [56] B. E. Launder, D. B. Spalding, The numerical computation of turbulent flows, *Computer Methods in Applied Mechanics and Engineering*, 3, 1974, pp. 269-289.
- [57] Laurence Gaston, Simulation numérique par éléments finis bidimensionnels du remplissage de moules de fonderie et étude expérimentale sur maquette hydraulique, *Ph.D. thesis, Ecole Nationale Supérieure des Mines de Paris*, 1997.
- [58] B. E. Launder, D. B. Spalding, The numerical computation of turbulent flows, *Computer Methods in Applied Mechanics and Engineering*, 3, 1974, pp. 269-289.
- [59] H. Le, Parviz Moin, and John Kim. Direct numerical simulation of turbulent flow over a backward-facing step. *J. of Fluid Mech.*, 330:349–374, 1997

Chapter 4

Implementation of turbulence models in incompressible flow solvers based on a finite element discretization

The present chapter is concerned with unsteady flow at high Reynolds number. The laminar to moderate flows discussed in the previous chapter are not applicable when turbulence occurs inside industrial furnaces. Two alternative procedures, the k-epsilon model and the Large Eddy Simulation model (LES) will be introduced and studied to simulate such flow regimes. Moreover, the stabilized finite element methods from the previous chapters will be used and applied for the resolution of the set of equations needed for the numerical modelling of turbulent flows. Finally, to compare and analyze the results, the developed models are tested on three representative benchmark problems and conclusions are drawn.

Chapter 4	131
Implementation of turbulence models in incompressible flow solvers based on a finite element discretization	131
4.1 Introduction to turbulence	132
4.2 Turbulence simulation	133
4.3 The k-epsilon turbulence model	135
4.3.1 The standard formulation	136
4.3.2 The boundary conditions	138
4.3.3 Enhanced wall treatment	144
4.3.4 Low Reynolds formulation	145
4.3.5 Finite element solution	148
4.3.6 Positivity of the solution	150
4.4 Large Eddy Simulation	151
4.4.1 Filtering equations	152
4.4.2 Subgrid-scale modeling	153
4.5 Benchmarks for the k-epsilon model	156
4.5.1 Validation: grid turbulence	156
4.5.2 Comte-Bellot	157
4.5.3 Flow over a backward-facing step	162
4.6 Flow behind an obstacle using LES model	169
4.7 Conclusion	172
References	173

4.1 Introduction to turbulence

It was declared by the famous British physicist in 1932, Horace Lamb, at the British Association for the Advancement of Science meeting: *“I am an old man now, and when I die and go to Heaven there are two matters on which I hope for enlightenment. One is quantum electrodynamics, and the other is the turbulent motion of fluids. And about the former I am really rather optimistic.”* Turbulence was always considered very difficult to model in classical physics and it remains the most important and not totally understood problem. It can be defined by random and unpredicted variation of the velocity and the pressure that occurs at high Reynolds numbers. In everyday life, we experience and observe turbulent flows around a boat, a plane, a stone in a river, a fast car and of course the flow inside the furnace (figure 1).

For more than a century, mathematicians and fluid dynamicists have been trying to understand turbulence in fluids, by analyzing the mechanisms that generate this disordered motion. They realized that as the Reynolds number increases, the flow becomes more turbulent and the requirements on resolution become more and more strict. The number of grid points and the smallness of the time steps required to solve the Navier-Stokes equations for all the relevant time and space scales of turbulent motion push the computation of turbulent flows in industrial equipment beyond the realms of present computing capabilities. For that reason the use of Direct Numerical Simulation (DNS) is still restricted for relatively moderate Reynolds numbers only. In CFD codes, this matter is overcome by the use of eddy viscosity models based on the Reynolds Averaged Navier-Stokes (RANS) equations and the LES model.

The main focus of the chapter is to provide such alternative methods for the numerical solution of turbulent fluid dynamics equations. In brief outline, this chapter is structured around the following questions. Which model we should use? How can we get reasonable results with an affordable computing cost? How much computing time do we need to simulate heat treatment furnaces? What is the required number of grids to fully describe the flows inside the furnace and around the heated objects? Answering these questions will require at least understanding, developing, implementing and validating these two turbulence models in our finite element library CIMLIB. Doing that, we open the choice to the user to decide which methods to use regarding the application in hand. Each method will offer the accuracy of the results in respect to the computational costs and the required computing time. Note that recently, with the support of parallel schemes the two models can nowadays be possible. But before going into details on current modelling procedures we summarize some of the important fundamental properties of turbulence.



Figure 1. Flows around a Lockheed L-1011 plane and F1 racing car

4.2 Turbulence simulation

Turbulent behaviour can be predicted by simply resolving the transient Navier-Stokes if only very fine mesh resolution and adequate time steps are used. But of course this requires an extremely large computer resource which is not nowadays affordable specifically when simulating heat treatment industrial furnaces. That's why most engineering computations involving turbulent flow processes will have to rely on models of turbulent flows, at least for the foreseeable future. This is especially true for heat treatment furnaces applications, where, in addition to turbulence models and set of equations, there are many other complexities such as radiation heat transfer, complex geometry, and so on.

Large numbers of models have been developed and studied in the last three decades. We can classify these modeling approaches into three categories: DNS, LES and RANS. As one progresses from DNS to RANS, more and more of turbulent motions are approximated and, therefore, require less computational resources.

In Direct Numerical Simulation we attempt to simulate and resolve all the scales of motion without approximation or the need of any additional modeling. DNS directly solves the Navier-Stokes equations described in the previous chapter. Since this approach aims to resolve all the spatial and temporal gradients, the application of DNS requires huge computational resources. Based on the Kolmogorov's theory [1], the grid size must get down to $h \approx \text{Re}^{-3/4}$ and the grid must contain approximately $\text{Re}^{9/4}$ vertices. A Reynolds number of $\text{Re} \approx 5 \cdot 10^5$ can be encountered in turbulent flow of industrial furnaces, so a reasonable number of vertices would be about 10^{13} . This is just an example to give the reader an idea about the huge amount of needed computational resources which are prohibitively expensive and why turbulence modeling is that important in our context. However, DNS can provide at the same time valuable information, difficult to obtain from experiments, about the interaction of small-scale and large-scale motions. More details can be found in [9, 11, 13, 14].

Unlike DNS, large eddy simulations are based on filtering and decomposing the scales into large-scale and small-scale (subgrid-scale) components. Since the large-scale are assumed to be more energetic than the small-scale and are the main contributors to the transport of conserved quantities, LES attempts to simulate more precisely and solve these scales and to only model the effect of the small-scale eddies. These simulations are also three-dimensional and time-dependent but are much less costly than DNS simulations. Later, we will introduce the fundamentals of LES, which include the filtered governing equations for LES; the subgrid-scale (SGS) models of LES that are used in the current study; the numerical methods in terms of the computational grid system, the discretization schemes, the numerical procedure used to solve the governing equations and the boundary conditions for wall. More details can be found in Germano *et al.* [2].

The Reynolds-averaged Navier-Stokes equation (RANS) determines ensemble-averaged flow parameters, such as air velocity and temperature using some turbulence modeling. The key point here is that all turbulent motions will be modeled. This averaging procedure will remove effectively all turbulent fluctuations. Consequently, much coarser grids can be used as the smaller turbulent eddies do not need to be captured. Therefore, two and three-dimensional simulations can be performed with significantly less computer resources when compared to DNS and LES simulations. This is the biggest advantage of the RANS approach, and the primary reason why it is most widely used CFD method in many industrial applications. However, while not solving the small-scale eddies, some additional closure models are required to introduce and approximate the turbulence effects. One of the most widely used model is the two-equation model, namely the k - ϵ will be described and detailed in the following section. This model is the first recommended one as a baseline model that succeed in expressing the main features of many turbulent flows by relying on just one characteristic length scale and time scale. More details can be found in [4, 5, 6].

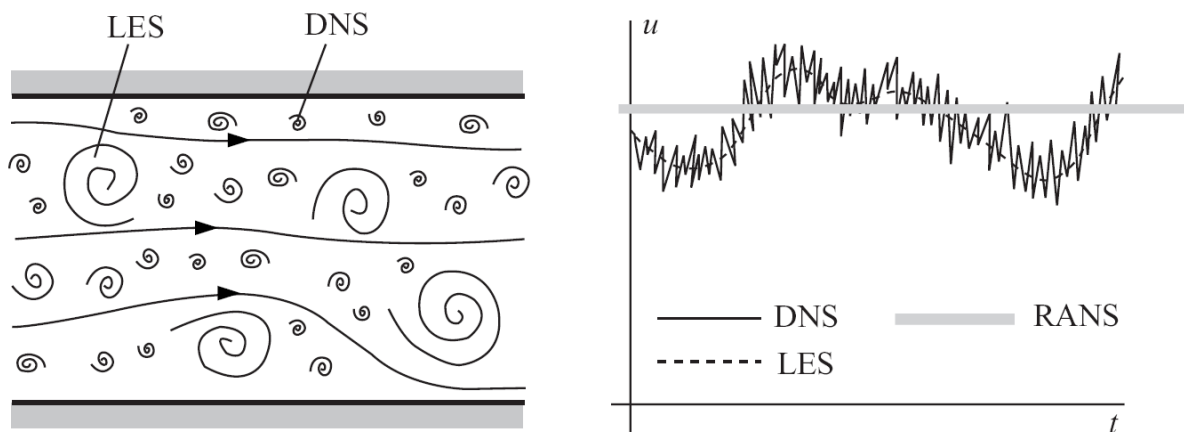


Figure 2. Schematic representations of scales in turbulent flow and their relationship with modeling approaches (adapted from Ferziger and Peric, 1996 [15])

The finite element implementation of both the k - ϵ and LES turbulence models for unsteady flows will be described and analyzed in this chapter. The use of stabilized finite element techniques described in the previous chapters will be applied to solve these turbulent models. We can count only few attempts on the implementation turbulence model at the CEMEF. All these attempts have served under the code THERCAST but none in the finite element library CIMLIB. More details about this subject can be found in [16, 5]. We certainly and often referred to the work of L. Gaston in [5] since to our knowledge it was considered as complete and detailed useful information about the description of the k - ϵ model. In this sense, the present work can be considered as a continuation of those references not only to deal with highly turbulent flows but also to open the choice to the user to decide which methods to use regarding the application in hand. Each method will offer the accuracy of the results in respect to the computational costs. Several numerical examples for solving the transient problems will show the benefits of the new modified scheme and conclusion will be drawn.

4.3 The k-epsilon turbulence model

In this section, details about the averaged Navier-Stokes equations using the Reynolds time-filtering or time-averaging technique will be presented. By applying those filters to the Navier-Stokes and continuity equations, we obtain a set of equations having an extra term corresponding to averaged products of fluctuating velocity components known by Reynolds stresses. The main idea was to assume that averaged quantities have only large-scale spatial-temporal variations and that the Reynolds stresses group and include all turbulence effects.

Later on, many methods were introduced to define and compute the Reynolds stresses; these techniques are often known by closure problem [3, 10, 12]. In our work, we have opted for a two-equation k- ϵ (turbulence kinetic energy and rate-of-dissipation energy) closure model to define the eddy viscosity for incompressible flows. This model usually involves transport equations for turbulence kinetic energy (TKE) and for a second turbulence variable, rate-of-dissipation energy, in order to evaluate the eddy viscosity. These two-equations of unsteady convection-diffusion-reaction type will be solved using the stabilized finite element method described in previous chapters. This model is the most popular model which has been used since 1970s. It is known to be effective in the far-wall zone, whereas, extra care must be paid in the near-wall zone. Additional wall functions must be added to close the model in the vicinity of those regions.

The main objective of the THOST project is to describe numerically the airflow and temperature field inside an industrial furnace where high convective heat sources are used. The thermal wall jet created by this kind of source can greatly influence the temperature distribution inside the enclosure. Therefore, advance turbulence model are needed to produce better results in particularly in the vicinity of the walls. This can be one among different reasons to extend the standard k- ϵ model by the low Reynolds number k- ϵ model under a suitable mesh scheme. We will also justify this choice later in chapter 6.

We start a presentation of the standard k- ϵ model which is mainly valid in the turbulent region (far-wall zone). The near-wall effects are simulated through wall functions which give boundary conditions for points situated in the turbulent zone. However, this procedure is not well adapted for complex flows, since the condition that the boundary must be in the turbulent zone cannot generally be respected rigorously. In our study, it was noticed that the use of an extended version of the k- ϵ model (low-Reynolds-number model) in combination with a wall function defined over the entire wall region is a much better choice. The appropriate choice of wall function in the near-wall zones is discussed in detail. A brief description of the solution strategy using a Newton-type method to solve for turbulence energy k and rate-of-dissipation energy ϵ is given in the same section. Finally we validate the model by simulating the turbulent flow between two plates and the backward facing step. Simulating results for a variety of flow are presented and discussed.

4.3.1 The standard formulation

In this section, we introduce the mathematical description of turbulent flows using time averaged Navier-Stokes equations. Based on assumptions stated previously, the main idea is to model the Reynolds stresses in terms of mean flow quantities and closes the set of equations. Recall that those turbulence models do not simulate the details of the turbulent motion but only the effect of turbulence on the mean-flow behaviour.

Besides the averaged Navier-Stokes equations, we can classify usually turbulence models according to the number of additional differential transport equations that need to solve [5]:

- 1) Zero equation models, the mixing length (l) model
- 2) One equation models
- 3) Two-equation models, the most popular of them being the k - ε model (ε is turbulent kinetic energy dissipation rate) presented by [4, 19]. We have opted for the k - ε model since it is the more used one for industrial applications. This model solves two additional partial differential equations but it offers reliable and accurate predictions in particularly in the presence of complicated domain geometries [17, 18]. We begin by representing any turbulence quantity $u(x,t)$ of interest as the sum of time-averaged component (resolvable scale) and a fluctuating component (unresolvable scale) [5]:

$$u(x,t) = \bar{u}(x,t) + u'(x,t) \quad \text{and} \quad \bar{u}(x,t) = \langle u \rangle \quad (4.1)$$

where $\langle . \rangle$ is the averaging (filtering) operator and the time averaged quantity may be obtained from

$$\bar{u}(x) = \langle u \rangle = \lim_{T \rightarrow \infty} \frac{1}{T} \int_t^{t+T} u(t) dt \quad \text{and} \quad \langle u' \rangle = 0 \quad (4.2)$$

As we can see, the mean value \bar{u} does not vary in time but only in space. As shown in the [5], by considering that the small-scale fluctuations of space-time are negligible, we can set the following properties with the Reynolds-averaging operation:

$$\langle u' \rangle = 0, \quad \langle \bar{u} \rangle = \bar{u}, \quad \langle \bar{u}u' \rangle = 0, \quad \langle uv \rangle = \bar{u} \bar{v} + \langle u'v' \rangle \quad (4.3)$$

Using these assumptions, the frequency spectrum of the small-scale fluctuations is far away from the large-scale fluctuations, i.e. no interaction exists between the two scales [20, 23]. Applying these filters to both the velocity components and the pressure yields the so-called Reynolds averaged Navier-Stokes equations:

$$\begin{aligned} \rho(\partial_t \bar{u} + \bar{u} \cdot \nabla \bar{u}) - \nabla \cdot (\mu \nabla \bar{u} + \nabla \bar{u}^T) + \nabla \bar{p} + \nabla \cdot \langle u' \otimes u' \rangle &= \rho g \quad \text{in } \Omega \times (0, T) \\ \nabla \cdot \bar{u} &= 0 \quad \text{in } \Omega \times (0, T) \end{aligned} \quad (4.4)$$

Equation (4.4) has the same form as the Navier-Stokes equations with the exception of the second-moment tensor (the last term on the right hand side of the first equation in Eq. 4.4). These extra terms act as apparent stresses due to turbulent motions and are called Reynolds stresses or turbulent stresses and usually denoted by \mathbf{R} . It contains the complete influence of the fluctuations field on the mean flow, in other words it represents the effect of the turbulence. Different methods were proposed to model this term. Here, in our work, we will use the standard k-e model [25], by setting R to the following form

$$\mathbf{R} = \mu_t (\nabla \bar{\mathbf{u}} + \nabla \bar{\mathbf{u}}^T) - \frac{2}{3} k \mathbf{I} \quad (4.5)$$

where k is the kinetic energy of turbulence. If we denote by ε the dissipation of the kinetic energy of turbulence than from dimensional analysis, the eddy viscosity μ_t will be modeled as the product of a characteristic velocity \sqrt{k} and a characteristic length $k^{3/2} / \varepsilon$ as follow:

$$\mu_t = \rho C_\mu \frac{k^2}{\varepsilon} \quad (4.6)$$

where

$$k = \frac{1}{2} \langle |u'|^2 \rangle \quad \text{and} \quad \varepsilon = \frac{\mu}{2} (\nabla u' + \nabla u'^T)$$

The computation of the turbulent eddy viscosity is supposed to emulate the effect of unresolved velocity fluctuations u' . The two turbulent quantities k and ε needed to compute the turbulent viscosity satisfy the following standard transport equations at each point of the domain:

$$\begin{aligned} \rho \left(\frac{\partial k}{\partial t} + \bar{\mathbf{u}} \cdot \nabla k \right) - \nabla \cdot \left[\left(\mu + \frac{\mu_t}{\sigma_k} \right) \nabla k \right] - \mu_t P + \rho \varepsilon &= 0 \\ \rho \left(\frac{\partial \varepsilon}{\partial t} + \bar{\mathbf{u}} \cdot \nabla \varepsilon \right) - \nabla \cdot \left[\left(\mu + \frac{\mu_t}{\sigma_\varepsilon} \right) \nabla \varepsilon \right] - C_{\varepsilon 1} \frac{\varepsilon}{k} \mu_t P + C_{\varepsilon 2} \rho \frac{\varepsilon^2}{k} &= 0 \end{aligned} \quad (4.7)$$

The standard values of the five empirical constants of the model are given in [19]

$$C_\mu = 0.09 \quad \sigma_k = 1.0 \quad \sigma_\varepsilon = 1.3 \quad C_{\varepsilon 1} = 1.44 \quad C_{\varepsilon 2} = 1.92 \quad (4.8)$$

and $P = \nabla \bar{\mathbf{u}} : (\nabla \bar{\mathbf{u}} + \nabla \bar{\mathbf{u}}^T)$ represents the production of turbulence.

Finally, replacing the stress tensor and rearranging the set of equations, one has to solve the following problem in $\Omega \times (0, T)$

$$\begin{aligned} \rho(\partial_t \bar{u} + \bar{u} \cdot \nabla \bar{u}) - \nabla \cdot ((\mu + \mu_t)(\nabla \bar{u} + \nabla \bar{u}^T)) + \nabla \tilde{p} &= \rho g \\ \nabla \cdot \bar{u} &= 0 \\ \rho \left(\frac{\partial k}{\partial t} + \bar{u} \cdot \nabla k \right) - \nabla \cdot \left[\left(\mu + \frac{\mu_t}{\sigma_k} \right) \nabla k \right] &= \mu_t P - \rho \varepsilon \\ \rho \left(\frac{\partial \varepsilon}{\partial t} + \bar{u} \cdot \nabla \varepsilon \right) - \nabla \cdot \left[\left(\mu + \frac{\mu_t}{\sigma_\varepsilon} \right) \nabla \varepsilon \right] &= C_{\varepsilon 1} \frac{\varepsilon}{k} \mu_t P - C_{\varepsilon 2} \rho \frac{\varepsilon^2}{k} \end{aligned} \quad (4.9)$$

together with the corresponding boundary and initial conditions.

The pressure has been modified into \tilde{p} by taking into account the isotropic part of the Reynolds stress tensor:

$$\tilde{p} = \bar{p} + \frac{2}{3} k \quad (4.10)$$

Remark 1. In what follows, the overbar ($\bar{\cdot}$) in the mean value of the variables shall be omitted to simplify the notation.

Close to a solid wall, the viscous effects predominate over turbulent ones. Therefore, these standard equations of the k - ε model are only valid at high Reynolds numbers and in the region away from a solid wall. Hence these equations have to be used in conjunction with an empirical wall function to overcome such drawback. We will discuss in the following various assumptions related to this subject [18, 20, 21, 23].

4.3.2 The boundary conditions

When applying the k - ε model to study the heat transfer and fluid flow inside industrial furnaces, the inflow and outflow conditions can be complicated due to the effects of up and down-stream obstacles, free stream turbulence, highly convective jet, etc. Recall also that this turbulence model is valid only in regions where the viscous terms are small compared with the turbulence effects. It is not valid in the near-wall zones, which include the viscous and buffer sublayers. The most popular approach to overcome these difficulties and assign the appropriate boundary conditions is not to consider the near-wall zones and employ wall functions instead. This section discusses in detail all these conditions.

Inflow condition

At the inflow boundary, for a prescribed velocity \mathbf{u} , the value of k can be computed using

$$k = c_{bc} |\mathbf{u}|^2 \quad (4.11)$$

where $c_{bc} \in [0.003, 0.02]$ is an empirical constant and $|u| = \sqrt{u \cdot u}$ is the Euclidian norm of the velocity. Usually c_{bc} is fixed to 0.02, see [5, 19] for more details. Once k is computed, the value of ε can be prescribed using

$$\varepsilon = \frac{C_\mu k^{3/2}}{L} \quad (4.12)$$

where L , a fixed constant, known as the characteristic length of the model.

Remark 2. These computed values of k and ε are extended into the interior domain as initial conditions.

Remark 3. The initial value of the turbulent viscosity can be directly computed using equation (4.6) together with (4.11) and (4.12)

Outflow condition

The treatment of the exit boundary condition is also important. At the outlet, a homogeneous Neumann (“do-nothing”) boundary condition should be applied. This would permit eddies in the flow to exit the domain without any adverse effect on the flow field inside the furnace.

$$n \cdot \nabla k = 0 \quad \text{and} \quad n \cdot \nabla \varepsilon = 0 \quad (4.13)$$

Remark 4. The numerical treatment of inflow and outflow boundary conditions does not present any difficulty. In the finite element framework, relations imply that the surface integrals resulting from integration by parts vanish and do not need to be assembled.

Boundary condition

If a non-slip boundary condition is used in turbulent flows, a large number of fine grids close to wall are needed, which is not practical at present due to computer limitations and long time heat treatment simulation. Moreover, near solid walls, the turbulence kinetic energy production is gradually reduced due to dominance of viscous effects. In this region, the large eddies dissipate their energy directly rather than transferring it to smaller scales as per the energy cascade. Therefore, although the strain rate can be expected to peak in the near-wall region due to steep velocity gradients, there will be a reduction in sub-grid scale stress. This effect is accounted for by damping the turbulent viscosity, μ_t , as the wall is approached. The usual way to damp this additional viscosity in the vicinity of the wall and to capture the near-wall effects without drastically increasing the number of unknowns is the use of wall models.

The first popular approach consists in avoiding the resolution of the Navier-Stokes equations and the two transport k - ε equations right up to the wall. Instead, the edge of the computational domain is placed at a small distance δ away from the wall in the high Reynolds number region. Empirical wall functions can then be derived and used to define boundary conditions at the edge of the modified domain, an internal boundary Γ_δ located at distance δ from the solid wall Γ_w . The subscript w and δ would mean at the wall and at the artificial wall boundary, see figure 3.

Remark 5. The topic of variable resolution in near-wall models can serve as a Ph.D. level thesis all on its own, and it is therefore well beyond the scope of our study. In our work, the purpose is to understand these approaches and to retain those that would well correspond for simulating heat treatment inside industrial furnaces. A complete description of this simulation will be given later in chapter 6. In what follows, we summarize the retained approaches.

At a small distance from the solid wall we begin to set the normal component of the velocity equal to zero, whereas tangential slip is permitted in turbulent flow simulations.

$$u \cdot n = 0 \quad (4.14)$$

To complete the previous statement and close the problem, we still need to prescribe the wall traction for the momentum equations (tangential stress) τ_w as well as the boundary values of k and ε on the wall. Since a boundary layer of width δ is removed from the computational domain Ω , the equations are now solved in the reduced domain Ω_δ subject to empirical boundary conditions (see figure 3.3).

To describe the asymptotic behavior of the different variables near a solid wall, as a first approach we imposed a combination of Neumann (tangential) and Dirichlet (normal) semi-empirical boundary conditions:

$$\tau_w = -\rho u_\tau^2 \frac{u}{|u|} \quad k_w = \frac{u_\tau^2}{\sqrt{C_\mu}} \quad \varepsilon_w = \frac{u_\tau^3}{\kappa \delta} \quad \text{on } \Gamma_\delta \quad (4.15)$$

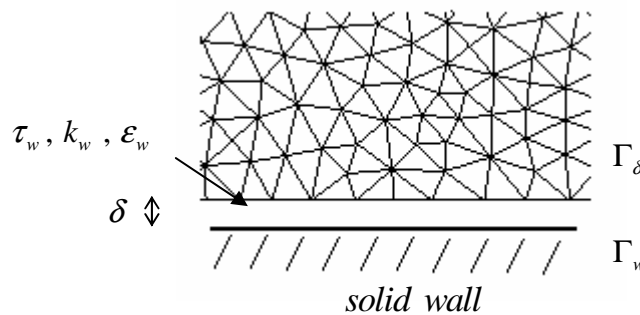


Figure 3. Discretization close to the wall

where τ_w is the shear stress tensor (opposite to local velocity), used as a Neumann boundary condition for the momentum equation in the tangential direction, κ is the Von Karman constant ($\kappa=0.41$) and u_τ is the friction velocity. Integration by parts in the weak form of the incompressible Navier-Stokes equations gives rise to a surface integral over the internal boundary Γ_δ which contains the prescribed traction:

$$\int_{\Gamma_\delta} \tau_w v ds = - \int_{\Gamma_\delta} -u_\tau^2 \frac{u}{|u|} v ds \quad (4.16)$$

It remains to determine the value of the friction velocity which is needed for the computation of (4.15).

Remark 6. The application of the no-penetration (free-slip) boundary condition (4.14) is nontrivial if the boundary of the computational domain is not aligned with the axes of the Cartesian coordinate system. Therefore, our formulation consists in computing first the normal vectors along the entire boundary domain by the use of the distance function. Consequently, the normal velocity component will set equal to zero using a simplified penalty method. The numerical implementation in our finite element library CIMLIB of this boundary condition as well as the friction law (4.16) has to be credited to the work of our colleagues Bruchon J. and Digonnet H [24]. Further details about this subject are published in [24]. It was shown that the use of such techniques developed in the framework of level set methods proves to be a simple yet efficient approach. The most straightforward way for computing the distance field is through the use of geometric brute force algorithm where the point-to-point distance is computed throughout the computational grid and the minimum distance for each point is stored. Once the distance field is computed, the normal to the entire boundary is defined by simply taking its gradient. This procedure will be applied only one time at the beginning of each simulation. Alternatively, Renato N. Elias *et al.* in [25] have proposed lately a fast marching method to compute the distance field using a finite element algorithm. A matter that needs further inspections in the near future.

Wall function implementation

In the region close to solid walls, wall function of Launder and Spalding 1974 [4] is usually used assuming that close to a solid wall the velocity and temperature can be described by universal logarithmic profiles. In this region, the turbulence variables k , ε and the shear stress τ_w are assumed to be constant and computed using (3.15). With these laws it is possible to express the mean velocity parallel to the wall by applying these boundary conditions for the momentum and turbulence transport equations rather than conditions at the wall itself. As outlined in the previous section, the viscous sublayer does not need to be resolved and the need for a very fine mesh is circumvented. In what follows, the last detail about the computation of the friction velocity will be given. From experimental work, it is known that near-wall flows have a characteristic multilayered structure within the boundary layer. It can divide it into three layers as shown in figure 4:

1. Viscous sublayer, where viscous stress dominated and molecular viscosity makes the flow behave close to laminar.
2. Buffer layer, where the laminar and turbulent properties of the flow are both important and of the same magnitude.
3. Fully turbulent layer, where the turbulent stress dominated.

Three scalar variables, i.e., scalar velocity u^+ , scalar coordinate y^+ , and scalar temperature T^+ , have been defined in the wall function approach: First, we set a local wall Reynolds number:

$$y^+ = \frac{\rho \delta}{\mu} \sqrt{\frac{\tau_w}{\rho}} \quad (4.17)$$

The velocity based on the wall shear stress is given by

$$u^+ = \frac{u}{\sqrt{\tau_w / \rho}} \quad (4.18)$$

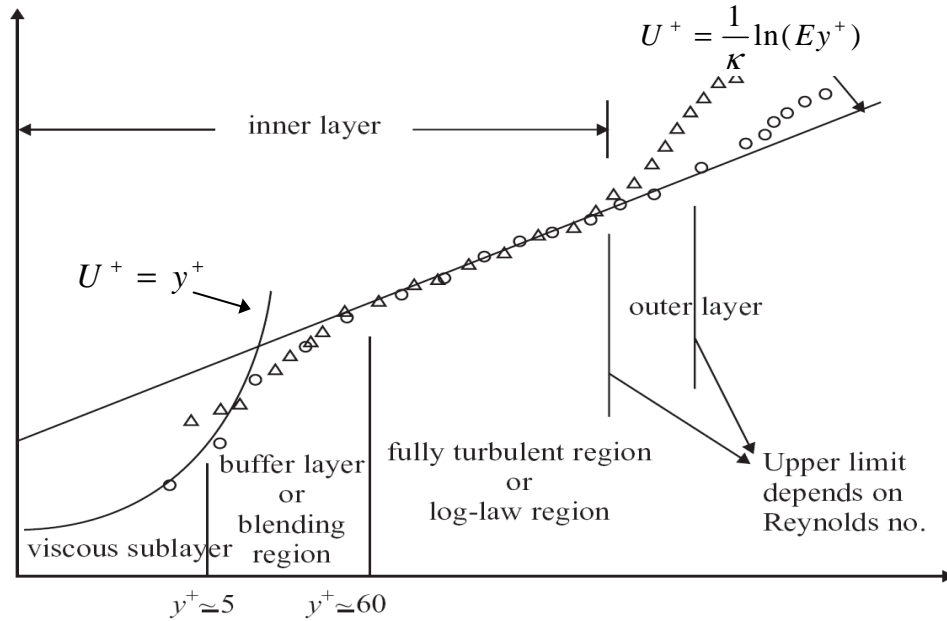


Figure 4. Flow structure near wall flows (adapted from Fluent user guide Vol. I [29])

where δ is the normal distance between the computational boundary and the wall and u is the tangent velocity as long as condition in (4.14) is imposed. When solving coupled problem, another non-dimensional number is used to characterize the temperature in the wall region:

$$T^+ = \frac{(T - T_w)u_\tau}{q_w / \rho c_p} \quad (4.19)$$

Recall that we are interested in computing the friction velocity $u_\tau \equiv \sqrt{\tau_w / \rho}$ which is located at distance δ from the wall. This can be done with the use of different relationships that exist between y^+ and u^+ depending on the magnitude of y^+ (see figure 4):

In the viscous sub-layer, we have

$$u^+ = y^+, \quad y^+ < 30 \quad (4.20)$$

In the inertial sub-layer, given by Launder and Spalding (1974) [4] and Smith (1984) [26]:

$$u^+ = \frac{1}{\kappa} \ln(Ey^+), \quad 30 < y^+ < 100 \quad (4.21)$$

where E is the roughness parameter. For smooth wall E is taken equal to 9.0.

An alternative way to ensure a direct transition between the laminar boundary layer and the turbulence zone is the use of the half-empirical law of Reichardt :

$$u^+ = 2.5 \ln(1 + 0.4y^+) + 7.8(1 - e^{-y^{+11}} - \frac{y^+}{11} e^{-0.33y^+}) \quad (4.22)$$

as suggested by Houghton and Carpenter (2003) [30].

The constants in equation (4.22) were obtained via comparison with experimental data. In our implementation, we have used equations (4.20) and (4.21). The distance δ at which the nodes is placed is at the discretion of the researcher; but generally it should not be too large in order to lie inside the wall region ($y^+ \leq 100$), but also not too small in order that the equations of the model remain valid ($y^+ \geq 30$).

Usually, we specify the value of δ over Γ_w at the beginning of the simulation, so that in order to find the friction velocity one must solve the nonlinear equation:

$$g(u_\tau) = |u| - u_\tau \frac{1}{k} (\ln Ey^+) = 0 \quad (4.23)$$

This equation can be solved iteratively by Newton's method [43, 47]

$$\begin{aligned} f(u_\tau) &= |u| - u_\tau \frac{1}{k} (\ln Ey^+) = 0 \\ u_\tau^{i+1} &= u_\tau^i - \frac{f(u_\tau^i)}{f'(u_\tau^i)} = u_\tau^i + \frac{|u| - U_\tau g(u_\tau^i)}{1/k + g(u_\tau^i)} \quad i = 1, 2, \dots \end{aligned} \quad (4.24)$$

$$\text{where } g(u_\tau^i) = \frac{1}{k} (\ln Ey_*^+) \quad \text{and} \quad y_*^+ = \max(20, \frac{\rho u_\tau \delta}{\mu})$$

The initialization is given by:

$$u_\tau^0 = \sqrt{\frac{\mu |u|}{\rho \delta}} \quad (4.25)$$

No iterations are performed if it turns out that $y^+ < 20$. In other words, it is equal to initial friction velocity in the viscous sublayer. The τ_w , k_w and ε_w are then calculated using equations (4.15) and used as boundary conditions for the following iterations. For further details regarding the implementation of wall laws the reader is referred to [20, 21].

Different strategies of wall functions have been studied over the past years. Recently, a two-velocity scale approach was used to enhance the behavior of the velocity near to the wall. In the following section, a brief summary about this method will be given. Although, the computations presented here were carried out using both the wall laws the two-layer k- ε model. Some comparisons will be given and conclusions will be drawn.

Remark 7. Another possibility could be successfully used in our work is to specify the value of y^+ over the boundary with wall law condition. The main advantage of this choice is that given y^+ no iterations that could fail to converge are needed anymore to be computed, the friction velocity can be evaluated in a direct manner. As a balancing drawback, now the distance δ depends on the solutions and can take different values at different points on the boundary. This is however not an issue when δ is negligible compared to the dimensions of the domain.

4.3.3 Enhanced wall treatment

Recently, most practitioners have used an alternative approach to improve the performance of the two-equation model in predicting near-wall flows [50, 51]. This approach is based on the use of two-scale velocities which offers some advantages in respect to the one-scale velocity presented in the previous section. It improves the prediction of the turbulent quantities in the regions where the friction to the wall decreases (e.g., the vicinity of a reattachment point at which τ_w is zero) while the turbulence are still at high level. This approach can also exhibit the correct heat transfer behavior at reattachment point.

We have followed closely the work of Grotjans and Menter (1998) and the details from [41]. The main idea is to use the logarithmic wall functions to derive Neumann boundary conditions for the turbulent variables rather than the use of Dirichlet boundary conditions described previously in (4.15). The comparisons made by [41, 43, 44, 45] have demonstrated the efficiency of the enhanced wall treatment. In the last section, we will provide similar benchmarks to assess this matter. As explained, the smallest wall distance for the definition of y^+ corresponds to point where the logarithmic layers meet the viscous sublayer. In this case, both linear and logarithmic functions (4.20) and (4.21) are assumed to hold. Hence, the optimal value of the parameter y^+ can be found by simply solving this nonlinear equation:

$$y^+ = \frac{1}{\kappa} \ln(Ey^+) \quad (4.26)$$

The resulting solution is given by $y_c^+ = 11.06$. As it was pointed out in Remark 7., for a given fixed value of y^+ the friction velocity can be directly computed from:

$$u_\tau = \frac{|u|}{y_c^+} \quad (4.27)$$

Consequently, the nonlinearity of (4.23) for computing the friction velocity is now taken into account implicitly in the computation of y_c^+ .

On the other hand, the wall shear stress will be now expressed using two-scale velocity:

$$\tau_w = -\rho u_\tau u_k \frac{u}{|u|} \quad \text{on } \Gamma_\delta \quad (4.28)$$

The new introduced velocity u_k called often *bulk velocity* is the velocity scale based on the turbulent kinetic energy and given by:

$$u_k = C_\mu^{0.25} \sqrt{k} \quad (4.29)$$

where k is now computed naturally and ‘floats’ at the boundary of the computational domain by setting the normal gradient to the wall equal to zero, and the velocity profile is given by:

$$u^+ = \begin{cases} y^+ & \text{for } y^+ < y_c^+ \\ \frac{1}{\kappa} \ln(Ey^+) & \text{for } y^+ > y_c^+ \end{cases} \quad (4.30)$$

Both the friction velocity and the TKE scale velocity are related using the modified dimensionless number:

$$y^+ = \frac{\rho \delta u_k}{\mu} \quad \text{and} \quad u^+ = \frac{|u|}{u_\tau} \quad (4.31)$$

To complete the previous statement and describe modified asymptotic behavior of the different variables near a solid wall, we imposed a new combination of Neumann and Dirichlet boundary conditions:

$$\frac{\partial k}{\partial n} = 0 \quad \varepsilon_w = \frac{u_k^3}{\kappa \delta} \quad \text{on } \Gamma_\delta \quad (4.32)$$

On the other hand levels of k remain high if the Neumann condition is adopted so that there is no difficulty in applying equation (4.28) with u_τ given by equation (4.27). The other types of boundary commonly encountered are not changed and treated in the same standard way (e.g. at inlet and outlet). To assess the implementations of the wall approaches, a comparisons between these two approaches will be given later in section 5. For the implementation issues of the two-scale velocity approach we have followed the work of [41, 43, 44].

Remark 8. The bridging y^+ value between the viscous and inertial sub-layers of 11.6 was based on Thangam & Hur theory (1991) [37]. Again, it is at the discretion of the researcher how this value is defined; e.g. Hassan & Barsamian (2001) [31] used 11.81.

4.3.4 Low Reynolds formulation

For complex flows, ensuring that each boundary grid point will be located in the turbulent layer can become quite a tedious task. Moreover, the real position δ of the boundary may become highly irregular in particularly when simulating heat transfer and turbulent flows inside industrial furnaces (see figure 5). This difficulty can be overcome by using the so-called low-Reynolds-number k - ε model, which is valid up to the wall. The computation can then cover the entire flow domain, including buffer and viscous zones and the mesh reaches the wall [38].

However, the computational cost would be much higher, since a very fine grid is needed for the wall region because of the very steep gradients and strong variations one finds there. This choice is justified in chapter 6, where we will show the reader that this additional nodes added in the vicinity of the wall become a must when simulating multi-domain applications.

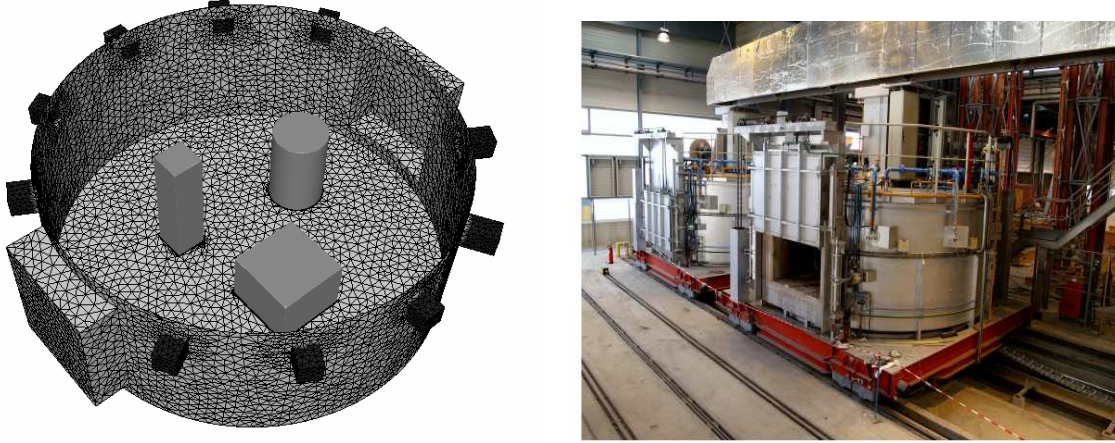


Figure 5. Complex configuration of an industrial furnace

The main idea of using the low-Reynolds-number model is that the two-equations (4.9) can now be applied to the viscous sublayer directly without the use of the wall function. Therefore, a suitable damping function must be introduced in the equations to damp the turbulent viscosity in the near-wall region, where it is known to be small. In the far-wall region, this function returns to 1 and produce the same good results for high Reynolds-numbers flows. Such modifications will improve the performance of the two-equation model in predicting the near-wall viscous layer for flows without separation.

The modified transport equations for the turbulence quantities satisfy at each point of the domain:

$$\begin{aligned} \rho \left(\frac{\partial k}{\partial t} + u \cdot \nabla k \right) - \nabla \cdot \left[\left(\mu + \frac{\mu_t}{\sigma_k} \right) \nabla k \right] - \mu_t P + \rho(\varepsilon + D) &= 0 \\ \rho \left(\frac{\partial \varepsilon}{\partial t} + u \cdot \nabla \varepsilon \right) - \nabla \cdot \left[\left(\mu + \frac{\mu_t}{\sigma_\varepsilon} \right) \nabla \varepsilon \right] - C_{\varepsilon 1} f_{\varepsilon 1} \frac{\varepsilon}{k} \mu_t P + C_{\varepsilon 2} f_{\varepsilon 2} \rho \frac{\varepsilon^2}{k} + \rho E &= 0 \quad (4.33) \\ \text{where } \mu_t &= \rho C_\mu f_\mu \frac{k^2}{\varepsilon} \end{aligned}$$

Compared with the standard k - ε equations, three damping functions f_μ , $f_{\varepsilon 1}$ and $f_{\varepsilon 2}$ and two additional terms (E and D) were introduced to provide a smooth transition from turbulent to laminar flow in the near-wall area. Many expressions for these functions can be founded in [38, 54, 55]. Since we extend the grid to the wall, then a suitable choice of these expressions must ensure on one hand that no terms goes to infinity as k approaches zero in the near-wall region and on the other hand it must provide appropriate boundary condition for ε .

We can find in [55] an interesting comparative study of five low Reynolds number k - ε models for predicting the flow and heat transfer characteristics. The authors have summarized and tested five models: Launder and Sharma [54], Changez, Hsieh and Chen [56], Abid [57]; Lam and Bremhorst [58] and Abe, Kondoh and Nagano [59]. Another alternative was suggested by Chien's in [38]. Here in our context, we have retained the expressions given by Chien [38] due to their simplicity and favorable numerical properties (see [43] for more details). Thus, the damping functions and the constants used in this model are as follow:

$$\begin{aligned}
 f_{\mu} &= 1 - \exp(-0.0115 y^+) \\
 f_{\varepsilon 1} &= 1 \\
 f_{\varepsilon 2} &= 1 - 0.22 \exp\left(-\frac{\rho k^2}{6\mu\varepsilon}\right)^2 \\
 D &= 2\left(\frac{\mu k}{\rho\delta^2}\right) \\
 E &= 2\left(\frac{\mu\varepsilon}{\rho\delta^2}\right)\exp(-y^+/2) \\
 C_{\mu} &= 0.09, \quad \sigma_k = 1.0, \quad \sigma_{\varepsilon} = 1.3, \quad C_{\varepsilon 1} = 1.35, \quad C_{\varepsilon 2} = 1.8
 \end{aligned} \tag{4.34}$$

As stated before, now only simple Dirichlet boundary conditions will be applied on the wall. The standard no-slip conditions for the velocity with zero values of k and ε are therefore implemented:

$$u_w = 0, \quad k_w = 0, \quad \varepsilon_w = 0 \quad \text{on } \Gamma_w \tag{4.35}$$

The specific role of each introduced functions that account for the low Reynolds numbers model is discussed briefly. In the first equation in (4.33), the introduced term D by Jones and Launder [53] is chosen so that the modified dissipation variable $\varepsilon = \tilde{\varepsilon} - D$ can be set equal to zero at the wall, a simple convenient boundary condition. The empirical constants in (4.34) shows a little diversity from those used in the standard k - ε model. This slight modification is determined from experimental data for a near-wall modeling.

As for the first damping function f_{μ} which multiplies the eddy viscosity in (4.33) was introduced to reduce and eliminate the direct effect of the molecular viscosity on the shear stress. Consequently, close to the wall, this function approaches zero, and thus it will damp completely the added turbulent viscosity. Whereas the function $f_{\varepsilon 2}$ was introduced to incorporate low Reynolds number effects in the destruction term of the ε equation. The function $f_{\varepsilon 1}$ and/or the extra term E got the same role; increasing the magnitude of the dissipation rate in the near wall region, thereby decreasing the values of k . These can results in a zero eddy viscosity at the wall. For more details about the use of these expressions where eight different models summarizing various assumptions and functions introduced to account for the low Reynolds number can be found in the famous reference [53].

In what follows, a description about the implementation of the finite element solver is discussed as well as the positivity of the numerical solutions. Several numerical examples are given in section 5 to assess the effectiveness of the adapted methods.

4.3.5 Finite element solution

The discretization in space for the incompressible Navier-Stokes equations and turbulence equations is performed by an unstructured grid stabilized finite element method. The method presented in chapter 2 for solving transient convection-diffusion-reaction equation is applied to the two-equation k - ε model (4.36). The variational multiscale method presented in chapter 3 is used for solving the Reynolds Averaged Navier-Stokes equations (4.23). Recall that the Galerkin formulation is obtained by multiplying these equations by an appropriate test functions, applying the divergence theorem to the diffusion terms and integrating over the domain of interest (see Section 2.3). Both the momentum and turbulence transport equations are dominated by convection and, as shown in the previous chapters, the standard Galerkin discretization of such equations leads to non-physical oscillations. Hence, stabilization methods presented previously are used to provide smooth solutions and to suppress these oscillations.

Before proceeding to the description of the finite element discretization of the equations to be solved [38], the first thing to be discussed is which iterative strategy should be used to linearize them. A special care should be adopted for linearization of the source and sink terms of k and ε transport equations in order to preserve the convergence. Many ideas were proposed in the literature, thus two modifications were retained.

The first as explained in [5] and proposed by [43] is to introduce an auxiliary parameter $\gamma = \varepsilon^i / k^i$ evaluated using the solution from the previous outer iteration in order to decouple and linearize these equations; and the second for practical implementation purposes is to linearize the nonlinear source term in the kinetic dissipation equation. These two modifications were also highlighted in [5] where both implicit and explicit formulation could be found. The author showed that these choices of decoupling the two-equation provide the needed robustness to deal with complex three-dimensional problems:

- 1) The destruction term in the turbulent kinetic energy equation is modified into a reaction term for a better stability as suggested by [5]:

$$\rho\varepsilon = \rho \frac{\varepsilon^i}{k^i} k \quad (4.36)$$

- 2) The destruction term in the dissipation equation is modified and linearized as follow:

$$C_{\varepsilon 2} \rho \frac{\varepsilon^2}{k} = 2C_{\varepsilon 2} \rho \frac{\varepsilon^i}{k^i} \varepsilon - C_{\varepsilon 2} \rho \frac{\varepsilon^{i^2}}{k^i} \quad (4.37)$$

where k^i and ε^i are the turbulent kinetic energy and dissipation at iteration i .

Therefore, the final linearized form of the k- ε equations can be written in the following form:

$$\begin{aligned} \underbrace{\rho\left(\frac{\partial k}{\partial t} + u \cdot \nabla k\right)}_{\text{Transient and convective terms}} - \underbrace{\nabla \cdot \left[\left(\mu + \frac{\mu_t}{\sigma_k} \right) \nabla k \right]}_{\text{Diffusion terms}} + \underbrace{\rho \gamma k}_{\text{Reaction terms}} &= \underbrace{\mu_t P}_{\text{Source terms}} \\ \underbrace{\rho\left(\frac{\partial \varepsilon}{\partial t} + u \cdot \nabla \varepsilon\right)}_{\text{Transient and convective terms}} - \underbrace{\nabla \cdot \left[\left(\mu + \frac{\mu_t}{\sigma_\varepsilon} \right) \nabla \varepsilon \right]}_{\text{Diffusion terms}} + \underbrace{C_{\varepsilon 2} \rho \gamma \varepsilon}_{\text{Reaction terms}} &= \underbrace{C_{\varepsilon 1} \gamma \mu_t P + C_{\varepsilon 2} \rho \gamma \varepsilon^i}_{\text{Source terms}} \end{aligned} \quad (4.38)$$

The strategy followed is to solve first the Navier-Stokes equations for the velocity and the pressure with the fields variables obtained from previous iteration and the updated wall boundary conditions. In the second phase of the solution procedure, the two-equation are solved for k and ε , respectively, using the updated flow velocity and the wall boundary condition. The iterations terminates when the convergence criteria is satisfied. The successive iterative solution algorithm is illustrated as follow:

- i. giving initial conditions u_0 , k_0 and ε_0
- ii. compute μ_t from k and ε
- iii. for μ_t given :
 1. solve the momentum and continuity equations
 2. solve the k -equation
 3. solve the ε -equation
 4. update μ_t and go to (iii)

The time derivatives are approximated by the Euler forward difference scheme. Following the lines on the use of stabilization methods for transient convection-diffusion-reaction equations discussed in the previous chapters, the space-time discretized global system of the two-equation turbulence model may be written in the following form:

Find k^i and ε^i such that, $\forall v \in V$

$$\begin{aligned} \left(\rho \frac{k^i - k^-}{\Delta t}, v \right) + \left(\rho u^{i-1} \cdot \nabla k^i, v \right) - \left(\left(\mu + \frac{\mu_t^{i-1}}{\sigma_k} \right) \nabla k^i, \nabla v \right) + \left(\rho \gamma^{j-1} k^i, v \right) \\ + \underbrace{\sum_K (\mathcal{R} k, \tau_K u^{i-1} \cdot \nabla v)_K}_{\text{streamline upwind}} + \underbrace{\sum_K (\mathcal{R} k, \tau_K^c u_{||}^{i-1} \cdot \nabla v)_K}_{\text{discontinuity-capturing}} = \left(\mu_t^{i-1} P^{i-1}, v \right) \end{aligned} \quad (4.39)$$

$$\begin{aligned} \left(\rho \frac{\varepsilon^i - \varepsilon^-}{\Delta t}, v \right) + \left(\rho u^{i-1} \cdot \nabla \varepsilon^i, v \right) - \left(\left(\mu + \frac{\mu_t^{i-1}}{\sigma_\varepsilon} \right) \nabla \varepsilon^i, \nabla v \right) + \left(C_{\varepsilon 2} \rho \gamma^{j-1} \varepsilon^i, v \right) \\ + \underbrace{\sum_K (\mathcal{R} \varepsilon, \tau_K u^{i-1} \cdot \nabla v)_K}_{\text{streamline upwind}} + \underbrace{\sum_K (\mathcal{R} \varepsilon, \tau_K^c u_{||}^{i-1} \cdot \nabla v)_K}_{\text{discontinuity-capturing}} = \left(C_{\varepsilon 1} \gamma^{j-1} \mu_t^{i-1} P^{i-1} + C_{\varepsilon 2} \rho \gamma^{j-1} \varepsilon^{i-1}, v \right) \end{aligned}$$

Subscript $\bar{\cdot}$ indicates the variable is computed using the solution from previous time step. As in Reference [9], the diffusion term, as well as the mean velocities is computed using the eddy viscosity from the previous iteration. Recall that the non-linear equations for the velocity and the pressure are solved using the Newton-Raphson iterations. For scalar equations, only fixed-point's iterations are performed. The resulting linear systems are generated directly in a compressed sparse row format, and solved iteratively using the generalized minimal residual method (GMRES) with ILU preconditioner [60].

4.3.6 Positivity of the solution

By definition, the turbulence variables are positive quantities. However due to oscillations in the numerical solution of these equations, if one of the turbulence variables becomes negative than the eddy viscosity may locally become negative. This will cause an immediate breakdown of the solution algorithm. Negative or small value in the denominator of the source terms can also lead to an improper sign or overly large values for μ_t or for some source terms. Enhanced the robustness of the algorithm is achieved if one can ensure that turbulence variables remain positive throughout the domain and during the course of iterations.

One way to preserve the positivity of the dependent variables was proposed by [52, 61] and consists of solving for their logarithms. By changing the dependent variables into $k=\ln(k)$ and $\varepsilon=\ln(\varepsilon)$, one can guarantee that k and ε will remain positive throughout the computations. Hence, the eddy viscosity will always remain positive. A detailed comparison of the traditional solution procedure and that solving for the logarithms may be found in references [61]. The main disadvantage of these techniques is the appearance of exponentials in the turbulence equations.

Another way to enhance robustness of the k - ε algorithm both k and ε are clipped to enforce positivity and to prevent these variables from taking overly small values. If k is too small it is replaced by $k = k_{\max} / c_k$ where k_{\max} is the maximum value found in the domain and c_k is a user supplied constant. When ε is too small and results in overly large value of μ_t , it is replaced by $\varepsilon = \rho C_\mu k^2 / (c_\varepsilon \mu)$ where c_ε is again a user supplied constant. However, changing the nodal value of the solution in an iterative process could lead to a deterioration of the stability of the equation. Although, this technique is commonly used by several authors as in [5].

Here in our context, we rely on the use of stabilization methods introduced in chapter 2 to reduce and possibly to eliminate numerical oscillations in the streamline direction (SUPG) and the solution gradient direction (SCPG). As shown in equation (4.39), two additional stabilizing terms were introduced; the first controls the oscillations in the direction of the streamline (SUPG) and the other controls the derivatives in the direction of the solution gradient. This can improve the result for convection dominated problems (SUPG), while the shock-capturing technique precludes the presence of overshoots and undershoots by increasing the amount of numerical dissipation in the neighborhood of layers and sharp gradients.

If we look further in the literature on this subject and we add our results from several numerical experiments we came to two main conclusions:

1. The use of advanced stabilization finite element methods plays an important role in preserving the positivity of the solution and retarding the appearance of numerical oscillations.
2. The instabilities in the solution of the classical Galerkin formulations of κ - ε equations is not caused only by the convection terms but also by the reaction terms.

This matter was also highlighted by the authors in [62]. By inspection of the formulation, they realized that is not the negative values of k and ε that really matter and need to be clipped, but instead the appearance of negative diffusion or reaction coefficients that cause the exponential growth of the solution. They proposed to limit these coefficients from below without any clipping or touching the nodal values of k or ε . The only adopted modifications introduced in the numerical resolution are:

1. The associated eddy viscosity μ_t is bounded from below by a small fraction α of the laminar viscosity μ :

$$\mu_t = \max \left(C_\mu \frac{(k^n)^2}{\varepsilon^n}, \alpha \mu \right) \quad (4.40)$$

2. Both the reaction terms and the source term in the ε -equation are limited from below:

$$\begin{aligned} \text{Reaction } (k) &= \max \left(\rho \frac{\varepsilon}{k}, 0 \right) \\ \text{Reaction } (\varepsilon) &= \max \left(C_{\varepsilon 2} \rho \frac{\varepsilon}{k}, 0 \right) \\ \text{Source } (\varepsilon) &= \max \left(C_{\varepsilon 1} \frac{\varepsilon}{k} \mu_t P + C_{\varepsilon 2} \rho \frac{\varepsilon^2}{k}, 0 \right) \end{aligned} \quad (4.41)$$

The above representations preclude division by zero or small values and guarantee nonnegative coefficients without manipulating the actual nodal values of k and ε .

4.4 Large Eddy Simulation

The LES method has been developed quickly in recent years and its future appears very promising with the modern developments in high performance computing (HPC) and parallel computing. Lesieur (1997) [64] pointed out that employing such sophisticated models offers high accuracy in respect to RANS models. In the LES simulations, the large-scale properties of the flow are computed directly from the filtered continuous Navier-Stokes equation while the subgrid-scale fields, which contain the fluctuations at smaller scales, are modelled.

Large eddy simulations are based on filtering and decomposing the scales into large-scale and small-scale (subgrid-scale) components. Therefore, the idea is to simulate more precisely and solve the contributions of the large, energy-carrying structures to momentum and energy transfer and to only model the effect of the small-scale eddies, which are not resolved numerically. These simulations are also three-dimensional and time-dependent but are much less costly than DNS simulations. The number of grid points required to resolve the outer layer is proportional to $Re^{0.4}$ while near the viscous sublayer it increases to $Re^{1.8}$ [65].

The filtered governing equations for LES, the subgrid-scale (SGS) models, the numerical methods and the discretization schemes using unstructured grids, the numerical procedure, and the boundary conditions for wall treatment and inflow and outflow settings are given in the next section. More details can be found in Germano *et al.* (1991) [2].

4.4.1 Filtering equations

In LES, the contribution of the large-scale is computed directly, and only the smallest scales of turbulence are modelled. To separate the large from the small scales, spatial filtering operation are applied. The flow is divided into a large scale \bar{u} and a subgrid scale u' (SGS)

$$u(x,t) = \bar{u}(x,t) + u'(x,t) \quad (4.42)$$

The large scale is defined by a filtering [17, 63]. For example, a one-dimensional filtered velocity can be obtained from

$$\bar{u}_i = \int G(x, x') u_i(x') dx' \quad (4.43)$$

where the bar represents grid filtering, and $G(x, x')$ is the filter function which determines the structure and size of the small scales. The filter function depends on the difference $(x-x')$ and on the filter width. The length scale is a length over which averaging is performed. The filtering procedure removes spatial fluctuations that are narrower than the characteristic length scale. Flow eddies larger than the length scale are 'large eddies' and smaller than the length scale are 'small eddies'. There are three commonly used filter kernels:

- 1- The Gaussian filter:

$$G(x_i) = \sqrt{\frac{6}{\pi\Delta_i}} \exp\left(\frac{-6x_i^2}{\Delta_i^2}\right) \quad (4.44)$$

- 2- The sharp Fourier cut-off filter:

$$G(x_i) = \frac{2 \sin\left(\frac{\pi x_i}{\Delta_i}\right)}{\pi x_i} \quad (4.45)$$

3- The tophat / box filter:

$$G(x_i) = \begin{cases} \frac{1}{\Delta_i} & \text{if } |x_i| \leq \frac{\Delta_i}{2} \\ 0 & \text{if } |x_i| > \frac{\Delta_i}{2} \end{cases} \quad (4.46)$$

where Δ_i is the filter width and $i=1, \dots, d$. Piomelli *et al* [34] pointed out that the Fourier and Gaussian filters were normally used for LES that applied spectral methods. For finite volume or finite difference, it was natural to use the box filter.

By applying the filtering on the Navier-Stokes equations, we remove the small turbulent scales and we derive the resolvable-scale equation. Through this procedure, a non-linear term are derived known as *subgrid-scale stress* (SGS) tensor and added to this equation which describes the effects of the unresolved scales. As shown for the RANS equation in section 2, the SGS tensor has to be modeled in order to close the equations.

The derived governing equations of LES take the following form:

$$\begin{aligned} \rho(\partial_t \bar{u} + \nabla \cdot (\bar{u} \otimes \bar{u})) - \nabla \cdot (2\mu S(\bar{u}) - \overline{u' \otimes u'}) + \nabla \bar{p} &= \rho g \quad \text{in } \Omega \times (0, T) \\ \nabla \cdot \bar{u} &= 0 \quad \text{in } \Omega \times (0, T) \end{aligned} \quad (4.47)$$

4.4.2 Subgrid-scale modeling

To model the effect of the small eddies and retain their contributions, two subgrid-scale models can be used: static and dynamic. The first, static, is known as the Smagorinsky model (1963) [35], and has been widely used for physically and geometrically complex flows of engineering relevance like, e.g. in combustion chambers. It is based on the equilibrium hypothesis which implies that the small scales dissipate entirely and instantaneously all the energy they receive from the large scales. Therefore, it assumes that the SGS Reynolds stresses in equation (4.47), $\tau := \overline{u' \otimes u'}$, are proportional to the rate of strain tensor $S(\bar{u})$

$$\tau^s := \overline{u' \otimes u'} = -2\mu_s S(\bar{u}) \quad (4.48)$$

with μ_s , the SGS eddy-viscosity given by:

$$\mu_s = (C_s \bar{\Delta})^2 |S| \quad (4.49)$$

The magnitude of the strain-rate tensor is defined as

$$|S| = (2S(\bar{u}) : S(\bar{u}))^{1/2} \quad \text{where} \quad S(\bar{u}) = \frac{\nabla \bar{u} + \nabla \bar{u}^T}{2} \quad (4.50)$$

The length scale Δ is related to the grid size and is often taken as the cubic root of the cell volumes, or chosen to be the averaged grid size, i.e., $\Delta = (\Delta x \Delta y \Delta z)^{1/3}$. Another possible definition already employed in LES with unstructured grids [66], and adopted in this work, is $\Delta = (Vol(K))^{1/3}$ in which $Vol(K)$ is the volume of the each element K of the corresponding mesh.

The Smagorinsky constant C_S needs to be specified prior to a simulation depending on the type of flow, the filter being used and the numerical method employed. For example, the theoretical value found by Lilly [67] is equal to 0.18 whereas Deardroff in [68] uses a smaller value $C_S = 0.1$ for a plan channel flow. As one can see, the Smagorinsky model is usually used due to its simplicity and very easy to implement, however it has two major drawbacks:

- 1- it introduces too much diffusion in particular in laminar regions and near walls
- 2- the parameter C_S is not optimally defined

In order to reduce the turbulent viscosity near walls and to account for the anisotropy of the turbulence, the Smagorinsky model is modified using the van Driest damping function [69]:

$$\mu_t = (C_S \bar{\Delta} f_\mu)^2 |S| \quad \text{where} \quad f_\mu = 1 - e^{-y^+/25} \quad (4.51)$$

with y^+ represents the dimensionless wall distance. As for the coefficient C_S , Germano (1991) in [2] and Lilly (1992) in [70] have introduced and developed the dynamic subgrid-scale model. They replaced the constant coefficient by a parameter $C_S(x,t)$ which evolves dynamically in space and time. To accomplish this, additional information is needed and must be captured, such as the unresolved stresses. This can be obtained using a second filtering operation known as *test filter*. The characteristic width of the test filter, $\tilde{\Delta}$, is assumed to be larger than the grid filter width Δ (usually $\tilde{\Delta} = 2\Delta$). By applying the test filter ($\tilde{\cdot}$) to the filtered governing equations of LES leads to the so-called subtest-scale stresses

$$\tau_{ij}^{ST} = \widetilde{u_i u_j} - \tilde{u}_i \tilde{u}_j \quad (4.52)$$

The Germano identity relates the subtest-scale stresses to the SGS stresses (Eq. 4.48) via

$$L_{ij} = \tau_{ij}^{ST} - \tilde{\tau}_{ij}^S \quad (4.53)$$

where L_{ij} denotes the Leonard stresses associated with the test filter.

It represents the contribution to the Reynolds stresses by scales whose length is intermediate between the filter width Δ and the test filter width $\tilde{\Delta}$. If we express the subtest-scale and the SGS stresses using the eddy-viscosity approach as in Eq. (4.48) together with Eq. (4.49), we obtain

$$\begin{aligned}\tau_{ij}^{ST} &= -2C_{ST} \tilde{\Delta}^2 \left| \tilde{S} \right| \tilde{S}_{ij} = C_{ST} \alpha_{ij} \\ \tilde{\tau}_{ij}^S &= \left[-2C_S \bar{\Delta}^2 \left| \bar{S} \right| \bar{S}_{ij} \right]^\sim = \left[C_S \beta_{ij} \right]^\sim\end{aligned}\quad (4.54)$$

where $[]^\sim$ means that the whole term enclosed in the brackets is test-filtered. Since the coefficient of the test filter cannot be resolved explicitly, Germano *et al.* (1991) [2] assumed that $C_{ST} \approx C_S$ and $\left[C_S \beta_{ij} \right]^\sim = C_S \tilde{\beta}_{ij}$. Replacing (4.52) into (4.53) together with the previous assumption, we get

$$L_{ij} - \frac{\delta_{ij}}{3} L_{kk} = -2C_S(x,t) M_{ij} \quad \text{where } M_{ij} = \alpha_{ij} - \beta_{ij} \quad (4.55)$$

Using the least-squares minimization proposed by Lilly [67], we obtain finally

$$C_S(x,t) = \frac{1}{2} \frac{\langle L_{ij} M_{ij} \rangle}{\langle M_{ij} M_{ij} \rangle} \quad (4.56)$$

Here $\langle \rangle$ denotes an ensemble-averaged in the homogeneous direction. This final averaging procedure proposed by Lilly reduces the large fluctuations of the C_S and produces stable results. For more details and other improved dynamic SGS models can be found in [63, 66, 34].

4.5 Benchmarks for the k-epsilon model

In this section, numerical calculations are performed for three applications: decay of grid turbulence, flow over a flat plate (Comte-Bellot) and flow over a backward facing step (BFS). These numerical tests, taken from [5], are considered important for validating the methodology and assessing the computational performance of the k - ϵ model. Additionally to that, computations using the low-Reynolds and two-scale velocity are given. Comparisons with experimental data and other numerical predictions are presented.

4.5.1 Validation: grid turbulence

In this example, already presented by [61] and validated in [5], we consider the decay of grid turbulence in a uniform flow. The objective of this test is to check the formulation and implementation of the coupled k - ϵ transport equations by comparing to the exact solution. The availability of the analytical solution provides a rigorous framework for assessment of solution accuracy.

By taking extremely low value of the viscosity from one hand and constant velocity from the other, the diffusion terms become negligible and the analytical solution of the coupled problem takes the following form:

$$\begin{cases} k(x) = k_0 \left[1 + \frac{\epsilon_0}{k_0} (C_{\epsilon_2} - 1)x \right]^{\frac{1}{1-C_{\epsilon_2}}} \\ \epsilon(x) = \epsilon_0 \left[1 + \frac{\epsilon_0}{k_0} (C_{\epsilon_2} - 1)x \right]^{\frac{C_{\epsilon_2}}{1-C_{\epsilon_2}}} \end{cases} \quad (4.57)$$

with $U_0 = 10 \text{ m/s}$, $k_0 = 5 \text{ m}^2/\text{s}^2$ and $\epsilon_0 = 10 \text{ m}^2/\text{s}^3$

The computational domain extends from $(0,0)$ to $(10,1)$. Dirichlet boundary conditions are applied at the inlet, while zero Neumann conditions are applied everywhere else. Figure 6 shows the geometry of the flat plate and the corresponding boundary conditions.

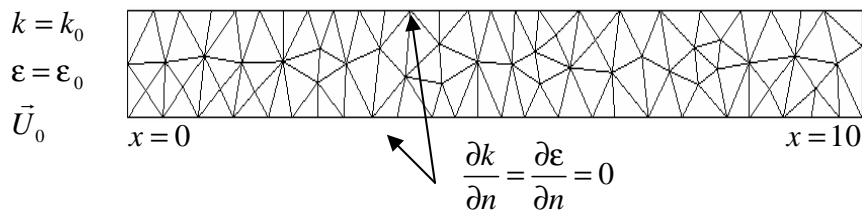


Figure 6. Geometry and boundary condition of the problem

Figure 7 shows the distribution of the turbulent kinetic energy and the turbulence dissipation along the x -axis. The numerical solutions are indistinguishable from the analytical solutions. This confirms the accuracy of predictions and ability of the code to deliver the right solution of this coupled problem.

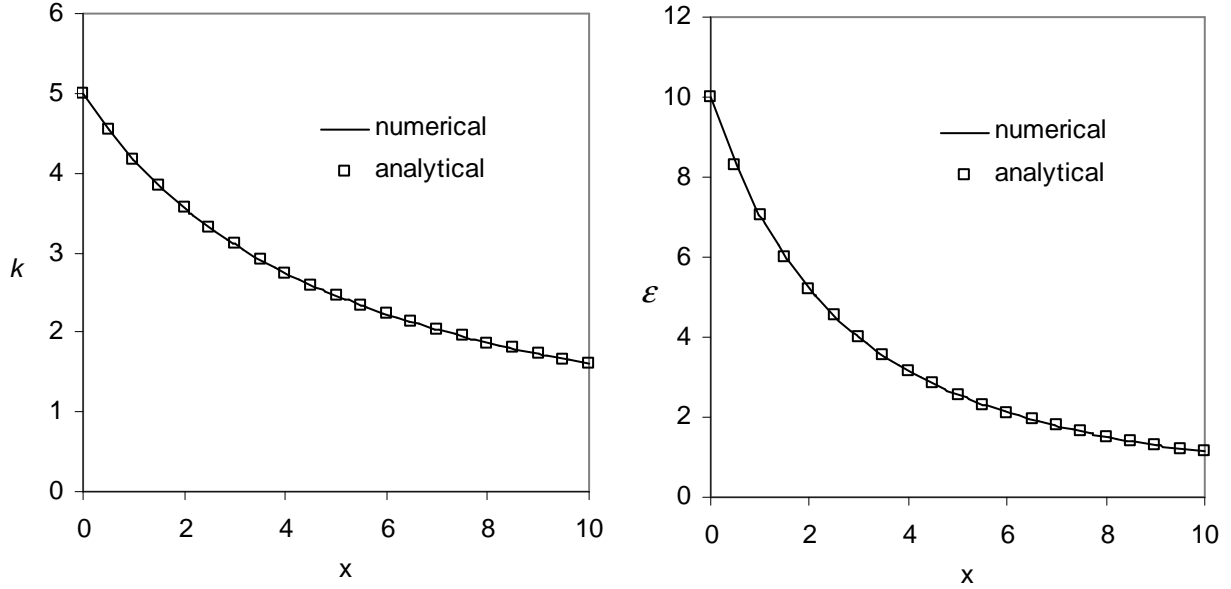


Figure 7. Grid turbulence solution along the x -axis

4.5.2 Comte-Bellot

The verified code is now applied to turbulent flow on a 2D duct. This test has played a central role in benchmarking the performance of the k - ϵ turbulence model. This flow has been experimentally studied by Comte-Bellot [22]. The different experimental parameters used in the simulation are taken from [5] and are given below:

- the half-width of the duct: $H=0.09m$;
- the velocity at the centre of the canal: $U_0=10.5 m/s$;
- the kinetic laminar viscosity (air) : $\nu=1.5 \cdot 10^{-5} m^2/s$;
- the density: $\rho=1.208 kg/m^3$;
- the obtained Reynolds number: $Re = 57000$
- time step: $\Delta t = 0.001s$

Since the solution of this problem is symmetric, we consider only half of the duct as shown in figure 8. Dirichlet boundary conditions for the turbulent variables are then applied at the inlet and computed using the given parabolic velocity U_{inlet} and the height H of the canal. Using Eq. (4.11) and (4.12) we obtain:

$$U_{inlet}(y) = U_0 - 3(U_0 - U_{moy}) \left(\frac{y}{H - \delta} \right)^2, \quad k_0 = 1.805 m^2 / s^2 \quad \text{and} \quad \epsilon_0 = 242.5 m^2 / s^3 \quad (4.58)$$

where $\delta=0.004m$ is the normal distance between the computational boundary and the wall and U_{avg} is the average velocity equal to $9.5 m/s$ (see [5] for more details).

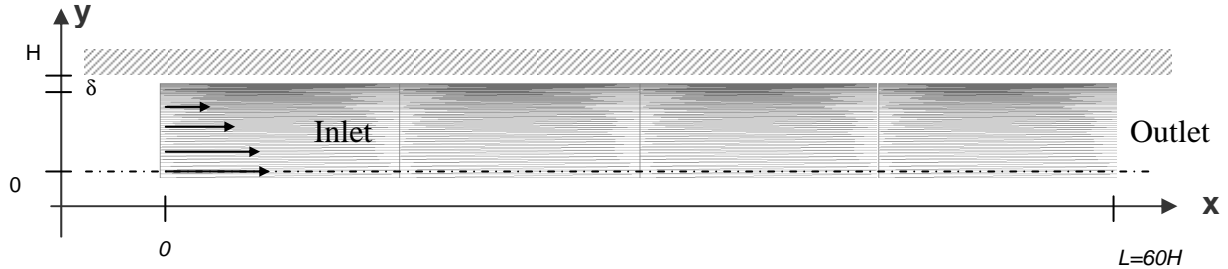


Figure 8. Problem set up of the Comte-Bellot 2D duct

The mesh, a rectangle of $H \times 60H$, is highly stretched near the wall and smoothly varying towards the centre. The minimum length along the y -direction for the coarse mesh and for the fine mesh is $3.64 \cdot 10^{-3}$ and $1.8 \cdot 10^{-3}$ respectively. For illustration, figure 9 and 10 show two cuts of the meshes used in our computations. The distance from the wall boundary to the nearest interior point corresponds to $y^+ \approx 100$.

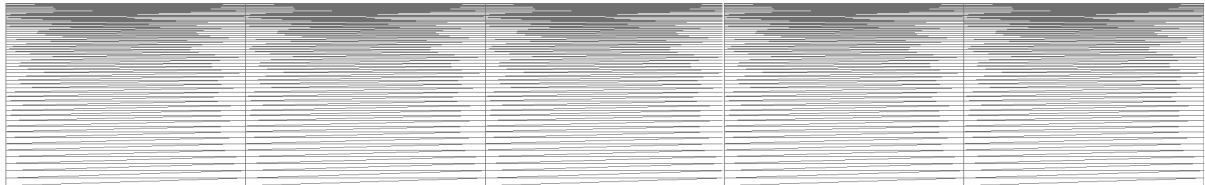


Figure 9. Coarse mesh of the half duct (3000 nodes)

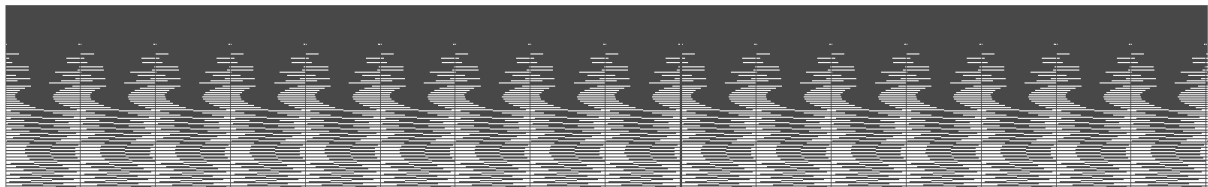


Figure 10. Fine mesh of the half duct (13000 nodes)

The goal of this example is to check the implementation of the code and at the same time to evaluate the performance of the standard $k-\varepsilon$ model with two different kinds of near-wall treatment: wall function implemented as Neumann (two-scale velocity model) vs. Dirichlet (one-scale velocity model) boundary conditions. Therefore, two numerical simulations were made to assess the influence of the mentioned boundary conditions. In the first section, results computed using the two-scale velocity approach are presented. Contours of the turbulent kinetic energy and the rate-of-dissipation energy are shown in figure 11 and 12. The velocity and the pressure profiles are displayed in the figure 13 and 14 respectively. The results are in complete agreement with the given reference [5].

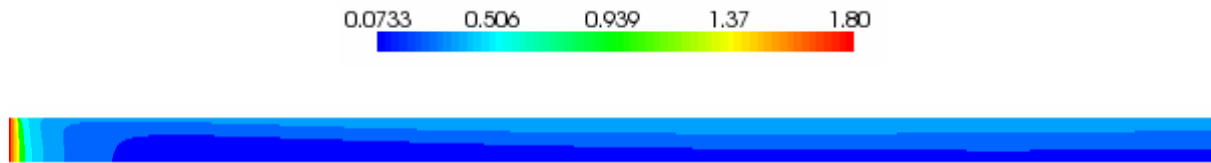


Figure 11. Variation of the turbulent kinetic energy

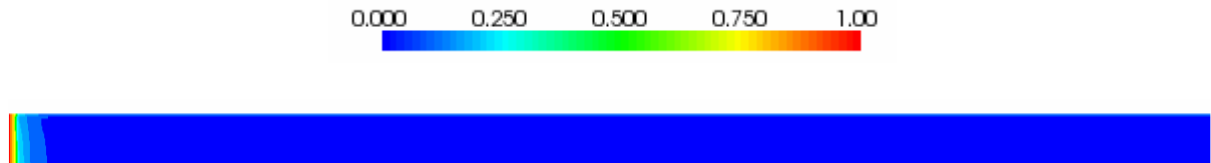


Figure 12. Variation of the rate-of-dissipation energy

In figure 15, we plot at the outlet-section the results for turbulence kinetic energy k , the rate-of-dissipation energy ε and the velocity U_x using the two-scale velocity model. The k -profile and ε -profile compares well with that obtained by experimental measurement in the near and far-wall regions. One can observe excellent agreement as well for the velocity profile. For more comparisons, we choose [5] as an additional reference solution. We can clearly see from figure 15 (left column) that all obtained profiles are in complete accordance.

Similar trends were observed using the standard k - ε model in the far-wall regions while different predictions occur in the near-wall regions. As shown in figure 16 the standard model gives a wrong behavior of the solution in the near-wall region. The reason for this behavior was pointed out in previous section and it is due to the use of Dirichlet boundary condition. Whereas using the two-scale velocity model which modifies the asymptotic behavior of the different variables near the solid wall and applies Neumann boundary conditions for the kinetic energy gives more appropriate results.

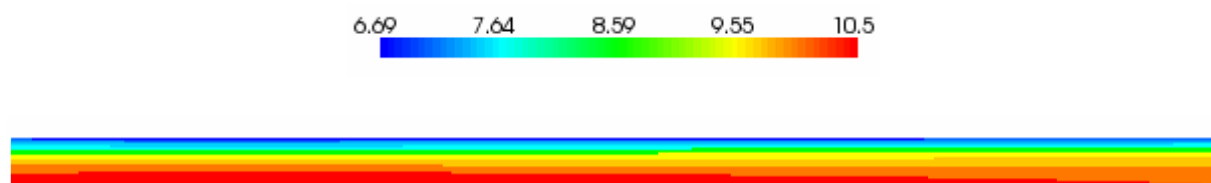


Figure 13. Variation of the velocity U_x



Figure 14. Variation of the pressure

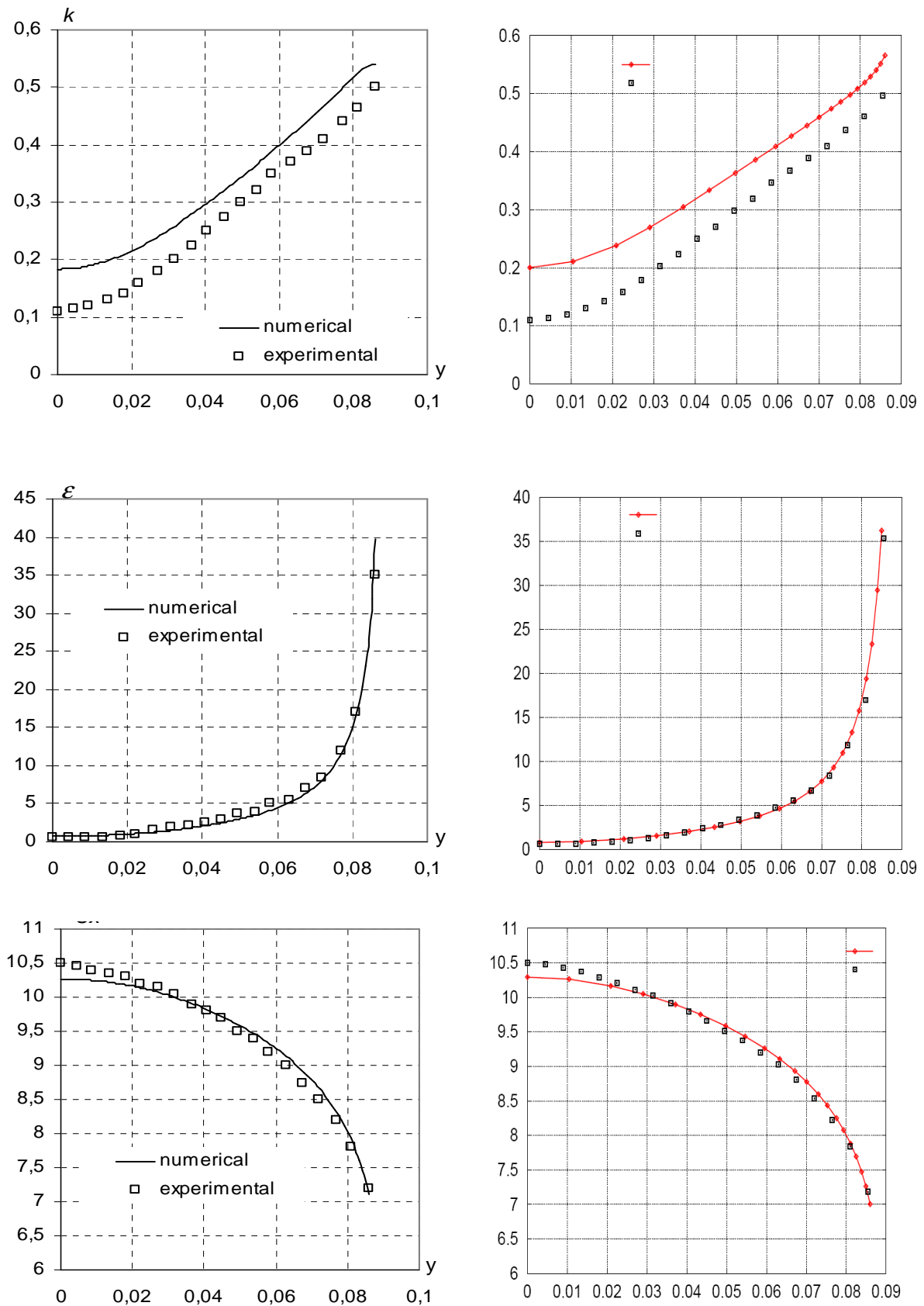


Figure 15. Solution profiles along the outlet-section: two-scale velocity model (left) reference solution [5] (right)

The differences between solutions computed using wall functions implemented in the strong and weak sense were also observed by [43]. The authors have pointed out that the use of Dirichlet boundary conditions for k and ϵ produced rather disappointing results, whereas the performance of Neumann boundary conditions is remarkably efficient for the near-wall treatment. Numerical results for the fine mesh are compared as well with the experimental data in figure 17. As can be seen, the agreements are good with a slight significant improvement in the results.

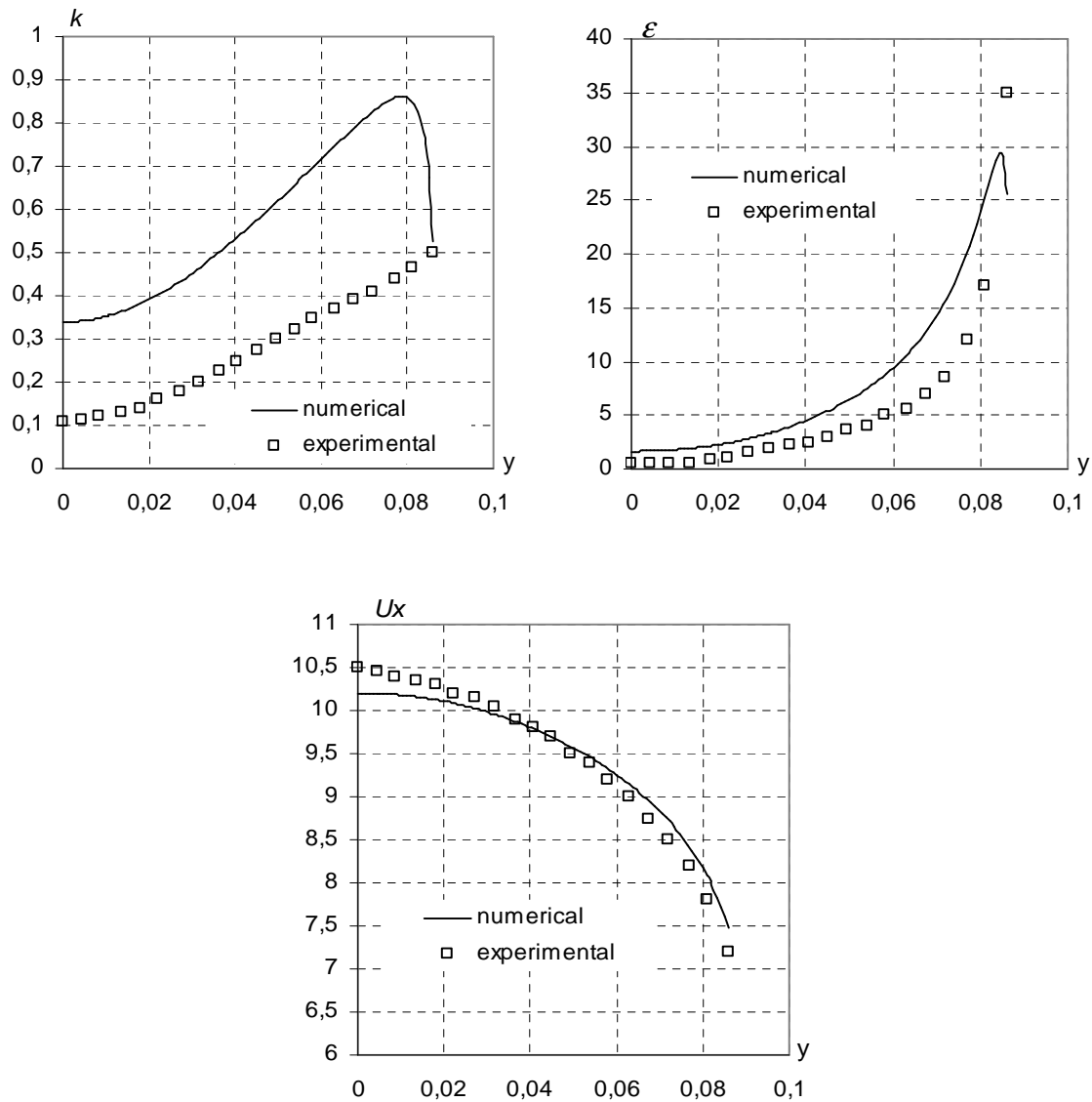


Figure 16. Solution profiles along the outlet-section using one-scale velocity model

We conclude from this example that the choice of a correct boundary condition for the turbulent variables is crucial. We have observed that the two-scale velocity model is superior to the standard model. By introducing the bulk velocity based on the turbulent kinetic energy and by letting k to be computed ‘naturally’ at the boundary of the computational domain, we improved the prediction of the turbulent quantities in the near wall regions and we obtained the correct behavior for all the profiles.

In the next section we present the last benchmark, the backward facing step. Computations in 2D and 3D are used to compare the performance of the turbulence model with the experimental measurement and to investigate the influence of the near-wall treatment.

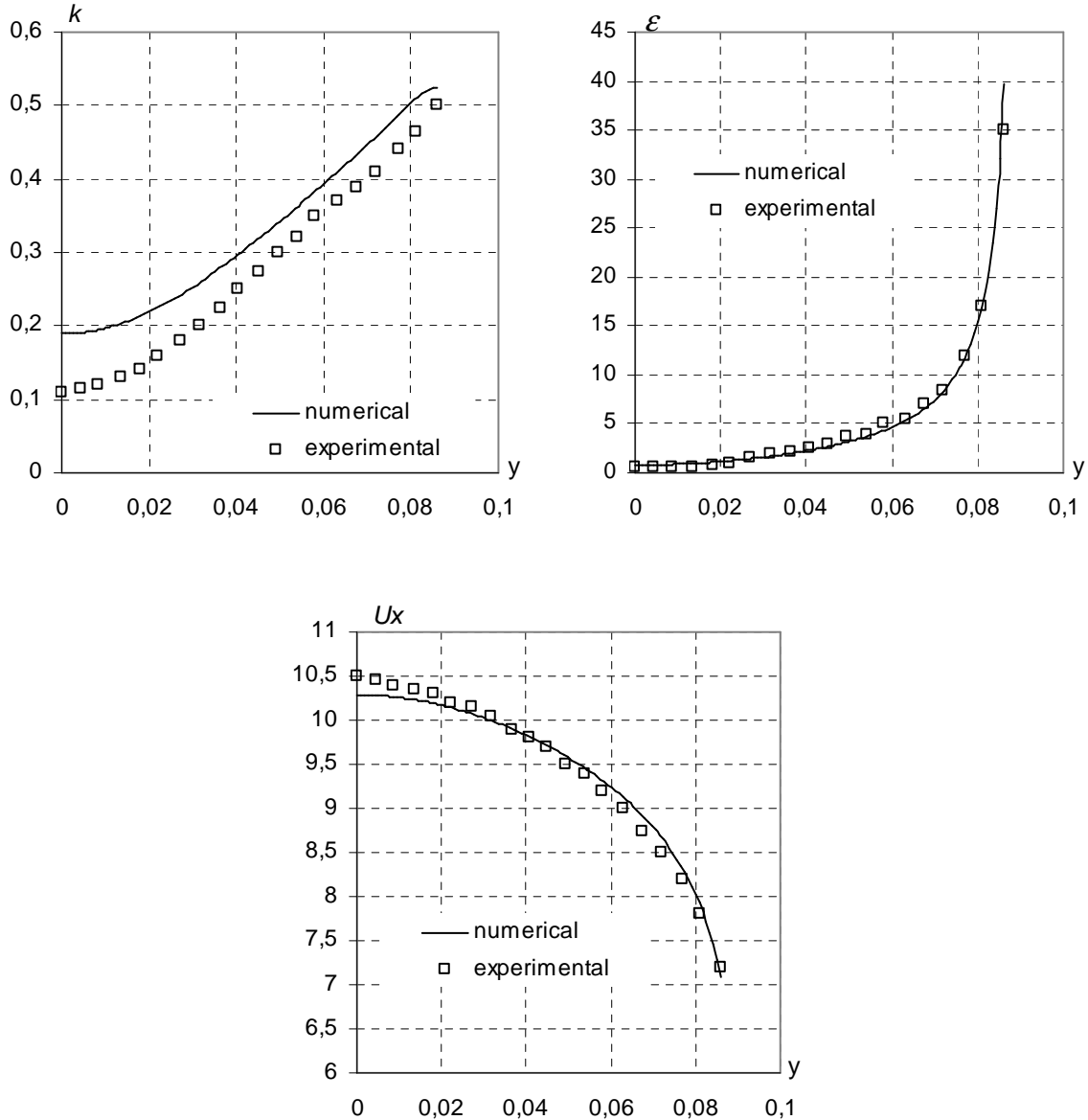


Figure 17. Solution profiles along the outlet-section using two-scale velocity model (fine mesh)

4.5.3 Flow over a backward-facing step

The flow of greatest interest in this thesis is the backward facing step flow. This problem has been the subject of a detailed experimental study by [3] and has served for many years as a benchmark for turbulent flow solvers. Figure 18 is a schematic diagram of channel flow over a backward-facing step.

The fully turbulent flow comes from the upstream of the step, forming thin boundary layer along the wall. When the channel suddenly expands at the step, the pressure gradients cause the new mixing layer to curve toward the wall and bifurcate at the reattachment point. One branch develops as a new boundary layer after the reattachment point and the other branch forms the recirculation region. Therefore, the flow undergoes rapid distortion in the region surrounding the reattachment point and subsequently relaxes downstream at this point.

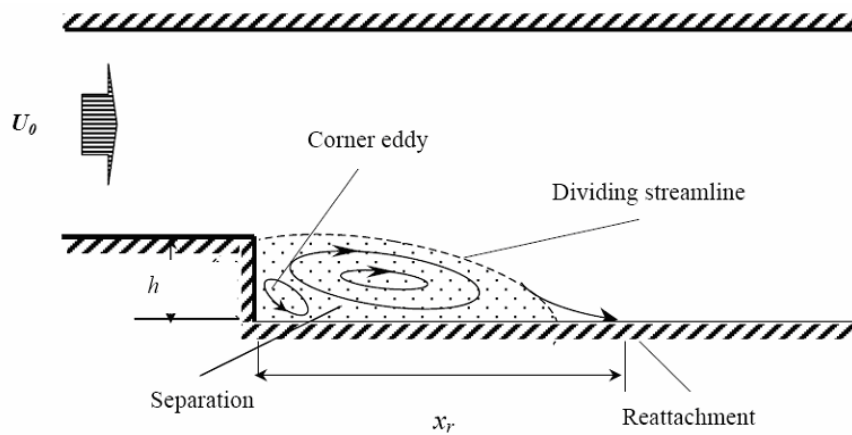


Figure 18. Schematic description of the turbulent flow over a backward-facing step (adapted from [36])

A critical parameter to assess the accuracy of the employed method is the reattachment length. Table I presents different values of the predicted length. Every author uses a variant of the $k-\epsilon$ model with wall functions and type of algorithm. The only possible causes for the differences observed between authors are the meshes used and details of the code implementation. Note that in [71, 72] the authors have proposed an adaptive finite element method for this benchmark.

Reference	Turbulence model	Recirculation length (L/H)
Kim <i>et al.</i>	experiment	7 ± 1
Mansour and Morel	$k-\epsilon$	5.2
Pollard	$k-\epsilon$	5.88
Rodi <i>et al.</i>	$k-\epsilon$	5.8
Launder <i>et al.</i>	ASM	6.9
Donaldson <i>et al.</i>	RSM	6.1
Ilegbusi and Spalding	modified $k-\epsilon$	7.2
Nallasamy and Chen	$k-\epsilon$	5.8
Ilinca <i>et al.</i>	$k-\epsilon$	6.2
Reference [5]	$k-\epsilon$	6

Table I. Recirculation length obtained using different methods adopted from [74]

The different experimental parameters used in the simulation are taken from [5] and are given below:

- the step height: $H=5.08\text{ cm}$;
- the velocity at the centre of the canal: $U_0=11.562\text{ m/s}$;
- the kinetic laminar viscosity (air) : $\nu=1.4\cdot 10^{-5}\text{ m}^2/\text{s}$;
- the density: $\rho=1.208\text{ kg/m}^3$;
- the obtained Reynolds number: $Re = 42000$
- time step: $\Delta t = 0.0002\text{ s}$

The inlet Dirichlet boundary conditions (at $x = -5H$) for the turbulent variables are given below and used as initial value:

$$k_0 = 0.78\text{ m}^2/\text{s}^2 \text{ and } \varepsilon_0 = 80.6\text{ m}^2/\text{s}^3 \quad (4.59)$$

The distance from the wall boundary to the nearest interior point corresponds to $y^+ \approx 100$. The geometry, the dimensions and the boundary conditions are shown in figure 19. At the outlet, the normal stress, the normal derivatives of k and ε and the velocity U_y are all set to zero. Wall functions were used on the boundary except for the inlet and the outlet. The 2D computational mesh consisted of approximately 12000 nodes. Local mesh refinement was employed in the vicinity of the walls and in the shear layer behind the step.

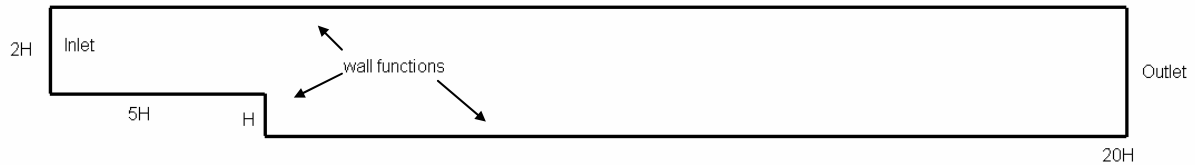
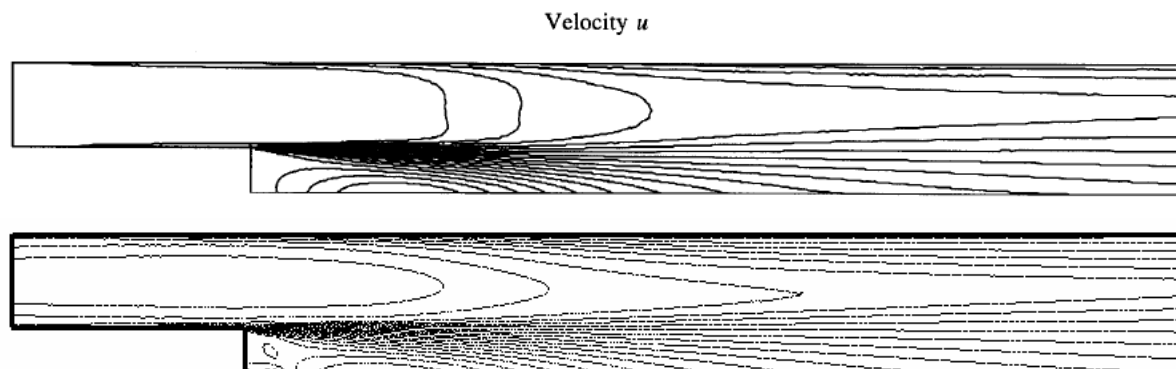


Figure 19. Computational domain for the backward-facing step [3]

The main objective is to evaluate the performance of the implemented method with three different kinds of near-wall treatment: wall functions implemented as Dirichlet and Neumann boundary conditions against the Low-Reynolds number model.

A first visual comparison of the steady-state solutions for all the turbulent variables and the averaged velocity is presented. We compare both solutions using the standard k - ε model. Contours of all variables are plotted in figure 20. Recall, that we choose the adaptive finite element method of [72] as reference due to the high accuracy of the results. A good agreement with the reference solution is shown for all the variables. However, as expected, we noticed a slight difference in particularly near the corner of the step where all variables exhibit strong variations and the bottom wall. The difference is due to the adaptive remeshing procedure (see [72]).



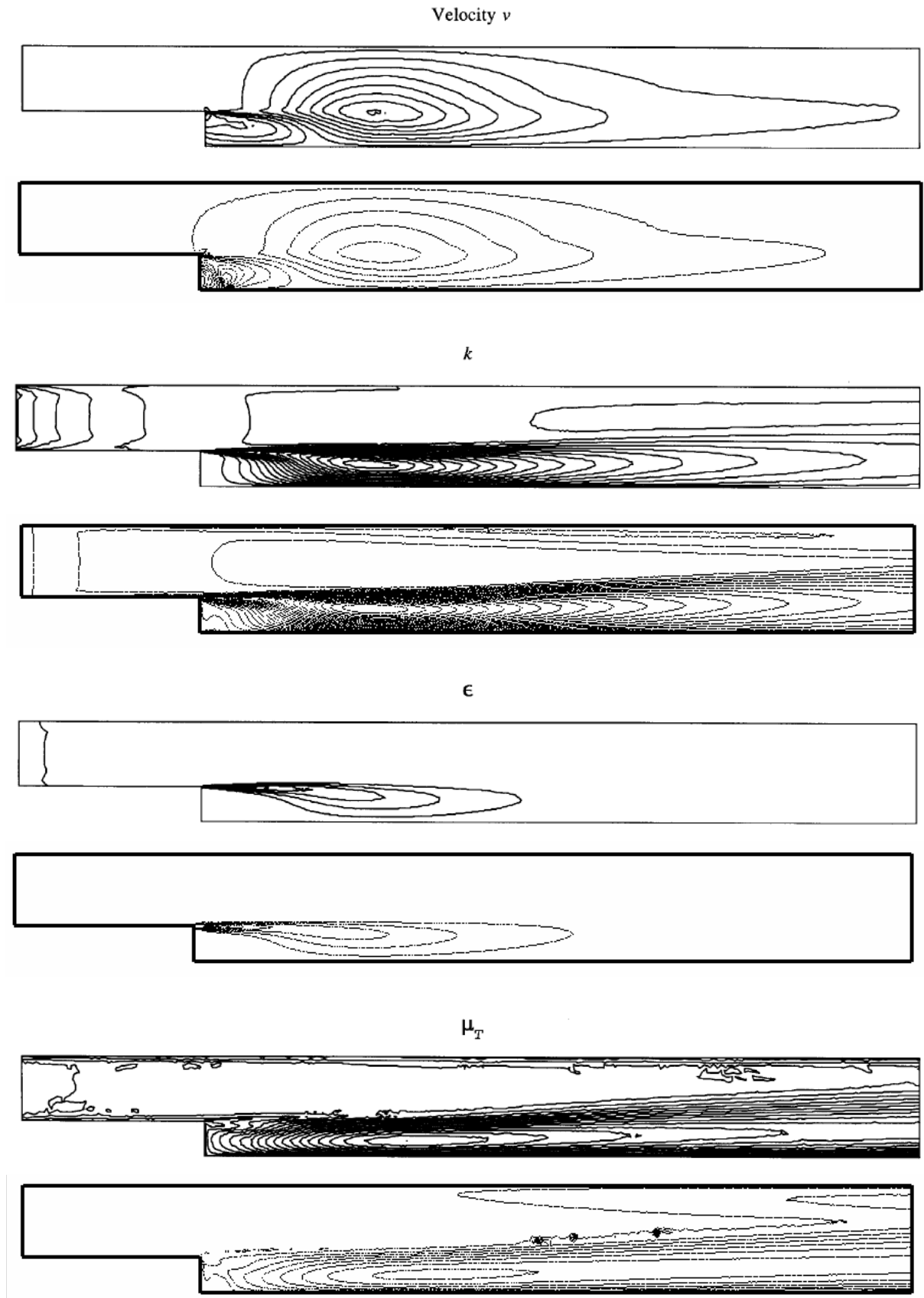


Figure 20. Steady state distribution: reference solution (top), standard $k-\epsilon$ solution (bottom)

An important evaluation criterion for this popular test problem is the recirculation length defined as $L = x / H$. Kim *et al.* (1980) [3] have experimentally determined the location of the reattachment point equal to $7H \pm H$. Different researchers obtained numerical values ranging from $4.8H$ to $7.0H$. Table II summarizes the results obtained for the length of the recirculation zone using different methods.

Reference	Turbulence model	Recirculation length
Kim <i>et al.</i>	experiment	7 ± 1
Mesh 1 (2D)	Standard model	5.9
Mesh 1 (2D)	Enhanced model	6.18
Mesh 1 (2D)	Low-Reynolds number model	5.79
Mesh 2 (3D- 21000 nodes)	Standard model	6.13
Reference [5]	Standard model	6

Table II. Recirculation length obtained using different methods

Results obtained by our calculation (Table II) compared well with the results obtained by different other authors (Table I). Figure 21 presents comparison of predicted and measured turbulence kinetic energy. As can be seen, the agreement is generally good for all stations. It should be noted that [72] provides results using an adaptive strategy that captured well the very thin layer and peak in the TKE profile in particularly at $x/H = 1.0$ and $x/H = 2.3$. However, far from the step and close to the upper wall, our predictions agree more with the experiments. We suspect that the main discrepancy could be due to the use of Neumann boundary conditions for the kinetic energy. By letting k to be computed ‘naturally’ at the boundary we improved the prediction of the turbulent quantities in the near wall regions and we obtained the correct behavior.

In the context of testing the implementation of two turbulent solvers using two different codes at the CEMEF, a three-dimensional test problem was done stimulatingly by [73] using the finite element code TherCast and the present implement method using the finite element library CIMLIB. The 3D computational mesh of the backward-facing step consisted of 71162 tetrahedral elements with 21514 nodes. Local mesh refinement was employed in the vicinity of the walls and in the shear layer behind the step. Further details about this test can be found in [73]. In Figure 22, the calculated velocity profiles for 6 different distances from the step are compared to one another and the experimental data from [3], and other numerical codes (such as THERCAST, Jaeger...).

The objective of this comparative study was to check the implementation of both the codes, the linearization of the coupled turbulent equations, the positivity of the solutions and the accuracy of the results. Figure 22 indicates that all the results all almost identical with one another and with the experimental measurements. The test has provided us a useful validation study for the implementation of the codes and the near-wall treatment methods. Finally, it is also worth mentioning that the profiles of k and ϵ do not suffer from spurious undershoots which are frequently observed in other computations. This can be attributed to the stabilization finite element discretization together with the positivity-preserving techniques mentioned in previous sections.

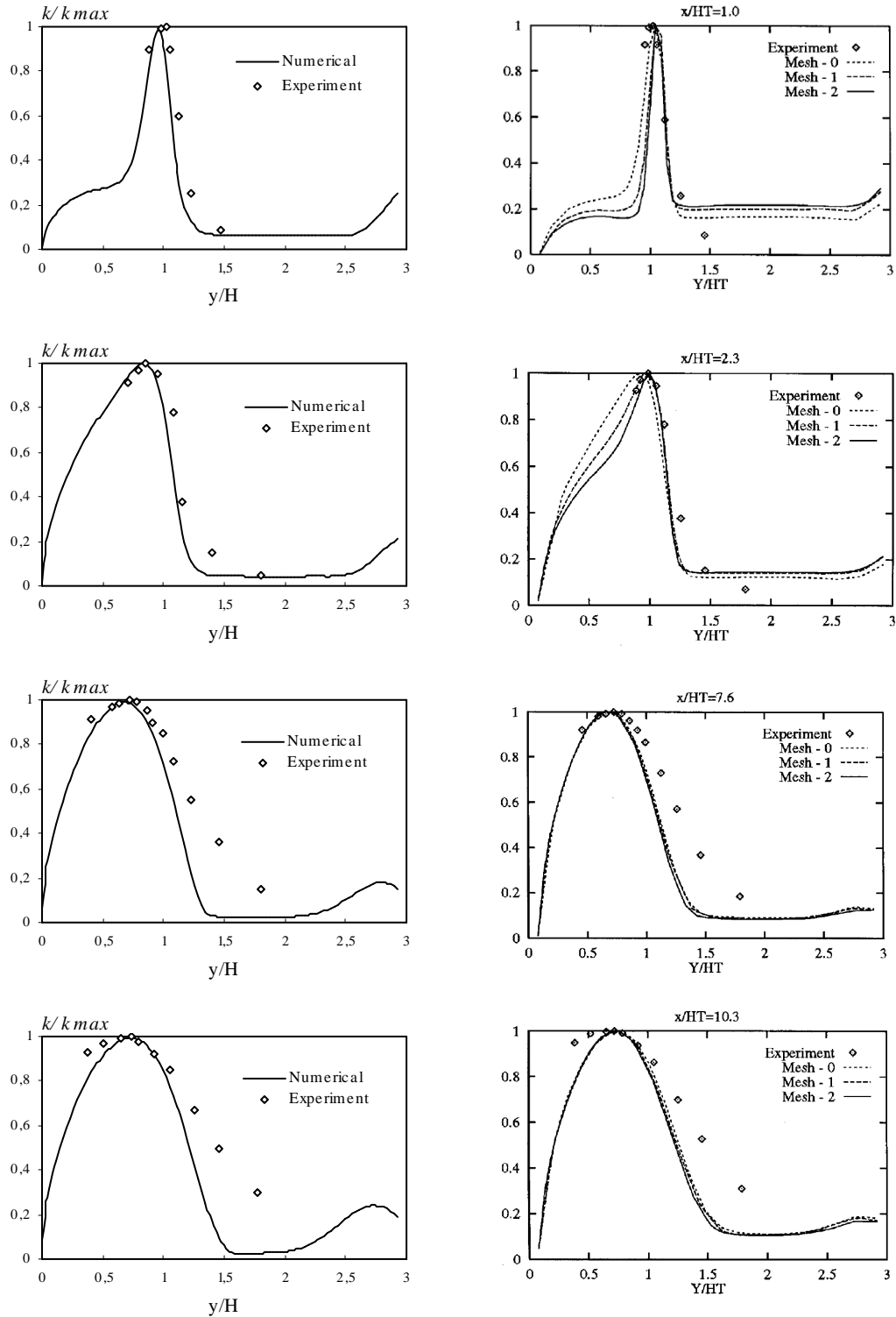


Figure 21. Distribution of turbulence kinetic energy: two-scale velocity (left) adaptive finite element method [72] (right)

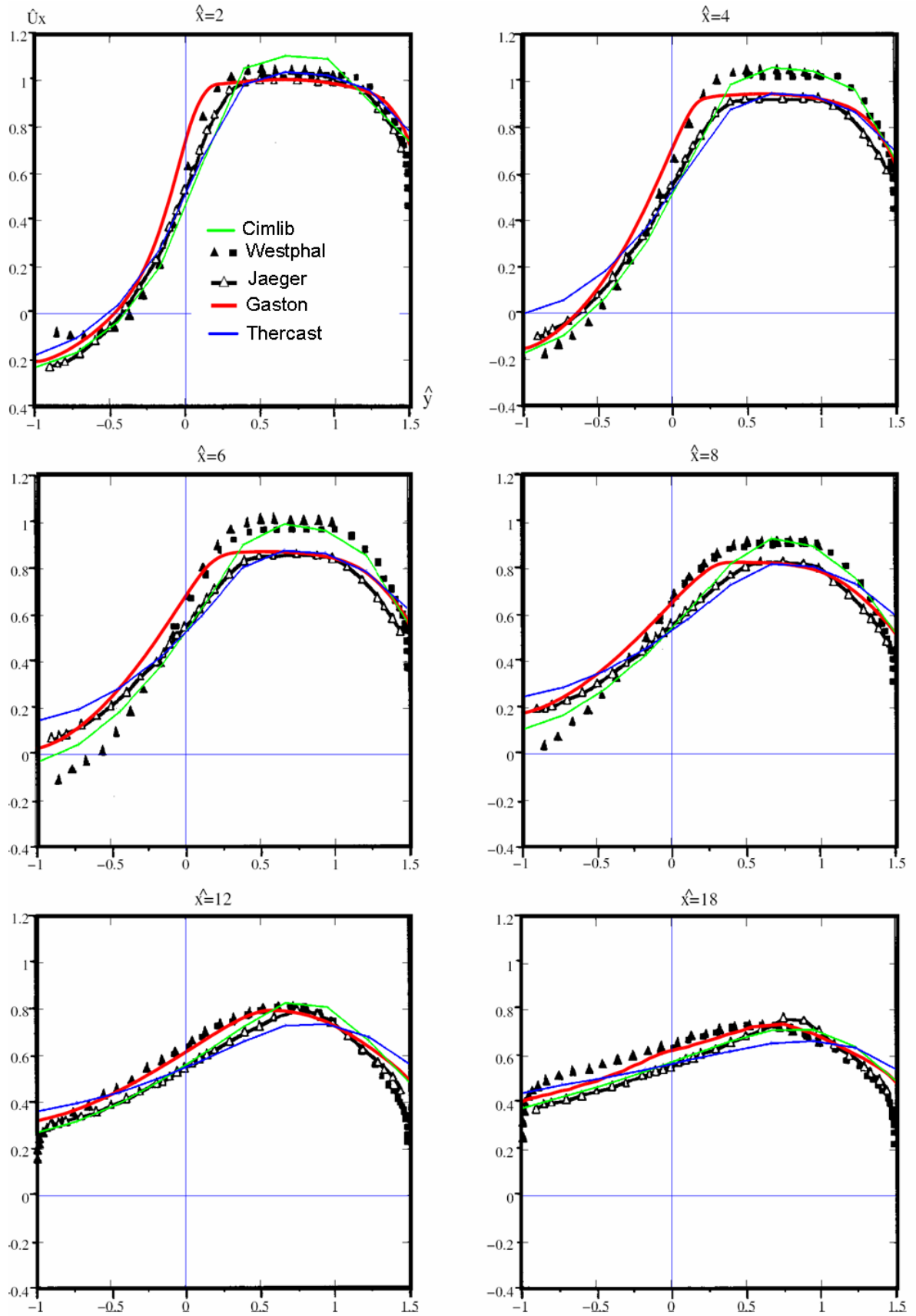


Figure 22. Measured and predicted streamwise velocity profiles at 6 different locations

4.6 Flow behind an obstacle using LES model

In this example, a turbulent unsteady flow past a square cylinder is analyzed to verify the proposed LES (Smagorinsky) model. The main focus of this numerical example is from one hand to offer a large diversity of numerical benchmarks and from the other hand it can be seen as an illustration of a flow past a heated ingot inside industrial furnaces. Recall that the objective is to validate the implementation of the code rather than comparing two different turbulent models. As mentioned in the introduction of the chapter, the idea was to open the choice to the user to decide which methods to use regarding the application in hand. Each method will offer the accuracy of the results in respect to the computational costs and the required computing time.

Here, even for relatively simple geometries, simulating such flows and the loading imposed on the bodies is a difficult task. Over the years, it has become clear in these calculations that statistical turbulence models have difficulties with such complex flows consequently, the large eddy simulation approach is more suitable in such situations as it resolves the large-scale unsteady motions and requires modeling only of the small-scale. Of course, the LES approach is computationally considerably more expensive, but the recent advances in computer performance and numerical methods have made LES calculations feasible.

This benchmark proposed by Lyn *et al.* [75, 79] has become a standard test case for unsteady turbulent flow of vortex-shedding past a square cylinder where different experimental measurements are given. It was shown that the occurrence and quality of vortex-shedding prediction depend strongly on the turbulence model used [76, 82]. Due to the excessive production of turbulent kinetic energy, the standard k - ϵ model was found to severely unpredicted the strength of the shedding motion. Improvement were carried out using the large eddy simulation and results can be found in [76, 77]. The RANS models the turbulence and resolves only the mean-flow structures whereas the LES resolves the eddies of turbulence itself. Consequently, RANS requires less spatial and temporal resolution while LES requires very long integration time to build an ensemble averaged solution. Full details concerning this test using different turbulence models are given by [76, 82].

We hope that this previous discussion would now answer the questions from the introduction of the chapter: “*Which model we should use?*” and “*How can we get reasonable results with an affordable computing cost?*”.

The mesh layout for this example as well as the boundary conditions is illustrated in figure 23. The dimensions shown in the figure are normalized by the length of the side of the square. The computational domain is discretized by 172264 elements and 32476 nodes. The inflow velocity is given equal to one and the Reynolds number is set to 22,000. Physical dimensions of our computations domain exactly matched to those of [78]. We choose the time step of 0.005, which is found to be sufficient to track unsteady characteristics of the flow. This paper among few, presents a stable finite element formulation to predict the behavior of high-speed wind passing bluff structures using the k-epsilon model.

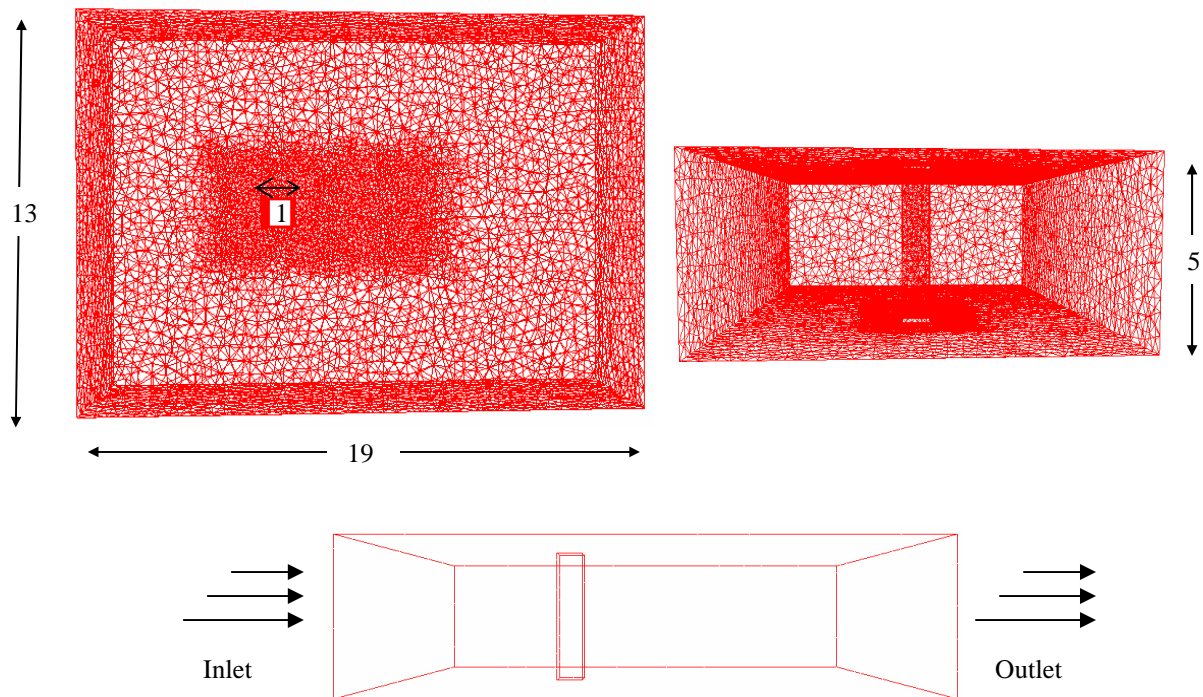


Figure 23. Computational domain for the flow past a square cylinder

For visualization and identification of instantaneous vortical structures, figure 24 shows instantaneous vortices distribution around the square cylinder predicted by the LES model at two different phases. Note that the more the grid system becomes finer, the more realistic structures with smaller scale structures can be captured.

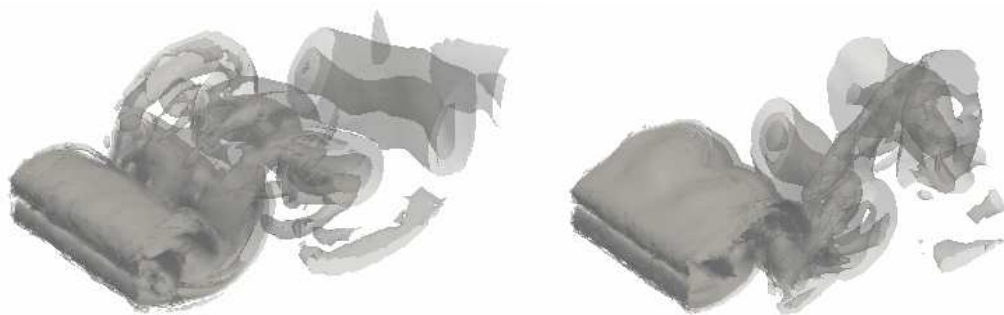


Figure 24. Instantaneous vorticity distribution past the square cylinder

Table III summarizes the dimensionless shedding frequency, the Strouhal number; $St=fD/U_0$ (f is the frequency, D is the section of the obstacle and U_0 is the given velocity), obtained in the present study and by different authors. This non-dimensional number can be considered important to quantify the properties of the periodic solution of the vortex street.

Reference	S_t Strouhal number
Present study	0.129
Exp. Lyn [79]	0.135
Exp. Duaro [80]	0.139
LES [81]	0.132
Standard k- ϵ [82]	0.124

Table III. Strouhal number obtained using different methods

As shown in table III, the Strouhal number is computed as 0.129, which is lower only by 5 percent compared to Lyn's experimental results [79]. Figure 25 displays the distribution of the time-mean velocity U along the centerline. Experimental data and results from different other authors are included. The authors in their study have used the RNG k - ϵ model (Figure 25 bottom). They have noticed that the data agree fairly well in the near-cylinder region and in front of the cylinder where the flow is basically inviscid while there are large differences in the wake region. Nevertheless, overall trends seem to be quite similar to the experimental results as well as results from others authors. An efficient and reliable numerical procedure for solving wind engineering problem in high Reynolds number flow regimes as well as many other comparisons on this test can be found in this reference.

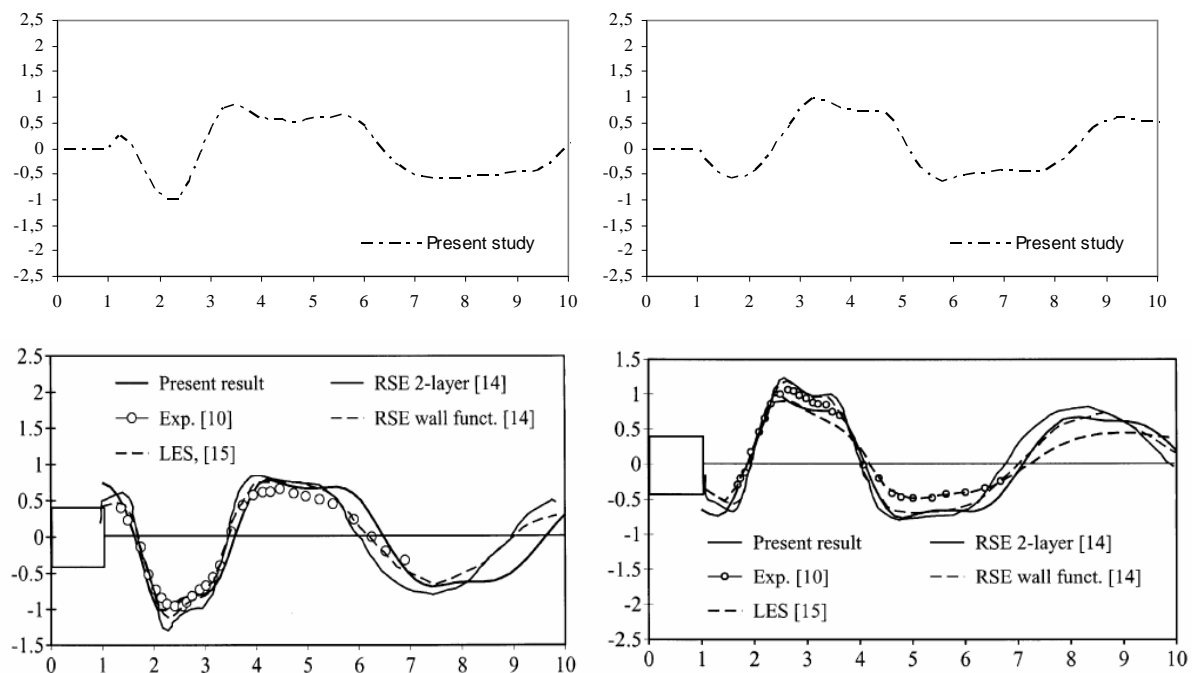


Figure 25. Lateral velocity along the centerline at two phases: Present result (up) and reference (bottom). The picture were adapted from [78]

4.7 Conclusion

In this chapter we have described two classical turbulence models to deal with unsteady flow at high Reynolds number. The motivation of using such models comes from the desire of solving turbulent flow problems inside industrial furnaces. Therefore, both the k -epsilon model and the Large Eddy Simulation model (LES) were introduced, analyzed and studied. The stabilized finite element methods was used and applied for the resolution of the set of equations. We can understand from the numerical experiments that a turbulence model should introduce the minimum amount of complexity while capturing the essence of the relevant physics. Consequently, the k - ϵ model, a traditional model attempts to strike the balance in this regard by sacrificing the details of the turbulence structures. It is still the most widely used turbulence modeling method in practical engineering applications. Whereas as opposed to the RANS approach, a major portion of the turbulent scales is numerically resolved within the LES model and offers more characteristics of the flow.

The performance and the efficiency of the overall models have been demonstrated using four benchmarks and conclusions were drawn. The flow around a square cylinder at a Reynolds number of 22000 has been chosen for a last validation of the Smagorinsky model. Although the given benchmarks do not contain all the complexity of simulating an industrial furnace, they are well suited for validation since both experimental data and numerical results from several authors are available. Summarizing, the originality of this work is the combination of stabilization methods, unstructured grids, implicit time advancing and turbulence models. All those elements are now features dedicated to industrial abilities of the method. Upcoming, more tests will be presented for coupled heat problem.

References

- [1] A. N. Kolmogorov, Dokl. Akad. Nauk SSSR, 30, 1941, pp. 229.
- [2] M. Germano, U. Pionelli, P. Moin, W. Cabot, a dynamic subgridscale eddy viscosity model, *Phys Fluids*, A3, 1991, pp. 1760-1765.
- [3] J.J. KIM, Investigation of separation and reattachment of turbulence shear layer: flow over a backward facing step, *Ph.D. Thesis, Stanford University*, 1978
- [4] B. E. Launder, D. B. Spalding, The numerical computation of turbulent flows, *Computer Methods in Applied Mechanics and Engineering*, 3, 1974, pp. 269-289.
- [5] Laurence Gaston, Simulation numérique par éléments finis bidimensionnels du remplissage de moules de fonderie et étude expérimentale sur maquette hydraulique, *Ph.D. thesis, Ecole Nationale Supérieure des Mines de Paris*, 1997.
- [6] B. E. Launder, D. B. Spalding, The numerical computation of turbulent flows, *Computer Methods in Applied Mechanics and Engineering*, 3, 1974, pp. 269-289.
- [7] H. Le, Parviz Moin, and John Kim. Direct numerical simulation of turbulent flow over a backward-facing step. *J. of Fluid Mech.*, 330:349–374, 1997
- [8] Kim, J., Moin, P. 1985 Application of fractionnal-step method to incompressible Navier Stokes equation, *J. Comp. Phys.* 59 308-323
- [9] Kim, J., Moin, P., Moser, R. 1987 Turbulence statistics in fully developed channel flow at low reynolds number, *J. Fluid Mech.* 177 133-166
- [10] Rodi, W., Mansour, N. N., and Michelassi, V., 1993 One Equation Near Wall Turbulence Modeling with the Aid of Direct Simulation Data, *ASME J. Fluids Eng.*, 115, pp. 196-205.
- [11] R.S. Rogallo. Numerical experiments in homogeneous turbulence. *NASA TM 81315*, 1981.
- [12] P.R. Spalart. Direct numerical simulation of a turbulent boundary layer up to $Re_\tau 1410$. *J. Fluid Mech.*, 187:61–98, 1988.
- [13] D.C. Wilcox. Turbulence modeling for CFD. *DCW Industries, La Canada, California*, 1993.
- [14] W.J. Feiereisen, W.C. Reynolds, and J.H. Ferziger. Numerical simulation of a compressible, homogeneous turbulent shear flow. *Rep. TF-13, Thermosci. Div., Dept. Mech. Eng., Stanford*, 1981.
- [15] Ferziger J.H. and Peric, M 1996, *Computational Methods for Fluid Dynamics*, Springer-Verlag, Berlin, Germany.

- [16] C. Bahloul, Etude numérique des phénomènes thermomécaniques pour la simulation tridimensionnelle du remplissage des moules de fonderie , *Ph.D. thesis, Ecole Nationale Supérieure des Mines de Paris*, 2000.
- [17] V. Haroutunian, M.S. Engelman and I. Hasbani, Segregated finite element algorithms for the numerical solution of large-scale incompressible problems. *Int. J. Numer. Methods Fluids* 17 (1993), pp. 323–348
- [18] V. Haroutunian and M.S. Engelman, Two-Equation Simulations of Turbulent Flows: A Commentary on Physical and Numerical Aspects, *ASME 1993 Winter Annual Meeting*, New Orleans, USA, 1993.
- [19] B.E. Launder and D.B. Spalding, *Mathematical Models of Turbulence*, Academic Press (1972).
- [20] B. Mohammadi and O. Pironneau, *Analysis of the K-Epsilon Turbulence Model*, WILEY, 1994 (Book).
- [21] B. Mohammadi and O. Pironneau, Unsteady Separated Turbulent Flows Computation with Wall-Laws and k- ϵ Model, *Computer Methods in Applied Mechanics and Engineering*, 1995.
- [22] G. Comte-Bellot, S. Corrsin, Simple Eulerian Time-Correlation of Full and Narrow-Band Velocity Signals in Grid-Generated Isotropic Turbulence, *JFM*, vol.48, pp:273-337, 1971.
- [23] S. Thangam, Analysis of Two-Equation Turbulence Models for Recirculating Flows, *ICASE report No. 91-61*, 1991.
- [24] Bruchon J, Dignonnet H, Coupez T. Using a signed distance function for the simulation of metal forming processes: Formulation of the contact condition and mesh adaptation. from a Lagrangian approach to an Eulerian approach. *International Journal for Numerical Methods in Engineering* 2008
- [25] R. N. ELIAS, M. A. D. MARTINS, A. L. G. A. COUTINHO, Simple Finite Element-Based Computation of Distance Functions in Unstructured Grids , *International Journal for Numerical Methods and Engineering*, (72):1095-1110, 2007
- [26] M. Smith, A practical method of two-equation turbulence modelling using finite elements, *Int.J. Num. Meth. Fluids*, 4, 321-336, (1984).
- [27] C. Taylor, C.E. Thomas and K. Morgan, Modelling flow over a backward-facing step using the FEM and the two-equation model of turbulence, *Int.J. Num. Meth. Fluids*, 1, 295-304, (1981).
- [28] T. Utnes, Two equation (k- ϵ) turbulence computations by the use of a finite element model, *Int.J. Num. Meth. Fluids*, 8, 965-975, (1988).
- [29] *Fluent v6.1 User's Guide*, Fluent Inc. (2003).

- [30] Houghton, E. L. & Carpenter, P. W. (2003), Aerodynamics for Engineering Students, 5th edition, *Butterworth-Heinemann*, Burlington, MA.
- [31] Hassan, Y. A. & Barsamian, H. R. 2001, New-wall modelling for complex flows using the large eddy simulation technique in curvilinear coordinates, *International Journal of Heat and Mass Transfer*, vol. 44, pp. 4009-4026.
- [32] Kim, J., Kline, S. J. & Johnston, J. P. 1978, Investigation of separation and reattachment of a turbulent shear layer: Flow over a backward-facing step, Rep. MD-37, *Thermosciences Division*, Dept. of Mech. Engng, Stanford University.
- [33] Krajnovic, S. 1998, Large-eddy simulation of the flow around a surface-mounted single cube in a channel, *Masters thesis*, Chalmers University of Technology.
- [34] Piomelli, U., Scotti, A. & Balaras E. 2001, Large-eddy simulations of turbulent flows, from desktop to supercomputer, Selected Papers and Invited Talks from the 4th International Conference on Vector and Parallel Processing, Berlin, 2001, Springer-Verlag, London, pp. 551-577.
- [35] Smagorinsky, J. 1963, General circulation experiments with the primitive equations. I. The basic experiment, *Mon. Weather Rev.*, vol. 91, pp. 99-164.
- [36] Speziale, C. G. & Ngo, T. 1988, Numerical solution of turbulent flow past a backward facing step using a nonlinear k-e model, *Int. J. Engng. Sci.*, vol. 10, pp. 1099-1112.
- [37] Thangam, S & Hur, N. 1991, A highly-resolved numerical study of turbulent separated flow past a backward-facing step, *International Journal of Engineering Science*, vol. 29, no. 5, pp. 607-615.
- [38] Chien K.-Y. (1982) Predictions of Channel and Boundary- Layer Flows with a Low-Reynolds-Number Turbulence Model., *AIAA J.* 20, pp.33-38.
- [39] Codina R. and Soto O. (1999) Finite Element Implementation of Two-Equation and Algebraic Stress Turbulence Models for Steady Incompressible Flows. *Int. J. Numer. Methods Fluids* 30 pp.309-333.
- [40] Engelman M. S., Sani R. L. and Gresho P. M. (1982) The Implementation of Normal and/or Tangential Boundary Conditions in Finite Element Codes for Incompressible Fluid Flow. *Int. J. Numer. Meth. Fluids* 2 pp.225-238.
- [41] Grotjans H. and Menter F. (1998) Wall Functions for General Application CFD Codes., ECCOMAS 98, *Proceedings of the 4th Computational Fluid Dynamics Conference*, John Wiley & Sons, pp.1112-1117.
- [42] Ilinca F., Héту J.-F. and Pelletier D. (1998) A Unified Finite Element Algorithm for Two Equation Models of Turbulence., *Comp. & Fluids* 27-3 pp.291-310.

- [43] D. Kuzmin, O. Mierka and S. Turek, On the implementation of the k-epsilon turbulence model in incompressible flow solvers based on a finite element discretization. 2007. *Int. J. Comp. Sci. Math.* 1 (2007) no. 2/3/4, 193-206.
- [44] E. Turgeon, D. Pelletier, J. Borggaard, Application of a sensitivity equation method to the k- ϵ model of turbulence, in: *Proceedings of the 15th AIAA Computational Fluid Dynamics Conference*, 2001.
- [45] Turgeon, E., Pelletier, D., Borggaard, J., Etienne, S. (2007). Application of a Sensitivity Equation Method to the K-Epsilon Model of Turbulence. *Optimization and Engineering*, 8(4), p. 341-372.
- [46] Lew A. J., Buscaglia G. C. and Carrica P. M. (2001) A Note on the Numerical Treatment of the k- Turbulence Model., *Int. J. of Comp. Fluid Dyn.* 14, pp.201-209.
- [47] Medic G. and Mohammadi B. (1999) NSIKE - an Incompressible Navier-Stokes Solver for Unstructured Meshes. *INRIA Research Report* 3644.
- [48] Thangam S. and Speziale C. G. (1992) Turbulent Flow Past a Backward-Facing Step: A Critical Evaluation of Two-Equation Models., *AIAA J.* 30-5, pp.1314-1320.
- [49] Turek S. and Kuzmin D. (2005) Algebraic Flux Correction III. Incompressible Flow Problems, In: Kuzmin D., Lohner R. and Turek S. (eds.) *Flux-Corrected Transport*, Springer, pp.251-296.
- [50] Menter FR (1994) Two-equation eddy-viscosity turbulence models for engineering applications. *AIAA J* 32:1598–1605
- [50] Chabard JP (1991) Projet N3S de mécanique des fluides-manuel théorique de la version 3. *Tech. Rep. EDF HE-41/91.30B*, Électricité de France
- [51] Ignat L, Pelletier D, Ilinca F (1998) Adaptive computation of turbulent forced convection. *Numer Heat Transf Part A* 34:847–871
- [52] Ilinca F (1996) Méthodes d'éléments finis adaptatives pour les écoulements turbulents. *PhD thesis*, École Polytechnique de Montréal
- [53] P. Jones and B.E. Launder, The prediction of laminarization with two equation model of turbulence. *Int. J. Heat Mass Transfer* 15 (1972), pp. 301–314
- [54] B. E. Launder and B. I. Sharma, Application of the energy-dissipation model of turbulence to the calculation of flow near a spinning disk, *Lett. Heat Mass Transfer* 1, 131-138, 1974
- [55] S.J. Wang and A.S. Mujumdar, A comparative study of five low Reynolds number k- ϵ models for impingement heat transfer, *Appl. Therm. Eng.* 25 (2005), pp. 31–44.

- [56] K.C. Chang, W.D. Hsieh and C.S. Chen, A modified low-Reynolds number turbulence model applicable to recirculating flow in pipe expansion, *ASME J. Fluids Eng.* 117 (1995), pp. 417–423.
- [57] R. Abid, Evaluation of two-equation turbulence models for predicting transitional flows, *Int. J. Eng. Sci.* 31 (1993), pp. 831–840.
- [58] C.K.G. Lam and K. Bremhost, A modified form of the k - ϵ model for prediction wall turbulence, *ASME J. Fluids Eng.* 103 (1981), pp. 456–460
- [59] K. Abe, T. Kondoh and Y. Nagano, A new turbulence model for predicting fluid flow and heat transfer in separating and reattaching flows I: flow field calculations, *Int. J. Heat Mass Transfer* 37 (1994), pp. 139–151.
- [60] Y. Saad and M.H. Schultz, GMRES: a generalized minimal residual algorithm for solving nonsymmetric linear systems. *SIAM J. Sci. Stat. Comput.* 7 (1986), pp. 856–869
- [61] Ilinca F, Pelletier D (1998) Positivity preservation and adaptive solution for the k - ϵ model of turbulence. *AIAA J* 36(1):44–51
- [62] Adrian J. Lew, Gustavo C. Buscaglia and Pablo M. Carrica, A note on the numerical treatment of the k - ϵ turbulence model, *International Journal of Computational Fluid Dynamics*, Volume 14, issue 3, 2001
- [63] M. Lesieur, O. Metais, New trends in large-eddy simulations of turbulence, *Annu. Rev. Fluid Mech.* 28 (1996) , 45-82
- [64] Lesieur, M., 1997: *Turbulence in Fluids*. Kluwer Academic Publishers, 515 pp..
- [65] D.R. Chapman, Computational Aerodynamics Development and Outlook, *AIAA J.*, vol. 17, no. 12, 1979, pp. 1293-1313
- [66] Okongo, N., Knight, D., and Zhou, G.2000. Large eddy simulation using an unstructured grid compressible Navier-Stokes algorithm. *International Journal of Computational Fluid Dynamics*13:303-326.
- [67] Lilly, D.K. 1967: The representation of small scale turbulence in numerical simulation experiments, *Proc. of the IBM Sci. Computing Symposium on Environ. Sciences*, Yorktown Heights, NY, 195 pp.
- [68] Deardroff, J.W. 1970, A numerical study of three-dimensional turbulent channel flow at large Reynolds numbers, *J. Fluid Mech*, 41
- [69] V. Driest, On turbulent flow near a wall, *J. Aeron. Sci.*, 23, No. 11 (1956).
- [70] Lilly D.K., A proposed modification of the germano subgrid-scale closure method, *Phys. Fluids A* 4 (3) (1992) 633-635

- [71] Ignat, L., Pelletier, D., Ilinca, F. (2000). A Universal Formulation of Two-Equation Models for Adaptive Computation of Turbulent Flows. *Computer Methods in Applied Mechanics and Engineering*, 189(4), p. 1119-1140.
- [72] Ilinca, F., Hetu, J.F., Pelletier, D. (1998). Unified Finite Element Algorithm for Two-Equation Models of Turbulence. *Computers & Fluids*, 27(3), p. 291-310.
- [73] Marc Henri (zvenks), Modélisation 3D par éléments finis du refroidissement primaire lors de la coulée continue d'aciers, *Ph.D. Thesis, Ecole des Mines de paris* (to appear)
- [74] Pelletier, D., Turgeon, E., Tremblay, D. (2004). Verification and Validation of Impinging Round Jet Simulations Using an Adaptive FEM. *International Journal for Numerical Methods in Fluids*, 44(7), p. 737-763.
- [75] D.A. Lyn and W. Rodi, The flapping shear layer by flow separation from the forward corner of a square cylinder, *J Fluid Mech* 267 (1994), pp. 353–379
- [76] Y. Zang, R.L. Street and J.R. Koseff, A dynamic mixed subgrid-scale model and its application to turbulent recirculating flows. *Phys. Fluids A* 5 12 (1993), pp. 3186–3196.
- [77] Rodi, W., 1997, Comparison of LES and RANS Calculations of the Flow Around Bluff Bodies, *J. Wind Eng. Ind. Aerodyn.*, 69–71, pp. 55–75.
- [78] Jeong U.Y., Koh H.M., and Lee H.S. (2002). Finite element formulation for the analysis of turbulent wind flow passing bluff structures using the RNG k- ϵ model. *J. Wind Eng. Ind. Aerod.* 90151–169.
- [79] D.A. Lyn, W. Rodi, Phase-averaged turbulence measurements in the separated shear region of flow around a square cylinder, in: *Proceeding of the. 23rd Cong. Int. Ass. Hydraulic Research*, Ottawa, Canada, August 21–25, 1989, A85–A92.
- [80] D.F.G. Durao, M.V. Heitor, J.C.F. Pereira, Measurements of turbulent and periodic flows around a square cross-section cylinder, *Exp. Fluids* (1998) 298–304.
- [81] S. Murakami, A. Mochida, On turbulent vortex shedding flow past 2-d square cylinder predicted by CFD, *J. Wind Eng. Ind. Aerodyn.* 54 (1995) 191–211.
- [82] W. Rodi, On the simulation of turbulent flow past bluff bodies, *J. Wind Eng. Ind. Aerodyn.* 48&47 (1993) 3–19.

Chapter 5

Immersed volume method for solving conjugate heat transfer

The present chapter is dedicated to develop a multidomain approach to solve the coupled heat problem and able to handle real complex geometries with different loading parts inside the furnace. First we present the complete description of the immersed volume method (IMV), which in turn is structured into three subsections: the use of the level-set approach to immerse and define heated objects, the unstructured and anisotropic mesh generation to adapt the interface between the fluid and the solid, and finally the thermo-physical properties of each subdomains are assigned using different mixing laws. The second part will be devoted to the resolution of the radiative transport equation (RTE) which constitutes an important ingredient for solving conjugate heat transfer. All the methods developed in previous chapters will now be coupled and used to study numerically problems arising in aero-thermo-mechanics inside industrial furnaces with different loadings. Finally, various numerical examples are considered for evaluating the proposed method and conclusions are drawn.

Chapter 5	179
Immersed volume method for solving conjugate heat transfer	179
5.1 Introduction	180
5.2 The immersed volume method	183
5.2.1 The signed distance function	183
5.2.2 The anisotropic mesh adaptation	185
5.2.3 Mixing laws	190
5.3 Radiative heat transfer	194
5.3.1 Introduction	195
5.3.2 The radiative transport equation (RTE)	196
5.3.3 Diffusive grey medium assumption	197
5.3.4 P1-model	199
5.3.5 Rosseland model	200
5.3.6 Conclusion and discussion	200
5.3.7 Combined natural convection and radiation in a square cavity	201
5.4 Applications	206
5.4.1 Forced and natural convection of conducting solids	206
5.4.2 Results and discussion	211
5.5 Conclusion	212
References	213

5.1 Introduction

The development of efficient methods to understand and simulate conjugate heat transfer for multi-components systems is among engineering challenges and still a need for industrials, especially in the case of the heat treatment of high-alloy steel by a continuously heating process inside industrial furnaces (see figure 1). Usually, the heat treatment sequence involves heating to a high temperature of an empty furnace followed by a controlled heating ingots placed at different locations inside. The thermal history of each ingot and the temperature distribution in the whole load are critical for the final microstructure and the mechanical properties of the treated workpieces and can directly determine their final quality in terms of hardness, toughness and resistance.

We have described in the previous chapters all the different numerical methods needed for solving the transient heat transfer and turbulent flows inside the furnaces. However, the modelling of the solid/fluid interaction problems and the thermal coupling are not yet treated. The main objective of this chapter is to present a multidomain approach to solve the conjugate heat transfer for which the three modes, convective, conductive and radiative heat transfer interfere simultaneously and in both the fluid part and the solid part. The proposed numerical method for modeling such multimaterial flows (fluid/solid) will be referred as the immersed volume method (IVM). A complete description and details about this method will be given. But first, we will discuss the driven motivation by revisiting some of the existing approaches that usually deal with such problems.

In recent years, there has been increasing interest in studying numerically a variety of engineering applications that involve thermal coupling of fluids and solids [1, 2, 3]. Most of the time, the general idea of these techniques consists in dividing the global domain into several local subdomains over each of which a local model (equation to be solved) can be analyzed independently. The global solution can then be constructed by suitably piecing together local solutions from individually modeled subdomains.

However, during the assembly, the coordination between the meshes can become complicated or even sometimes infeasible. Other alternative approaches have been applied for multi-phase flows problems and are available in the literature, such as the ghost fluid method introduced by Fedkiw *et al.* (1999) [4], the immersed boundary method [5, 6], domain decomposition [7], and the X-FEM [8]. They introduced and improved enrichment functions for material interfaces and voids by means of the level set representations of surfaces.

Nevertheless, in general when using all these techniques, one still need to know the value of the heat transfer coefficients between the two domains which ensures, as a Neumann/Dirichlet boundary conditions, the heat transfer at the air/solid interface. In fact, industrials perform many experimental tests to obtain such heat transfer coefficients. But, when dealing with a large diversity of shapes, dimensions and physical properties of these metals to quench, such operations can become rapidly very costly and time consuming.

In the present study, the proposed method aims to overcome this drawback. The main idea is to retain the use of the monolithic formulation and coupling it to some additional features that could allow a better and accurate resolution, in particularly at the interface between the fluid and solid. Recall that the monolithic resolution, based on the levelset approach consists in considering a single grid for both air and solid for which only one set of equations need to be solved. Consequently, different subdomains are treated as a single fluid with variable material properties. One important feature till now is that by solving the whole domain in a fully monolithic way there is no need of empirical data so as to determine the heat transfer coefficient. The heat exchange at the interface is replaced naturally by solving the convective fluid in the whole domain. Note also that different numerical methods introduced in the previous chapters could be used to solve the conjugate and coupled problem without additional efforts. Numerically, the communication between the solid and the fluid is obtained naturally without any further assumption and force modelling. In other words, there is no need for some coupling engines specifically designed to handle data exchange and algorithmic control signals between solid region and fluid region.

The second feature of this method is the use advanced research in the anisotropic mesh adaptation to adapt the interface between two different materials. The proposed mesh generation algorithm allows the creation of meshes with extremely anisotropic elements stretched along the interface, which is an important requirement for conjugate heat transfer and multi-component devices with surface conductive layers [12]. Many research efforts have been devoted to analyze and improve the accuracy, stability, conservation and robustness of different immersed boundary method. This is obviously required when following an interface all along the computations. But in the present study, the solid, the heated objects inside the furnace, are considered fixed and, consequently, a preadapted meshing is totally affordable. All these previously cited techniques can at a certain degree explicitly be replaced by this proposed locally interface refinement that can generate a quasi conforming mesh with an acceptable cost.

The interface between solid and fluid is only defined by a zero isovalue of the distance function; hence the calculations of the classical boundary integrals that account for the radiative heat transfer between the solid and the fluid are no longer applicable. The contribution of the radiations to the heat transfers is assessed by solving the radiative transfer equation (RTE) and by computing volumetric source terms. Two simple models, the 'Rosseland approach' and the P1-model are introduced and implemented.

It is important to mention also that the same strategy has already been introduced in [9] *et al.*, [10] and in [11], but the context was clearly different. In [9], the authors have proposed to use the metric properties of the distance function for simulating two bodies in contacts in a forging process. Details about the formulation of the contact condition, mesh adaptation as well as the computation of the distance function are given. On the other hand, in [10], the use of this method was highlighted by several numerical examples such as extrusion and industrial mixing processes. In [11], the authors illustrate the ability of this approach to accurately describe nucleation and grain growth in the context of recrystallization in a polycrystalline material. More details about the method can be also found in [13]. Here, we intend to apply the same strategy for simulating conjugate heat transfers and turbulent flows inside a furnace in the presence of heated industrial parts.

The outline of the chapter is as follows: first, we present a detailed description of the immersed volume method using both the level set function and the anisotropic mesh adaptation. Section 3 presents the suitable radiative heat transfer models. In section 4, various numerical examples are considered for evaluating the proposed method. Comparisons with the experimental results are presented in section 5. Finally, conclusions and perspectives are outlined.

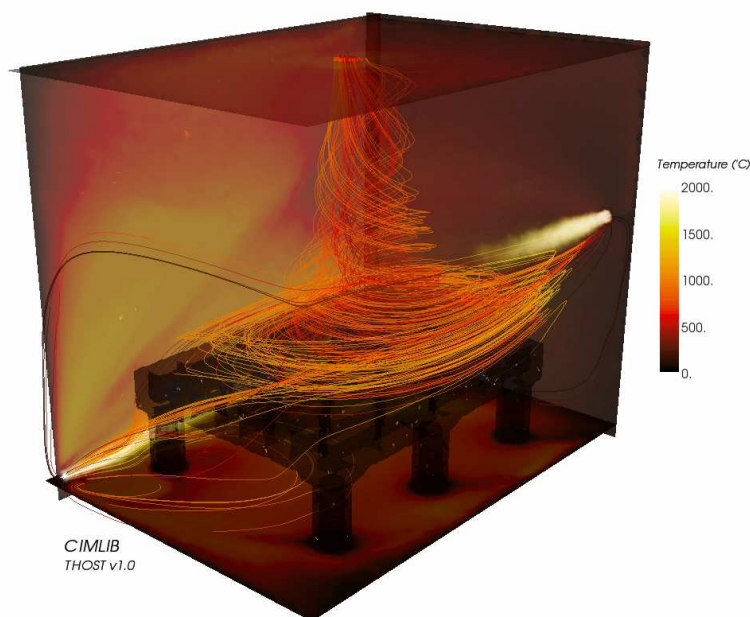


Figure 1. Heat treatment furnace: turbulent flow and conjugate heat transfer with radiation in a multidomain approach

5.2 The immersed volume method

The comprehensive description of the immersed volume method (IMV) is structured into three subsections. In the first section, the level-set approach is presented and used to describe, position and immerse heated objects inside the furnace; next the anisotropic mesh adaptation algorithm needed to refine the interface between the fluid and the solid is explained, and finally a brief review on mixing different thermo-physical properties for each subdomains is highlighted.

5.2.1 The signed distance function

In this section, brief details about computing the distance function and capturing the interface between a solid body and the surrounding fluid are presented. The algorithm used to compute the signed distance function has to be credited to Bruchon *et al.* and it is detailed in [9]. Distances are widely used in applications ranging from computer vision, physics and computer graphics and have been the subject of research of many authors in the last decade. We can find it in wide variety of problems such as: image reconstructing, multiphase flows and others [14, 15, 17]. In our context, we employed the distance function only as a geometric tool to initialize a given surface inside the furnace.

The most straightforward way for computing distance fields is through the use of a geometric brute force algorithm where the point-to-point distance is computed throughout the computational grid and the minimum distance for each point is stored. If Ω is a closed domain and $\Omega_{solid} \subset \Omega \subset \mathfrak{R}^d$ with piecewise smooth boundary Γ , then the signed distance function $\alpha(\vec{x})$ is defined as:

$$\alpha(\vec{x}) = \begin{cases} -d(\vec{x}, \Gamma) & \text{if } \vec{x} \notin \Omega_{solid} \\ d(\vec{x}, \Gamma) & \text{if } \vec{x} \in \Omega_{solid} \end{cases} \quad (5.1)$$

and the needed distance is given by

$$d(\vec{x}, \Gamma) := \min_{x_p \in \Gamma} \|\vec{x} - \vec{x}_p\| \quad (5.2)$$

For simple geometries, this function can be obtained from an implicit representation. For example, if the smooth boundary of a circle (see figure 2) with center $(0.5, 0.5)$ and radius $(R=0.25)$ is given by:

$$\Gamma_{(C,R)} = \{\vec{x} \in \Omega \mid d(\vec{x}) = R\} \quad \text{and} \quad d(\vec{x}) = \|\vec{x} - R\|^2 \quad \forall \vec{x} \in \Omega \quad (5.3)$$

Then the signed distance function implies simply: $\alpha(\vec{x}) = R - d(\vec{x})$.

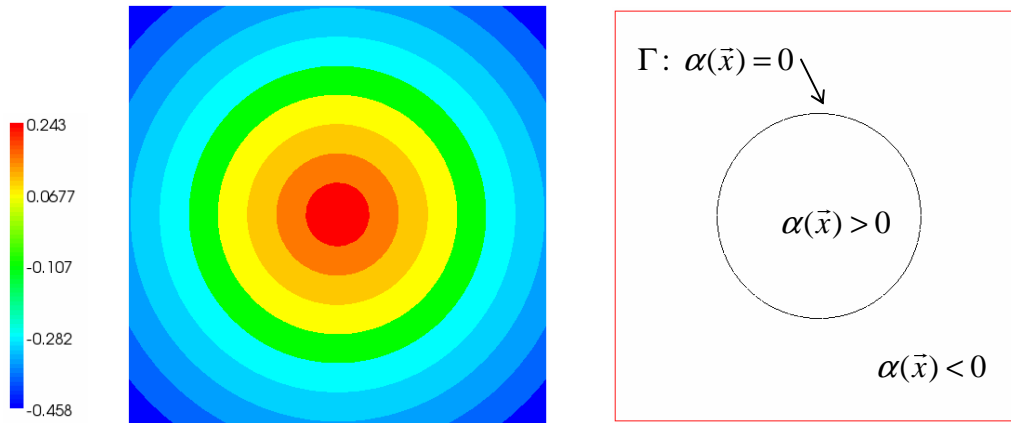


Figure 2. Definition of the signed distance function and representation of a circle

However, for complex geometry, such as industrial heated parts, the surface can not be given by any implicit function and it will be estimated from a discrete surface representation. Note also, that the brute force algorithms are infeasible due their high computational cost.

There exists a variety of algorithms to compute the distance function, which can be classified in two categories:

- i. *Geometric calculation*: The signed distance function is computed from the surface directly.
- ii. *PDE methods*: The signed distance function is a solution of a partial differential equation; the Eikonal equation [23, 46].

In the literature, most of the available methods for computing distance fields are developed for Cartesian grids, while little attention has been devoted to unstructured meshes. The study of more efficient methods for computing distance functions is still an open research area. [9, 14]. However, in the CIMLIB library, a modified fast algorithm for computing the distance function has been developed and implemented. Based on the geometric calculation, a new parameter, referred as the ‘quality parameter’ is introduced to compute the sign of the function as well as a hierarchical representation of the surface mesh is used to reduce as much as possible the computation time and cost. All the details including the algorithm can be found in [9]. The use of this computed distance function was also highlighted by many 3D applications with more complex configuration and can be found in [13, 15, 17, 18].

Recall that in our study, all the objects inside the furnace are considered fixed, and the computation of their respective distance functions is done only one time at the beginning of the resolution. Thus, the proposed algorithm is highly recommended in terms of accuracy and CPU time in particularly for three dimensional problems.

5.2.2 The anisotropic mesh adaptation

Accurate calculation of the temperature distribution along the fluid-solid interface is critical for a correct modelling of industrial experiments. When the heat flux is directed through the interface, the difficulty arises due to the presence of high gradients of temperature and due to the discontinuity of the material properties. If this latter is not aligned with the element edges, it may intersect the element arbitrarily such that the accuracy of the finite element approach can be compromised.

In this section, we introduce the second feature of the IVM method by proposing a strategy to adapt automatically the interfaces between subdomains. The level-set function described in previous section is coupled to an anisotropic mesh adaptation [36, 37, 39, 12, 13]. The mesh becomes locally refined around the zero isovalue of the level-set function which enables to sharply define the interface and to save a great number of elements compared to classical isotropic refinement. This anisotropic adaptation is performed by constructing a metric map that allows the mesh size to be imposed in the direction of the distance function gradient.

First, let us remind that all the meshes presented in this work have been generated through CIMLIB by the MTC mesher and remesher. It is based on a topological optimization technique that, by considering the quality of the elements, improves the mesh topology. The 3D tetrahedral, unstructured, isotropic or anisotropic mesh generator was developed by T. Coupez. and detailed in [16, 19, 20, 40, 41, 42, 43, 44].

Here, a brief review on building this metric map is presented. Further detailed are also given in the last section (4.5). This subject has been extensively studied in our lab and used by many researcher [24, 25, 26]. The main idea is to build a certain metric \mathcal{M} , a symmetric positive-definite matrix, that allows the creation of meshes with extremely anisotropic elements stretched along the interface. This forms an important ingredient for conjugate heat transfer and multi-component devices with surface conductive layers.

Therefore, if the metric \mathcal{M} can be regarded as a tensor whose eigenvalues are related to the mesh sizes, and whose eigenvectors define the directions for which these sizes are applied, then one can think about imposing small element sizes along the direction of the distance function gradient $\nabla\alpha$, and keeping the same background size in the orthogonal direction $\nabla\alpha^\perp$. In other words, the proposed metric takes the following form:

$$\mathcal{M} = m^2(\nabla\alpha \otimes \nabla\alpha^T) + \varepsilon^2 I \quad (5.4)$$

Where I is the identity tensor, ε and m are two positive-real parameters. This simply means that using this metric leads to a mesh size of $1/\sqrt{m^2|\nabla\alpha|^2 + \varepsilon^2}$ in the direction of $\nabla\alpha$ and to a mesh size of $1/\varepsilon$ in the direction of $\nabla\alpha^\perp$.

However, since only the interface separating both subdomains is the region of interest, this pushes us to build a general metric map that is equal to an isotropic metric in the far-interface region and equal to the previous constructed metric (5.4) in the vicinity of the interface. Accordingly, the general metric map takes the following form:

$$\mathcal{M} = \begin{cases} \varepsilon^2 I & \text{if } |\alpha| > e/2 \\ (\frac{N}{e} - \varepsilon^2) B + \varepsilon^2 I & \text{if } |\alpha| < e/2 \end{cases} \quad (5.5)$$

$$\text{where } B = \frac{\nabla \alpha \otimes \nabla \alpha^T}{\|\nabla \alpha\|^2}$$

where N is the number of elements required in a certain thickness e .

As shown in figure 3 which presents a close-up on the interface zone at the end of the anisotropic adaptation process, the mesh has been gradually refined when approaching the interface. Consequently, only additional nodes are locally added in this region, whereas the rest of domain has maintained the same background size: an important feature that keeps the computational work devoted to the grid generation low.

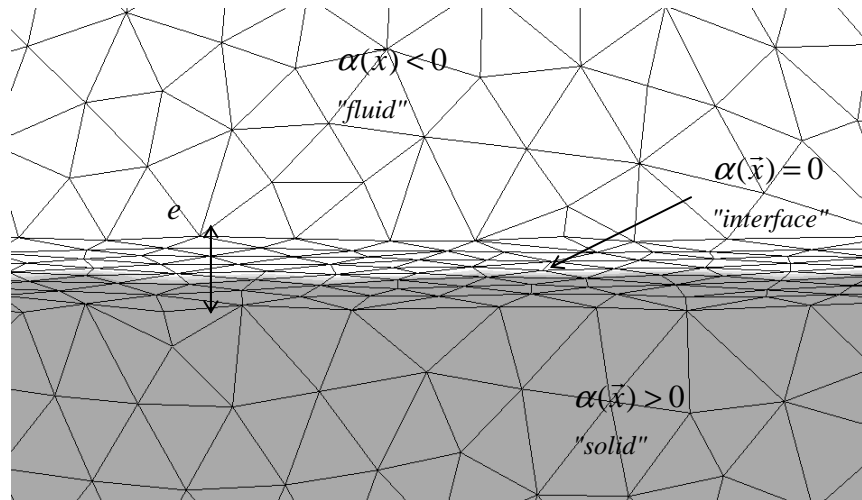


Figure 3. Interface refinement using anisotropic mesh adaptation: a zoom on the interface

The proposed mesh generation algorithm works well for 2D or 3D geometries and can easily handle arbitrary geometries. Next, some numerical examples are given to illustrate the effectiveness of the proposed mesh algorithm.

5.2.2.1 Two simple geometries

We consider two ingots placed in a 3D enclosure. Starting from a coarse mesh, we generate the multidomain metric and we adapt the mesh to this metric. After several iterations, one can clearly see from figure 4 that the interface between these objects and the surroundings is well adapted. Figure 5 shows that the refinement at the interface is anisotropic, while the rest of the domain has kept the same background size.

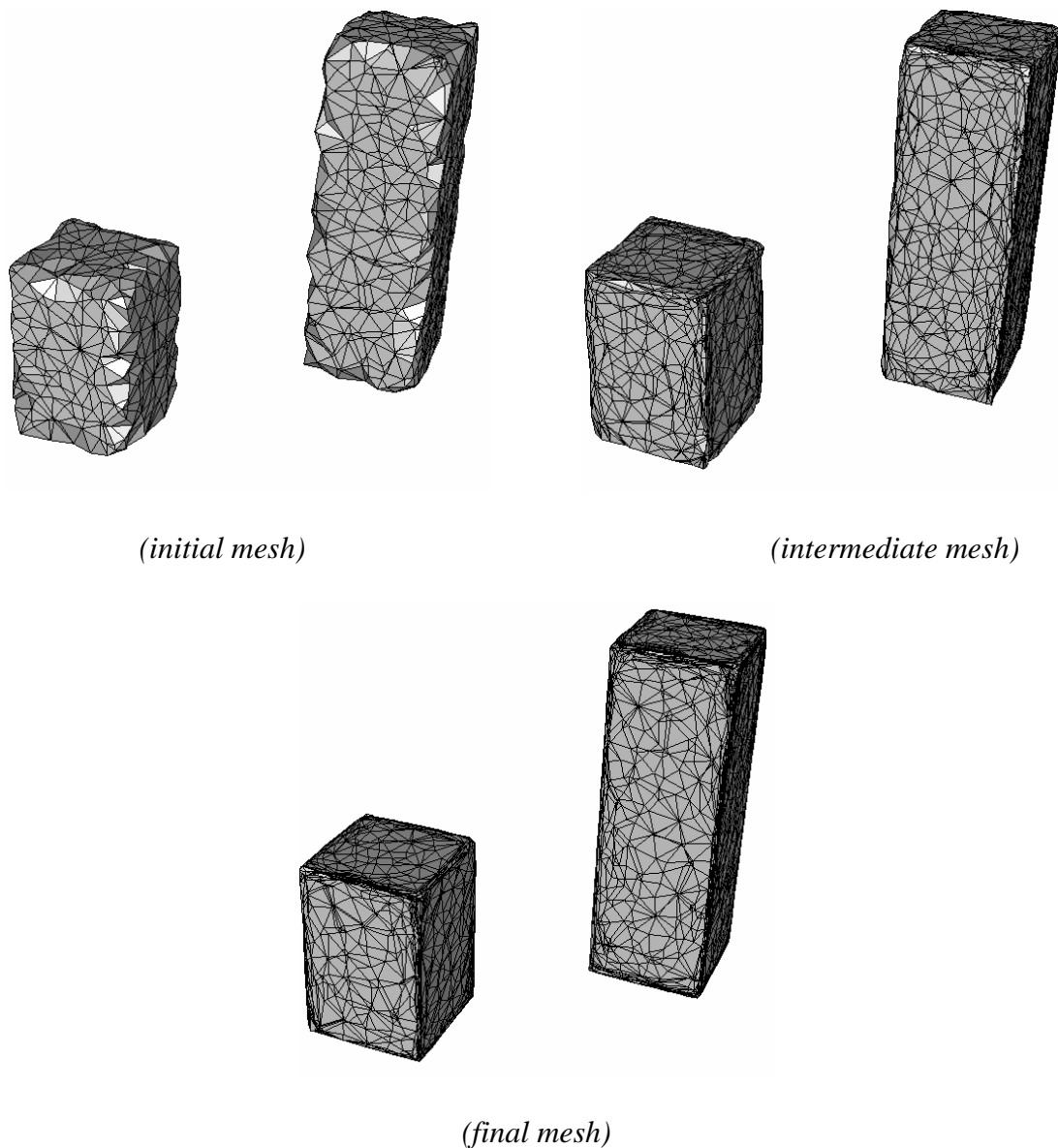


Figure 4. Iteration between the metric computation and the mesh generator

Note also, when using an anisotropic mesh, with elements stretched in a 'right' direction, one could allow not only to save a lot of elements but also to well describe the geometry in terms of curvature, angles, etc. Contrary to others techniques, this promising method can provide an alternative to body-fitted mesh for very complex geometry. In the

following example we consider a more complex problem: the immersion of a support grid inside an industrial furnace.

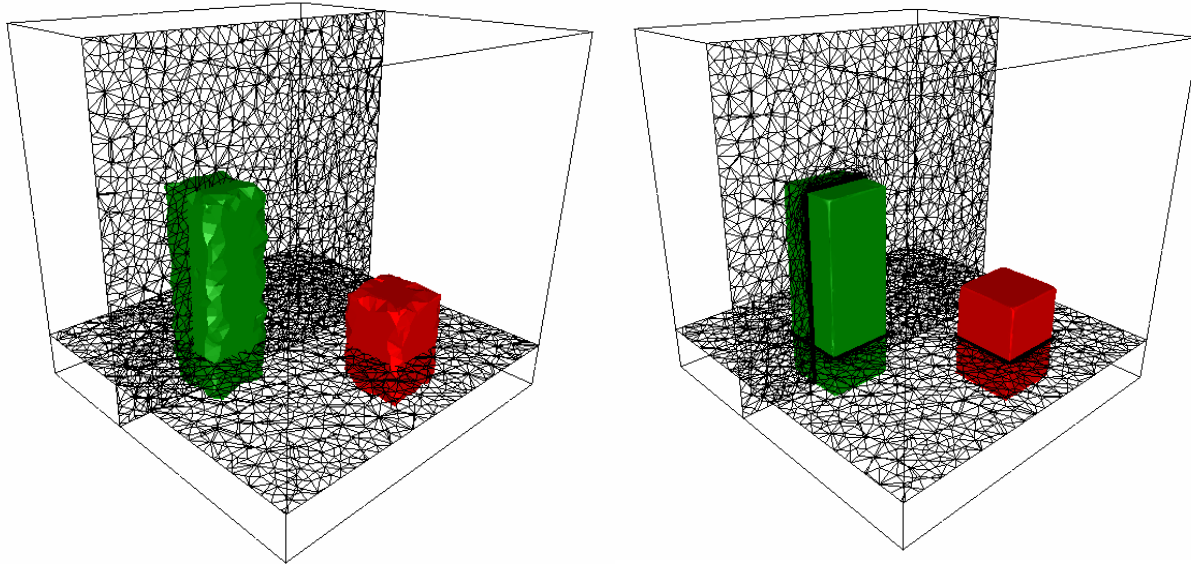


Figure 5. Zero isovalue of the immersed solid bodies

5.2.2.2 Support grid inside a furnace

Figure 6 presents a $1m^3$ gas-fired furnace provided by our industrial partner Terreal-France. This furnace is used for continuous heat treatment of terra-cotta products positioned usually on a support grid. The support is made by six cylindrical object and flat grid all placed in the center of the furnace as shown in figure 6 (right). Such geometries can not be given by any implicit function and the distance function must be computed.



Figure 6. $1m^3$ furnace (left) and the support grid (right)

By applying the IVM method, the level-set function identifies automatically the complete support grid body from the surrounding air and then applies the anisotropic mesh adaptation at the interface. The computations of the coupled heated problem and the results for this furnace are given in the last section. Figure 7 shows the resulting unstructured meshes after several iterations.

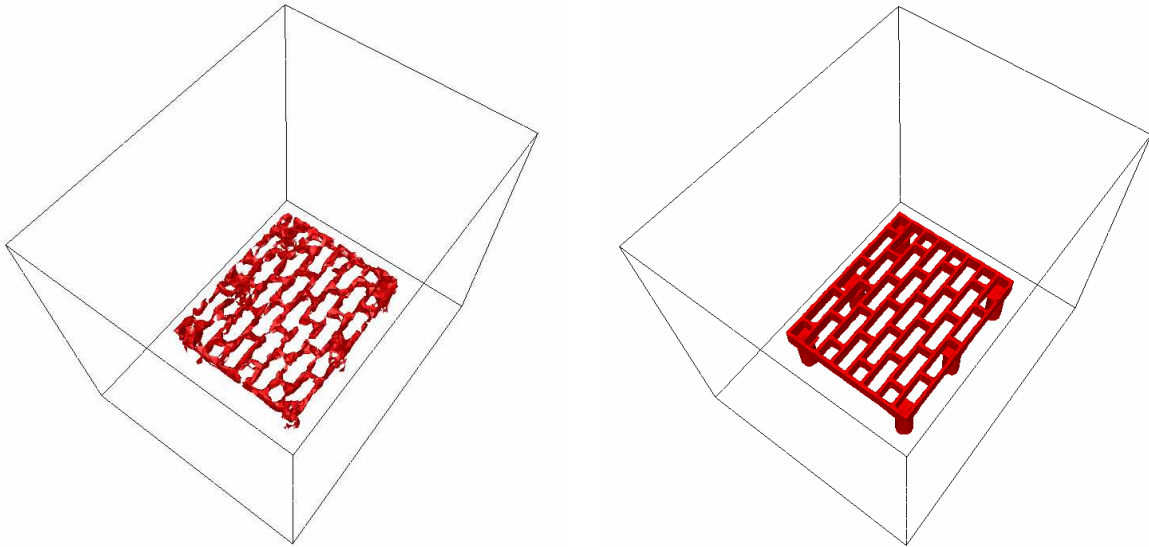


Figure 7. Difference between the initial mesh (left) and the final mesh (right)

The algorithm progressively detects and refines the support grid leading to a well respected shape in terms of curvature, angles, etc. All the small details in this given geometry can be captured accurately (see figure 8).

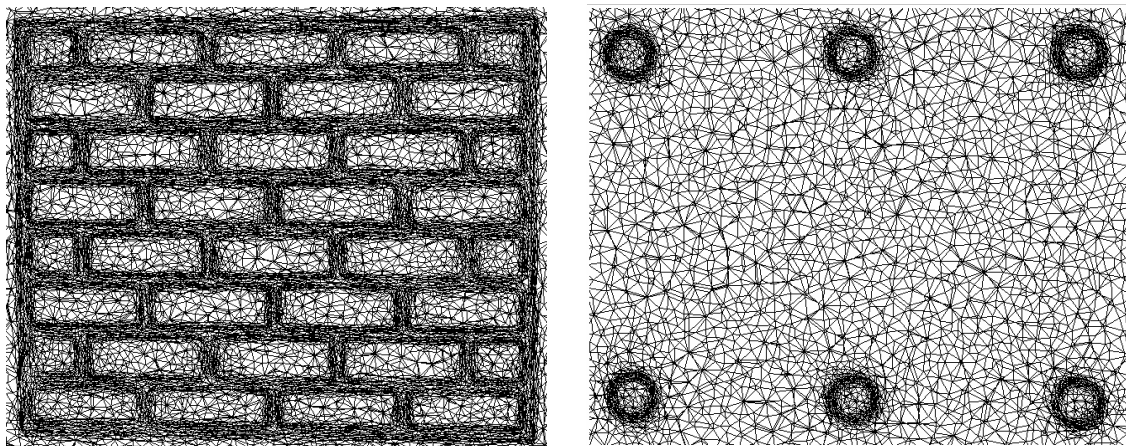


Figure 8. Two cuts of the support grid at different level

More examples and computational results are given in the last sections. As a conclusion, we have showed that the proposed anisotropic algorithm can capture accurately very complex industrial geometries. Although additional nodes are added to the initial

computational domain, we obtain very accurate interface which is an important requirement for conjugate heat transfer and multi-component devices with surface conductive layers.

Finally, once the mesh is well adapted along the interface, we use different mixing laws to distribute the material between each physical subdomain (solid/fluid). This last feature of the IVM method is presented in the following section.

5.2.3 Mixing laws

The geometry and thermodynamic properties of the solid domain are characterized by the signed distance function. The location of the air is then deduced by complementarity and does not require the introduction of an additional distance function. The air-solid mixture can now be treated as a single fluid whose effective properties are defined using continuous heterogeneity between their coefficients. Consequently, the coupled heat problem is simultaneously solved over the entire domain including both fluid and solid regions with variable material properties.

There exist in the literature roughly two categories of methods to compute the effective material properties. The first is based on numerical homogenization method which considers the dimension and geometry of periodic porous subdomains [27]. The other category, usually called mixture rules, relies on a ‘characteristic function’ of constituent materials and assumes no microstructure. Since our focus in this study is the heat treatment of large loads inside enclosures it is more convenient that the material distribution between each physical domain be described by means of the level set function.

The characteristic function of the solid domain is simply defined by the Heaviside step function H as :

$$H(\alpha) = \begin{cases} 1 & \text{if } \alpha(\bar{x}) > 0 \\ 1/2 & \text{if } \alpha(\bar{x}) = 0 \\ 0 & \text{if } \alpha(\bar{x}) < 0 \end{cases} \quad (5.6)$$

The physical and thermodynamic properties in the domain are then calculated as a function of $H(\alpha)$; for instance, the mixed temperature is calculated using a linear interpolation between the values of the temperature in the fluid and the solid:

$$T = T_{solid} H(\alpha) + T_{fluid} (1 - H(\alpha)) \quad (5.7)$$

However, using the Heaviside function described above leads to poor numerical results due to the assumed zero thickness of the interface and of course due to the sharp changes in the material properties.

Instead, we can use an alternative description of the interface as proposed by Sussman *et al.* [28]; Unverdi and Tryggvason [29]; and Sussman *et al.* [30]. It should be noted that there exist another approach proposed by Kang *et al.* [31] which treats the interface in a sharp fashion using jump conditions at the interface.

The idea is to give the interface a fixed thickness that is proportional to the spatial mesh size, and substitute the Heaviside function described above by a smoothed function given by:

$$H(\alpha) = \begin{cases} 1 & \text{if } \alpha(\bar{x}) > \varepsilon \\ \frac{1}{2} \left(1 + \frac{\alpha(\bar{x})}{\varepsilon} + \frac{1}{\pi} \sin\left(\frac{\pi \alpha(\bar{x})}{\varepsilon}\right) \right) & \text{if } |\alpha(\bar{x})| \leq \varepsilon \\ 0 & \text{if } \alpha(\bar{x}) < -\varepsilon \end{cases} \quad (5.8)$$

where ε is a small parameter such that $\varepsilon = O(h)$, known as the interface thickness, and h is the averaged mesh size in the vicinity of the interface.

“Recall that the IVM method couples at the same time all the three features described previously. This will result in a **smoothed Heaviside** function based on the **distance function** and able to assign the right thermodynamic properties on each side of the extremely **refined** interface. Consequently, the distribution of the materials properties will again respect the zero assumed thickness of the interface between a solid and a fluid”. This is actually an advantage of the IVM method over traditional multimaterial structures.

In addition to the use of the smoothed characteristic function, we still need a prescription for evaluating the appropriate mixture law at the interface for all the materials properties [32]. We conducted a large research on problems treating multiple materials with different properties in particularly, the conjugate heat transfer problem where convective heat transfer in the fluid and conductive heat transfer in the solid are handled simultaneously [32, 33, 34, 35]. A closer inspection on the mixture formulation of different materials reveals that the use of linear variation for the thermal conductivities cannot handle the abrupt change at the interface and would lead to inaccurate results. “Thus a proper formulation is highly desirable” [32].

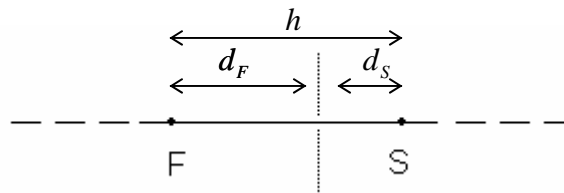


Figure 9. The interface between two domain and the distances associated with the interface

The effective thermal conductivity calculated using a linear variation is given by:

$$k_{eff} = k_F f(\alpha) + k_S (1 - f(\alpha)) \quad (5.9)$$

where $f(\alpha) = d_S/h$ is an example of the interpolation factor.

In [32], the author explained that it is not the local value of conductivity at the interface that is important (equation 5.9), it is rather the continuity of temperature and heat flux across the interface. The heat flux that leaves one control volume through a particular face must be identical to the heat flux that enters the next control volume through the same face (see figure 9). Otherwise, the overall balance would not be satisfied.

Therefore, in the absence of the source term, a steady one-dimensional analysis of the heat flux at the interface leads simply to:

$$q_{\Gamma_i} = \frac{T_F - T_S}{d_F / k_F + d_S / k_S} = \frac{T_F - T_S}{h / k_{eff}} \quad (5.10)$$

As a result, the appropriate expression for the effective thermal conductivity yields:

$$k_{eff} = \left(\frac{1 - f(\alpha)}{k_F} + \frac{f(\alpha)}{k_S} \right)^{-1} \quad (5.11)$$

This formulation, known as the harmonic average mean, basically reflects the requirement that diffusion flux should be the same even when calculated by different representative subdomains. Full details, demonstrations and complete analysis can be found in [32]. This is one conclusion about the mixture formulation among different others.

A closed details as well as the influence on the use of different mixture rules are given in [45]. To simplify the exposition, only the retained formulas are given. The global material properties for the coupled heat transfer problem such as density ρ , initial temperature T_0 , dynamic viscosity μ , heat capacity C_p and thermal conductivity, are defined by the following laws:

$$\begin{aligned} \rho &= \rho_{solid} H(\alpha) + \rho_{fluid} (1 - H(\alpha)) \\ \mu &= \mu_{solid} H(\alpha) + \mu_{fluid} (1 - H(\alpha)) \\ \rho C_p &= \rho C_{p_{solid}} H(\alpha) + \rho C_{p_{fluid}} (1 - H(\alpha)) \\ \rho C_p T_0 &= \rho C_{p_{solid}} T_{solid} H(\alpha) + \rho C_{p_{fluid}} T_{fluid} (1 - H(\alpha)) \\ k &= \left(\frac{H(\alpha)}{k_{fluid}} + \frac{1 - H(\alpha)}{k_{solid}} \right)^{-1} \end{aligned} \quad (5.12)$$

The sensitivity of the model to the estimation of the effective thermal conductivity and the interface representation is assessed using the following simple example. We consider in this test the transient conduction between two domains; a small squared heated solid immersed inside a cold cavity. The ratio of material properties across the interface is very large. Table I presents the different values used in this example. All walls of the cavity are maintained at adiabatic condition. Subject only to these boundary conditions, the analytical solution of this example is easily derived. The temperature evolution across the interface is presented in figure 11. Three type of interface are considered (figure 10). Two different mixture formulations for the thermal conductivity are used.

Domain	Temperature °C	Density kg/m ³	Heat capacity J/Kg°C	Conductivity W/m°C
Fluid	20°C	1.2	1000	0.02
Solid	400°C	2500	1000	175

Table I. Materials properties and initial temperature for both subdomains

The sharp discontinuity of the properties of the material across the interface and the presence of high gradients of temperature change this simple numerical example into a complicated one. From a numerical point of view, the sudden cooling of the hot immersed body inside a cold cavity is at the origin of so-called thermal shocks which cause spurious oscillations in the solution. To overcome this difficulty, the enriched finite element method presented in section 2.5. has been applied.

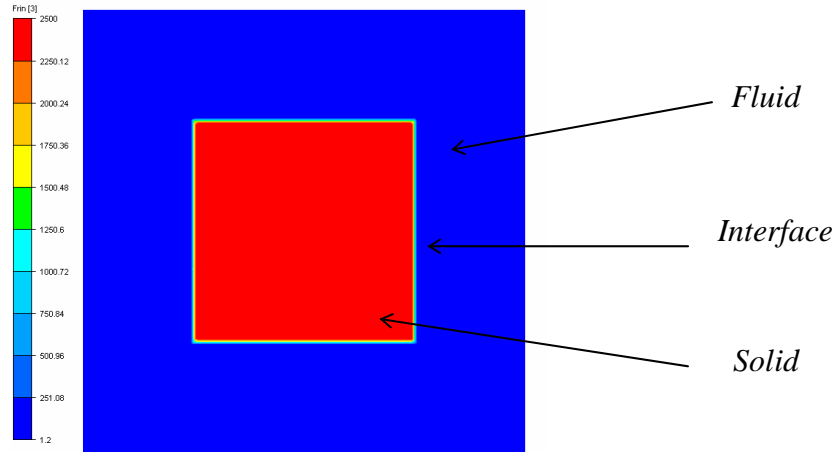


Figure 10. Density distribution across the interface

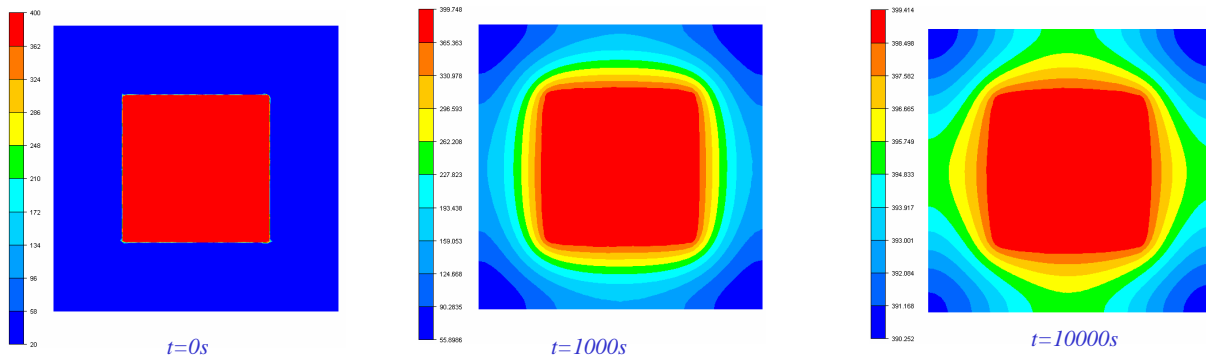


Figure 11. Temperature evolution across the interface

A comparison between the results obtained by the three cases is summarized in Table II.

Mixture law	No interface	Conform interface	Refined interface (IVM)
Simple	4.1%	6.4%	1.73%
Appropriate	0.15%	0.14%	0.12%

Table II. The relative error obtained using different mixture rules

As expected, predictions for the resulting temperature seem to be less sensitive to the interface refinement when using the appropriate mixture law (equation 5.11) for the thermal conductivity. However, when simple laws (equation 5.9) are used, the temperature decreases rapidly and fails to predict the appropriate behaviour. The closest prediction to the analytical solution is obtained by using the harmonic mean formulation together with a refined interface.

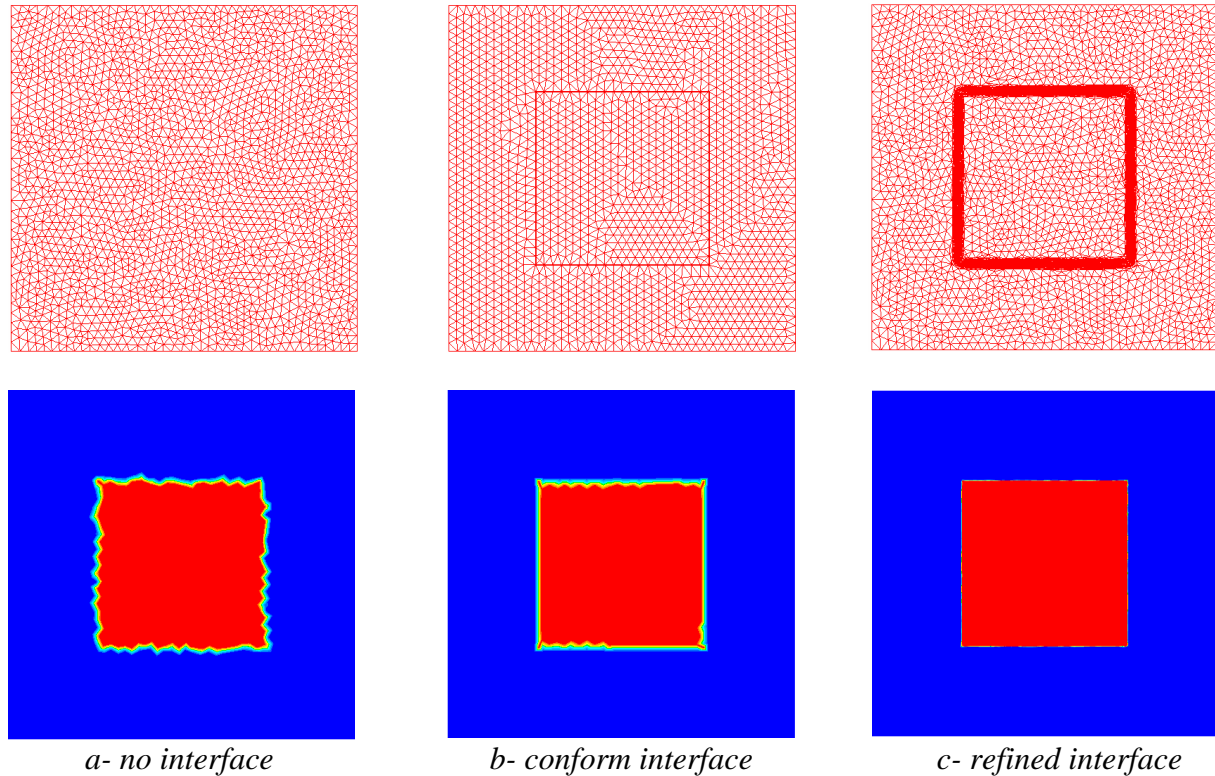


Figure 12. Distribution of the thermal conductivity across different interfaces

The influence for using different mixture rules on other coefficient as viscosity or the density have been also investigated in the given reference [45]. The majority of published work confirms that the effect of other materials properties is less important compared to the effect of thermal conductivity.

Having presented an initial validation of the IMV model, we proceed now to more detailed description on the radiative heat transfer; these include presentation of the radiative transport equation (RTE), the proposed models and 2D numerical validation. Finally, in the last sections, various results for the fluid and thermal flow processes simulated are illustrated in order to enhance the physical understanding of the phenomena taking place inside industrial furnaces.

5.3 Radiative heat transfer

The overall efficiency, the quality of the heated ingots and the production rates can be related directly to the accuracy of the thermal radiation model in industrial furnaces. We agree that thermal radiation exchange is the dominant mode of heat transfer in most furnaces and it depends on many factors including position, local temperature and composition. However, the prediction of radiative transfer is very complex due to the multidimensional and spectral nature of radiation. Recently, many works have been devoted to introduce some simplifications and assumptions suited to some particular application and modelling approach. Therefore, in this section we introduce some basic models to solve radiative heat transfer. In other words, the main focus of this section is structured around the following two questions: How do we predict radiative heat transfer inside industrial furnaces? Which model we should use that can be adapted to the IVM approach described previously?

Two kinds of radiation heat transfer occur inside a furnace enclosure: from workpieces to workpieces and from furnace (flame, hot combustion gases...) to workpieces. Many studies have been done to simulate the radiative exchange between solids [65], while other works mainly focus on the gas radiative heat transfer [48, 49]. However, there are few studies that deal with both type of exchange. Summarizing, heat transfer and turbulent flows between furnace and workpieces, among workpieces and inside workpieces simultaneously are extremely complicated and to our knowledge this work can be considered among the few attempts to attempt such objectives [52, 53, 54].

The topic of analyzing different approaches to model accurately radiation inside furnaces can serve as a Ph.D. level thesis all on its own and need further inspections. However, for validation purposes, we have conducted a research trying to find the best fitted radiative heat transfer models that could complement, even as a start, the IVM approach. In what follows, we summarize the retained methods.

5.3.1 Introduction

Radiative heat transfers occur in several physical processes such as combustion, nuclear reactor safety, and of course furnaces. However, due to its complexity, it was generally neglected or replaced by some semi-empirical assumptions in many numerical computations. Such complexity can be characterized by the high computational cost, need of chemical database, or the important uncertainty concerning the optical properties of the participating media and surfaces.

At the same time, radiation can strongly interact with convection in many situations of engineering interest. As highlighted in the following numerical example, the influence of radiation on natural convection is generally stronger than that on forced convection due to inherent coupling between the temperature and the flow fields in enclosures.

In the full simulation of combustion systems, the radiative transfer, which is an integro-differential equation, must be solved along with the partial differential equations of material, momentum, energy transport and chemical reactions as a fully coupled system. The most accurate procedures available in the literature for computing radiative transfer are the zonal and Monte-Carlo methods (Modest, McGraw Hill, 1993 [58]). However, these methods are not generally applied in combustion calculations due to their large computational time and storage requirements. Note also that these equations are in non-differential form, a significant inconvenience when solved in conjunction with the differential equations of flow and combustion.

In the current work, we are interested in modelling the energy transport in high-temperature gases using the CFD codes. Therefore, the models for solving the radiative transfer must be compatible with the numerical methods employed to solve the reacting flow equations. The zonal and Monte Carlo methods for solving the radiative transfer problem are incompatible with the mathematical formulations used in CFD codes, and require prohibitive computational resources for the desired spatial resolution. The discrete-ordinate and transfer methods (DOM/DTM, [63, 64]) appear to be reasonable compromises for solving the radiative transfer equations, but still one has to deal with large systems of algebraic equations, resulting from discretizing angle and space coordinates, that may deteriorate the efficiency of the CFD code.

Other approximated models for radiative transfer have also been derived and widely used in the literature. For instance we mention the diffusion approach (Rosseland, [50,58]) and the simplified P_N equations, when the medium under consideration is isotropic and optically thick (opaque). In fact, in an opaque medium the system is close to a radiative equilibrium for which assumptions of diffusion and simplified P_N equations are satisfied. Hence, in spite of the weaknesses of such approaches, especially when dealing with anisotropic or transparent (optically thin) media, *i.e.* when the system is far from the radiative equilibrium, they provide significant improvements for predicting interactions between radiation and matter. The following table summarizes a comparison of the different methods for modelling radiation transfer in furnaces:

Model	Description	Advantages	Disadvantages
Monte Carlo models	Uses random numbers to simulate and track individual beams of radiation through a furnace enclosure.	-easy for complex geometries -handle shadowing effects -model scattering, specular reflectors and spectral wall properties.	-incompatible with CFD equations -random behaviour does not guarantee the convergence.
Flux models	Direct solution of the RTE equation by subdividing the directional variation into a small number of angles in which radiation intensity is assumed to be constant.	-valid to non-homogeneous absorbing and scattering media. -compatible with CFD model	-all surface are diffusive -over-prediction of radiation
Zonal models	Radiation heat balance equations are solved using radiation exchange factors between each zone pair.	-simple model, does not require complex solution techniques -valid to non-grey gases	-invalid for non-homogeneous gases -incompatible with CFD -high computational cost
The DTM	Applies features of the above three methods	-easy for complex geometries -valid for non-homogeneous gases	-less accurate than the Zone method

Here in this study, we shall restrict ourselves to the flux models which can be applied to non-homogeneous absorbing media and they are well suited to application in CFD models.

5.3.2 The radiative transport equation (RTE)

The general equation of radiative transport is given by Eq. (5.13) [50]. The transport equation describes how radiant energy is affected as it travels through a medium along a direction s .

$$s \cdot \nabla I(r, s) = -(k_a + k_s)I(r, s) + k_a I_b + \frac{k_s}{4\pi} \int_{4\pi} I(r, s') \phi(s, s') d\Omega' + S_c \quad (5.13)$$

In the above, s and r denote a unit vector along the direction of the radiation intensity I and the local position vector, respectively. k_a and k_s stands for the absorption and scattering coefficients respectively. Φ is a probability function, formally known as the phase function, and S_c represents the resulting radiative source term. Ω' denotes the solid angle. The specific role of each introduced functions that account for the RTE model is discussed briefly. (see [58, 59])

The first term on the right hand side represents the attenuation of the incident energy by the extinction properties of the medium and constitutes a negative change in the incident energy. The second term represents the amount of energy which is emitted into the s direction by mass located along that direction. Energy which is attenuated and converted to internal energy may subsequently be emitted. The third term is shown in terms of the absorption coefficient k_a ; it is written this way to show that equal magnitudes of energy are absorbed and re-emitted in order when there is thermodynamic equilibrium. I_b is the blackbody intensity emitted by the medium at the local temperatures at position s .

The last terms represents what may be called "Inscattering", which is defined as that amount of energy from other directions which is scattered into the s direction after interacting with neighbouring elements. The probability function, Φ , scales the scattering of the neighbouring elements according to the uniformity or isotropy of the resulting scattered radiation. Inscattering causes a positive change to the local intensity. Further details can be found in [56, 57].

5.3.3 Diffusive grey medium assumption

The equation of radiation transport is an integro-differential equation. It is complex to apply this equation due to the nature of the required information (seven variables in particular Φ) and the need to find the intensity for each location within the medium and for each angular orientation.

Since solving equation (5.13) is often prohibitive in terms of CPU time, approximations can be made for varying situations which greatly simplify the analysis. The diffusion approximation, introduced by [59] presents one of the most important simplification. It is valid when the local intensity within the medium is a result of local emissions only; that is, emissions from distant elements are either absorbed or scattered and consequently diminished.

In [58] the author shows that the accurate knowledge of frequential and directional properties is not always necessary and depends on the considered applications. Recall that studying the spectrum of a star and analysing the medium in which the beams go through require a very accurate resolution as far as the frequencies are concerned. Similarly, when one is interested by the anisotropic aspect of the intensity to study the surrounding radiative sources, one has to treat very accurately the angular dependency. However, when the global thermodynamic exchanges between the material and the radiative beam are the main concern, averaged values of frequential and directional properties are 'often sufficient'. In the case of radiative exchanges in a furnace, this last approach, the diffuse grey medium assumption can be considered.

We begin by introducing the representative macroscopic quantities needed to derive the diffusive radiative model. By integrating the specific radiative intensity over the whole electromagnetic spectrum, for all directions and over all the wavelengths λ , the radiative energy, the vector of radiative flux and the tensor of radiative pressure are defined as:

$$\begin{aligned} E_{ray} &= \frac{1}{c} \int_{4\pi} \int_0^\infty I_\lambda(r, s) d\lambda d\Omega' \\ q_{ray} &= \int_{4\pi} \int_0^\infty I_\lambda(r, s) s d\lambda d\Omega' \\ \bar{\bar{P}}_{ray} &= \frac{1}{c} \int_{4\pi} \int_0^\infty I_\lambda(r, s) s \otimes s d\lambda d\Omega' \end{aligned} \quad (5.14)$$

Remark 1. The radiative energy is usually referred by engineers and researcher as the incident radiative intensity $G_{ray} = c E_{ray}$ where c is the speed of light.

For diffusive grey medium, we assume that the absorption coefficient is independent form the frequency and direction. Thus, according to the Bouguer Law, [59] the mean absorption coefficient can be defined by:

$$k = \frac{-1}{L_m} \ln(1-a) \quad (5.15)$$

where a is the macroscopic absorptivity of the medium.

L_m stands for the mean path length. In practical calculation, it can be considered as the characteristic size of the furnace which reads (see [59]):

$$L_m = C \frac{4V}{S} \quad (5.16)$$

where V and S are respectively the volume and the surface area of the furnace and C is a correction factor typically taken as 0.9. Alternate mean beam lengths are based on the grid cell size as follows:

$$L_m = C \frac{4\Delta V}{\Delta S} \quad (5.17)$$

with $\Delta V = \Delta x \Delta y \Delta z$ and $\Delta S = 2(\Delta x \Delta y + \Delta y \Delta z + \Delta z \Delta x)$. The definition adopted in the numerical computations is based on computing an appropriate volume and surface of the considered simplex when using unstructured grid [66].

Based on the work of Modest [59], the author provides a comprehensive derivation for the diffusion approximation. The main conclusion that we can get is that the divergence of the radiative heat flux represents the difference between the energy emitted from a point through thermal radiation and the incident energy form all other points in the domain and is given by:

$$\nabla \cdot q_{ray} = k(4\pi\sigma T^4 - G_{ray}) \quad (5.18)$$

where σ is the Stefan–Boltzmann constant, $5.670 \times 10^{-8} \text{ W.m}^{-2}.\text{K}^{-4}$

As a conclusion, solving now for the incident radiation G_{ray} yields the required volumetric source term $\nabla \cdot q_{ray}$. This source term is introduced back into the energy equation ensuring as a sink/load source the radiative heat transfer in the enclosure. Two basic models are studied and implemented in this work to solve the incident radiation G : the P1-model and the Rosseland model.

5.3.4 P1-model

The P1 model has been used for a number of years in the calculation of radiation transfer for industrial computational fluid dynamics (CFD), particularly in the simulation of combustion systems. In these applications, it was assumed that the absorption coefficient is constant, or an effective value was found, which is a function of composition and temperature, by some averaging technique such as the weighted-sum-of-grey-gases [59]. For the calculation of high temperature heated objects and the surrounding hot gases, such a degree of approximation is unacceptable, but a full integration over frequency is too computationally expensive. The averaged absorption coefficient (equation 1.3.3) can be used to solve the P1 equation. The governing equations for the P1 model are derived in detail in [51, 58, 59]. It was shown that under this diffusive limit, there is a link between the radiative pressure tensor and the radiative energy referred as the closure relation:

$$P_r = \frac{1}{3} E_r \mathbb{I} \quad (5.19)$$

with \mathbb{I} the identity tensor.

Such a closure relation together with (5.14) and (5.18) enables to express the radiative flux as a linear function of the incident intensity gradient:

$$q_{ray} = -\frac{1}{3k} \nabla G_{ray} \quad (5.20)$$

For completeness, inserting the last expression into the radiative energy equation (RTE) leads to the well-known P1 diffusion-reaction equation:

$$-\nabla \cdot \left(\frac{1}{3k} \nabla G_{ray} \right) + kG_{ray} = 4k\sigma T^4 \quad (5.21)$$

The boundary condition for the P1 model is derived and discussed in detail in [57] and is given by:

$$\frac{\partial G}{\partial n} = \frac{e_w}{2(2-e_w)} (4k\sigma T_w^4 - G_w) \quad (5.22)$$

where e_w stands for the emissivity at the wall, the subscript w indicates the value at the wall and the direction n is normal to the wall and points into the gas. This expression, used usually in neutron diffusion theory, is known as the Marshak boundary condition [51, 57].

5.3.5 Rosseland model

The Rosseland approximation has been established in [47] by a method based on a multiscale expansion in powers of the emissivity. In [50], the same Rosseland approximation is introduced for a reduced version of the grey model neglecting the time derivative in the energy balance equation. Compared to the P1 model, the Rosseland approximation introduces a supplementary simplification by approximating the radiative intensity using the Planck distribution [58]. It follows that the grey incident radiative intensity reads:

$$G_{ray} = 4\sigma T^4 \quad (5.23)$$

The grey radiative flux is expressed as:

$$q_{ray} = -\frac{4\sigma}{3k} \nabla(T^4) \approx -\frac{16\sigma T^3}{3k} \nabla T \quad (5.24)$$

As shown in equation (5.24), the Rosseland model accounts for radiation losses through the use of a diffusive source term in the energy equation through an additional conductivity denoted by:

$$k_{ray} = -\frac{16\sigma T^3}{3k} \quad (5.25)$$

The radiation problem thus reduces to a simple conduction problem with strongly temperature dependent conductivity.

5.3.6 Conclusion and discussion

The limitations of the so-called Rosseland approximation have been extensively studied in the literature. In general, despite the simplicity of this model, it predicts nearly uniform temperatures and neglects directional dependence while assuming that all energy is directly converted into radiation energy. These assumptions lead to poor numerical results when simulating industrial furnaces with heated objects.

On the other hand, the P1 approach requires the solution of a radiation transport equation (RTE), and it is based on the assumption that radiation is continuous throughout the domain. It works best with participating media. The results of the P1 model are expected to yield better results inside the furnace with participating heated objects considering the modest calculation effort. Therefore, the one with the lowest computational effort, the P1 model, should be chosen for the time being. However, if the temperature distribution is important, this model, known to be a diffusion model, can yield over-predict radiation and must be replaced. This will be the subject of further investigations and future works.

Since the IVM method used is shown as an attractive way to solve a coupled heat treatment problem by numerical simulation. Some needed improvements have been identified, mainly regarding the radiative heat transfer. An improved directional method in the CIMBLIB library is identified by the work of T. Kłoczko [67, 68] for future works.

The natural assumption for a heterogeneous medium (solid/fluid) is to consider it as a single fluid with different opacities (absorption coefficients). Therefore, the effective medium is obtained using the IVM method and by defining an effective opacity (absorption coefficients) using an arithmetic mean formulation:

$$k_a = k_{a \text{ solid}} H(\alpha) + k_{a \text{ fluid}} (1 - H(\alpha)) \quad (5.26)$$

We restrict ourselves to the case where the two opacities exhibit a high-contrast ration: one of the component is diffusive and opaque (solid part) whereas the other one is not and is considered as non-participating medium (fluid part). It is noticed that solving the radiative transport equation (RTE) in both domains generates a volume source term rendered by the sharp discontinuity of the temperature and the materials properties. This source term is introduced into the energy equation ensuring the continuous cooling/heating of the immersed objects.

More details about using the Rosseland approximation for radiative transfer in heterogeneous media can be found in [69, 70]. Both methods are implemented in the CIMLIB library, but only the P1 model is used in this study. For simple configuration inside an enclosure and in the presence of a heated object, the proposed effective opacities approach is considered as a first attempt. A complete study taking into account different objects and shadowing is a work on progress. The remainder of the chapter is structured as follows. In the next section, we present a 2D test case for validating the P1-model equation. In section 4, we give more simulation and numerical results on the effective opacity of the mixture.

5.3.7 Combined natural convection and radiation in a square cavity

One of the most popular benchmark in CFD computations is the laminar flow in a two-dimensional square cavity with differentially heated sidewalls. This test has been widely used as a benchmark for the validation of numerical codes and has been analyzed by a number of authors [60, 61]. The velocity and the temperature equations are coupled due to the buoyancy force and solved. Consequently, the flow inside the enclosure is driven by the temperature differences. The ratio of these two temperature differences is a very important factor to decide the heat transfer and flow characteristics of the enclosure.

Here, in the present study, the main focus is restricted to validate the implementation of the P1-model and to evaluate the influence of the radiative heat transfer inside the cavity. The problem description and boundary conditions are shown in figure 13. The left wall is kept at a constant cold temperature of $T_c=1000 \text{ K}$, whereas the right wall is kept at a constant high temperature of $T_h=2000 \text{ K}$. Other two walls are maintained at adiabatic condition. The radiation effects are assumed to be negligible in the first study case and active with absorption coefficients of 0.2 and 5 in the second one. We assume that the fluid properties are to be constant, except for the density in the buoyancy term, which allows Boussinesq approximation. The gravitational acceleration is taken parallel to the isothermal walls.

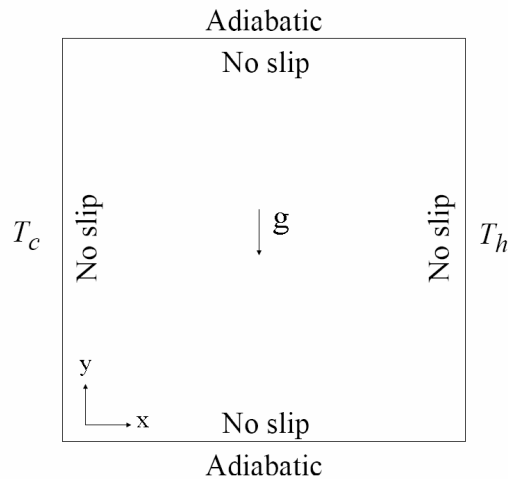


Figure 13. Schematic domain and boundary conditions

Radiation effects on convection can be quite important in the context of many industrial applications involving high temperatures such as nuclear power plant, gas turbines, and various propulsion engines for aircraft, missiles, satellites, and space technology. Ali *et al.* [71] studied the natural convection-radiation interaction in boundary layer flow over horizontal surfaces. Hossain and Pop [72] considered the effect of radiation on free convection of an optically dense viscous incompressible fluid along a heated inclined flat surface maintained at uniform temperature placed in a saturated porous medium. Hossain and Takhar [73] investigated the radiation effect on the mixed convection flow of an optically dense viscous incompressible fluid over vertical flat plate.

In the present study, we analyzed the combined effect of radiation and heat absorption coefficient on the natural convection flow inside an enclosure [74]. In order to validate the accuracy of the present implemented solver, the results are compared with the numerical calculations obtained by Fluent [55-75]. The Prandtl number is taken to be 0.71 , and the Rayleigh number based on the length of the cavity is 5.10^5 . Note that the values of all physical properties and operating conditions (e.g., gravitational acceleration) have been adjusted to yield the desired Prandtl, Rayleigh, and Planck numbers and were adapted from Fluent user guide [75].

Let us remind some dimensionless numbers relevant in the coupled heat transfer and fluid flow. First, the Rayleigh number, a non-dimensional number, is the buoyant force divided by the product of the viscous drag and the rate of heat diffusion, it is given by:

$$Ra = \frac{\rho g \beta (T_h - T_c) L^3}{\mu k} \quad (5.27)$$

where β is the coefficient of thermal expansion of the fluid, $\Delta T = T_h - T_c$ is the temperature difference between the right hot and left cold walls in the figure separated by width L , k is the thermal diffusivity of the fluid, μ the dynamic viscosity and ρ the density of the fluid. It represents the ratio between the conduction and the convection for a given fluid in a certain

geometry configuration. Once the Ra exceeds a critical value, the dominant energy transport mechanism in the fluid becomes the convection.

The Prandtl number Pr is a dimensionless number representing the ratio of the kinematic viscosity to the thermal diffusivity of a fluid and is an important control variable in thermal convection. It is defined as:

$$Pr = \frac{c_p \mu}{k} = \frac{\text{viscous diffusion rate}}{\text{thermal diffusion rate}} \quad (5.28)$$

The division of the Rayleigh number by the Prandtl number gives the Grashof number, an interesting dimensionless number in fluid dynamics and heat transfer that approximates the ratio of the buoyancy to viscous force acting on a fluid. It frequently arises in the study of situations involving natural convection and it is given by:

$$Gr = \frac{g \beta (T_h - T_c) L^3}{\nu^2} \quad (5.29)$$

where ν is the kinematic viscosity.

Finally, the Boussinesq approximation used for many natural-convection flows states that density differences are sufficiently small to be neglected, except where they appear in terms multiplied by g , the acceleration due to gravity. The essence of the Boussinesq approximation is that the difference in inertia is negligible but gravity is sufficiently strong to make the specific weight appreciably different between the two fluids. Consequently, the force term in the momentum equation change into:

$$(\rho - \rho_0)g \approx -\rho_0 \beta (T - T_0)g \quad (5.30)$$

where ρ_0 is the constant density of the flow, T_0 is the operating temperature, and β is again the thermal expansion coefficient.

In order to obtain the field of velocities, pressures, temperature and the incident radiation, the energy equation, the P1-model and the Navier-Stokes equations using the Boussinesq approximation are coupled and solved simultaneously. Figure 14 and 15 shows at convergence state, the isotherms and streamlines obtained using a pure natural convection compared to those obtained by the conjugate convection-radiation problem (absorption coefficient $k=0.2$ and $k=5$).

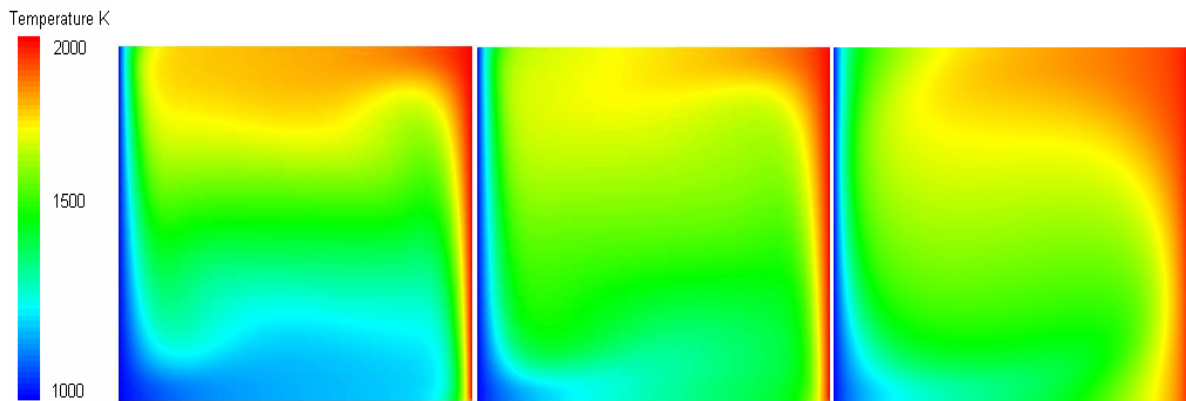


Figure 14. Temperature contours: without radiation (left); with radiation $k=0.2$ (center); with radiation $k=5$ (right)

The classical recirculatory patterns observed are due to the natural convection in the cavity. At a low optical thickness ($k=0.2$), radiation should not have that large influence on the flow. The flow pattern is expected to be similar to that obtained with no radiation. However, for high optical thickness ($k=5$), the radiative source term becomes more important. In this case, one single circulation cell was formed and flow strength increases. With the increase of natural convection mechanism the flow pattern becomes very symmetric and the temperature distribution becomes more homogeneous as shown in figure 14 (right).

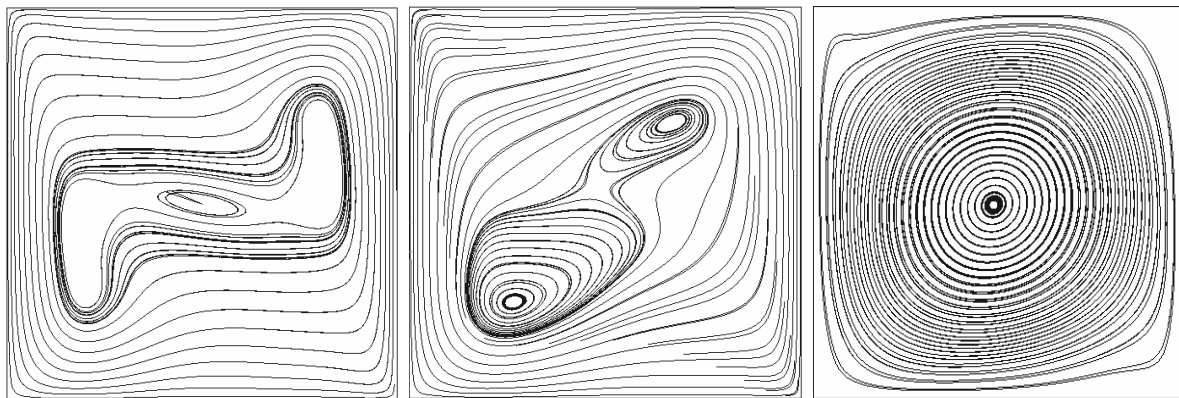


Figure 15. General streamline pattern: pure convection (left); with radiation $k=0.2$ (center); with radiation $k=5$ (right)

The velocity profiles for u_y along $y=0.5$ are shown in figure 16. The numerical solutions are indistinguishable from the reference solutions. This confirms the validity of the implemented finite element radiative solver. These plots show the effect of the radiation parameter on the velocity fields. It is noticed that increasing the radiation parameter plays an important role inside the enclosure and enhances the velocity profile. These behaviors are expected inside a furnace enclosure.

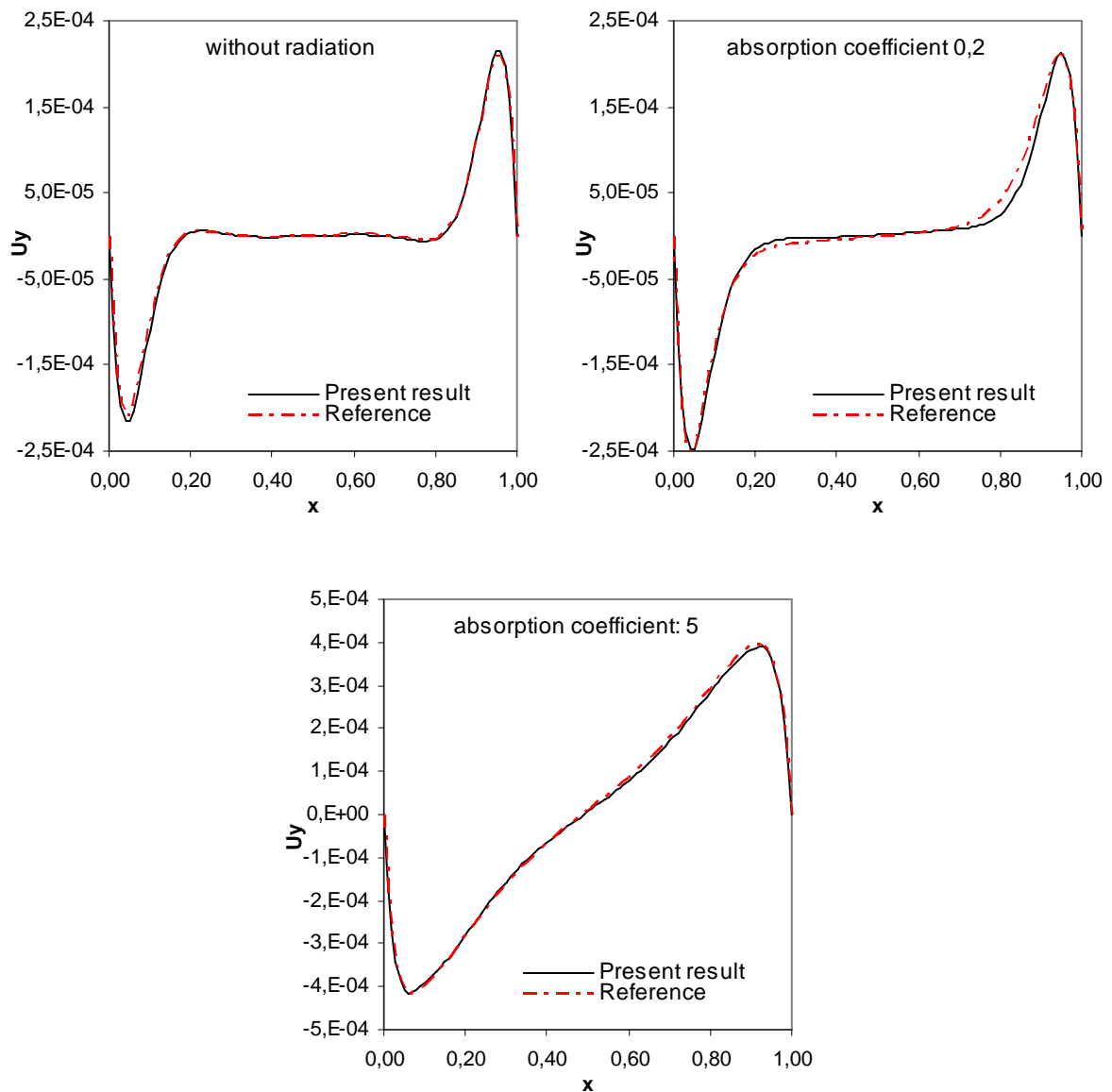


Figure 16. Velocity profiles for u_y along $y=0.5$

We can conclude from this simple example that radiation can strongly interact with convection in many situations. The influence of radiation on natural convection was highlighted and plays an important role due to inherent coupling between the temperature and the flow fields in enclosures.

5.4 Applications

The main objective of this last section is to provide a numerical investigation of conjugate heat transfer and turbulent airflow in a full-scale industrial furnace. This type of application allows improvement in the productivity with very low capital investment, consequently reducing energy consumption. In addition, experimental tests have demonstrated that the furnace performance may be improved significantly by design optimization. A design optimization involves finding the best geometry of the furnace, which include the furnace dimensioning, positioning and type of the burners, positioning of exhaust ports, positioning and arrangement of the treated ingots. Because of great complexity of the problem, the large diversity of shape and large number of parameters variables involved, a complete analysis is only possible with the aid of powerful numerical codes and computers.

We can find in the literature several recent works dedicated to the numerical investigation of combustion processes with different models [78, 79, 80]. The present work attempts to provide an additional contribution by simulating the heat treatment process inside an industrial furnace using the IVM approach. The advantage of the proposed method can be resumed by the following points:

- The model produces detailed information simultaneously in both domains: the treated ingots and the surrounding hot air
- Easy for the designer to simulate several different operational situations
- Capable of handling multiple parts in 3-D.
- Inexpensive for the designer to simulate conjugate problems: conduction in the solid and convection in the rest of the domain by solving one set of equations
- Accurate representation of the fluid-solid interface
- No need for previous experimental tests to deduce the transfer heat coefficient that ensures the heat exchange between subdomains.

However, experiments must be performed in order to provide better understanding of the physics involved as well as to produce real data against which the model results should be compared.

5.4.1 Forced and natural convection of conducting solids

In this section, we will propose three numerical examples to illustrate the IVM approach from heat transfer and turbulent fluid dynamics points of view. We consider three cases:

- cases (a) and (b) the continuous heating of immersed ingots by forced convection.
- case (c) considers the air-cooling by natural convection of two heated objects inside an enclosure.

The radiation in these examples is considered negligible. Figure 17 illustrates the simplified pre-heated furnace geometry, which has a rectangular shape, with one ingot (case a) and two ingots (case b) inside located on the lower surface at arbitrary position. Figure 18 illustrates the air cooling of two heated ingots in a simplified cold enclosure. The materials properties affected to each domains, the initial conditions and the parameters used in these test are presented in table III and IV respectively.

Domain	Temperature °C	Density kg/m ³	Heat capacity J/Kg°C	Conductivity W/m°C
Fluid	250°C	1.2	1000	0.02
Solid (s)	50°C	100	1000	175

Table III. Material properties for case (a) and (b)

Domain	Temperature °C	Density kg/m ³	Heat capacity J/Kg°C	Conductivity W/m°C
Fluid	20°C	1.2	1000	0.02
Solid (1)	500°C	100	1000	175
Solid (2)	250°C	100	1000	175

Table IV. Material properties for case (c)

The levelset function is first applied to define and positioned the treated objects. The second step consists in deriving the anisotropic adapted mesh that describes very accurately the interface between the workpieces and the surrounding air. Recall that the mesh algorithm allows the creation of extremely stretched elements along the interface, which is an important requirement for multimaterial problem with surface conductive layers. The additional nodes are added only at the interface region keeping the computational cost low.

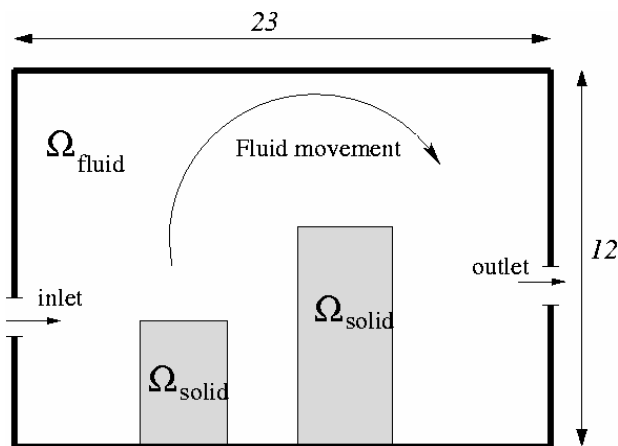


Figure 17. Schematic diagram and boundary condition; case (a) and (b)

Once the mesh is well adapted along the interface, the material distribution between each physical domain can be described by means of the level set function. Consequently, the same set of equations; momentum equations, energy equation, the turbulent kinetic and dissipation energy equations (k-epsilon model), is simultaneously solved over the entire domain including both fluid and solid regions with variable material properties (see table III, and IV).

Note also that the interface between the solid and the fluid is rendered by the zero isovalue of the distance function; hence the calculations of the classical boundary conditions to ensure the heat exchange between the subdomains are no longer applicable on their interfaces.

The state of art in the proposed thermal coupling analysis lies in that the heat transfer between the solid and the air at the interface has been treated “naturally”, i.e. without the use or a previous knowledge of any heat transfer coefficient.

The discretization in space for the incompressible Navier-Stokes equations, the heat transfer equation and the turbulence equations is performed by an unstructured grid stabilized finite element method. Thus, the numerical oscillations and thermal shocks are well captured and smooth solutions are obtained.

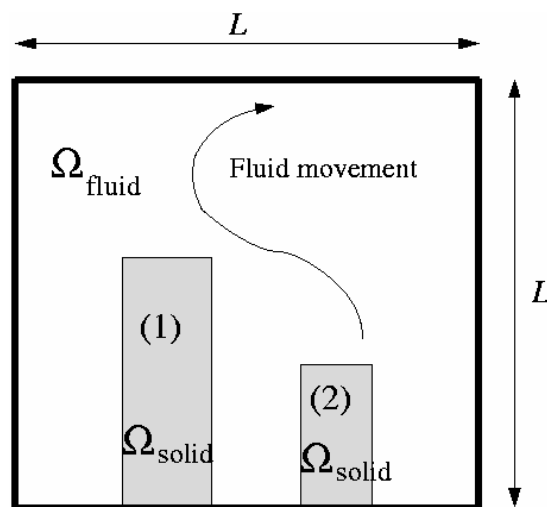


Figure 18. Schematic diagram and boundary condition; case (c)

The evolution of the isotherms at different time steps inside the simplified furnace is illustrated in Figure 19. The hot air is pumped from the left inlet at 2m/s at a fixed temperature of 1000°C. The air is vented out the enclosure through the outlet positioned at left vertical wall. Standard wall function is applied on the rest of the boundary. The shape of the treated object is well capture and respected by applying the anisotropic mesh adaptation.

The ingots slow down the injected air from the burner and slightly influence the main air circulation inside the domain. This explains the difference in the flow pattern between the two cases.

When the hot fluid passes across the volume of the furnace, it induces a turbulent and recalculating motion within the geometry. This forced convection is caused by the interaction of the moving stream and the stationary fluid inside the furnace. The temperature distribution clearly indicates this expected flow pattern. The air movement around the workpieces is interesting; i.e. it allow studying the influence of different arrangements and positions to optimize the heat treatment. A number of vortexes between the objects and the surroundings can be observed due to the turbulence dissipation and mixing between the hot and cold air.

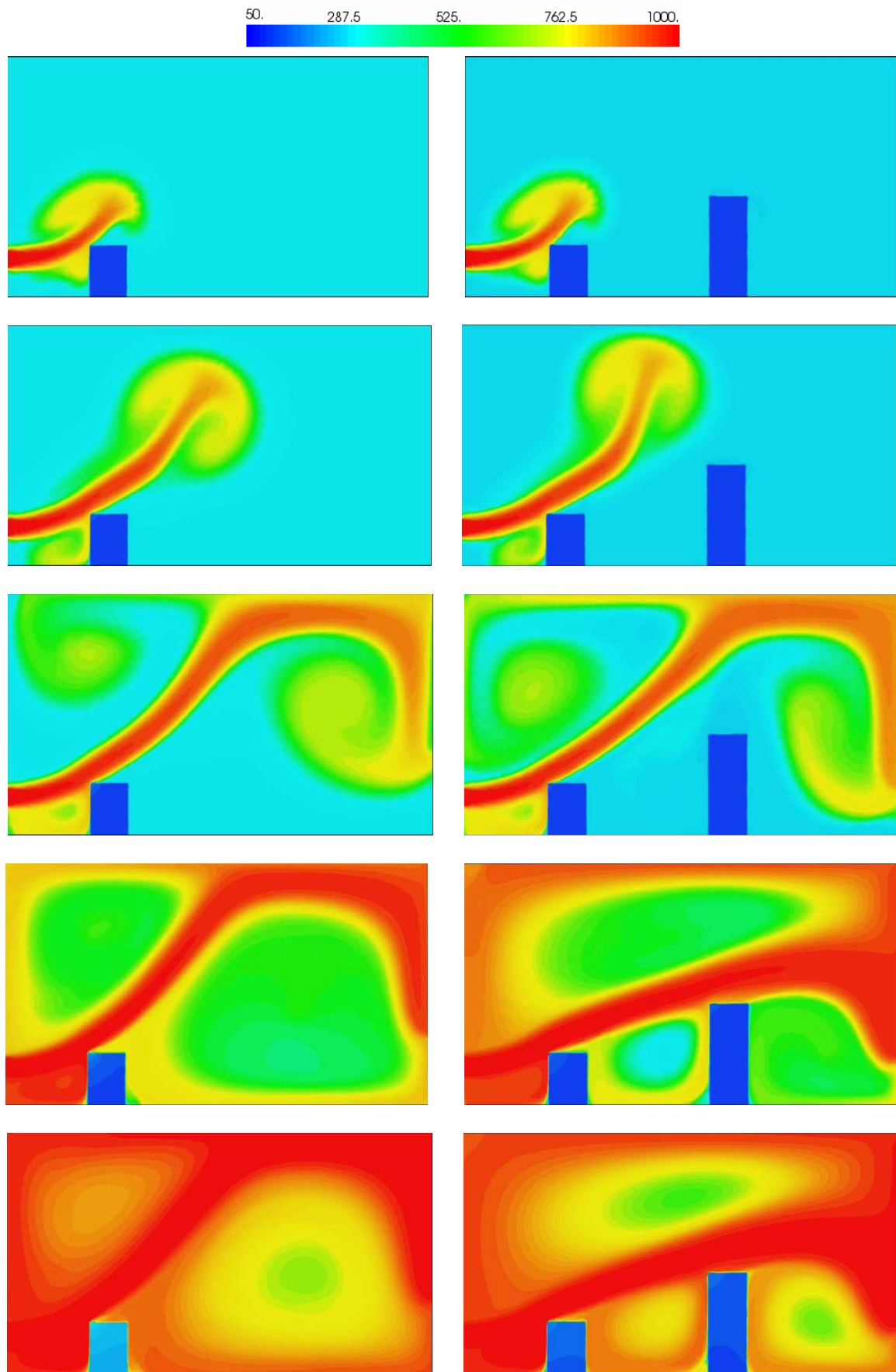
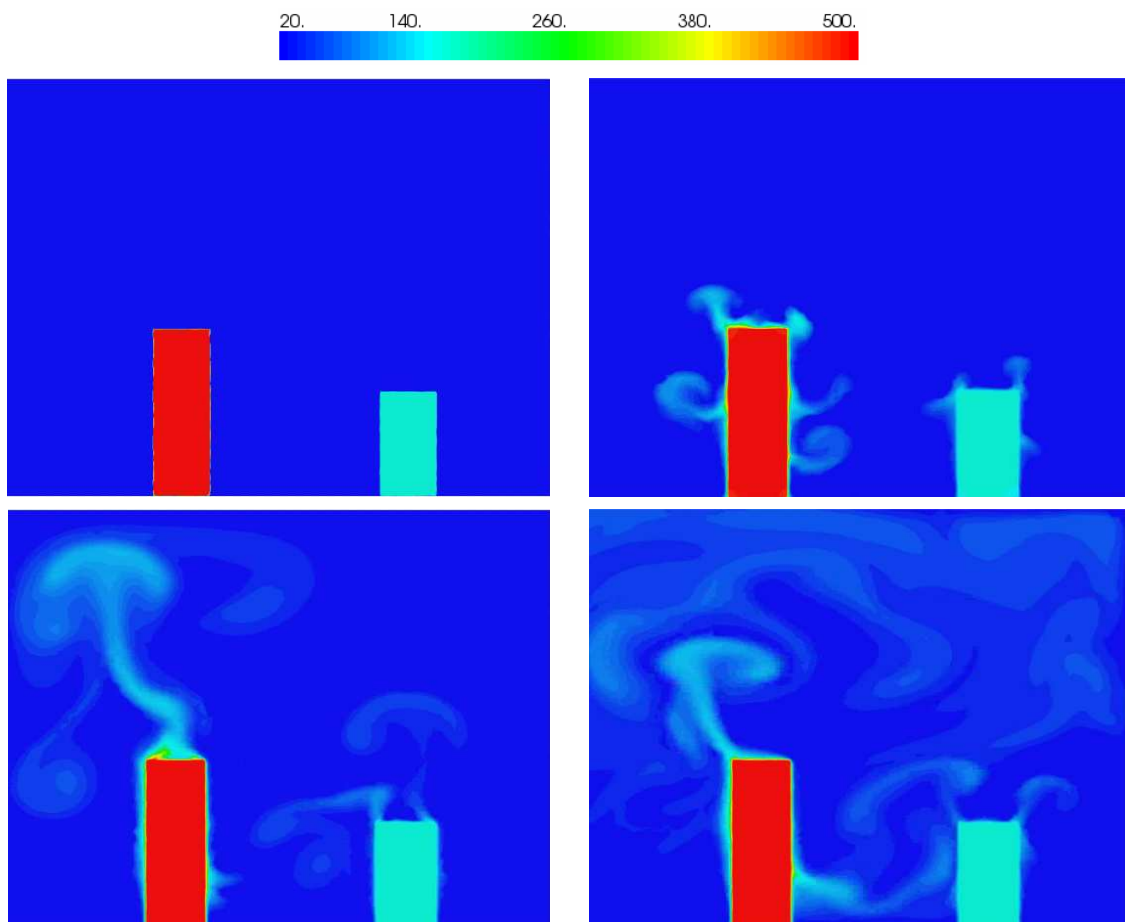


Figure 19. Temperature distribution at different time step

In the next example we consider the air-cooling by natural convection of the heated ingots. Natural convection in an enclosed container has received a great deal of attention by research community due to the importance in many engineering devices. Most of the research has concentrated on the vertical differentially heated square problem where one side wall is at a relatively hot temperature and the other side wall is at a relatively cold temperature and the top and bottom of the enclosure are adiabatic, while less attention was devoted to the presence of conduction bodies (except recently, [62, 76, 77]).

The radiation effects are assumed to be negligible. We assume that the fluid properties are to be constant, except for the density in the buoyancy term, which allows Boussinesq approximation. The gravitational acceleration is taken parallel to the vertical walls. Figure 20 shows the evolution of the temperature distribution at different time steps inside the simplified enclosure. Initially, the air inside the enclosure has the same cold temperature and is at rest. As the air inside becomes heated by conduction coming from both heated ingots, the temperature increases and the expected recirculation appears. Once again, the geometry of the objects immersed in the enclosure is respected due to the high efficacy of the mesh adaptation [36, 37, 38].



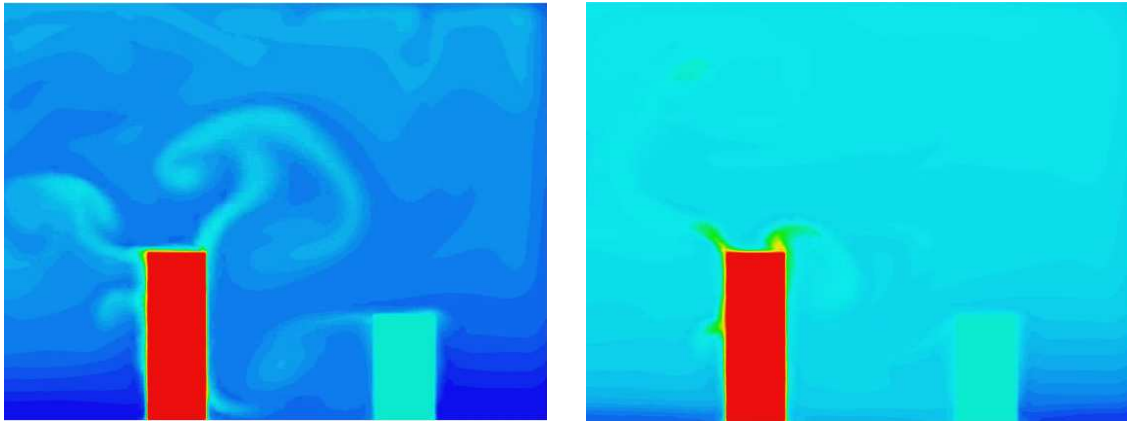


Figure 20. Temperature distribution at different time step

5.4.2 Results and discussion

Three simple numerical computations were presented to assess and illustrate the general ingredients of the IVM method. Although the geometry is simple, we always choose sharp gradients in the temperature and high discontinuity in the material properties to test the effectiveness of the implemented methods and also to be close as much as we can to the real industrial cases.

A very important common characteristic of solid–fluid heterogeneous media is still how to resolve the discontinuity in physical properties across their interfaces. In the IVM method, the level-set function identifies automatically the solid part from the fluid region and applies the anisotropic mesh adaptation at the interface. Conductivities are then calculated using a harmonic mean formulation [32] in order to handle the abrupt changes in the material properties. Thus, we automatically well establish the continuity of temperature and heat flux across the interface.

Also note that the use of high value of the relative kinematics viscosity in solid region would make the velocity components negligibly small by solving the momentum equations and hence the no-slip condition on the refined interface is satisfied. Therefore, the energy equation is reduced to transient heat conduction equation for the solid body, because its convection terms vanish. The implemented stabilized finite element method (section 2.5) is well adapted to the IVM approach and shown to be effective in capturing the thermal shocks at the interface. More examples and comparisons with the literature are given next.

Concerning the solid domain, we have used the penalty method known as Standard Solid Penalty (SSP) approach, which uses simply a constant high viscosity in the solid region to mark the solid body without adding extra constraints.[15]. However, it is also well-known that the involved flow solver can face some problems with strongly discontinuous coefficients. Moreover, the influence of discontinuity that means the viscosity ratio between the solid and the fluid is not clear yet. Since choosing finite value parameters for viscosity as an approximation for the infinite values for real solid can lead to penetration from the surrounding flow into this object. However, this internal diffusion is mainly related to the

actual size of viscosity and the time scale for observing such perturbations may be much larger than the actual time interval calculation. Summing up, the combination of the local mesh adaptation and the use of iterative solvers together with the smoothed distribution of the viscosity across the interface may overcome this drawback and lead to good numerical behaviour.

Since the idea is to investigate how well we can replace boundary conditions between two subdomains by volumetric source terms, various benchmarks, numerical examples and experimental validation are presented in the next sections. Simple 2D and 3D benchmarks to demonstrate the effectiveness of the proposed approach are given in chapter 6. Further investigations on more complex situations will be given. The last section is devoted to the main conclusion and computations for a real industrial furnace.

5.5 Conclusion

The flow regimes have been simulated by solving simultaneously the coupled flow and heat transfer processes inside different enclosures. An immersed volume method is introduced to identify inside each enclosure the surrounding air and the solid subdomains based on the levelset approach. Adaptive anisotropic local grid refinement was employed for capturing the sharp discontinuities of the fluid-solid interface. The temperature variation across the interface was calculated assuming heat flux continuity; for all variables in the computational domain containing solid and fluid, a parametric investigation has revealed that the harmonic formulation for the thermal conductivity provided better predictions against the experimental data available. The IVM approach was tested on two numerical examples showing a promising tool for simulating thermal coupling of solids and fluids. The volumetric radiation was introduced and detailed. Two simple models are implemented and tested. Various benchmarks and more complex numerical examples are given in the next chapter. The numerical results of forced turbulent convection inside industrial furnace are also included.

References

- [1] Houzeaux G, Codina R. An overlapping Dirichlet/Robin domain decomposition method. *Journal of Computational and Applied Mathematics* 2003; 158(2):243-276.
- [2] Felippa CA. Partitioned analysis for coupled mechanical systems. *Engineering Computations* 1988; 5:123-133.
- [3] Principe J, Codina R. A numerical approximation of the thermal coupling of fluids and solids. *International Journal for Numerical Methods in Fluids* 2009; 59:1181-1201.
- [4] Fedkiw R, Aslam T, Merriman B, , Osher S. A non-oscillatory eulerian approach to interfaces in multimaterial flows (the ghost fluid method). *Journal of Computational Physics* 1999; 152:457.
- [5] Fadlun E, Verzicco R, Orlandi P, Mohd-Yusof J. Combined immersed boundary finite difference methods for three-dimensional complex flow simulations. *Journal of Computational Physics* 2000; 161:35-60.
- [6] Peskin CS. The immersed boundary method. *Acta Numerica* 2002; 11:1-39.
- [7] Rixen D, Gosselet P. Domain decomposition methods applied to challenging engineering problems. *16th International Conference on Domain Decomposition Method*, New-York, 2005; 564-581.
- [8] Sukumar N, Moes N, Moran B, Belytschko T. Extended finite element method for three dimensional crack modeling. *International Journal for Numerical Methods in Engineering* 2000; 48(11):1549-1570.
- [9] Bruchon J, Digonnet H, Coupez T. Using a signed distance function for the simulation of metal forming processes: Formulation of the contact condition and mesh adaptation. from a Lagrangian approach to an Eulerian approach. *International Journal for Numerical Methods in Engineering* 2008; online.
- [10] Valette R, Coupez T, David C, Vergnes B. A direct 3D numerical simulation code for extrusion and mixing processes. *International Polymer Processing XXIV* 2009; 2:141-147.
- [11] Bernacki M, Chastel Y, Coupez T. Level set method for the numerical modelling of primary recrystallization in the polycrystalline materials. *Scripta Materialia* 2008; 58(12):1129-1132.
- [12] Gruau C, Coupez T. 3D tetrahedral, unstructured and anisotropic mesh generation with adaptation to natural and multidomain metric. *Computer Methods in Applied Mechanics and Engineering* 2005; 194:4951-4976
- [13] T. Coupez, H. Digonnet, Y. Mesri, Adaptive Anisotropic Parallel Mesh Adaptation with Applications to Interface Capturing Problem, *17 th Mesh Round Table*. Pittsburgh, 2008

- [14] R. N. ELIAS, M. A. D. MARTINS, A. L. G. A. COUTINHO, Simple Finite Element-Based Computation of Distance Functions in Unstructured Grids , *International Journal for Numerical Methods and Engineering*, (72):1095-1110, 2007
- [15] Laure P, Beaume G, Basset O, Silva L, Coupez T. Les méthodes numériques pour les écoulements de fluides chargés. *1er colloque du GDR interactions fluide structure*, 2005.
- [16] T. Coupez, Génération de maillage et adaptation de maillage par optimisation locale. *Revue européenne des éléments finis* 2000; 9(4):403-423.
- [17] Valette R, Bruchon J, Digonnet H, Laure P, Leboeuf M, Silva L, Vergnes B, Coupez T. Méthodes d'interaction fluide-structure pour la simulation multi-échelles des procédés de mélange. *Mécanique et Industries* 2007; 8(3):251-258.
- [18] T. Coupez, Réinitialisation convective et locale des fonctions levelset pour le mouvement de surfaces et d'interfaces, in: *Journées Activités Universitaires de Mécanique*
- [19] T. Coupez, "A mesh improvement method for 3D automatic remeshing". *4th International Conference of Numerical Grid Generation in Computational Fluid Dynamics and Related Fields*. Swansea, Wales 6th - 8th April 1994.
- [20] T. Coupez. Grandes transformations et remaillage automatique. *PhD thesis*, Ecole Nationale supérieure des mines de Paris, 1991.
- [21] Basset O. Simulation numérique d'écoulements multi-fluides sur grille de calcul. *PhD Thesis, Ecole Nationale Supérieure des Mines de Paris* 2006.
- [22] T. Coupez. Parallel adaptive remeshing in 3d moving mesh finite element. In B.K. Soni and al., editors, *Numerical Grid Generation in Computational Field Simulation*, volume 1, pages 783–792. Mississippi University, 1996.
- [23] M. Kimura and H. Notsu. A level set method using the signed distance function, *Japan Journal of Industrial and Applied Mathematics* 19 (2002), no. 3, 415{446.
- [24] Basset O. Simulation numérique d'écoulements multi-fluides sur grille de calcul. *PhD Thesis, Ecole Nationale Supérieure des Mines de Paris* 2006.
- [25] Beaume Grégory. Modélisation et simulation de l'écoulement d'un fluide complexe. *PhD Thesis, Ecole Nationale Supérieure des Mines de Paris* 2008.
- [26] Gruau Cyril, Génération de métriques pour adaptation anisotrope de maillages, applications à la mise en forme des matériaux.. *PhD Thesis, Ecole Nationale Supérieure des Mines de Paris* 2004.
- [27] Bendsoe M., Kikuchi N. 1988 Generating Optimal Topologies in Structural Design Using a Homogenization Method, *Comp. Meth. Appl. Mech. Eng.* 71, 197-224.

- [28] M. Sussman, P. Smereka and S. Osher, A level set approach for computing solutions to incompressible two-phase flow, *Journal of Computational Physics* 114 (1994), pp. 146–159
- [29] O.S. Unverdi and G. Tryggvason, A front-tracking method for viscous, incompressible, multi-fluid flows, *Journal of Computational Physics* 100 (1992), pp. 25–37.
- [30] M. Sussman, A.S. Almgren, J.B. Bell, L.H. Howell, P. Colella and W.L. Welcome, An adaptive level set approach for incompressible two-phase flows, *J. Comput. Phys.* 148 (1999), pp. 81–124.
- [31] M. Kang, R.P. Fedkiw and X.D. Liu, A boundary condition capturing method for multiphase incompressible flow, *J. Sci. Comput.* 15 (2000), pp. 323–360
- [32] S. V. Patankar, Numerical Heat Transfer and Fluid Flow, Series in Computational and Physical Processes in Mechanics and Thermal Sciences, *Taylor & Francis*, 1980.
- [33] G. Iaccarino and S. Moreau, Natural and forced conjugate heat transfer in complex geometries on Cartesian adapted grids, *J. Fluids Eng.* 128 (2006), pp. 838–846
- [34] S. Kang, An improved immersed boundary method for computation of turbulent flows with heat transfer. *Ph.D. Thesis*, Stanford University, 2008.
- [35] Z. Yu, X. Shao and A. Wachs, A fictitious domain method for particulate flows with heat transfer, *J. Comput. Phys.* 217 (2006), pp. 424–452
- [36] B.Glut, T. Coupez and J.-L. Chenot, Automatic mesh generator for complex 2-D domains - Application to moving geometries in forming processes, *Journal of Materials Processing Technology*, 34, pp. 69-76, 1992.*
- [37] T. Coupez and J.-L. Chenot, Mesh topology for mesh generation problems - Application to three-dimensional remeshing, Numerical Methods in Industrial Forming Processes, Ed. by J. L. CHENOT *et al*, A.A. BALKEMA, Rotterdam, pp. 237-242, 1992.
- [38] T. Coupez, Maillage et remaillage automatique 3D par une technique générale d'amélioration de topologie, journée d'étude CSMA "vers l'automatisation des calculs éléments finis", *Edts Jean-Pierre Pelle et Paul-Louis George, INRIA Rocquencourt* (1994)
- [39] T. Coupez, A mesh improvement method for 3d automatic remeshing, In N.P. Weatherill *et al.*, *Numerical Grid Generation in Computational Fluid Dynamics and Related Fields*, pages 615--626. Pineridge Press, 1994.
- [40] T. Coupez, Automatic remeshing in three-dimensional moving mesh finite element analysis of industrial forming, *Numerical Methods in Industrial Forming Processes - NUMIFORM 95*, pages 407--412. A.A. Balkema, 1995.
- [41] T. Coupez, Mesh generation and adaptive remeshing by a local optimisation principle/, in NAFEMS world congress 97, pages 1051--1060. NAFEMS Ltd, Glasgow, 1997.

- [42] T. Coupez, L. Fourment, and J. L. Chenot, Adaptive solutions in industrial forming process simulation, in P. Ladeveze and J. T. Oden, editors, *New Advances in Adaptive Computational Mechanics*, Pages 365--382, Elsevier, 1997.
- [43] T. Coupez, Adaptive meshing for forming processes, in M. Cross *et al*, editor, *Numerical Grid Generation in Computational Field Simulation*, U. of Greenwich (UK), eds. Mississippi State University, 3-19, 1998
- [44] T. Coupez, E. Bigot, 3D Anisotropic mesh generation and adaptation with applications. *European Congress on Computational Methods in Applied Sciences and Engineering*, ECCOMAS 2000, CD-Rom, Barcelona, 2000.
- [45] G. Strotos M. Gavaises A. Theodorakakos G. Bergeles, Numerical investigation of the cooling effectiveness of a droplet impinging on a heated surface, *International Journal of Heat and Mass Transfer*, vol.51(no.19-20), 2008
- [46] 19. Sethian JA, Vladimirov A. Fast methods for the Eikonal and related Hamilton Jacobi equations on unstructured meshes. *Proceedings of the National Academy of Sciences* 2000; 97(11):5699–5703.
- [47] Siegel R and Howell J, Thermal Radiation Heat Transfer, *McGraw Hill*, New York, (1972).
- [48] Cheng P 1966 Dynamics of a radiating gas with applications to flow over a wavy wall *AIAA J.* 4 238–45
- [49] Becker H A, Liu F and Bindar Y 1998 A comparative study of radiative heat transfer modelling in gas-fired furnaces using the simple grey gas and the weighted sum of grey gasses models, *Int. J. Heat Mass Transfer* 41 3357–71
- [50] Siegel R and Howell J R 1981 Thermal Radiation Heat Transfer 2nd edn (New York: Hemisphere)
- [51] Marshak R E 1947 Note on the spherical harmonic method as applied to the milne problem for a sphere, *Phys. Rev.* 71 443–6
- [52] E. Hachem, H. Dignonnet, E. Massoni and T. Coupez, Heat transfer modeling inside industrial furnaces, *8th. World Congress on Computational Mechanics (WCCM8) 5th. European Congress on Computational Methods in Applied Sciences and Engineering (ECCOMAS 2008)*, Venice, 2008
- [53] E. Hachem, E. Massoni and T. Coupez, Immersed volume technique for solving natural convection, conduction and radiation of a hat-shaped disk inside an enclosure, *15th International Conference on Finite Elements in Flow Problems*, Tokyo 2009
- [54] T. Coupez, E. Hachem and H. Dignonnet, Stabilized finite element method for heat transfer and fluid flow inside industrial furnaces, *15th International Conference on Finite Elements in Flow Problems*, Tokyo 2009

- [55] FLUENT computational fluid dynamics software, Version 5. New Hampshire: Fluent Corp.; 1998
- [56] M.F. Modest, Two-dimensional radiative equilibrium of a gray medium in a plane layer bounded by gray non-isothermal walls, *J Heat Transfer* 96C (1974), pp. 483–488.
- [57] M.F. Modest, Radiative equilibrium in a rectangular enclosure bounded by gray non-isothermal walls, *JQSRT* 15 (1975), pp. 445–461
- [58] F. Modest, Radiative heat transfer (2nd ed.), Academic Press, New York (2003).
- [59] R. Siegel and J.R. Howell, Thermal Radiation Heat Transfer (3rd ed.), Hemisphere Publishing Corp., New York (1992).
- [60] G. de Vahl Davis, Natural convection of air in a square cavity, a benchmark numerical solution, *Int. J. Numer. Methods Fluids* 3 (1962), pp. 249–264.
- [61] A. Yucel, S. Acharaya and M.L. Williams, Natural convection and radiation in a square enclosure, *Numerical Heat Transfer* 15 (1989), pp. 261–277
- [62] M. Y. Ha, I.-K. Kim, H. S. Yoon, K. S. Yoon, J. R. Lee, S. Balachandar, H. H. Chun, Two-dimensional and unsteady natural convection in a horizontal enclosure with a square body, *Numerical heat transfer. Part A, Applications* 41 (2) (2002) 183-210.
- [63] W.A. Fiveland, Discrete-ordinates solution of the radiative transport equation for rectangular enclosures, *J Heat Transfer* 106 (1984), pp. 699–706
- [64] W.A. Fiveland (1984). Discrete ordinates solution of the radiative transport equation for rectangular enclosures. *Journal of Heat Transfer, Transactions of ASME*, 106(4), 699–705.
- [65] R.A. Bialecki (1993). Solving Heat Radiation Problems Using the Boundary Element Method, volume 15 of Topics in Engineering. *Computational Mechanics Publications*, Southampton UK and Boston USA.
- [66] Okongo, N., Knight, D., and Zhou, G.2000. Large eddy simulation using an unstructured grid compressible Navier-Stokes algorithm. *International Journal of Computational Fluid Dynamics*13:303-326.
- [67] T. Kloczko. Radiative Heat Transfer: Basics and first simulations. *Technical Report*, CEMEF, 2009.
- [68] T. Kloczko. Immersed volume method for radiative heat transfer: theory and validation. *First International Conference on Computational Methods for Thermal Problem ThermaComp2009* , September 8-10, 2009, Naples, Italy.
- [69] M. Larini, F. Giround, B. Porterier, J.C. Loraud, A multiphase formulation of fire propagation in heterogeneous combustible media, *Int. J. Heat Mass Transfer* 41 (1997) 881-897.

- [70] Deutsch, C.; Vanderhaegen, D., Radiative transfer in statistically heterogeneous mixtures, *AIP Conference Proceedings*, Volume 152, pp. 416-427 (1986).
- [71] Ali, M. M., Chen, T. S., Armaly, B. F.: Natural convection-radiation interaction in boundary layer flow over horizontal surface. *AIAA J.22*, 1797–1803 (1984).
- [72] Hossain, M. A., Pop, I., Ahmed, M.: MHD free convection from an isothermal plate inclined at a small angle to the horizontal. *Int. J. Theor. Appl. Fluid Mech.* (to appear).
- [73] Hossain, M. A., Takhar, H. S.: Radiation effect on mixed convection along a vertical plate with uniform surface temperature. *Heat Mass Transfer* 31, 243–248 (1996).
- [74] K. Huang, M. Ferraro, E. Hachem and K. Mocellin, Study of the radiation and natural convection phenomena, *Post Master Professional Certificate, COMPUMECH Ecole Nationale Supérieure des Mines de Paris*, February 2008
- [75] *Fluent v6.1 User's Guide*, Fluent Inc. (2003).
- [76] M. Y. Ha, J. J. Mi, A numerical study on three-dimensional conjugate heat transfer of natural convection and conduction in a differentially heated cubic enclosure with a heat generating cubic conducting body, *International Journal of Heat and Mass Transfer* 43 (23) (2000) 4229-4248.
- [77] M. K. Das, K. S. K. Reddy, Conjugate natural convection heat transfer in an inclined square cavity containing a conducting block, *International Journal of Heat and Mass Transfer* 49 (2006) 4987-5000.
- [78] Goldin, G. M., and Menon, S. A., 1998, "Comparison of Scalar PDF Turbulent Combustion Models," *Combust. Flame*, 113(3), pp. 442–453.
- [79] Song, G., Bjorge, T., Holen, J., and Magnussen, B. F., 1997, "Simulation Of Fluid Flow And Gaseous Radiation Heat Transfer In A Natural Gas-Fired Furnace," *Int. J. Numer. Methods Heat Fluid Flow*, 7, pp. 169–182.
- [80] Nieckele, A. O., Naccache, M. F., Gomes, M. S. P., and Kobayashi, W., 1997, Numerical Simulation of a Three Dimensional Aluminum Melting Furnace," *Proc. 4th Int. Conf. on Technology and Combustion for a Clean Environment, Portugal*, II (36.3), pp. 15–20.

Chapitre 6

Immersed volume method for solving conjugate heat transfer and turbulent flows

Chapitre 6	219
Immersed volume method for solving conjugate heat transfer and turbulent flows	219
6.1 Immersed volume method for solving natural convection, conduction and radiation of a hat-shaped disk inside an enclosure	221
6.2 Stable mixed-finite element method for incompressible flows with high Reynolds number.....	245
6.3 Finite element solution to handle complex heat and fluid flows in industrial furnaces using the immersed volume method.....	275
6.4 Numerical simulation in a full-scale industrial furnace	303

6.1 Immersed volume method for solving natural convection, conduction and radiation of a hat-shaped disk inside an enclosure

*** see attached paper**

Immersed volume technique for solving natural convection, conduction and radiation of a hat-shaped disk inside an enclosure

E. Hachem^{a,*}, T. Kloczko^{a,1}, H. Dignonnet^{a,2}, T. Coupez^{a,3}

^a Ecole des Mines de Paris, Centre de Mise en Forme des Matériaux (CEMEF), UMR CNRS 7635, Sophia-Antipolis, France

Abstract

An immersed volume method for time-dependent, three-dimensional, conjugate heat transfer and fluid flow is presented in this paper. The incompressible Navier-Stokes equations and the heat transfer equations are discretized using a stabilized finite element method. The interface of the immersed disk is defined and rendered by the zero isovalues of a level set function. This signed distance function allows turning different thermal properties of each component into homogeneous parameters and it is coupled to a direct anisotropic mesh adaptation process providing a better capturing of the interface without affecting the initial background mesh. Thus, a single set of equations is solved for both fluid and solid with different thermal properties which can reduce the computational costs. On the other hand, using stabilized finite element method for the Navier-Stokes and the convection-diffusion equations allows the control of spurious oscillations and thermal shocks yielding very accurate results. The proposed method demonstrates the capability of the model to simulate an unsteady three-dimensional heat transfer flow of natural convection, conduction and radiation in a cubic enclosure with the presence of a conducting body (inconel 718). Results are assessed by comparing the predictions with the experimental data.

Key words: Stabilized Finite Elements, natural convection, heat conduction, radiative transfer, immersion volume technique

1. Introduction

The development of efficient methods to understand and simulate conjugate heat transfer for multi-components systems is one of the most engineering challenges and still a need for industrials, especially in the case of the heat treatment of high-alloy steel by a continuously cooling. Usually, the heat treatment sequence involves heating to a high temperature followed by a controlled cooling so as to enhance the particular microstructures and the combinations of properties such as hardness, toughness and resistance. The most important part for hardening steel results from the cooling of the body in a liquid or a gas that rapidly extracts heat. A good description of the operations performed during heat treating of steel is available in [1] and [2]. It was stated that the rate of cooling in the heated disk depends on the heat removal characteristics of the cooling medium (*e.g.* air), the thermal characteristics of the alloy (*e.g.* inconel 718), and the section thickness of the disk. Fully hardened steel can be only obtained at a sufficiently high rate of cooling conditions. In practice, industrials have to carry out many experimental tests to attain this critical

☆

☆☆

* Corresponding author, Tel.: +33 (0)4 93 95 74 58

Email addresses: Elie.Hachem@mines-paristech.fr (E. Hachem), Thibaud.Kloczko@mines-paristech.fr (T. Kloczko), Hugues.Dignonnet@mines-paristech.fr (H. Dignonnet), Thierry.Coupez@mines-paristech.fr (T. Coupez)

¹ Tel.: +33 (0)4 93 67 89 39

² Tel.: +33 (0)4 93 95 75 94

³ Tel.: +33 (0)4 93 95 75 94

December 2, 2009

rate of cooling. Hence, resorting to numerical experiments is expected to save both time and economical resources. A first step to design an industrial numerical tool for the simulation of involved quenching processes is the modelling of the transient air cooling of a heated body inside an enclosure. The present paper aims at presenting a direct method to study and analyse all the phenomena taking place in such a complex configuration, from a fluid dynamics and heat transfer point of view. We especially insist on the representation of the physical domains (air and solid in the present case), and how to deal with these domains both in terms of accuracy and computational costs. In recent years, there has been increasing interest in studying numerically a variety of engineering applications that involve coupling between different physical phenomena [3, 4, 5]. Most of the time, such analyses may be accomplished by dividing the global domain into several local subdomains over each of which a local model (equation to be solved) can be analyzed independently. The global solution can then be constructed by suitably piecing together local solutions from individually modelled subdomains. However, during the assembly, it is often too cumbersome, or even infeasible, to coordinate the meshes over separate subdomains. Many alternative approaches have been applied for multi-phase flows problems and are available in the literature, such as the ghost-fluid method introduced by Fedkiw *et al.* in [6], the immersed boundary method [7, 8], the domain decomposition [9], the X-FEM [10]. In general, they introduced and improved enrichment functions for material interfaces and voids by means of the level set representations of surfaces. Nevertheless, when using all these techniques, one still need to know the value of the heat transfer coefficients between the two domains which ensures, as a Neumann/Dirichlet boundary conditions, the heat transfer at the air/solid interface. Frequently, industrials perform many experimental tests to obtain such heat transfer coefficients. But, when dealing with a large diversity of shapes, dimensions and physical properties of these metals to quench, such operations can become rapidly very costly and time consuming.

In the present study, the proposed method aims to overcome this drawback by considering a single grid for both air and solid for which only one set of equations need to be solved. This technique, known as immersed volume method (IVM), makes the use of a signed distance function (level-set function method [11, 12]) that allows turning thermal properties of each component into homogeneous parameters. Thus, by solving the whole domain in a fully monolithic way there is no need of empirical data so as to determine the heat transfer coefficient. The heat exchange at the interface is replaced naturally by solving the convective fluid in the whole domain. Additionally, solving the radiative transport equation (RTE) in both domains generates a volume source term rendered by the sharp discontinuity of the temperature and the materials properties. This source term is introduced into the energy equation ensuring the continuous cooling of the hat shaped disk. As a last features of this method, we make the use of our advanced research in the anisotropic mesh adaptation to adapt the interface between two different materials. The proposed mesh generation algorithm allows the creation of meshes with extremely anisotropic elements stretched along the interface, which is an important requirement for conjugate heat transfer and multi-component devices with surface conductive layers [13, 14]. Numerically, the communication between the solid and the fluid is obtained naturally without any further assumption and force modelling. Many research efforts have been devoted to analyze and improve the accuracy, stability, conservation and robustness of the immersed boundary method. This is obviously required when following an interface all along the computations. In our context, the solid, the heated disk, is considered fixed and, consequently, a preadapt meshing is totally affordable. All these cited techniques are explicitly replaced by a locally refined mesh that can, at certain degree, generate a conforming mesh with such low cost.

It is important to mention that the present approach has already been introduced in [15], [16] and in [17], where the strategy is similar but the context is clearly different. In [15], the authors have proposed to use the metric properties of the distance function for simulating two bodies in contacts in a forging process. Details about the formulation of the contact condition, mesh adaptation as well as the computation of the distance function are given. On the other hand, in [16], the use of this method was highlighted by several numerical examples such as extrusion and industrial mixing processes. In [17], this method was adapted to the context of the numerical modelling of recrystallization in a polycrystalline material, the authors illustrate the ability of this approach to accurately describe nucleation and grain growth. Here, we intend to apply the same strategy for simulating conjugate heat transfers and fluid flows inside an enclosure in the presence of a conducting body.

From a numerical point of view, the sudden cooling of hot solid immersed inside a gas fluid is at the origin of so-called thermal shocks which cause spurious oscillations in the solution. In order to circumvent this issue, a stabilized finite element method is used for both Navier-Stokes [18, 19, 20, 21] and the convection-diffusion equations [22, 23, 24]. As far as the radiative terms are concerned, the radiative transfer equation is solved separately using the so-called P-1 method [25].

The outline of the paper is as follows: first, we present the time-dependent, three-dimensional, conjugate heat transfer and fluid flow problem. Section 2 presents the discretization as well as the stabilized finite element method for solving these equations. A detailed description of the immersed volume method using both the level set function and the anisotropic mesh adaptation is given in section 3. In section 4, the numerical performance of the presented method is demonstrated by means of 2D test cases and a 3D real industrial problem. Comparisons with the experimental results are presented. Finally, conclusions and perspectives are outlined.

2. Governing equations

This section is devoted to the mathematical formulation of the 3D heat transfer and fluid flow around a hat-shape disk inside an enclosure. For illustration, figure 20 shows the geometry and the schematic diagram of the treated problem. The governing equations are considered to be three-dimensional, unsteady and incompressible. Thermo-physical and mechanical properties are assumed to depend on both the temperature and the relative position in the computational domain, in fact, discontinuous. Indeed, as mentioned in introduction, the same computational domain is used to represent both gas and solid. More details about the key feature of the proposed monolithic resolution are presented further. The computation of the heat transfer and the fluid flow requires to solve simultaneously the Navier-Stokes and energy equations. Moreover, in order to take into account the radiation effects, the radiative transfer equation has to be solved. Hence, the resulting governing equations are the following:

- i) the dynamic of the flow is given by the Navier-Stokes equations including the Boussinesq approximation:

$$\begin{cases} \nabla \cdot \mathbf{u} = 0 & \text{in } \Omega \\ \rho (\partial_t \mathbf{u} + \mathbf{u} \cdot \nabla \mathbf{u}) - \nabla \cdot (2\mu \boldsymbol{\varepsilon}(\mathbf{u}) - p \mathbf{I}_d) = \rho_0 \beta (T - T_0) \mathbf{g} & \text{in } \Omega \\ \mathbf{u} = \mathbf{0} & \text{in } \partial\Omega \end{cases} \quad (1)$$

where \mathbf{u} is the velocity vector, ρ the density, p the pressure, T the temperature, μ the dynamic viscosity, $\boldsymbol{\varepsilon}(\mathbf{u}) = (\nabla \mathbf{u} + {}^t \nabla \mathbf{u})/2$ the deformation-rate tensor, ρ_0 and T_0 reference density and temperature, β the thermal expansion coefficient and \mathbf{g} the gravity vector.

- ii) the heat transfers are governed by the energy equation:

$$\begin{cases} \rho C_p (\partial_t T + \mathbf{u} \cdot \nabla T) - \nabla \cdot (\lambda \nabla T) = f - \nabla \cdot \mathbf{q}_r & \text{in } \Omega \\ T(\mathbf{x}, t) = T_{\text{wall}} & \text{in } \partial\Omega \\ T(\mathbf{x}, 0) = T_0(\mathbf{x}) & \text{in } \partial\Omega \end{cases} \quad (2)$$

where ρ is the density, C_p the specific heat, λ the heat conduction coefficient of the whole medium. f is the external source term and \mathbf{q}_r is the radiative heat flux that has to be computed.

- iii) the contribution of the radiations to the heat transfers is assessed using the radiative transfer equation (RTE) coupled with the so-called P-1 radiation method. This latter enables to simplify the RTE equation so that the incident radiation is computed by solving the following system:

$$\begin{cases} \nabla \cdot \left(\frac{1}{3\kappa} \nabla G \right) - \kappa G = 4\kappa\sigma T^4 & \text{in } \Omega \\ \frac{\partial G_w}{\partial n} = \frac{3\kappa\epsilon_w}{2(2 - \epsilon_w)} (4\sigma T_w^4 - G_w) & \text{in } \partial\Omega \end{cases} \quad (3)$$

where G is the incident radiation, κ is the mean absorption coefficient which is calculated using the Bouger law [26], σ is the Stefan-Boltzmann constant and ϵ_w denotes the emissivity of the wall surfaces. Under grey gas assumption (see [25]), the divergence of radiative flux from equation (2) that accounts for the volumetric radiation is given by:

$$-\nabla \cdot \mathbf{q}_r = \kappa (G - 4\kappa\sigma T^4) \quad (4)$$

3. Immersed Volume Method

The immersed volume method is based on solving a single set of equations for the whole computational domain and treating the different subdomains as a single fluid with variable material properties. This section presents the complete description of the method, which in turn is structured into three subsections: immerse and define the heated object using the level-set function, apply the anisotropic mesh adaptation in the vicinity of the interface solid-air and mix the thermo-physical properties for both domains.

3.1. Level set approach

In many two-phase flows encountered in industrial applications, multi-material properties, such as density and viscosity, vary deterministically across the interface. This discontinuity in the properties makes such flows much involved to model. In particular, simulating conjugate heat transfer for which the three modes, convective, conductive and radiative heat transfer interfere simultaneously is a challenging task. Here, the material distribution between each physical domains and the refined interface are described by means of the so-called level set method. In practice, a signed distance function is used to localize the interface of the immersed body and initialize the desirable properties on both sides of this latter. Recall that in our context, the solid being fixed, the interface is static. Let Ω_f , Ω_s and Γ_i be respectively the fluid domain, the solid domain and the interface. They verify:

$$\Omega_f \cup \Omega_s = \Omega \quad \text{and} \quad \Omega_f \cap \Omega_s = \Gamma_i \quad (5)$$

For each node of the computational domain Ω , the level set function α which is the signed distance from the interface reads:

$$\alpha(\mathbf{x}) = \begin{cases} > 0 & \text{if } \mathbf{x} \in \Omega_f, \\ 0 & \text{if } \mathbf{x} \in \Gamma_i, \\ < 0 & \text{if } \mathbf{x} \in \Omega_s. \end{cases} \quad (6)$$

The physical and thermodynamic properties in the domain are then smoothed and calculated as a function of α ; for instance, the mixed density is calculated using a linear interpolation between the values of the density in the fluid and the solid:

$$\rho = \rho_f H(\alpha) + \rho_s (1 - H(\alpha)) \quad (7)$$

where H is a smoothed Heaviside function given by:

$$H(\alpha) = \begin{cases} 1 & \text{if } \alpha > \varepsilon \\ \frac{1}{2} \left(1 + \frac{\alpha}{\varepsilon} + \frac{1}{\pi} \sin\left(\frac{\pi\alpha}{\varepsilon}\right) \right) & \text{if } |\alpha| \leq \varepsilon \\ 0 & \text{if } \alpha < -\varepsilon \end{cases} \quad (8)$$

where ε is a small parameter such that $\varepsilon = O(h)$, known as the interface thickness, and h is the averaged mesh size in the vicinity of the interface. Further details about the algorithm used to compute the distance are available in [15].

3.2. Anisotropic mesh adaptation

Accurate calculation of the temperature distribution along the air-solid interface is critical for a correct modelling of industrial experiments. When the heat flux is directed through the interface, the difficulty arises due to the discontinuity of the properties of the material across the interface together with the presence of high gradients of temperature. If this latter is not aligned with the element edges, it may intersect the element arbitrarily such that the accuracy of the finite element approach can be compromised. In order to circumvent this issue, the level-set process is thus coupled to an anisotropic mesh adaptation as described in [14]. The idea of this method is to pre-adapt the mesh at the interface. The mesh becomes locally refined which enables to sharply define the interface and to save a great number of elements compared to classical isotropic refinement. This anisotropic adaptation is performed by constructing a metric map that allows the mesh size to be imposed in the direction of the distance function gradient. Let us briefly described the

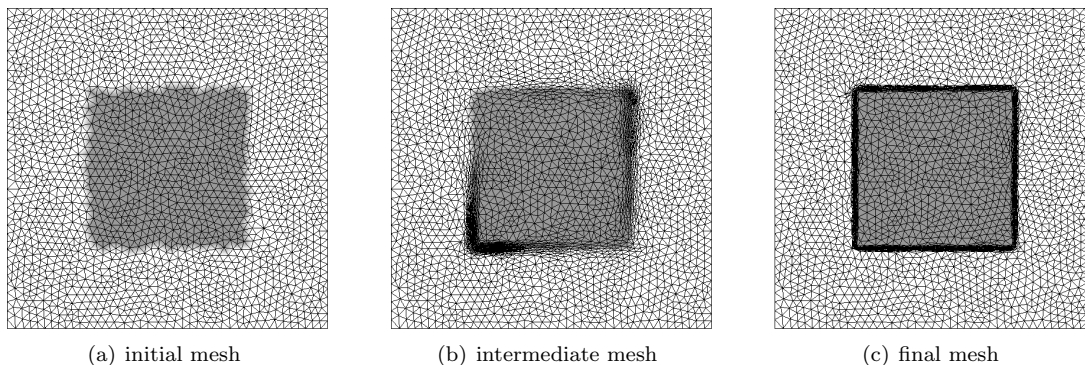


Figure 1: Mesh adaptation process in the vicinity of the interface.

main principles of this technique. First of all, one has to resort to a so-called metric which is a symmetric positive defined tensor representing a local base that modify the distance computation, such that:

$$\|\mathbf{x}\|_{\mathbb{M}} = \sqrt{{}^t\mathbf{x} \cdot \mathbb{M} \cdot \mathbf{x}}, \quad \langle \mathbf{x}, \mathbf{y} \rangle_{\mathbb{M}} = {}^t\mathbf{x} \cdot \mathbb{M} \cdot \mathbf{y}. \quad (9)$$

The metric \mathbb{M} can be regarded as a tensor whose eigenvalues are related to the mesh sizes, and whose eigenvectors define the directions for which these sizes are applied. For instance, using the identity tensor, one recovers the usual distances and directions of the Euclidean space. In our case the direction of mesh refinement is given by the unit normal to the interface which corresponds to the gradient of the level set function: $\mathbf{x} = \nabla\alpha/|\nabla\alpha|$. A default mesh size, or background mesh size, h_d is imposed far from the interface and it is reduced as the interface comes closer. A likely choice for the mesh size evolution is the following:

$$h = \begin{cases} h_d & \text{if } |\alpha(\mathbf{x})| > e/2 \\ \frac{2h_d(m-1)}{m e} |\alpha(\mathbf{x})| + \frac{h_d}{m} & \text{if } |\alpha(\mathbf{x})| \leq e/2 \end{cases} \quad (10)$$

Eventually, at the interface, the mesh size is reduced by a factor m with respect to the default value h_d . Then this size increases until equalling h_d for a distance that corresponds to the half of a given thickness e . The unit normal to the interface \mathbf{x} and the mesh size h defined above, lead to the following metric:

$$\mathbb{M} = C(\mathbf{x} \otimes \mathbf{x}) + \frac{1}{h_d} \mathbb{I} \quad \text{with} \quad C = \begin{cases} 0 & \text{if } |\alpha(\mathbf{x})| \geq e/2 \\ \frac{1}{h^2} - \frac{1}{h_d^2} & \text{if } |\alpha(\mathbf{x})| < e/2 \end{cases} \quad (11)$$

where \mathbb{I} is the identity tensor. This metric corresponds to an isotropic metric far from the interface (with a mesh size equal to h_d for all directions) and to an anisotropic metric near the interface (with a mesh size

equal to h in the direction \mathbf{x} and equal to h_d in the others). In practice, the mesh is generated in several steps using, through the CIMLIB library, the MTC mesher and remesher developed by [13]. Further details on the anisotropic mesh generation can be found in [14]. The proposed mesh generation algorithm works well for 2D or 3D geometries. It allows the creation of meshes with extremely anisotropic elements stretched along the interface, which is an important requirement for conjugate heat transfer and multi-component devices with surface conductive layers. The grid is only then modified in the vicinity of the interface which keeps the computational work devoted to the grid generation low. Note that the proposed method can easily handle arbitrary geometries and the mesh generated is not sensitive to small geometries.

Figure 1 illustrates some steps of the refinement process for a 2D square body immersed in a cavity. At the beginning of the adaptation, the immersed surface of the small squared body is not aligned with the mesh. Several steps are necessary to pre-adapt the interface between both adjoining materials. As shown in figure 2 which presents a close-up on the interface zone at the end of the anisotropic adaptation process, the mesh has been gradually refined when approaching the interface. Consequently, only additional nodes are locally added in this region, whereas the rest of domain keeps the same background size. Note also,

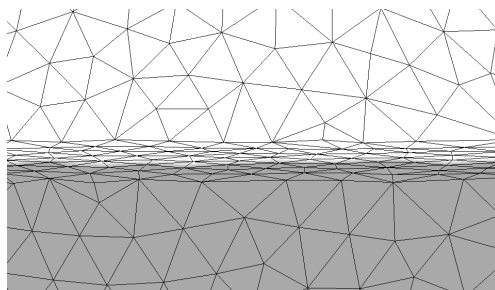


Figure 2: Zoom on the interface zone after anisotropic adaptation

when using an anisotropic mesh, with elements stretched in a 'right' direction, one could allow not only to save a lot of elements but also to well describe the geometry in terms of curvature, angles, etc. Contrary to others techniques, this promising method can provide an alternative to body-fitted mesh for very complex geometry.

3.3. Mixing laws

The geometry and thermodynamic properties of the solid domain are characterized by the signed distance function. The location of the air is then deduced by complementarity and does not require the introduction of an additional distance function. The air-solid mixture can now be treated as a single fluid whose effective properties are defined using mainly linear interpolations between their coefficients as previously evoked in expression (7). The smoothed Heaviside function defined in (8) enables to assign the right properties on each side of the interface. The global material properties introduced in systems of equations (1)-(4), such as density, initial temperature, dynamic viscosity, heat capacity and emissivity, are defined by the following laws:

$$\begin{aligned}
 \rho &= \rho_f H(\alpha) + \rho_s (1 - H(\alpha)) \\
 \mu &= \mu_f H(\alpha) + \mu_s (1 - H(\alpha)) \\
 \rho C_p &= (\rho_f C_{pf} H(\alpha) + \rho_s C_{ps} (1 - H(\alpha))) \\
 \rho C_p T &= \rho_f C_{pf} T_f H(\alpha) + \rho_s C_{ps} T_s (1 - H(\alpha)) \\
 \kappa &= \kappa_f H(\alpha) + \kappa_s (1 - H(\alpha))
 \end{aligned} \tag{12}$$

The use of linear interpolation for the thermal conductivity would lead to inaccurate results. In order to handle this abrupt changes at the interface, we use instead the harmonic mean formulation as suggested by

Patankar [27]:

$$\lambda = \left(\frac{H(\alpha)}{\lambda_f} + \frac{1 - H(\alpha)}{\lambda_s} \right)^{-1} \quad (13)$$

This formulation basically reflects the requirement that diffusion flux should be the same even when calculated by different representative subdomains. Concerning the solid domain, we have used the penalty

Properties	Air	Inconel 718
density ρ [kg/m ³]	1.25	
heat capacity C_p [J/(kg K)]	1000	
viscosity μ [kg/(m s)]	1.9e-5	–
conductivity λ [W/(m K)]	0.0262	
emissivity ϵ	–	0.7

Table 1: Properties of materials.

method known as Standard Solid Penalty (SSP) approach, which uses simply a constant high viscosity in the solid region to mark the solid body without adding extra constraints [28, 29].

3.4. The main objectives

It is noticeable that by immersing the body inside the volume, the interface Γ_i is no more explicitly known and the related surface integrals are no more applicable. The interface is only defined by the zero level of the distance function. In a gas quenching, the domain of temperatures in such heat transfer by radiation is of importance only in an early stage of the quenching process. Only heat transfer by conduction within the metal and by convection between the metal to be quenched and the quenching fluid is of interest in the present paper. The convective thermal transport from a surface to a fluid in motion is known to be related to the heat transfer coefficient h_c , the surface-to-fluid temperature difference, and the wetted surface area Γ_i in the form:

$$q = \int_{\Gamma_i} h_c (T - T_{\text{ext}}) d\Gamma, \quad (14)$$

where T_{ext} is the averaged temperature of the surroundings; and the radiative heat transfer still at the interface

$$\int_{\Gamma_i} \sigma \epsilon (T^4 - T_{\text{ext}}^4) d\Gamma, \quad (15)$$

where σ is the Stefan-Boltzmann constant and ϵ is the emissivity.

Once the object is immersed inside the computational domain using our technique, the need of geometric boundary conditions vanishes and is replaced by the zero level of the level set function. Thus, the boundary conditions (14–15) at the solid’s interface are no longer applicable. Our alternate approach consists in simulating the conjugate heat transfer by solving the coupled problem (1)–(4) for both the surrounding air and the heated object. We emphasize that the computation of the heat transfer coefficient h_c can be a difficult task since it needs experimental data and often requires to solve inverse problem. It can be therefore a limiting issue for practical applications when one needs to change the geometry of the object, the physical parameters, the number and the position of the objects, the surrounding fluid (air, water, etc). On the other hand, our approach can be apply to any complex problem since it only requires the material properties of the different media.

4. Stabilized Finite-Element method

In this section, we describe briefly the Galerkin finite-element approximation and the corresponding stabilization methods for the resulting discrete system of equations (1)-(4). Based on a partition \mathcal{T}_h of Ω into set of N_{el} elements K , the functional spaces for the velocity $V := (H_0^1(\Omega))^{nsd}$ and the pressure $P := C^0(\bar{\Omega}) \cap L_0^2(\Omega)$ are approached by the following finite dimensional spaces spanned by continuous piecewise polynomials:

$$\begin{aligned} V_h &= \left\{ \mathbf{u} \in (H_0^1(\Omega))^{nsd} \mid \mathbf{u}|_K \in P^1(K)^{nsd}, \forall K \in \mathcal{T}_h \right\} \\ P_h &= \left\{ p \in C^0(\bar{\Omega}) \cap L_0^2(\Omega) \mid p|_K \in P^1(K), \forall K \in \mathcal{T}_h \right\} \end{aligned} \quad (16)$$

The weak formulation of the incompressible Navier-Stokes equations reads:

$$\left\{ \begin{array}{l} \text{Find } \mathbf{u} \in V_h \text{ and } p \in P_h \text{ such that:} \\ \forall \mathbf{w} \in V_h, q \in P_h, B(\mathbf{u}; \mathbf{u}, p; \mathbf{w}, q) = 0 \\ B(\mathbf{v}; \mathbf{u}, p; \mathbf{w}, q) = \rho(\partial_t \mathbf{u}, \mathbf{w}) + \rho(\mathbf{v} \cdot \nabla \mathbf{u}, \mathbf{w}) + (2\mu \boldsymbol{\varepsilon}(\mathbf{u}) : \boldsymbol{\varepsilon}(\mathbf{w})) - (p, \nabla \cdot \mathbf{w}) - (f, \mathbf{w}) + (\nabla \cdot \mathbf{u}, q) \end{array} \right. \quad (17)$$

where f is the given force vector. It is well known that the classical finite element approximation for the flow problem may fail because of two reasons: the compatibility condition known by the inf-sup condition or Brezzi-Babuska condition which required an appropriate pair of the function spaces for the velocity and the pressure [30, 31, 32, 33, 24] and when the convection dominates [18]. Therefore, we employ stable finite element formulation based on the enrichment of the functional spaces with space of bubble functions known as Mini element [34, 35, 36]. The special choice of bubble functions enables us to employ static condensation procedure giving rise to a stabilized formulation for equal-order linear element. A detailed description on the implementation of the finite element solver using the P1+/P1-based mixed finite element method can be found in [37, 28, 38].

Equations (2) and (3) can be represented by a single scalar transient convection-diffusion-reaction equation which reads:

$$\partial_t \varphi + \mathbf{u} \cdot \nabla \varphi + \nabla \cdot (\alpha \nabla \varphi) + r \varphi = f \quad (18)$$

where φ is the scalar variable, \mathbf{u} the velocity vector, α the diffusion coefficient, r the reaction coefficient and f a source term. The solution strategy for solving these equations is similar to that used for the equations of motion. Again, the spatial discretization is performed using approximation spaces. Thus, the Galerkin formulation is obtained by multiplying these equations by an appropriate test functions, applying the divergence theorem to the diffusion terms and integrating over the domain of interest. Following the lines on the use of stabilisation methods for transient convection-diffusion-reaction equations as discussed in [24, 39], the stabilized weak form of equation (18) reads:

$$\left\{ \begin{array}{l} \text{Find } \varphi \in S_h \text{ such that, } \forall w \in W_h \\ (\partial_t \varphi + \mathbf{u} \cdot \nabla \varphi, w) + (\alpha \nabla \varphi, \nabla w) + (r \varphi, w) \\ + \underbrace{\sum_K (\mathcal{R}(\varphi), \tau_{\text{SUPG}} \mathbf{u} \cdot \nabla w)_K}_{\text{streamline upwind}} + \underbrace{\sum_K (\mathcal{R}(\varphi), \tau_{\text{SCPG}} \tilde{\mathbf{u}} \cdot \nabla w)_K}_{\text{discontinuity-capturing}} = (f, w) \end{array} \right. \quad (19)$$

where S_h and W_h are standard test and weight finite element spaces (the scalar counterpart of the vector space defined in (16)) and $\mathcal{R}(\varphi)$ is the appropriate residual of equation (18). As shown in equation (19), two additional stabilizing terms were introduced; the first controls the oscillations in the direction of the streamline (SUPG) [18, 40] and the other controls the derivatives in the direction of the solution gradient (SCPG) [41]. This can improve the result for convection dominated problems while the shock-capturing

technique precludes the presence of overshoots and undershoots by increasing the amount of numerical dissipation in the neighborhood of layers and sharp gradients. The evaluation of the τ_{SUPG} and τ_{SCPG} stabilizations terms follows the definition described in [18, 41, 42]. The time derivatives are approximated by the Euler forward difference scheme.

The algebraic problems resulting from the finite element formulation are assembled and solved using the conjugate residual method associated to the incomplete LU preconditioner from the PETSc (Portable Extensive Toolkit for Scientific Computation) library. A master-slave parallel strategy was used [38, 12], involving SPMD (Single Program, Multiple Data) modules and the MPI (Message Passing Interface) library standard. The computations of the 3D conjugate heat transfer have been obtained using 8 2.4 Ghz Opteron cores in parallel (linked by an Infiniband network).

5. Validation for 2D cases

In this section, we want to validate the accuracy and the efficiency of the immersed volume method over relatively simple 2D test cases. All the numerical simulations were carried out by using the CIMLIB finite element library. This C++ library, which is highly parallel, is developed at CEMEF by the team of Coupez and Digonnet (see [38]). The three first simulations are quite academic. The results obtained with our code, referred as IVM, are then compared with those obtained either by analytical solution or by other approaches.

5.1. A one-dimensional example

In this example, already presented and validated in [5], we consider a simple one-dimensional domain with two different materials (fluid and solid). The objective of this test is to check the formulation and implementation of the proposed method by comparing results to the exact solution. The availability of the analytical solution provides a rigorous framework for assessment of solution accuracy. The authors, as in here, have described different aspects related to the numerical approximation of thermal coupling between a fluid and a solid by proposing two alternatives to treat the interface coupling. For more details about the proposed algorithm and their interesting results, consult [5]. The computational domain is split into two subdomains $\Omega_F = [-1, 0]$ and $\Omega_S = [0, 1]$. The distribution of the conductivities, presented in figure 3, is

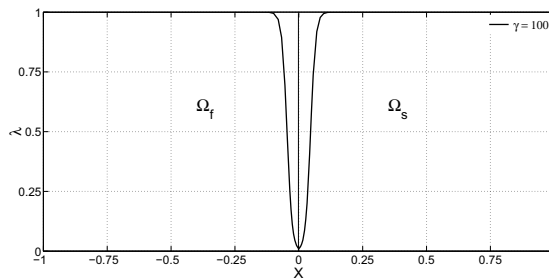


Figure 3: Distribution of thermal conductivity in each subdomain.

given, for both subdomains, by:

$$\begin{aligned} \lambda_F &= \frac{1 - e^{-\gamma}}{1 - e^{-\gamma} + \gamma e^{\gamma x}} \\ \lambda_S &= \frac{1 - e^{-\gamma}}{1 - e^{-\gamma} + \gamma e^{-\gamma x}} \end{aligned} \tag{20}$$

where γ is a measure of the boundary layer width. Dirichlet boundary conditions, namely $T(x = -1) = 1$ and $T(x = 1) = -1$, are applied at both extremities while zero Neumann conditions are applied everywhere else. Subject only to these boundary conditions, the problem can be considered as one-dimensional case for

which the exact solution takes the following form:

$$\begin{aligned} T_F(x) &= \frac{1}{2} \left(-x + \frac{1 - e^{\gamma x}}{1 - e^{-\gamma}} \right) \\ T_S(x) &= \frac{1}{2} \left(-x - \frac{1 - e^{-\gamma x}}{1 - e^{-\gamma}} \right) \end{aligned} \tag{21}$$

By applying the IVM method, the level-set function identifies automatically the solid region from the fluid region and then applies the anisotropic mesh adaptation at the interface. Figure 4 shows the resulting

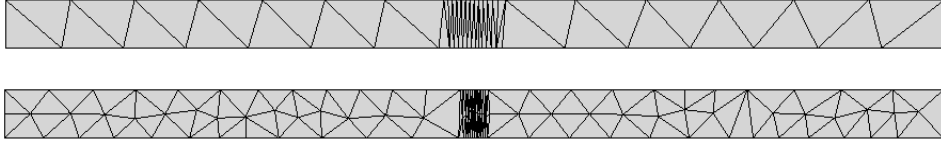


Figure 4: Anisotropic adapted grids. Top: coarse grid with 10 elements in each subdomain. Bottom: fine grid with 20 elements in each subdomain.

unstructured meshes which consists of 10 and 20 elements along the x-direction in each subdomain. The distributions of the temperature along the x-axis are presented in figure 5. The numerical solutions are

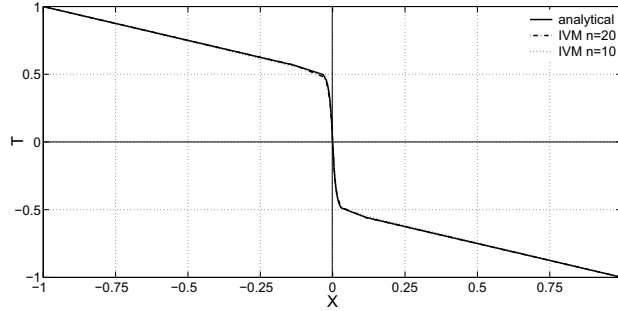


Figure 5: Finite element solution obtained using the IVM with anisotropic adapted meshes of 10 and 20 elements and compared with the analytical solution.

indistinguishable from the analytical solution. This confirms the accuracy of predictions and ability of the code to deliver the right solution of this multi-material problem. Inspired by the reference, we have solved this problem again using three different unstructured meshes of 10, 20 and 40 elements, adapted isotropically near the interface. As expected, some differences can be observed in particular near the interface when using

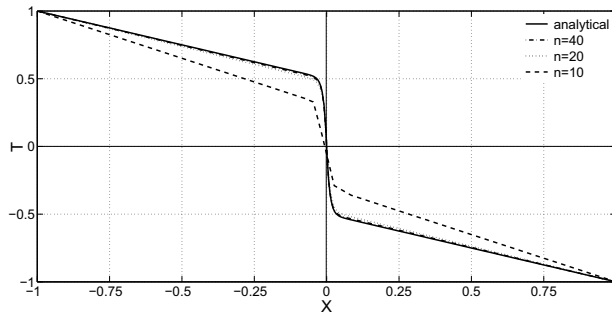


Figure 6: Finite element solution obtained using the IVM with isotropic adapted meshes of 10, 20 and 40 elements and compared with the analytical solution.

coarser meshes (figure 6). Whereas as shown previously in figure 5, the IVM method gives much better results in the case of a coarse discretization. The reason for this behaviour was pointed out in previous section and it is due to the use of extremely anisotropic elements stretched along the interface, which is an important requirement for conjugate heat transfer with surface conductive layers.

5.2. Conduction and radiation heat transfer

In this example, circular and square solids, initially at a temperature of $T = 1000^{\circ}C$, are cooled in presence of air at atmospheric conditions. The cooling process is mainly due to the radiative heat transfer between the hot surface of the bodies and the air. High temperature gradient appears at the interface and a conduction heat transfer between the core and the surface is established leading to the cooling of the whole body. We compute the cooling for both solids using two different methods. The first one, the classical approach, consists in treating the solids as single entities (*cf.* figures 7(a) and 7(c)). The radiative exchange with the surrounding air is computed by the means of the boundary conditions and the use of the heat transfer coefficients (14–15). The second approach, referred as IVM, consists in enlarging the computational

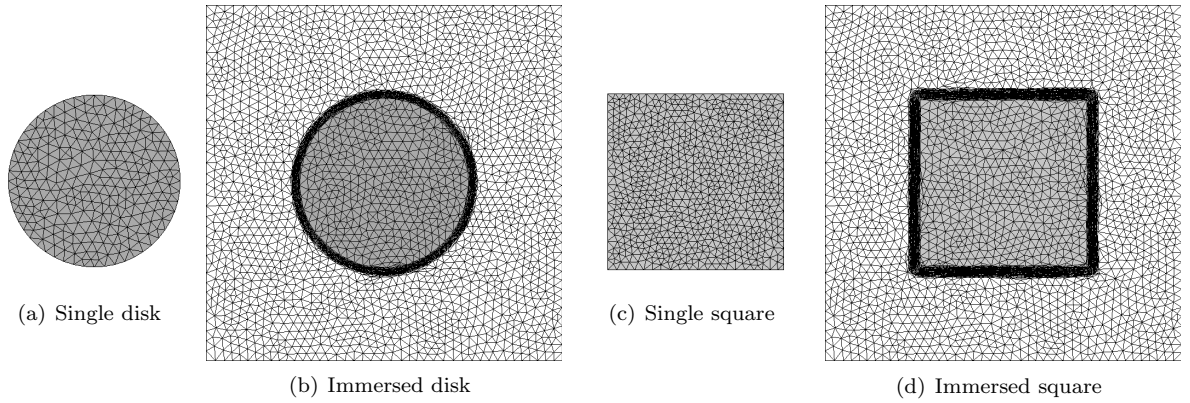


Figure 7: Computational domains for each case and each method.

domain so as to compute the heat transfer in both air and solid domain. The bodies are therefore immersed inside a square cavity filled by the air. The remeshing process coupled to the level set function enables to capture accurately the air-solid interface as shown in figures 7(b) and 7(d). The radiative exchange is naturally taken into account inside the equation without using additional heat transfer coefficients.

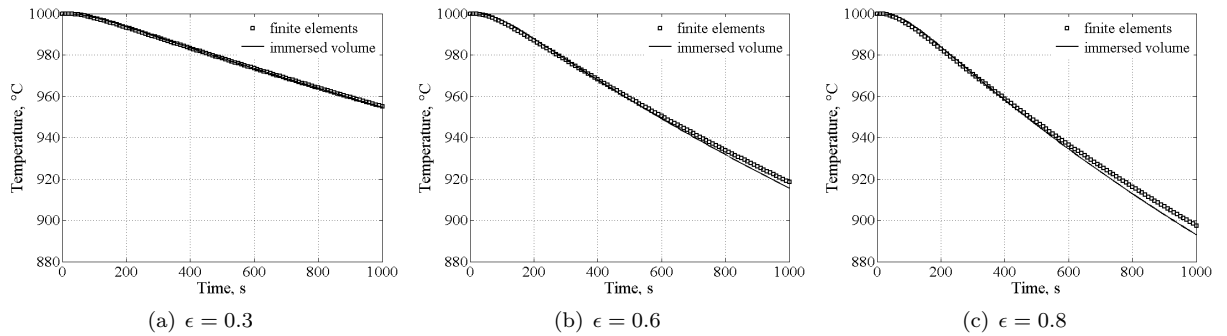


Figure 8: Temperature evolution of a circular body for different emissivity.

Figures 8 to 10 display the distribution of the temperature at different locations inside the solid body and for different emissivities. As can be seen, the agreement is generally good for all stations. However, far from the center and close to the interface, slight differences in the solution are observed. We suspect that the

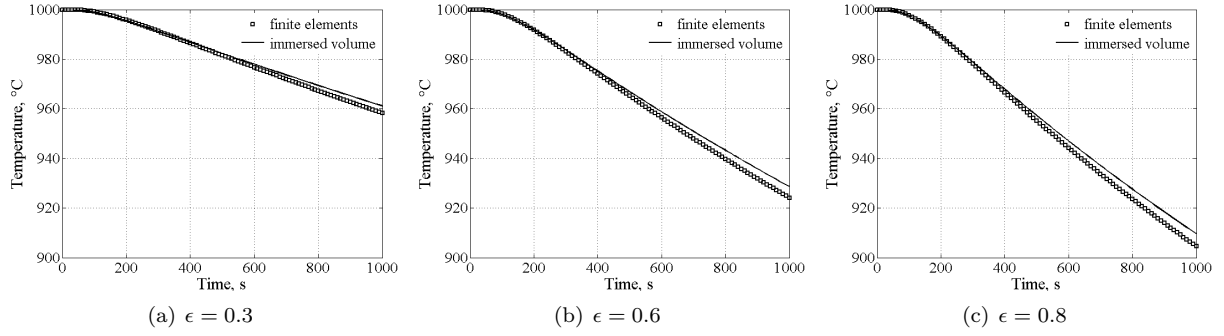


Figure 9: Temperature evolution of a square body for different emissivity.

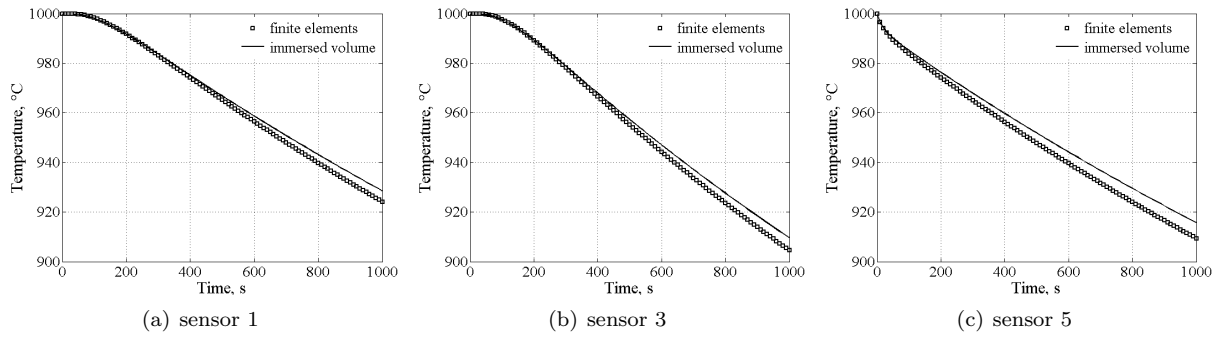


Figure 10: Temperature evolution of a square body with $\epsilon = 0.8$ at different locations.

main discrepancy could be due to the use of the P-1 radiation model which in general neglect the directional influence and known to be a little bit diffusive. However, the approach of this model is relatively simple and computationally cheap.

5.3. Enclosed square body in a differentially heated 2D square cavity

This test has been widely used as a benchmark for numerical methods and has been analyzed by a number of authors ([43], [44], [45], [46], [47]). The velocity and the temperature equations are coupled due

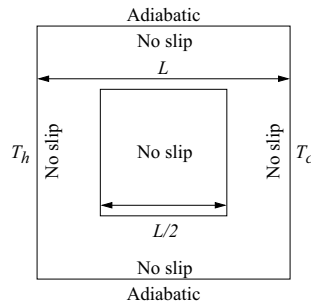


Figure 11: Enclosed square body in a differentially heated 2D square cavity: problem set-up.

to the buoyancy force and solved in the presence of a conducting body placed in the centre of the enclosure. Consequently, the flow inside the enclosure is driven by two temperature differences: the first across the enclosure and the second caused by the squared body. The ratio of these two temperature differences, the thermal conductivity ratio and the heat capacity ratio are very important factors to decide the heat transfer and flow characteristics of the enclosure. Many authors investigated these ratios and the effects of

Rayleigh numbers on variations of streamlines, isotherms and the averaged Nusselt numbers. More details can be found in [46] and [48]. Here, in the present study, the main focus is only restricted to evaluate the performance of the IVM method in terms of multi-domain representation.

The problem description and boundary conditions are shown in figure 11. The left wall is kept at a constant high temperature of T_h , whereas the right wall is kept at a constant low temperature of T_c . Other two walls are maintained at adiabatic condition. The radiation effects are assumed to be negligible. We

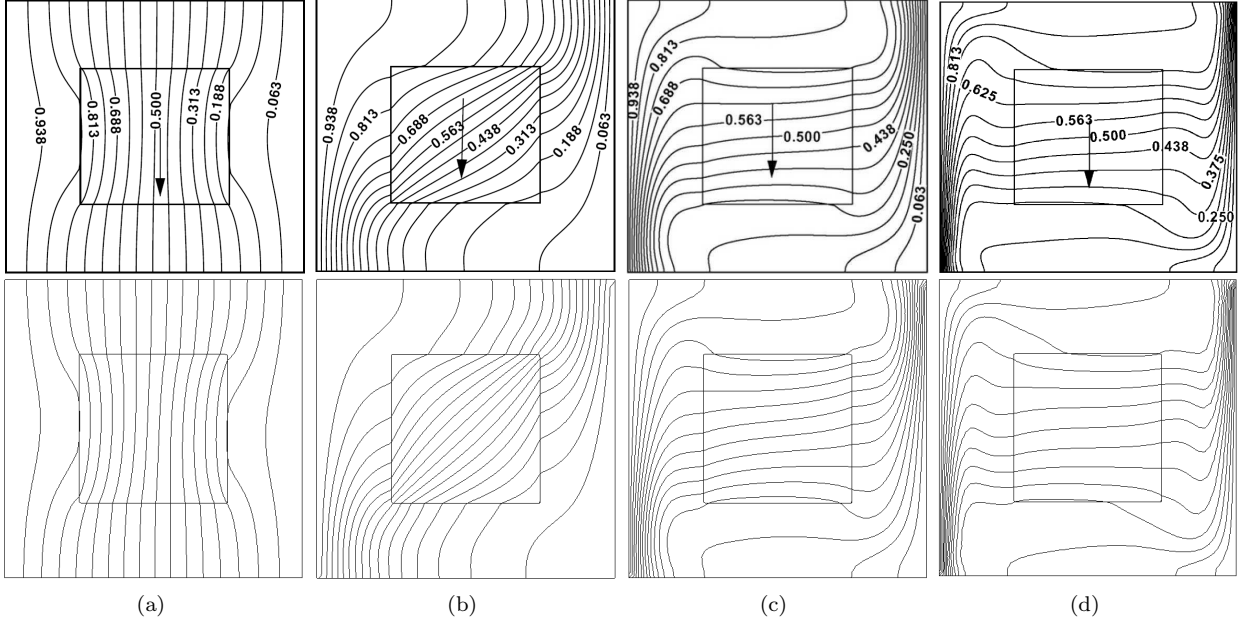


Figure 12: Distribution of isotherms for the conducting body for different Rayleigh numbers: $\lambda^* = 0.2$, (a) $Ra = 10^3$; (b) $Ra = 10^4$; (c) $Ra = 10^5$; (d) $Ra = 10^6$ Top: reference solutions. Bottom: present work.

assume that the fluid properties are to be constant, except for the density in the buoyancy term, which allows Boussinesq approximation. The gravitational acceleration is taken parallel to the isothermal walls. The solid conducting body placed at the centre of the enclosure with thermal conductivity λ_s . The Prandtl number, Pr is taken to be 0.71 corresponding to air. The thermal conductivity ratio $\lambda^* = \lambda_s/\lambda_f$ is taken to be equal 0.2 and 5. Rayleigh number varies from 10^3 up to 10^6 . All these given values were adopted from [49]. In this reference, the authors have investigated also the influence of the angle of inclination of the cavity. Results of their studies are detailed in [49]. By applying the IVM method, the level-set function identifies automatically the solid square body from the fluid region and then applies the anisotropic mesh adaptation at the interface. As noticed in the given reference, when the $\lambda^* = 0.2$, the thermal conductivity of the fluid is 20 times larger than that of heat generating conducting body, consequently the value of maximum temperature in the enclosure decreases slightly with increasing Rayleigh number. The calculated Nusselt number for $Ra = 10^5$ is equal to 4.633 which is in good agreement with the values of [50, 46, 51]. The isotherms obtained from the present calculation for different Rayleigh numbers are shown in figure 12 and compared with results obtained by [49], showing good agreement between them. Same computations have been repeated using different thermal conductivity ratio, $\lambda^* = 5$ (see figure 13). In this case also, good agreement has been obtained by comparing the results with those available in [48] and [49]. It is noticed that with higher values of λ^* , better conductive heat transfer occurs within the squared body and the isotherms are more clustered near the hot and cold walls.

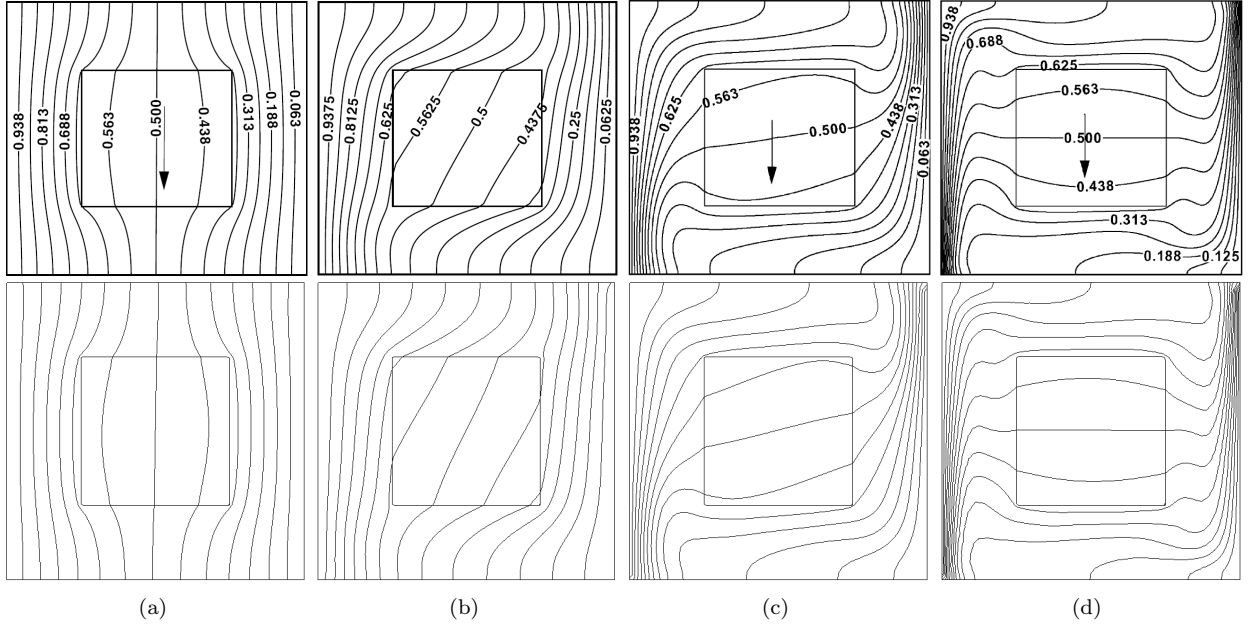


Figure 13: Distribution of isotherms for the conducting body for different Rayleigh number: $\lambda^* = 5$, (a) $Ra = 10^3$; (b) $Ra = 10^4$; (c) $Ra = 10^5$; (d) $Ra = 10^6$. Top: reference solutions. Bottom: present work.

5.4. Mixed convection in a plane channel: the Poiseuille-Bénard flow

In this section, we want to validate the numerical performance of the immersed volume method over a common benchmark involving two-dimensional thermally coupled flows. This test, known as the Poiseuille-Bénard flow, consisting in a channel flow between two infinite parallel plates is frequently used for validating unsteady coupled heat transfer. Both forced and natural convection are present and the limiting flow is time-dependent.

5.4.1. Problem setup

It mainly consists of a two-dimensional laminar flow in a horizontal channel suddenly heated from below under conditions which result in a thermally convective instability. This problem was solved in [52] as a benchmark for open boundary flows using a finite difference method and a fine grid. It has been extensively

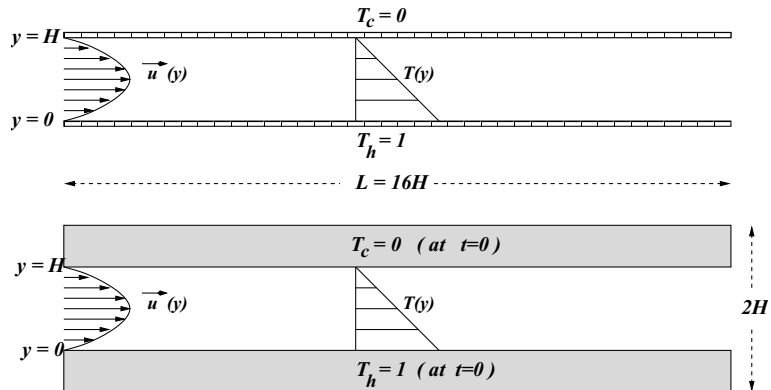


Figure 14: Problem definition

used by other researchers because of its growing interest in many applications and engineering problems such as the fabrication of microelectronic circuits using the chemical vapour deposition process [53, 54].

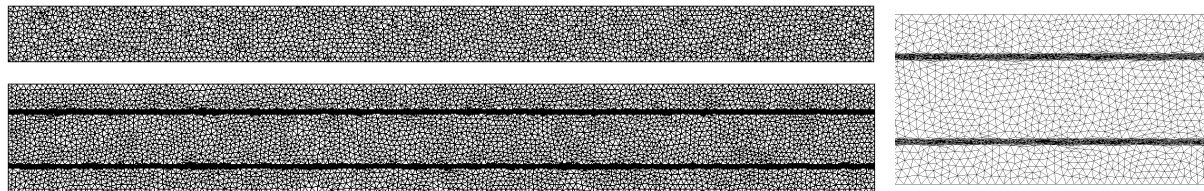


Figure 15: Left: Meshes for single domain and multi-domain cases. Right: close-up on the interface between fluid and solid for the multi-domain case.

Here in our study, two test cases are considered to lead this validation. For both of them, a rectangular enclosure is regarded. However, in order to apply the IVM approach, the domain is enlarged by replacing the top and bottom walls by a solid body (see figure 14). The imposed boundary conditions used in the classical approach are then replaced by two highly conductive solid bodies initially taken at the required temperature. The results obtained using the classical approach with boundary conditions; the IVM method and the reference solutions [52] are then plotted on both domains and compared one to another.

Our purpose is then to first validate the finite element implementation of the coupled problem by comparing our prediction to the given reference, and second, to assess the effectiveness of the IVM method on an extended domain using thick horizontal walls. We expect such conclusions from the following numerical experiments:

- i) The IVM method yields same results as the classical approach from a fluid dynamics, convective flow and heat transfer point of view;
- ii) The proposed approach seems promising to simulate multidomain flows and to replace the use of imposed boundary conditions by corresponding conductive solid bodies.

Several experimental and numerical studies have been carried out on natural/forced convection heat transfer in enclosures under boundary conditions; however, studies about partially divided enclosures are rarely investigated. Such applications range from cooling of electronic devices or industrial workpieces, jet impingement, enhancement of room air, heat exchanger design and many others [55, 56, 57, 58].

The proposed approach seems to be completely suitable for simulating such multi-material problems. It first computes the level set function that identifies automatically the solid part from the fluid region and then applies the anisotropic mesh adaptation at the interface. Thus, a single set of equations (1) is solved for the whole computational domain by treating the different subdomains as a single fluid with variable material properties. Figure 14 shows the two diagrams of the calculation domain and boundary conditions. The first domain consists of the 2D horizontal channel occupying the domain $[0, 16] \times [0, 1]$ and the second one of $[0, 16] \times [0, 2]$. A parabolic inlet velocity profile is prescribed at $x = 0$, whereas the outlet is left free. The top and the bottom walls are respectively maintained at temperatures T_c and T_h in the classical approach (top of figure 14), whereas, for the IVM method, the two additional solid bodies are initially taken at temperature T_c and T_h (bottom of figure 14). Note also that the fluid in the channel is initially linearly stratified in temperature and is flowing with a parabolic velocity distribution.

At solid-fluid interfaces, conductivities are calculated using a harmonic mean formulation [27] in order to handle abrupt changes in the material properties. Thus, we automatically well establish the continuity of temperature and heat flux across the interface. The temperature gradient inside the solid walls is extremely low due to the use of high thermal conductivity ($\lambda = 10^6$).

Moreover, setting the relative kinematics viscosity very high value in the solid regions satisfies the zero velocity in these regions and hence the no-slip condition on the interface is also satisfied. Therefore, the convective terms in the energy equation drop out and the equation reduces to the transient conduction equations in the solid. The stabilized finite element methods are employed to discretized and solve the coupled heat transfer inside the enclosure.

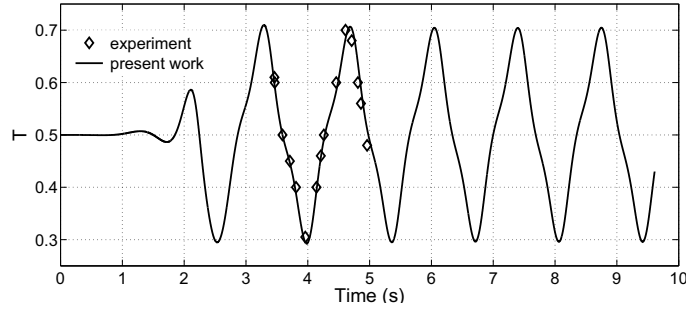


Figure 16: The temperature evolution at the mid-height of the duct compared with the calculations of Evans and Paolucci.

The aim of this numerical test is not to study the effect of conducting horizontal walls in terms of thickness and conductivity ratios, it is more to analyse the general behaviour of the solution on extended domains. The radiation effects are assumed to be negligible. We assume that the fluid properties are to be constant, except for the density in the buoyancy term, which allows Boussinesq approximation. The gravitational acceleration is taken perpendicular to the solid walls.

5.4.2. Analysis of the results

Calculations were carried out using a 10×40 linear triangular elements unstructured mesh and a time step is chosen equal to 0.001 as in [59] to capture the physics accurately. The Reynolds number Re is taken to be equal to 10, the Froude number Fr is fixed at $1/150$ and the Peclet number Pe is $20/3$. For such values, taken from [52], the ratio of forced to natural convections forces is small, the resulting flow consists of transverse travelling waves. In the above definitions, ν and α are the kinematic viscosity and the thermal diffusivity respectively, β is the coefficient of volume expansion and g is the magnitude of the gravitational field.

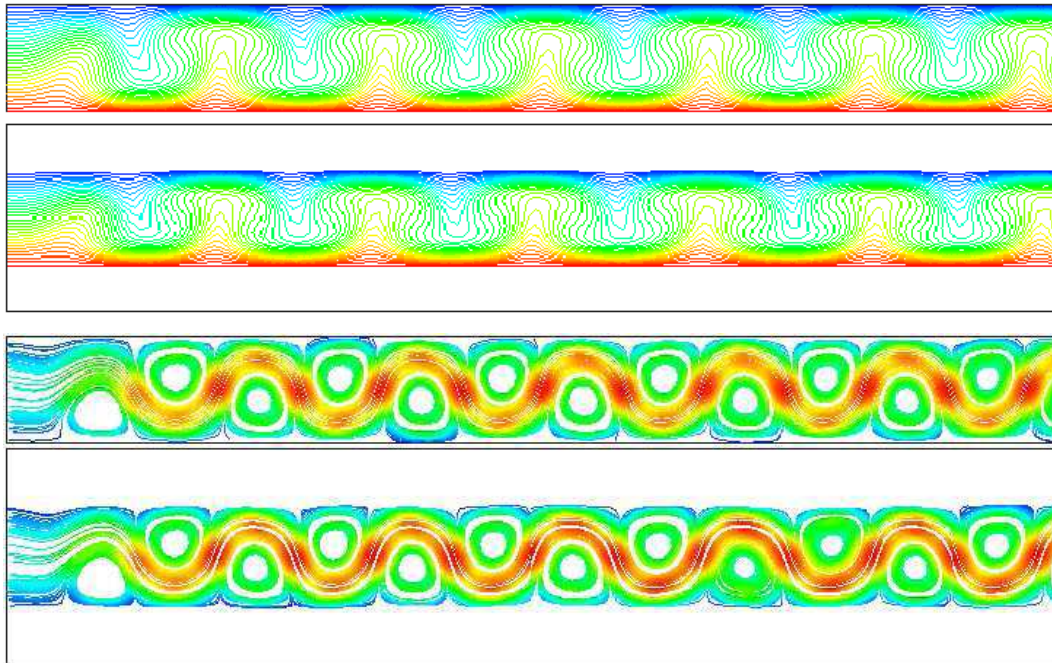


Figure 17: Comparison of the isotherms and the streamlines between the classical approach and the IMV method.

The time history of the temperature T , captured at a mid-height of the duct five channel heights downstream of the entrance $(5, 0.5)$, is shown in figure 16 and compared to a one period evolution from [52]. The agreement between the two calculations shows that the present coupled solvers accurately predicts the temporal behaviour of the temperature. The temporal period of oscillation was predicted by the highest

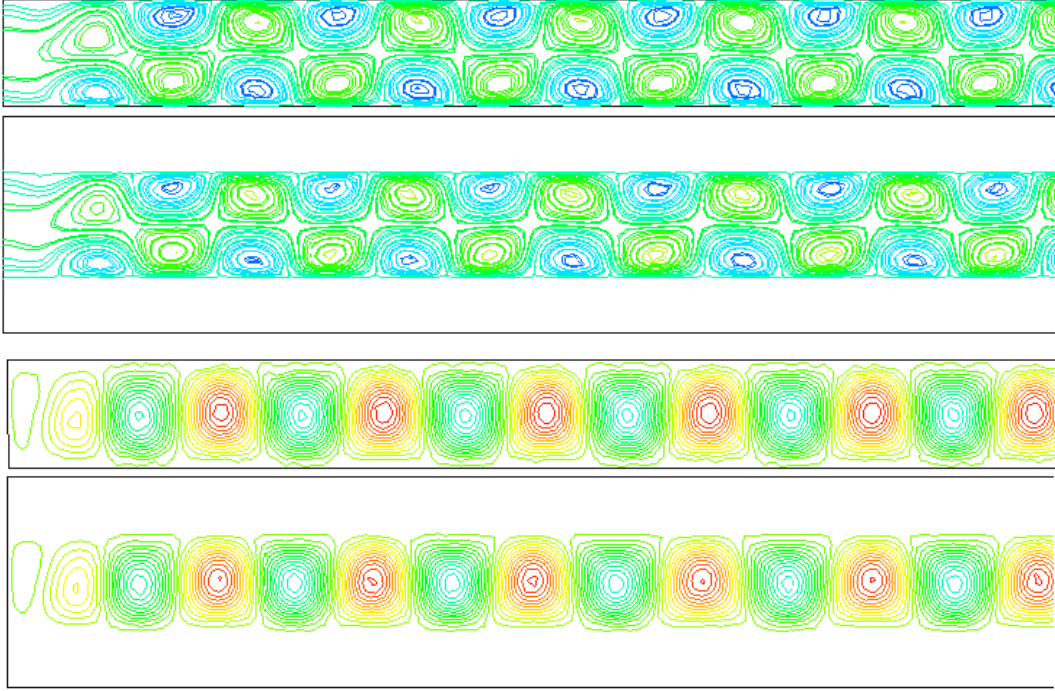


Figure 18: Comparison of the velocity components between the classical approach and the IMV method.

resolution calculation of Evan and paolucci to be 1.306, which is 3.3% less than that predicted by the present calculation, which is 1.35. The difference is not visible in the comparison in figure 16 and can be explained due to the coarser mesh used in the present study. A comparison of isotherms, streamlines, and velocity

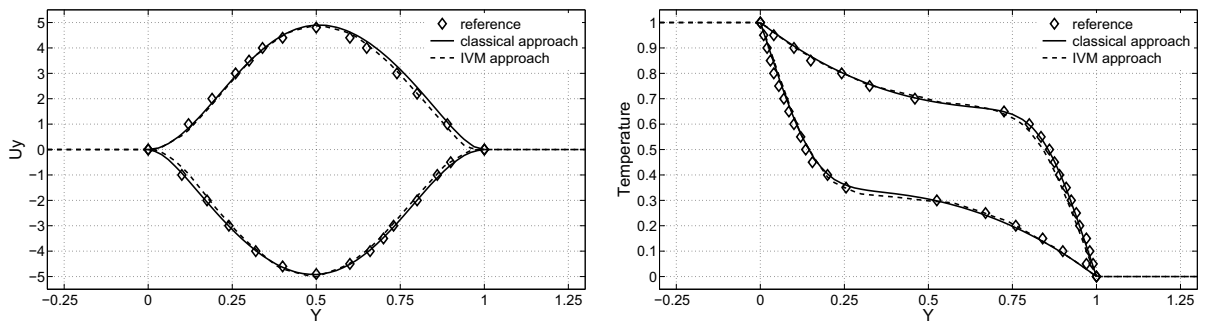


Figure 19: Comparison between an unsteady calculation and the calculations of Evans and Paolucci: the vertical velocities and the temperature.

components at a time t_c that corresponds to a minimum in the temperature at the position $(x = 5.0, y = 0.5)$ between the classical approach (with zero wall thickness) and the IVM approach (with a thick horizontal walls) over the first half of the computed domain are depicted in figures 17 and 18. As shown due to high conductivity and high viscosity of the solid wall, the fluid behaves as the classical approach and both results

are almost identical.

Finally, temperature and velocity distributions along two locations obtained on both domains are illustrated in figure 19 and compared to the reference solutions. Two locations are compared, one at $x = 4.97$ and the other at $x = 10.01$. Those two positions represent a strong negative (resp. positive) value of the vertical velocity where the flow is directed towards the bottom wall (resp. top). Afresh, all the results are almost indistinguishable between both approaches. The temperature profile shows the steep gradient near the hot wall as opposed to the more shallow change near the cool wall on top.

6. Air cooling of an enclosed hat-shaped disk

6.1. Sketch of the experiment

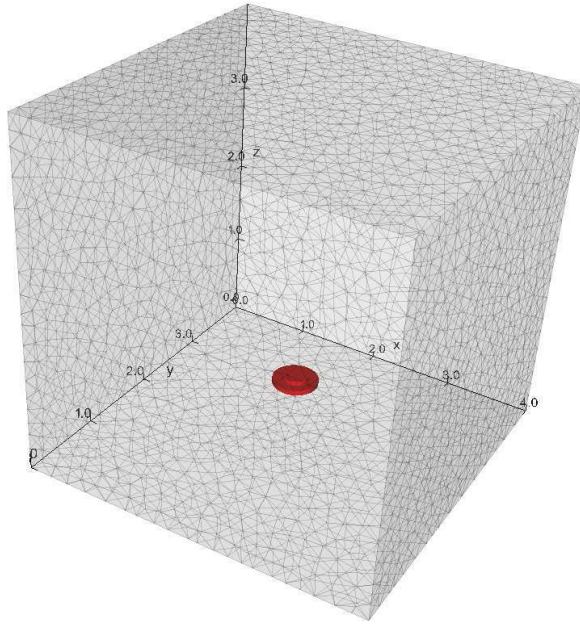


Figure 20: Problem set-up: hat shaped disk inside an enclosure

A 3D Inconel-718 hat shape disk is initially taken at a temperature of $1160\text{ }^{\circ}\text{C}$ and placed inside an enclosure filled by air at atmospheric conditions. The complete set-up of this experiment is given in figures 20 and 23. We start by deriving an anisotropic adapted mesh that describes very accurately the interface between air and solid. In figure 21, one can clearly see that, after a reduced number of steps, the shape of the disk is well respected by the mesh. Only additional nodes are locally added in this region which enables to sharply define the interface, whereas the rest of domain kept the same background size. Once the mesh is well adapted along the interface, the material distribution between each physical domains can be described by means of the level set function (see figure 22). Consequently, the same set of equations (1)-(4) is simultaneously solved over the entire domain including both fluid and solid regions with variable material properties (see table 1). It should be pointed out that the sharp discontinuity of thermal conductivities at the interface between the fluid and the solid regions are handled by harmonic mean formulation. Thus, we automatically well establish the continuity of temperature and heat flux across the interface. Also note that the use of high value of the relative kinematics viscosity in solid region would make the velocity components negligibly small by solving the momentum equations. The energy equation is then reduced to transient heat conduction equation for the solid body, because its convection terms vanish. Summarizing, one can clearly see that regardless the increasing requirement of computational storage and time, the global solution procedure facilitates the code programming, making it possible and easier to solve conjugate heat transfer problem.

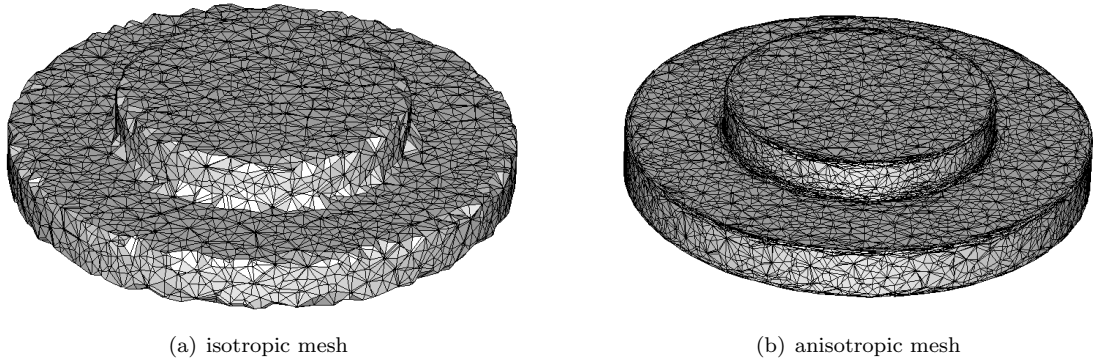


Figure 21: Quality of the interface across the adaptation process.

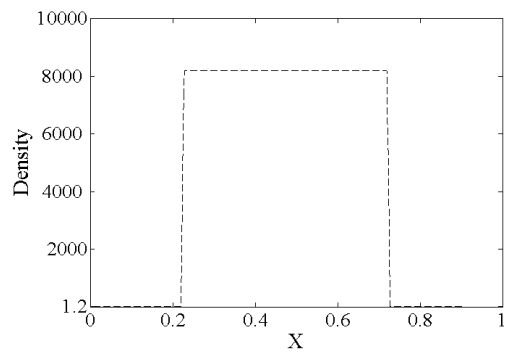


Figure 22: Distribution of the density across the air/solid interface.

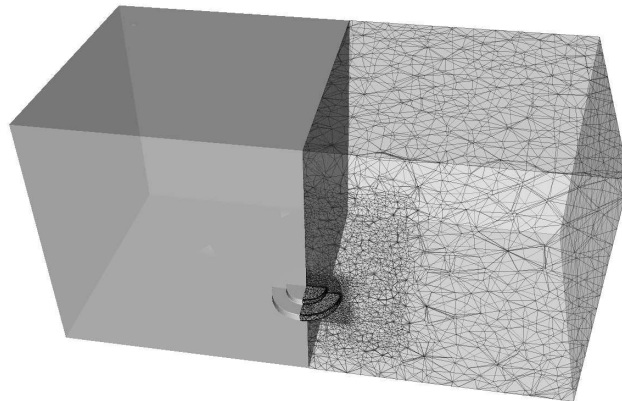


Figure 23: Immersed body in the computational domain.

6.2. Analysis of the results

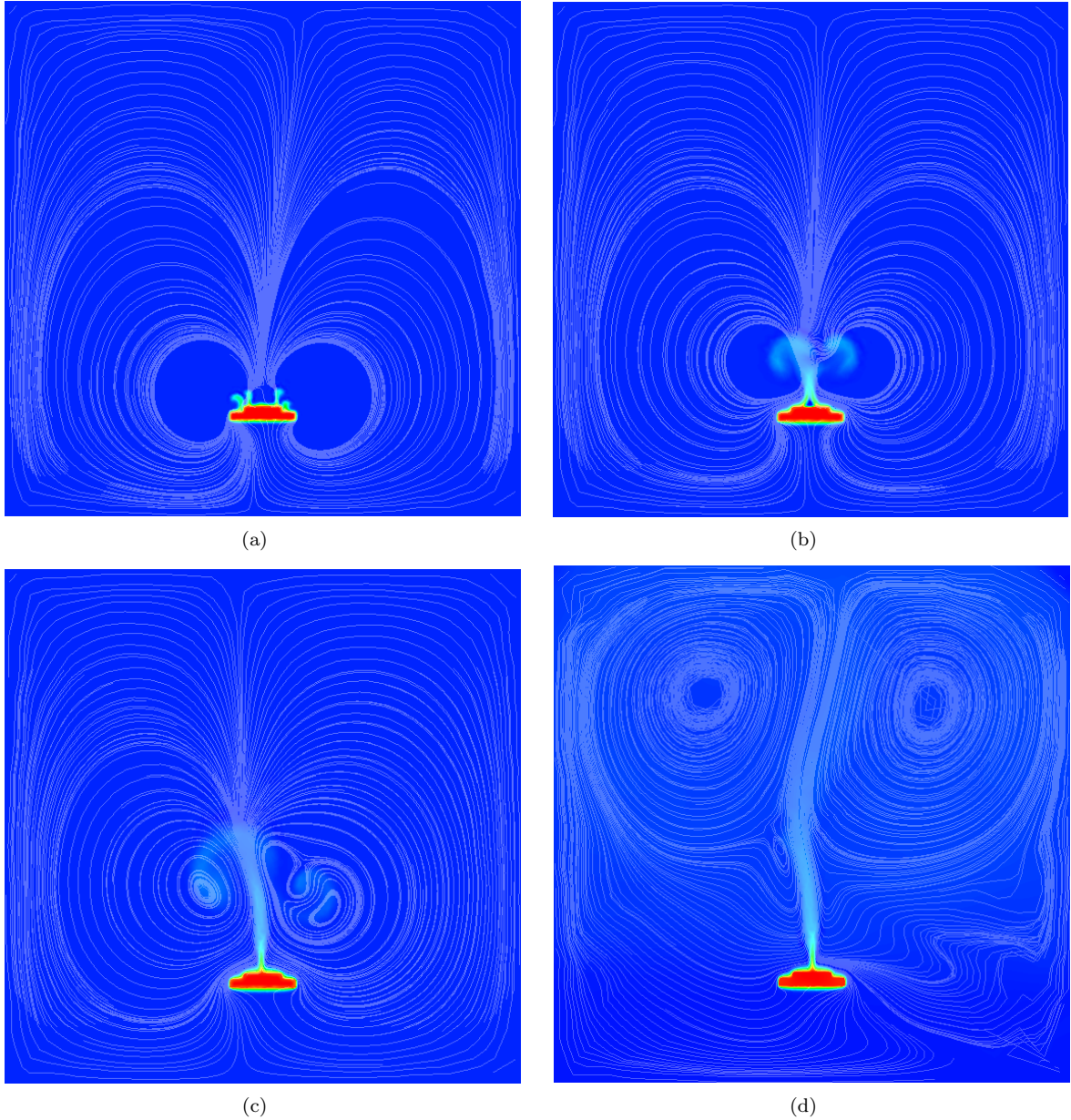


Figure 24: Evolution of temperature distribution and streamlines during the cooling.

Recall that the interface between solid and fluid is only the zero level of the distance function; hence the calculations of the boundary integrals of systems (1)-(4) are no longer applicable. The state of art in this coupled convection-conduction-radiation analysis (1)-(4) lies in that the heat transfer between the solid and the air at the interface has been treated “naturally”, *i.e.* without the use or a previous knowledge of any heat transfer coefficient. Moreover, by solving the P-1 radiative model in both domains it generates a volume source term rendered by the sharp discontinuity of the temperature and the materials properties (*i.e.* emissivity). As shown in the second section, this source term is introduced back into the energy equation ensuring the continuous cooling of the hat shaped disk. Figure 24 shows the evolution of the temperature

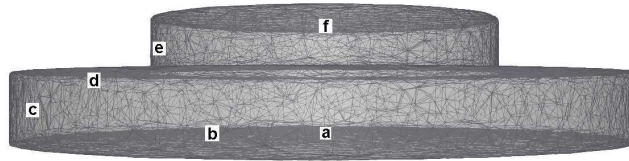


Figure 25: Positions of the thermal sensors

at different time steps as well as the convective effects from the Boussinesq model. The streamlines and the temperature distribution clearly indicate the expected flow pattern. It is characterized by a hot fluid rising above the heated disk in the form of ascending thermal plumes. Once it reaches the top wall, it returns to the heated solid forming two counter-rotating recirculation movements.

6.3. Comparison with experimental data

The hat shaped disk was instrumented with 6 thermal sensors at different locations (see figure 26). Data were acquired via a computer controlled data acquisition system, tabulated and then reported by our industrial partner. A comparison of experimentally measured temperature results with the numerical simulation results at these different locations is shown in figure 26. As can be seen, the agreement is generally good (within $\pm 5\%$) for all stations. However, the discrepancy shown at the top flat surface of the heated disk (sensor f) indicates that a more sophisticated radiative transfer model may be needed to improve solution and account for a better directional influence. This issue will be the subject of further investigations.

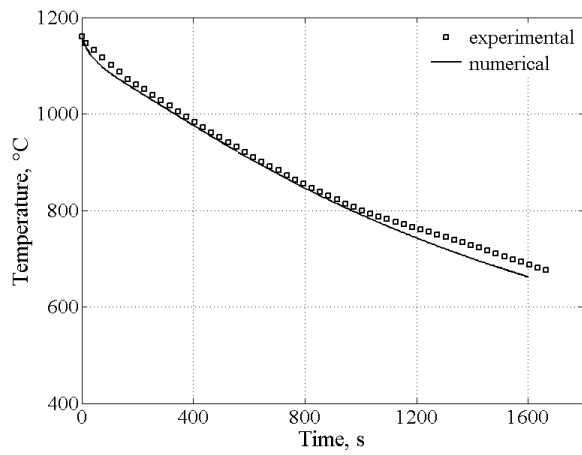
Summing up, for any different geometry, even if we consider a new studied solid, it is shown that the proposed method only requires to define the composite material properties without any knowledge or previous experiment needed to deduce the heat transfer coefficient. It is also worth mentioning that the profiles of the temperature does not suffer from spurious oscillations (undershoots or overshoots) which are frequently observed in the presence of high temperature gradients at the interface or in convection dominated problems across the enclosure. This can be attributed to the stabilization finite element discretization applied on the system of equations (1)-(4).

7. Conclusion

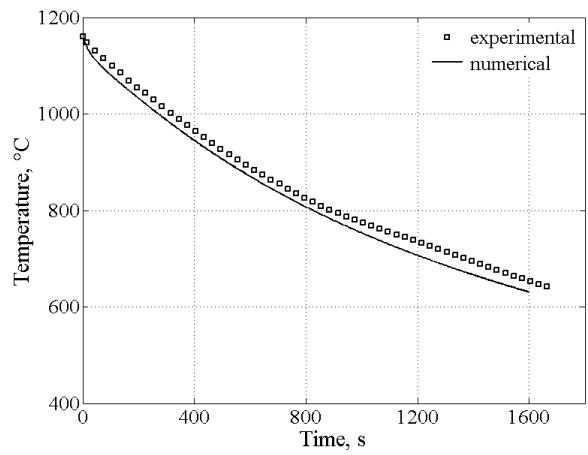
In this paper we have described different aspects related to the numerical approximation of thermal coupling between a fluid and a solid. Our approach, referred as the IVM method, solve one set of equation in both domains with different materials properties. This has allowed us to propose alternatives to classical boundary conditions (mixed-convection and radiation) and heat transfer coefficients that insure the heat exchange between each subdomains. The sharp discontinuity of the material properties was captured by an anisotropic refined solid-fluid interface. The robustness of the method to compute the flow and heat transfer with large materials properties differences is demonstrated. The applications of the stabilized finite element formulations for incompressible flows with thermal coupling to 2D and 3D test problems with conducting bodies were also highlighted. The numerical tests show that the proposed scheme can produce the accurate numerical solutions to unsteady flows. The validation with experimental results for the air cooling of a hat-shaped disk allow us to use the same approach to model similar quenching process in different other conditions without the need of experimentally computed heat transfer coefficients.

Acknowledgment

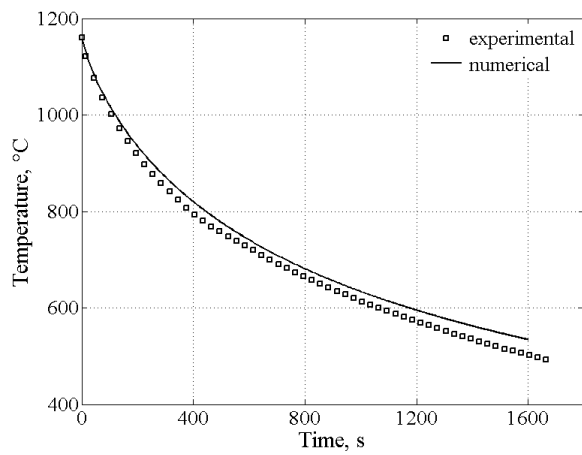
The authors gratefully acknowledge support from the ADEME, CIM Team and the companies involved in the THOST project managed by Science Computer and Consultants (SCC). They are also sincerely grateful to Snecma for supplying the experimental data and the full support for this work.



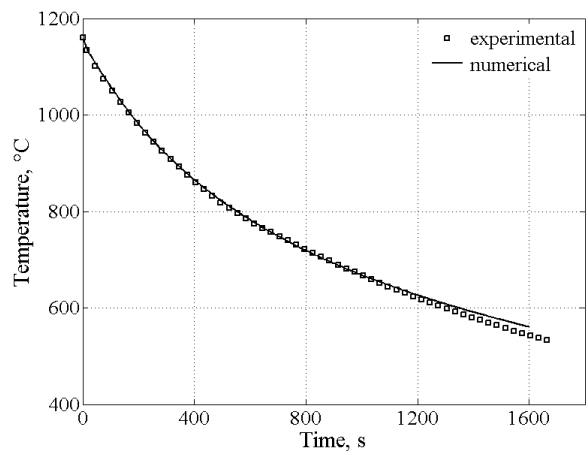
(a)



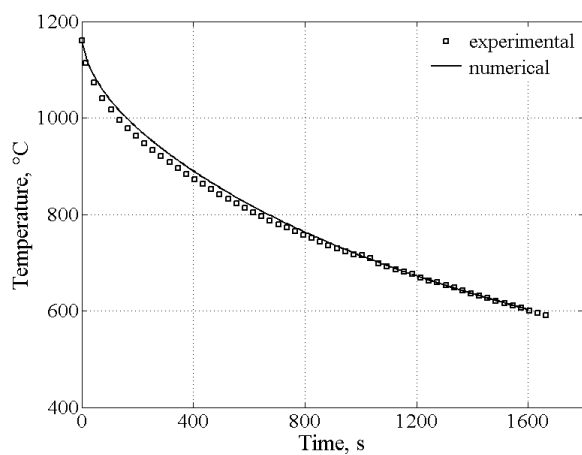
(b)



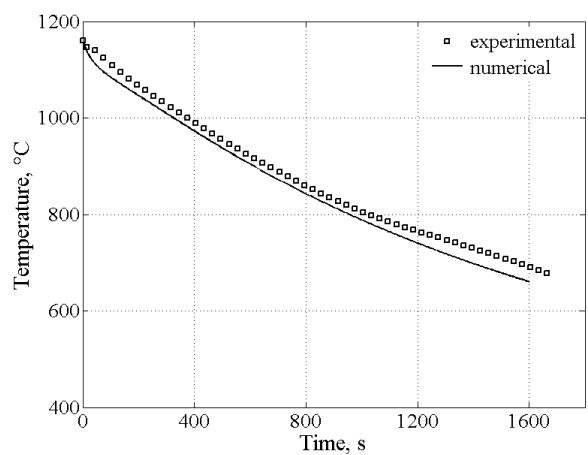
(c)



(d)



(e)



(f)

Figure 26: Comparison of temperature profiles between experimental and numerical results. From top to bottom and from left to right: sensors a, b, c, d, e, f.

References

- [1] G. E. Totten, C. E. Bates, N. A. Clinton, *Quenchants and Quenching Technology*, ASM International, 1993.
- [2] M. De Oliveira, D. R. Garwood, R. A. Wallis, Quenching of aerospace forgings from high temperatures using air-assisted, atomized water sprays, *Journal of Materials Engineering and Performance* 11 (1) (2002) 80–85.
- [3] G. Houzeaux, R. Codina, An overlapping Dirichlet=Robin domain decomposition method, *Journal of Computational and Applied Mathematics* 158 (2) (2003) 243–276.
- [4] C. A. Felippa, Partitioned analysis for coupled mechanical systems, *Engineering Computations* 5 (1988) 123–133.
- [5] J. Principe, R. Codina, A numerical approximation of the thermal coupling of fluids and solids, *International Journal for Numerical Methods in Fluids* 59 (2009) 1181–1201.
- [6] R. Fedkiw, T. Aslam, B. Merriman, S. Osher, A Non-oscillatory Eulerian Approach to Interfaces in Multimaterial Flows (The Ghost Fluid Method), *Journal of Computational Physics* 152 (1999) 457.
- [7] E. Fadlun, R. Verzicco, P. Orlandi, J. Mohd-Yusof, Combined Immersed Boundary Finite-Difference Methods for three-dimensional Complex Flow Simulations, *Journal of Computational Physics* 161 (2000) 35–60.
- [8] C. S. Peskin, The immersed boundary method, *Acta Numerica* 11 (2002) 1–39.
- [9] D. Rixen, P. Gosselet, Domain decomposition methods applied to challenging engineering problems, in: *16th International Conference on Domain Decomposition Method*, New-York, 564–581, 2005.
- [10] N. Sukumar, N. Moës, B. Moran, T. Belytschko, Extended Finite Element Method for Three-Dimensional Crack Modeling, *International Journal for Numerical Methods in Engineering* 48 (11) (2000) 1549–1570.
- [11] T. Coupez, Réinitialisation convective et locale des fonctions level set pour le mouvement de surfaces et d’interfaces, in: *Journées Activités Universitaires de Mécanique*, 2000.
- [12] R. Valette, J. Bruchon, H. Digonnet, P. Laure, M. Leboeuf, L. Silva, B. Vergnes, T. Coupez, Méthodes d’interaction fluide-structure pour la simulation multi-échelles des procédés de mélange, *Mécanique et Industries* 8 (3) (2007) 251–258.
- [13] T. Coupez, Génération de maillage et adaptation de maillage par optimisation locale, *Revue européenne des éléments finis* 9 (4) (2000) 403–423.
- [14] C. Gruau, T. Coupez, 3D Tetrahedral, Unstructured and Anisotropic Mesh Generation with Adaptation to Natural and Multidomain Metric, *Computer Methods in Applied Mechanics and Engineering* 194 (2005) 4951–4976.
- [15] J. Bruchon, H. Digonnet, T. Coupez, Using a signed distance function for the simulation of metal forming processes: Formulation of the contact condition and mesh adaptation. From a Lagrangian approach to an Eulerian approach, *International Journal for Numerical Methods in Engineering* online.
- [16] R. Valette, T. Coupez, C. David, B. Vergnes, A Direct 3D Numerical Simulation Code for Extrusion and Mixing Processes, *International Polymer Processing XXIV* 2 (2009) 141–147.
- [17] M. Bernacki, Y. Chastel, T. Coupez, Level set method for the numerical modelling of primary recrystallization in the polycrystalline materials, *Scripta Materialia* 58 (12) (2008) 1129–1132.
- [18] A. Brooks, T. Hughes, Streamline upwind/Petrov-Galerkin formulations for convection dominated flows with particular emphasis on the incompressible Navier-Stokes equations, *Computer Methods in Applied Mechanics and Engineering* 32 (1982) 199–259.
- [19] L. Franca, S. Frey, Stabilized finite element methods: II. The incompressible Navier-Stokes equations, *Computer Methods in Applied Mechanics and Engineering* 99 (1992) 209–233.
- [20] R. Codina, Stabilization of incompressibility and convection through orthogonal sub-scales in finite element methods, *Computer Methods in Applied Mechanics and Engineering* 190 (13-14) (2000) 1579–1599.
- [21] R. Codina, Stabilized finite element method for the transient Navier-Stokes equations based on a pressure gradient projection, *Computer Methods in Applied Mechanics and Engineering* 182 (3-4) (2000) 277–300.
- [22] F. Brezzi, A. Russo, Choosing bubbles for advection-diffusion problems, *Mathematical Models and Methods in Applied Sciences* 4 (1994) 571–587.
- [23] L. Franca, F. C., Bubble functions prompt unusual stabilized finite element methods, *Computer Methods in Applied Mechanics and Engineering* 123 (1995) 229–308.
- [24] R. Codina, Comparison of some finite element methods for solving the diffusion-convection-reaction equation, *Computer Methods in Applied Mechanics and Engineering* 156 (1998) 185–210.
- [25] M. F. Modest, *Radiative Heat Transfer*, McGraw-Hill, New-York, 1993.
- [26] R. Siegel, J. Howell, *Thermal Radiation Heat Transfer*, Taylor & Francis, New-York, 2002.
- [27] S. V. Patankar, *Numerical Heat Transfer and Fluid Flow*, Series in Computational and Physical Processes in Mechanics and Thermal Sciences, Taylor & Francis, 1980.
- [28] P. Laure, G. Beaume, O. Basset, L. Silva, T. Coupez, Les Méthodes Numériques Pour Les coulements De Fluides Chargés, in: *1er colloque du GDR interactions fluide-structure*, 2005.
- [29] J.-B. Ritz, S. Marie, A Numerical Continuous Model for the Hydrodynamics of Fluid Particle Systems, *International Journal for Numerical Methods in Fluids* 30 (1999) 1067–1090.
- [30] F. Brezzi, J. Douglas, Stabilized mixed methods for the Stokes problem, *Numerische Mathematik* 53 (1988) 225–236.
- [31] F. Brezzi, J. Pitkranta, On the stabilization of finite element approximations of the Stokes problem, *Efficient Solutions of Elliptic Systems*, *Notes on Numerical Fluid Mechanics* 10 (1984) 11–19.
- [32] L. Franca, T. Hughes, Two classes of mixed finite element methods, *Computer Methods in Applied Mechanics and Engineering* 69 (1988) 89–129.
- [33] R. Codina, J. M. González-Ondina, G. Díaz-Hernández, J. Principe, Finite element approximation of the modified Boussinesq equations using a stabilized formulation, *International Journal for Numerical Methods in Fluids* 57 (2008) 1305–1322.
- [34] D. Arnold, F. Brezzi, M. Fortin, A stable finite element for the Stokes equations, *Calcolo* 23 (4) (1984) 337–344.

- [35] F. Brezzi, M. Bristeau, L. Franca, M. Mallet, G. Rog, A relationship between stabilized finite element methods and the Galerkin method with bubble functions, *Computer Methods in Applied Mechanics and Engineering* 96 (1992) 117–129.
- [36] R. Bank, B. Welfert, A comparison between the mini element and the Petrov-Galerkin formulations for the generalized Stokes problem, *Computer Methods in Applied Mechanics and Engineering* 83 (1990) 61–68.
- [37] T. Coupez, S. Marie, From a Direct to a Parallel Iterative Solver in 3D Forging Simulation, *International Journal of Supercomputer Applications And High Performance Computing* 11 (4) (1997) 277–285.
- [38] H. Dignonnet, T. Coupez, Object-oriented programming for fast and easy development of parallel applications in forming processes simulation, in: *Computational Fluid and Solid Mechanics 2003*, 1922–1924, 2003.
- [39] S. Badia, R. Codina, Analysis of a stabilized finite element approximation of the transient convection-diffusion equation using an ALE framework, *Journal on Numerical Analysis* 44 (2006) 2159–2197.
- [40] T. Hughes, L. Franca, M. Balestra, A new finite element formulation for computational fluid dynamics: V. Circumventing the Babuska-Brezzi condition: A stable Petrov-Galerkin formulation of the Stokes problem accommodating equal-order interpolations, *Computer Methods in Applied Mechanics and Engineering* 59 (1987) 85–99.
- [41] A. Galeão, E. do Carmo, A consistent approximate upwind Petrov-Galerkin method for convection-dominated problems, *Computer Methods in Applied Mechanics and Engineering* 68 (1) (1988) 83–95.
- [42] E. Hachem, *Stabilized Finite Element Method for Heat Transfer and Turbulent Flows inside Industrial Furnaces*, Ph.D. thesis, Ecole Nationale Supérieure des Mines de Paris, 2009.
- [43] G. de Vahl Davis, Natural convection of air in a square cavity: a benchmark solution, *International Journal for Numerical Methods in Fluids* 3 (1983) 249–264.
- [44] D. M. Kim, R. Viskanta, Study of the effects of wall conductance on natural convection in differentially oriented square cavities, *Journal of Fluid Mechanics* 144 (1984) 153–176.
- [45] Q.-H. Deng, G.-F. Tang, Numerical visualization of mass and heat transport for conjugate natural convection/heat conduction by streamline and heatline, *International Journal of Heat and Mass Transfer* 45 (2002) 2373–2385.
- [46] M. Y. Ha, J. J. Mi, A numerical study on three-dimensional conjugate heat transfer of natural convection and conduction in a differentially heated cubic enclosure with a heat-generating cubic conducting body, *International Journal of Heat and Mass Transfer* 43 (23) (2000) 4229–4248.
- [47] J. Y. Oh, M. Y. Ha, K. C. Kim, Numerical study of heat transfer and flow of natural convection in an enclosure with a heat-generating conducting body, *Numerical heat transfer. Part A, Applications* 31 (3) (1997) 289–303.
- [48] J. M. House, T. F. Beckermann, C. ad Smith, Effect of a centered conducting body on natural convection heat transfer in an enclosure, *Numerical Heat Transfer* 18 (1990) 213–225.
- [49] M. K. Das, K. S. K. Reddy, Conjugate natural convection heat transfer in an inclined square cavity containing a conducting block, *International Journal of Heat and Mass Transfer* 49 (2006) 4987–5000.
- [50] G. D. Mallinson, G. de Vahl Davis, Three-dimensional natural convection in a box: a numerical study, *Journal of Fluid Mechanics* 83 (1977) 1–31.
- [51] M. Y. Ha, I.-K. Kim, H. S. Yoon, K. S. Yoon, J. R. Lee, S. Balachandar, H. H. Chun, Two-dimensional and unsteady natural convection in a horizontal enclosure with a square body, *Numerical heat transfer. Part A, Applications* 41 (2) (2002) 183–210.
- [52] G. Evans, S. Paolucci, The thermoconvective instability of plane Poiseuille flow heated from below: a proposed benchmark solution for open boundary flows, *International Journal for Numerical Methods in Fluids* 11 (1990) 1001–1013.
- [53] B. J. Curtis, J. P. Dismukes, Effects of natural and forced convection in vapor phase growth systems, *J. Crystal Growth* 17 (1972) 128.
- [54] H. K. Moffat, K. F. Jensen, Three-dimensional flow effects in silicon CVD in horizontal reactors, *J. Electro. Chem. Soc.* 135 (1988) 459–471.
- [55] M. W. Nansteel, R. Greif, Natural convection in undivided and partially divided rectangular enclosures, *Journal of Heat Transfer* 103 (1981) 623–629.
- [56] M. Amin, *International Journal of Heat and Mass Transfer* 34 (1991) 2691–2701.
- [57] D. Olson, L. Glicksman, *Journal of Heat Transfer* 112 (1991) 640–647.
- [58] I. Dagtekin, H. F. Oztop, *International Communications in Heat and Mass Transfer* 28 (2001) 823–834.
- [59] E. A. Sewall, D. K. Tafti, A time-accurate variable property algorithm for calculating flows with large temperature variations, *Computers and Fluids* 37 (2008) 51–63.

6.2 Stable mixed-finite element method for incompressible flows with high Reynolds number

*** see attached paper**

Stable mixed-finite element method for incompressible flows with high Reynolds number

E. Hachem^{1,*,\dagger}, B. Rivaux¹, T. Kloczko¹, H. Dignonnet¹ and T. Coupez¹

¹ *Ecole des Mines de Paris, Centre de Mise en Forme des Matériaux (CEMEF), UMR CNRS 7635, Sophia-Antipolis, France.*

SUMMARY

In the following paper, we discuss some implementation aspects of stabilization finite element methods for the resolution of the 3D time-dependent incompressible Navier-Stokes equations. The proposed method is based on the use of stable mixed formulation, which consists of continuous piecewise linear functions enriched with a bubble function for the velocity and piecewise linear functions for the pressure. This choice of element is stable and satisfies the so-called 'Babuska-Brezzi' condition. However, for simulating high Reynolds number, an extension of this method based on the multiscale approach is used. We assess the behaviour and accuracy of the proposed mixed-stable approximation on two test cases. First, the lid-driven square cavity at Reynolds number up to 50,000 is compared with the highly resolved numerical simulations and second, the lid-driven cubic cavity up to $Re = 12,000$ is compared with the experimental data. Results show that the present implementation is able to exhibit good stability and accuracy properties for high Reynolds number flows using unstructured meshes.

KEY WORDS: mixed-stable finite elements, high Reynolds number, 2D & 3D lid-driven cavity

1. INTRODUCTION

The incompressible Navier-Stokes equations are used to model a number of important physical phenomena, including pipe flow, flow around airfoils, weather, blood flow and convective heat transfer inside industrial furnaces. Significant emphasis has been placed in the literature on developing stabilized formulations robust enough to model complex flows at high Reynolds number [1, 2, 3, 4].

It is known that the Galerkin approximation of the Navier-Stokes equations may fail because of two reasons. Firstly, for convection dominated flows, for which it appears layers where the solution and its gradient exhibit rapid variation, the classical Galerkin approach leads to oscillations of the solution in these layer regions which can spread quickly and pollute the entire solution domain. Secondly, the use of inappropriate combinations of interpolation

*Correspondence to: Ecole des Mines de Paris, Centre de Mise en Forme des Matériaux (CEMEF), UMR CNRS 7635, Sophia-Antipolis, France.

^{\dagger}E-mail: Elie.Hachem@mines-paristech.fr

functions to represent the velocity and pressure fields [5, 6] yields instable schemes. These instabilities associated are usually circumvented by addition of stabilization terms to the Galerkin formulation.

The present work aims at retaining the advantages of using linear approximations (P1 finite elements) regarding the accuracy and the computational cost, especially for 3D real applications. But it is well known that the combination of P1-P1 approximation for the velocity and the pressure does not lead to a stable discretization since it fails to satisfy the Babuska-Brezzi condition.

Many measures may be distinguished to solve and get around these two difficulties, the instabilities in advection-dominated regime and the velocity-pressure compatibility condition. A very popular method was firstly proposed by Arnold, Brezzi and Fortin [7] for the Stokes problem. It was suggested to enrich the functional spaces with space of bubble functions known as Mini-element. Since the bubble functions vanish on each element boundary, they can be eliminated and statically condensed giving rise to a stabilized formulation for equal-order linear element. Later, in [8], it was pointed out that resorting to these local bubbles is equivalent to use residual-based stabilized schemes with a natural way of choosing the stabilization parameters: the selection of the optimal bubble function reproducing the appropriate choice of the stability parameter. Thus, it is clear that the bubble can take different shapes for the diffusive dominated regime and for the advection-dominated flow regime. For example, it was shown in [9, 10] that upwind bubbles could be used to reproduce the SUPG stabilization. A standard reference for mixed finite element methods is the book of Brezzi and Fortin [11]. A brief history on residual based stabilisation methods can be found in Brezzi *et al.* [12], the book of Donea and Huerta [13], all the articles by Hughes *et al.* [14, 15, 16, 17] on multiscale methods and SUPG/PSPG methods by Tezduyar [18]. The Unusual Stabilised finite element method was introduced by Franca and Farhat in [19]. Codina and co-workers introduced lately recent developments of residual based stabilisation methods using orthogonal subscales and time dependent subscales [20, 21, 22, 23]. These methods are very promising and can be regarded as an open door to turbulence. At the same level, one can find a complete description on the use of variational multiscale method for turbulent flows in [24, 25, 26] where a three scale separation method was developed and applied. In diffusion dominant cases, the Mini-element formulation of the problem yields acceptable results. However, when the convection terms dominate, the results can be impaired and an extension for this method is needed. In the past three decades, various numerical methods were developed to overcome this problem [14, 9, 27, 28]. In the present work, the multiscale approach introduced by [29] is applied to deal with the dominance of the inertial term. The main contributions of this work are a systematic study of the variational multiscale method for three-dimensional problems and an implementation of a consistent formulation suitable for large problems with high Reynolds number and unstructured meshes. Using the mixed stable finite element method, we construct a stable scheme for the approximation of the velocity and the pressure and by using the variational multiscale framework we add the needed stabilizing term for the convection dominated problems. We demonstrate the performance of the method for a number of two-dimensional and three-dimensional problems for Reynolds up to 50,000 and 12,000 respectively.

The outline of the paper is as follows: first, we present the time-dependent, three-dimensional, Navier-Stokes problem. In section 3, we present the classical mixed variational formulation to solve the Stokes problem. The stabilizing schemes from a variational multiscale point of view to deal with convection dominated problems is described and presented in

;

section 4. In section 5, the numerical performance of the presented method is demonstrated by means of 2D and 3D test cases. Comparisons with the literature results are presented. Finally, conclusions and perspectives are outlined.

2. THE INCOMPRESSIBLE NAVIER-STOKES EQUATIONS

Let $\Omega \subset \mathbb{R}^{n_{sd}}$ be the spatial domain at time $t \in [0, T]$, where n_{sd} is the number of space dimensions. Let Γ denote the boundary of Ω . We consider the following velocity-pressure formulation of the Navier-Stokes equations governing unsteady incompressible flows:

$$\begin{cases} \rho(\partial_t \mathbf{u} + \mathbf{u} \cdot \nabla \mathbf{u}) - \nabla \cdot \boldsymbol{\sigma} = \mathbf{f} & \text{in } \Omega \times [0, T] \\ \nabla \cdot \mathbf{u} = 0 & \text{in } \Omega \times [0, T] \end{cases} \quad (1)$$

$$\quad (2)$$

where ρ and \mathbf{u} are the density and the velocity, \mathbf{f} the body force vector per unity density and $\boldsymbol{\sigma}$ the stress tensor which reads:

$$\boldsymbol{\sigma} = 2\mu \boldsymbol{\varepsilon}(\mathbf{u}) - p \mathbf{I}_d \quad (3)$$

with p and μ the pressure and the dynamic viscosity, \mathbf{I}_d the identity tensor and $\boldsymbol{\varepsilon}$ the strain-rate tensor defined as

$$\boldsymbol{\varepsilon}(\mathbf{u}) = \frac{1}{2}(\nabla \mathbf{u} + {}^t \nabla \mathbf{u}) \quad (4)$$

Essential and natural boundary conditions for equation (1) are:

$$\mathbf{u} = \mathbf{g} \quad \text{on } \Gamma_g \times [0, T] \quad (5)$$

$$\mathbf{n} \cdot \boldsymbol{\sigma} = \mathbf{h} \quad \text{on } \Gamma_h \times [0, T] \quad (6)$$

Γ_g and Γ_h are complementary subsets of the domain boundary Γ . Functions \mathbf{g} and \mathbf{h} are given and \mathbf{n} is the unit outward normal vector of Γ . As initial condition, a divergence-free velocity field $\mathbf{u}_0(\mathbf{x})$ is specified over the domain Ω_t at $t = 0$:

$$\mathbf{u}(\mathbf{x}, 0) = \mathbf{u}_0(\mathbf{x}) \quad (7)$$

3. CLASSICAL MIXED VARIATIONAL FORMULATION

3.1. Weak formulation of the incompressible Navier-Stokes equations

The function spaces for the velocity, the weighting function space and the scalar function space for the pressure are respectively defined by:

$$V = \{ \mathbf{u}(\mathbf{x}, t) \mid \mathbf{u}(\mathbf{x}, t) \in H^1(\Omega)^{n_{sd}}, \mathbf{u} = \mathbf{g} \text{ on } \Gamma_g \} \quad (8)$$

$$Q = \left\{ p(\mathbf{x}, t) \mid p(\mathbf{x}, t) \in L^2(\Omega), \int_{\Omega} p \, d\Omega = 0 \right\} \quad (9)$$

;

The weak form of the system (1-2) consists in finding $(\mathbf{u}, p) \in V \times Q$ such that:

$$\begin{cases} \rho(\partial_t \mathbf{u}, \mathbf{w})_\Omega + \rho(\mathbf{u} \cdot \nabla \mathbf{u}, \mathbf{w})_\Omega + (\boldsymbol{\sigma}(p, \mathbf{u}), \boldsymbol{\varepsilon}(\mathbf{w}))_\Omega = (\mathbf{f}, \mathbf{w})_\Omega + (\mathbf{h}, \mathbf{w})_{\Gamma_h} & \forall \mathbf{w} \in V_0 \\ (\nabla \cdot \mathbf{u}, q)_\Omega = 0 & \forall q \in Q_0 \end{cases} \quad (10)$$

where $(\varphi, \psi)_\Omega = \int_\Omega \varphi \psi d\Omega$ is the standard scalar product in $L^2(\Omega)$. The Galerkin approximation consists in decomposing the domain Ω into N_{el} elements K such that they cover the domain and there are either disjoint or share a complete edge (or face in 3D). Using this partition \mathcal{T}_h , the above-defined functional spaces (8) and (9) are approached by finite dimensional spaces spanned by continuous piecewise polynomials such that:

$$V_h = \{\mathbf{u}_h \mid \mathbf{u}_h \in C^0(\Omega)^{n_{sd}}, \mathbf{u}_h|_K \in P^1(K)^{n_{sd}}, \forall K \in \mathcal{T}_h\} \quad (11)$$

$$Q_h = \{p_h \mid p_h \in C^0(\Omega), p_h|_K \in P^1(K), \forall K \in \mathcal{T}_h\} \quad (12)$$

The Galerkin discrete problem consists therefore in solving the following mixed problem:

Find a pair $(\mathbf{u}_h, p_h) \in V_h \times Q_h$, such that: $\forall (\mathbf{w}_h, q_h) \in V_{h,0} \times Q_h$

$$\begin{cases} \rho(\partial_t \mathbf{u}_h, \mathbf{w}_h)_\Omega + \rho(\mathbf{u}_h \cdot \nabla \mathbf{u}_h, \mathbf{w}_h)_\Omega \\ \quad + (2\mu \boldsymbol{\varepsilon}(\mathbf{u}_h) : \boldsymbol{\varepsilon}(\mathbf{w}_h))_\Omega - (p_h, \nabla \cdot \mathbf{w}_h)_\Omega = (\mathbf{f}, \mathbf{w}_h)_\Omega + (\mathbf{h}, \mathbf{w}_h)_{\Gamma_h} \\ (\nabla \cdot \mathbf{u}_h, q_h)_\Omega = 0 \end{cases} \quad (13)$$

3.2. Classical mixed formulation: the Stokes problem

This paragraph is devoted to the brief presentation of the classical stable mixed-formulation for the Stokes problem which can be derived by introducing the Mini-element and the corresponding static condensation [11]. This formulation is stable for equal-order interpolation for the velocity and the pressure fields (satisfies the inf-sup condition) and has already been implemented in the CIMLIB library and validated in [30, 31].

The finite element formulation of the classical mixed formulation for the Stokes equations reads:

Find a pair $(\mathbf{u}_h, p_h) \in V_h \times Q_h$, such that:

$$\begin{cases} (2\mu \boldsymbol{\varepsilon}(\mathbf{u}_h) : \boldsymbol{\varepsilon}(\mathbf{w}_h))_\Omega - (p_h, \nabla \cdot \mathbf{w}_h)_\Omega = (\mathbf{f}, \mathbf{w}_h)_\Omega & \forall \mathbf{w}_h \in V_{h,0} \\ (\nabla \cdot \mathbf{u}_h, q_h)_\Omega = 0 & \forall q_h \in Q_h \end{cases} \quad (14)$$

The velocity functional space is enriched by the discrete space associated to the bubble function [7]:

$$V' = \{\mathbf{u}' \mid \mathbf{u}'|_K \in P^1(K)^{n_{sd}} \cap H_0^1(K)^{n_{sd}}, \forall K \in \mathcal{T}_h\} \quad (15)$$

The choice of this bubble function is continuous inside the element, considered as linear on each sub-triangle and vanishes at the boundary of K . The velocity field is now an element of the function space generated by the following direct sum $V_h \oplus V'$. In other words, we use continuous piecewise linear functions enriched by bubbles for the velocity and piecewise linear

;

functions for the pressure. The mixed-finite element approximation of problem (14) can now be written as follows:

Find a pair $(\mathbf{u}, p_h) \in V = V_h \oplus V' \times Q_h$, such that:

$$\begin{cases} (2\mu\boldsymbol{\varepsilon}(\mathbf{u}) : \boldsymbol{\varepsilon}(\mathbf{w}))_{\Omega} - (p_h, \nabla \cdot \mathbf{w})_{\Omega} = (\mathbf{f}, \mathbf{w})_{\Omega} & \forall \mathbf{w} \in V_0 \\ (\nabla \cdot \mathbf{u}, q_h)_{\Omega} = 0 & \forall q_h \in Q_h \end{cases} \quad (16)$$

Since the fine-scale problem is independent and uncoupled at the element level and vanishes on the element boundaries, the system (16) can be decomposed into:

$$\begin{cases} (2\mu\boldsymbol{\varepsilon}(\mathbf{u}_h) : \boldsymbol{\varepsilon}(\mathbf{w}_h))_{\Omega} - (p_h, \nabla \cdot \mathbf{w}_h)_{\Omega} = (\mathbf{f}, \mathbf{w}_h)_{\Omega} \\ (2\mu\boldsymbol{\varepsilon}(\mathbf{u}') : \boldsymbol{\varepsilon}(\mathbf{w}'))_{\Omega} - (p_h, \nabla \cdot \mathbf{w}')_{\Omega} = (\mathbf{f}, \mathbf{w}')_{\Omega} \\ (\nabla \cdot (\mathbf{u}_h + \mathbf{u}'), q_h)_{\Omega} = 0 \end{cases} \quad (17)$$

As the fine-scale space is assumed to be orthogonal to the finite element space, the crossed viscous terms in both equations of (17) vanished [32].

3.3. Matrix formulation

Equations of system (17) give rise to the following global system to solve:

$$\begin{bmatrix} A_{ww} & 0 & {}^t A_{wq} \\ 0 & A_{bb} & {}^t A_{bq} \\ A_{wq} & A_{bq} & 0 \end{bmatrix} \begin{bmatrix} \mathbf{u}_h \\ \mathbf{u}' \\ p_h \end{bmatrix} = \begin{bmatrix} B_w \\ B_b \\ B_q \end{bmatrix} \quad (18)$$

where

$$\begin{aligned} A_{ww}(\mathbf{u}_h) &= (2\mu\boldsymbol{\varepsilon}(\mathbf{u}_h) : \boldsymbol{\varepsilon}(\mathbf{w}_h))_{\Omega} , & A_{bb}(\mathbf{u}') &= (2\mu\boldsymbol{\varepsilon}(\mathbf{u}') : \boldsymbol{\varepsilon}(\mathbf{w}'))_{\Omega} , \\ A_{wq}(\mathbf{u}_h) &= -(\nabla \cdot \mathbf{u}_h, q_h)_{\Omega} , & A_{bq}(\mathbf{u}') &= -(\nabla \cdot \mathbf{u}', q_h)_{\Omega} , \\ {}^t A_{wq}(p_h) &= -(p_h, \nabla \cdot \mathbf{w}_h)_{\Omega} , & {}^t A_{bq}(p_h) &= -(p_h, \nabla \cdot \mathbf{w}')_{\Omega} , \\ B_w &= (\mathbf{f}, \mathbf{w}_h)_{\Omega} , & B_b &= (\mathbf{f}, \mathbf{w}')_{\Omega} , & B_q &= 0 . \end{aligned} \quad (19)$$

The static condensation process consists in solving the second line for the bubble function \mathbf{u}' and inserting the result into the third line of (18) which yields the condensed matrix scheme for large-scale unknowns \mathbf{u}_h and p_h :

$$\begin{bmatrix} A_{ww} & {}^t A_{wq} \\ A_{wq} & \tilde{A}_{qq} \end{bmatrix} \begin{bmatrix} \mathbf{u}_h \\ p_h \end{bmatrix} = \begin{bmatrix} B_w \\ \tilde{B}_q \end{bmatrix} \quad (20)$$

where

$$\tilde{A}_{qq} = A_{bq} A_{bb}^{-1} {}^t A_{bq} \quad \text{and} \quad \tilde{B}_q = {}^t A_{bq} A_{bb}^{-1} B_b \quad (21)$$

It is clear that taking into account locally the influence of fine scales (bubble functions) upon the resolved large scales has introduced new stabilizing terms and has modified the components of the global matrix. The new operator \tilde{A}_{qq} provides a so-called pressure stabilization while the new right hand side \tilde{B}_q ensures consistency. Finally, we obtain a stable mixed formulation for the velocity and pressure system of equations as previously presented in [31].

;

4. STABLE MULTISCALE VARIATIONAL APPROACH

In this section the general equations of time-dependent Navier-Stokes equation are solved. The stabilizing schemes from a variational multiscale point of view are described and presented. The velocity and the pressure spaces are enriched by a space of bubbles that cures the spurious oscillations in the convection-dominated regime as well as the pressure instability.

4.1. Basic principles of the multiscale approach

Following the lines in [29], we consider an overlapping sum decomposition of the velocity and the pressure fields into resolvable coarse-scale and unresolved fine-scale $\mathbf{u} = \mathbf{u}_h + \mathbf{u}'$ and $p = p_h + p'$. Likewise, we regard the same decomposition for the weighting functions $\mathbf{w} = \mathbf{w}_h + \mathbf{w}'$ and $q = q_h + q'$. The unresolved fine-scales are usually modelled using residual based terms that are derived consistently. The static condensation consists in substituting the fine-scale solution into the large-scale problem providing additional terms, tuned by a local time-dependent stabilizing parameter, that enhance the stability and accuracy of the standard Galerkin formulation for the transient non-linear Navier-Stokes equations. In order to represent these fine-scales, different bubble functions (similar to the Mini-element) may be used. The selection of the optimal bubble function reproduces the appropriate choice of the stability parameter [9, 8].

The enrichment of the functional spaces is performed as follows: $V = V_h \oplus V'$, $V_0 = V_{h,0} \oplus V'_0$, $Q = Q_h \oplus Q'$ and $Q_0 = Q_{h,0} + Q'_0$. Thus, the mixed-finite element approximation of problem (13) can read:

$$\begin{aligned} & \text{Find a pair } (\mathbf{u}, p) \in V \times Q, \text{ such that: } \forall (\mathbf{w}, q) \in V_0 \times Q_0 \\ & \left\{ \begin{array}{l} \rho(\partial_t(\mathbf{u}_h + \mathbf{u}'), (\mathbf{w}_h + \mathbf{w}'))_{\Omega} + \rho((\mathbf{u}_h + \mathbf{u}') \cdot \nabla(\mathbf{u}_h + \mathbf{u}'), (\mathbf{w}_h + \mathbf{w}'))_{\Omega} \\ \quad + (2\mu\boldsymbol{\varepsilon}(\mathbf{u}_h + \mathbf{u}') : \boldsymbol{\varepsilon}(\mathbf{w}_h + \mathbf{w}'))_{\Omega} \\ \quad - ((p_h + p'), \nabla \cdot (\mathbf{w}_h + \mathbf{w}'))_{\Omega} = (\mathbf{f}, (\mathbf{w}_h + \mathbf{w}'))_{\Omega} + (\mathbf{h}, (\mathbf{w}_h + \mathbf{w}'))_{\Gamma_h} \\ (\nabla \cdot (\mathbf{u}_h + \mathbf{u}'), (q_h + q'))_{\Omega} = 0 \end{array} \right. \end{aligned} \quad (22)$$

As shown previously, these equations can be split into two sub-problems by separating the two scales. Integrating by parts within each element, we obtain the so-called coarse-scale problem

$$\left\{ \begin{array}{l} \rho(\partial_t(\mathbf{u}_h + \mathbf{u}'), \mathbf{w}_h)_{\Omega} + \rho((\mathbf{u}_h + \mathbf{u}') \cdot \nabla(\mathbf{u}_h + \mathbf{u}'), \mathbf{w}_h)_{\Omega} + (2\mu\boldsymbol{\varepsilon}(\mathbf{u}_h) : \boldsymbol{\varepsilon}(\mathbf{w}_h))_{\Omega} \\ \quad - ((p_h + p'), \nabla \cdot \mathbf{w}_h)_{\Omega} = (\mathbf{f}, \mathbf{w}_h)_{\Omega} + (\mathbf{h}, \mathbf{w}_h)_{\Gamma_h} \quad \forall \mathbf{w}_h \in V_{h,0} \\ (\nabla \cdot (\mathbf{u}_h + \mathbf{u}'), q_h)_{\Omega} = 0 \quad \forall q_h \in Q_{h,0} \end{array} \right. \quad (23)$$

and the fine-scale problem

$$\left\{ \begin{array}{l} \rho(\partial_t(\mathbf{u}_h + \mathbf{u}'), \mathbf{w}')_K + \rho((\mathbf{u}_h + \mathbf{u}') \cdot \nabla(\mathbf{u}_h + \mathbf{u}'), \mathbf{w}')_K + (2\mu\boldsymbol{\varepsilon}(\mathbf{u}') : \boldsymbol{\varepsilon}(\mathbf{w}'))_K \\ \quad - ((p_h + p'), \nabla \cdot \mathbf{w}')_{\Omega} = (\mathbf{f}, \mathbf{w}')_{\Omega} + (\mathbf{h}, \mathbf{w}')_{\Gamma_h} \quad \forall \mathbf{w}' \in V'_0 \\ (\nabla \cdot (\mathbf{u}_h + \mathbf{u}'), q')_{\Omega} = 0 \quad \forall q' \in Q'_0 \end{array} \right. \quad (24)$$

;

To derive our stabilized formulation, we first solve the fine scale problem, defined on the sum of element interiors and written in terms of the time-dependant large-scale variables. Then we substitute the fine-scale solution back into the coarse problem (23), thereby *eliminating the explicit appearance of the fine-scale while still modelling their effects*. At this stage, three important remarks have to be made:

- i) when using linear interpolation functions, the second derivatives vanish as well as all terms involving integrals over the element interior boundaries;
- ii) as the fine-scale space is assumed to be orthogonal to the finite element space, the crossed viscous terms vanish in (23) and (24) [32];
- iii) for the sake of clarity, only Dirichlet boundary conditions are considered, generalization to other types of boundary conditions being straightforward.

4.2. The fine scale sub-problem

Rearranging the terms of equation (24) leads to:

$$\begin{cases} \rho(\partial_t \mathbf{u}', \mathbf{w}')_{\Omega} + \rho((\mathbf{u}_h + \mathbf{u}') \cdot \nabla \mathbf{u}', \mathbf{w}')_{\Omega} \\ \quad + (2\mu \boldsymbol{\varepsilon}(\mathbf{u}') : \boldsymbol{\varepsilon}(\mathbf{w}'))_{\Omega} + (\nabla p', \mathbf{w}')_{\Omega} = (\mathcal{R}_M, \mathbf{w}')_{\Omega} \quad \forall \mathbf{w}' \in V'_0 \\ (\nabla \cdot \mathbf{u}', q')_{\Omega} = (\mathcal{R}_C, q')_{\Omega} \quad \forall q' \in Q'_0 \end{cases} \quad (25)$$

with \mathcal{R}_M and \mathcal{R}_C the momentum and continuity residuals, respectively:

$$\begin{aligned} \mathcal{R}_M &= \mathbf{f} - \rho \partial_t \mathbf{u}_h - \rho(\mathbf{u}_h + \mathbf{u}') \cdot \nabla \mathbf{u}_h - \nabla p_h \\ \mathcal{R}_C &= -\nabla \cdot \mathbf{u}_h \end{aligned} \quad (26)$$

Here, some assumptions have to be made in order to deal with the time-dependency and the non-linearity of the momentum equation of the subscale system (25):

- i) the subscales are not tracked in time, therefore, quasi-static subscales are considered here (see [33] for a justification of this choice); however, the subscale equation remains quasi time-dependent since it is driven by the large-scale time-dependent residual;
- ii) the convective velocity of the non-linear term may be approximated using only large-scale part so that $(\mathbf{u}_h + \mathbf{u}') \cdot \nabla(\mathbf{u}_h + \mathbf{u}') \approx \mathbf{u}_h \cdot \nabla(\mathbf{u}_h + \mathbf{u}')$.

Consequently, the fine-scale problem reduces to the following:

$$\begin{cases} \rho(\mathbf{u}_h \cdot \nabla \mathbf{u}', \mathbf{w}')_{\Omega} + (2\mu \boldsymbol{\varepsilon}(\mathbf{u}') : \boldsymbol{\varepsilon}(\mathbf{w}'))_{\Omega} + (\nabla p', \mathbf{w}')_{\Omega} = (\mathcal{R}_M, \mathbf{w}')_{\Omega} \quad \forall \mathbf{w}' \in V'_0 \\ (\nabla \cdot \mathbf{u}', q')_{\Omega} = (\mathcal{R}_C, q')_{\Omega} \quad \forall q' \in Q'_0 \end{cases} \quad (27)$$

With regard to the work of [31], two important extensions can be identified. The first one consists in considering the advection terms in equation (27) and the second one is that the small-scale pressure is included. These two extensions are essential for simulating high convection-dominated flows. Indeed, it is known, from the works of Wall *et al.* [34], Tezduyar and Osawa [35], that considering the small-scale pressure as an additional variable enables to complete the continuity condition on the small-scale level. It provides additional stability especially when increasing Reynolds number. However, solving the small-scale equation for

;

both the velocity and the pressure is somewhat complicated. Franca and co-workers [5] proposed a separation technique of the small-scale unknowns. They replaced the small-scale continuity equation by the small-scale pressure Poisson equation (PPE). Since only the effect of the small-scale pressure Poisson equation on the large-scale equation must be retained, Franca and Oliveira [36] showed that rather than solving this equation it could be approximated by way of an additional term in the fashion of a stabilizing term as follows:

$$p' \approx \tau_C \mathcal{R}_C \quad (28)$$

In this work, we adopt the definition proposed by Codina in [20] for the stabilizing coefficient:

$$\tau_C = \left(\left(\frac{\mu}{\rho} \right)^2 + \left(\frac{c_2 \|\mathbf{u}\|_K}{c_1 h} \right)^2 \right)^{1/2} \quad (29)$$

where c_1 and c_2 are two constants independent from h , h being the characteristic length of the element. Once this stabilizing coefficient τ_C has been defined, expression (28) can be inserted into the large scale equation (23). Then, it remains to deal with the small scale momentum equation. Codina has shown in [20] that the small scale velocity is exclusively driven by the residual of the large scale momentum equation and not by the residual of the continuity equation. Consequently, in order to eliminate the effects of the small scale pressure in the small scale momentum equation, we impose $p' = 0$. Finally, the method can be regarded as a combination of a stable formulation (Mini-element) plus a stabilizing strategy. Indeed, the stable formulation, described previously for the Stokes problem, is applied to the velocity field while the fine scale pressure is modelled using a stabilizing method.

Now, it remains to solve the small-scale momentum equation. Following Masud and Khurram [27] and without loss of generality, the fine scale fields can be expanded using bubble functions on individual elements:

$$\mathbf{u}' = \sum_{K \in \mathcal{T}_h} \mathbf{u}'_K b_K \quad \text{and} \quad \mathbf{w}' = \sum_{K \in \mathcal{T}_h} \mathbf{w}'_K b_K \quad (30)$$

where b_K represents the bubble shape functions, \mathbf{u}'_K denotes the vector of coefficients for the fine scale velocity field and \mathbf{w}'_K represents the coefficients for the fine scale weighting function. Inserting expressions (30) into the fine scale momentum equation (27) yields:

$$\sum_{K \in \mathcal{T}_h} \rho (\mathbf{u}_h \cdot \nabla b_K \mathbf{u}'_K, b_K \mathbf{w}'_K)_K + (2\mu \boldsymbol{\varepsilon}(b_K \mathbf{u}'_K) : \boldsymbol{\varepsilon}(b_K \mathbf{w}'_K))_K = \sum_{K \in \mathcal{T}_h} (\mathcal{R}_M, b_K \mathbf{w}'_K)_K \quad (31)$$

Since the bubble functions vanish on element boundaries, the previous expression simplifies into:

$$\rho (\mathbf{u}_h \cdot \nabla b_K \mathbf{u}'_K, b_K \mathbf{w}'_K)_K + (2\mu \boldsymbol{\varepsilon}(b_K \mathbf{u}'_K) : \boldsymbol{\varepsilon}(b_K \mathbf{w}'_K))_K = (\mathcal{R}_M, b_K \mathbf{w}'_K)_K \quad \forall K \in \mathcal{T}_h \quad (32)$$

Taking the constant vector of coefficients \mathbf{u}'_K and \mathbf{w}'_K out of the integral and exploiting arbitrariness of \mathbf{w}'_K , one gets:

$$\mathbf{u}'_K = \frac{1}{\rho (\mathbf{u}_h \cdot \nabla b_K, b_K)_K + (2\mu \boldsymbol{\varepsilon}(b_K) : \boldsymbol{\varepsilon}(b_K))_K} \cdot (\mathcal{R}_M, b_K)_K \quad \forall K \in \mathcal{T}_h \quad (33)$$

Assuming that the large scale momentum residual \mathcal{R}_M is constant, the fine scale velocity on each element K can read:

$$\mathbf{u}'|_K = \tau_K \mathcal{R}_M \quad \forall K \in \mathcal{T}_h \quad (34)$$

;

where τ_K is the stabilization parameter which has been naturally obtained after the resolution of the fine scale sub-problem:

$$\tau_K = \frac{b_k \int_K b_k d\Omega}{\rho (\mathbf{u}_h \cdot \nabla b_K, b_K)_K + (2\mu\boldsymbol{\varepsilon}(b_K) : \boldsymbol{\varepsilon}(b_K))_K} \quad \forall K \in \mathcal{T}_h \quad (35)$$

The effect of the bubble is now condensed in this elemental parameter. Obviously, the choice of the bubble functions affects the value of the stability parameter. In expression (35), both convection and viscous regime are represented. However, using the same bubble function for the trial function and the weighting function leads to the cancellation of the convection term. Indeed, under the assumption that \mathbf{u}_h is piecewise constant, the choice of the Mini-element yields:

$$(\mathbf{u}_h \cdot \nabla b_K, b_K)_K = 0 \quad \forall K \in \mathcal{T}_h \quad (36)$$

As pointed out in [9], a way to recover the convection term is to resort to upwind bubbles. Such a choice enables to reproduce naturally the coefficient of the SUPG stabilization method. This issue has been also highlighted by Masud *et al.* in [27], they propose to use different order of interpolation functions for the trial and the weighting functions in the skew part of (35). In order to extract the structure of the stability parameter τ_K , we employ a combination of standard bubble shape function b_K and upwind shape functions b_K^u in the fine scale field \mathbf{w}' :

$$\mathbf{w}'|_K = \mathbf{w}'_K b_K^* = \mathbf{w}'_K (b_K + b_K^u) \quad (37)$$

Introducing the modified \mathbf{w}' into (33) leads to the modified form of the stabilization parameter τ_K :

$$\tau_K = \frac{b_k \int_K b_k^* d\Omega}{\rho (\mathbf{u}_h \cdot \nabla b_K, b_K^*)_K + (2\mu\boldsymbol{\varepsilon}(b_K) : \boldsymbol{\varepsilon}(b_K))_K} \quad \forall K \in \mathcal{T}_h \quad (38)$$

As we use linear interpolations, the upwind part drops out directly in the viscous term.

4.3. The coarse scale sub-problem

Let us consider the coarse scale problem of the expression (23) including the assumptions made for the fine scale fields:

$$\left\{ \begin{array}{l} \rho (\partial_t \mathbf{u}_h, \mathbf{w}_h)_\Omega + (\rho \mathbf{u}_h \cdot \nabla \mathbf{u}_h, \mathbf{w}_h)_\Omega + (\rho \mathbf{u}_h \cdot \nabla \mathbf{u}', \mathbf{w}_h)_\Omega + (2\mu\boldsymbol{\varepsilon}(\mathbf{u}_h) : \boldsymbol{\varepsilon}(\mathbf{w}_h))_\Omega \\ \quad - (p_h, \nabla \cdot \mathbf{w}_h)_\Omega - (p', \nabla \cdot \mathbf{w}_h)_\Omega = (\mathbf{f}, \mathbf{w}_h)_\Omega \quad \forall \mathbf{w}_h \in V_{h,0} \\ (\nabla \cdot \mathbf{u}_h, q_h)_\Omega + (\nabla \cdot \mathbf{u}', q_h)_\Omega = 0 \quad \forall q_h \in Q_{h,0} \end{array} \right. \quad (39)$$

Applying integration by parts to the third terms in the first equation of (39) and to the second term in the second equation, then substituting the expressions of both the fine-scale pressure (28) and the fine-scale velocity (34), we get:

$$\left\{ \begin{array}{l} \rho (\partial_t \mathbf{u}_h, \mathbf{w}_h)_\Omega + (\rho \mathbf{u}_h \cdot \nabla \mathbf{u}_h, \mathbf{w}_h)_\Omega - \sum_{K \in \mathcal{T}_h} (\tau_K \mathcal{R}_M, \rho \mathbf{u}_h \nabla \mathbf{w}_h)_K + (2\mu\boldsymbol{\varepsilon}(\mathbf{u}_h) : \boldsymbol{\varepsilon}(\mathbf{w}_h))_\Omega \\ \quad - (p_h, \nabla \cdot \mathbf{w}_h)_\Omega + \sum_{K \in \mathcal{T}_h} (\tau_C \mathcal{R}_C, \nabla \cdot \mathbf{w}_h)_K = (\mathbf{f}, \mathbf{w}_h)_\Omega \quad \forall \mathbf{w}_h \in V_{h,0} \\ (\nabla \cdot \mathbf{u}_h, q_h)_\Omega - \sum_{K \in \mathcal{T}_h} (\tau_K \mathcal{R}_M, \nabla q_h)_K = 0 \quad \forall q_h \in Q_{h,0} \end{array} \right. \quad (40)$$

;

Finally, substituting the residual of the momentum equation and expanding all the additional terms, we obtain a modified coarse scale equations expressed solely in terms of coarse scale functions. The new modified problem can now be decomposed into four main terms: the first one is the Galerkin contribution, the second and the third terms take into account the influence of the fine-scale velocity on the finite element components and the last term models the influence of the fine-scale pressure onto the large-scale problem:

$$\begin{aligned}
& \underbrace{\rho(\partial_t \mathbf{u}_h + \mathbf{u}_h \cdot \nabla \mathbf{u}_h, \mathbf{w}_h)_\Omega + (2\mu \boldsymbol{\varepsilon}(\mathbf{u}_h) : \boldsymbol{\varepsilon}(\mathbf{w}_h))_\Omega - (p_h, \nabla \cdot \mathbf{w}_h)_\Omega + (\nabla \cdot \mathbf{u}_h, q_h)_\Omega - (\mathbf{f}, \mathbf{w}_h)_\Omega}_{\text{Galerkin terms}} \\
& + \underbrace{\sum_{K \in \mathcal{T}_h} \tau_K (\rho(\partial_t \mathbf{u}_h + \mathbf{u}_h \cdot \nabla \mathbf{u}_h) + \nabla p_h - \mathbf{f}, \rho \mathbf{u}_h \nabla \mathbf{w}_h)_K}_{\text{Upwind stabilization terms}} \\
& + \underbrace{\sum_{K \in \mathcal{T}_h} \tau_K (\rho(\partial_t \mathbf{u}_h + \mathbf{u}_h \cdot \nabla \mathbf{u}_h) + \nabla p_h - \mathbf{f}, \nabla q_h)_K}_{\text{Pressure stabilization terms}} \\
& + \underbrace{\sum_{K \in \mathcal{T}_h} (\tau_C \nabla \cdot \mathbf{u}_h, \nabla \cdot \mathbf{w}_h)_K}_{\text{grad-div stabilization term}} = 0 \quad \forall \mathbf{w}_h \in V_{h,0}, \quad \forall q_h \in Q_{h,0}
\end{aligned} \tag{41}$$

When compared with the Galerkin method (13), the proposed stable formulation involves additional integrals that are evaluated element wise. These additional terms, obtained by replacing the approximated \mathbf{u}' and p' into the large-scale equation, represent the effects of the sub-grid scales and they are introduced in a consistent way to the Galerkin formulation. All of these terms enable to overcome the instability of the classical formulation arising in convection dominated flows and to satisfy the inf-sup condition for the velocity and pressure interpolations. Moreover, the last term in equation (41) provides additional stability at high Reynolds number [37].

For sake of simplicity in the notation and for a better representation of all the additional terms in equation (41), the condensation procedure of the small-scale into the large scale is masked under these stabilizing parameters. However, from the implementation point of view, the structure of the stabilizing parameters is computed naturally via the element-level matrices.

4.4. Time advancing

In the present study, the time derivative is discretized using a simple first order Euler formulae while an implicit scheme is used for the other terms. To illustrate this point, let us focus on the coarse scale momentum equation including the small scale pressure simplification. In this

;

case, the weak form of the implicit scheme reads:

$$\begin{aligned} & \rho \left(\frac{\mathbf{u}_h^{n+1} - \mathbf{u}_h^n}{\Delta t^n}, \mathbf{w}_h \right)_{\Omega} + (\rho \mathbf{u}_h \cdot \nabla \mathbf{u}_h, \mathbf{w}_h)_{\Omega}^{n+1} + (\rho \mathbf{u}_h \cdot \nabla \mathbf{u}', \mathbf{w}_h)_{\Omega}^{n+1} \\ & + (2\mu \boldsymbol{\varepsilon}(\mathbf{u}_h^{n+1}) : \boldsymbol{\varepsilon}(\mathbf{w}_h))_{\Omega} - (p_h^{n+1}, \nabla \cdot \mathbf{w}_h)_{\Omega} + (\tau_C \nabla \cdot \mathbf{u}_h^{n+1}, \nabla \cdot \mathbf{w}_h)_{\Omega} = (\mathbf{f}^n, \mathbf{w}_h)_{\Omega} \end{aligned} \quad (42)$$

where the exponent n denotes the current time iteration while the exponent $(n+1)$ represents the next time level we want to compute. The resulting implicit scheme (42) is obviously non-linear because of the non-linear nature of the convective terms. In order to circumvent this issue, we resort to a classical Newton-Raphson linearization procedure. The implicit Newton-Raphson iterative scheme reads:

$$\begin{aligned} & \rho \left(\frac{\mathbf{u}_h^{n,i+1} - \mathbf{u}_h^n}{\Delta t^n}, \mathbf{w}_h \right)_{\Omega} + (\rho \mathbf{u}_h \cdot \nabla \mathbf{u}_h, \mathbf{w}_h)_{\Omega}^{n,i+1} + (\rho \mathbf{u}_h \cdot \nabla \mathbf{u}', \mathbf{w}_h)_{\Omega}^{n,i+1} \\ & + (2\mu \boldsymbol{\varepsilon}(\mathbf{u}_h^{n,i+1}) : \boldsymbol{\varepsilon}(\mathbf{w}_h))_{\Omega} - (p_h^{n,i+1}, \nabla \cdot \mathbf{w}_h)_{\Omega} + (\tau_C \nabla \cdot \mathbf{u}_h^{n,i+1}, \nabla \cdot \mathbf{w}_h)_{\Omega} = (\mathbf{f}^n, \mathbf{w}_h)_{\Omega} \end{aligned} \quad (43)$$

where the exponent $(n, i+1)$ denotes the $(i+1)^{\text{th}}$ iteration of the Newton-Raphson procedure which uses as initial guess the solution at time level n . The linearization of the convective terms consists in keeping only first order terms at the $(i+1)^{\text{th}}$ Newton iteration as follows:

$$\begin{aligned} (\mathbf{u}_h \cdot \nabla \mathbf{u}_h)^{n,i+1} &= (\mathbf{u}_h^{n,i} + (\mathbf{u}_h^{n,i+1} - \mathbf{u}_h^{n,i})) \cdot \nabla (\mathbf{u}_h^{n,i} + (\mathbf{u}_h^{n,i+1} - \mathbf{u}_h^{n,i})) \\ &= \mathbf{u}_h^{n,i} \cdot \nabla \mathbf{u}_h^{n,i+1} + \mathbf{u}_h^{n,i+1} \cdot \nabla \mathbf{u}_h^{n,i} - \mathbf{u}_h^{n,i} \cdot \nabla \mathbf{u}_h^{n,i} \\ &\quad + (\mathbf{u}_h^{n,i+1} - \mathbf{u}_h^{n,i}) \cdot \nabla (\mathbf{u}_h^{n,i+1} - \mathbf{u}_h^{n,i}) \\ &\approx \mathbf{u}_h^{n,i} \cdot \nabla \mathbf{u}_h^{n,i+1} + \mathbf{u}_h^{n,i+1} \cdot \nabla \mathbf{u}_h^{n,i} - \mathbf{u}_h^{n,i} \cdot \nabla \mathbf{u}_h^{n,i} \end{aligned} \quad (44)$$

with $\mathbf{u}_h^{n,i}$ the value of the velocity at the previous Newton iteration. Owing to we use quasi-static bubble functions, the third term of equation (43) reduces to:

$$(\mathbf{u}_h \cdot \nabla \mathbf{u}')^{n,i+1} \approx \mathbf{u}_h^{n,i} \cdot \nabla \mathbf{u}'^{n,i+1} \quad (45)$$

The complete linearized Newton-Raphson scheme finally reads:

$$\begin{aligned} & \rho \left(\frac{\mathbf{u}_h^{n,i+1}}{\Delta t^n} + \mathbf{u}_h^{n,i} \cdot \nabla \mathbf{u}_h^{n,i+1} + \mathbf{u}_h^{n,i+1} \cdot \nabla \mathbf{u}_h^{n,i}, \mathbf{w}_h \right)_{\Omega} + (\rho \mathbf{u}_h^{n,i} \cdot \nabla \mathbf{u}'^{n,i+1}, \mathbf{w}_h)_{\Omega} \\ & + (2\mu \boldsymbol{\varepsilon}(\mathbf{u}_h^{n,i+1}) : \boldsymbol{\varepsilon}(\mathbf{w}_h))_{\Omega} - (p_h^{n,i+1}, \nabla \cdot \mathbf{w}_h)_{\Omega} + (\tau_C \nabla \cdot \mathbf{u}_h^{n,i+1}, \nabla \cdot \mathbf{w}_h)_{\Omega} \\ & = \left(\mathbf{f}^n + \rho \frac{\mathbf{u}_h^n}{\Delta t^n} + \mathbf{u}_h^{n,i} \cdot \nabla \mathbf{u}_h^{n,i}, \mathbf{w}_h \right)_{\Omega} \end{aligned} \quad (46)$$

4.5. Matrix formulation of the problem

When applied to both the coarse scale system and the fine scale system, the previous scheme gives rise to a linear system that remains to be solve. This system can be put naturally under

;

the following matrix form:

$$\begin{bmatrix} A_{ww} & {}^t A_{wb} & {}^t A_{wq} \\ A_{wb} & A_{bb} & {}^t A_{bq} \\ A_{wq} & A_{bq} & 0 \end{bmatrix} \begin{bmatrix} \mathbf{u}_h \\ \mathbf{u}' \\ p_h \end{bmatrix} = \begin{bmatrix} B_w \\ B_b \\ B_q \end{bmatrix} \quad (47)$$

where

$$\begin{aligned} A_{ww}(\mathbf{u}_h) &= \rho \left(\frac{\mathbf{u}_h^{n,i+1}}{\Delta t^n} + \mathbf{u}_h^{n,i} \cdot \nabla \mathbf{u}_h^{n,i+1} + \mathbf{u}_h^{n,i+1} \cdot \nabla \mathbf{u}_h^{n,i}, \mathbf{w}_h \right)_{\Omega} \\ &\quad + \left(2\mu \boldsymbol{\varepsilon}(\mathbf{u}_h^{n,i+1}) : \boldsymbol{\varepsilon}(\mathbf{w}_h) \right)_{\Omega} + \left(\tau_C \nabla \cdot \mathbf{u}_h^{n,i+1}, \nabla \cdot \mathbf{w}_h \right)_{\Omega} \\ A_{bb}(\mathbf{u}') &= \rho \left(\mathbf{u}_h^{n,i} \cdot \nabla \mathbf{u}'^{n,i+1}, \mathbf{w}' \right)_{\Omega} + \left(2\mu \boldsymbol{\varepsilon}(\mathbf{u}'^{n,i+1}) : \boldsymbol{\varepsilon}(\mathbf{w}') \right)_{\Omega} \\ A_{wb}(\mathbf{u}_h) &= \rho \left(\frac{\mathbf{u}_h^{n,i+1}}{\Delta t^n} + \mathbf{u}_h^{n,i} \cdot \nabla \mathbf{u}_h^{n,i+1} + \mathbf{u}_h^{n,i+1} \cdot \nabla \mathbf{u}_h^{n,i}, \mathbf{w}' \right)_{\Omega} \\ A_{wq}(\mathbf{u}_h) &= - \left(\nabla \cdot \mathbf{u}_h^{n,i+1}, q_h \right)_{\Omega} \\ A_{bq}(\mathbf{u}') &= - \left(\nabla \cdot \mathbf{u}'^{n,i+1}, q_h \right)_{\Omega} \\ B_w &= \left(\mathbf{f}^n + \rho \frac{\mathbf{u}_h^n}{\Delta t^n} + \mathbf{u}_h^{n,i} \cdot \nabla \mathbf{u}_h^{n,i}, \mathbf{w}_h \right)_{\Omega} \\ B_b &= \left(\mathbf{f}^n + \rho \frac{\mathbf{u}_h^n}{\Delta t^n} + \mathbf{u}_h^{n,i} \cdot \nabla \mathbf{u}_h^{n,i}, \mathbf{w}' \right)_{\Omega} \\ B_q &= 0 \end{aligned} \quad (48)$$

One can notice that, in the present case of the quasi-static bubble assumption, the following simplification holds:

$${}^t A_{wb}(\mathbf{u}') = \rho \left(\mathbf{u}_h^{n,i} \cdot \nabla \mathbf{u}'^{n,i+1}, \mathbf{w}_h \right)_{\Omega} \quad (49)$$

The static condensation process, previously detailed, which consists in solving the second line involving \mathbf{u}' and inserting the solution into the first and third lines of system (47) results into the condensed matrix scheme for large-scale unknowns \mathbf{u}_h and p_h that reads:

$$\begin{bmatrix} \tilde{A}_{ww} & {}^t \tilde{A}_{wq} \\ \tilde{A}_{wq} & \tilde{A}_{qq} \end{bmatrix} \begin{bmatrix} \mathbf{u}_h \\ p_h \end{bmatrix} = \begin{bmatrix} \tilde{B}_w \\ \tilde{B}_q \end{bmatrix} \quad (50)$$

with

$$\begin{aligned} \tilde{A}_{ww} &= A_{ww} - {}^t A_{wb} A_{bb}^{-1} A_{wb} & {}^t \tilde{A}_{wq} &= {}^t A_{wq} - {}^t A_{wb} A_{bb}^{-1} {}^t A_{bq} \\ \tilde{A}_{wq} &= A_{wq} - A_{bq} A_{bb}^{-1} A_{wb} & \tilde{A}_{qq} &= -A_{bq} A_{bb}^{-1} {}^t A_{bq} \\ \tilde{B}_w &= B_w - {}^t A_{wb} A_{bb}^{-1} B_b & \tilde{B}_q &= -A_{bq} A_{bb}^{-1} B_b \end{aligned} \quad (51)$$

;

Taking into account locally the influence of unresolved fine scales upon the resolved large scales has introduced new stabilizing terms and modified the components of all the matrices while the effect of the fine-scale pressure has been added directly to the first matrix by a stabilizing term. This matrix formulation can be put in relation with the classic expression (41) as follows:

- i) the modified terms \tilde{A}_{ww} and \tilde{A}_{wq} incorporate the upwind stabilization terms provided by ${}^t A_{wb} A_{bb}^{-1} A_{wb}$ and $A_{bq} A_{bb}^{-1} A_{wb}$;
- ii) similarly, the modified operators ${}^t \tilde{A}_{wq}$ and \tilde{A}_{qq} contain the pressure stabilization terms ${}^t A_{wb} A_{bb}^{-1} {}^t A_{bq}$ and $A_{bq} A_{bb}^{-1} {}^t A_{bq}$;
- iii) eventually, the right hand side components have been modified to ensure consistency by means of ${}^t A_{wb} A_{bb}^{-1} B_b$ and $A_{bq} A_{bb}^{-1} B_b$.

5. NUMERICAL EXAMPLES

In order to assess the main characteristics of the formulation previously presented and test its feasibility in the context of high-performance computing, two examples are analyzed. They were chosen to cover different flow regimes, from laminar to turbulence, and to deal with engineering applications as well. Please note that the RB-VMS computations shown in the following qualify this formulation as an important tool to be used within the realm of simulation of real flows. That is especially due to the fact that it does not require any LES-type modeling and, thus, can be applied to any region of the domain, regardless of the flow regime.

5.1. Driven flow cavity problem (2-D)

Now we numerically solve the lid-driven flow problem. This test has been widely used as a benchmark for numerical methods and has been analyzed by a number of authors [38, 39, 40, 41]. The problem description, boundary conditions and the corresponding meshes are shown in figure 1. Dirichlet boundary conditions prescribe on the upper boundary at $y = 1$, and elsewhere on Γ . The source term is identical to zero. The viscosity is adjusted in order to obtain Reynolds number of 1, 000, 5, 000, 10, 000, 20, 000, 33, 000 and 50, 000. Zero pressure is prescribed at the lower left corner.

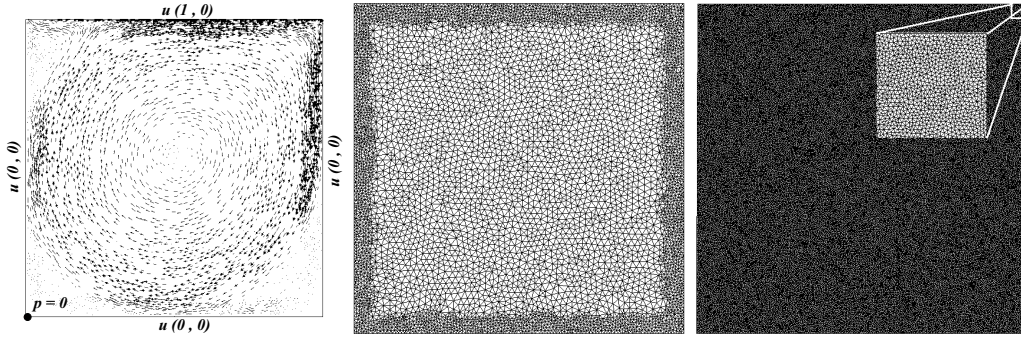


Figure 1. Problem settings: boundary conditions (left) , coarse mesh (center) , fine mesh (right).

Two meshes of linear finite elements have been used in the calculations. The coarse one is

;

Table I. Minimum and maximum values of the pressure for various numerical methods for the coarse mesh (64×64) and for $\text{Re} = 10000$.

	Present work	USFEM	Two-level method	Three-level method
p_{\min}	-0.1319	-0.0975	-0.0730	-0.0904
p_{\max}	0.9142	0.8774	1.0465	1.1278

made of 64×64 elements, refined near the walls of the cavity. The fine mesh is made of 180×180 elements. All numerical experiments are compared to the very known references of Ghia *et al.* [38] and Erturk *et al.* [42]. The authors in [38] applied a second-order accurate finite difference method using a fine grid of 257×257 while in [42] the 2-D steady incompressible Navier-Stokes equations was solved using a very efficient finite difference numerical method (fourth order compact formulation) on a very fine grid of 601×601 . We consider that the steady state is reached when the normalized velocity deviations within one step are lower than a chosen tolerance of 10^{-6} . Recall that the main interest is to compare the performance of our scheme described in the previous section and the behaviour of the solution for high Reynolds number flows. Therefore, a first set of numerical experiments has been performed using our scheme. The velocity profiles for u_x and u_y along $x = 0.5$ and $y = 0.5$ respectively are shown in figure 2. Comparing these results with the given reference, one can clearly see the improvement of the new scheme in the solution in particularly when the Reynolds number increases. Hence, we conclude that the absence of the pressure subscale and the convection terms in the small-scale problem renders an extremely diffusive solution even on a very fine mesh. For high Reynolds number, the results are underestimated with respect to the new formulation and they are very inaccurate. However, the solution of the modified scheme is in excellent agreement with the reference in all situations. Some other interesting quantities than plotting the velocity profiles are available in the literature. In [43], the authors have studied and analyzed the pressure and the vortex formation and comparisons were made using several numerical methods for different Reynolds number. In the following, we will get a closer look on the pressure isolines for Reynolds number 10000 and compared our results to the given reference. Table I and figure 3 show a very good agreement of our modified scheme with the given reference. As in [31], we proceed our comparisons by investigating the location of the respective vortex centers. Figure 4 shows the computed flow fields in terms of the velocity magnitude and the corresponding streamlines. As expected, using the fine mesh 180×180 the solutions exhibit additional counter-rotating vortices in or near the cavity corners as Re increases. It is known that this problem involves a primary vortex, while for higher Reynolds numbers secondary vortices appear in the corners of the domain. As the Reynolds number increases, the location of the centers of these vortices change, secondary vortex has the tendency to break on two new vortex and consequently their number increases (see figures 4 and 5). The effect of the Reynolds number on the genesis of new vortices inside the cavity is presented in the following graph. Figure 6 highlights by order of appearance the location of these expected vortices. The location of the centers of these vortices together with corresponding values from references solutions are summarized in tables III and IV. Qualitatively and quantitatively, the results are similar to reference solutions and a good agreement is observed, although the mesh used here is coarser than the one used

;

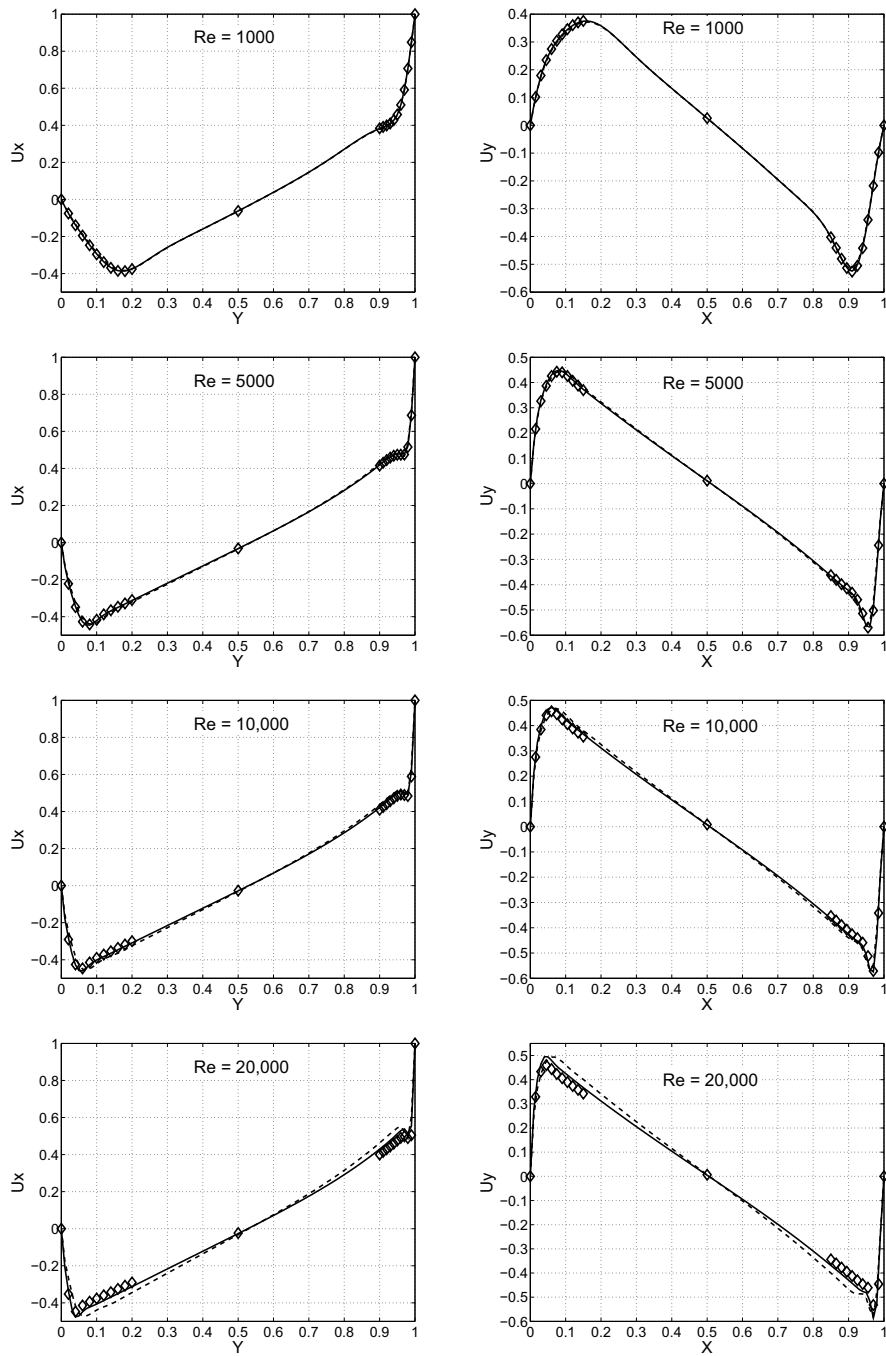


Figure 2. Left: velocity profile for u_x along $x = 0.5$. Right: velocity profile for u_y along $y = 0.5$. The dashed and solid lines denote the coarse and the fine meshes respectively while the symbols represent the reference.

;

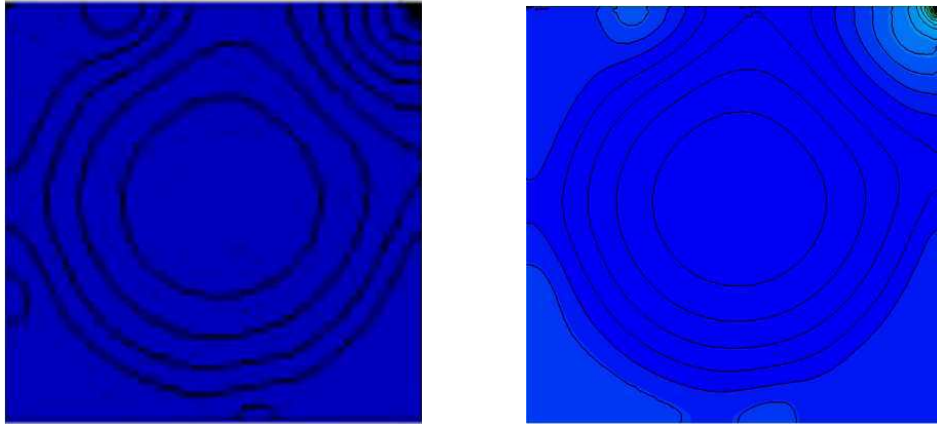


Figure 3. Pressure isolines on colored pressure distribution.
Left: two-level method [43]. Right: present work.

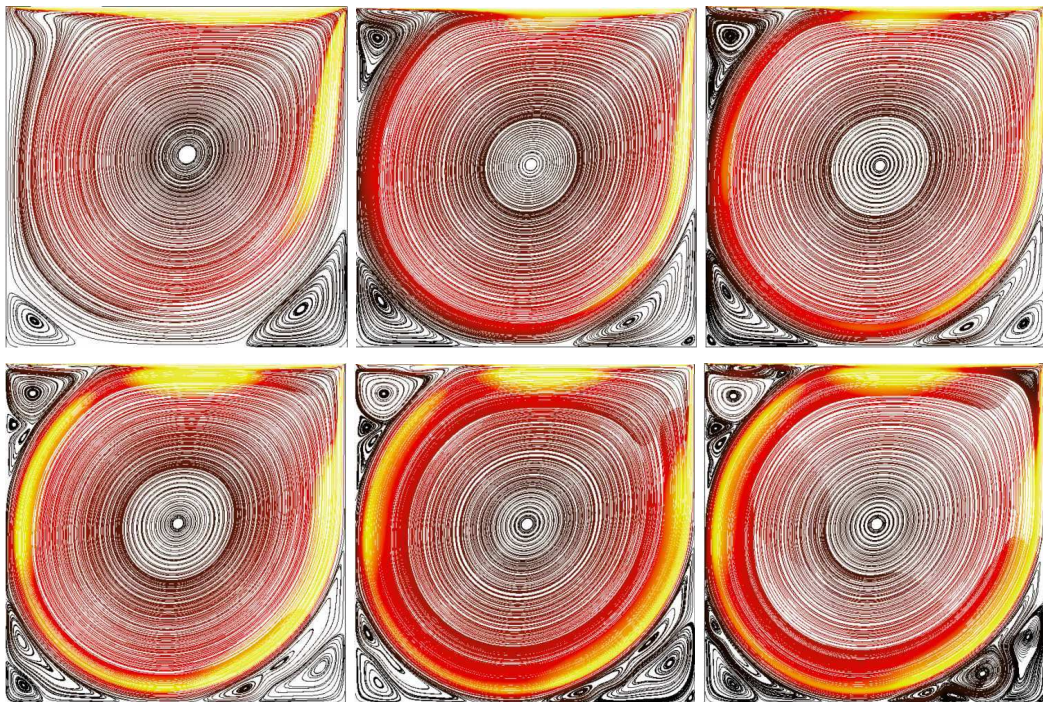


Figure 4. Streamline on colored velocity distribution from top-left to bottom-right: $Re = 1000, 5000, 10000, 20000, 33000$ and 50000 with 180×180 mesh.

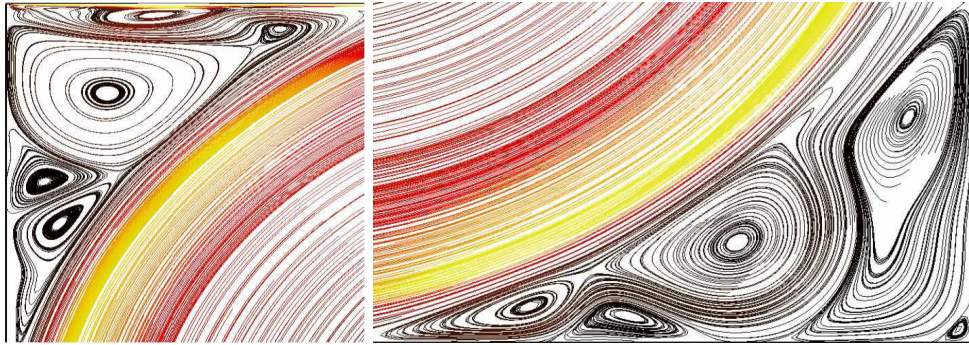


Figure 5. A magnified view of various secondary vortices near the cavity corners for $Re = 50000$.

Table II. Number of resolved vortices in function of the Reynolds number.

Reynolds	Vortices amount
1,000	3
5,000	5
10,000	6
20,000	8
30,000	10
50,000	13

in the reference. We have used as reference [38] for number of Reynolds less than 10,000, and

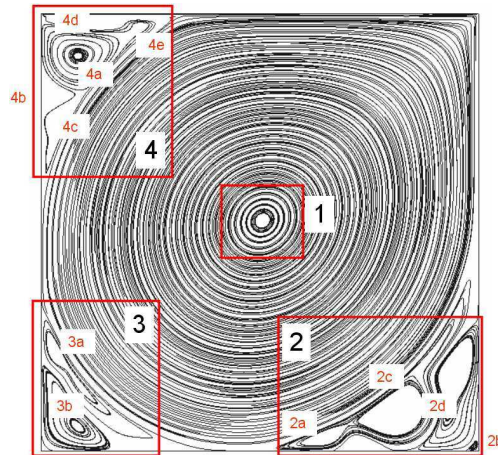


Figure 6. Location of the resolved vortices in order of appearance

[42] for $Re = 20,000$. To our knowledge, results for Reynolds number 33,000 and 50,000 using

Table III. Location of vortex centers (coordinate x, coordinate y) for the two first zones (V_1 , V_2).

Reynolds values		10,000	20,000	33,000	50,000
V_{1a}	Current	(0.5110, 0.5310)	(0.5080, 0.5280)	(0.506, 0.527)	(0.506, 0.526)
	Reference	(0.5117, 0.5330)	(0.5100, 0.5267)	--	--
V_{2a}	Current	(0.7670, 0.0594)	(0.7060, 0.0416)	(0.667, 0.0350)	(0.654, 0.0309)
	Reference	(0.7656, 0.0586)	(0.7267, 0.0450)	--	--
V_{2b}	Current	(0.9330, 0.0689)	(0.9290, 0.1060)	(0.926, 0.119)	(0.99, 0.0112)
	Reference	(0.9336, 0.0625)	(0.9300, 0.1033)	--	--
V_{2c}	Current		(0.808, 0.115)	(0.863, 0.178)	(0.816, 0.0857)
	Reference		--	--	--
V_{2d}	Current			(0.986, 0.017)	(0.95, 0.194)
	Reference			--	--
V_{2e}	Current				(0.732, 0.0218)
	Reference				--

Table IV. Location of vortex centers (coordinate x, coordinate y) for the two last zones (V_3 , V_4).

Reynolds values		10,000	20,000	33,000	50,000
V_{3a}	Current	(0.0589, 0.1600)	(0.0489, 0.1820)	(0.0375, 0.206)	(0.0307, 0.226)
	Reference	(0.0586, 0.1641)	(0.0483, 0.1817)	--	--
V_{3b}	Current	(0.0160, 0.0191)	(0.0536, 0.0511)	(0.0692, 0.0602)	(0.0831, 0.0556)
	Reference	(0.0156, 0.0195)	(0.0567, 0.0533)	--	--
V_{4a}	Current	(0.0710, 0.9110)	(0.0802, 0.9120)	(0.0852, 0.911)	(0.0839, 0.908)
	Reference	(0.0703, 0.9141)	(0.0817, 0.9133)	--	--
V_{4b}	Current		(0.0255, 0.82)	(0.0339, 0.811)	(0.0317, 0.809)
	Reference		(0.0233, 0.82)	--	--
V_{4c}	Current		(0.0539, 0.783)	(0.0537, 0.774)	(0.0446, 0.763)
	Reference		--	--	--
V_{4d}	Current				(0.126, 0.988)
	Reference				--
V_{4e}	Current				(0.228, 0.972)
	Reference				--

linear stabilised finite elements methods are considered very rare. We notice a very interesting behaviour of these computations which will be subject of further investigations. The velocity profiles for u_x and u_y along $x = 0.5$ and $y = 0.5$ respectively for Reynolds number 33,000 and 50,000 are shown in figure 7. Another set of numerical experiments was conducted in

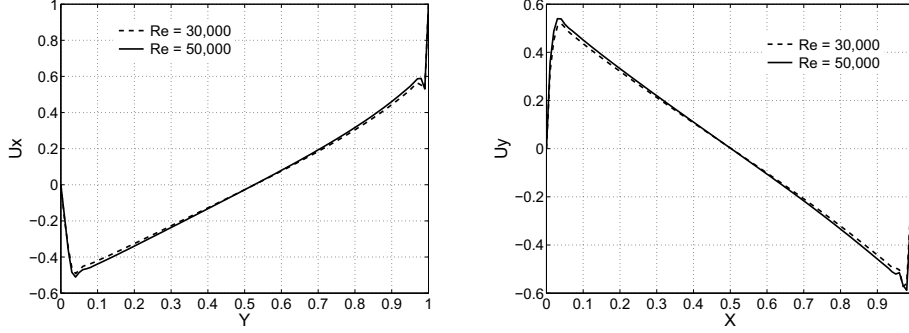


Figure 7. Velocity profile for u_x along $x = 0.5$ (left) and u_y along $y = 0.5$ (right).

order to study the convergence of the new scheme. We performed a mesh sensitivity study to validate the capability of the method. Therefore, five different unstructured grids were used for these comparisons with a mesh of 16×16 , 32×32 , 64×64 , 80×80 and 125×125 elements respectively. The Reynolds number is chosen to be equal to 5,000. We compute the error of the velocity solution using the L^2 -norm for all mesh sizes h as follows:

$$\text{err}(h) = \left(\sum_{x,y} (u_{\text{ref}}^i - u_k^i)^2 \right)^{1/2} \quad \forall h \quad (52)$$

Results are compared to [42] obtained by employing a high-order accurate finite difference method on a 601×601 mesh. The approximation error is plotted in figure 8 and shows the expected improvement in the results. The velocity profiles employing different grid resolutions together with the reference solution are shown in figure 9. Note that the present method converges rather rapidly to the given benchmark solution.

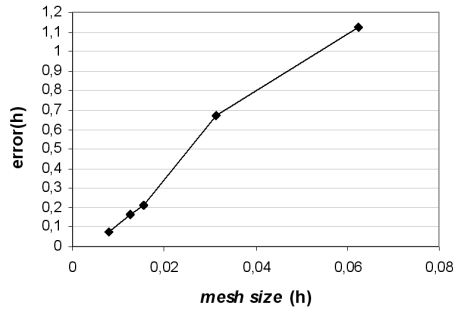


Figure 8. Evolution of the error in function of the mesh size h .

;

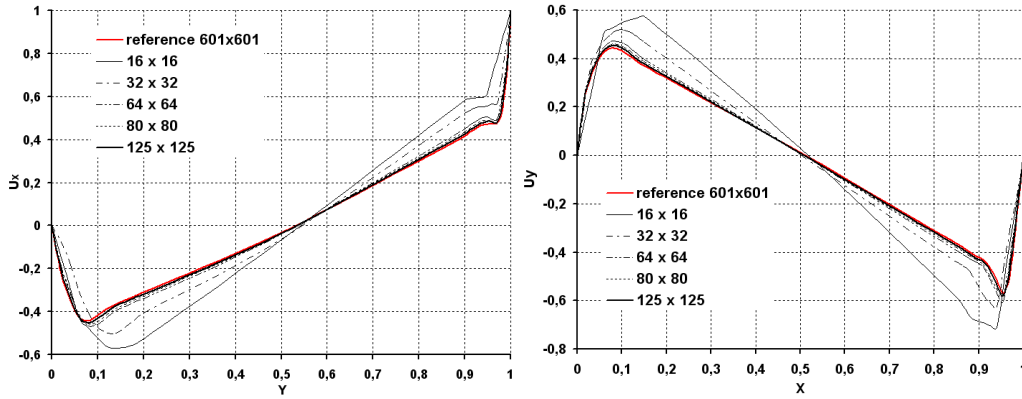


Figure 9. Velocity profile using different meshes. Left: u_x along $x = 0.5$. Right: u_y along $y = 0.5$.

We conclude this numerical example by examining the computer demands. The number of time steps needed to reach the steady state with $\Delta t = 0.1s$, as well as the required CPU time, are reported in figure 10. Within each time step only a single iteration is performed. As expected, the required CPU time increases with the rise of the Reynolds number. This is due to the fact that more physical time iterations are necessary to yield the solution; the ratio $\frac{\text{CPU time}}{\text{real time}}$ remaining quite constant in all cases.

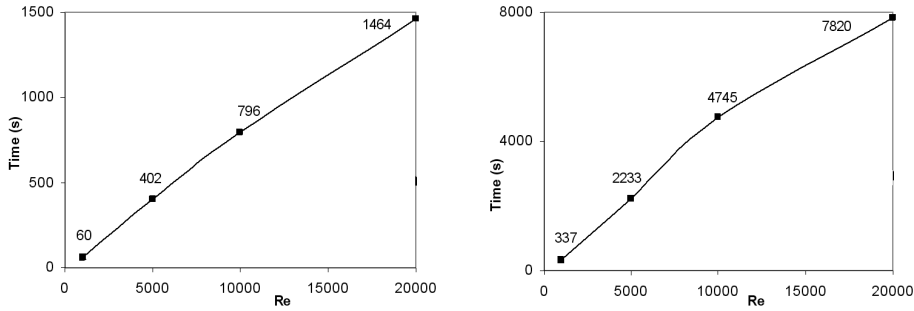


Figure 10. Required physical time (left) and CPU time (right) to reach the steady state for different Reynolds number.

5.2. Three-dimensional lid-driven cavity flow

In many industrial, environmental and geophysical flows, the 3D lid-driven cavity flow can be seen as an interesting re-circulating flow. The flow is confined in a cubic domain with the upper wall moving at a constant speed (see figure 11 for details). Although the geometry is simple, complex physical phenomena occurs inside the cubic cavity. Contrary to the 2D case presented in the previous section, new phenomena can be captured with the 3D simulations. The presence of side-walls confining the full flow modifies the flow pattern so that three-dimensional structures that significantly altered the primary flow in the central plane are produced.

Recently, the use of three-dimensional numerical simulation becomes a very interesting tool for

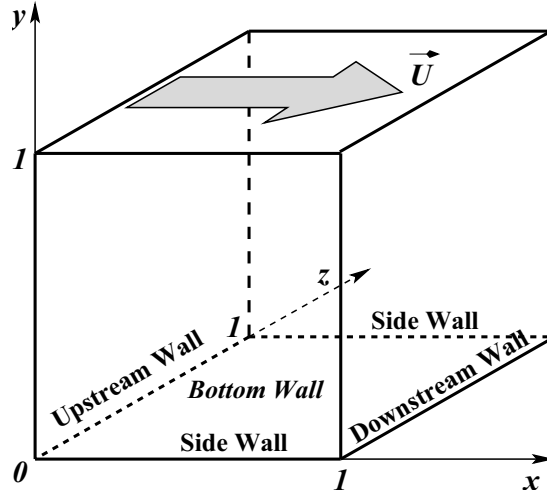


Figure 11. Sketch of the 3D lid driven cavity problem

investigating such physical phenomena in particularly thanks to the increase of technological advances in computer hardware and parallel computing.

A literature review on the 3D problem shows that in fact by examining a plane parallel to the downstream wall, corner eddies were caused at the juncture of the side-walls and the ground while downstream secondary vortices appeared. Moreover, due to centrifugal forces along the downstream, eddy separation surface were found along the span. These vortices are often

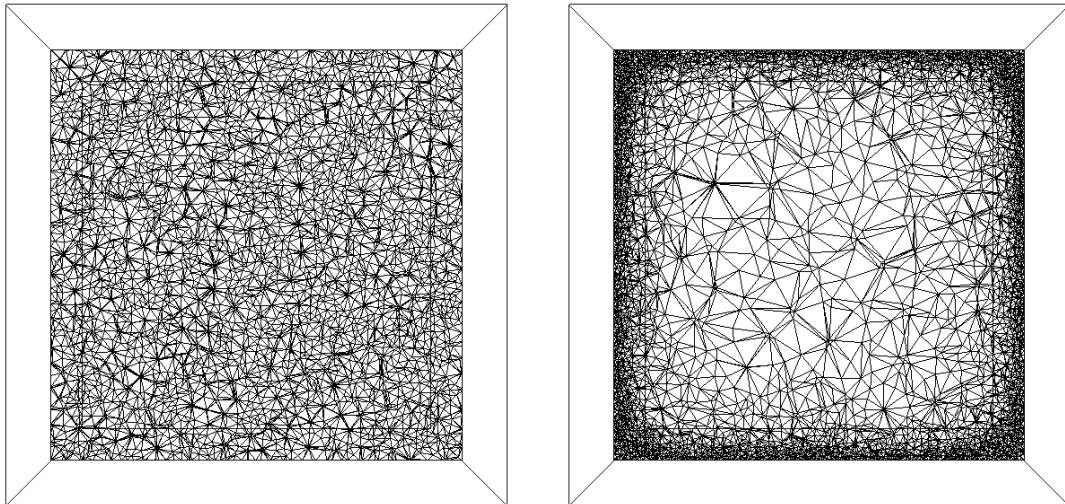


Figure 12. Heterogeneous isotropic mesh for 3D lid-driven cavity flow.

known as Taylor-Görter-like (TGL) vortices in reference to their curvature-induced origins. As shown in the 2D numerical test, the number and location of these vortices were also function of Reynolds number. The experimental visualization of these vortices were first accomplished at Stanford University by Koseff *et al.* [44, 45]. The numerical prediction of these vortices has to be credited to the work of Freitas *et al.* [46, 47]. It was mentioned that not only corner vortices in the vicinity of the vertical end-walls were observed but also locally spreading TGL vortices. For instance, eight pairs of TGL vortices were observed for $Re \approx 3,000$. For higher Reynolds numbers, regular unsteadiness is no longer sustained and thus evolved into turbulence.

From a numerical point of view, it is worth noticing that most of the computations were made using structured grids due to the simplicity of the geometry in order to capture the flow phenomenon accurately. Consequently, few calculations were performed using unstructured grids. Here, in this work, two unstructured tetrahedral grids were employed to simulate the lid-driven cavity flow: the first referred as the coarse mesh, consists of 36,282 nodes and 192,080 linear tetrahedral elements, and the second referred as the fine mesh consists of 238,580 nodes and 1,229,089 linear tetrahedral elements with grid clustering near the six cavity walls. These grids are displayed in figure 12. Aiming at comparing our results with the given reference, the two different meshes employed here are formed by approximately the same number of elements (see [48] for the coarse mesh and [49] for the fine mesh).

The initial velocity in the flow is set to zero everywhere except on the lid surface. The viscosity is adjusted to obtain the desired Reynolds number. The computational results for $Re = 1,000$, $Re = 3,200$ and $Re = 12,000$ are compared to the results from Tang *et al.* [50], Zang *et al.* [51] and Prasad and Koseff [52] respectively. The fluid motion is generated by the top lid that moves in the x -direction with a constant velocity $U_0 = 1m/s$. However, in order to avoid discontinuity in Dirichlet boundary conditions, we resort to the following velocity profile in the manner of [53] or [49].

$$U_x = U_0 \left(1 - \left(\frac{2x}{L} \right)^{18} \right)^2 \left(1 - \left(\frac{2y}{L} \right)^{18} \right)^2 \quad (53)$$

where L is the size of the cavity. For all the remaining walls, no-slip conditions are applied.

Following the lines in [49] a fixed time step of $0.1s$ is employed and 20,000 time steps (2,000 time units) are performed. Since the detailed convergence analysis is not within the goals of this paper, only the velocity profiles in the mid-plane are plotted and compared with the reference solutions. It is worth to mention that for $Re \geq 3,200$, all the experimental and numerical observations reported by Koseff [44, 45] and Zang [51], showed that the steady state does not exist but the transient behaviours become periodic. Consequently, a time interval, for which oscillations of the velocity field occur, was identified and statistical studies in this period were carried out in order to obtain the mean velocity profiles. Figure 13 show the velocity profiles of u_x component on the vertical centreline and u_z component on the horizontal centreline of the symmetry plane $z = 0.5$ for $Re = 1,000$, $Re = 3,200$ and $Re = 12,000$, respectively. The symbols denote the results of the reference data extracted from their figures. All the velocity profiles are in good agreement with profiles reported by the given references. As mentioned previously, as the flow is unsteady, the instantaneous velocity at the same time step is different from the experimental results. Only the time-averaged velocity profile of fully developed flow is plotted and agrees well with the experimental results. The profile is the average value of 100 dimensionless time units. The differences with the experimental results is most probably

;

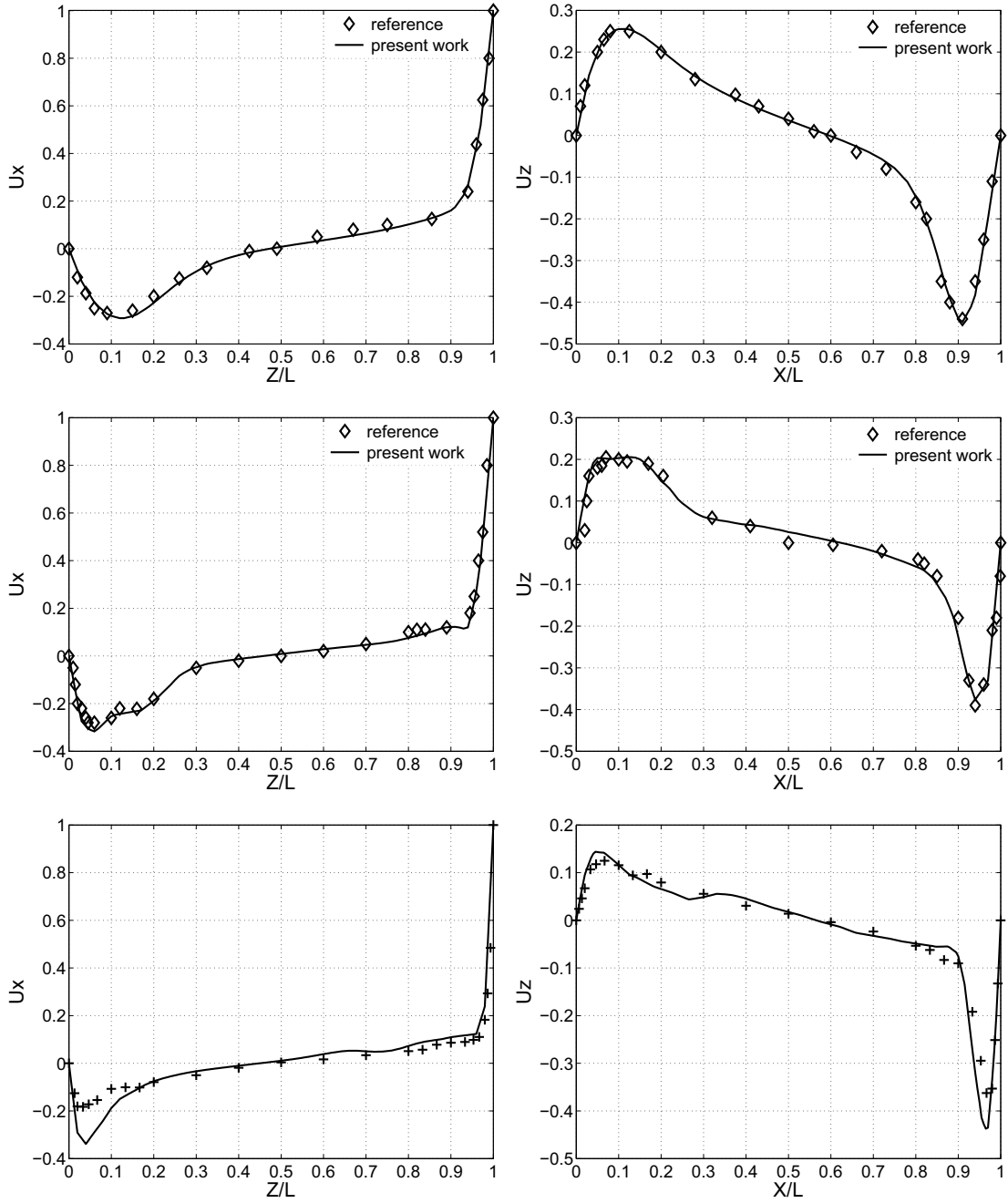


Figure 13. Comparison of velocity profiles in the mid-plane $y = 0.5$ with reference data (symbols) from [50] for $Re = 1,000$ (top), [51] for $Re = 3,200$ (middle) and [52] for $Re = 12,000$ (bottom). Left: mean value of velocity in the x -direction. Right: mean value of velocity in the z -direction.

;

due to the fact that the grid is not fine enough to simulate accurately such complex fluid phenomena. However, as a first implementation, the agreement between the present and the experimental results has been considered satisfactory.

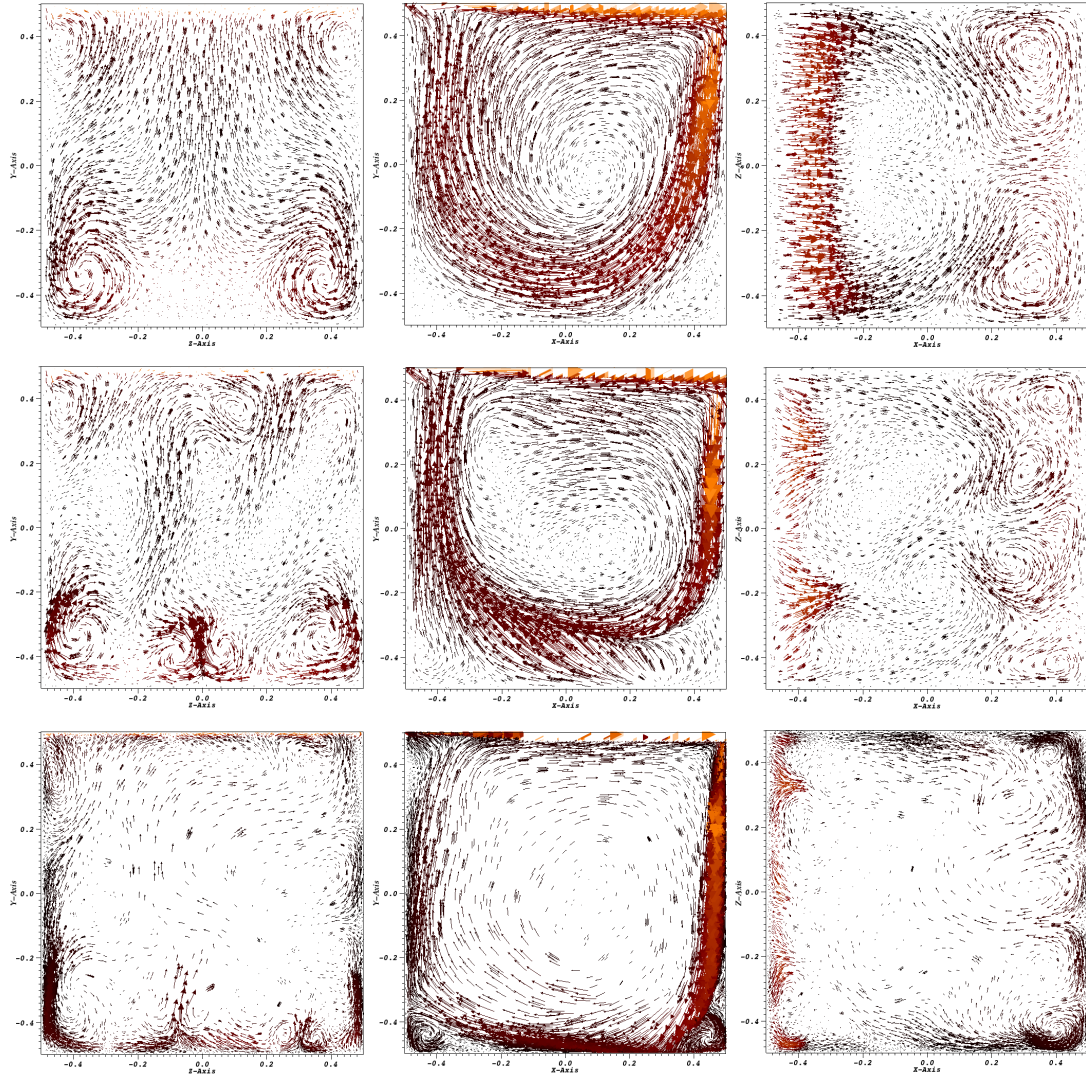


Figure 14. Comparison of velocity vectors for different Reynolds number: $Re = 1,000$ (top); $Re = 3,200$ (middle) and $Re = 12,000$ (bottom) along different planes: plane $y-z$ (left); plane $x-y$ (middle); plane $z-x$ (right).

In order to reveal the Taylor-Görtler structures, we investigate the flow vectors, after 2,000 time units, on the three middle planes $x = 0.5$, $y = 0.5$ and $z = 0.5$. At $Re = 1,000$, a primary vortex appearing in the plane $x-y$ is coming with two secondary contra-rotating vortices next to the downstream and bottom walls as shown in planes $y-z$ and $z-x$. Moreover, two additional

;

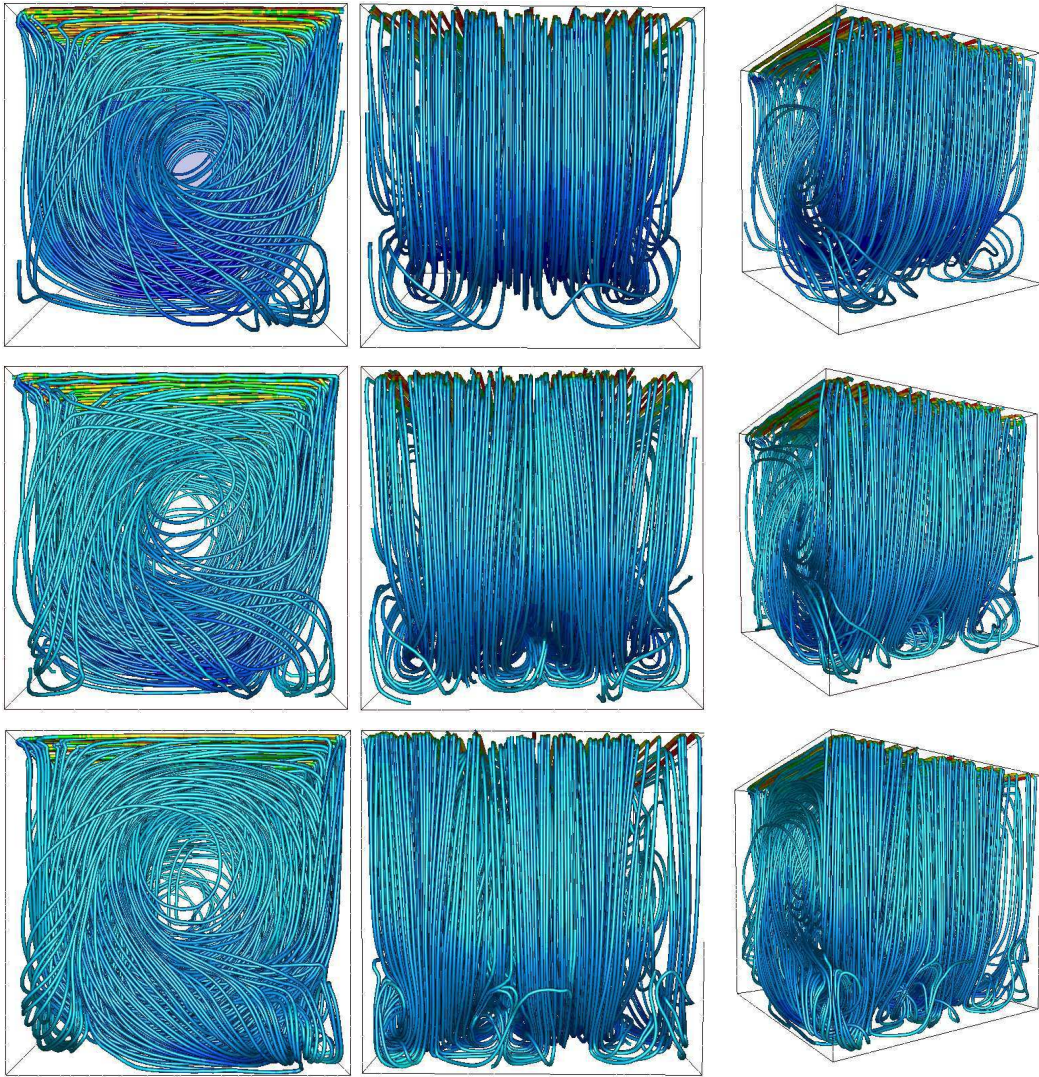


Figure 15. Comparison of observed streamtraces for different Reynolds number: $Re = 1,000$ (top); $Re = 3,200$ (middle) and $Re = 12,000$ (bottom) on different views: front view (left); side view (middle); oblique view (right).

vortices can be observed in the top corners of plane y - z . The steadiness of the flow is clearly highlighted by its symmetry. These results are in perfect agreement with those of Yang *et al.* [54] and Wong and Baker [55]. When the Reynolds number increases, the centre of the primary vortex moves toward the centre of the cube in the same way than the two-dimensional lid-driven square cavity. Furthermore, the size of the secondary vortices decreases while their number is rising. The flow loses its symmetry indicating that it becomes unsteady. Although no quantitative measurements were reported in the given references, similar behaviour of the velocity field was reported by [46, 56, 57].

For high Reynolds number ($Re = 12,000$), the complexity of the flow is clearly emphasized by the streamtraces displayed in figure 15. The flow structure is composed by a primary eddy, a downstream secondary eddy, an upstream tertiary eddy and a corner eddy. As the Reynolds number increases, the observed particle trajectory exhibits a qualitatively new feature; no longer is the particle confined to a single side of the cavity, but instead, the particle can pass from one side to the other, and back again given sufficient time, in apparent violation of mirror symmetry. As shown by front view in figure 15, the corresponding spiralling path explores the full width of the cavity.

6. CONCLUSION

In this paper, an unstructured finite element incompressible Navier-Stokes solver, based on the use of a mixed stable and stabilized approach has been successfully developed for the study of 2D and 3D unsteady incompressible flows at high Reynolds numbers. The method is applied to the lid-driven cavity problem for both steady and unsteady flows at Reynolds number up to 50,000 for the 2D case and up to 12,000 for the 3D case. All the results obtained were compared with numerical solutions obtained by other researchers and are in very good agreement with benchmark results in the literature.

ACKNOWLEDGMENT

The authors gratefully acknowledge support from the ADEME, CIM Team and the companies involved in the THOST project managed by Science Computer and Consultants (SCC).

REFERENCES

1. Yang H, Chen T, Zhu Z. Numerical study of forced turbulent heat convection in a straight square duct. *International Journal of Heat and Mass Transfer* 2009; **52**:3128–3136.
2. Yagi H, Kawahara M. Optimal shape determination of a body located in incompressible viscous fluid flow. *Computer Methods in Applied Mechanics and Engineering* 2007; **196**:5084–5091.
3. Oñate E, Valls A, García J. Modeling incompressible flows at low and high Reynolds numbers via a finite calculus–finite element approach. *Journal of Computational Physics* 2007; **224**(1):332–351.
4. Hachem E. Stabilized finite element method for heat transfer and turbulent flows inside industrial furnaces. PhD Thesis, Ecole Nationale Supérieure des Mines de Paris 2009.
5. Franca L, Nesliturk A, Stynes M. On the stability of residual-free bubbles for convection-diffusion problems and their approximation by a two-level finite element method. *Computer Methods in Applied Mechanics and Engineering* 1998; **166**:35–49.

;

6. Nesliturk A. Approximating the incompressible Navier-Stokes equations using a two level finite element method. PhD Thesis, University of Colorado 1999.
7. Arnold D, Brezzi F, Fortin M. A stable finite element for the Stokes equations. *Calcolo* 1984; **23**(4):337–344.
8. Canuto C, Van Kemenade V. Bubble-stabilized spectral methods for the incompressible navier-stokes equations. *Computer Methods in Applied Mechanics and Engineering* 1996; **135**:35–61.
9. Brezzi F, Russo A. Choosing bubbles for advection-diffusion problems. *Mathematical Models and Methods in Applied Sciences* 1994; **4**:571–587.
10. Russo A. Bubble stabilization of finite element methods for linearized incompressible Navier-Stokes equations. *Computer Methods in Applied Mechanics and Engineering* 1996; **132**:335–343.
11. Brezzi F, M F. *Mixed and Hybrid Finite Element Methods*. No. 15 in Springer Series in Computational Mathematics, Springer-Verlag: New-York, 1991.
12. Brezzi F, Franca L, Hughes T, Russo A. Stabilization techniques and subgrid scales capturing. *Conference of the State of the Art in Numerical Analysis*, York, England, 1996.
13. Donea J, Huerta A. *Finite Element Methods for Flow Problems*. New-York, 2003.
14. Brooks A, Hughes T. Streamline upwind/Petrov-Galerkin formulations for convection dominated flows with particular emphasis on the incompressible Navier-Stokes equations. *Computer Methods in Applied Mechanics and Engineering* 1982; **32**:199–259.
15. Hughes T. Multiscale phenomena: Green’s functions, the Dirichlet-to-Neumann formulation, subgrid scale models, bubbles and the origin of stabilized methods. *Computer Methods in Applied Mechanics and Engineering* 1995; **127**:387–401.
16. Brezzi F, Franca L, Hughes T, Russo A. $b = \int g$. *Computer Methods in Applied Mechanics and Engineering* 1997; **145**:329–339.
17. Hughes TJR, Scovazzi G, Bochev PB, Buffa A. A multiscale discontinuous Galerkin method with the computational structure of a continuous Galerkin method. *Computer Methods in Applied Mechanics and Engineering* 2006; **195**(19-22):2761–2787.
18. Tezduyar T, Shih R, Mittal S, Ray S. Incompressible flow computations with stabilized bilinear and linear equal-order-interpolation velocity-pressure elements. *Computer Methods in Applied Mechanics and Engineering* 1992; **95**:221–242.
19. Franca L, C F. Bubble functions prompt unusual stabilized finite element methods. *Computer Methods in Applied Mechanics and Engineering* 1995; **123**:229–308.
20. Codina R. Stabilization of incompressibility and convection through orthogonal sub-scales in finite element methods. *Computer Methods in Applied Mechanics and Engineering* 2000; **190**(13-14):1579–1599.
21. Codina R. Stabilized finite element method for the transient Navier-Stokes equations based on a pressure gradient projection. *Computer Methods in Applied Mechanics and Engineering* 2000; **182**(3-4):277–300.
22. Codina R. Pressure stability in fractional step finite element methods for incompressible flows. *Journal of Computational Physics* 2001; **170**(1):112–140.
23. Codina R, Principe J. Dynamic subscales in the finite element approximation of thermally coupled incompressible flows. *International Journal for Numerical Methods in Fluids* 2007; **54**:707–730.
24. Gravemeier V. Scale-separating operators for variational multiscale large eddy simulation of turbulent flows. *Journal of Computational Physics* 2006; **212**(2):400–435.
25. Gravemeier V. A consistent dynamic localization model for large eddy simulation of turbulent flows based on a variational formulation. *Journal of Computational Physics* 2006; **218**(2):677–701.
26. Gravemeier V, Gee MW, Kronbichler M, Wall WA. An algebraic variational multiscalemultigrid method for large eddy simulation of turbulent flow. *Computer Methods in Applied Mechanics and Engineering* 2009; (In Press).
27. Masud A, Khurram RA. A multiscale/stabilized finite element method for advection-diffusion equation. *Computer Methods in Applied Mechanics and Engineering* 2004; **193**:1997–2018.
28. Scovazzi G. A discourse on Galilean invariance, SUPG stabilization, and the variational multiscale framework. *Computer Methods in Applied Mechanics and Engineering* 2007; **196**(4-6):1108–1132.
29. Hughes TJR, Feijoo GR, Mazzei L, Quincy JN. The variational multiscale method a paradigm for computational mechanics. *Computer Methods in Applied Mechanics and Engineering* 1998; **166**:3–24.
30. Dignonnet H, Coupez T. Object-oriented programming for fast and easy development of parallel applications in forming processes simulation. *Computational Fluid and Solid Mechanics 2003*, 2003; 1922–1924.
31. Basset O. Simulation numérique d’écoulements multi-fluides sur grille de calcul. PhD Thesis, Ecole Nationale Supérieure des Mines de Paris 2006.
32. Coupez T. Stable-stabilized finite element for 3D forming calculation. *Technical Report*, CEMEF 1996.
33. Dubois T, Jauberteau F, Temam R. *Dynamic Multilevel Methods and the Numerical Simulation of Turbulence*. Cambridge University Press: Cambridge, 1999.
34. Wall WA, Bischoff M, Ramm E. A deformation dependent stabilization technique, exemplified by EAS elements at large strains. *Computer Methods in Applied Mechanics and Engineering* 2000; **188**(4):859–871.

35. Tezduyar TE, Osawa Y. Finite element stabilization parameters computed from element matrices and vectors. *Computer Methods in Applied Mechanics and Engineering* 2000; **190**(3-4):411–430.
36. Franca LP, Oliveira SP. Pressure bubbles stabilization features in the Stokes problem. *Computer Methods in Applied Mechanics and Engineering* 2003; **192**:1929–1937.
37. Behr MA, Franca LP, E TT. Stabilized finite element methods for the velocity-pressure-stress formulation of incompressible flows. *Computer Methods in Applied Mechanics and Engineering* 1993; **104**(1):31–48.
38. Ghia U, Ghia KN, Shin CT. High-Re solutions for incompressible flow using the Navier-Stokes equations and a multigrid method. *Journal of Computational Physics* 1982; **48**(3):387–411.
39. Schreiber R, Keller HB. Driven cavity flows by efficient numerical techniques. *Journal of Computational Physics* 1983; **49**:310–333.
40. Botella O, Peyret R. Benchmark spectral results on the lid-driven cavity flow. *Computers and Fluids* 1998; **27**(4):421–433.
41. Sahin M, Owens RG. A novel fully-implicit finite volume method applied to the lid-driven cavity problem. part i: high Reynolds number flow calculations. *International Journal for Numerical Methods in Fluids* 2003; **42**:57–77.
42. Erturk E, Corke TC, Gokcol. Numerical solutions of 2-D steady incompressible driven cavity flow at high Reynolds numbers. *International Journal for Numerical Methods in Fluids* 2005; **48**(7):747–774.
43. Gravemeier V, Wall WA, Ramm E. Numerical solution of the incompressible Navier-Stokes equations by a three-level finite element method. *Computational Fluid and Solid Mechanics* 2003; :915–918.
44. Koseff JR, Street RL, Gresho PM, Upson CD, Humphrey JAC, To JW. A three-dimensional lid-driven cavity flow: experiment and simulation. *Third International Conference on Numerical Methods in Laminar and Turbulent Flow*, Seattle, WA, 1983; 564–581.
45. Koseff JR, Street RL. Visualization studies of a shear driven three-dimensional recirculating flow. *Journal of Fluids Engineering* 1984; **106**:21–29.
46. Freitas CJ, Street RL, Findikakis AN, Koseff JR. Numerical simulation of three dimensional flow in a cavity. *International Journal for Numerical Methods in Fluids* 1985; **5**:561–575.
47. Freitas CJ, Street RL. Non-linear transport phenomena in a complex recirculating flow: a numerical investigation. *International Journal for Numerical Methods in Fluids* 1988; **8**:769–802.
48. Popiolek TL, Awruch AM, Teixeira PRF. Finite element analysis of laminar and turbulent flows using LES and subgrid-scale models. *Applied Mathematical Modelling* 2006; **30**(2):177–199.
49. Lins EF, Elias RN, Guerra GM, A RF, Coutinho AL. Edge-based finite element implementation of the residual-based variational multiscale method. *International Journal for Numerical Methods in Fluids* 2009; **61**:1–22.
50. Tang LQ, Cheng T, Tsang TTH. Transient solutions for three-dimensional lid-driven cavity flows by a least-squares finite element method. *International Journal for Numerical Methods in Fluids* 1995; **21**:413–432.
51. Zang Y, Street RL, Koseff JR. A dynamic mixed subgrid-scale model and its application to turbulent recirculating flows. *Physics of Fluids* 1993; **A5**:3186–3196.
52. Prasad AK, Koseff JR. Reynolds number and end-wall effects on a lid-driven cavity flow. *Physics of Fluids* 1989; **A1**:208–218.
53. Bouffanais R, Leriche E, Deville MO. Large-eddy simulation of the flow in a lid-driven cubical cavity. *Physics of Fluids* 2007; **19**(5):055108.
54. Yang JY, Yang SC, Chen YN, Hsu CA. Implicit weighted ENO schemes for the three-dimensional incompressible Navier-Stokes equations. *Journal of Computational Physics* 1998; **146**(1):464–487.
55. Wong KL, Baker AJ. A 3D incompressible Navier-Stokes velocity-vorticity weak form finite element algorithm. *International Journal for Numerical Methods in Fluids* 2002; **38**:99–123.
56. Koseff JR, Street RL. The lid-driven cavity flow: a synthesis of qualitative and quantitative observations. *Journal of Fluids Engineering* 1984; **106**:390–398.
57. Koseff JR, Street RL. On end wall effects in a lid-driven cavity flow. *Journal of Fluids Engineering* 1984; **106**:385–389.

6.3 Finite element solution to handle complex heat and fluid flows in industrial furnaces using the immersed volume method

*** see attached paper**

Finite element solution to handle complex heat and fluid flows in industrial furnaces using the immersed volume technique

E. Hachem^{1,*,\dagger}, T. Kloczko¹, H. Digonnet¹ and T. Coupez¹

¹ *Ecole des Mines de Paris, Centre de Mise en Forme des Matériaux (CEMEF), UMR CNRS 7635, Sophia-Antipolis, France.*

SUMMARY

A mathematical and numerical model to design an industrial software solution able to handle real complex furnaces configurations in terms of geometries, atmospheres, parts positioning, heat generators and physical thermal phenomena has been developed. A 3D-dimensional algorithm based on stabilized finite element methods (SFEM) for solving the momentum, energy, turbulence and radiation equations is presented. An immersed volume method for thermal coupling of fluids and solids is introduced. It consists in considering a single 3D grid of the furnace and solving one set of equations for both fluid and solid with different thermal properties which can reduce the computational costs. A level set function enables to define precisely the position and the interface of any objects inside the furnace and to provide homogeneous physical and thermodynamic properties for each subdomain. Furthermore, in order to ensure an accurate capture of the discontinuities that characterize the strongly heterogeneous domain, we resort to an anisotropic mesh adaptation algorithm based on the variations of the level set function. The proposed method demonstrates the capability of the model to simulate an unsteady three dimensional heat transfers and turbulent flows in an industrial furnace with the presence of three conducting solids.

KEY WORDS: Immersion volume technique; level set method; anisotropic mesh adaptation; mixing laws; radiative heat transfer.

1. INTRODUCTION

The analysis of transient heating characteristics of the steel in a heating furnace has attracted considerable attention during the past few decades since the furnace process should have lower energy consumption and pollutant emissions [1, 2]. In addition, requirement of the uniform temperature distribution inside the volume and the treated workpieces greatly increases the importance of accurate and fast prediction of furnace process because this determines the quality of the steel product in terms of hardness, toughness and resistance. Intrinsically, the resulting hot gas flow within the furnace influences the heat transfer process through

*Correspondence to: Ecole des Mines de Paris, Centre de Mise en Forme des Matériaux (CEMEF), UMR CNRS 7635, Sophia-Antipolis, France.

^{\dagger}E-mail: Elie.Hachem@mines-paristech.fr

conduction in the solids, convection, and thermal radiation simultaneously [3]. However, complex three-dimensional structure of the furnace including the thermal coupling of fluids and solids, turbulent convection, thermal radiation, location of the ingots, the burners, and the given geometry make the problem difficult to analyze accurately and economically. Therefore, models and methods for predicting the furnace behaviour and heat transfer processes of the workpieces are highly demand.

The main objective of this paper is to present a multidomain approach to solve the conjugate heat transfer for which the three modes, convective, conductive and radiative heat transfer interfere simultaneously and in both the fluid part and the solid part. The proposed numerical method for modelling such multimaterial flows (fluid/solid) will be referred as the immersed volume method (IVM) [4]. A complete description and details about this method will be given. But first, we will discuss the driven motivation by revisiting some of the existing approaches that usually deal with such problems.

In recent years, there has been increasing interest in studying numerically a variety of engineering applications that involve thermal coupling of fluids and solids [5, 6, 7]. Most of the time, the general idea of these techniques consists in dividing the global domain into several local subdomains over each of which a local model (equation to be solved) can be analyzed independently. The global solution can then be constructed by suitably piecing together local solutions from individually modelled subdomains. However, during the assembly, the coordination between the meshes can become complicated or even sometimes infeasible. Other alternative approaches have been applied for multi-phase flows problems and are available in the literature, such as the ghost fluid method introduced by Fedkiw *et al.* in [8], the immersed boundary method [9, 10], the domain decomposition [11], the X-FEM [12]. They introduced and improved enrichment functions for material interfaces and voids by means of the level set representations of surfaces.

Nevertheless, in general when using all these techniques, one still need to know the value of the heat transfer coefficients between the two domains which ensures, as a Neumann/Dirichlet boundary conditions, the heat transfer at the air/solid interface. In fact, industrials perform many experimental tests to obtain such heat transfer coefficients. But, when dealing with a large diversity of shapes, dimensions and physical properties of these metals to quench, such operations can become rapidly very costly and time consuming.

In the present study, the proposed method aims to overcome this drawback. The main idea is to retain the use of the monolithic formulation and coupling it to some additional features that could allow a better and accurate resolution, in particularly at the interface between the fluid and solid. Recall that the monolithic resolution, based on the levelset approach consists in considering a single grid for both air and solid for which only one set of equations need to be solved. Consequently, different subdomains are treated as a single fluid with variable material properties. One important feature till now is that by solving the whole domain in a fully monolithic way there is no need of empirical data so as to determine the heat transfer coefficient. The heat exchange at the interface is replaced naturally by solving the convective fluid in the whole domain. Numerically, the communication between the solid and the fluid is obtained naturally without any further assumption and force modelling. In other words, there is no need for some coupling engines specifically designed to handle data exchange and algorithmic control signals between solid region and fluid region.

The second feature of this method is the use of our advanced research in the anisotropic mesh adaptation to adapt the interface between two different materials [4, 13, 14, 15]. The proposed

;

mesh generation algorithm allows the creation of meshes with extremely anisotropic elements stretched along the interface, which is an important requirement for conjugate heat transfer and multi-component devices with surface conductive layers [16]. Many research efforts have been devoted to analyze and to improve the accuracy, stability, conservation and robustness of different immersed boundary method. This is obviously required when following an interface all along the computations. However, in the present study, as the solid, the heated objects inside the furnace are considered fixed, a preadapt meshing is totally affordable. All these previously cited techniques can at a certain degree explicitly be replaced by this proposed locally interface refinement that can generate a quasi conforming mesh with an acceptable cost. Recall that the interface between solid and fluid is nothing but a zero isovalue of the distance function; hence the calculations of the classical boundary integrals that account for the radiative heat transfer between the solid and the fluid are no longer applicable. The contribution of the radiations to the heat transfers is assessed by solving the radiative transfer equation (RTE) and by computing volumetric terms that acts as an energy source terms via divergence of radiative heat flux.

The present approach has already been introduced in the works of Bruchon *et al.* [13], Valette *et al.* [14] and Bernacki *et al.* [15]. If the strategy is similar, the context is clearly different. In [13], the authors have proposed to use the metric properties of the distance function for simulating two bodies in contacts in a forging process. Details about the formulation of the contact condition, mesh adaptation as well as the computation of the distance function are given. On the other hand, in [14], the use of this method was highlighted by several numerical examples such as extrusion and industrial mixing processes. In [15], the authors illustrate the ability of this approach to accurately describe nucleation and grain growth in the context of recrystallization in a polycrystalline material. The present study intends to apply the same strategy for simulating conjugate heat transfers and turbulent fluid flows inside a furnace in the presence of heated industrial parts.

From a numerical point of view, the sudden heating of solid is at the origin of so-called thermal shocks which cause spurious oscillations in the solution. In order to circumvent this issue, a stabilized finite element method is used for both Navier-Stokes [17, 18, 19, 20] and the convection-diffusion equations [21, 22, 23]. As far as the radiative terms are concerned, the radiative transfer equation is solved separately using the so-called P-1 method [24].

The outline of the paper is as follows: first, we present the time-dependent, three-dimensional, conjugate heat transfer and fluid flow problem. The section 2 presents the discretization as well as the stabilized finite element method for solving these equations. A detailed description of the immersed volume method using both the level set function and the anisotropic mesh adaptation is given in section 3. In section 4, the numerical performance of the presented method is demonstrated by means of 2D test cases and a 3D real industrial problem. Comparisons with the literature results are presented. Finally, conclusions and perspectives are outlined.

;

2. GOVERNING EQUATIONS

2.1. Navier-Stokes equations

Let $\Omega \subset \mathbb{R}^d$, $d = 2, 3$, be the spatial computational domain with boundary $\partial\Omega$. In order to compute the motion of an unsteady, viscous, incompressible, non-isothermal flow with buoyancy forces, one has to solve the coupled non-linear system provided by the Navier-Stokes equations including the Boussinesq approximation:

$$\begin{cases} \nabla \cdot \mathbf{u} = 0 & \text{in } \Omega & (1) \\ \rho(\partial_t \mathbf{u} + \mathbf{u} \cdot \nabla \mathbf{u}) - \nabla \cdot (2\mu \boldsymbol{\varepsilon}(\mathbf{u}) - p \mathbf{I}_d) = \rho_0 \beta (T - T_0) \mathbf{g} & \text{in } \Omega & (2) \\ \rho C_p (\partial_t T + \mathbf{u} \cdot \nabla T) - \nabla \cdot (\lambda \nabla T) = f - \nabla \cdot \mathbf{q}_r & \text{in } \Omega & (3) \end{cases}$$

where \mathbf{u} is the velocity vector, p the pressure and T the temperature. Equation (1) is the expression of the incompressibility constraint. Equation (2) that describes the momentum conservation features the density ρ , the dynamic viscosity μ , the deformation-rate tensor $\boldsymbol{\varepsilon}(\mathbf{u}) = (\nabla \mathbf{u} + {}^t \nabla \mathbf{u})/2$, the reference density and temperature ρ_0 and T_0 , the thermal expansion coefficient β and the gravitational acceleration \mathbf{g} . Eventually, equation (3) denotes the energy conservation and it involves the constant pressure heat capacity C_p , the specific thermal conductivity λ , a volume source term f and the heat radiative flux \mathbf{q}_r .

2.2. Turbulence model

The turbulent aspect of flows in furnaces requires the use of dedicated models to compute the flow field. In the present work, we solve the Reynolds-averaged Navier-Stokes problem derived from the equations (1)-(3) and we resort to the standard $k - \varepsilon$ model to close the system. The RANS equations read:

$$\begin{cases} \nabla \cdot \mathbf{u} = 0 & \text{in } \Omega & (4) \\ \rho(\partial_t \mathbf{u} + \mathbf{u} \cdot \nabla \mathbf{u}) - \nabla \cdot (2\mu_e \boldsymbol{\varepsilon}(\mathbf{u}) - p_e \mathbf{I}_d) = \rho_0 \beta (T - T_0) \mathbf{g} & \text{in } \Omega & (5) \\ \rho C_p (\partial_t T + \mathbf{u} \cdot \nabla T) - \nabla \cdot (\lambda_e \nabla T) = f - \nabla \cdot \mathbf{q}_r & \text{in } \Omega & (6) \end{cases}$$

where the averaged values of the unknowns are the velocity \mathbf{u} , the effective pressure p_e and the temperature T . The system (4)-(6) features the effective viscosity μ_e and the effective thermal conduction λ_e which are given by:

$$\mu_e = \mu + \mu_t \quad \text{and} \quad \lambda_e = \lambda + \frac{C_p \mu_t}{\text{Pr}_t} \quad (7)$$

with Pr_t the turbulent Prandtl number. The turbulent viscosity μ_t in expression (7) is a function of the turbulent kinetic energy k and the turbulent dissipation ε that reads:

$$\mu_t = \rho C_\mu \frac{k^2}{\varepsilon} \quad (8)$$

;

with C_μ an empirical constant usually equal to 0.09. To assess μ_t , the introduced variables k and ε are computed using two transport equations that read:

$$\left\{ \begin{array}{l} \rho(\partial_t k + \mathbf{u} \cdot \nabla k) - \nabla \cdot \left(\left(\mu + \frac{\mu_t}{\text{Pr}_k} \right) \nabla k \right) = P_k + P_{kb} - \rho\varepsilon \quad \text{in } \Omega \quad (9) \\ \rho(\partial_t \varepsilon + \mathbf{u} \cdot \nabla \varepsilon) - \nabla \cdot \left(\left(\mu + \frac{\mu_t}{\text{Pr}_\varepsilon} \right) \nabla \varepsilon \right) = \frac{\varepsilon}{k} (C_{1\varepsilon} P_k + C_{3\varepsilon} P_{\varepsilon b} - C_{2\varepsilon} \rho\varepsilon) \quad \text{in } \Omega \quad (10) \end{array} \right.$$

In equations (9) and (10), P_k represents the production of turbulent kinetic energy due to the mean velocity gradients, P_{kb} is the production due to the buoyancy effects, Pr_k and Pr_ε are the turbulent Prandtl number for k and ε respectively, while $C_{1\varepsilon}$, $C_{2\varepsilon}$ and $C_{3\varepsilon}$ are model constants. The production terms P_k and P_{kb} are modelled as follows:

$$P_k = 2\mu_t(\boldsymbol{\varepsilon}(\mathbf{u}) : \boldsymbol{\varepsilon}(\mathbf{u})) \quad \text{and} \quad P_{kb} = -\frac{\mu_t}{\rho \text{Pr}_g} \mathbf{g} \cdot \nabla \rho \quad (11)$$

Finally, it remains to assess the real pressure from the effective pressure and the turbulent kinetic energy, which is carried out in the following manner:

$$p = p_e - \frac{2}{3} \rho k \quad (12)$$

2.3. Radiative transfer model

2.3.1. Gray gas assumption The gray gas model may often be sufficient for furnace applications since, most of the time, surfaces are fairly rough and, as a result, reflect in a relatively diffuse fashion. Furthermore, if the radiative properties do not vary much across the spectrum then the gray gas simplifications may be valid. According to Modest [24], in the case of a gray medium, the divergence of the heat radiative flux that appears in equation (3) or (6) relies on the local temperature and the incident radiation as follows:

$$-\nabla \cdot \mathbf{q}_r = \kappa (G - 4\kappa\sigma T^4) \quad (13)$$

where G denotes the incident radiation, κ is the mean absorption coefficient and σ the Stefan-Boltzmann constant.

2.3.2. The P-1 approximation Equation (13) clearly establishes the necessity of getting an expression of G in order to assess the divergence of \mathbf{q}_r . This can be achieved by considering the radiative transfer equation (RTE) that may be found in [25]. In the present study, one resorts to the so-called P-1 radiation model that is the simplest case of the P-N model to express radiation intensity by means of series of spherical harmonics (*cf.* [24, 25] for more details). Using this approach enables to simplify the RTE into an elliptical partial differential equation in terms of the incident radiation G as follows:

$$\left\{ \begin{array}{l} \nabla \cdot \left(\frac{1}{3\kappa} \nabla G \right) - \kappa G = 4\kappa\sigma T^4 \quad \text{in } \Omega \\ \frac{\partial G_w}{\partial n} = \frac{3\kappa\epsilon_w}{2(2 - \epsilon_w)} (4\sigma T_w^4 - G_w) \quad \text{in } \partial\Omega \end{array} \right. \quad (14)$$

where subscript w denotes wall quantities, n is the normal to the wall and ϵ_w the emissivity of the wall.

2.3.3. Radiative properties In the context of gray-medium assumption, the mean absorption coefficient κ can be derived from the emissivity ϵ of the material using the Bouguer's law which reads:

$$\kappa = -\frac{1}{L_m} \ln(1 - \epsilon) \quad (15)$$

where L_m is the mean beam length defined as:

$$L_m = 3.6 \frac{\Delta V}{\Delta S} \quad (16)$$

For unstructured grids, ΔV and ΔS are appropriate measures of volume and surface for each element of the mesh.

2.4. Non dimensional parameters

In practice, relevant dimensionless numbers are used in our numerical experiments. They read:

$$\begin{aligned} \text{Re} &:= \frac{\rho U L}{\mu} && \text{Reynolds number} \\ \text{Pe} &:= \frac{\rho C_p U L}{\lambda} && \text{Peclet number} \\ \text{Gr} &:= \frac{\rho^2 \beta g L^3 \Delta T}{\mu^2} && \text{Grashof number} \\ \text{Pr} &:= \frac{C_p \mu}{\lambda} && \text{Prandtl number} \\ \text{Ra} &:= \frac{\rho^2 C_p \beta g L^3 \Delta T}{\mu \lambda} && \text{Rayleigh number} \\ \text{Fr} &:= \frac{U^2}{g L \Delta T} && \text{Froude number} \end{aligned} \quad (17)$$

where L is the characteristic length of the problem, U the characteristic velocity and ΔT the characteristic temperature difference. These numbers are related by $\text{Ra} = \text{Gr} \cdot \text{Pr}$, $\text{Fr} = \text{Re}^2 \cdot \text{Gr}^{-1}$ and $\text{Re} = \text{Pe} \cdot \text{Pr}^{-1}$.

2.5. Boundary conditions

At the inflow boundary, for a prescribed velocity \mathbf{u} , the value of k can be computed using:

$$k_{\text{inlet}} = c_{\text{bc}} \cdot |\mathbf{u}|^2 \quad (18)$$

where c_{bc} is fixed to 0.02 as an empirical constant. Once k is computed, the value of ε can be prescribed using:

$$\varepsilon_{\text{inlet}} = \frac{C_\mu \cdot k^{3/2}}{L} \quad (19)$$

with L , a fixed constant, known as the characteristic length of the model [26]. These computed values of k and ε are extended into the interior domain as initial conditions.

At the outflow, the following homogeneous Neumann boundary conditions are applied:

$$\mathbf{n} \cdot \nabla k = 0 \quad \text{and} \quad \mathbf{n} \cdot \nabla \varepsilon = 0 \quad (20)$$

;

On the rest of the computational boundary a combination of Neumann and Dirichlet conditions is imposed by using classical wall function introduced in [27] which describe the asymptotic behaviour of the different variables near the wall. If the boundary mesh nodes are located in the logarithmic region, we impose the wall shear stress given by :

$$\tau_w = \rho U^{*2} \quad (21)$$

where U^* is the friction velocity evaluated by solving the equation:

$$\frac{U}{U^*} = \frac{1}{k} \ln \left(\frac{\rho E \delta}{\mu} U^* \right) \quad (22)$$

where U is the tangential velocity, δ is the distance to the wall, k is the Von Karman constant (typically equal to 0.41) and E is a roughness parameter taken equal to 9.0 for smooth walls. Imposing the wall shear stress corresponds to a non-homogeneous Neumann boundary condition for the momentum equation in the tangential direction. The normal component of the velocity is set to zero. The turbulent kinetic energy and its dissipation on the boundary of the mesh are given as function of the friction velocity [27]:

$$k_w = \frac{U^{*2}}{\sqrt{C_\mu}} \quad \text{and} \quad \varepsilon_w = \frac{U^{*3}}{k_w \delta} \quad (23)$$

Boundary conditions at a wall for the energy equation are enforced through a temperature wall function similar to that used for the momentum equations. The effective heat flux in the wall function is computed as :

$$q_w = \mathbf{n} \cdot \mathbf{q}_w = \frac{\rho C_p C_\mu^{1/4} k_w (T_w - T)}{T^+} \quad (24)$$

where T_w is the wall temperature and T^+ is the normalized temperature given in [28].

3. IMMERSED VOLUME TECHNIQUE

The immersed volume technique consists in dealing with only one computational domain for both fluid and solid. Hence, the domain can be viewed as a composite material made of several components. In order to provide very accurate results, such a method must gather three key ingredients: a level set function, an anisotropic mesh adaptation and appropriate mixing laws to describe the properties of the composite material. The following paragraphs aim at detailing these three items.

3.1. Level set approach

The so-called level set approach enables to represent the interface between solid and fluid as a zero level of a smooth function. In practice, a signed distance function is used to localize the interface and initialize the material properties on both sides of this latter. In our context, the solid being fixed, the interface is static. Let Ω_f , Ω_s and Γ_i represent respectively the fluid domain, the solid domain and the interface. They verify:

$$\Omega_f \cup \Omega_s = \Omega \quad \text{and} \quad \Omega_f \cap \Omega_s = \Gamma_i \quad (25)$$

;

For each node of the computational domain Ω , the level set function α which is the signed distance from the interface reads:

$$\alpha(\mathbf{x}) = \begin{cases} > 0 & \text{if } \mathbf{x} \in \Omega_f, \\ 0 & \text{if } \mathbf{x} \in \Gamma_i, \\ < 0 & \text{if } \mathbf{x} \in \Omega_s. \end{cases} \quad (26)$$

The physical and thermodynamic properties in the domain are then calculated as a function of α ; for instance, the mixed density is calculated using a linear interpolation between the values of the density in the fluid and the solid:

$$\rho = \rho_f H(\alpha) + \rho_s (1 - H(\alpha)) \quad (27)$$

where H is a smoothed Heaviside function given by:

$$H(\alpha) = \begin{cases} 1 & \text{if } \alpha > \varepsilon \\ \frac{1}{2} \left(1 + \frac{\alpha}{\varepsilon} + \frac{1}{\pi} \sin\left(\frac{\pi\alpha}{\varepsilon}\right) \right) & \text{if } |\alpha| \leq \varepsilon \\ 0 & \text{if } \alpha < -\varepsilon \end{cases} \quad (28)$$

ε being a small parameter such that $\varepsilon = O(h)$ and h the averaged mesh size in the vicinity of the interface.

3.2. Anisotropic mesh adaptation

Accurate calculation of the temperature distribution along the air-solid interface is critical for a correct modelling of industrial experiments. When the heat flux is directed through the interface, the difficulty arises due to the discontinuity of the properties of the material across the interface. If this latter is not aligned with the element edges, it may intersect the element arbitrarily such that the accuracy of the finite element approach can be compromised. In order to circumvent this issue, the level-set process is thus coupled to an anisotropic mesh adaptation as described in [16]. The idea of this method is to gradually refine the mesh when approaching the interface. In this way, the mesh becomes locally refined which enables to sharply define the interface and to save a great number of elements with respect to classical isotropic refinement. This anisotropic adaptation is performed by constructing a metric map that allows the mesh size to be imposed in the direction of the distance function gradient. Let us briefly describe the main principles of this technique. First of all, one has to resort to a so-called metric which is a symmetric positive defined tensor representing a local base that modify the distance computation, such that:

$$\|\mathbf{x}\|_{\mathbb{M}} = \sqrt{{}^t\mathbf{x} \cdot \mathbb{M} \cdot \mathbf{x}}, \quad \langle \mathbf{x}, \mathbf{y} \rangle_{\mathbb{M}} = {}^t\mathbf{x} \cdot \mathbb{M} \cdot \mathbf{y}. \quad (29)$$

The metric \mathbb{M} can be regarded as a tensor whose eigenvalues are related to the mesh sizes, and whose eigenvectors define the directions for which these sizes are applied. For instance, using the identity tensor, one recovers the usual distances and directions of the Euclidean space. In our case the direction of mesh refinement is given by the unit normal to the interface which corresponds to the gradient of the level set function: $\mathbf{x} = \nabla\alpha/|\nabla\alpha|$. A default mesh size, or

;

background mesh size, h_d is imposed far from the interface and it is reduced as the interface comes closer. A likely choice for the mesh size evolution is the following:

$$h = \begin{cases} h_d & \text{if } |\alpha(\mathbf{x})| > e/2 \\ \frac{2h_d(m-1)}{m e} |\alpha(\mathbf{x})| + \frac{h_d}{m} & \text{if } |\alpha(\mathbf{x})| \leq e/2 \end{cases} \quad (30)$$

Eventually, at the interface, the mesh size is reduced by a factor m with respect to the default value h_d . Then this size increases until equalling h_d for a distance that corresponds to the half



Figure 1. Mesh adaptation in the vicinity of the interface: from the initial mesh to the final mesh.

of a given thickness e . The unit normal to the interface \mathbf{x} and the mesh size h defined above, lead to the following metric:

$$\mathbb{M} = C(\mathbf{x} \otimes \mathbf{x}) + \frac{1}{h_d} \mathbb{I} \quad \text{with} \quad C = \begin{cases} 0 & \text{if } |\alpha(\mathbf{x})| \geq e/2 \\ \frac{1}{h^2} - \frac{1}{h_d^2} & \text{if } |\alpha(\mathbf{x})| < e/2 \end{cases} \quad (31)$$

where \mathbb{I} is the identity tensor. This metric corresponds to an isotropic metric far from the interface (with a mesh size equal to h_d for all directions) and to an anisotropic metric near the interface (with a mesh size equal to h in the direction \mathbf{x} and equal to h_d in the others).

;

In practice, the mesh is generated in several steps using, through the CIMLIB library, the MTC mesher developed by T. Coupez [29]. This mesher is based on a topological optimisation technique available in [16] for the anisotropic case. At each step of the refinement process, the mesh size converges locally toward the target size. Figure 1 illustrates the steps of the refinement process for a three ingots immersed inside the three-dimensional furnace. Figure 2 shows the computational domain at the end of the anisotropic adaptation process, it clearly emphasizes the mesh refinement along all the interfaces whereas the rest of the domain keeps the same background mesh size.



Figure 2. Computational domain after anisotropic adaptation

3.3. *Mixing laws*

The immersed volume technique implies that the material which is treated in the equations is a composite one. Hence, it is necessary to define the physical and thermodynamic properties of such a material. To achieve this, linear interpolations are mainly used between the values of the properties in the fluid and the solid as previously evoked in expression (27). The smoothed Heaviside function defined in (28) enables to assign the right properties on each side of the interface. The material properties introduced in systems of equations (1-3)-(13), such as density, initial temperature, dynamic viscosity, constant pressure heat capacity and

;

mean absorption coefficient, are defined as:

$$\begin{aligned}
\rho &= \rho_f H(\alpha) + \rho_s (1 - H(\alpha)) \\
\mu &= \mu_f H(\alpha) + \mu_s (1 - H(\alpha)) \\
\rho C_p &= (\rho_f C_{pf} H(\alpha) + \rho_s C_{ps} (1 - H(\alpha))) \\
\rho C_p T &= \rho_f C_{pf} T_f H(\alpha) + \rho_s C_{ps} T_s (1 - H(\alpha)) \\
\kappa &= \kappa_f H(\alpha) + \kappa_s (1 - H(\alpha))
\end{aligned} \tag{32}$$

However, as far as the thermal conductivity is concerned, linear interpolation would lead to inaccurate results. According to [30], one has to resort to the following law to ensure the conservation of the heat flux:

$$\lambda = \left(\frac{H(\alpha)}{\lambda_f} + \frac{1 - H(\alpha)}{\lambda_s} \right)^{-1} \tag{33}$$

Table I. Properties of materials.

Properties	Air	Inconel 718
density ρ [kg/m ³]	1.25	
heat capacity C_p [J/(kg K)]	1000	
viscosity μ [kg/(m s)]	1.9e-5	–
conductivity λ [W/(m K)]	0.0262	
emissivity ϵ	–	0.7

3.4. Originality of the method

Usually, the simulation of the heat transfer between two media requires additional boundary conditions of Neumann/Dirichlet type. Such conditions typically describe the convection transfer at the interface

$$\int_{\Gamma_i} h_c (T - T_{\text{ext}}) d\Gamma, \tag{34}$$

where h_c is the heat transfer coefficient and T_{ext} is the averaged temperature of the surroundings. Similarly, the radiative heat transfer is computed using the classical boundary condition:

$$\int_{\Gamma_i} \sigma \epsilon (T^4 - T_{\text{ext}}^4) d\Gamma, \tag{35}$$

where σ is the Stefan-Boltzmann constant and ϵ is the emissivity.

Once the object is immersed inside the computational domain using the IVM, the need of geometric boundary conditions vanishes and is replaced by the zero level of the level set

;

to that used for the equations of motion. Again, the spatial discretization is performed using approximation spaces. Thus, the Galerkin formulation is obtained by multiplying these equations by an appropriate test functions, applying the divergence theorem to the diffusion terms and integrating over the domain of interest. Following the lines on the use of stabilisation methods for transient convection-diffusion-reaction equations as discussed in [23, 42], the stabilized weak form of equation (38) reads:

$$\left\{ \begin{array}{l} \text{Find } \varphi \in S_h \text{ such that, } \forall w \in W_h \\ (\partial_t \varphi + \mathbf{u} \cdot \nabla \varphi, w) + (\alpha \nabla \varphi, \nabla w) + (r\varphi, w) \\ + \underbrace{\sum_K (\mathcal{R}(\varphi), \tau_{\text{SUPG}} \mathbf{u} \cdot \nabla w)_K}_{\text{streamline upwind}} + \underbrace{\sum_K (\mathcal{R}(\varphi), \tau_{\text{SCPG}} \tilde{\mathbf{u}} \cdot \nabla w)_K}_{\text{discontinuity-capturing}} = (f, v) \end{array} \right. \quad (39)$$

where S_h and W_h are standard test and weight finite element spaces (the scalar counterpart of the vector space defined in (36)) and $\mathcal{R}(\varphi)$ is the appropriate residual of equation (38). In equation (39), two additional stabilizing terms have been introduced; the first controls the oscillations in the direction of the streamline (SUPG) [17, 43] and the other controls the derivatives in the direction of the solution gradient (SCPG) [44, 41]. This can improve the result for convection dominated problems while the shock-capturing technique precludes the presence of overshoots and undershoots by increasing the amount of numerical dissipation in the neighborhood of layers and sharp gradients. The evaluation of the τ_{SUPG} and τ_{SCPG} stabilizations terms follows the definition described in [17, 44, 41]. The time derivatives are approximated by the Euler forward difference scheme.

The algebraic problems resulting from the finite element formulation are assembled and solved using the conjugate residual method associated to the incomplete LU preconditioner from the PETSc (Portable Extensive Toolkit for Scientific Computation) library. A master-slave parallel strategy was used [40, 45], involving SPMD (Single Program, Multiple Data) modules and the MPI (Message Passing Interface) library standard. The computations of the 3D conjugate heat transfer have been obtained using 8 2.4 Ghz Opteron cores in parallel (linked by an Infiniband network).

5. VALIDATION FOR 2D CASES

In this section, we want to validate the numerical performance of the immersed volume method over two numerical tests involving two-dimensional thermally coupled flows. All the numerical simulations were carried out by using the CIMLIB finite element library. This C++ library, which is highly parallel, is developed at CEMEF by the team of Coupez and Digonnet (see [40]).

The transient natural convection of low-Prandtl-number fluids in a differentially heated square cavity is solved at first using a classical approach and compared to the published results. This preliminary step enables us to use the classical approach as a reference in order to validate the IVM method. Two test cases are then considered to lead this validation. For both of them, a square enclosure is regarded. However, in order to apply the IVM approach, the domain is enlarged by replacing the left wall by a solid body. The results obtained using

;

classical and IVM methods are then plotted on both domains and compared one to another. The main purpose is to show that IVM method must yield same results as the classical one from a fluid dynamics, turbulent flow and heat transfer point of view. We expect such conclusions from the following numerical experiments:

- i) The IVM method performed well on both conjugate laminar and turbulent mixed convection and conduction in lid-driven enclosure with thick vertical wall.
- ii) The proposed approach seems promising to simulate turbulent flow and heat transfer inside industrial furnaces in the presence of heated workpieces.

5.1. Transient natural convection of low-Prandtl-number fluids

The study of flow and heat transfer for lid-driven enclosures offers an interesting test to validate numerical solution algorithms [46, 47, 48]. It has been extensively used by researchers

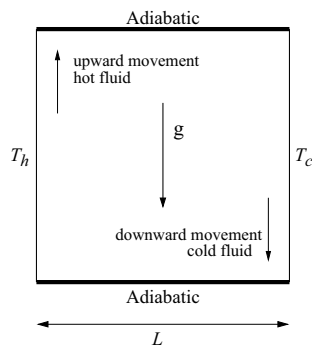


Figure 3. Set-up of the differentially heated square cavity.

because of its growing interest in many applications such as materials processing, metallurgy, crystal growth and many others [49, 46, 50, 47]. In [46], the authors repeated the numerical example taken from [49] which consists in solving the classical flow in a cavity with differentially heated vertical walls with low Prandtl number. It was shown that under such condition the flow exhibits a Hopf bifurcation that leads to an oscillating flow pattern. This particular example is still an interesting and challenging problem especially under transient conditions. Correspondingly, the authors in [46] showed that by tracking the subscales and keeping their effects in the thermal coupling problems, higher accuracy is obtained in the solution and the stability of the coupled problem is improved in respect to other classical stabilized finite-element methods. Our purpose here is first to validate the finite element implementation of the coupled problem by comparing our prediction to the given reference, and second, to assess the effectiveness of the IVM method on an extended domain using a thick vertical wall. The problem is schematically shown in figure 6 which is a square enclosure with a side length L . Both top and bottom surfaces of the enclosure are insulated *i.e.* the zero heat flux boundary condition is prescribed. The vertical walls are maintained at different T_h (hot) and T_c (cold) constant temperatures. Homogeneous Dirichlet boundary conditions are prescribed everywhere on the boundary for the velocity. The radiation effects are assumed to be negligible. We assume that the fluid properties are to be constant, except for the density in the buoyancy term,

;

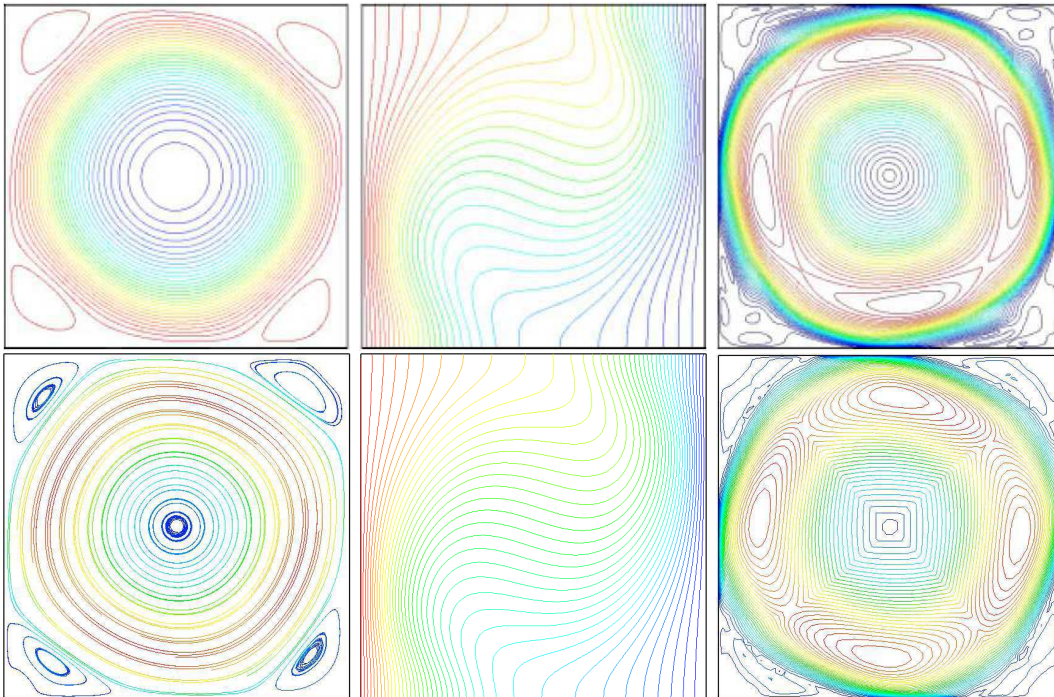


Figure 4. Comparison of the present results (bottom) with the reference ones (top) in [46].
Left: streamlines. Middle: isotherms. Right: velocity norm.

which allows Boussinesq approximation. The gravitational acceleration is taken parallel to the isothermal walls. Calculations were carried out using a 61×61 unstructured mesh refined near the walls and a time step of 0.002. The Prandtl number Pr is taken to be equal to 0.005 and the Grashof number Gr is fixed at $5 \cdot 10^6$. For such unusual values, taken from [49, 46], oscillations are predicted with a dimensionless frequency of 12.2. Note that under certain conditions, these convective oscillations appear in many low Prandtl number fluids as the crystal metal, the liquid metals in casting, nuclear reactor safety and many other applications. More details can be found in [49, 51, 48]. All computations have been carried out by starting with a fluid at rest. The expected flow is basically formed by one main centred circulation limited by the lateral confinement and four different recirculation located at the corners as shown in figure 4. The streamlines, the isotherms and the velocity norm obtained at a certain time step from the present calculation are exposed in figure 4 and compared with results obtained by Codina and Principe in [46], showing good agreement between them. The time history of the velocity U_x , captured at a mid right-hand corner of the cavity (0.9571, 0.5043), is shown in figure 5 and compared well to results from [49]. As expected, the flow field oscillates with a dimensionless frequency of 12.18 which is in very good accordance to the reference value.

;

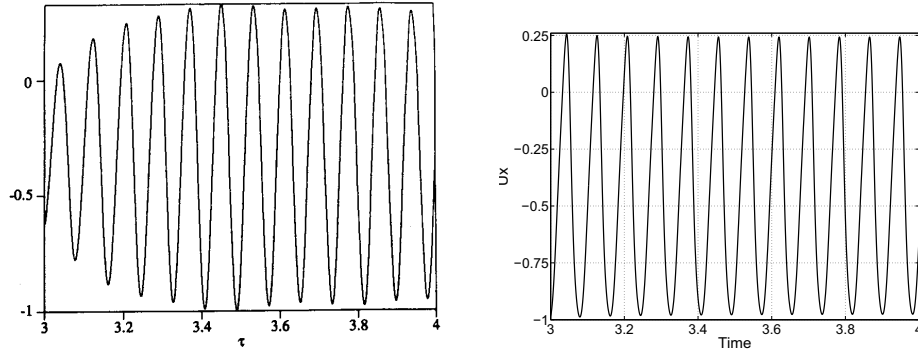


Figure 5. Time series of U_x at mid-right corner of the cavity: present work (left); reference (right).

5.2. Conjugate-mixed convection with a thick vertical wall

To evaluate the performance of the IVM method in terms of multi-domain representation, we extend our domain by adding a vertical thick wall on the left side of the cavity (see figure 6). Several experimental and numerical studies have been carried out on natural convection heat transfer in enclosures under boundary conditions, however, studies about a partially divided enclosures are rarely investigated [52]. Such applications concern cooling of electronic devices, jet impingement [53], enhancement of room air [54], flow and temperature distribution in heat loaded furnaces [55], heat exchanger design [56], etc.

The IVM approach, initially implemented and validated in [4], was shown to be completely suitable for simulating such multi-material problems. In the present study, we aim to

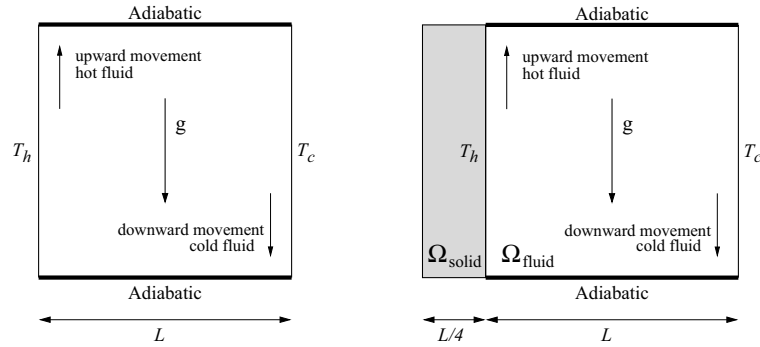


Figure 6. Schematic of the problem with domain and boundary conditions used. Case 1: square enclosure with left and right walls differentially heated. Case 2: the same square enclosure with a thick left vertical wall.

extend the validation on conjugate heat transfer and turbulent flow problems, in particularly, for simulating industrial furnaces with heated objects inside. A very important common characteristic of solidfluid heterogeneous media is still how to resolve the discontinuity in physical properties across their interfaces. In the IVM method, the level set function identifies automatically the solid part from the fluid region and applies the anisotropic mesh adaptation

at the interface [4]. The proposed mesh generation algorithm allows the creation of meshes

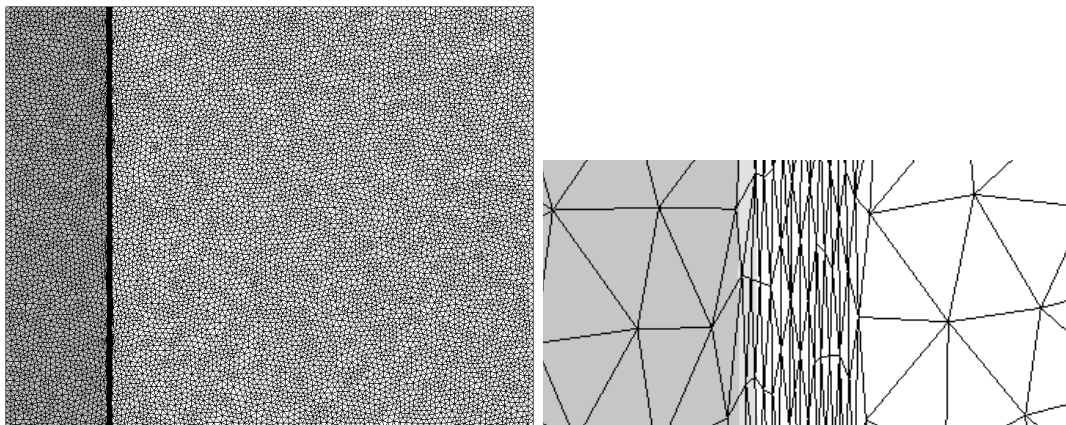


Figure 7. Left: computational domain with a left thick wall. Right: close-up along the interface.

with extremely anisotropic elements stretched along the interface (*cf.* figure 7), which is an important requirement for conjugate heat transfer and multi-component devices with surface conductive layers [52].

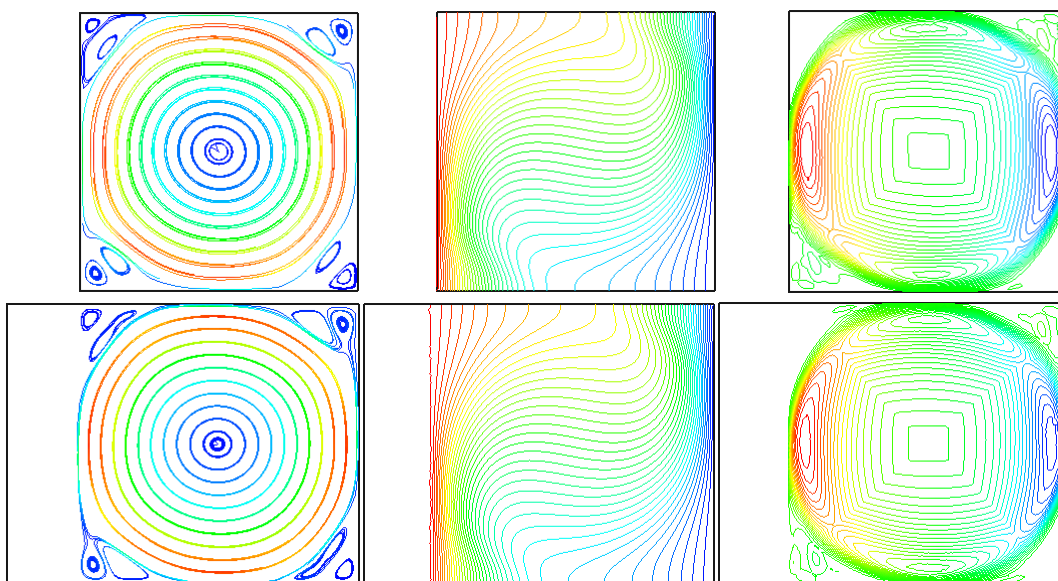


Figure 8. Comparison between the IVM method (bottom) and the classical approach (top).
Left: streamlines. Middle: isotherms. Right: velocity norm.

Thus, a single set of equations (1)-(3) is solved for the whole computational domain by treating the different subdomains as a single fluid with variable material properties. At solid-

;

fluid interfaces, conductivities are calculated using a harmonic mean formulation [30] in order to handle abrupt changes in the material properties. Thus, we automatically well establish the continuity of temperature and heat flux across the interface. The solid domain have a dimensionless thickness of $0.25L$ and is initially taken at T_h (hot) constant temperature. The temperature gradient inside the solid wall is extremely low due to the use of high thermal conductivity ($\lambda = 10^6$). Moreover, setting the relative kinematics viscosity very high value in the solid region satisfies the zero velocity in this region and hence the no-slip condition on the interface is also satisfied. Therefore, the convective terms in the energy equation drop out and the equation reduces to the transient conduction equations in the solid. The stabilized finite element methods are employed to discretize and solve the coupled heat transfer inside the enclosure.

The aim of this numerical test is not to study the effect of conducting left wall in terms of thickness and conductivity ratios, it is more to analyse the general behaviour of the solution on extended domains. As it was shown in [4], the idea is to investigate how well

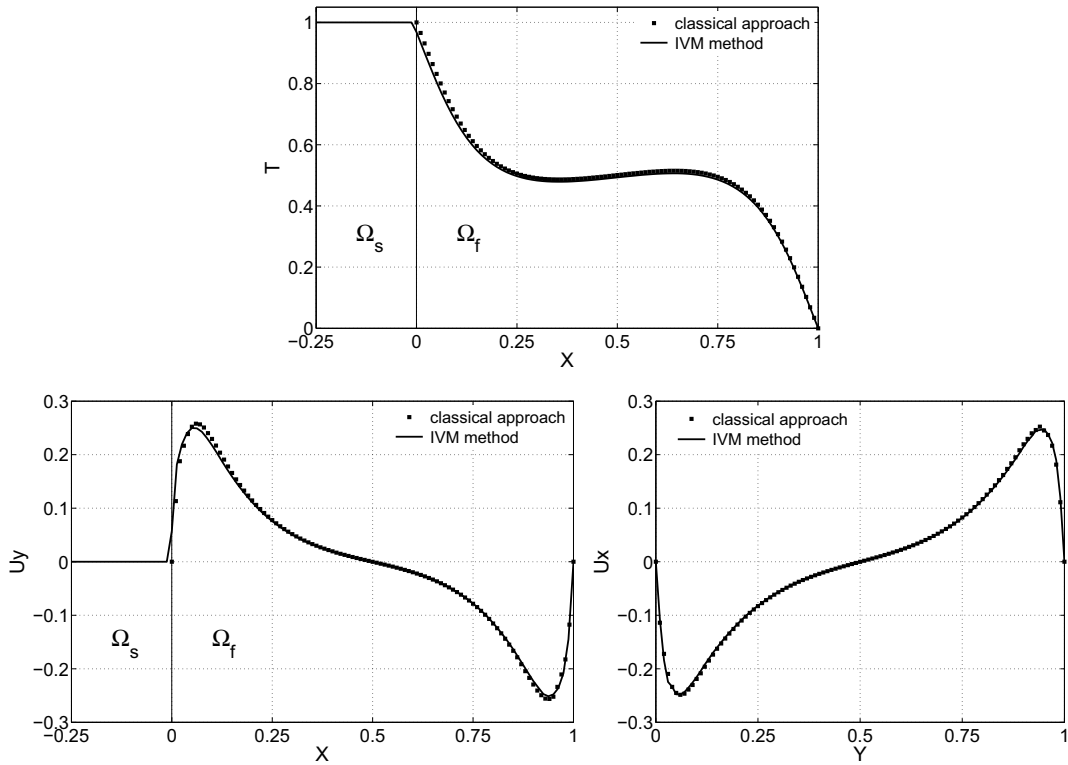


Figure 9. Comparison between the IVM method and the classical approach. Top: T along the x centerline. Left: U_y along the x centerline. Right: U_x along the y centerline.

the boundary conditions between two subdomains by volumetric source terms can be replaced. Several benchmarks in [4] demonstrate the effectiveness of the proposed approach. Here, this investigation is continued and carried out over more complex situations.

;

The Prandtl number and the Grashof number are chosen to be under the threshold of oscillation for this test. Thus, the flow and temperature showed a gradual approach to a steady state without any oscillation. A comparison of streamlines, isotherms and velocity norm between the classical approach (with zero wall thickness) and the IVM approach (with a thick vertical wall) are depicted in figure 8. As shown, the streamlines are almost circular in shape with very weak circulations at the corners and the obtained results are in complete agreement. Due to high conductivity of the solid wall, the fluid behaves as the classical lid-driven cavity problem. Finally, temperature and velocity distributions along the centrelines obtained on both domains are illustrated in figure 9. Afresh, all the results are almost indistinguishable between both approaches.

5.3. Forced turbulent convection in a partially divided square enclosure

In this section same computational domains have been used to solve forced turbulent convection heat transfer on a solid wall. This example can be seen as a simplified model of a gas-

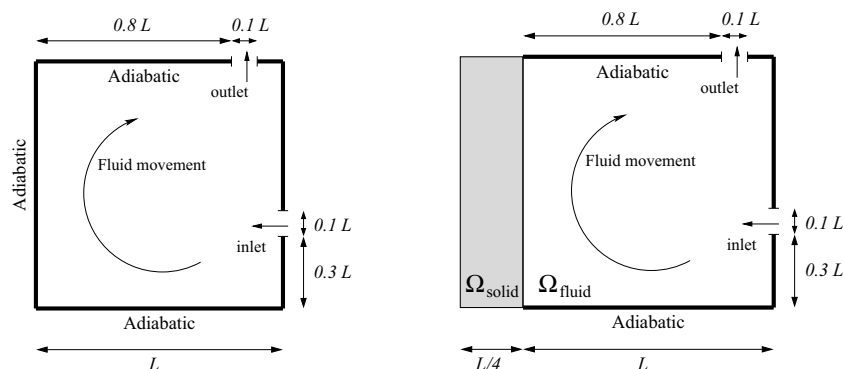


Figure 10. Schematic of the problem with domain and boundary conditions used. Left: square enclosure. Right: the same square enclosure with a thick left vertical wall.

fired furnace. The heated air is pumped into the enclosure from the right inlet located at $y = 0.3L$. The velocity magnitude is $0.5m/s$, and the temperature is fixed at $1273K$. At all other boundaries, adiabatic condition for the temperature equation is applied. The air is vented out the enclosure through the outlet positioned at $x = 0.8L$ on the top wall. For illustration, figures 10 and 11 show the schematic diagram and the sequence of the treated problem.

Unlike the previous test cases, the highly turbulent characteristic of the flow requires to solve the $k - \varepsilon$ model (4)-(6) with the standard logarithm wall functions [27]. Furthermore, to preclude possible numerical oscillations in the regions of high convection and high gradients, both the SUPG and SCPG stabilisation methods are included. The dimensionless parameters involved in the problem are the Peclet number ($Pe = 1,000$) and the Reynolds number ($Re = 50,000$).

As in the previous section, once the interface is refined, the material properties for each subdomains are dispersed. Two additional equations, the turbulent kinetic energy and dissipation are coupled and solved on both domains. Note that the use of high value for the relative kinematics viscosity in solid region makes the velocity components negligibly small and satisfies the no-slip condition at the refined interface. Therefore, as shown for the energy

;

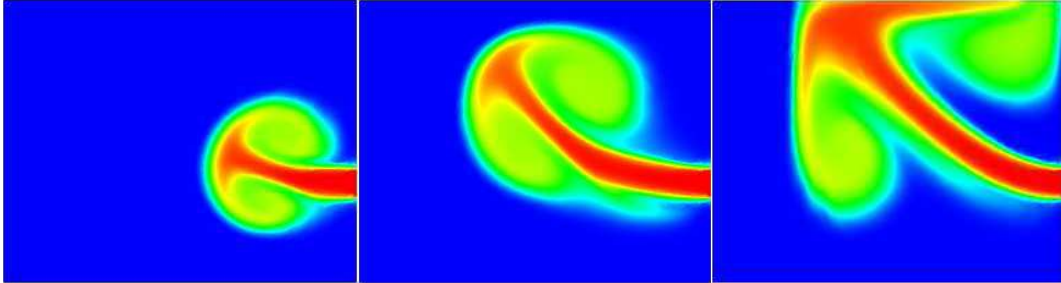


Figure 11. Sequence of the air injection at different time steps.

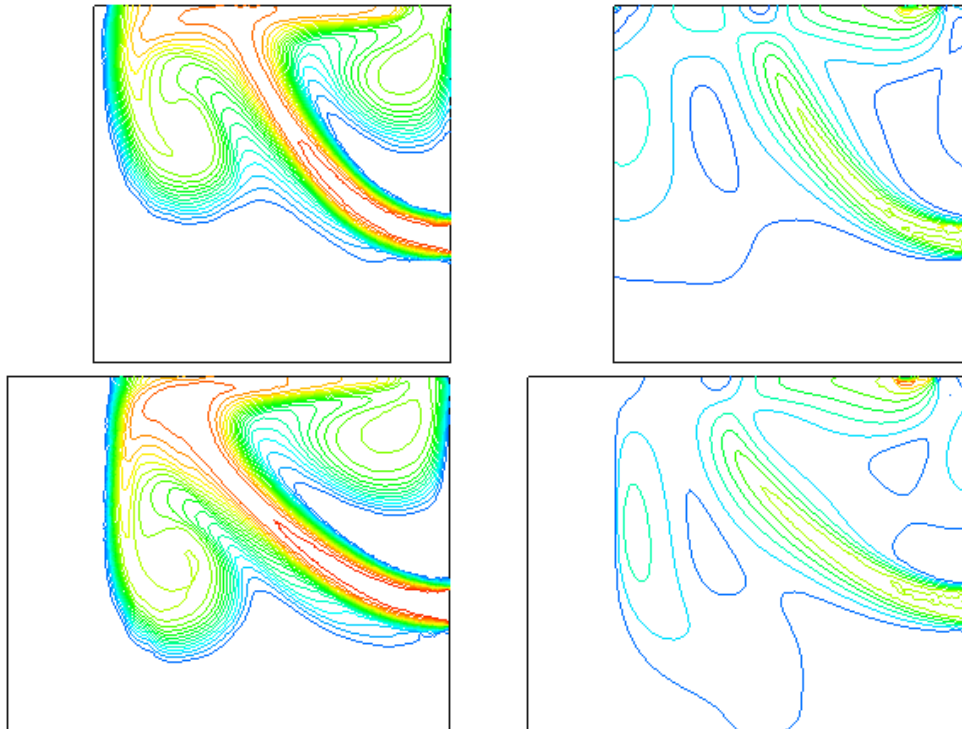


Figure 12. Comparison between the IVM method (bottom) and the classical approach (top).
Left: isotherms. Right: velocity norm.

equations, all the convective terms as well as the source (*i.e.* destruction) terms in the two-equations of the $k-\varepsilon$ model drop out. To complete, the solution gradients of the $k-\varepsilon$ model is

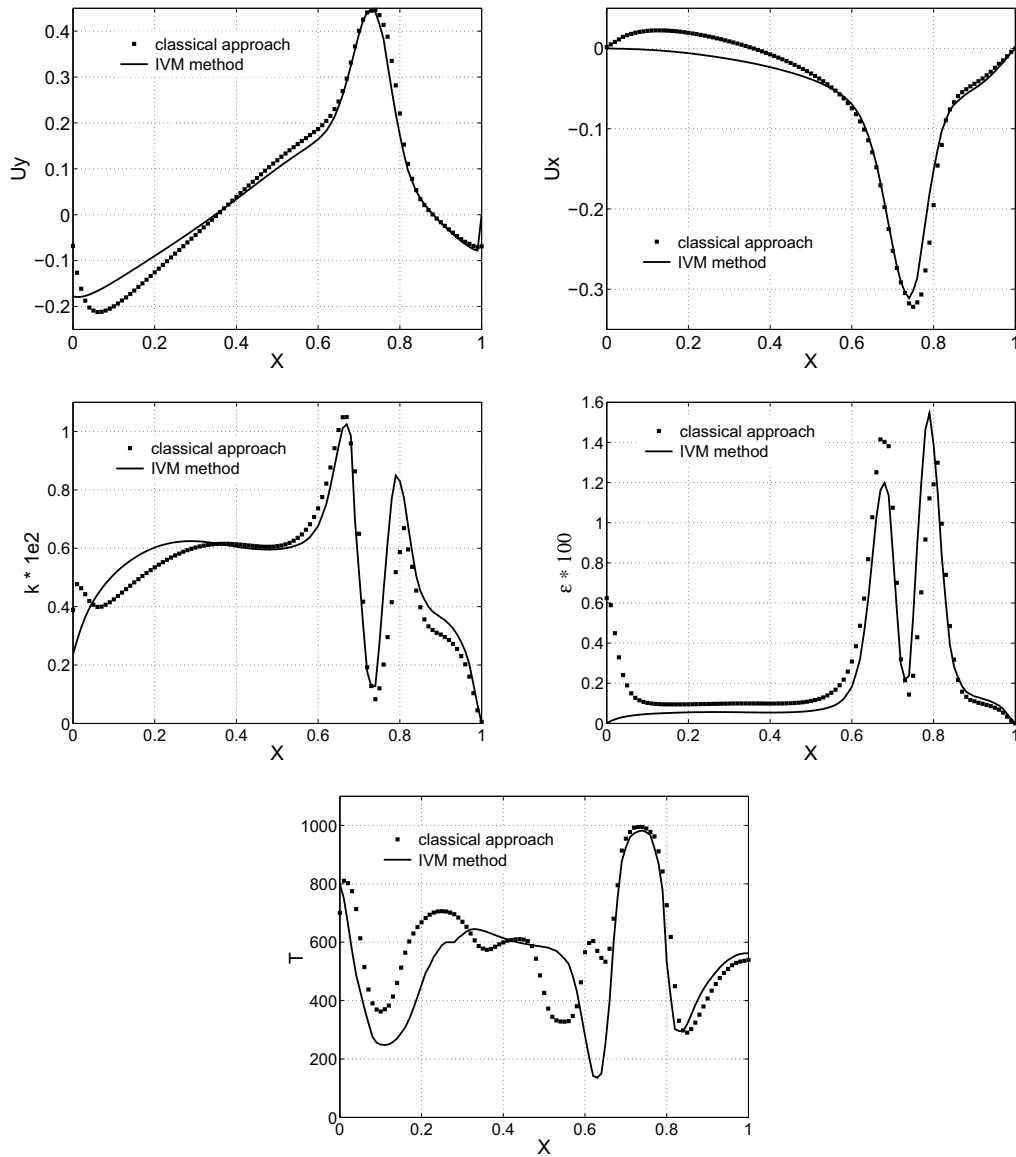


Figure 13. Comparison between the IVM method and the classical approach along the x centerline. Top left: velocity U_x . Top right: velocity U_y . Middle left: turbulent kinetic energy $k \cdot 10^2$. Middle right: turbulent dissipation $\varepsilon \cdot 10^2$. Bottom: temperature T .

extremely low inside the solid wall due to the fact that the high introduced relative kinematics viscosity is proportional to the diffusion terms in both turbulent equations (9)-(10) .

;

Figure 12 shows a good agreement between both approaches for the temperature and the velocity norm contours at a certain time step. As expected, the use of high viscosity in the solid region satisfies the zero velocity in this region and hence the no-slip condition on the extremely refined interface is also verified. Moreover, due to the low conductivity of the solid wall, a quasi adiabatic surface is observed and reported.

In figure 13, the distributions of the velocity profiles, the temperature, the turbulent kinetic energy and the turbulence dissipation are plotted along the line $y = 0.5$ at time $t = 20s$. This stage corresponds to the fully development of the turbulent flow before it reaches a quasi-steady state. Similar trends and good agreement between the two approaches are observed in all the solutions. However, in the near-wall region, some differences in the solution exist. We suspect that the main discrepancy could be due to the use of a simple wall function implemented as Dirichlet boundary conditions in the classical approach. On the other hand, in the IVM approach, the turbulent quantities are computed naturally at the interface. The differences between solutions computed using wall functions implemented in the strong and weak sense were also observed in [57] and [41]. It was shown that the use of Dirichlet boundary conditions for k and ε produced rather disappointing results, whereas the performance of Neumann boundary conditions is remarkably efficient for the near-wall treatment. The authors have pointed out that by letting k to be computed "naturally" at the boundary, they improved the prediction of the turbulent quantities in the near wall regions and they obtained the correct behaviour. This matter will be the subject of further investigations in a near future.

5.4. 3D test case

As a final example, the heat transfer and turbulent flow inside an industrial furnace is considered. Figure 2 shows three ingots taken initially at $333K$ and positioned at different locations inside the furnace. All computations have been conducted by starting with a fluid at rest and at a constant temperature of $333K$.

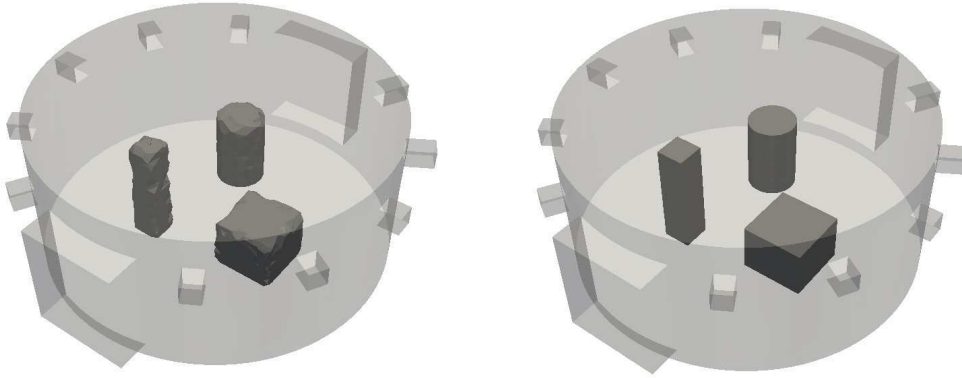


Figure 14. Computational domain inside the furnace. Left: initial geometry. Right: final geometry.

The heated air is pumped into the furnace from 10 different inlets forming a circle of $6m$ diameter at $1.7m$ from the ground. The velocity magnitude of each burner is $10m/s$, and the corresponding temperature is fixed at $1073K$. At all other boundaries, adiabatic condition for

the temperature equation is applied for sake of simplicity. The air is vented out the furnace through the outlet positioned at the centre-top wall (at $z = 2.42m$). The volume mesh used in the computations has 57,012 nodes and 304,785 tetrahedral elements. The time-step is equal to 0.001s. The 3D computations have been obtained using 32 2.4Ghz Opteron cores in parallel (linked by an Infiniband network) [40]. We start by deriving an anisotropic adapted mesh that describes very accurately the interface between the three workpieces and the surrounding air. In figure 14, one can clearly see that, after a reduced number of steps, the shapes of the ingots are well respected by the mesh. Only additional nodes are locally added at the interface

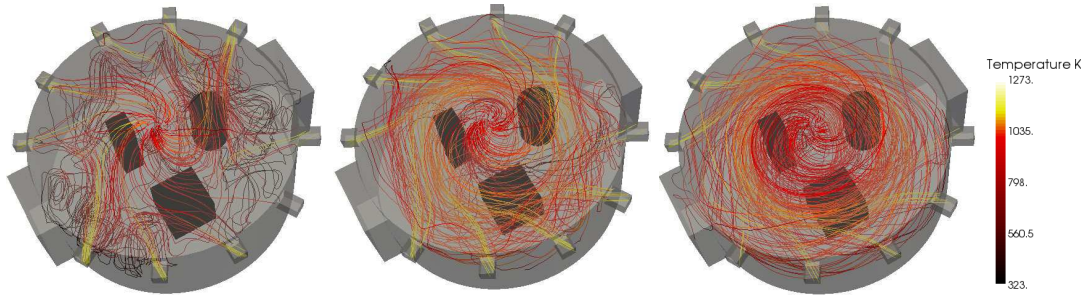


Figure 15. Streamlines and isotherms inside the furnace at different time steps.

region, whereas the rest of domain keeps the same background size. Once the mesh is well adapted along the interface, the material distribution between each physical domain can be described by means of the level set function. Consequently, the same set of equations (1)-(3) is simultaneously solved over the entire domain including both fluid and solid regions with variable material properties (see table I).

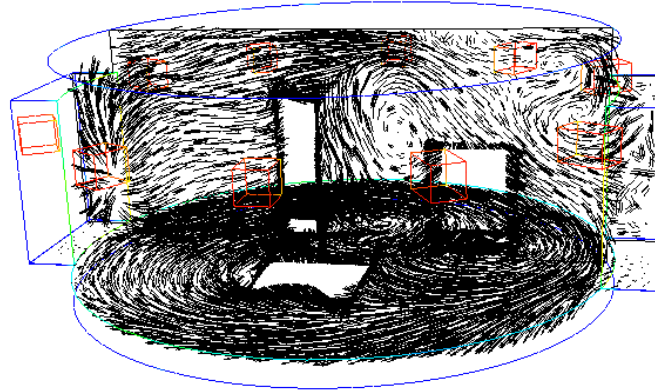


Figure 16. Velocity vectors in the midplane of the furnace.

As the interface between solid and fluid is only the zero level of the distance function, the calculations of the boundary integrals of systems (1)-(3) are no longer applicable on their interfaces. The state of art in the thermal coupling analysis (1)-(3) lies in that the heat transfer

;

Table II.

Location	Average temperature (K)	Average velocity (m/s)
Near wall	706	45
Near center	526	45

between the solid and the air at the interface has been treated naturally, *i.e.* without the use of a previous knowledge of any heat transfer coefficient. Moreover, we replace the classical boundary conditions (35) by solving the P-1 radiative model (14) in both domains which generates a volume source term for the energy equation.

Figure 15 shows the evolution of the isotherms and the streamlines at different time steps. When the hot fluid passes across the volume of the furnace, it induces a turbulent and recirculating motion within the geometry. This forced convection is caused by the interaction of the moving stream and the stationary fluid inside the furnace. The streamlines and the temperature distribution clearly indicate the expected flow pattern. The air movement around the workpieces is quite complex and the temporal evolution is chaotic. A number of small vortexes inside different buffer zones can be observed in figure 16. They are due to the turbulence dissipation and mixing between the hot and cold air. On the vertical plane cutting through the ingots, we see, as expected, the solid region satisfies the zero velocity and, hence, the no-slip condition on the extremely refined interface is also verified. The obstacles (3 ingots) slow down the air circulation in the central zone of the furnace and slightly influence the main air circulation along the walls. Table II provides the average temperature and average velocity values at two different locations: one at intermediate distance between the ingots and the walls and the other at the centre of the furnace between the ingots. Figure 17 shows the temperature

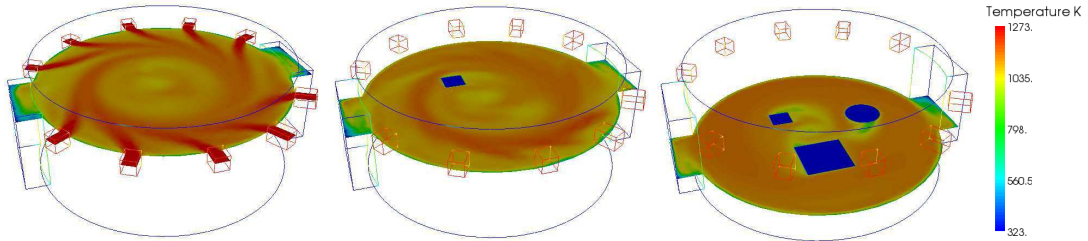


Figure 17. Temperature distribution on three parallel planes inside the furnace.

distribution on three mutually parallel planes in the furnace. The amount of energy required to increase the temperature of the three loads by a few hundred degrees is considerable both in real application and computational studies. The present results, as exposed in figure 17, describe the five first minutes of the heating process during which the immersed solids only gain few degrees above their initial temperature. Such a 3D computation has yet required 4 days on 32 cores. Hence, a great effort is still necessary to supply fast algorithms in order to calculate this kind of full heating sequences in reasonable reducing time.

These numerical results indicate that the IVM approach is suitable for the parallel

;

numerical simulation of industrial furnaces with different loads. The method is now applied in the consortium THOST, "Thermal optimization system", which groups many industrial partners. Such calculations allow to predict different parameters and to understand the flow characteristics for heat treatment furnaces. Future investigation will be concerned with experimental comparisons and time reducing models.

6. CONCLUSION

In this paper, we have presented a numerical investigation of natural and forced convection heat transfer, airflow in industrial furnace. The applications of the stabilized finite element formulations for incompressible turbulent flows with thermal coupling to 2D and 3D test problems with conducting bodies are highlighted. We have also described different aspects related to the numerical approximation of thermal coupling between a fluid and a solid. Our approach, referred as the IVM method, solve one set of equation in both domains with different materials properties. This has allowed us to propose alternatives to classical boundary conditions (mixed-convection and radiation) and heat transfer coefficients that insure the heat exchange between each subdomains. The numerical tests show that the proposed scheme can produce the accurate numerical solutions to unsteady laminar and turbulent flows. In some of the cases, we were able to compare our results to those reported in the literature. The favourable nature of the comparisons in those cases and the reasonable nature of the results in the other cases increased our confidence in and demonstrated a good potential for formulations developed.

ACKNOWLEDGMENT

The authors gratefully acknowledge support from the ADEME, CIM Team and the companies involved in the THOST project managed by Science Computer and Consultants (SCC). They are also sincerely grateful to Aubert & Duval for supplying the experimental data and the full support for this work.

REFERENCES

1. Ishii T, Zhang C, Sugiyama S. Numerical modeling of an industrial aluminium melting furnace. *Journal of Energy Resources Technology* 1998; **120**:276–284.
2. Nieckele AO, Naccache MF, Gomes MSP. Numerical modeling of an industrial aluminium melting furnace. *Journal of Energy Resources Technology* 2004; **126**:72–81.
3. Song G, Bjorge T, Holen J, Magnussen BF. Simulation of fluid flow and gaseous radiation heat transfer in a natural gas-fired furnace. *International Journal of Numerical Methods for Heat and Fluid Flow* 1997; **7**:169–182.
4. Hachem E, Kloczko T, Dignonnet H, Coupez T. Immersed volume technique for solving natural convection, conduction and radiation of a hat-shaped disk inside an enclosure. *Submitted to Journal of Computational Physics* -; -:-.
5. Houzeaux G, Codina R. An overlapping Dirichlet=Robin domain decomposition method. *Journal of Computational and Applied Mathematics* 2003; **158**(2):243–276.
6. Felippa CA. Partitioned analysis for coupled mechanical systems. *Engineering Computations* 1988; **5**:123–133.

;

7. Principe J, Codina R. A numerical approximation of the thermal coupling of fluids and solids. *International Journal for Numerical Methods in Fluids* 2009; **59**:1181–1201.
8. Fedkiw R, Aslam T, Merriman B, Osher S. A non-oscillatory eulerian approach to interfaces in multimaterial flows (the ghost fluid method). *Journal of Computational Physics* 1999; **152**:457.
9. Fadlun E, Verzicco R, Orlandi P, Mohd-Yusof J. Combined immersed boundary finite-difference methods for three-dimensional complex flow simulations. *Journal of Computational Physics* 2000; **161**:35–60.
10. Peskin CS. The immersed boundary method. *Acta Numerica* 2002; **11**:1–39.
11. Rixen D, Gosselet P. Domain decomposition methods applied to challenging engineering problems. *16th International Conference on Domain Decomposition Method*, New-York, 2005; 564–581.
12. Sukumar N, Moës N, Moran B, Belytschko T. Extended finite element method for three-dimensional crack modeling. *International Journal for Numerical Methods in Engineering* 2000; **48**(11):1549–1570.
13. Bruchon J, Dignonnet H, Coupez T. Using a signed distance function for the simulation of metal forming processes: Formulation of the contact condition and mesh adaptation. from a Lagrangian approach to an Eulerian approach. *International Journal for Numerical Methods in Engineering* 2008; **online**.
14. Valette R, Coupez T, David C, Vergnes B. A direct 3D numerical simulation code for extrusion and mixing processes. *International Polymer Processing XXIV* 2009; **2**:141–147.
15. Bernacki M, Chastel Y, Coupez T. Level set method for the numerical modelling of primary recrystallization in the polycrystalline materials. *Scripta Materialia* 2008; **58**(12):1129–1132.
16. Gruau C, Coupez T. 3D tetrahedral, unstructured and anisotropic mesh generation with adaptation to natural and multidomain metric. *Computer Methods in Applied Mechanics and Engineering* 2005; **194**:4951–4976.
17. Brooks A, Hughes T. Streamline upwind/Petrov-Galerkin formulations for convection dominated flows with particular emphasis on the incompressible Navier-Stokes equations. *Computer Methods in Applied Mechanics and Engineering* 1982; **32**:199–259.
18. Franca L, Frey S. Stabilized finite element methods: Ii. the incompressible Navier-Stokes equations. *Computer Methods in Applied Mechanics and Engineering* 1992; **99**:209–233.
19. Codina R. Stabilization of incompressibility and convection through orthogonal sub-scales in finite element methods. *Computer Methods in Applied Mechanics and Engineering* 2000; **190**(13-14):1579–1599.
20. Codina R. Stabilized finite element method for the transient Navier-Stokes equations based on a pressure gradient projection. *Computer Methods in Applied Mechanics and Engineering* 2000; **182**(3-4):277–300.
21. Brezzi F, Russo A. Choosing bubbles for advection-diffusion problems. *Mathematical Models and Methods in Applied Sciences* 1994; **4**:571–587.
22. Franca L, C F. Bubble functions prompt unusual stabilized finite element methods. *Computer Methods in Applied Mechanics and Engineering* 1995; **123**:229–308.
23. Codina R. Comparison of some finite element methods for solving the diffusion-convection-reaction equation. *Computer Methods in Applied Mechanics and Engineering* 1998; **156**:185–210.
24. Modest MF. *Radiative Heat Transfer*. McGraw-Hill: New-York, 1993.
25. Siegel R, Howell J. *Thermal Radiation Heat Transfer*. Taylor & Francis: New-York, 2002.
26. Jones WP, Launder BE. The prediction of laminarization with a two-equation model of turbulence. *International Journal of Heat and Mass Transfer* 1972; **15**(2):301–314.
27. Launder BE, Spalding DB. The numerical computation of turbulent flows. *Computer Methods in Applied Mechanics and Engineering* 1974; **3**(2):269–289.
28. Han Z, Reitz RD. A temperature wall function formulation for variable-density turbulent flows with application to engine convective heat transfer modeling. *International Journal of Heat and Mass Transfer* 1997; **40**(3):613–625.
29. Coupez T. Génération de maillage et adaptation de maillage par optimisation locale. *Revue européenne des éléments finis* 2000; **9**(4):403–423.
30. Patankar SV. *Numerical Heat Transfer and Fluid Flow*. Series in Computational and Physical Processes in Mechanics and Thermal Sciences, Taylor & Francis, 1980.
31. Brezzi F, Douglas J. Stabilized mixed methods for the Stokes problem. *Numerische Mathematik* 1988; **53**:225–236.
32. Brezzi F, Pitkranta J. On the stabilization of finite element approximations of the Stokes problem. *Efficient Solutions of Elliptic Systems, Notes on Numerical Fluid Mechanics* 1984; **10**:11–19.
33. Franca L, Hughes T. Two classes of mixed finite element methods. *Computer Methods in Applied Mechanics and Engineering* 1988; **69**:89–129.
34. Codina R, González-Ondina JM, Díaz-Hernández G, Principe J. Finite element approximation of the modified boussinesq equations using a stabilized formulation. *International Journal for Numerical Methods in Fluids* 2008; **57**:1305–1322.
35. Arnold D, Brezzi F, Fortin M. A stable finite element for the Stokes equations. *Calcolo* 1984; **23**(4):337–344.
36. Brezzi F, Bristeau M, Franca L, Mallet M, Rog G. A relationship between stabilized finite element methods

;

- and the Galerkin method with bubble functions. *Computer Methods in Applied Mechanics and Engineering* 1992; **96**:117–129.
37. Bank R, Welfert B. A comparison between the mini element and the Petrov-Galerkin formulations for the generalized Stokes problem. *Computer Methods in Applied Mechanics and Engineering* 1990; **83**:61–68.
 38. Coupez T, Marie S. From a direct to a parallel iterative solver in 3D forging simulation. *International Journal of Supercomputer Applications And High Performance Computing* 1997; **11**(4):277–285.
 39. Laure P, Beaume G, Basset O, Silva L, Coupez T. Les méthodes numériques pour les coulements de fluides chargés. *1er colloque du GDR interactions fluide-structure*, 2005.
 40. Dignonnet H, Coupez T. Object-oriented programming for fast and easy development of parallel applications in forming processes simulation. *Computational Fluid and Solid Mechanics 2003*, 2003; 1922–1924.
 41. Hachem E. Stabilized finite element method for heat transfer and turbulent flows inside industrial furnaces. PhD Thesis, Ecole Nationale Supérieure des Mines de Paris 2009.
 42. Badia S, Codina R. Analysis of a stabilized finite element approximation of the transient convection-diffusion equation using an ale framework. *Journal on Numerical Analysis* 2006; **44**:2159–2197.
 43. Hughes T, Franca L, Balestra M. A new finite element formulation for computational fluid dynamics: V. circumventing the Babuska-Brezzi condition: A stable Petrov-Galerkin formulation of the Stokes problem accommodating equal-order interpolations. *Computer Methods in Applied Mechanics and Engineering* 1987; **59**:85–99.
 44. Galeão A, do Carmo E. A consistent approximate upwind Petrov-Galerkin method for convection-dominated problems. *Computer Methods in Applied Mechanics and Engineering* 1988; **68**(1):83–95.
 45. Valette R, Bruchon J, Dignonnet H, Laure P, Leboeuf M, Silva L, Vergnes B, Coupez T. Méthodes d'interaction fluide-structure pour la simulation multi-échelles des procédés de mélange. *Mécanique et Industries* 2007; **8**(3):251–258.
 46. Codina R, Principe J. Dynamic subscales in the finite element approximation of thermally coupled incompressible flows. *International Journal for Numerical Methods in Fluids* 2007; **54**:707–730.
 47. Nicolás A, Bermúdez B. 2d thermal/isothermal incompressible viscous flows. *International Journal for Numerical Methods in Fluids* 2005; **48**:349–366.
 48. Bhave P, Narasimhan A, Rees DAS. Natural convection heat transfer enhancement using adiabatic block: optimal block size and Prandtl number effect. *International Journal of Heat and Mass Transfer* 2006; **49**:3807–3818.
 49. Mohamad AA, Viskanta R. Transient natural convection of low-Prandtl-number fluids in a differentially heated cavity. *International Journal for Numerical Methods in Fluids* 1991; **13**:61–81.
 50. Yuçel N, Özdem AH. Natural convection in partially divided square enclosures. *Heat and Mass Transfer* 2003; **40**:167–175.
 51. Wakitani S. Numerical study of three-dimensional oscillatory natural convection at low Prandtl number in rectangular enclosures. *Journal of Heat Transfer* 2001; **123**:77–83.
 52. Liaqat A, Baytas AC. Conjugate natural convection in a square enclosure containing volumetric sources. *International Journal of Heat and Mass Transfer* 2001; **44**:3273–3280.
 53. Kondaraju S, Kondaraju JS. Hybrid turbulence simulation of spray impingement cooling: The effect of vortex motion on turbulent heat flux. *International Journal for Numerical Methods in Fluids* 2009; **59**(6):657–676.
 54. Yongson O, Badruddin IA, Zainal ZA, Narayana PAA. Airflow analysis in an air conditioning room. *Building and Environment* 2007; **42**(3):1531–1537.
 55. Kim MY. A heat transfer model for the analysis of transient heating of the slab in a direct-fired walking beam type reheating furnace. *International Journal of Heat and Mass Transfer* 2007; **450**(1):3740–3748.
 56. Laguerre O, Ben Amara S, Moureh J, Flick D. Numerical simulation of air flow and heat transfer in domestic refrigerators. *Journal of Food Engineering* 2007; **81**(1):144–156.
 57. Kuzmin D, Mierka O, Turek S. On the implementation of the k-epsilon turbulence model in incompressible flow solvers based on a finite element discretization. *International Journal of Computing Science and Mathematics* 2007; **2/3/4**:193–206.

6.4 Numerical simulation in a full-scale industrial furnace

E. Hachem^{*}, H. Digonnet^{*}, E. Massoni^{*}, H. Lemerrier⁺ and T. Coupez^{*}

^{} Centre For Material Forming (CEMEF), École des Mines de Paris*

06904 Sophia-Antipolis, France

⁺ Terreal, Research and Development department, 15, rue Pagès, 92150 SURESNES

Abstract

In this paper, a heat treatment furnace was simulated by using Computational Fluid Dynamics to investigate thermal performance of the furnace and the heating process. The furnace is used to heat and treat terra-cotta products impellers to obtain the required microstructure and mechanical properties. CFD simulation provides a useful tool to predict the temperature evolution in the furnace and within the walls and the support grid. The model consists of turbulent flow, thermal radiation and conjugate heat transfer. A 3D stabilized finite element methods is used to solve the conjugate heat problem. An immersed volume method (IVM) is applied to treat the fluid/solid interactions. Temperature measurements were carried in different location and are compared to the experimental results.

Keywords: Finite elements, stabilization, heat conduction, static condensation

*** This section is a preprint and subject for a future publication**

Introduction

The prediction of the transient heat transfer inside the furnace and inside the steel charge is presented. This procedure couples a numerical solution of the turbulent fluid flow, thermal radiation and conjugate convection-conduction heat transfer inside the furnace including the charges, the surrounding air and the treated walls. The heating process of industrial furnaces represents a critical step to achieve the correct temperature and metallurgical properties of the treated workpieces. Many factors play an important role in the heat treatment process such as: minimisation of local temperature gradients, insuring a uniform temperature within the load, avoiding at maximum all surface defects such as skid marks, minimising energy usage and maximising furnace capacity.

The design of a computational fluid dynamics (CFD) tool is invaluable for the exploration of these physical phenomena, investigation of process sensitivities and optimisation procedures.

The study and development of stabilized finite element methods (chapter 1-4) able to handle such complex flow become more evident to obtain good predictions of the temperature solution at different locations inside the furnace and again, the immersed volume method (IVM) is applied to treat the fluid-solid interactions.

Application

Here in this study, we aim to present seven minutes of heating process for an industrial furnace given by our industrial partners. The furnace was modelled as a rectangular section duct, $1.5 \times 1.3 \times 1.1 \text{ m}^3$ forming one heat transfer zone. The hot gas is pumped into the furnace through two burners located on the vertical wall at 75 m/s each having a constant temperature of 1100°C .



Figure 1. 1 m^3 furnace (left) and the support grid (right)

Domain	Temperature $^\circ\text{C}$ at $t=0\text{s}$	Density kg/m^3	Heat capacity $\text{J/Kg}^\circ\text{C}$	Conductivity $\text{W/m}^\circ\text{C}$
Gas(air)	250°C	1.2	1000	0.02
Solid (s)	250°C	2300	960	20
Walls	250°C	90	950	0.2

Table I. Materials properties and initial temperature

Figure 1 illustrates the furnace geometry where a support grid is positioned on the bottom wall while in Figure 2, the location of the burners on both left and right sidewalls are presented. The materials properties used in this test, as well as the initial conditions and different parameters are presented in table I. The air is vented out the enclosure through the outlet positioned at the centre of top wall.



Figure 2. Left and right burners located on the vertical walls

By applying the IVM method, the levelset function first detects and defines the treated objects. The second step consists in deriving the anisotropic adapted mesh that describes very accurately the interface between the workpieces, the walls and the surrounding air. Recall that the mesh algorithm allows the creation of extremely stretched elements along the interface, which is an important requirement for multimaterial problem with surface conductive layers. The additional nodes are added only at the interface region keeping the computational cost low. Note that although the support is made by six different cylindrical objects and one flat grid, however, as shown in figure 3, the shape of these treated objects is well captured and respected by applying the proposed anisotropic mesh adaptation.

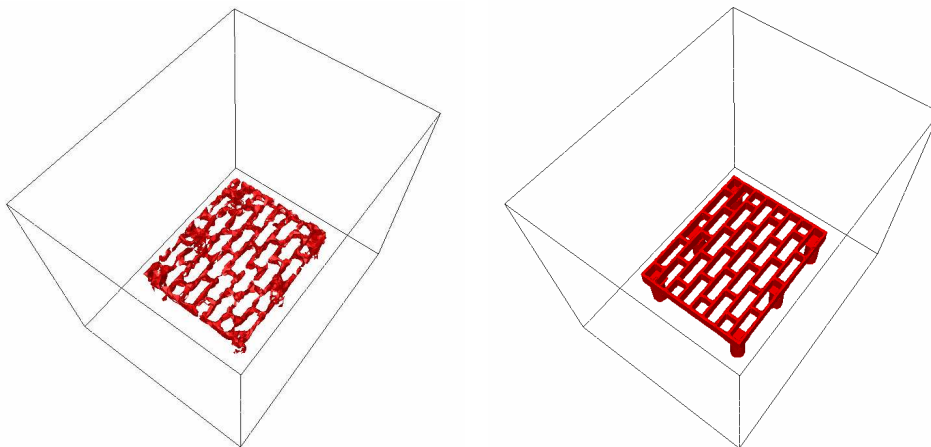


Figure 3. Difference between the initial mesh (left) and the final mesh (right)

The algorithm progressively detects and refines the support grid and the walls leading to a well respected shape in terms of curvature, angles, etc. All the small details in this given geometry can be captured accurately (see figure 4). Note that the the final mesh used for the numerical simulation consists of 155015 nodes and 896539 linear tetrahedral elements.

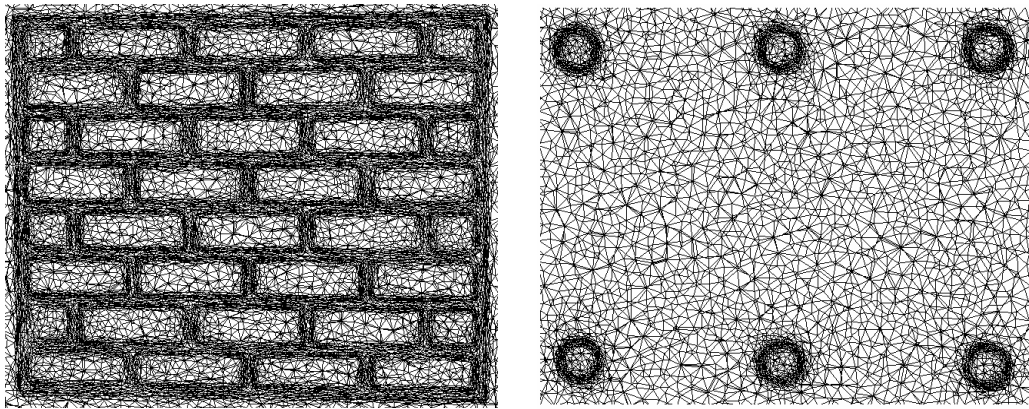


Figure 4. Two verticals cuts in the volume at different heights of the support grid

Once the mesh is well adapted along the interfaces between the walls, the support grid and the volume of the furnace, the material distribution between each physical domain can be described by means of the level set function. Consequently, the same set of equations; momentum equations, energy equation, the turbulent kinetic and dissipation energy equations, is simultaneously solved over the entire domain including both fluid and solid regions with variable material properties.

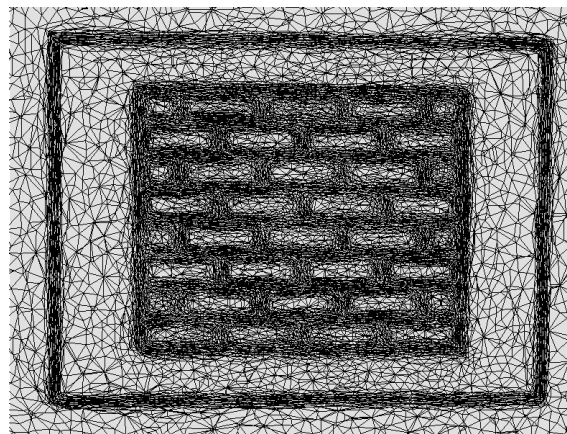


Figure 5. Detailed view of the anisotropic mesh adaptation along the treated walls

Recall that the interface between the solid and the fluid is rendered by the zero isovalue of the distance function; hence the calculations of the classical boundary conditions to ensure the heat exchange between the subdomains (air-solid and air-walls) are no longer applicable on their interfaces (figure 6 and 7). The state of art in the proposed thermal coupling analysis lies in that the heat transfer at any interfaces has been treated “naturally”, i.e. without the use or a previous knowledge of any heat transfer coefficient.

Usually, the heat transfer coefficient between two subdomains can be obtained through experimental tests or empirical rules, but in the presence of complex geometries and flows, different configurations of the furnace (changing the speed of gas, changing the initial temperature, changing in the burner’s temperature...) such operations can become rapidly very costly and time consuming.

Summing up, for any different geometry, even if we consider a new studied solid, it is shown that the proposed method only requires to define the composite material properties to ensure the corresponding heat transfer.

The discretization in space for the incompressible Navier-Stokes equations, the heat transfer equation and the turbulence equations is performed by an unstructured grid stabilized finite element method. Thus, the numerical oscillations and thermal shocks are well captured and smooth solutions are obtained.

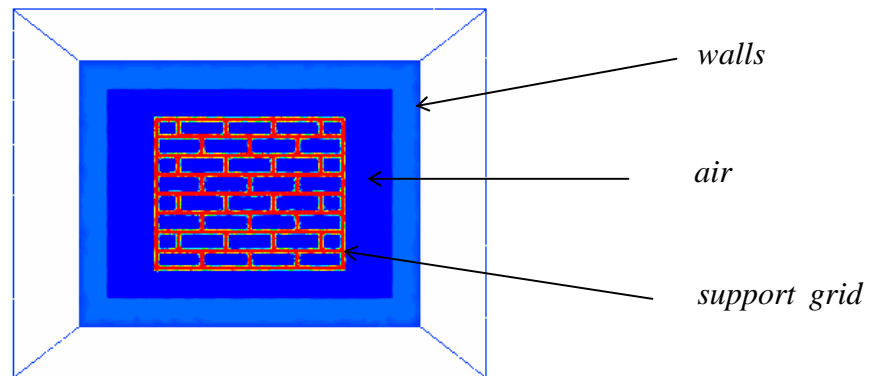


Figure 6. A top view of the density distribution along the walls, the atmosphere and the support grid

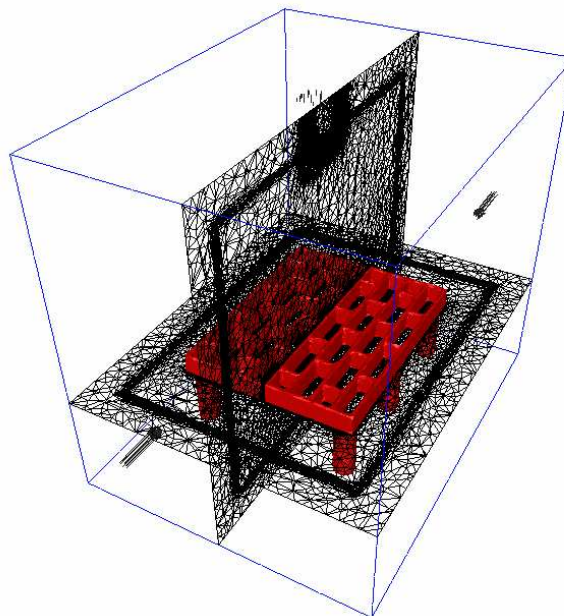


Figure 7. Two cuts in the final mesh at different positions. Locations of the burners, the outlet and the support grid

Note that at fluid-solid interfaces, conductivities are calculated using a harmonic mean formulation in order to handle abrupt changes in the material properties. Thus, we automatically well establish the continuity of temperature and heat flux across the interfaces. Moreover, setting the relative kinematics viscosity very high value in the solid regions, the walls and the support, satisfies the zero velocity in these regions and hence the no-slip condition on the interface is also satisfied. Therefore, the convective terms in the energy equation drop out and the equation reduces to the transient conduction equations in the solid.

The aim of this numerical test is not to study the effect of the heating process for any optimisation or manufacturing processes, in terms of speed of gas, initial and inlet temperature or other factors; it is more to analyse the general behaviour of the solution in the presence of the extended domains.

Both radiation effects of the gas and the walls are considered in the computations. The emissivity is assumed to be equal 0.05 for the gas and 0.45 for the walls. We assume that the fluid properties depend on the temperature, in particularly the density of the gas in the buoyancy term, which allows Boussinesq approximation. The gravitational acceleration is taken parallel to the solid walls. Calculations were carried out using a time step equal to 0.001s to capture the physics accurately. The Reynolds number is assumed to be equal to 10^6 . All the given parameters used for the numerical simulations do not reflect the true measurements from the experimental tests, due to the complexity of the materials, the gas composition and other technical issues. However, we made sure that the chosen parameters have at least the real physical representations and are appropriate to simulate the real test. The 3D computations have been obtained using 32 2.4 Ghz Opteron cores in parallel (linked by an Infiniband network)

The main objective of the THOST project is to describe numerically the airflow and temperature field inside an industrial furnace where high convective heat sources are used. The thermal wall jet created by this kind of source can greatly influence the temperature distribution inside the enclosure. Therefore, advance turbulence model are needed to produce better results in particularly in the vicinity of the walls. This can be one among different reasons to extend the standard $k-\epsilon$ model by the low Reynolds number $k-\epsilon$ model under a suitable mesh scheme. We will also justify this choice later in chapter 6.

We start a presentation of the standard $k-\epsilon$ model which is mainly valid in the turbulent region (far-wall zone). The near-wall effects are simulated through wall functions which give boundary conditions for points situated in the turbulent zone. However, this procedure is not well adapted for complex flows, since the condition that the boundary must be in the turbulent zone cannot generally be respected rigorously. In our study, it was noticed that the use of an extended version of the $k-\epsilon$ model (low-Reynolds-number model) in combination with a wall function defined over the entire wall region is a much better choice. The appropriate choice of wall function in the near-wall zones is discussed in detail. A brief description of the solution strategy using a Newton-type method to solve for turbulence energy k and rate-of-dissipation energy ϵ is given in the same section. Finally we validate the model by simulating the turbulent flow between two plates and the backward facing step. Simulating results for a variety of flow are presented and discussed.

If a non-slip boundary condition is used in turbulent flows, a large number of fine grids close to wall are needed, which is not practical at present due to computer limitations and long time heat treatment simulation. Moreover, near solid walls, the turbulence kinetic energy production is gradually reduced due to dominance of viscous effects. In this region, the large eddies dissipate their energy directly rather than transferring it to smaller scales as per the energy cascade. Therefore, although the strain rate can be expected to peak in the near-wall region due to steep velocity gradients, there will be a reduction in sub-grid scale stress. This effect is accounted for by damping the turbulent viscosity, ν_t , as the wall is approached. The usual way to damp this additional viscosity in the vicinity of the wall and to capture the near-wall effects without drastically increasing the number of unknowns is the use of wall models.

Results and discussions

For illustration purposes, we present in figure 8 the evolution of the isotherms at two different locations and at a certain time step ($t=70s$) inside the furnace.

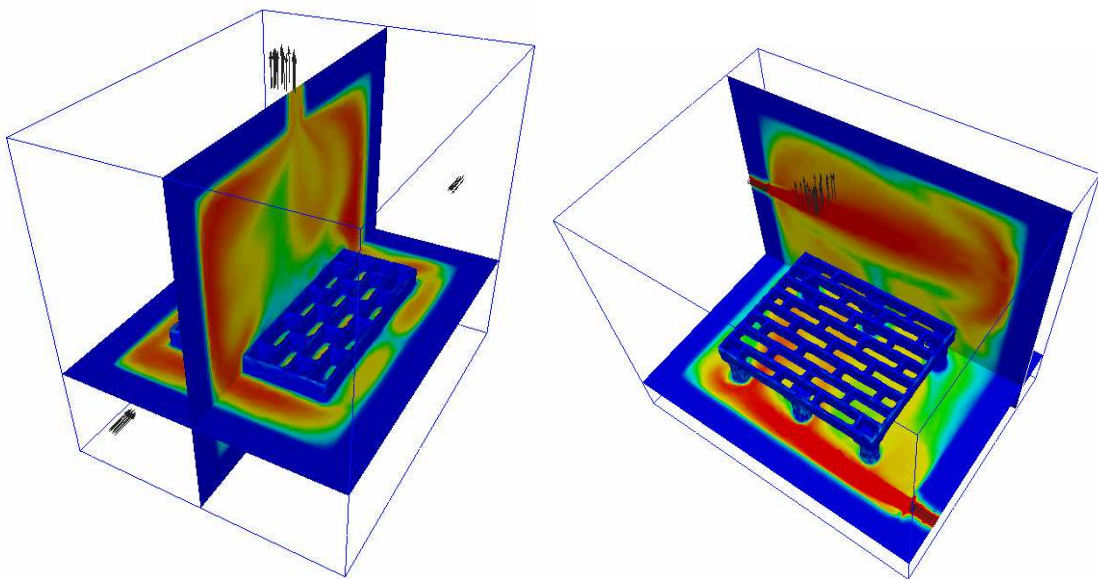


Figure 8. Temperature distribution in the furnace atmosphere and within the support.

The temperature distribution clearly indicates the expected flow pattern. At the solid's level, we observe that the injected air from the bottom burner is slowed down and slightly influence the main air circulation in the lower part of the domain. This explains the difference in the flow pattern between the two burners. When the hot fluid passes across the volume of the furnace, it induces a turbulent and recalculating motion within the geometry. This forced convection is caused by the interaction of the moving stream and the stationary fluid inside the furnace.

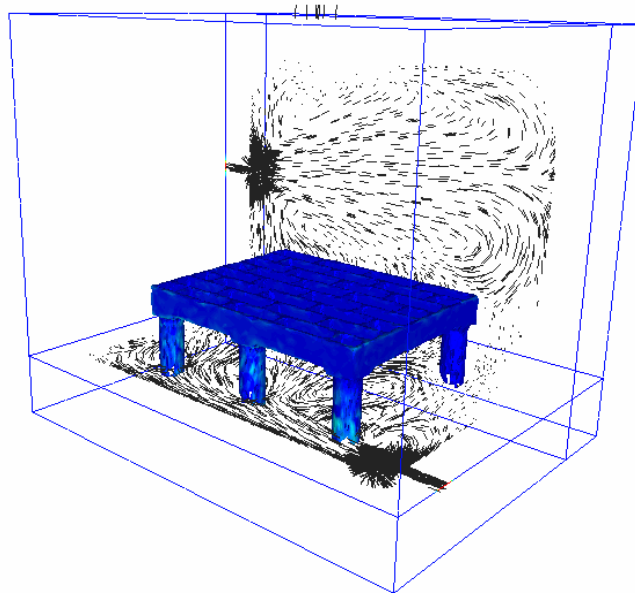


Figure 9. Velocity distribution in the furnace atmosphere and around the support.

The air movement around the workpieces is interesting; i.e. it allows studying the influence of different arrangements and positions to optimize the heat treatment. A number of vortices between the objects and the surroundings can be observed due to the turbulence dissipation and mixing between the hot and cold air (see figure 9).

In order to reveal in details the unsteady complex structures and the flow pattern, we investigate in figure 10, 11 and 12 the vectors along the x-z, x-y and y-z planes respectively at four different positions after 200 time units. In each plane, the cross section is positioned near the first burner, then it moves towards the centre of the furnace passing through the support grid and the outlet and finally it ends up near the second burner. The two opposing burners are positioned far from the centre so that the flames jets do not meet. It is shown that once the flames hit the walls and deviate towards the centre it forms a slight counter clockwise rotating flow. Near the centre of the furnace and between the two pair of flames, a full rotating gas flow is formed, which is ended near the impeller top-surface and exits through the outlet.

One can also observe as shown in Fig.11 (x-y plane) that the centre of a primary vortex moves toward the centre in the upper part of the furnace and secondary vortices appear clearly in different corners. This phenomenon is similar to that shown in the three-dimensional lid-driven cubic cavity.

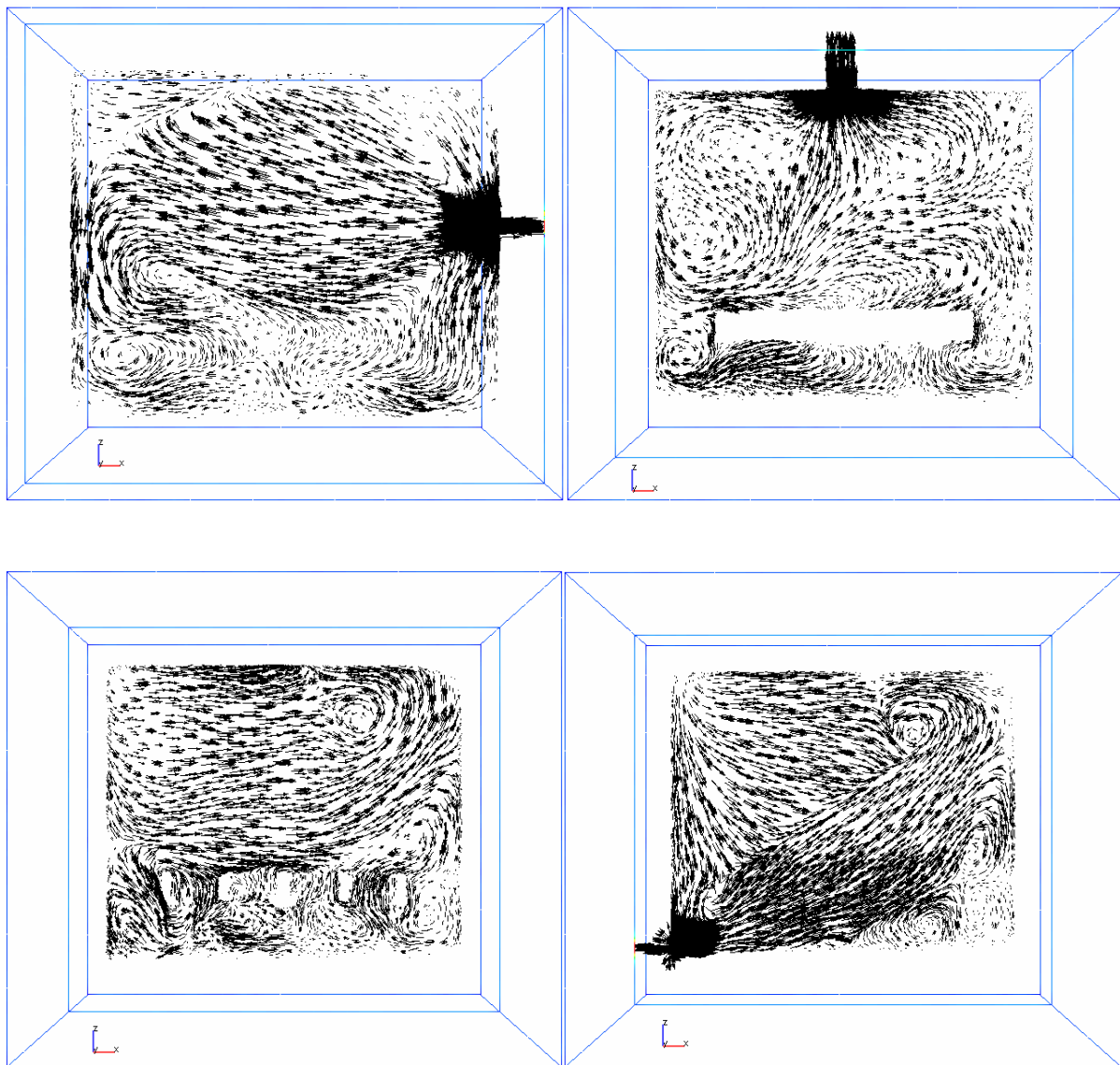


Figure 10. Velocity distribution in the furnace and around the support. (x - z plane)

On all vertical planes cutting through the support grid and the surrounding walls in figures 10-12, we see as expected, the solid region satisfies the zero velocity and, hence, the no-slip condition on the extremely refined interface is also verified. For instance, the support grid slows down the air circulation in the lower part of the furnace and slightly influences the main recirculation along the walls. This explains why the upper part of the furnace is more heated than the lower part. The air movement around the workpieces is quite complex and the temporal evolution is chaotic. An important number of small vortices inside different buffer zones can be observed. They are due to the turbulence dissipation and mixing between the hot and cold air.

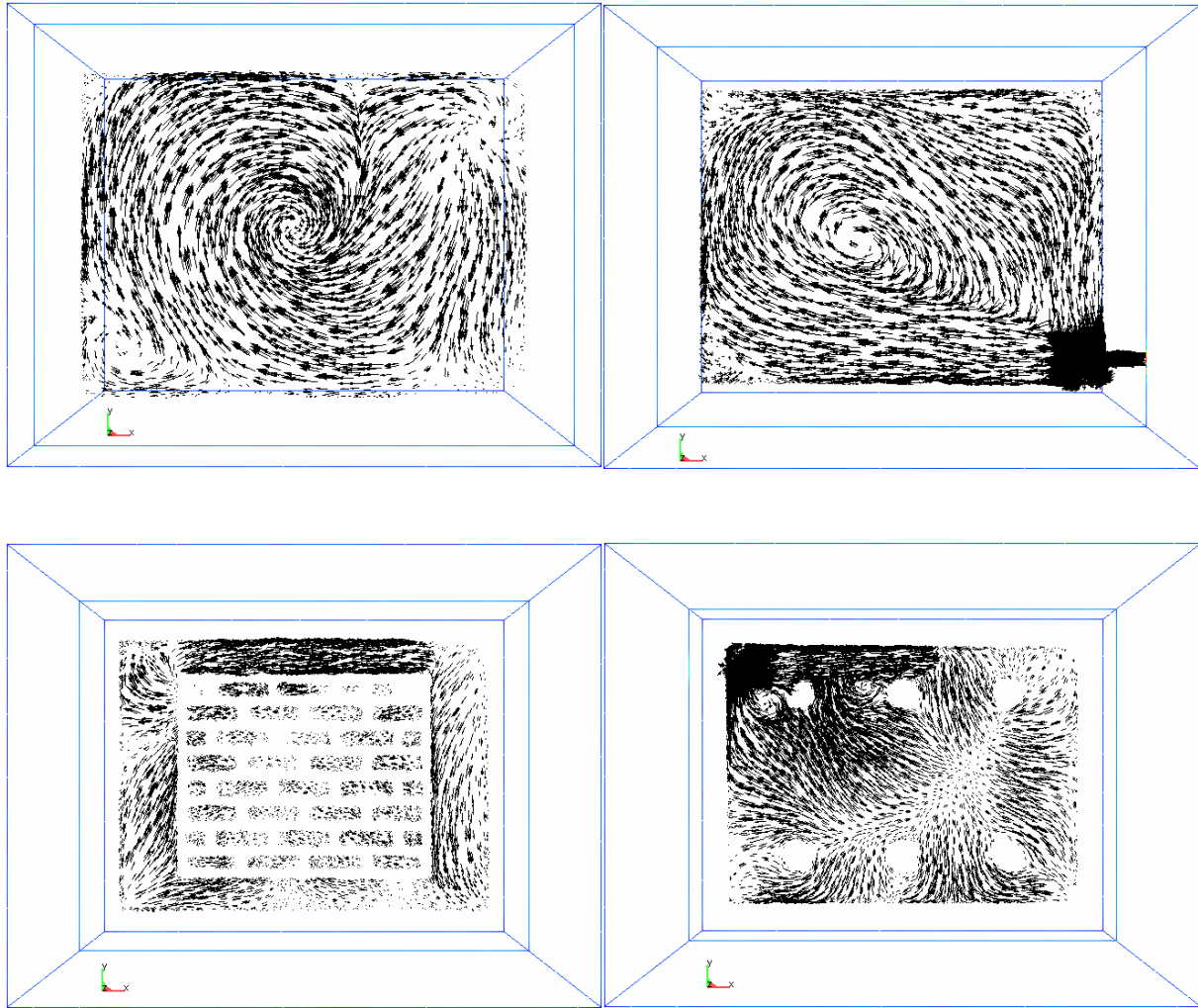


Figure 11. Velocity distribution in the furnace and around the support. (x - y plane)

It is also worth mentioning that the profiles of the temperature do not suffer from spurious oscillations (high undershoots or overshoots) which are frequently observed in the presence of high temperature gradients at the interface or in convection dominated problems across the enclosure. This can be attributed to the stabilization finite element discretization applied on the system of equations. However, there is still some regions where the solution (temperature, turbulent kinetic energy or the dissipation rate energy) exhibits some overshoots or undershoots. But they are very localized and will not affect the overall solution and do not lead to global instability. It could be avoided by refining and adapting the grid in these regions using for example a posteriori error estimator coupled to an anisotropic mesh adaptation strategy. A point that needs also further investigations.

Recall that the contribution of the radiations to the heat transfers is assessed by solving the radiative transfer equation (RTE) (discussed in the previous chapter) over the whole domain and by computing volumetric terms that acts as an energy source terms via divergence of radiative heat flux. These source terms, rendered by the discontinuity of both the temperature and the emissivity across the interfaces, replace the classical boundary conditions that usually are applied at the interface between two subdomains.

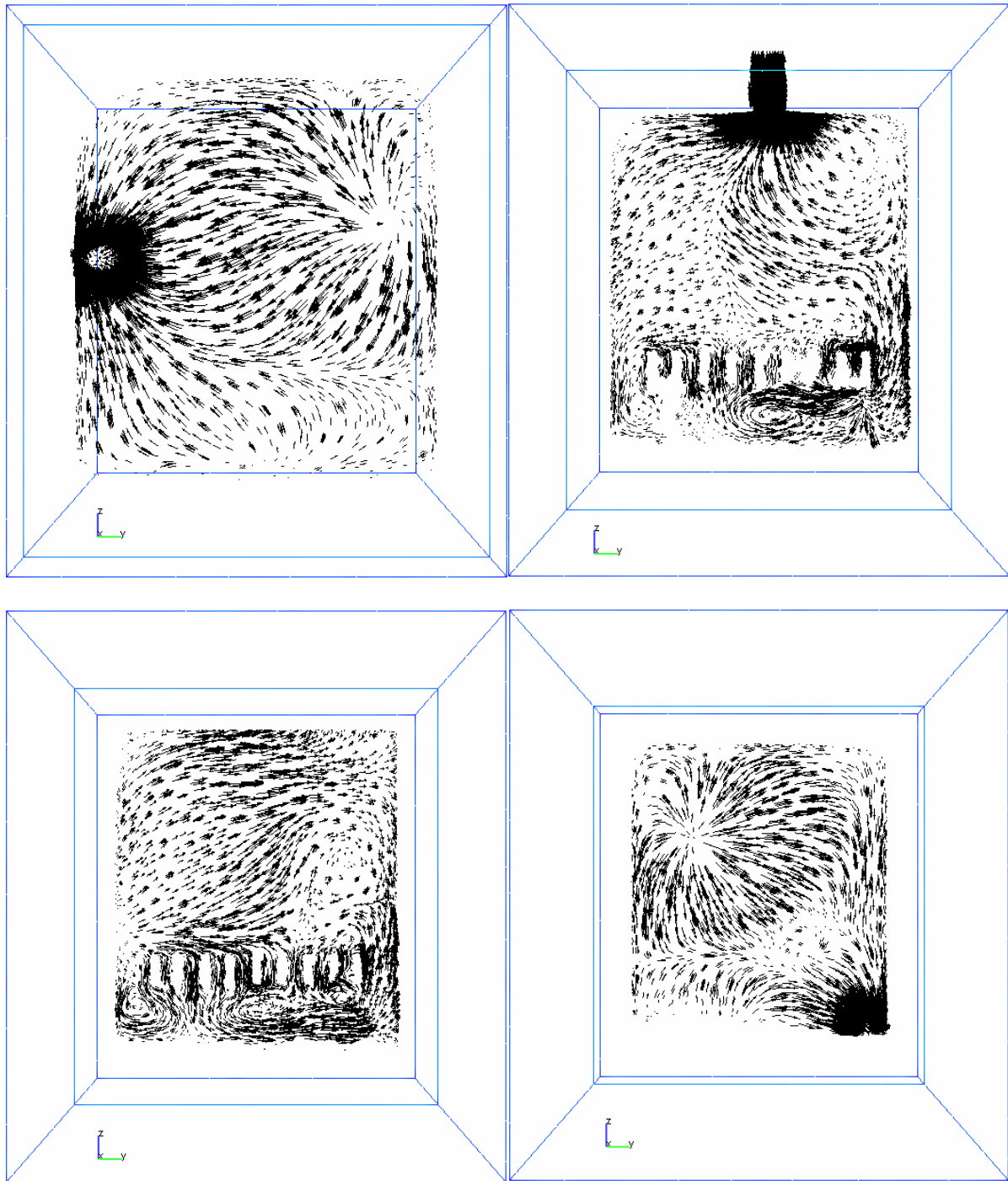


Figure 12. Velocity distribution in the furnace and around the support. (y-z plane)

To get better information on the temperature evolution around the immersed objects, we present in figure 13 the temperature distribution on six different planes in the furnace at a certain time step. The amount of energy required to increase the temperature of the loads by a few hundred degrees is considerable both in real application and computational studies. The immersed solids gain only few degrees above their initial temperature. Such a 3D computation has yet required 5 days on 32 cores. Hence, a great effort is still necessary to supply fast algorithms in order to calculate this kind of full heating sequences in reasonable reducing time.

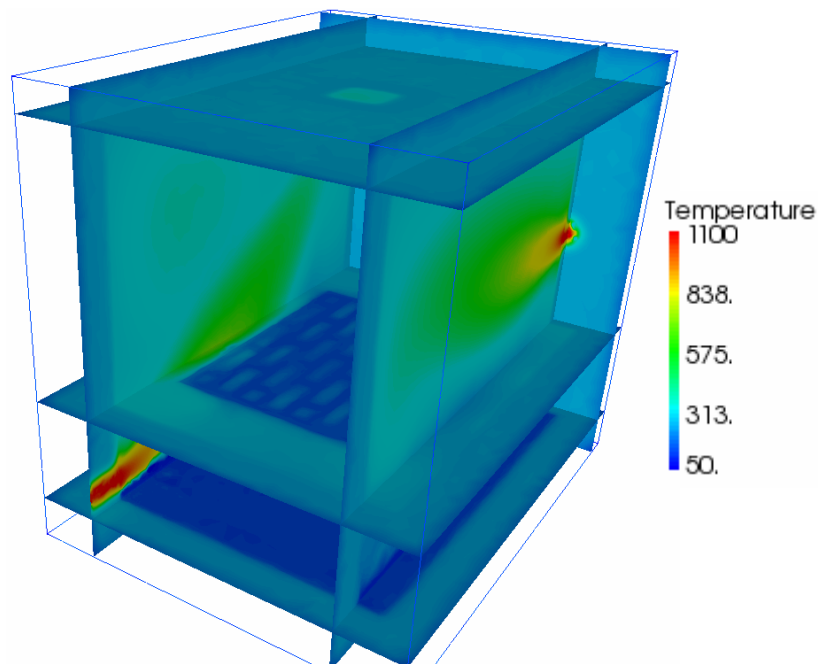


Figure 13. Temperature distribution in the furnace and around the support at a given time step.

Figure 14 and 15 shows the evolution of the isotherms and the streamlines at different time steps ($t= 1.25s, 9.61s, 27.08s, 58.77s, 116.57s$ and $222s$). When the hot air passes across the volume of the furnace through the burners, it induces a turbulent and recirculating motion within the geometry. This forced convection is caused by the interaction of the moving stream and the fluid at rest inside the furnace. The streamlines and the temperature distribution clearly indicate the expected flow pattern. Again, as shown due to high viscosity of the solid walls and the support, the no-slip boundary condition is verified and only transient conduction is solved in those regions.

These numerical results indicate that the IVM approach is suitable for the parallel numerical simulation of industrial furnaces with different loads. The method is now applied and used in the consortium THOST, "Thermal optimization system", which groups many industrial partners. Such calculations allow to predict different parameters and to understand the flow characteristics for heat treatment furnaces. Future investigation will be concerned with experimental comparisons and time reducing models.

Finally, the time history of the temperature captured at the centres of the sidewalls is shown in figure 16 and compared to the experimental results given by our industrial partners. According to the analysis made by our industrial partners, it is shown that during the first 150s the average temperature inside the volume and on the walls is approximately the same. At this stage, the temperature of 250°C was recorded and used as initial temperature for the numerical computations.

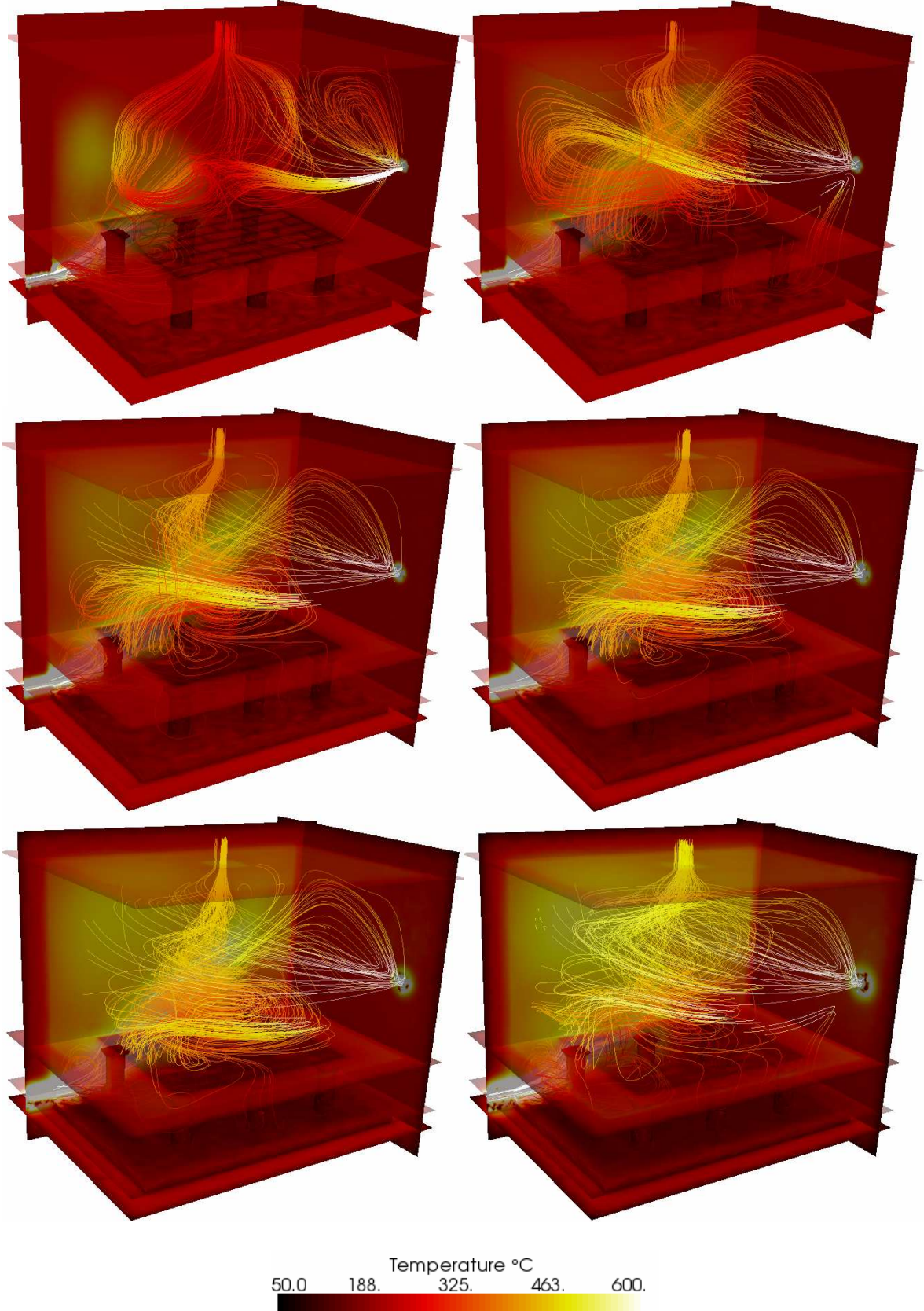


Figure 14. The evolution of isotherms and streamlines at different time step (side view)

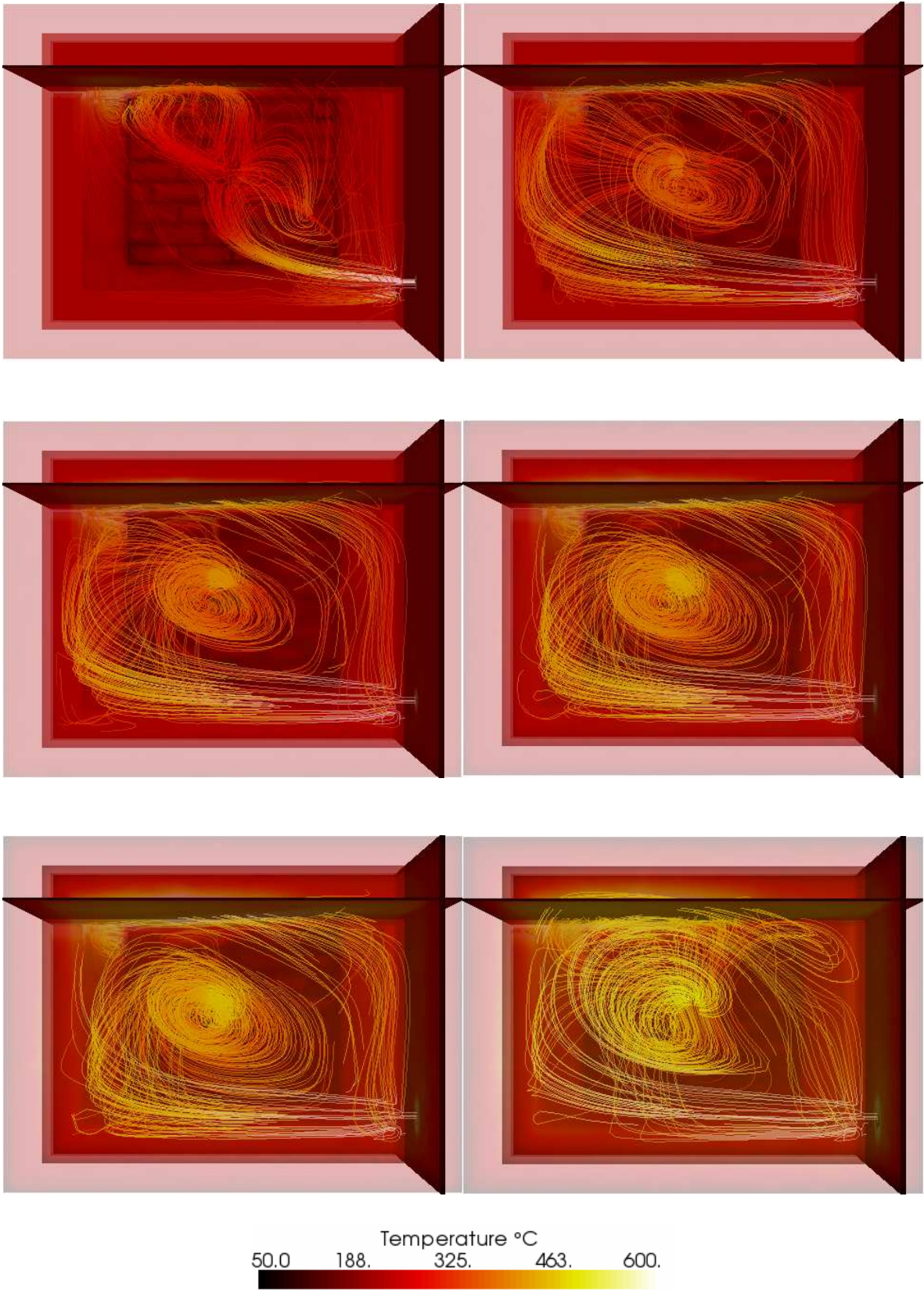


Figure 15. The evolution of isotherms and streamlines at different time step (top view)

The walls were instrumented with many thermal sensors at different locations. Data were acquired via a computer controlled data acquisition system, tabulated and then reported by our industrial partner. All the experimental results on the walls (resp. inside the volume) were approximately the same. Therefore, only their average temperature was plotted. The average temperature on the walls was referred as the 'Zone 1' while the average temperature in the centre was referred as 'Zone 2'.

A comparison of experimentally measured temperature results with the numerical simulation results at these locations is shown in figure 16. As can be seen, the agreement is generally good for all stations. However, the difference respect to the experimental results may be due to different factors. We will state here only the important one. First, the use of the correct physical properties as well as the appropriate initial conditions can play an important role on the final results. From the numerical point of view, we can say that the use of a fine enough grid could be more appropriate to simulate accurately such complex fluid phenomena. Moreover, such discrepancies in the results clearly indicate that a more sophisticated radiative transfer model may be needed to improve the solution and account for a better directional influence. This issue will be the subject of further investigations.

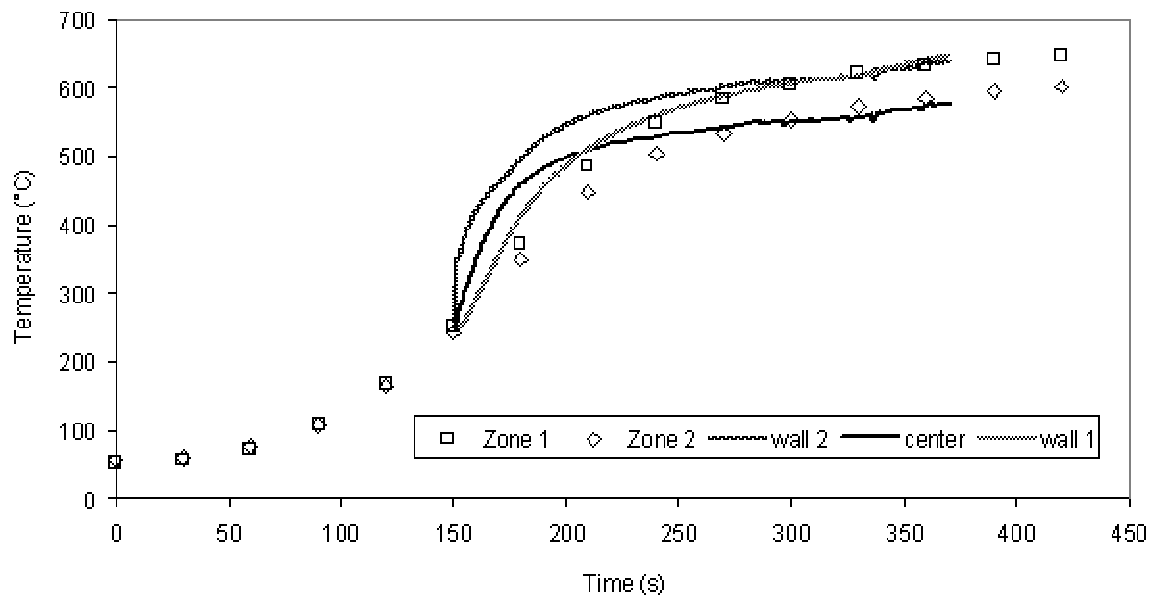


Figure 16. Temperature-time profile at different locations in the furnace

Conclusion

This paper presents the CFD simulation of the heating process of a loaded industrial furnace. The simulation presented in this work has provided a useful tool to predict the temperature evolution at the same time in the furnace and within the walls and the support grid. The 3D stabilized finite element methods developed in this work was used to solve the turbulent flows, the conjugate heat transfer and the thermal radiation problem. The fluid-solid interactions were treated using the immersed volume method (IVM). Temperature measurement data on the walls and inside the volume was the used to validate the present CFD model. The heating profile was reasonably predicted by the simulation. As a first implementation, the agreement between the present and the experimental results can be considered satisfactory. The proposed approach seems promising to simulate turbulent flow and heat transfer inside industrial furnaces in the presence of different heated workpieces.

Chapitre 7

Conclusions and Perspectives

The objective of this thesis is the development of an efficient method which is able to simulate complex flow problems inside industrial furnaces including fluid-solid interaction phenomena. Such simulation involves turbulent flows, conjugate heat transfer (convection and conduction) and thermal radiation all in a multi-component formulations. The tools used in this thesis are the Finite Element Method (FEM) and Computational Fluid Dynamics (CFD). This method is shown as an attractive way to solve the turbulent flow and heat transfer in the furnace chamber and it can be applied for a variety of furnace geometry and boundary conditions.

Therefore, the first part of the thesis consisted in developing different numerical methods for modeling the heat transfer and turbulent flows. Standard finite element method normally exhibits global spurious oscillations in convection-dominated problems, especially in the vicinity of sharp gradients. More advanced methods in the stabilization context were proposed in chapter 2 and 3.

In chapter 2, the need for the stabilization methods in the case of time-dependent convection diffusion reaction problems has been revisited. The Streamline Upwind Petrov-Galerkin (SUPG) and the Shock Capturing Petrov-Galerkin (SCPG) methods were introduced and implemented. In the case of transient diffusion problems, a space-time stabilized finite element method referred as 'Enriched-Method with time interpolation' has been presented and analysed to treat thermal shock in numerical heat transfer. The most important part of this chapter is the application of these stabilized formulations to the heat transfer equation needed later for simulation of heat treatment inside industrial furnaces.

A method able to handle flows at high Reynolds number in three-dimensional computations was discussed in chapter 3. We have described in this chapter a stabilized finite element method for the transient incompressible Navier-Stokes equations based on the variational multiscale (VMS) principle, e.g. the decomposition of the unknowns into large scale and fine scale. The motivation of using these advanced methods comes from the desire of extending the existed solver in order to deal with highly convection-dominated flows which occurs mainly in the furnace chamber. The bottom line of the proposed approach was to keep the previous implementation of the stable velocity-pressure formulation and to extend it by taking into account the small-scale pressure and the convection terms in the fine scale equations. Results for the unsteady Navier-Stokes equations obtained via the new modified scheme have been compared with the reference and analyzed. The numerical experiments show that the method is stable. The performance and the efficiency of the overall new scheme have been demonstrated using five benchmarks.

In chapter 4, the background of turbulence models is worked out in order to justify the choice of the particular method that must be used to simulate a real industrial furnace. Two classical turbulence models were introduced, analyzed and studied: the k -epsilon model and the Large Eddy Simulation (LES) model. The motivation of using such models comes from the desire of solving highly turbulent flow problems, e.g. the air velocity coming out from the burners into the furnace chamber could reach 75 m/s. Again, the stabilized finite element methods proposed in chapter 2 and 3 was used and applied for the resolution of the set of turbulent equations. Most importantly, we concluded from the numerical experiments that a chosen turbulence model should introduce the minimum amount of complexity while capturing the essence of the relevant physics. Consequently, the k - ϵ model, a traditional model attempts to strike the balance in this regard by sacrificing the details of the turbulence structures, was adopted. An improved version of this model appropriate for multi-components simulation was also introduced and adopted in this work. However, the question of which suitable model must be used to simulate accurately turbulent flows in the furnace chamber requires certain attention. Our main objective remained on understanding and implementing these models to open the choice to the user to decide which methods one must use regarding the application in hand. We explicated briefly that each method offers the accuracy of the results in respect to the computational costs and the required computing time. Finally, the performance and the efficiency of the overall models have been demonstrated using four benchmark and comparisons with both experimental and numerical results from several authors were presented.

As mentioned in chapter 5, thermal radiation exchange plays an important role on the overall efficiency, the quality of the heated ingots and the production rates since it is the dominant mode of heat transfer in most furnaces. Therefore, the second section of this chapter was dedicated to search and review different models for solving the radiative heat transfer. The main objective was to find the best fitted model with a certain capability to take into account fluid-solid interactions phenomena (gas-walls-heated ingots). Two thermal radiation models were chosen and discussed, implemented and adapted to our multi-components problem.

A multidomain approach to solve the conjugate heat transfer for which the three modes, convective, conductive and radiative heat transfer interfere simultaneously and in both the fluid part and the solid part was introduced in chapter 5. This element represents the most important ingredient of this work. In the first section of chapter 5, we showed that the proposed numerical technique for modeling such multimaterial flows (fluid/solid), referred as the immersed volume method (IVM), allows a simple and accurate resolution, in particularly at the interface between the fluid and solid. Full description, details and examples about this method are discussed in this chapter. One important feature of the proposed approach is that all the three-dimensional stabilized finite-element (SFEM) methods developed in the first part of the thesis, which are needed for solving the transient heat transfer and turbulent flows inside the furnaces, are completely suited with this approach without additional efforts.

The immersed volume method is based on the use of an adaptive anisotropic local grid refinement by means of the levelset function to well capture the sharp discontinuities of the fluid-solid interface, e.g. physical properties. We have used a mesh generation algorithm that allows the creation of meshes with extremely anisotropic elements stretched along the interface. This turned out to be an important requirement for conjugate heat transfer and multi-component devices with surface conductive layers. The strategy was to only add nodes locally at the interface, whereas the rest of domain keeps the same background size. Note also, when using an anisotropic mesh, with elements stretched in a 'right' direction, one could allow not only to save a lot of elements but also to well describe the geometry in terms of curvature, angles, etc. Contrary to others techniques, this promising method can provide an alternative to body fitted mesh for very complex geometry.

To resume, the main idea in chapter 5 was to retain the use of the monolithic formulation and coupling it to such additional features (IVM). This allows a better and accurate resolution, in particularly at the interface between the fluid and solid. From the other hands, the computation of the heat transfer coefficient, which usually is used as a boundary conditions to insure the heat exchange between two subdomains, can be a difficult task since it needs experimental data and often requires solving inverse problems. This is a limiting issue for practical applications when one needs to change the geometry of the object, the physical parameters, the number and the position of the objects, the surrounding fluid (air, water, etc...).

However, we have chosen in this work to consider a single grid for both air and solid for which only one set of equations need to be solved. Consequently, different subdomains are treated as a single fluid with variable material properties. The important aspect of the chosen strategy is that by solving the whole domain in a fully monolithic way there is no need of empirical data so as to determine the heat transfer coefficient between the treated solid and the surrounding fluid. The heat exchange at the interface is replaced naturally by solving the convective fluid in the whole domain. Numerically, the communication between the solid and the fluid was obtained directly without any further assumption and force modelling. In other words, there is no need for some coupling engines specifically designed to handle data exchange and algorithmic control signals between solid region and fluid region. In the last section of chapter 5, the IVM approach was tested on two numerical examples showing a promising tool for simulating thermal coupling of solids and fluids.

Various benchmarks and more complex numerical examples are given in chapter 6. The numerical results of forced turbulent convection inside industrial furnace are also included.

The simulation of the heating process of a loaded 3D industrial furnace is presented in the last section. The prediction of the temperature profiles at the same time in the furnace and within the walls and the support grid are presented. The fluid-solid interactions were treated using the immersed volume method (IVM). Temperature measurement data on the walls and inside the volume was the used to validate the present CFD model.

The focus in this work is on a new concept for numerical methods to estimate the temperature distributions at the same time in the furnace and within the workpieces under specified furnace geometry, thermal schedule, parts loading design, initial operation conditions, and performance requirements.

However, the practically relevant test cases to achieve higher treatment efficiency are not in the scope of this work. Therefore, in future works with the proposed IVM method and the implemented finite element solvers, it is important to prove the usefulness of the proposed concept with a number of further real industrial cases. Possible applications, where the features of the coupled solver are desirable, are for example simulations of quenching and cooling process (ThosT II).

Since simulation of the heat treatment sequence of workpieces in heat treatment furnaces followed by a controlled cooling process is of great importance for the prediction and control of the ultimate microstructure of the workpieces but specially the reduction of both energy consumption and pollutant emissions, then the construction of a model to simulation and to study the effect of quenching on the microstructure and mechanical property coupled to a multi-phase transformation model are possible extensions of the current work.

Clearly, a number of other considerations have to be taken into account for more accurate predictions of temperature profiles in the furnace chamber. Here is the list of several important steps towards enhanced simulation tools for more realistic problems:

The development of a more sophisticated radiative transfer model to improve solution and account for a better directional influence (the M1 model).

A better determination of temperature wall functions for high Rayleigh number in multidomain problems.

The development of fast algorithms in order to simulate full heating sequences in reasonable reducing time (e.g. POD, adaptive time-step, ...)

Anisotropic mesh adaptation for finite element method using a posteriori error estimates